On the electromagnetic field of a proton beam as a basis for range verification in particle therapy

An analytical and simulation-supported analysis

Martin Rädler

München 2022

On the electromagnetic field of a proton beam as a basis for range verification in particle therapy

An analytical and simulation-supported analysis

Über das elektomagnetische Feld eines Protonenstrahls als Basis für die Reichweitenüberprüfung in der Partikeltherapie

Eine analytische und simulationsgestützte Analyse

Dissertation
der Fakultät für Physik
der Ludwig-Maximilians-Universität
München

vorgelegt von
Martin Rädler
aus Buchloe

München, den 10. Oktober 2022

Erstgutachter: Prof. Dr. Marco Riboldi
Zweitgutachter: Prof. Dr. Joao Seco
Tag der mündlichen Prüfung: 21. November 2022

ZUSAMMENFASSUNG

Die Bestrahlung von Tumorzellen mit ionisierenden Strahlen mit dem Ziel sie unschädlich zu machen gehört zu den Hauptpfeilern der Krebsbehandlung. Zu diesem Zweck werden externe Strahlen bestehend aus schweren geladenen Teilchen wie Protonen eingesetzt, die aufgrund ihres vorteilhaften Tiefendosisprofils, des so genannten Bragg-Peaks, eine sehr konforme Dosisabgabe ermöglichen. Dies gestattet eine effektive Schonung von gesundem Gewebe und gefährdeten Organen, insbesondere im Vergleich zum konventionellen Ansatz mit Röntgenstrahlen. Die endliche Eindringtiefe der Protonen in den Patienten, die so genannte Reichweite, ist jedoch mit Unsicherheiten behaftet, die zu einer erheblichen Unterdosierung im Tumor und einer übermäßigen Dosis in lebensnotwendigen Organen führen können. Ungenauigkeiten können von der Bildgebung, anatomischen Veränderungen, der Positionierung des Patienten, um nur einige zu nennen, herrühren. Solche Risikofaktoren schränken das volle Potenzial der Protonentherapie ein und machen die Verwendung von Sicherheitsmargen um das Tumorvolumen herum erforderlich, was die Gesamtdosis für das gesunde Gewebe erhöht. Daher ist die Entwicklung von Methoden zur Überprüfung der Protonenreichweite in vivo ein aktives Forschungsgebiet. Die bekanntesten Herangehensweisen stützen sich auf die Positronen-Emissions-Tomographie (PET), die prompt gamma (PG) Bildgebung oder die Messung von thermoakustischen Wellen. Diese Methoden sind jedoch in vielerlei Hinsicht eingeschränkt, z. B. durch ein geringes Signal-Rausch-Verhältnis oder eine schwierige Detektion, was Raum für die Entwicklung neuer Ideen und Methoden lässt.

Kürzlich wurde vorgeschlagen, das elektrische Feld der Primärprotonen als Grundlage für eine alternative Methode zur Überprüfung der Reichweite zu verwenden. Die vorliegende Arbeit zielt darauf ab, die Möglichkeiten und Grenzen eines solchen Ansatzes zu untersuchen. Der erste Teil befasst sich mit einer umfassenden analytischen Charakterisierung des elektromagnetischen Feldes, das von einem Protonenstrahl ausgeht und wie es von biologischem Gewebe beeinflusst wird. Dabei werden die Auswirkungen der Form des Strahlpulses, der Permittivität, der Leitfähigkeit und der Gewebegrenzen berücksichtigt. Im Gegensatz zu bisherigen Ergebnissen wurde festgestellt, dass die Ladungsrelaxation, die auf die Ionenleitfähigkeit von biologischem Gewebe zurückzuführen ist, einen enormen Einfluss auf das elektrische Feld hat, so dass es sich innerhalb von Nanosekunden abschwächt. Das elektrische Feld eignet sich daher nicht als Grundlage für die Reichweitenüberprüfung, auch unter Berücksichtigung des Auswascheffekts, der durch die schnelle Umverteilung der Ladungen entsteht. Das magnetische Feld hingegen wird davon nicht beeinflusst und profitiert von der annähernd konstanten Stromdichte. Sie nimmt nicht mit der abnehmenden Teilchengeschwindigkeit ab, sondern wird aufgrund der ebenfalls zunehmenden Ladungsdichte zur Reichweite hin aufrechterhalten. Das zugehörige Magnetfeld weist keinen ausgeprägten Peak im Bereich der Reichweite auf, sondern folgt einem flachem, aber charakteristischen Profil entlang der Strahlachse, aus dem die Reichweite bestimmt werden könnte. Schließlich wurde eine eingehende Analyse des Frequenzspek-

trums durchgeführt, wobei es in die bekannten Bestandteile zerlegt wurde.

Der zweite Teil zielte darauf ab, einige der vereinfachenden Annahmen aufzuheben und die Auswirkungen von Kernreaktionen, Energie- und Reichweitenstreuung, lateraler Streuung, Strahldurchmesser und Sekundärteilchen zu untersuchen. Mit Schwerpunkt auf den Sekundärelektronen wurden speziell dafür vorgesehene Monte-Carlo-Simulationen (MC) durchgeführt, bei denen die Elektronen bis hinunter zu 10 eV nachverfolgt wurden. Obwohl sie wesentlich zahlreicher sind als die primären Protonen, reduzieren sie die Gesamtstromdichte nur um 10%. Die Hauptgründe dafür sind ihr überwiegend isotroper Fluss und ihre kurze Lebensdauer, was sich aus einer eingehenden Phasenraumanalyse ergeben hat. Die aus den MC-Simulationen extrahierte Stromdichte diente als Ausgangspunkt für eine numerische Magnetfeldbestimmung mittels Finite-Elemente-Analyse. Dabei wurde festgestellt, dass der Intensitätsverlust aus Kernreaktionen, der Elektronenstrom und der radiale Protonenstrom eine kleine, aber nicht vernachlässigbare Längsverschiebung gegenüber dem analytischen Ergebnis aus dem ersten Teil verursachen. Darüber hinaus wurden die Zufallsschwankungen der Stromdichte quantifiziert und im Rahmen einer Messung als vernachlässigbar eingestuft. Schließlich wurde gezeigt, dass der Strahldurchmesser keinen Einfluss auf das messbare Magnetfeld hat. Zusammenfassend kann gesagt werden, dass die Ergebnisse des ersten Teils, abgesehen von geringfügigen Abweichungen, unter realistischeren Annahmen bestätigt werden konnten.

Im letzten Teil wird die Anwendbarkeit des analytischen Ansatzes auf einfache inhomogene Targets erweitert. Mit Hilfe eines Green'schen Funktionsansatzes wurden die Auswirkungen von Gewebegrenzen für einen realistischeren Strahl, der die HF-Struktur des Beschleunigers einschließt, untersucht. Auch die Möglichkeit, die Strahlintensität künstlich zu modulieren, um das gesuchte Signal vom Umgebungsrauschen (Bioelektrizität) zu trennen, kann mit der gleichen Methode untersucht werden. Vorläufige Ergebnisse zeigten, dass die Grenzflächen nicht vernachlässigt werden können, was aufgrund der vergleichsweise großen Reflexionskoeffizienten zu einer Gesamtverringerung des transmittierten Signals führt. Außerdem hängt das longitudinale Profil des magnetischen Feldes von der Modulationsfrequenz ab. Schließlich wurde das Potenzial der untersuchten Methode zur Reichweitenverifizierung im Hinblick auf die derzeitigen technischen Möglichkeiten evaluiert.

ABSTRACT

Targeting tumor cells with ionizing radiation in an effort to eliminate them is a mainstay of cancer treatment. External beams of heavy charged particles, such as protons, are applied for such purposes and have the potential to enable highly conformal dose delivery due to their favorable depth dose profile, i.e. the so-called Bragg peak. This allows an effective sparing of healthy tissues and organs at risk, especially when compared to the conventional approach with x-rays. The finite penetration depth of protons within the patient, known as the range, is however subject to uncertainties, which can lead to significant underdosage in the tumor and excessive dose to critical structures. Inaccuracies can originate from imaging, anatomical changes, patient positioning, just to name a few. Such risk factors limit the full potential of proton therapy and necessitate the utilization of safety margins around the tumor volume, which increases the overall dose to healthy tissue. Hence, the development of methodologies to verify the proton range in vivo is an active field of research. The most prominent candidates rely on positron emission tomography (PET), prompt gamma (PG) imaging or the detection of thermoacoustic waves. These methods, however, are limited in several aspects, such as low signal-to-noise ratios or challenging detection, leaving room for new ideas and methods to be developed.

Recently, it has been suggested to use the electric field of the primary protons as a basis for an alternative range verification method. The present work aims to investigate the possibilities and limitations of such an approach. The first part is concerned with an exhaustive analytical characterization of the electromagnetic field that originates from a proton pencil beam and how it is affected by biological tissues. The impact of the beam pulse shape, permittivity, conductivity and tissue boundaries are considered. Contradictory to previous results, it has been found that the charge relaxation, which originates from the ionic conductivity of biological tissues, has a huge impact on the electric field, causing it to diminish in a nanosecond time scale. The electric field is thus not suitable as a basis for range verification, considering also the washout effect, that the rapid redistribution of charges creates. The magnetic field, on the other hand, is not affected by the latter and benefits from the approximate constancy of the current density. It does not drop together with the decreasing particle velocity, but is upheld due to the equally increasing charge density towards the range. The associated magnetic field does not show a distinctive peak at the range but follows a smooth yet characteristic profile along the beam axis, from which the range could be determined. Finally, an in-depth analysis of the frequency spectrum has been carried out, separating it into well-known constituents.

The second part aimed to lift some of the simplifying assumptions, investigating the impact of nuclear reactions, energy and range straggling, lateral scattering, beam spot size and secondary particles. With an emphasis on the secondary electrons, dedicated Monte Carlo (MC) simulations were conducted, tracking them down to 10 eV. Despite being significantly more numerous than the primary protons, they reduce the overall current density by only 10%. The main reasons are their mostly isotropic flow and short lifetimes, which

followed from a thorough phase space analysis. The current density extracted from the MC simulations served as an input for a numerical magnetic field estimation via finite element analysis. Thereby, it has been found that the loss of intensity from nuclear reactions, the electron current and the radial proton current introduce a small but non-negligible longitudinal shift with respect to the analytical result from the first part. In addition, the random current density fluctuations were quantified and deemed negligible in the context of a measurement. Finally, it has been shown that the beam spot size has no impact on the detectable magnetic field. In summary, barring minor deviations, the findings from the first part have been confirmed under more realistic assumptions.

The last part expand the applicability of the analytical approach to simple inhomogeneous targets. Through a Green's function approach, the impact of boundaries for a more realistic beam, which includes the RF structure from the accelerator, has been examined. Also, the possibility to modulate the beam intensity artificially in an effort to separate the sought signal from ambient noise (bioelectricity) can be investigated with the same method. Preliminary results indicated that the boundaries cannot be neglected causing an overall reduction of the transmitted signal due to the comparatively large reflection coefficients. Also, the longitudinal magnetic field profile depends on the modulation frequency. Finally, the potential of the range verification method under consideration has been evaluated with respect to current technological capabilities.

"Electromagnetic induction as a phenomenon in which one of the fields creates the other is an illusion."

Oleg D. Jefimenko [1]

CONTENTS

LIST OF ACRONYMS

Notation	Description
AOI	Area of interest
CBCT	Cone beam computed tomography
CDF	Cumulative distribution function
CDI	Current density imaging
CPU	Central processing unit
CSDA	Continuous slowing down approximation
CT	Computed tomography
CTV	Clinical target volume
CW	Continuous wave
DC	Direct current
DNA_5	Geant4-DNA physics list, option 5
FDTD	Finite difference time domain
FEA	Finite element analysis
FET	Fermi-Eyges theory
FLASH	Radiotherapy with dose rates above 40 Gy/s
FWHM	Full width at half maximum
GTV	Gross tumor volume
ICRU	International Commission on Radiation Units and Measurements
IMPT	Intensity modulated proton therapy
IMRT	Intensity modulated radiation therapy
LET	Linear energy transfer
LHS	Left-hand side
LINAC	Linear accelerator
LU	Lower upper (decomposition)
MC	Monte Carlo
MCS	Multiple Coulomb scattering
MEG	Magnetoencephalography
MOM	Method of moments
MRI	Magnetic resonance imaging
NIST	National Institute of Standards and Technology
OAR	Organs at risk
OM	Optical magnetometry
PDF	Probability density function
PET	Positron emission tomography
PG	Prompt gamma

Notation	Description
PMF	Probability mass function
PMMA	Poly(methyl methacrylate)
PS	Phase space
PSF	Point spread function
PTV	Planning target volume
QGSP_BIC	Geant4 physics list
RBE	Relative biological effectiveness
RF	Radio frequency
RHS	Right-hand side
SNR	Signal-to-noise ratio
RSD	Relative standard deviation
RSP	Relative stopping power
S2C2	IBA's superconducting synchrocyclotron
SFUD	Single field, uniform dose
SQUID	Superconducting quantum interference device
WKB	Wentzel–Kramers–Brillouin approximation

1 INTRODUCTION AND MOTIVATION

Cancer is among the leading causes of death worldwide and with almost ten million mortalities in 2020 [2] only second to cardiovascular diseases. It is characterized by an uncontrolled proliferation of tumor cells, which damages surrounding tissues and can spread to further organs (metastasis) with potentially lethal consequences for the patient [3]. Nowadays, there are multiple treatment options, with the three main ones being surgery, systemic therapy (such as chemotherapy or hormonal treatments) and radiation therapy. Oftentimes, combinations of those are used. About a quarter of all patients eventually receive radiotherapy, while recommendations to enhance overall survival are as high as fifty percent [4]. The present work is concerned with radiotherapy, being a non-invasive cancer treatment, that aims at killing the tumor cells by external radiation. It relies on the different response of tumor cells and healthy tissue upon receiving ionizing radiation, which spans a *therapeutic window* with respect to the amount of radiation to be administered. Within this window, one can effectively target tumor cells, while keeping complications of normal tissue low, due to their enhanced repair mechanisms [5]. Certainly, an optimal sparing of healthy tissue is desirable.

These days, different types of radiation are used therapeutically, while the treatment with photons is considered as the *conventional* approach. In fact, the first breast cancer treatment with an x-ray tube occurred already in 1896, only one year after the discovery of x-rays [7]. 50 years later, when radiation therapy based on x-rays had been well established, technologies capable of accelerating heavy charged particles, such as protons, to relevant therapeutic energies, were being developed. With his 1946 paper, Wilson [8] can be credited with the first published suggestion to use them for cancer treatment: *"It must have occurred to many people that [protons, deuterons, and alpha particles] now become of considerable therapeutic interest."* Since then, an extraordinary amount of research, technological development and standardization (ICRU) have enabled clinical particle therapy. As of August 2022, there are 119 particle therapy facilities in operation [9] and a total of more than 300,000 patients have been treated with either protons or heavier ions. Nonetheless, these numbers are small when compared to the number of new cases annually, so the majority of patients are treated conventionally. Operated with comparatively simple and compact LINACs (linear accelerators), photon therapy is significantly more cost effective when compared to proton therapy, requiring expensive, large and complex accelerators (see Sec. 2.3) and infrastructure [10]. However, the sustained interest in proton therapy is primarily based on their favorable depth dose profile, shown in Fig. 1.1.

The interactions of high energetic photons with biological tissues are dominated by Rayleigh scattering, Compton scattering, the photoelectric effect and pair production [12]. These are single scattering events, which affect a certain fraction of photons upon traversing a slab of material. Since this can occur at any depth, the energy deposited per unit mass (dose; see Sec. 2.2) decreases approximately exponentially for x-rays. Deviations from this

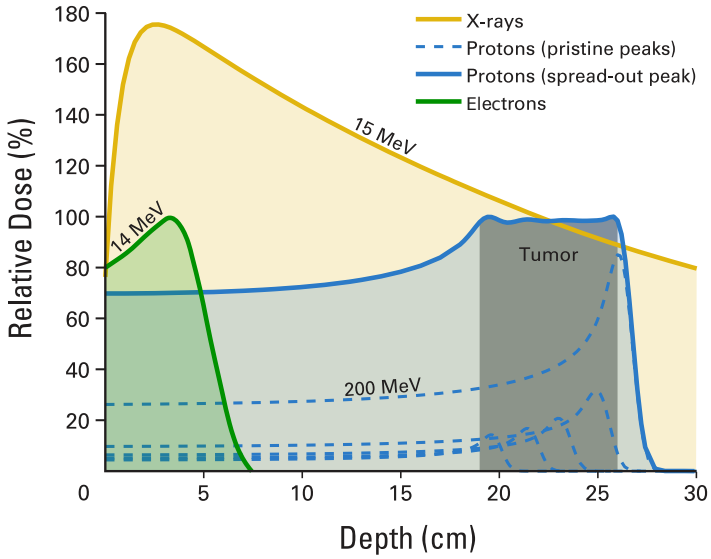

Figure 1.1: Comparison of depth dose profiles from different particles. Adapted from [6].

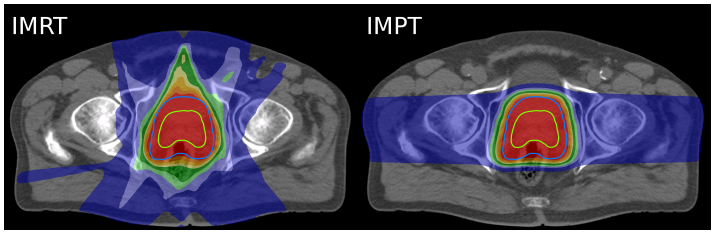

Figure 1.2: Comparison of the dose distributions for a treatment with photons (left) and protons (right). Courtesy of G. Landry. Originally published in [11].

law occur at the entrance (buildup region), since the energy is primarily transferred to electrons moving along with the photons. The passage of charged particles is quite the contrary. Every proton undergoes a myriad of small interactions with the electrons of the target, which become more frequent as the particle decelerates. This has two consequences: (a) particles with therapeutic energies have a finite *range* within the body and (b) they deposit a large amount of their energy at or close to the range, which leads to the so-called *Bragg peak* [13]. The depth of the Bragg peak depends on the initial energy of the primary protons and can be adjusted to target the tumor. A more detailed description of the interaction between protons and biological tissues can be found in Sec. 2.1. Usually, the target exceeds the longitudinal extent of the Bragg peak so that a superposition of Bragg peaks with different energies and intensities is necessary, referred to as the *spread-out Bragg peak*. Thereby, one can achieve a uniform and highly conformal coverage of the tumor with minimum entrance dose to healthy tissue. This constitutes the distinct advantage over photons, which deposit the majority of their energy within the first few centimeters so that one needs to distribute it by irradiating the tumor from many different angles [14]. The aforementioned sparing of healthy tissue is hence optimized with heavy charged particles. Aside from the purely physical argument (Bragg peak vs. exponential fall off), more evidence is currently accumulating that proton therapy has the ability to enhance the overall survival when compared to photon therapy [15–17], despite the ethical challenges

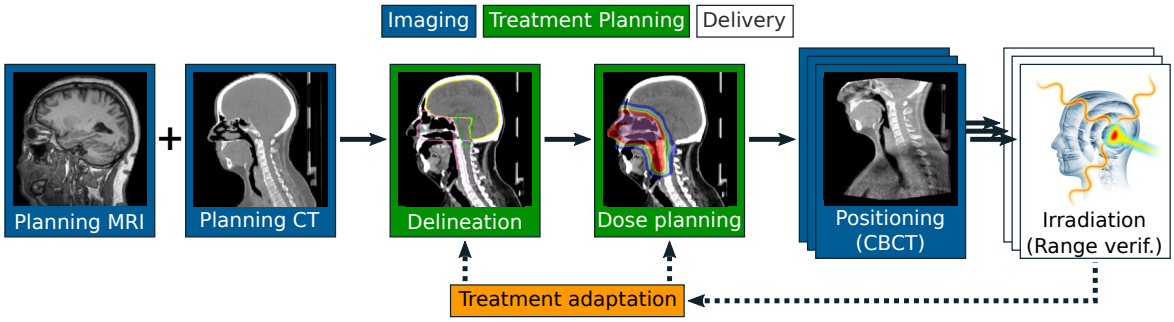

Figure 1.3: Simplified proton therapy workflow, including the desired range verification, which is currently not part of clinical practice. The necessary conversion from Hounsfield units to RSP (see Eq. (2.3)) is not explicitly shown. The individual images were adapted from [18].

in study design and in particular running *randomized controlled trials*. Before addressing the specific concern of this work, a brief overview of the particle therapy workflow is presented in the following.

1.1 Adaptive radiation therapy workflow with protons

A simplified proton therapy workflow is sketched in Fig. 1.3. As a first step, one needs to identify the site and extent of the tumor. Based on computed tomography (CT) images and ideally paired with magnetic resonance images (MRI) and/or positron emission tomography (PET) images, physicians delineate the visible part of the tumor, called the *gross tumor volume* (GTV) [19]. Non-visible and microscopic tumor cells, that likely surround the GTV, are taken into account by adding a certain margin around the GTV, resulting in the *clinical target volume* (CTV). Further safety margins account for various uncertainties, described below, leading finally to the *planning target volume* (PTV). The delineation also includes the surrounding *organs at risk* (OAR), which could be affected by excessive irradiation. In the subsequent planning stage, a dose, usually in the order of 60 Gy, is prescribed to the PTV and optimized to maximize target coverage and minimize dose to the OARs. In particular, in *single field uniform dose* (SFUD) delivery, one optimizes the fields from different angles individually to each yield a uniform dose in the target, which is then superimposed [13]. *Intensity modulated proton therapy* (IMPT) on the other hand, allows for non-uniform fields from different angles, so only when added together, they cover the PTV uniformly. Prior to the dose delivery, which is sub-divided into fractions, modern facilities ensure the patient positioning through three-dimensional cone beam CT (CBCT) images [11]. In current clinical practice, irradiation constitutes the last step. Yet, unless one can guarantee that the sharp distal fall-off actually hits its target, the full potential of proton therapy cannot be exploited. And in fact, uncertainties of the range have a large impact and numerous sources, as discussed in the following.

1.2 Range uncertainties

In a comprehensive roadmap article on *proton therapy physics and biology* from more than twenty of the leading experts in the field [20], Tony Lomax from the PSI (Paul Scherrer Institut, Villigen, Switzerland) entitled his description of uncertainties in particle therapy with "*uncertainly precise*". His phrasing offers a concise description of the conflict in particle

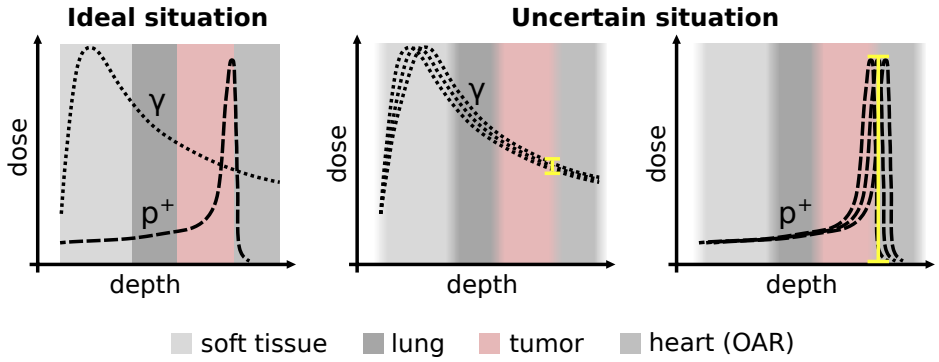

Figure 1.4: Impact of uncertainties on photon and proton therapy. The dose differences at the distal edge have been highlighted by the yellow bars. Adapted from [21].

therapy between the highly localized dose delivery enabled through the Bragg peak and the risks that come with the uncertainties, which cannot be ignored. To be more specific, the core issue is schematically shown in Fig. 1.4. When taking uncertainties along the beam line into account, as indicated by the blurring in Fig. 1.4, shifts in the depth dose profiles of protons might lead to significant under/over dosage in tumor/OAR, respectively.

Lomax has identified *fourteen* causes of uncertainties, divided into six categories, which shall be briefly summarized in the following. Already *diagnosis, staging and the delineation* of the tumor show strong inter observer variability [22], which may be mitigated through machine learning-based methods [23]. *Biological uncertainties* are another major category concerning the tumor response to ionizing radiation [24]. Considering variable relative biological effectiveness (RBE) (see Sec. 2.2) is one approach to take this into account. *Positioning and anatomical changes* (weight loss/gain, tumor shrinkage/growth) are more geometrical uncertainties. Treatment plan adaptation based on e.g. the daily CBCT positioning image [25] has been described as "mandatory" [26]. *Imaging* as the starting point of the treatment workflow (see Fig. 1.3) is subject to uncertainties, primarily due to the conversion of the Hounsfield units (HU) of the planning CT to the relative stopping power (RSP; see Eq. (2.3)) necessary for planning [27]. Dual energy CT or proton CT [28] have been shown to reduce such uncertainties. Uncertainties originating from *dose calculation* are the fifth category, which can be improved through Monte Carlo (MC) dose planning [29]. Finally and considered the least contributing are *machine delivery uncertainties*, which are managed through appropriate quality assurance. Methods to reduce the uncertainties have been mentioned for each category. Many more efforts are ongoing, further listed in [20].

These uncertainties have profound consquences on the clinical practice, one of which are the safety margins (CTV→PTV). A systematic evaluation of range uncertainties has been carried out by Paganetti [31]. Without biological effects and assuming a MC-based treatment planning, he estimates a total range uncertainty of $2.4\% + 1.2$ mm. Accordingly, clinical margins have a similar magnitude, as shown in Fig. 1.5. Also, such uncertainties force clinicians to choose sub-optimal plans, whenever OARs could be targeted through over- or undershoots [21]. An example is shown in Fig. 1.6. If it were not for range uncertainties, one would choose a *single-field plan* with minimal dose to healthy tissue. However, with the heart lying right behind the tumor along the beam line, the risk of delivering an excessive dose to the OAR is too high. The safest option, less susceptible to range uncertainties, is a *multi-field plan*, yet it delivers a larger amount of dose to healthy tissue. A common compromise is the depicted *patched-field plan* with reduced risk of targeting the

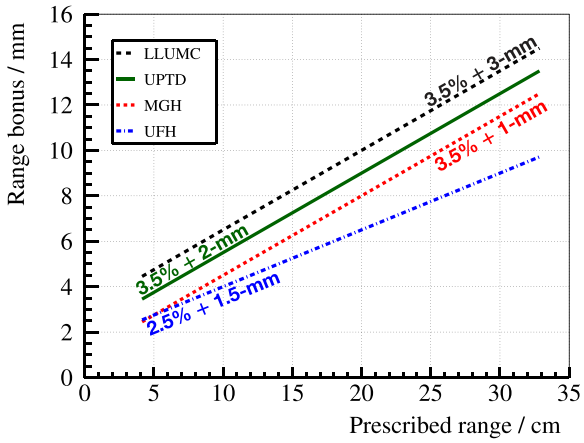

Figure 1.5: Range uncertainty margins in clinical practice at the Loma Linda University Medical Center (LLUMC), Universitäts Protonen Therapie Dresden (UPTD), Massachusetts General Hospital (MGH) and the University of Florida Health Proton Therapy Institute (UFH). The figure has been adapted from [30], which is based on data from [31], published back in 2012. Very recently, dual energy CT has enabled to reduce the UPTD margins to 2.0% + 2 mm for prostate cancer [32].

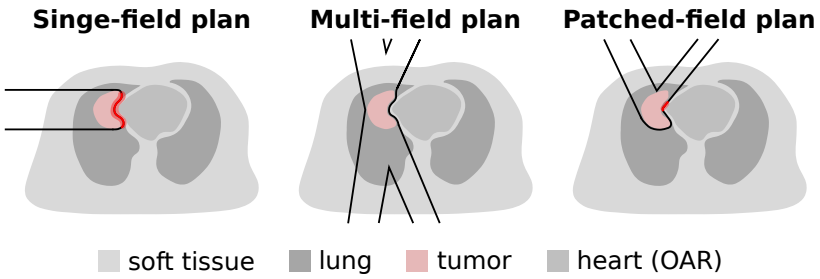

Figure 1.6: Treatment planning strategies and their susceptibility to range uncertainties. The *single-field plan* corresponds to the scenario depicted in Fig. 1.4. Adapted from [21].

OAR.

Except for the first two uncertainty categories, a precise in vivo knowledge of the dose deposition and in particular the position of the Bragg peak could help to overcome the remaining four sources of uncertainty by enabling an ideally real time adaptive radiotherapy (see Fig. 1.3). Hence, the development of *range verification techniques* is a very active field of research, which will be described in the following.

1.3 Ion beam range verification

Three physical processes form the basis of the currently investigated non-invasive in vivo range verification approaches: (a) β^+-emission from radioactive isotopes, (b) prompt gammas emitted after fast nuclear de-excitations and (c) ultrasound waves that originate from minute but rapid temperature changes. All of them are either directly[1] or indirectly caused by the primary protons and schematically visualized in Fig. 1.7. In the following, they will

[1]The signal is not generated by secondaries, but the primary protons themselves.

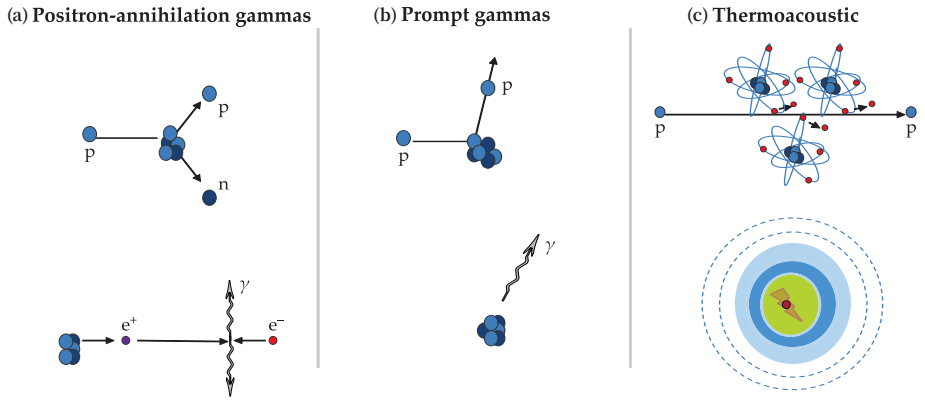

Figure 1.7: Physical interactions of the primary protons with the target exploited for range verification. Adapted from [33].

be briefly outlined in the same order. For more comprehensive reviews, refer to [20,33–35]. Besides, proton radiography [36] and MRI [37] have been suggested. Since the former can only detect cumulative range variations along the projection (beam) line and the latter is caused by a late tissue response to radiation, they cannot be considered an *on-line* range verification approach and are thus beyond the scope of this work.

Positron emission tomography (PET) While passing through biological tissues, proton beams produce radioactive isotopes through nuclear fragmentation. The most dominant β^+-emitters among those are ^{11}C, ^{15}O and ^{13}N [38], while a more complete list can be found in [39]. Through a PET scanner, one may detect and correlate the 511 keV photon pairs (with opposite momenta) created by the positron-electron annihilation to reconstruct the activity for beam monitoring. First experiments were already carried out in 1969 by Maccabee et al. [40]. Therein, they credit C. A. Tobias, who initially investigated the activation of tissues upon charged particle irradiation back in 1947, for the suggestion to locate the Bragg peak by observing the activity of the β^+-emitters. Since then, many groups have studied range verification with PET [41–47]. The half-lifes of the isotopes range from 2 to 20 minutes [39], so to avoid data loss, one ideally combines the particle beam with the PET scanner (*in-beam*). The major advantage is that PET detection and irradiation run simultaneously so that more statistics can be collected. Nonetheless, it requires dedicated configurations (oftentimes only dual-head instead of full-ring scanners [44,48]) due to geometrical limitations and entails challenging reconstruction [47]. A more cost effective approach is to use an already available scanner [49,50], to which the patient is transported after the treatment (*offline*). The biggest disadvantages here are the loss of activity while moving the patient and positioning uncertainties. A hybrid approach is an *in-room* PET [51], which at least shortens the transport time. Unfortunately, β^+-emissions do not show a sharp distal fall off at the range, since it takes high energies for primaries to cross the Coulomb barrier, which is rarely surpassed by the low energy protons close to the Bragg peak [52]. In order to carry out a range verification, one needs to compare the detected signal to a simulation of the delivered irradiation [51] or a reference measurement [48]. Clinical studies are ongoing and have been reported in [53,54]. However, range verification through PET remains intrinsically limited through the biological washout [55] during the long acquisition times. Moreover, it cannot provide real time monitoring and suffers from the prompt gamma background [56], described in the following.

Prompt gamma (PG) Just like the β^+-emitters, prompt gammas (PG) are a result of inelastic nuclear interactions between ion beams and the target. As abundantly present in biological tissues, the main sources of PGs are ^{12}C, ^{16}O and ^{14}N [57, 58], which can emit a PG upon proton impact through a fast excitation-deexcitation transition. Specifically, these processes are in the sub-nanosecond time scale, hence the name *prompt* gamma, which overcomes issues from delayed emissions and washout [34]. The detection is more challenging, due to the higher photon energies (2-7 MeV [57]), yet PGs have lower production thresholds (better correlation with the range) and higher overall yield when compared to PET [59]. Since the first suggestion in 2003 [60] many groups have worked on PG-based range verification and in fact, PG imaging comprises a whole family of techniques reliant on the same principle. For instance, one-dimensional profiles along the beam line are obtained through passively collimated systems, such as the *multi-slit camera* [61] or the *knife-edge slit camera* [62]. On the other hand, three-dimensional images can be retrieved without mechanical collimation via a *Compton camera* system [63, 64]. In combination with collimation, another technique (*prompt gamma spectroscopy*) relies on resolving the energy spectrum of the PGs [65]. Range determination has also been carried out by measuring the time of gamma ray emission along the proton path, i.e. *prompt gamma timing* [66, 67]. Finally, some isotopes (^{10}C, ^{14}O) emit both a positron and leave the daughter nucleus in an excited state, leading to a third photon in coincidence with the annihilation photon pair [68]. To this end, two prototypes have reached clinical stage [69, 70]. Just as in PET (relying on nuclear processes), a range verification through PGs generally requires a comparison to a reference [71].

Ionoacoustics As opposed to the previous two methods, ionoacoustics is a non-nuclear, direct and cost effective method for range verification. It relies on the *thermoacoustic effect* and is similar to *photoacousitc imaging*. In case of ions, the deposited energy leads to a thermal expansion and thus to an acoustic wave, predominantly at the range. Detecting this wave with high frequency transducers ($\sim$ MHz) allows a reconstruction of the Bragg peak through time-of-flight measurements. Early clinical experiments began in 1991 [72,73], followed later by more fundamental experiments [74–76]. Yet, to obtain a useful signal, one requires pencil beam scanning (see Sec. 2.4) instead of passive delivery and a specific (pulsed) beam structure (see Sec. 2.3.3). With dedicated accelerators and transducers, new experimental [77–80] and simulation studies [81, 82] followed in the mid 2010s. A major issue is the large amount of dose necessary to overcome the low signal-to-noise ratio (SNR), hence more recent efforts aim to enhance the signal strength [83]. Also, complexity due to heterogeneities remains challenging.

1.4 Topic and thesis outline

The range verification methods presented above are limited in several ways. To recapitulate, PET suffers from washout and relies on delayed β^+-decays so that it cannot be considered as candidate for *real-time* range verification. While PGs overcome both of these issues, they are more challenging to detect, due to their higher energies and lack of intrinsic collimation. Generally, with both the emission of positrons and PGs being the result of nuclear reactions, for which protons need a certain energy to overcome the Coulomb barrier, the correlation to the Bragg peak is not straightforward. Secondly, they are both *indirect* methods, insofar that the detected signal does not originate from the primary protons, but secondaries instead. While one might overcome these limitations by choosing a range verification through ionoacoustics (direct method), its low SNR and issues with heterogeneities are major chal-

lenges. Hence, the present work seeks to investigate a novel range verification approach based on the electromagnetic field that originates from the primary protons. As opposed to PET, PG and ionoacoustics, this approach does not have rich history, i.e. very little work has been done thus far. A first suggestion goes back to a conference in 2011 [84]. Caspers made a rough estimate of the electric field strength and the time scale within which it vanishes. He concludes that "the proposed concept should be further investigated by detailed simulations." Secondly, Albert et al. [85] further investigated the electric field for an application to range verification via analytical methods. (What exactly has been done by Albert et al. is further described in Chapter 4.) This thesis takes the work from Albert et al. as a starting point of an extensive analytical and simulation-supported investigation. The goal is to provide a fundamental analysis of the electromagnetic field of a proton beam in biological tissues. The possibilities and limitations of such an approach are still to be explored. With the limited existing prior efforts, this work is to a large degree also a methodological development and seeks to provide a general understanding of the topic. An already appealing characteristic, is that this approach would be a direct method, based on simple principles. To quote the second reviewer of the work presented in Chapter 5: "Range verification in proton therapy still is a field requiring new ideas and methods to be developed."

With this goal in mind, the present thesis is structured as follows. Chapter 2 covers the basic proton therapy physics including some technical aspects of particle accelerators relevant for the presented calculations. A summary of the classical electromagnetic theory follows in Chapter 3, containing also dedicated analytical and numerical methods. Chapter 4 then provides a detailed analytical description of the electromagnetic field of an idealized proton pencil beam. The contributions from the fifth chapter is based on more realistic Monte Carlo simulations and primarily seeks to investigate the impact of secondary electrons. Also, the impact of tissue boundaries and the RF structure of the accelerators are further analyzed in Chapter 6. Finally, the work is summarized in Chapter 7 with some concluding remarks and future perspectives. Consequently, Chapters 4 to 6 do not contain individual conclusions, but provide motivation for the subsequent chapters.

2 FUNDAMENTALS OF PROTON THERAPY

This chapter summarizes some basics of proton therapy. It begins with the most relevant physical interactions, whose impact on the electromagnetic field will be investigated in Chapter 5. How one obtains the average proton path from the stopping power, is subsequently described when introducing the continuous slowing down approximation. The concept of *dose*, which has already been qualitatively introduced in Fig. 1.1, is presented thereafter in more detail. Finally some technical aspects about particle accelerators and dose delivery follow. The present overview is more or less limited to the aspects that are necessary for the investigations in Chapters 4 to 6 and their discussions. An exhaustive introduction can be found in the book of Paganetti [13], whereas the review article from Newhauser and Zhang [86] is an easily accessible reference. On the other hand, Podgoršak's book [87] is more concerned with a detailed description of the interactions and their cross sections.

2.1 Physics aspects of proton therapy

The fundamental physics aspects of charged particle therapy with an emphasis on protons will be summarized in the following. In particular, the interactions of the projectiles with the target causing stopping, energy straggling, scattering and nuclear reactions will be quantified. These processes, which are depicted in Fig. 2.1, lead to the well-known Bragg peak (see Fig. 1.1) and the pencil beam dose distribution (see Fig. 2.12). Beginning with the stopping power, which describes the energy loss and deceleration of the primary protons.

2.1.1 Stopping power

The stopping power is defined as the (negative) average kinetic energy loss $\mathrm{d}Q$ per unit path length $\mathrm{d}z$ of a particle traversing a medium: $S = -\,\mathrm{d}Q/\mathrm{d}z$. For charged particles, one separates the stopping power into the *radiation stopping power* S_{rad} and the *collision stopping power* S_{col}: $S = S_{\mathrm{rad}} + S_{\mathrm{col}}$ [87]. The former is caused by interactions between the projectile and the nucleus, which results in bremsstrahlung. The corresponding rate of energy loss is proportional to the inverse square of the particle mass m_{p}, since it depends on the particles acceleration (deflection). Accordingly, S_{rad} is more relevant for light charged particles, such as electrons, but negligible for heavy charged particles when compared to their collision stopping power (collisions between the projectile and the target's electrons), which is described by the Bethe-Bloch formula [87]:

$$S_{\mathrm{col}} = n_{\mathrm{e}} \frac{4\pi}{m_{\mathrm{e}} c_0^2} \left(\frac{q_{\mathrm{e}}^2}{4\pi\varepsilon_0} \right)^2 \frac{z_{\mathrm{p}}^2}{\beta^2} \left[\log\left(\frac{W_{\mathrm{m}}}{I_{\mathrm{e}}} \right) - \beta^2 - \frac{C}{Z} - \frac{\delta}{2} \right], \tag{2.1}$$

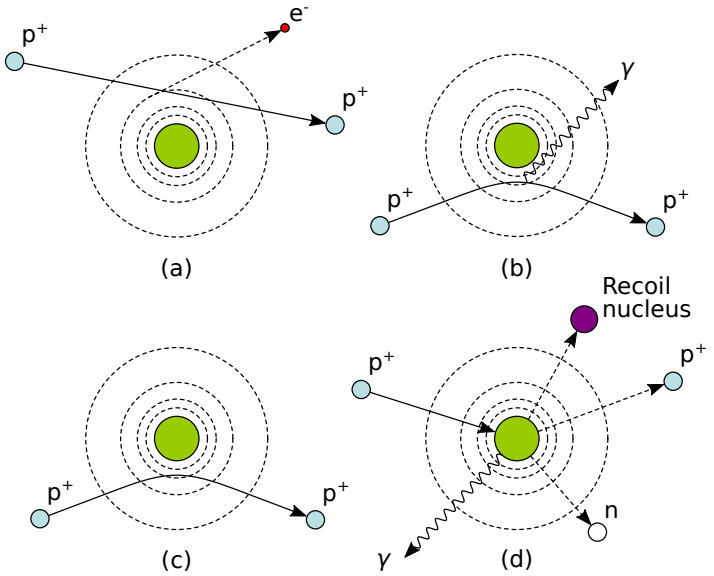

Figure 2.1: Interactions of swift and heavy charged particles with a target. They consist of (a) collisions with orbital electrons, which are on average described by the Bethe-Bloch formula, (b) radiative energy loss due to bremsstrahlung (negligible for heavy charged particles), (c) elastic scattering and (d) head-on collisions (nuclear reactions) leading to a wide range of secondaries. Adapted from [86].

where

$$W_\mathrm{m} = \frac{2m_\mathrm{e}c_0^2\beta^2\gamma^2}{1 + 2\gamma(m_\mathrm{e}/m_\mathrm{p}) + (m_\mathrm{e}/m_\mathrm{p})^2} \overset{m_\mathrm{p} \gg m_\mathrm{e}}{\approx} 2m_\mathrm{e}c_0^2\beta^2\gamma^2 \tag{2.2}$$

is the largest possible energy transfer between the projectile and an electron from the target with mass m_e. For ion beam therapy, it is significantly lower than the projectile mass so that $m_\mathrm{e}/m_\mathrm{p} \ll 1$, enabling the approximation in Eq. (2.2). Moreover c_0 is the speed of light in vacuum, $\beta = v/c_0$ is the particle velocity v relative to c_0, $\gamma = 1/\sqrt{1-\beta^2}$ is the Lorentz factor, q_e is the elementary charge, ε_0 is the vacuum permittivity, z_p is the projectile's charge in units of q_e, I_e is the ionization potential of the target and n_e is the electron density of the target medium, which can be calculated as $n_\mathrm{e} = \varrho N_A Z/A$. Therein, ϱ is the density of the target, $N_A \approx 6.022 \times 10^{23}$ mol^{-1} is Avogadro's constant, Z is the atomic number of the medium and A is its atomic mass in units of g/mol. The last two terms in the square brackets of Eq. (2.1) are correction terms. C/Z is the shell correction that relaxes the assumption that the projectile velocity is much larger than the velocity of the target electrons. The latter is not valid for low energies, where the shell correction contributes. The density effect correction $\delta/2$ takes into account that the polarization of the medium reduces the contributions from more distant electrons, which is more relevant at relativistic energies. Both corrections were introduced by Fano in 1963 [88]. Without them, Eq. (2.1) is the result of a relativistic and quantum mechanical calculation that was presented by Bethe in 1930 [89].

The stopping power of *water* is considered throughout this thesis. While different tissues are modeled electromagnetically through the permittivity (see Sec. 3.2.2), the *relative stopping power* (RSP) to water will be used in order to model different tissues [92]:

$$\mathrm{RSP} = \frac{S_\mathrm{t}}{S_\mathrm{w}} = \frac{n_\mathrm{e,t}}{n_\mathrm{e,w}} \frac{\log(W_\mathrm{m}/I_\mathrm{e,t}) - \beta^2}{\log(W_\mathrm{m}/I_\mathrm{e,w}) - \beta^2} \approx \frac{n_\mathrm{e,t}}{n_\mathrm{e,w}}, \tag{2.3}$$

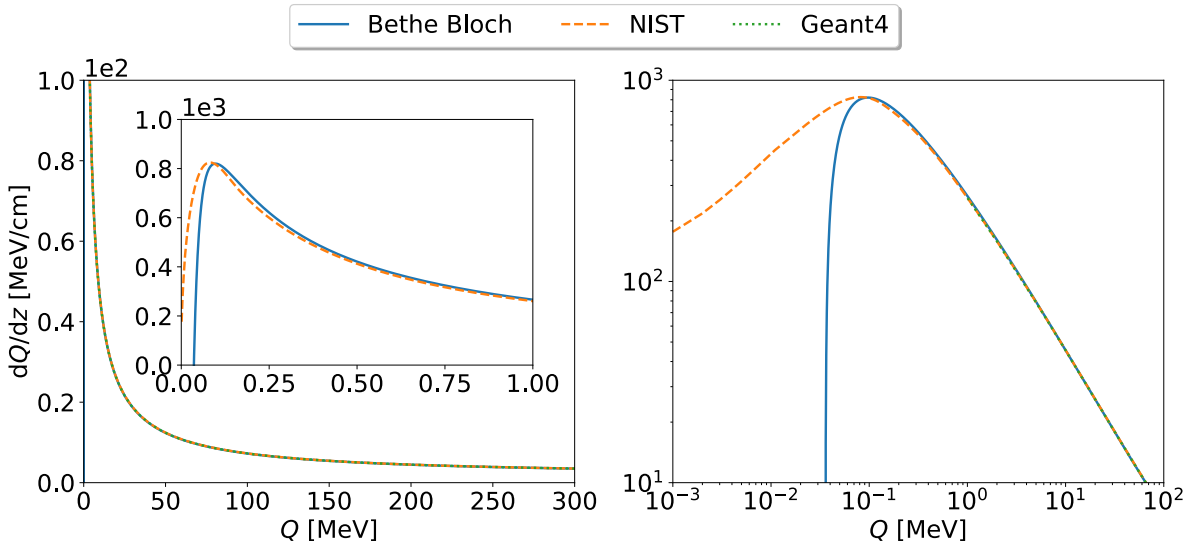

Figure 2.2: Stopping power of water for energies between 1 keV and 300 MeV shown in a linear scale (left) and logarithmic scale (right). The graph labeled with "Bethe Bloch" shows Eq. (2.1) without the correction terms, while "NIST" and "Geant4" are tabulated data [90, 91]. In particular, $\varrho = 0.99823\ \mathrm{g/cm^3}$, $A = 18.01528\ \mathrm{g/mol}$, $Z = 10$ and $I_\mathrm{e} = 78\ \mathrm{eV}$ has been used. Over a wide range of energies, Eq. (2.1) without the corrections terms offers a close description of the more accurate stopping power data.

where the subscripts stand for target (t) and water (w) and the correction terms were neglected. Under the assumption that the target's mean ionization potential is homogeneous and that it can be approximated by the ionization potential of water $I_{\mathrm{e,w}}$, which is reasonable for biological tissues, the RSP becomes energy independent. In other words, one can obtain the stopping power of a target by simply rescaling the stopping power of water with the RSP value.

Tabulated stopping power data within $1 \leq Q/\mathrm{MeV} \leq 300$ and $\Delta Q = 1$ MeV, which has been extracted from Geant4 simulations [91], has been used for the work presented in Chapter 4. It is labeled as "Geant4" in Fig. 2.2. Alternatively, the stopping power tables from the National Institute of Standards and Technology (NIST) [90], which provides stopping power data over a wide energy from 1 keV to 10 GeV, far above the therapeutic energy window, has been leveraged. It is also shown in Fig. 2.2, labeled as "NIST". The NIST library contains the correction terms and provides data that is valid to very low energies. In the same figure, both tabulated stopping power data are compared to Eq. (2.1) without the correction terms. In the logarithmic scale, one can clearly see the dominant $1/\beta^2$ proportionality of S for large energies as an approximately straight line.

2.1.2 Energy and range straggling

The gradual energy loss of the primary protons is a statistical process, which is subject to random fluctuations. The Bethe-Bloch formula (Eq. (2.1)) only describes the *average*. The variability can be attributed to randomness of the impact parameter and the transferred momenta [93]. This means that two protons with an identical initial state (energy, position, momentum) follow nonetheless different paths with different ranges. The shape of the associated distributions depends on the energy loss. It changes from a Landau distribution, valid for only few interactions, to a normal distribution [94].

Since a therapeutic beam that completely stops within the target is considered, a depth-

dependent quantification of the energy and range straggling, parameterized through the standard deviation of normal distributions, is desired. More than a century ago, a first theoretical description has been put forward by Bohr [95]. When relativistic effects are taken into account [96], the variance of the energy can be described by

$$\sigma_Q^2(z) = \int_0^z T[Q(Q_{\text{in}}, z')]\mathrm{d}z', \qquad (2.4) \qquad\qquad T(Q) = C_T \frac{1-\beta^2(Q)/2}{1-\beta^2(Q)}, \qquad (2.5)$$

where Eq. (2.4) is known as the *relativistic Bohr formula* and Eq. (2.5) is *Bohr's straggling parameter* [97]. The depth dependent energy $Q(Q_{\text{in}}, z)$ is obtained through the *continuous slowing down approximation* (CSDA), which is described below in Sec. 2.1.5. The associated proportionality constant is given by $C_T = 4\pi n_{\text{e}} q_{\text{e}}^4/(4\pi\varepsilon_0)^2 z_{\text{p}}^2$, which is approximately $C_T \approx 0.087\ \text{MeV}^2/\text{cm}$ for protons decelerating in water. $T(Q)$ becomes constant in the non-relativistic regime ($\beta \ll 1$) so that the variance increases linearly with the distance z along the beam line. In other words, σ_Q increases as the square root of the depth, which is the original non-relativistc result from Bohr. However, Eq. (2.4) becomes increasingly inaccurate towards large z, which led to the work of Symon [98]. He realized that Eq. (2.4) can be considered a low-order approximation of a more fundamental theory. A more accurate analysis through the *transport*, i.e. *Boltzmann equation* [96] leads to a set of differential equations, expanded over the central moments of the energy distribution. Taking the second moment (variance) and expanding it up to the first order, leads to the following differential equation:

$$\mathrm{d}\sigma_Q^2/\mathrm{d}z = T - 2(\partial S/\partial Q)\sigma_Q^2. \qquad (2.6)$$

The zeroth order approximation is obtained by dropping the second term on the RHS of Eq. (2.6), which is again Bohr's formula. Starting from Eq. (2.6), Tschalär [99] also provided a thorough and noteworthy investigation of energy straggling. The conceptual differences between Bohr's and Symon's theory have been pointed out by Payne [100], stating that it also includes that particles with different energies lose energy at different rates instead of a fixed and depth-dependent rate. He also figured that Eq. (2.6) has a closed form solution when parameterized through the energy:

$$\frac{\sigma_Q^2(Q)}{S^2(Q)} = \frac{\sigma_Q^2(Q_{\text{in}})}{S^2(Q_{\text{in}})} + \int_Q^{Q_{\text{in}}} \frac{T(Q')}{S^3(Q')}\mathrm{d}Q', \qquad (2.7)$$

where $\sigma_Q^2(Q_{\text{in}})$ is the initial energy spread at the initial energy Q_{in}. How this energy uncertainty translates to an uncertainty of the particles position along the path and eventually the penetration depth follows from the first order uncertainty propagation:

$$\sigma_z^2(Q) \approx \left(\frac{\partial z(Q)}{\partial Q}\right)^2 \sigma_Q^2(Q) = \frac{\sigma_Q^2(Q)}{S^2(Q)}, \qquad (2.8)$$

where the CSDA has been used in the second step. At the range, σ_z is referred to as *range straggling*, which broadens the Bragg peak (see Fig. 1.1). In Fig. 2.3, the predictions generated from Eqs. (2.7) and (2.8) were compared to results obtained from Monte Carlo simulations. Therein σ_Q and σ_z were parametrized through depth z instead of the energy Q, which is achieved through the CSDA (see Sec. 2.1.5). The MC data (DNA_5) is the one generated in Chapter 5 (see Sec. 5.1.4 for details). To obtain $\sigma_Q^{\text{DNA\_5}}$, the data has been binned with a relatively small $\Delta z = 0.1$ mm, otherwise the energy loss within each bin broadens the distribution beyond the theoretical expectation. In fact, the increasing discrepancy for

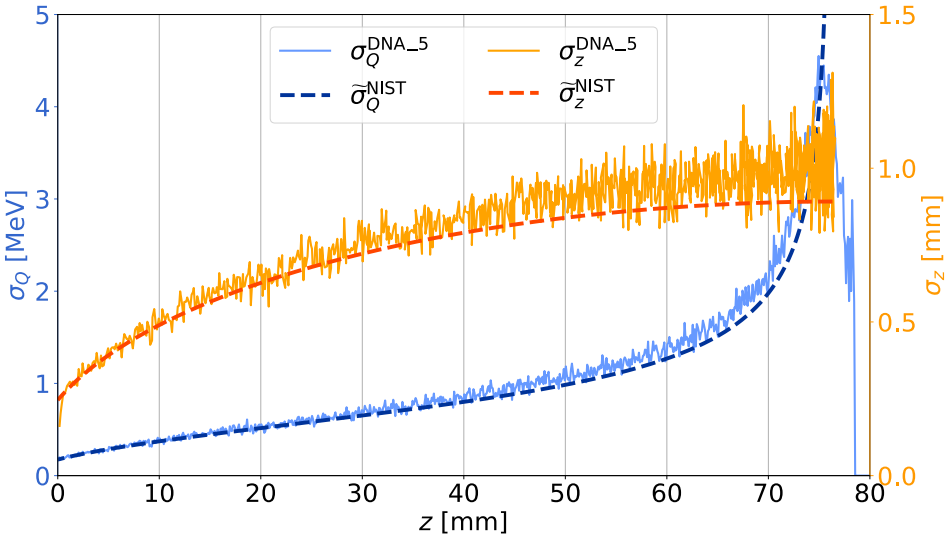

Figure 2.3: Energy ($\widetilde{\sigma}_Q^{\mathrm{NIST}}$) and penetration depth straggling ($\widetilde{\sigma}_z^{\mathrm{NIST}}$) as a function of the depth z. They were calculated via Eqs. (2.7) and (2.8) and are based on the *modified stopping power* (hence the tilde) being described in Appendix B.4, to enable a better comparability to the Monte Carlo DNA_5 data (see Sec. 5.1.4), which has been added for reference. Both data and theory use $\sigma_Q(Q_{\mathrm{in}} = 100\ \mathrm{MeV}) = 0.174\ \mathrm{MeV}$.

$z > 30$ mm is likely explained by the same reasoning. Subsequently, normal distributions were fitted to the energy histogram of each bin. Vice versa for $\sigma_z^{\mathrm{DNA\_5}}$: first energy binning ($\Delta Q = 0.1$ MeV) followed by fitting the z-histograms. Generally a good agreement between theory and simulation can be observed. In addition to the given sources, the derivations from first principles of the expressions from above have concisely been summarized in [101].

2.1.3 Multiple Coulomb scattering

Charged particles traversing matter undergo multiple Coulomb interactions with the nuclei of the target, which causes deflections from their initial direction (see Fig. 2.1 (c)). They gradually accumulate, resulting in an effective widening of the beam cross section and the angular distribution. The *Fermi-Eyges theory (FET)* provides a probabilistic description for this phenomenon, being a comparatively simple Gaussian theory. A more complete albeit more complicated theory has been put forward by Molière [102–104], taking larger single scattering events into account, which leads to longer tails at the distribution. Nonetheless, the FET provides an apt description for 99% of the distribution [105], which shall suffice for the application below.

The geometry of FET is reduced to a two-dimensional plane along the initial direction z and one perpendicular coordinate x (see Fig. 2.4). In addition, one introduces a scattering angle θ_x lying in the same plane. The deflections are generally small, yet for normalization purposes $\theta_x \in \mathbb{R}$ rad. This causes no inconsistencies, since the vast majority of the distribution lies within a couple of degrees. How this geometry translates to a three-dimensional cylindrical coordinate system will be shown further below. To quantify the strength of scattering, one introduces the *scattering power*. It is defined as the rate of change along z with respect to the variance of θ_x:

$$T_\theta \equiv \frac{\mathrm{d}\left\langle \theta_x^2 \right\rangle}{\mathrm{d}z}. \tag{2.9}$$

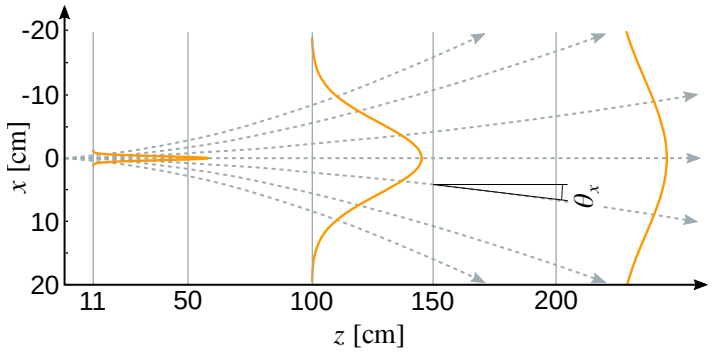

Figure 2.4: Geometry of the Fermi-Eyges theory (FET). It describes how an initially collimated beam at $z_0 = x_0 = \theta_{x,0} = 0$ broadens through multiple Coulomb scattering. The scale applies to 6 MeV electrons in air, which can also be described by FET. The sketch is based on Fig. 6 of [106].

In its simplest form, it can be derived from the classical Rutherford scattering cross section [107], which leads to $T_\theta^{\text{ICRU}} = (E_s/pv)^2/X_s$, where pv is the product of the particle's velocity and momentum, $E_s = \sqrt{2\pi/\alpha} m_e c^2 \approx 15.0$ MeV, $\alpha \approx 1/137$ is the fine-structure constant and X_s is the *scattering length*. The latter is a collection of material dependent constants (analogous to the radiation length X_0), which is approximately $X_s \approx 46.88$ cm for water [108]. The aforementioned ICRU [109] recommendation from 1984 has been improved by numerous authors, including Gottschalk [108], who provides an excellent overview and introduces $T_\theta^{\text{dM}} = f^{\text{dM}}(pv, p_1v_1) \times T_\theta^{\text{ICRU}}$. $f^{\text{dM}}(pv, p_1v_1)$ is a non-local scaling factor, depending on the initial product of momentum and velocity p_1v_1.

By analyzing the infinitesimal changes, Fermi derived a partial differential equation (transport equation) for the evolution of the probability density function of a particle along the beam line, where $P(z, x, \theta_x)\mathrm{d}x\mathrm{d}\theta_x$ is the probability to find the proton at depth z within the lateral interval $[x, x + \mathrm{d}x]$ traversing with the angle $[\theta_x, \theta_x + \mathrm{d}\theta_x]$:

$$\frac{\partial P}{\partial z} = -\theta_x \frac{\partial P}{\partial x} + \frac{T_\theta}{2} \frac{\partial^2 P}{\partial \theta_x^2}. \tag{2.10}$$

Fermi did not publish this himself, but gave Rossi and Greisen [110] the permission to do so. Finding a solution of Eq. (2.10) is not straightforward. Fermi has solved it under the assumption that the energy loss is negligible, which may have been valid for his interests (cosmic rays) but is not applicable to therapeutic beams. In a very short but all the more important paper, Eyges [111] derived a solution of Eq. (2.10) that allows for energy loss. Through a two-dimensional Fourier transform and the *method of characteristics* he obtained the following solution, which is given with the notation from Gottschalk [105]:

$$P(z, x, \theta_x) = \frac{1}{2\pi\sqrt{B_A}} \exp\left(-\frac{A_0 x^2 - 2A_1 x\theta_x + A_2\theta_x^2}{2B_A}\right), \tag{2.11}$$

where

$$A_n(z) \equiv \int_0^z (z - z')^n T_\theta(z')\mathrm{d}z', \qquad n = \{0, 1, 2\} \tag{2.12}$$

are the "moments" of the scattering power. The result is a simple binomial distribution, i.e. the exponent may also be written as $-\mathbf{x}^{\mathrm{T}}\underline{\mathrm{B}}_A^{-1}\mathbf{x}/2$, where $\mathbf{x}^{\mathrm{T}} = (x \;\; \theta_x)$, $\underline{\mathrm{B}}_A$ is the covariance matrix and $B_A \equiv \det(\underline{\mathrm{B}}_A) = A_0A_2 - A_1^2$ is the determinant of the covariance matrix. It

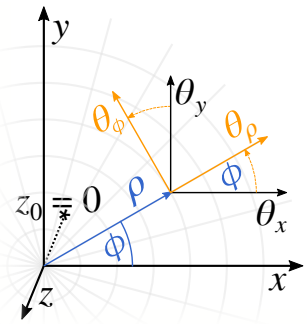

Figure 2.5: The polar coordinate system (ρ, ϕ) is linked to the local Cartesian coordinate system $(\theta_\rho, \theta_\phi)$, which is rotated by the same angle ϕ.

follows that[1] $A_0 = \langle \theta_x^2 \rangle$, $A_1 = \langle x\theta_x \rangle$ and $A_2 = \langle x^2 \rangle$, which can also be shown by evaluating the expectation values explicitly. The initial condition of Eq. (2.11) is chosen so that it describes a point-particle starting from $z = x = \theta_x = 0$ (explicitly: $P(0, x, \theta) = \delta(x)\delta(\theta_x)$), which is what is depicted in Fig. 2.4. To describe the evolution of a beam, one needs to convolve Eq. (2.11) with the lateral beam distribution. If the latter happens to be a normal distribution with a cross section of σ_b^2, then simply $A_2 \to A_2 + \sigma_b^2$, since $A_2 = \langle x^2 \rangle$. Note that Eq. (2.11) only applies to targets that are laterally homogeneous, while the scattering power may change along z. In other words, the beam must be sufficiently small. An excellent analysis of Eq. (2.11) can be found in [105], while explicit derivations of the formulas above are summarized in [101].

Eq. (2.11) is symmetric with respect to the two lateral scattering directions x and y, hence a complete Cartesian description is given by $P(z, x, \theta_x)P(z, y, \theta_y)\mathrm{d}x\mathrm{d}\theta_x\mathrm{d}y\mathrm{d}\theta_y$, which shall be transformed to cylindrical coordinates (see Fig. 2.5). $(x, y) \to (\rho\cos\phi, \rho\sin\phi)$ is used together with the radial and azimuthal scattering angles $(\theta_\rho, \theta_\phi) = (\theta_\rho\cos\phi - \theta_\phi\sin\phi, \theta_\rho\sin\phi + \theta_\phi\cos\phi)$. As expected, the result is ϕ-independent. The cylindrical data collection (see Sec. 5.1.1) corresponds to ϕ-integration. θ_ϕ is normally distributed around zero $\forall\rho, \theta_\rho$, hence it is also eliminated through integration. The result differs only slightly from Eq. (2.11):

$$P(z, \rho, \theta_\rho) = \frac{1}{\sqrt{2\pi A_2 B_A}} \exp\left(-\frac{A_0\rho^2 - 2A_1\rho\theta_\rho + A_2\theta_\rho^2}{2B_A}\right), \tag{2.13}$$

which is normalized with respect to $\rho\mathrm{d}\rho\mathrm{d}\theta_\rho$.

2.1.4 Secondaries

Besides the dominant Coulomb interactions with the electrons of the target, a fraction of the primaries undergo *nuclear reactions*. One distinguishes between *elastic* and *inelastic* interactions [113]. The former are the Coulomb interactions with the target nuclei, which lead to scattering but leave the primary particles unchanged in terms of energy. They have already been described in the previous section. *Inelastic* interactions, on the other hand, do not conserve the kinetic energy, can produce a large variety of secondary particles and may cause excitations to higher internal quantum states, which decay through the emission of

[1] Or alternatively by definition, combining Eqs. (2.9) and (2.12).

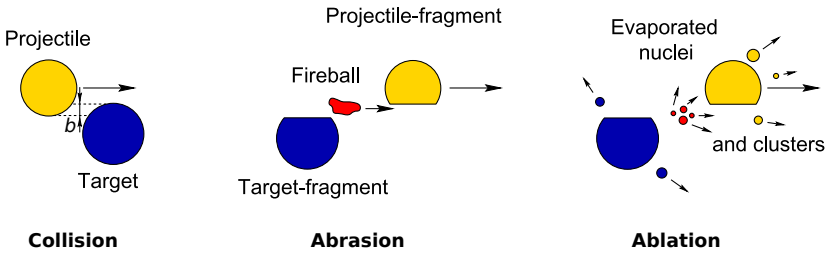

Figure 2.6: Abrasion-ablation model for nuclear interactions. Adapted from [112].

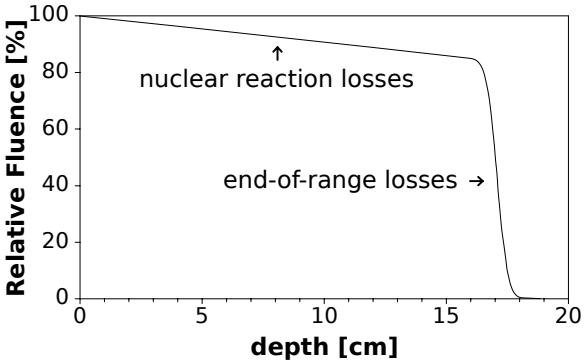

Figure 2.7: Reduction of the primary proton fluence of a 160 MeV proton beam in water. Adapted from [86].

energetic photons (gammas). The latter is depicted in Fig. 2.1 (d). One may describe such head-on collisions with the abrasion-ablation model (see Fig. 2.6). Nucleons are ripped off during the rapid abrasion stage, forming a high energetic *fireball*, which decays into stable fragments in the subsequent ablation. In the high energy regime, one may describe the nuclear interaction cross section through the Bradt–Peters formula [114]

$$\sigma_n = \pi r_0^2 \left(A_\mathrm{p}^{1/3} + A_\mathrm{t}^{1/3} - b\right), \tag{2.14}$$

where r_0 is the nucleon radius, A_p and A_r are the atomic mass numbers of the projectile and target, respectively and b is the impact parameter that quantifies the overlap between interacting nuclei, as shown in Fig. 2.6. Towards lower energies one needs to introduce corrections, which are further described in [113]. By traversing the distance $\mathrm{d}z$, the fraction $\Phi\, n\, \sigma_n \mathrm{d}z$ (n is the number density of the target) of the total fluence Φ undergoes a nuclear reactions with target. By analyzing the infinitesimal changes, one obtains an exponential law:

$$\mathrm{d}\Phi = -\Phi\, n\, \sigma_n \mathrm{d}z, \quad \Leftrightarrow \quad \Phi(z) = \Phi_0 e^{-n\sigma_n z}. \tag{2.15}$$

The reduction of fluence related to nuclear ractions is schematically shown in Fig. 2.7. The most relevant fragments with respect to the dose are secondary protons, alpha-particles ^{3}He ions, deuterium and tritium (see Fig. 2.8). The impact of heavy secondaries, such as O, N, C, B and Be, has been analyzed in [115].

As stated above, the primary protons mainly lose their kinetic energies through numerous interactions with target electrons, which are thus by far the most common secondaries. Their microscopic behavior is usually not discussed in particle therapy-related literature [13, 86] as the energy is considered to be deposited once it is transmitted to the

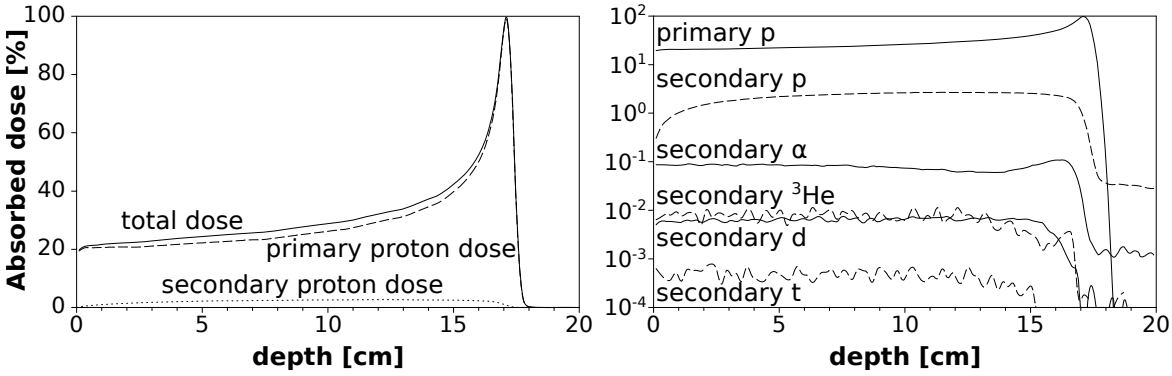

Figure 2.8: Contributions of secondary particles to the dose of a 160 MeV proton beam in water (Monte Carlo simulation). Adapted from [116].

electrons. Yet, as moving charged particles, they need to be considered for the present work, since they contribute to the total current density.

The secondary electron kinetic energy (W) distribution, after overcoming the mean ionization potential of 78 eV [117], is shown in Fig. 2.9. De Vera [118] describes it through the differential inverse mean free path, convolved (i.e. weighted) with the energy distribution of the primary protons $\mathrm{d}\Lambda^{\mathrm{conv}}_{\mathrm{ioniz}}/\mathrm{d}W$, from which they estimate the average kinetic energy of the secondary electrons in water. It slightly decreases towards the range, but can be approximated by 55 eV. This allows an estimate of the expected total number of secondary electrons per primary proton with say 100 MeV: $100\ \mathrm{MeV}/(78+55)\ \mathrm{eV} \approx 7.5 \times 10^5$. Comparable ionization numbers can also be found in an earlier work of the same author [119]. The theoretical basis that leads to the energy distribution shown in Fig. 2.9. is further described in [120–122]. What is more relevant for the present work is the directionality of the secondary electrons. It is dictated by the *binary encounter peak angle* [123]. The derivation is effectively the same as *Compton scattering* so that the energy of the secondary electron determines the polar scattering angle [124, 125]

$$\theta = \begin{cases} \mathcal{U}_{[0,\pi]} & W < 100\ \mathrm{eV} \\ \arccos\left(\sqrt{W/W_{\mathrm{m}}}\right) & W \geq 100\ \mathrm{eV} \end{cases}, \tag{2.16}$$

where $\mathcal{U}_{[a,b]}$ denotes a uniform distribution in $[a, b]$ and W_{m} has been defined in Eq. (2.2). The azimuthal ejection angle is always $\phi \in \mathcal{U}_{[0,2\pi]}$. It follows from Eq. (2.16) that the high energy electrons scatter more strongly in the forward direction. An almost perpendicular scattering angle to the primary proton path ($\theta \approx \pi/2$) occurs for low energies close to the threshold value of 100 eV. Below that, it is assumed to be entirely random.

2.1.5 Continuous slowing down approximation

The continuous slowing down approximation (CSDA) provides an idealized average estimate of the depth dependent energy of a particle in a given medium. It is calculated from first principles [126]

$$z(Q) = \int_0^{z(Q)} \mathrm{d}z' = \int_{Q_{\mathrm{in}}}^{Q} \frac{\mathrm{d}Q'}{-\mathrm{d}Q'/\mathrm{d}z'} = \int_{Q_{\mathrm{in}}}^{Q} \frac{\mathrm{d}Q'}{S(Q')}, \tag{2.17}$$

where Q_{in} is the initial energy at $z = 0$. When Eq. (2.17) is integrated down to $Q = 0$, then it can be used to calculate the range. For the work presented in Chapters 4 and 6, it

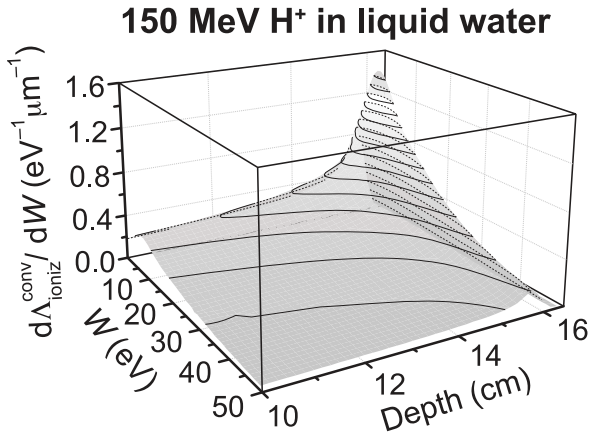

Figure 2.9: Differential inverse mean free path of the primary protons. Adapted from [118].

has been used to estimate the average path of a single point particle in water (equivalent) targets. Having the aforementioned tabulated stopping power data, Eq. (2.17) is evaluated numerically, where obtaining the inverse $Q(z)$ is particularly simple. Subsequently, this is mapped to a depth dependent velocity $v(z)$, where the connection to the kinetic energy follows from relativistic kinematics [127]

$$\beta = \frac{\sqrt{Q}\sqrt{Q+2E_0}}{Q+E_0}, \tag{2.18}$$

where $E_0 = m_0 c_0^2$ is the rest energy of the particle, which is $E_0 \approx 938.272$ MeV for protons, and m_0 is its rest mass. For $Q \ll E_0$, Eq. (2.18) reduces to the classical limit $\beta \approx \sqrt{2Q/E_0}$ or more commonly known as $v \approx \sqrt{2Q/m_0}$. A relativistic approach is nonetheless necessary, since e.g. protons with an initial energy of 150 MeV move approximately with half the speed of light. The depth dependent time is estimtated in analogy to the CSDA:

$$t(z) = \int_0^{t(z)} \mathrm{d}t' = \int_0^z \frac{\mathrm{d}z'}{\mathrm{d}z'/\mathrm{d}t'} = \int_0^z \frac{\mathrm{d}z'}{v(z')}, \tag{2.19}$$

where by definition $v = \mathrm{d}z/\mathrm{d}t$. Finally, the time-dependent particle position and velocity are obtained by another inversion: $f_z(t) \equiv z(t)$ and $\dot{f}_z(t) \equiv v(t)$. The acceleration $\ddot{f}_z(t)$ follows from $\dot{f}_z(t)$ by numerical differentiation with respect to time. For Eq. (2.17), the Geant4-based stopping power is used for the work from Chapter 4 and otherwise the stopping power from NIST. Since the former ends at 1 MeV, the velocity has been extrapolated via a Taylor expansion down to zero. The necessary coefficients were estimated numerically through the asymmetric (backwards) finite differences at the velocity that corresponds to 1 MeV. Subsequently, the position and acceleration were also extended by numerical integration and differentiation, respectively. Thereby, a perhaps unrealistic but complete proton path has been obtained with a well-defined range and a velocity of zero at the range. The proton path data with an initial energy of 150 MeV is shown in Fig. 2.10. In Fig. 2.11, the same results for the NIST data are shown, where the data has not been further extrapolated, since the stopping power data reaches down to 1 keV, which is sufficiently close to resting. Yet, the velocity is nonzero at the last time sample and thereby discontinuous. This leads to a jump in the acceleration, which has been avoided with the extrapolated Geant4 data, since the study from Chapter 4 investigates the proportionality of the electromagnetic

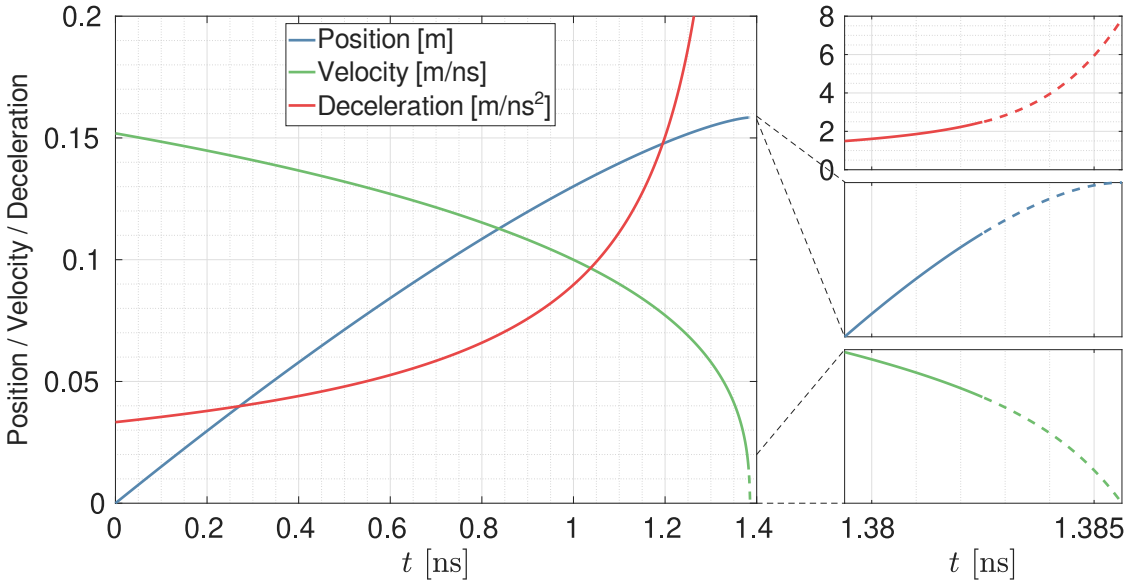

Figure 2.10: Average path of a 150 MeV proton decelerated in water, as calculated from the Geant4 stopping power. The dashed lines are the extrapolated data.

field to $\ddot{f}_z(t)$. Comparing the extrapolated deceleration from the Geant4 data, as shown in the upper right panel of Fig. 2.10, to the more accurate one based on the NIST data and depicted in the upper right panel of Fig. 2.11, good agreement in terms of magnitude can be observed. Both peak at about 8 m/ns^2. Effectively, the decrease of the stopping power beyond 0.1 MeV (see Fig. 2.2) is neglected for the path shown in Fig. 2.10. Overall, the deceleration times at clinical energies are in the nanosecond range so that electromagnetic fields in the GHz range can be expected.

2.2 Dose and dose rate

The dose D is defined as the deposited energy E per unit mass m: $D \equiv \mathrm{d}E/\mathrm{d}m$ and is measured in units of Gy $=$ J/kg. It is an important quantity in clinical practice, being prescribed by physicians to be administered to the tumor. A typical clinical dose is in the order of 60 Gy, which is usually delivered in smaller fractions of about 2 Gy. The *fractionation* helps to spare normal tissue, which regenerates faster than the tumor tissue. The definition from above is more specifically referred to as *physical dose* and is distinguished from the *effective dose*. This distinction is necessary, since different kinds of therapeutic beams (photons, electrons, protons, carbon ions etc.) have a different biological effect, i.e. a given amount of physical dose does not lead to the same amount of cell death when administered with for instance photons versus protons. To compensate for the differences, one introduces the *relative biological effectiveness (RBE)* as the ratio between a reference dose (from photons or electrons) to the dose from a different species (e.g. protons) that achieves the same effect (isoeffectiveness) [128]. In clinical practice, one usually assumes RBE $= 1.1$ for protons, which means that one delivers about 10% less physical dose, when treating with protons over photons. This higher effectiveness is explained by the higher *linear energy transfer (LET)*. Protons deposit their energy in a small volume around the proton track, which increases the chances of cell death through double strand breaks. Replacing the constant value of 1.1 by a more accurate *variable RBE* is also under investigation [129]. A rough

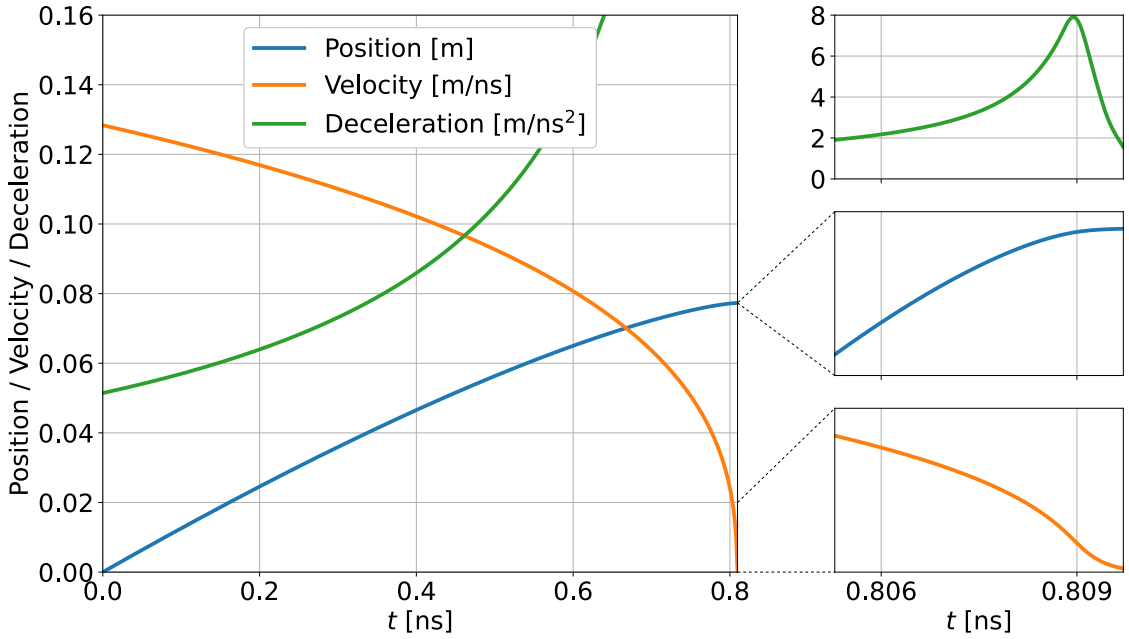

Figure 2.11: Average path of a 100 MeV proton decelerated in water, as calculated from the NIST stopping power data.

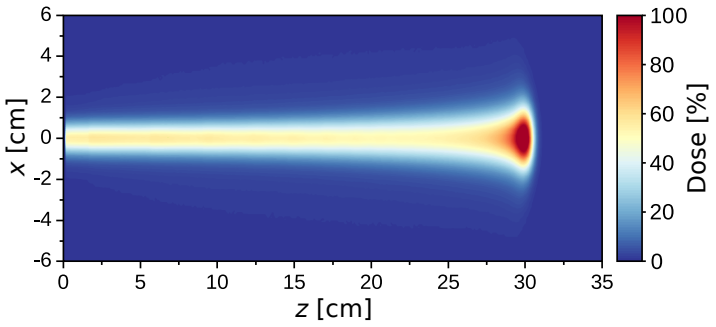

Figure 2.12: Dose distribution of a 220 MeV proton pencil beam in water. Adapted from [130].

approximation of the dose of a proton pencil beam is sought for the present work, hence it will suffice to focus on the physical dose in the following. By replacing the mass m through the density $\varrho = m/V$, where V is the volume, and the deposited energy by the stopping power S, one can represent the definition of the dose as [13]

$$D = \Phi_A \, S/\varrho, \tag{2.20}$$

where $\Phi_A = \mathrm{d}N/\mathrm{d}A$ is the proton fluence, i.e. the number of particles N flowing perpendicularly through the unit area A. Since $S \propto n_\mathrm{e} \propto \varrho$ (see Eq. (2.1)), one refers to S/ϱ as the *mass stopping power*. The proportionality to the stopping power explains the Bragg peak (see Fig. 1.1). Since it increases towards the range, so does the dose. An exemplary dose profile of a proton beam in water is shown in Fig. 2.12. By differentiating Eq. (2.20) with respect to time, one obtains the *dose rate* $\dot{D} \equiv \mathrm{d}D/\mathrm{d}t$. With the current given as $I = q_\mathrm{e}\Phi$, where $\Phi = \mathrm{d}N/\mathrm{d}t$ is the particle rate, and the longitudinal current density defined as $J = \mathrm{d}I/\mathrm{d}A$, one gets $\dot{D} = J/q_\mathrm{e} \; S/\varrho$. One may well approximate the initial lateral current

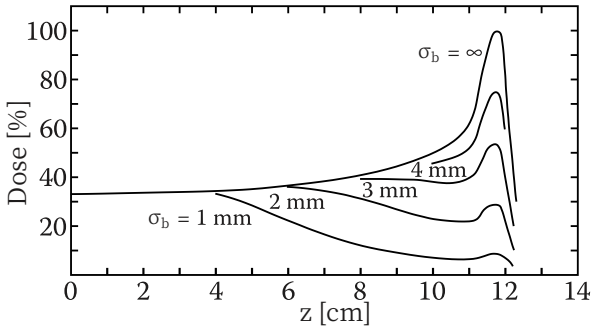

Figure 2.13: Dose on the central beam axis of a proton beam in water with a range of about 12 cm. Towards small spot sizes σ_b, lateral scattering causes deviations from the expected Bragg peak. Adapted from [86].

density profile of a proton pencil beam through a normal distribution:

$$J_{\text{in}}(x,y) = I/(2\pi\sigma_b^2)\exp\left[-(x^2+y^2)/(2\sigma_b^2)\right], \tag{2.21}$$

where σ_b is the beam spot size. J_{in} is normalized such that when laterally integrated, it yields the beam current I. The stopping power of the initial energy is necessary to estimate the dose rate at the entrance region. For $Q_{\text{in}} = 100$ MeV and water as the target, one has $S \approx 7.28$ MeV/cm (see Fig. 2.2). Along the central beam axis $(x, y = 0)$, the dose rate of a pencil beam in water ($\varrho \approx 1$ g/cm^3) at the entrance region is

$$\dot{D}_{\text{in}}[\text{Gy/s}] \approx 1.16\frac{I\ [\text{nA}]}{(\sigma_b\ [\text{cm}])^2}. \tag{2.22}$$

To obtain the dose at the Bragg peak from the entrance dose, Gottschalk [13] adds a scaling factor of $f_{\text{BP}} \approx 3.5$. The energy modulation necessary for larger longitudinal fields (spread-out Bragg peak) diminishes the ratio between entrance and target dose, described by another scaling factor $f_{\text{MOD}} < 1$. In addition, lateral scattering distributes the energy over a wider range, which also reduces the dose (see Fig. 2.13). These corrections are all of order one and approximately cancel, so that the entrance dose is considered a reasonable estimate of a proton pencil beam dose.

To deliver the dose within a reasonable time, a standard requirement for the accelerator is to administer a dose of 2 Gy to a volume of one liter ($10 \times 10 \times 10$ cm^3) within one minute [131]. With Eq. (2.22), one may confirm that the necessary beam current lies in the order of 0.1 nA. In 2014, Favaudon et al. [132] reported less damage to healthy tissues in mice experiments with an equal effectiveness against tumor cells after irradiation with ultra high dose rates. They coined the term FLASH for dose rates above 40 Gy/s, which is orders of magnitude larger than the conventional approach described above (≤ 0.03 Gy/s). Their findings have gained considerable interest in the scientific community, ranging from further confirmations of the FLASH effect [133–135], general debates [136,137], discussions regarding technical challenges and safety towards clinical applicability [138,139], to the first patient being treated with FLASH radiotherapy [140], only five years after its suggestion. In addition, a dedicated conference[2] is held since 2021. For particle therapy, average beam currents above 300 nA are necessary [141], which is within the capabilities of some accelerators

[2]Flash Radiotherapy & Particle Therapy Conference: `https://frpt-conference.org/`.

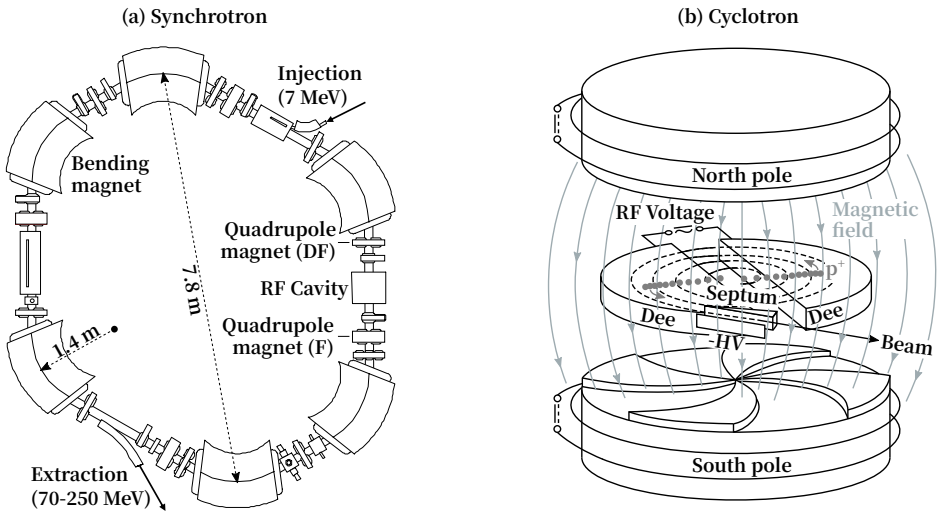

Figure 2.14: Comparison of clinical particle accelerators. (a) shows the synchrotron that has been designed by Hitachi for the *MD Anderson Cancer Center*. The main components have been labeled, including the focusing (F) and defocusing (DF) magnets. The remaining ones are described in [143], from where the sketch has been adapted. (b) is an "exploded" view containing the main constituents of a cyclotron. It has been adapted from [144].

(see Sec. 2.3). For the present work, delivery with FLASH dose rates is of particular interest, since the magnetic field, being the basis of the investigated range verification approach, scales with the beam current.

2.3 Particle accelerators

For the analytical calculations and the Monte Carlo-based simulations below, beam pulse parameters based on clinical particle accelerators were chosen. In the following, some basic characteristics of the three most commonly used accelerators are described: synchrotrons, cyclotrons and synchrocyclotrons. Out of the 119 proton therapy centers currently in operation (as of August 2022 [9]), 45 use synchrotrons, 60 cyclotrons and 15 synchrocyclotrons[3]. In addition, there are another 69 facilities under construction or in planning, which will operate with 18, 40 and 11 of the same accelerator types, respectively. Only a brief overview will be presented, while for instance Paganetti [13] or Humphries [142] offer more detailed descriptions. The following begins with the synchrotron, which was built for the first hospital-based proton therapy facility, i.e. the Loma Linda Medical Center, which started operation in 1992.

2.3.1 Synchrotrons

A synchrotron (see Fig. 2.14 (a)) keeps protons on a circular orbit through bending magnets and focused via quadrupole magnets. In each turn they pass through an RF acceleration device, which gradually increases their energy. This process takes about half a second, during which the protons travel approximately 10^6 times around the ring. To maintain the ions on a constant radius, one needs to increase the strength of the bending magnets *synchronously*, hence the name. The same goes for the RF frequency, which needs to be adjusted to the

[3]The Institut Méditerranéen De ProtonThérapie (IMPT) in Nice has both a cyclotron and a synchrocyclotron.

increasing revolution frequency (1-10 MHz). Protons can only be accelerated at a specific phase of the RF cavity, which is why they travel in batches. Generally, the operation of a synchrotron runs in cycles, lasting a couple of seconds in total. 10^{10}-10^{11} protons from an ion source[4] are pre-accelerated by linear accelerators to approximately 2-7 MeV and subsequently injected into the ring. They are then accelerated to the desired energy (70-250 MeV) and afterwards gradually extracted (over 0.5-5 seconds). One may choose a different energy for each cycle, yet the process lasts too long for the energy modulation necessary for proton therapy. The energy is then further modulated at the nozzle (through e.g. modulator wheels or ridge filters) to adjust the range, while the synchrotron energy is only adjusted for different angles. Advantages of synchrotrons are the energy flexibility, smaller energy spread, lower power consumption compared to the cyclotron, little creation of radioactivity due to beam losses and that low energy protons have the same intensity as higher energies, since one does not require up-stream degraders. They are currently also the only option for heaver ions, such as carbon ions. Disadvantages are the pulsed operation and that they are comparatively large (6-8 meters). The numbers given above show that cyclotrons and synchrocyclotrons are more frequently used. Their principle will be shown in the following.

2.3.2 Isochronous cyclotrons

Instead of traveling with a fixed radius, protons in cyclotrons (see Fig. 2.14 (b)) are accelerated within an external magnetic field, so that they spiral outwards while gaining energy through an RF system. The ion source sits in the center and creates protons by ionizing hydrogen gas through energetic electrons. They are picked up by the closest electrode ("puller") of the RF system, which accelerates them with two to four electrodes[5]. They are driven by a strong RF (50-100 MHz) voltage between 30 and 100 kV with currents in the kiloampere range, requiring good vacuum and cooling. The acceleration is consequently rather rapid compared to synchrotrons. For instance, a four-electrode RF operated at 60 kV yields a gain of approximately 0.48 MeV per turn so that it only takes about 530 turns to arrive at the maximum energy of 250 MeV. Having reached the outer edge of the magnet, they are extracted through a so-called *septum* and an opposing electrode to be further guided to the beam transport system. They cannot be extracted at a lower radius so that a cyclotron creates a fixed energy, which requires degrading to the desired energy. Strong magnetic fields[6] (2-3.5 T) are necessary with pole radii below one meter. A cyclotron is referred to as *isochronous* if the magnetic field is adjusted to maintain a constant period duration for each radius. To account for relativistic effects, one needs to increase the field strength for larger radii, which creates a vertical instability. A spiral-shaped hill and valley pattern on the poles reestablishes the focus, as shown in Fig. 2.14 (b). Even though it is pulsed at the RF frequency, the beam of a cyclotron is considered CW (continuous wave), which is one major advantage. The relatively simple and compact design (3.5-5 m radius; single room installation) contributes to its popularity. More detailed descriptions regarding medical cyclotrons can be found in [144,145].

2.3.3 Synchrocyclotrons

A synchrocyclotron is a special type of cyclotron. The setup is mostly the same as the one shown in Fig. 2.14 (b). As the name suggests, a synchronization differentiates it from a

[4] Ionized for instance by microwaves.

[5] The electrodes were shaped like the letter "D" in early designs, hence the name *Dees*.

[6] Modern cyclotrons use superconducting coils.

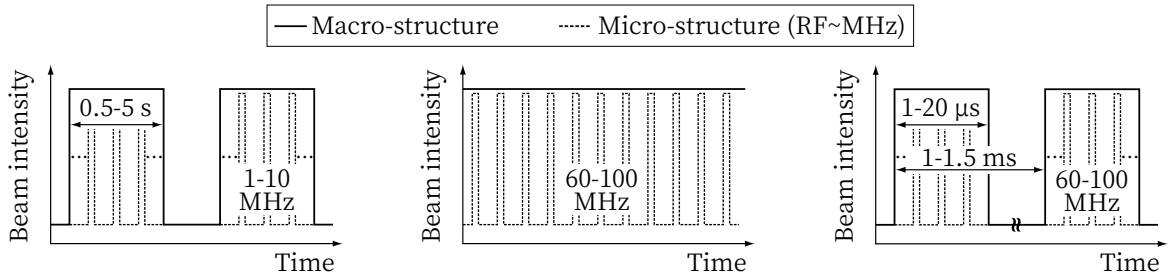

(a) Synchrotron (~0.5 Hz) (b) Cyclotron (CW) (c) Synchrocyclotron (~1 kHz)

Figure 2.15: Macro- and micro-pulse structure of the accelerator types discussed in Sec. 2.3. The frequency range of the macroscopic structure is given in the parenthesis. In addition, the given RF frequencies (microscopic structure of the beam) correspond to the following time structure: (a) 25-200 ns and (b) & (c) 1-3 ns.

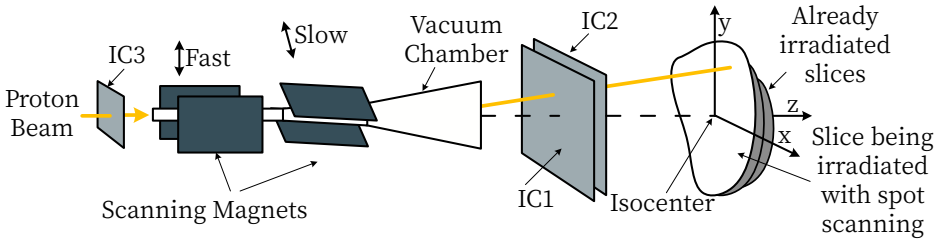

Figure 2.16: Pencil beam scanning in particle therapy (IC: Ionization chamber). Adapted from [152].

isochronous cyclotron. In particular, instead of increasing the magnetic field towards larger radii, one modulates the RF frequency *synchronously* to the increasing mass. The beam is consequently pulsed (lasting few microseconds), where repetition rates of about 1 kHz are achievable. For the present work, a synchrocyclotron, such as IBA's superconducting synchrocyclotron (S2C2) [146], serves as a guideline regarding the chosen beam pulse parameters. Its maximum average beam current and pulse duration vary in the literature between ∼20-200 nA [141,146,147] and 7-10 µs [146,148,149]. The maximum possible peak beam current of 18 µA is given in [141]. The large difference between the average and peak beam current is due to the low duty cycle in the order of 1%. The macro- and micro-pulse structure of the previously discussed accelerators were visually summarized in Fig. 2.15. Feasibility studies of particle based FLASH radiotherapy also provide good summaries of accelerator parameters [139,150,151]. Generally, the RF-based acceleration of all three accelerator types imposes a micro-pulsing of the same frequency. For the cyclotron, this leads to the particles of different energies being concentrated on radial lines having the same phase, as indicated in Fig. 2.14. This substructure is somewhat slower (lower frequency) for synchrotrons compared to cyclotrons or synchrocyclotrons due to their larger particle orbits.

2.4 Dose delivery

The results presented in Chapters 4 to 6 focus on a single proton pencil beam, which entails that a dose delivery through pencil beam scanning, as shown in Fig. 2.16. To administer the dose to the three-dimensional target, one first subdivides the volume into slices along

the beam line and adjusts the particle energy necessary to reach each depth. A pair of scanning magnets then deflects the collimated proton pencil beam to scan across the two-dimensional plane. This is done using either a "'step-and-shoot" method or a continuous beam with raster scanning. For the latter, one can either vary the beam intensity or the scanning speed. Further details are provided in [13], together with the passive scattering technique, which is not considered here.

3 ELECTROMAGNETIC THEORY

The electromagnetic theory plays a major role for the entire thesis, seeking to investigate the electric and magnetic field of a proton pencil beam in water and various other biological tissues. In particular, the results from this work are based on the *classical theory* described by the *Maxwell's equations*. A quantum mechanical description will not be necessary, as the investigated dimensions are guided by the size and range of standard clinical proton beams. Nonetheless, charge quantization is oftentimes considered, relying on solutions of the Maxwell equations for point particle charge and current densities. This chapter primarily covers some well established basics (Maxwell equations, interface conditions, point particle charge and current density), some specific topics (permittivity & conductivity model of biological tissues) and also techniques that have been developed or adjusted for the present work and have been published as supplementary materials (convolutional superposition, finite element analysis for a cylindrical geometry).

As widely established, vectorial quantities are printed **bold**, scalar quantities in *italics* and matrices are underlined. The real and imaginary parts of a complex quantity c are denoted with prime and double prime, if not stated otherwise: $c = c' + ic''$, where $c', c'' \in \mathbb{R}$. Partial derivatives are occasionally abbreviated as $\partial/\partial t \rightarrow \partial_t$.

3.1 Maxwell equations

Central to the entire thesis are the four macroscopic Maxwell equations. Given the free charge and current density ρ_f and $\mathbf{J}_\mathrm{f}$, they govern the electromagnetic fields [153]:

$$\nabla \cdot \mathbf{D} = \rho_\mathrm{f}, \qquad \text{(Gauß' law)} \tag{3.1a}$$

$$\nabla \cdot \mathbf{B} = 0, \qquad \text{(Gauß' law for magnetism)} \tag{3.1b}$$

$$\nabla \times \mathbf{E} = -\frac{\partial}{\partial t}\mathbf{B}, \qquad \text{(Maxwell-Faraday equation)} \tag{3.1c}$$

$$\nabla \times \mathbf{H} = \mathbf{J}_\mathrm{f} + \frac{\partial}{\partial t}\mathbf{D}, \qquad \text{(Ampère's circuital law)} \tag{3.1d}$$

where $\mathbf{E}$ and $\mathbf{B}$ are the electric field and magnetic flux density[1], while $\mathbf{D}$ and $\mathbf{H}$ are the electric displacement field and the magnetic field strength. The latter are related to the former through the so-called *constitutive relations*:

$$\mathbf{D}(\mathbf{r}, t) = \int_{-\infty}^{\infty} \varepsilon(t - t')\mathbf{E}(\mathbf{r}, t')\mathrm{d}t' = \varepsilon(t) * \mathbf{E}(\mathbf{r}, t), \tag{3.2}$$

$$\mathbf{H}(\mathbf{r}, t) = \mathbf{B}(\mathbf{r}, t)/\mu, \tag{3.3}$$

[1] Throughout this work, $\mathbf{B}$ is referred to as the *magnetic field* instead of *magnetic flux density*.

where ε is the permittivity and μ is the permeability. Some underlying assumptions have already simplified Eqs. (3.2) and (3.3), which could grow to arbitrary complexity when modeling non-linear effects in an anisotropic medium and a non-local response [154] (generally: $\mathbf{D} = \mathbf{D}(\mathbf{E}, \mathbf{B})$ and $\mathbf{H} = \mathbf{H}(\mathbf{E}, \mathbf{B})$). The latter requires power expansions with respect to the fields and a tensor representation of the permittivity and permeability. This will be neglected, considering only weak electromagnetic fields in biological tissues. Yet, in Eq. (3.2) a time-delayed response has been allowed for, i.e. that the displacement field at time t can be influenced by the electric field from $t' \leq t$. This is modeled through a convolutional law in the time domain. With the integral ranging across $\mathbb{R}$, one needs to ensure that $\varepsilon(t < 0) = 0$, otherwise the electric field "from the future" could influence the present displacement field, which would break the causality. Eq. (3.3) could also be stated as a convolutional law. For this purpose, one introduces the magnetization $\mathbf{M}$ as $\mathbf{H} = \mathbf{B}/\mu_0 - \mathbf{M}$ and $\mathbf{M}(\mathbf{r}, t) = \chi_\mathrm{m}(t) * \mathbf{H}(\mathbf{r}, t)$, where μ_0 is the vacuum permeability and χ_m is the magnetic susceptibility. In the time-independent case, the latter is also defined through the material dependent permeability $\mu = \mu_0(1 + \chi_\mathrm{m})$. Magnetic susceptibility effects in biological tissues are generally small, but can lead to minor distortions in MRI imaging [155]. Therein, the magnetic susceptibility is quantified as $|\chi_\mathrm{m}| \simeq 10^{-5}$, which is why it is entirely neglected throughout this work.

The Maxwell equations together with the constitutive relations form a complex set of differential equations. It is considerably simpler (if not the only option with a complex permittivity model ε) to solve them in the Fourier domain. Throughout this work, both the Fourier transform with respect to time ($t \to \omega$, where ω is the angular frequency) and the Fourier transform with respect to time and space ($(\mathbf{r}, t) \to (\mathbf{k}, \omega)$, where $\mathbf{k} = (k_x, k_y, k_z)^\mathrm{T}$ are the spatial frequencies) are considered. With the Fourier transform defined in Eqs. (A.1a) and (A.1b) and the transforms of the derivatives from Eqs. (A.2a) to (A.2c), Eqs. (3.1a) to (3.1d) transform to

$$\nabla \cdot \widetilde{\mathbf{D}} = \tilde{\rho}_\mathrm{f}, \tag{3.4a}$$
$$\nabla \cdot \widetilde{\mathbf{B}} = 0, \tag{3.4b}$$
$$\nabla \times \widetilde{\mathbf{E}} = -i\omega\widetilde{\mathbf{B}}, \tag{3.4c}$$
$$\nabla \times \widetilde{\mathbf{H}} = \tilde{\mathbf{J}}_\mathrm{f} + i\omega\widetilde{\mathbf{D}}, \tag{3.4d}$$

$$-i\mathbf{k} \cdot \widetilde{\widetilde{\mathbf{D}}} = \tilde{\tilde{\rho}}_\mathrm{f}, \tag{3.5a}$$
$$-i\mathbf{k} \cdot \widetilde{\widetilde{\mathbf{B}}} = 0, \tag{3.5b}$$
$$-i\mathbf{k} \times \widetilde{\widetilde{\mathbf{E}}} = -i\omega\widetilde{\widetilde{\mathbf{B}}}, \tag{3.5c}$$
$$-i\mathbf{k} \times \widetilde{\widetilde{\mathbf{H}}} = \tilde{\tilde{\mathbf{J}}}_\mathrm{f} + i\omega\widetilde{\widetilde{\mathbf{D}}}. \tag{3.5d}$$

The following notation will be used throughout this work: scalar and vector quantities that are only time-wise Fourier transformed are accented with a single tilde $\widetilde{(\circ)}$, while the four-dimensional Fourier transform with respect to space and time is denoted with a double tilde $\widetilde{\widetilde{(\circ)}}$. One major motivation to work with the Fourier domain is that Eq. (3.2) turns multiplicative:

$$\widetilde{\mathbf{D}}(\mathbf{r}, \omega) = 2\pi\hat{\tilde{\varepsilon}}(\omega)\widetilde{\mathbf{E}}(\mathbf{r}, \omega) \equiv \tilde{\varepsilon}(\omega)\mathbf{E}(\mathbf{r}, \omega), \tag{3.6}$$

where the factor of 2π from Eq. (A.5) has been collected within $\tilde{\varepsilon}$. In the simplest case $\varepsilon(t) = \varepsilon_0\delta(t)$, where Eq. (3.2) simplifies to $\mathbf{D}(\mathbf{r}, t) = \varepsilon_0\mathbf{E}(\mathbf{r}, t)$ so that its Fourier transform should be $\widetilde{\mathbf{D}}(\mathbf{r}, \omega) = \varepsilon_0\widetilde{\mathbf{E}}(\mathbf{r}, \omega)$. It follows from Eq. (A.1a) that for this example $\hat{\tilde{\varepsilon}}(\omega) = \varepsilon_0/2\pi$ so that Eq. (3.6) is consistent. Yet $\tilde{\varepsilon}(\omega) = \varepsilon_0$ is simpler and more natural and will therefore be used throughout this thesis.

An important yet implicit consequence of the Maxwell equations is the continuity equation. It follows by taking the divergence of Eq. (3.1d) in combination with Eq. (3.1a):

$$\nabla \cdot \mathbf{J}_\mathrm{f} + \frac{\partial}{\partial t}\rho_\mathrm{f} = 0, \tag{3.7}$$
$$\nabla \cdot \tilde{\mathbf{J}}_\mathrm{f} + i\omega\tilde{\rho}_\mathrm{f} = 0. \tag{3.8}$$

The Maxwell equations can simplify under certain conditions through the introduction of the scalar potential φ and the vector potential $\mathbf{A}$. Since, according to Eq. (3.1b), the divergence of the magnetic field vanishes, it can be represented through the curl of the vector potential. Regarding the electric field, the vector potential representation of the magnetic field in combination with Faraday's law (Eq. (3.1c)) leads to $\nabla \times (\mathbf{E} + \partial_t \mathbf{A}) = 0$. Consequently, $\mathbf{E} + \partial_t \mathbf{A}$ is *irrotational* so, according to the Helmholtz decomposition, it can be represented by a gradient field: $\mathbf{E} + \partial_t \mathbf{A} = -\nabla\varphi$ [156]. Altogether, the electric and magnetic field are then related to the scalar and vector potential through

$$\mathbf{E} = -\nabla\varphi - \frac{\partial}{\partial t}\mathbf{A}, \tag{3.9}$$

$$\mathbf{B} = \nabla \times \mathbf{A}. \tag{3.10}$$

Eqs. (3.9) and (3.10) satisfy Eqs. (3.1b) and (3.1c) by definition and in combination with Eqs. (3.1a) and (3.1d) lead to two (coupled) equations for the scalar and vector potential. However, since the laws for $\mathbf{E}$ and $\mathbf{B}$ remain unchanged under the associated gauge transformations, one may simplify the equations for φ and $\mathbf{A}$ by fixing the gauge appropriately. Due to the convolutional law from Eq. (3.2), the following is easier stated in the Fourier domain with respect to time, where Eqs. (3.9) and (3.10) become

$$\widetilde{\mathbf{E}} = -\nabla\widetilde{\varphi} - i\omega\widetilde{\mathbf{A}}, \tag{3.11}$$

$$\widetilde{\mathbf{B}} = \nabla \times \widetilde{\mathbf{A}}. \tag{3.12}$$

A common choice is the Lorenz gauge ($\nabla \cdot \mathbf{A} + \mu_0\varepsilon_0\partial_t\varphi = 0$), which decouples the equations for the scalar and vector potential for a homogeneous and non-dispersive medium. The same holds true for a dispersive medium, if one adds the convolutional permittivity law from Eq. (3.2) to the gauge, which is again a product in the Fourier domain:

$$\nabla \cdot \widetilde{\mathbf{A}} + i\omega\mu\tilde{\varepsilon}\widetilde{\varphi} = 0. \tag{3.13}$$

Using Eq. (3.13), Gauss's law (Eq. (3.4a)) and Ampère's circuital law (Eq. (3.4d)) simplify to decoupled wave equations for both the scalar and vector potential

$$[\nabla^2 + \omega^2\mu\tilde{\varepsilon}(\omega)]\widetilde{\varphi} = -\tilde{\rho}_\mathrm{f}/\tilde{\varepsilon}(\omega), \tag{3.14}$$

$$[\nabla^2 + \omega^2\mu\tilde{\varepsilon}(\omega)]\widetilde{\mathbf{A}} = -\mu\tilde{\mathbf{J}}_\mathrm{f}. \tag{3.15}$$

In classical electromagnetic theory, the flow of energy is described by the Poynting theorem. By introducing the Poynting vector $\mathbf{S} = \mathbf{E} \times \mathbf{H}$ and the energy density $u = (\mathbf{E} \cdot \mathbf{D} + \mathbf{B} \cdot \mathbf{H})/2$ one can derive the Poynting theorem from the Maxwell equations

$$\nabla \cdot \mathbf{S} = -\Bigg(\underbrace{\mathbf{E} \cdot \frac{\partial \mathbf{D}}{\partial t} + \mathbf{H} \cdot \frac{\partial \mathbf{B}}{\partial t}}_{\partial u / \partial t}\Bigg) - \mathbf{E} \cdot \mathbf{J}_\mathrm{f}. \tag{3.16}$$

3.2 Electromagnetic tissue response

The target's electromagnetic properties have a major impact on the fields. How they are taken into account and modeled is described in the following.

3.2.1 Polarization and bound charge and current density

While the magnetization $\mathbf{M}$ has already been introduced and simultaneously neglected due to the low magnetic susceptibility of biological tissues, the same cannot be stated for the polarization $\mathbf{P}$ and the electric susceptibility χ_e, which is discussed in this section.

For simplicity and since the corresponding bound charge will only be used for heuristic arguments, a homogeneous domain will be considered, i.e. $\varepsilon(\mathbf{r}) = \varepsilon$. Also, the following discussion simplifies in the temporal frequency domain due to the convolutional law from Eq. (3.2). Formally, the polarization is introduced as

$$\widetilde{\mathbf{D}}(\mathbf{r},\omega) = \varepsilon_0\widetilde{\mathbf{E}}(\mathbf{r},\omega) + \widetilde{\mathbf{P}}(\mathbf{r},\omega), \tag{3.17}$$

where ε_0 is the vacuum permittivity. In a linear and isotropic medium, the polarization is proportional to the electric field

$$\widetilde{\mathbf{P}}(\mathbf{r},\omega) = \varepsilon_0\widetilde{\chi}_\mathrm{e}(\omega)\widetilde{\mathbf{E}}(\mathbf{r},\omega), \tag{3.18}$$

$$\tilde{\varepsilon}(\omega) = \varepsilon_0(\underbrace{1+\widetilde{\chi}_\mathrm{e}(\omega)}_{\tilde{\varepsilon}_\mathrm{r}(\omega)}), \tag{3.19}$$

where Eq. (3.19) follows from the consistency between Eqs. (3.6) and (3.17) and also the relative permittivity $\tilde{\varepsilon}_\mathrm{r} = \tilde{\varepsilon}/\varepsilon_0$ has been introduced. By letting $\widetilde{\chi}_\mathrm{e} \to 0$, where $\widetilde{\chi}_\mathrm{m} = 0$ has already been assumed, the Maxwell equations simplify so the so-called *microscopic* Maxwell equations or the Maxwell equations in vacuum. If one holds on to the then simplified constitutive relation (now $\widetilde{\chi}_\mathrm{e} \neq 0$) without collecting the polarization within the permittivity, then the polarization gives rise to what can be interpreted as bound charge. In particular, Eq. (3.4a) in combination with Eq. (3.17) can be rearranged to $\nabla\cdot(\varepsilon_0\widetilde{\mathbf{E}}) = \tilde{\rho}_\mathrm{f} - \nabla\cdot\widetilde{\mathbf{P}}$, where $\tilde{\rho}_\mathrm{b} = -\nabla\cdot\widetilde{\mathbf{P}}$ is the sought bound charge. As Eq. (3.7) only covers the free charge and current density, an associated bound current must be introduced. This time, it follows from Eq. (3.4d) together with Eq. (3.17): $\tilde{\mathbf{J}}_\mathrm{b} = i\omega\widetilde{\mathbf{P}}$. Keep in mind that $\chi_\mathrm{m} = 0$ has been set, otherwise $\tilde{\mathbf{J}}_\mathrm{b}$ would have an additional term related to the magnetization. By definition, the bound charge and current density satisfy a separate continuity equation: $\nabla\cdot\tilde{\mathbf{J}}_\mathrm{b} + i\omega\tilde{\rho}_\mathrm{b} = 0$. Finally, since the displacement field can be expressed through the polarization (by combining Eqs. (3.17) and (3.18)) and its divergence is the bound charge, while the divergence of the displacement field is the free charge (Eq. (3.4a)), one may express the bound charge through the free charge:

$$\tilde{\rho}_\mathrm{b}(\mathbf{r},\omega) = -\frac{\widetilde{\chi}_\mathrm{e}(\omega)}{1+\widetilde{\chi}_\mathrm{e}(\omega)}\tilde{\rho}_\mathrm{f}(\mathbf{r},\omega). \tag{3.20}$$

Recall that this only holds in a homogeneous environment, i.e. $\widetilde{\chi}_\mathrm{e}(\mathbf{r},\omega) = \widetilde{\chi}_\mathrm{e}(\omega)$.

3.2.2 Permittivity

A convolutional time-dependent permittivity is associated with a frequency-dependent permittivity model. This frequency dependence is known as *dispersion* [157], where also the refractive index depends on the frequency. For convenience, the relative permittivity to the vacuum permittivity $\varepsilon_\mathrm{r}(t) = \varepsilon(t)/\varepsilon_0$ is discussed. One of the simplest, yet non-trivial permittivity models is the Debye model [158]. It assumes an exponential relaxation with a half-life of $\tau\log 2$:

$$\varepsilon_\mathrm{r}(t) = \varepsilon_\infty\delta(t) + (\varepsilon_s - \varepsilon_\infty)\exp(-t/\tau)/\tau\;\theta(t). \tag{3.21}$$

The instantaneous response for high frequencies is given by ε_∞, while the permittivity settles to the static value ε_s for constant (DC) fields. In the Fourier domain, the Debye model becomes

$$\tilde{\varepsilon}_\mathrm{r}(\omega) = \varepsilon_\infty + \frac{\Delta\varepsilon}{1+i\omega\tau} = \Bigg(\underbrace{\varepsilon_\infty + \frac{\Delta\varepsilon}{1+\omega^2\tau^2}}_{\varepsilon'_\mathrm{r}}\Bigg) + i\Bigg(\underbrace{-\frac{\omega\tau\,\Delta\varepsilon}{1+\omega^2\tau^2}}_{\varepsilon''_\mathrm{r}}\Bigg), \tag{3.22}$$

Table 3.1: Parameters for the Cole-Cole model from Eq. (3.23) taken from Sasaki. et al. [165]. The resonance angular frequencies $\omega_j = 2\pi f_j$ are originally given as frequencies f_j and have been rescaled. The parameters for water are taken from [159] ($\omega_1 = 1/\tau$).

	ε_∞	ω_1 [GHz]	$\Delta\varepsilon_1$	α_1	ω_2 [MHz]	$\Delta\varepsilon_2$	α_2	σ_{DC} [S/m]
Muscle (Parallel)	3.91	113.1	55.0	0.165	4.90	663	0.387	0.633
Gray matter	12.7	117.5	32.2	0.075	14.8	1170	0.315	0.173
Liver	4.52	106.2	36.8	0.107	7.04	2550	0.219	0.140
Lung (Inflated)	4.44	101.2	14.6	0.001	20.2	646	0.181	.0842
Fat	2.32	126.3	2.14	0.002	51.8	19.7	0.259	.0222
Water (37°)	4.0	161.3	70.1	0.000	-	-	-	-

where $\Delta\varepsilon = \varepsilon_s - \varepsilon_\infty$ and it has been separated into its real part $\varepsilon'_{\mathrm{r}}$ and imaginary part $\varepsilon''_{\mathrm{r}}$. Eq. (3.22) reduces to ε_s for $\omega \to 0$ and ε_∞ for $\omega \to \infty$ so that its real part follows a step-like shape (in a logarithmic plot), smoothly changing from ε_s to ε_∞ at $\omega_1 = 1/\tau$. Its imaginary part, on the other hand, peaks at ω_1. Despite its strongly simplifying assumptions, it can be used to model water, where $\tau = 6.2$ ps, $\varepsilon_s = 74.1$ and $\varepsilon_\infty = 4$ [159]. A better description over a wider frequency range can still be achieved with the same model and multiple resonances [160]. The Debye model forms the basis for more sophisticated permittivity models by simple analytical modifications. For instance the Havriliak–Negami relaxation, Cole–Davidson equation or the Cole-Cole model are commonly used [161]. For biological tissues, Gabriel et al. have determined parameters for the latter with multiple resonance frequencies ω_j in an extensive three-paper series [159, 162, 163]:

$$\tilde{\varepsilon}_{\mathrm{r}}(\omega) = \varepsilon_\infty + \sum_{j=1}^{n} \frac{\Delta\varepsilon_j}{1 + (i\omega/\omega_j)^{1-\alpha_j}}. \tag{3.23}$$

where $\Delta\varepsilon_1 = \varepsilon_1 - \varepsilon_\infty$, $\Delta\varepsilon_j = \varepsilon_j - \varepsilon_{j-1}$ for $1 < j < n$ and $\Delta\varepsilon_n = \varepsilon_s - \varepsilon_{n-1}$ for $n > 1$. Starting from ε_∞ at $\omega \to \infty$, the real part of the permittivity rises at each ω_j by $\Delta\varepsilon_j$. The value at $\omega \to 0$ is still ε_s. The newly introduced parameter α_j controls the width or steepness of the steps.

For frequencies below 1 THz, one may identify three major dispersions for soft tissues: α ($\sim$ kHz), β ($\sim$ 10 MHz) and γ ($\sim$ 100 GHz), given as angular frequencies. The first two are attributed to ionic diffusion processes and capacitive charging of cellular membranes [164]. The third one has probably the simplest explanation, as it is related to the molecular dipole structure of water. Gabriel et al. adds a fourth dispersion at around 10 Hz. Throughout this work, fast processes based on the high energy proton kinematics are studied, with their stopping times in the nanosecond range. Just like the work of Albert et al. [85], only the β and γ resonances ($n = 2$ in Eq. (3.23)) are therefore included. Regarding the latter, more recent measurements were carried out by Sasaki et al. [165]. Their results for a few select tissues are collected in Table 3.1 and have been used to plot Eq. (3.23) in Fig. 3.1 (a). Accordingly, Eq. (3.23) is valid between 1 MHz and up to hundreds of GHz, where also the majority of the energy in the frequency domain is contained. Also, towards visible frequencies, Eq. (3.22) for water does not apply anymore, as it does not model its transparency.

While the Cole-Cole model is a simple algebraic modification of the Debye model in the Fourier domain (adding the power α_j), its time domain behavior does not have a simple description. To study its behavior in the time domain, one may introduce the Mittag-Leffler

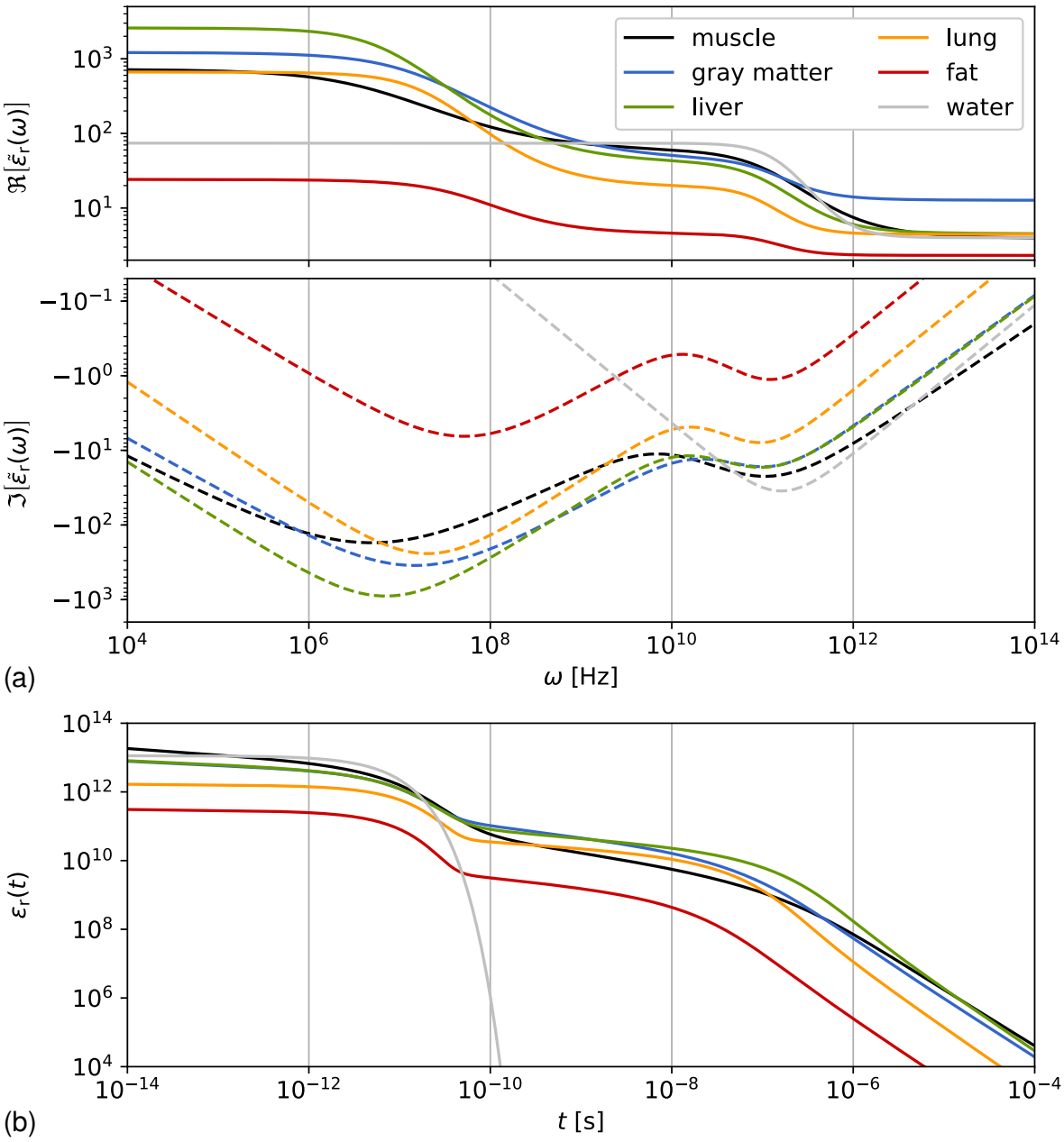

Figure 3.1: Relative permittivity of various biological tissues and water as described through the Cole-Cole model from Eq. (3.23) with the parameters listed in Table 3.1. (a) shows the real and imaginary part of the relative permittivity in the frequency domain, while (b) shows the same in the time domain. Eq. (3.25) has been used for the latter. Note that it does not and cannot include the δ-peak at $t = 0$ weighted with ε_∞.

function

$$\mathrm{E}_{\alpha,\beta}(t) = \sum_{n=0}^{\infty} \frac{t^n}{\Gamma(\alpha n + \beta)}, \tag{3.24}$$

where $\Gamma(n) = (n-1)!$ is the continuation of the factorial. According to Holm [166], which is based on the work of Garrappa et al. [167], the inverse Fourier transform of the Cole-Cole equation is given by

$$\mathcal{F}^{-1}\left\{ \frac{1}{1 + (i\omega/\omega_j)^{1-\alpha_j}} \right\} = \omega_j (\omega_j t)^{-\alpha_j} \, \mathrm{E}_{1-\alpha_j, 1-\alpha_j}\Big[-(\omega_j t)^{1-\alpha_j} \Big]. \tag{3.25}$$

Letting $\alpha_j \to 0$, one gets $\mathrm{E}_{1,1}(t) = \exp(t)$, which follows directly from Eq. (3.24), so that Eq. (3.25) is consistent with Eq. (3.21). Through Eq. (3.25), one can represent Eq. (3.23) in the time domain, which is shown in Fig. 3.1 (b). The implementation of Eq. (3.24) from [168] has been used. The permittivities of the tissues modeled with Eq. (3.23) have a longer lasting impact then the purely exponential model of water, which drops sharply after $\tau = 6.2$ ps.

Eventually, the scalar and vector potential or the electric and magnetic fields are represented in the Fourier domain. Since they are real valued, their frequency spectra are symmetric with respect to the origin i.e. $\omega = 0$ (see Eq. (A.6)). It is therefore sufficient to consider, for example, only positive frequencies. In Eq. (3.22), one can see that the imaginary part of the permittivity is negative for positive frequencies. With the Fourier transform given in Eqs. (A.1a) and (A.1b) this is true in a more general sense, which follows from the *Kramers-Kronig* relations [153]. They relate the real and imaginary parts of the electric susceptibility $\tilde{\chi}_\mathrm{e}(\omega) = \chi'_\mathrm{e}(\omega) + i\chi''_\mathrm{e}(\omega)$ to one another:

$$\chi'_\mathrm{e}(\omega) = -\frac{1}{\pi}\mathcal{P}\int_{-\infty}^{\infty} \frac{\chi''_\mathrm{e}(\omega')}{\omega' - \omega}\mathrm{d}\omega', \tag{3.26}$$

$$\chi''_\mathrm{e}(\omega) = \frac{1}{\pi}\mathcal{P}\int_{-\infty}^{\infty} \frac{\chi'_\mathrm{e}(\omega')}{\omega' - \omega}\mathrm{d}\omega'. \tag{3.27}$$

Recall that they are adjusted to fit Eqs. (A.1a) and (A.1b), which is why the sign differs compared to [153]. With $\tilde{\chi}_\mathrm{e}(\omega) = \tilde{\varepsilon}_\mathrm{r}(\omega) - \varepsilon_\infty$, Eq. (3.22) satisfies Eqs. (3.26) and (3.27). Usually $\tilde{\chi}_\mathrm{e}(\omega) = \tilde{\varepsilon}_\mathrm{r}(\omega) - 1$, but $\tilde{\chi}_\mathrm{e}(\omega \to \infty)$ has to vanish, since a polarization for arbitrarily high frequencies is unphysical. For ordinary matter, the real part of the permittivity is always positive ($\chi'_\mathrm{e}(\omega) > 0$) and symmetric (see Eq. (A.6)). Eq. (3.27) is a convolution of $\chi'_\mathrm{e}(\omega')$ with the kernel $-1/\omega'$, where for $\omega > 0$, the majority of $\chi'_\mathrm{e}(\omega')$ has a negative weight so that $\chi''_\mathrm{e}(\omega > 0) < 0$. The same also applies to the permittivity, so that one can state:

$$\Im[\tilde{\varepsilon}(\omega > 0)] < 0. \tag{3.28}$$

This constraint is necessary for some of the steps below.

When studying the impact of boundaries (Chapter 6) and the propagation through the target, it is instructive to consider the refractive index n and the absorption coefficient α. They are motivated as follows. In a homogeneous and source-free environment, Eqs. (3.4a) to (3.4d) simplify to wave equations for both the electric and magnetic field $\widetilde{\mathbf{F}} = \{\widetilde{\mathbf{E}}, \widetilde{\mathbf{B}}\}$: $\nabla^2\widetilde{\mathbf{F}} + \omega^2/\tilde{c}^2\widetilde{\mathbf{F}} = 0$, where $1/\tilde{c}^2 = \mu\tilde{\varepsilon}$. The necessary algebraic manipulations can be found in numerous textbooks on electromagnetism, e.g. [169]. The result is a wave that moves with the speed of light $\tilde{c}$ in the medium. The ratio to the speed of light in vacuum c_0 is the (complex) refractive index $\tilde{n} = c_0/\tilde{c} = \sqrt{\tilde{\varepsilon}_\mathrm{r}}$. Here, $\mu_\mathrm{r} = \mu/\mu_0 \approx 1$ has been assumed, just as in Eq. (3.3). Separating both the refractive index and the permittivity into their real and imaginary parts, one can express the refractive index through the permittivity: $\varepsilon'_\mathrm{r} + i\varepsilon''_\mathrm{r} = (n' + in'')^2 \Rightarrow n' = \sqrt{(\varepsilon'_\mathrm{r} + |\tilde{\varepsilon}_\mathrm{r}|)/2}$ and $n'' = \varepsilon''_\mathrm{r}/(2n')$. n' plays an important role in the reflection and refraction at the boundaries, while n'' is related to the absorption.

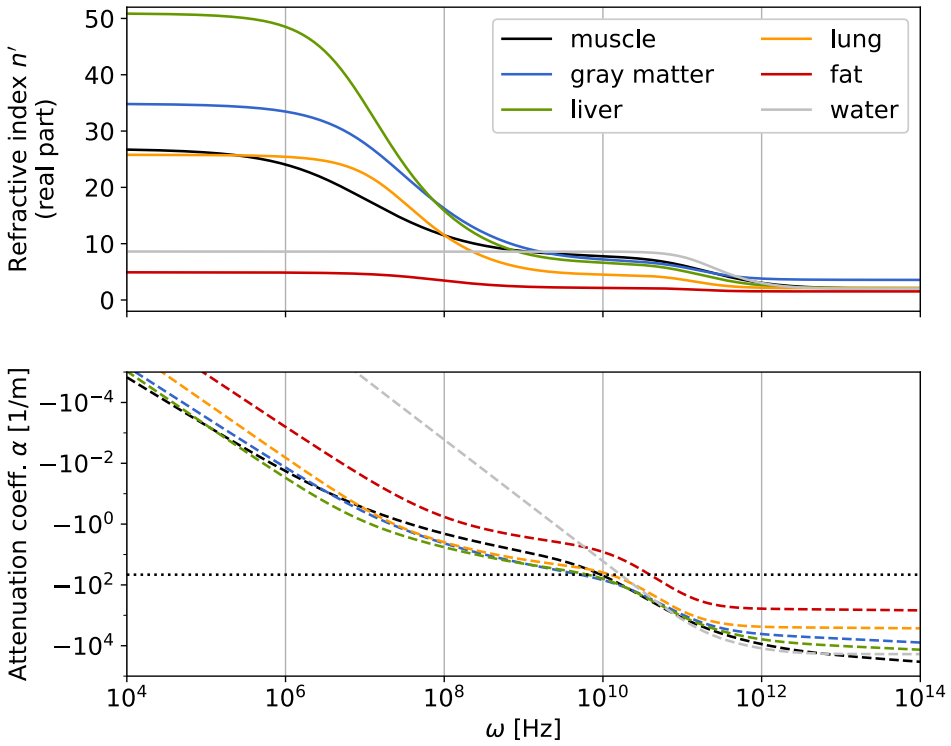

Figure 3.2: Real part of the complex refractive index $\tilde{n} = n' + in'' = \sqrt{\tilde{\varepsilon}_r}$ (top) and the attenuation coefficient defined as $\alpha = 2n''\omega/c_0$ (bottom). $\tilde{\varepsilon}_\mathbf{r}$ is modeled according to Eq. (3.23) (Cole-Cole model) with the parameters given in Table 3.1.

The wave equation is generally solved by $\widetilde{E}_x, \widetilde{B}_y \propto \exp(-i\tilde{n}\omega/c_0 z)$ for a wave propagating along z. Since $\omega\tilde{n}$ has a negative imaginary part (see Eq. (3.28)), the intensity, which is proportional to the square of the fields, decreases with $\exp(2n''\omega/c_0 z) = \exp(\alpha z)$, where the attenuation coefficient $\alpha = 2n''\omega/c_0$ [170] has been introduced. It is a more meaningful way to represent the impact of the imaginary part of the permittivity. Both the refractive index and the absorption coefficient are shown in Fig. 3.2. With the exponential law, one can also determine which frequencies are absorbed within the approximate target dimensions of $z \simeq 10$ cm. For $\alpha < \log(0.01)/z$, 99% of the wave is absorbed, which is shown as the horizontal dotted line in Fig. 3.2, where one sees that frequencies above $\sim$ 10 GHz are suppressed.

3.2.3 Conductivity

In a conducting medium, a conductivity current $\mathbf{J}_c$ emerges in the presence of an (external) electric field, which is described by Ohm's law [154]

$$\mathbf{J}_c(\mathbf{r},t) = \int_{-\infty}^{\infty} \sigma(t-t')\mathbf{E}(\mathbf{r},t')\mathrm{d}t', \qquad (3.29) \qquad\qquad \tilde{\mathbf{J}}_c(\mathbf{r},\omega) = \tilde{\sigma}(\omega)\tilde{\mathbf{E}}(\mathbf{r},\omega), \qquad (3.30)$$

where σ is the conductivity. Eq. (3.29) is again stated as a general convolutional law, just as Eq. (3.2), so that the 2π is also collected within $\tilde{\sigma}(\omega)$ in Eq. (3.30), like Eq. (3.6). For simplicity and based on the work of Gabriel et al. [163], which shows comparatively flat conductivity profiles as a function of the frequency, a time and frequency independent conductivity is assumed. In particular, it will be approximated by its DC conductivity:

$\sigma(t) = \sigma_{\mathrm{DC}}\delta(t)$, so that Ohm's law becomes very simple:

$$\mathbf{J}_{\mathrm{c}} = \sigma_{\mathrm{DC}}\mathbf{E}. \tag{3.31}$$

As stated in Eqs. (3.4a) to (3.4d), the Maxwell equations do not describe conductivity phenomena. Yet, they can easily be modified by adding the conductivity current $\tilde{\mathbf{J}}_{\mathrm{c}} = \sigma_{\mathrm{DC}}\widetilde{\mathbf{E}}$ to the RHS of Eq. (3.4c). Together with Eq. (3.6), one can re-define the permittivity so that the conductivity term is collected within it [154, 171, 172]:

$$\tilde{\varepsilon}_{\mathrm{c}}(\omega) = \tilde{\varepsilon}(\omega) - i\frac{\sigma_{\mathrm{DC}}}{\omega}. \tag{3.32}$$

The conductivity values of the biological tissues investigated, were already given in the last column of Table 3.1. By introducing the conductivity current, one also effectively introduces a conductivity charge $\tilde{\rho}_{\mathrm{c}} = i\sigma_{\mathrm{DC}}/\omega\,\nabla\cdot\widetilde{\mathbf{E}}$, analogous to the bound charge as discussed in Sec. 3.2.1. By definition, they also satisfy a separate continuity equation: $\nabla\cdot\tilde{\mathbf{J}}_{\mathrm{c}} + i\omega\tilde{\rho}_{\mathrm{c}} = 0$.

3.3 Interface conditions

Except for Chapter 6, the Maxwell equations are solved in a homogeneous environment in this thesis. In order to introduce a tissue boundary, one may use the *interface conditions*. The focus lies in the following on the electric field, since for the magnetic field, the permeability gradients were already assumed to be low in Eq. (3.3), as described in the text thereafter. The interface conditions state that the perpendicular ($\perp$) component of the displacement field is discontinuous in the presence of some surface charge density ρ_{s} and that the tangential ($\parallel$) electric field is continuous [153, 154]:

$$D^a_\perp - D^b_\perp = \varepsilon^a E^a_\perp - \varepsilon^b E^b_\perp = \rho_{\mathrm{s}} \tag{3.33}$$

$$\mathbf{E}^a_\parallel - \mathbf{E}^b_\parallel = 0, \tag{3.34}$$

where the superscripts refer to the materials a & b on opposite sides of the boundary. They are derived by applying the integral representation of the Maxwell equations, which follow from Gauß' or Stokes' theorem, to infinitesimal volumes/areas around the boundary. By the same approach, one can also derive a similar condition based on the combination of the continuity equation (Eq. (3.7)) and Ohm's law (Eq. (3.31)) [173]:

$$\sigma^a E^a_\perp - \sigma^b E^b_\perp = -\,\partial\rho_{\mathrm{s}}/\partial t\ . \tag{3.35}$$

By combining Eqs. (3.33) and (3.35), one can eliminate the surface charge density ρ_{s}. In the Fourier domain ($\partial/\partial t \rightarrow i\omega$), one arrives at an interface condition, that allows a direct mapping from the field in a to b, without having to calculate the surface charge density [173]:

$$\big[\underbrace{\tilde{\varepsilon}^a(\omega) - i\sigma^a_{\mathrm{DC}}/\omega}_{\tilde{\varepsilon}^a_{\mathrm{c}}(\omega)}\big]E^a_\perp - \big[\underbrace{\tilde{\varepsilon}^b(\omega) - i\sigma^b_{\mathrm{DC}}/\omega}_{\tilde{\varepsilon}^b_{\mathrm{c}}(\omega)}\big]E^b_\perp = 0, \tag{3.36}$$

where conductivity has been collected within the permittivity as in Eq. (3.32). When represented as $\tilde{\varepsilon}^a_{\mathrm{c}}(\omega)E^a_\perp - \tilde{\varepsilon}^b_{\mathrm{c}}(\omega)E^b_\perp = 0$, Eq. (3.36) is similar to Eq. (3.33), where the surface charge density appears to be neglected, but is actually taken into account through the conductivity terms. It is crucial to keep in mind that Eqs. (3.33) and (3.34) were separately derived from Gauß' and Faraday's law. When isolated from one another, they only apply to static fields that originate from static sources. This is a major simplifying assumption, which limits their applicability. For instance, they cannot be used to model the reflection/transmission of an electromagnetic wave at a boundary. Further limitations are discussed in Chapter 4, when they are taken into consideration.

3.4 Point particle charge and current density

The analytical approach in Chapters 4 and 6 is based on the solutions of the electromagnetic field from individual point particles. Accordingly, the corresponding source terms, i.e. the point particle charge and current density, are necessary. Fundamentally, they are related to one another. By definition, the current density J is the amount of charge $\mathrm{d}q$ that flows perpendicularly through the area $\mathrm{d}A$ within the time $\mathrm{d}t$: $J = \mathrm{d}q/(\mathrm{d}t\mathrm{d}A) = \mathrm{d}I/\mathrm{d}A$, where $I = \mathrm{d}q/\mathrm{d}t$ is the current. When the individual particles move with the velocity v, then the time interval may be represented as $\mathrm{d}t = \mathrm{d}s/v$, where $\mathrm{d}s$ is the perpendicular distance that the particles travel within $\mathrm{d}t$. Together with $\mathrm{d}A$, this spans a volume $\mathrm{d}V = \mathrm{d}s\mathrm{d}A$, so that the current density may be written as $J = \mathrm{d}q/(\mathrm{d}s\mathrm{d}A)\, v = \mathrm{d}q/\mathrm{d}V\, v = \rho\, v$, where the charge density $\rho = \mathrm{d}q/\mathrm{d}V$ is by definition the amount of charge per unit volume. Therefore, one may express the current density through the particle velocity vector $\mathbf{v}$ and the free charge density [154]:

$$\mathbf{J}_\mathrm{f}(\mathbf{r},t) = \rho_\mathrm{f}(\mathbf{r},t)\mathbf{v}(\mathbf{r},t). \tag{3.37}$$

One can describe the charge density of a moving point particle through a shifted delta function. The point particle path is described through $\mathbf{r}_\mathrm{p}(t)$ with its velocity $\mathbf{v}_\mathrm{p}(t) = \mathrm{d}\mathbf{r}_\mathrm{p}(t)/\mathrm{d}t$. Together with Eq. (3.37), one obtains [153]

$$\rho_\mathrm{f}(\mathbf{r},t) = q_\mathrm{e}\delta^3(\mathbf{r}-\mathbf{r}_\mathrm{p}(t)), \tag{3.38}$$

$$\mathbf{J}_\mathrm{f}(\mathbf{r},t) = q_\mathrm{e}\mathbf{v}_\mathrm{p}(t)\delta^3(\mathbf{r}-\mathbf{r}_\mathrm{p}(t)), \tag{3.39}$$

where $q_\mathrm{e} \approx 1.602 \times 10^{-19}$ C is the elementary charge. By definition, Eqs. (3.38) and (3.39) satisfy the continuity equation from Eq. (3.7) and are thus valid source terms. For computational reasons it is convenient to introduce the charges at $t = 0$, so that the field from $t < 0$ does not have to be calculated. To do so, one multiplies both the charge and current density by a step function with respect to the time: $\rho_\mathrm{f}(\mathbf{r},t) \to \rho_\mathrm{f}(\mathbf{r},t)\theta(t)$ and $\mathbf{J}_\mathrm{f}(\mathbf{r},t) \to \mathbf{J}_\mathrm{f}(\mathbf{r},t)\theta(t)$. An inadvertent consequence, however, is that the new charge and current density do not satisfy the continuity equation anymore. In particular, it is replaced by a generalized continuity equation, which includes a source term σ_s: $\partial\rho_\mathrm{f}/\partial t + \nabla\cdot\mathbf{J}_\mathrm{f} = \sigma_\mathrm{s}$, where $\sigma_\mathrm{s} = q_\mathrm{e}\delta^3(\mathbf{r})\delta(t)$ and $\mathbf{r}_\mathrm{p}(t=0) = \mathbf{0}$ has been assumed. Such a source term is sensible, as it actually gives rise to a new charge, which is created at $t = 0$. Coping with the situation that Eq. (3.7) is not satisfied is more relevant for numerical solutions of Maxwell or related equations [174,175]. For the present work, an approach similar to [176] is considered, whereby one modifies the free current density as

$$\mathbf{J}_\mathrm{f} \to \mathbf{J}_\mathrm{f} - \mathbf{\Sigma}_\mathrm{s}, \tag{3.40}$$

$$\sigma_\mathrm{s} = \nabla\cdot\mathbf{\Sigma}_\mathrm{s}, \tag{3.41}$$

where the additional current $\mathbf{\Sigma}_\mathrm{s}$ needs to satisfy Eq. (3.41). One can equivalently introduce an additional charge density as $\rho_\mathrm{f} \to \rho_\mathrm{f} - \Sigma_\mathrm{s}$, which could also account for the source term. It can e.g. be a charge that sits at the center for $t < 0$ and vanishes at $t = 0$ ($\Sigma_\mathrm{s} = q_\mathrm{e}\delta^3(\mathbf{r})\theta(-t)$) or a charge with an opposite sign that is simultaneously created at $t = 0$ ($\Sigma_\mathrm{s} = -q_\mathrm{e}\delta^3(\mathbf{r})\theta(t)$). In the first case, the net charge is at all times equal to q_e, while it vanishes at all times in the second case, which is equivalent to a pair production. Parts of the preceding discussion were also published in [177], yet the implications of Eq. (3.40) on the electromagnetic field will be discussed in the dedicated Chapter 4.

3.5 Superposition

Since the Maxwell equations are linear with respect to the source terms ρ_f and $\mathbf{J}_\mathrm{f}$, one can superimpose the point particle solutions to obtain a field that is generated by a beam,

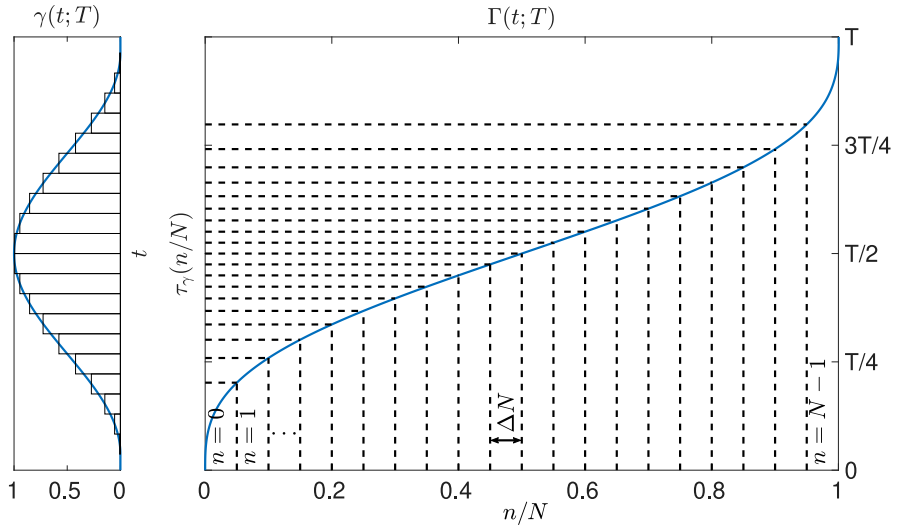

Figure 3.3: Connection between the beam shape function $\gamma(t)$ and the launch time function $\tau_\gamma(n/N)$ in the case of an exemplary raised cosine distribution $\gamma(t) = 2/T \sin^2(\pi t/T)$, for $t \in [0, T]$. The dashed lines indicate the uniform evaluation of τ_γ at n/N, which leads to a non-uniform $\gamma(t)$ on the LHS.

consisting of individual particles. Formally, the combined field of a beam $\mathbf{F}^b$ is the sum of the time-shifted point particle solutions $\mathbf{F}^\delta$:

$$\mathbf{F}^b(\mathbf{r}, t) = \sum_{n=0}^{N-1} \mathbf{F}^\delta(\mathbf{r}, t - \tau_\gamma(n/N)), \tag{3.42}$$

where $\tau_\gamma(n/N)$ returns the time when the n$^{\text{th}}$ particle is launched. $\mathbf{F} = \{\mathbf{E}, \mathbf{B}\}$ serves here as a placeholder for the electric or magnetic field. In total, N particles are superimposed. In general $\tau_\gamma : [0,1] \to \mathbb{R}$, but more practically $\tau_\gamma : [0,1] \to [0,T]$, where the first particle is launched at time zero ($\tau_\gamma(0) = 0$) and the last is launched at time T ($\tau_\gamma(1) = T$). For example, when the particles are launched linearly, then the launch time function is given by $\tau_\gamma(n/N) = n/N \cdot T = n\Delta\tau$, where $\Delta\tau = T/N$ is the time delay between two consecutive protons, which is determined by the proton beam current from the accelerator. A non-linear case is depicted in Fig. 3.3.

In order to simplify the evaluation of Eq. (3.42), the discrete sum of individual particles shall be turned into a continuous stream. The conditions under which this approximation holds will be discussed below. The total charge $q_{\text{tot}} = Nq_e$ is kept constant while allowing for infinitely many infinitesimal contributions. In particular, if N particles are being released, then $\tau_\gamma(n/N)$ will be evaluated uniformly at $\Delta N = 1/N$ increments. The number of individual charges is increased by letting $\Delta N \to 0$:

$$\begin{aligned}\mathbf{F}^b(\mathbf{r}, t) &\approx N \lim_{\Delta N \to 0} \sum_{n=0}^{1/\Delta N - 1} \mathbf{F}^\delta(\mathbf{r}, t - \tau_\gamma(n\Delta N))\Delta N \\ &= N \int_0^1 \mathbf{F}^\delta(\mathbf{r}, t - \tau_\gamma(n))\mathrm{d}n,\end{aligned} \tag{3.43}$$

where $N\Delta N = 1$ has been inserted in the first step. Instead of constructing a τ_γ and evaluating Eq. (3.43), which is not necessarily simpler than Eq. (3.42), a change of variables of the form $t' = \tau_\gamma(n)$ is performed. For this purpose, the inverse is defined as $\tau_\gamma^{-1}(t') \equiv$

$\Gamma(t')$ and in turn its derivative as $\partial_{t'}\Gamma(t') \equiv \gamma(t')$. With the help of Fig. 3.3, one can assign a meaning to these functions, which is inspired by the inverse transform sampling theorem [178]. It says that in order to obtain random samples distributed according to $\gamma(t)$, one samples $n \in \mathcal{U}_{[0,1]}$ and evaluates them at $\tau_\gamma(n)$. Since τ_γ is by definition evaluated uniformly (see Eq. (3.42)), $\gamma(t)$ can be interpreted as the beam shape distribution. In addition $\gamma(t)$ and $\Gamma(t)$ are related to one another like a probability density function (PDF) and its cumulative density function (CDF). Specifically the normalization is guaranteed by definition. Recall that $\tau_\gamma : [0,1] \to \mathbb{R}$ so that $\Gamma = \tau_\gamma^{-1} : \mathbb{R} \to [0,1]$. Consequently $\gamma(t)$ satisfies

$$\int_{-\infty}^{\infty} \gamma(t)\mathrm{d}t = 1. \tag{3.44}$$

Together with the original number of particles $N\gamma(t)$ can be interpreted as a launch rate and $N\gamma(t)\mathrm{d}t$ is the number of particles that are released within $\mathrm{d}t$. Finally, the aforementioned change of variables is completed via

$$\frac{\mathrm{d}n}{\mathrm{d}t'} = \frac{\mathrm{d}}{\mathrm{d}t'}\tau_\gamma^{-1}(t') = \frac{\mathrm{d}}{\mathrm{d}t'}\Gamma(t') = \gamma(t'), \tag{3.45}$$

so that Eq. (3.43) simplifies to a convolution between the point particle field and the beam shape function:

$$\mathbf{F}^b(\mathbf{r},t) = N\int_{-\infty}^{\infty} \mathbf{F}^\delta(\mathbf{r},t-t')\gamma(t')\mathrm{d}t' = N\mathbf{F}^\delta(\mathbf{r},t) * \gamma(t). \tag{3.46}$$

At first sight, Eq. (3.46) is still not simpler than Eq. (3.42), since instead of a sum, one now needs to evaluate a convolution integral. Yet, the point particle fields are solved in the frequency domain, where also the convolution theorem applies. It states that a convolution in the time domain corresponds to a product in the frequency domain so that in order to obtain the field that originates from a beam, one merely needs to multiply the frequency domain point particle solution with the Fourier transform of the beam shape function and carry out the inverse Fourier transform:

$$\widetilde{\mathbf{F}}^b(\mathbf{r},\omega) = 2\pi N\widetilde{\mathbf{F}}^\delta(\mathbf{r},\omega)\tilde{\gamma}(\omega) \qquad \Rightarrow \qquad \mathbf{F}^b(\mathbf{r},t) = 2\pi N\int_{-\infty}^{\infty} \widetilde{\mathbf{F}}^\delta(\mathbf{r},\omega)\tilde{\gamma}(\omega)e^{i\omega t}\mathrm{d}\omega. \tag{3.47}$$

The factor of 2π originates from Eq. (A.5). In summary, a major simplification has been achieved but one needs to remind that Eq. (3.46) is an approximation. In reality, individual particles give rise to individual electric and magnetic fields, which are eventually superimposed. The approximation holds only if the point particle fields are sufficiently large or the distance between adjacent particles is sufficiently small. In the following, the latter shall be quantified. For simplicity, the dispersion of the tissue is neglected, i.e. considering the beam before it enters the target as it drifts freely through space/air. Since the density increases downstream (see Fig. 5.8) and the width of a point particle field increases with the decreasing particle velocity (relativistic effect - see below), evaluating the approximation with the initial energy/velocity is a rather conservative estimate.

The electric and magnetic field that originates from a point particle, which moves with the velocity v along the z-axis: $\mathbf{r}_\mathrm{p}(t) = (0,0,vt)^\mathrm{T}$, forms the staring point of the following. Its radial electric field can be found by Lorentz-boosting the classical Coulomb field [153,179]: $E_\rho(\mathbf{r},t) = q_e/(4\pi\varepsilon_0)\,\gamma\rho/\sqrt{\rho^2+\gamma^2(z+vt)^2}^3$, where $\gamma = 1/\sqrt{1-\beta^2}$ is the Lorentz factor, $\beta = v/c_0$ is the particle velocity relative to the speed of light and $\rho = \sqrt{x^2+y^2}$ is the perpendicular distance to the path. The azimuthal magnetic field has the same spatial and temporal behavior and is just rescaled with respect to E_ρ: $B_\phi(\mathbf{r},t) = \beta/c_0\,E_\rho(\mathbf{r},t)$. Both follow a

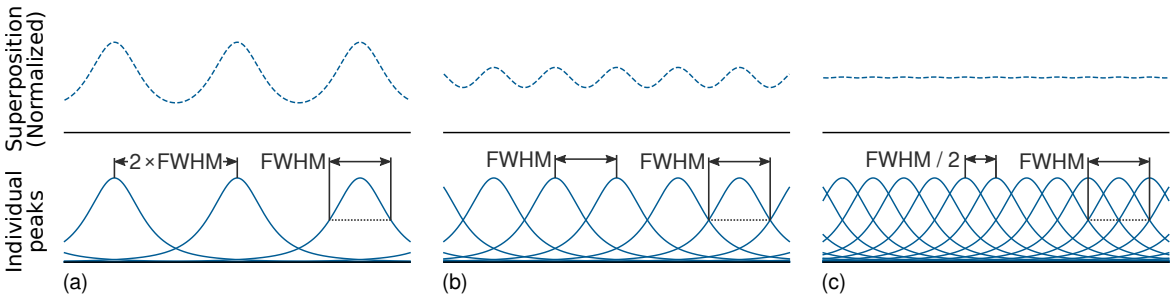

Figure 3.4: Qualitative superposition (dashed lines) of the radial electric or azimuthal magnetic point particle fields in vacuum (solid lines). The longitudinal separation is given in units of the point particle FWHM and ranges from (a) $2 \times$ FWHM to (c) FWHM/2.

bell-shaped curve with a full width at half maximum (FWHM) of $2\sqrt{2^{2/3}-1}\,\rho/\gamma \approx 1.5\,\rho/\gamma$. For the purposes under consideration, it needs to be ensured that in the superposition, the individual particles cannot be distinguished. A standard criterion when studying the resolution and in particular how well individual features can be distinguished, e.g. in optics or medical imaging, is the FWHM of the point spread function (PSF). If two sources are separated by less than the FWHM of the PSF, then they cannot be resolved [180]. A qualitative portrayal is shown in Fig. 3.4. Effectively, E_ρ and B_ϕ are the PSFs of the point particle.

The longitudinal separation depends on the initial beam energy Q_{in} and current I. The average time delay between two consecutive protons is given by $\Delta t_p = q_e/I$. The corresponding longitudinal distance is related to Δt_p through the initial velocity v_{in}: $\Delta z_p = v_{\text{in}} \Delta t_p$. The latter, in turn, is determined by the initial kinetic energy (see Eq. (2.18)). Note that for this analysis, the random fluctuations from the accelerator are neglected. Finally, a validity criterion of Eq. (3.46) can be stated:

$$\Delta z_p < \text{FWHM}/2 \quad \Leftrightarrow \quad v_{\text{in}}\, q_e/I < \sqrt{2^{2/3}-1}\,\rho/\gamma. \tag{3.48}$$

FWHM/2 has been chosen instead of just FWHM, based on Fig. 3.4. Eq. (3.48) is visualized in Fig. 3.5. It is shown that this validity criterion depends only weakly on the initial kinetic energy. Several results, presented in this thesis, consider the fields at $\rho \sim 10$ cm. For a wide range of beam currents, Eq. (3.46) applies at this distance.

If Eq. (3.46) does not apply, Eq. (3.42) can still be simplified to a certain extent. By Fourier transforming both sides of Eq. (3.42), one can make use of the linearity of the Fourier transform by extracting the sum and then apply the shift property from Eq. (A.4):

$$\begin{aligned}\widetilde{\mathbf{F}}^b(\mathbf{r},\omega) &= \sum_{n=0}^{N-1} \mathcal{F}\Big\{\mathbf{F}^\delta(\mathbf{r}, t-\tau_\gamma(n/N))\Big\} \\ &= \widetilde{\mathbf{F}}^\delta(\mathbf{r},\omega) \sum_{n=0}^{N-1} e^{-i\omega\tau_\gamma(n/N)}.\end{aligned} \tag{3.49}$$

Just as in Eq. (3.47), the result is yet again a product in the Fourier domain between the point particle solution and the equivalent of $\tilde{\gamma}(\omega)$. Similar to Eq. (3.43), it is consistent with

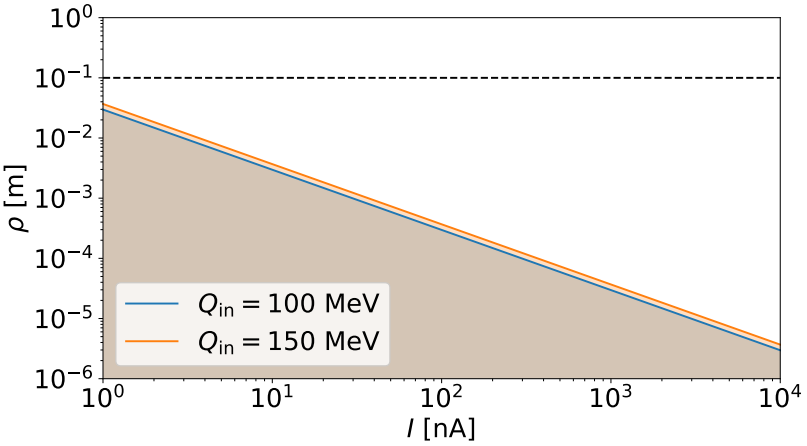

Figure 3.5: Validity of Eq. (3.46) according to Eq. (3.48) as a function of the beam current I and the distance from the central beam axis ρ. Eq. (3.46) does not apply in the shaded area, i.e. for too low radii or currents. The dashed line marks $\rho = 10$ cm.

Eq. (3.47) in the limit $\Delta N \to 0$:

$$\begin{aligned} N \lim_{\Delta N \to 0} \sum_{n=0}^{1/\Delta N - 1} e^{-i\omega\tau_\gamma(n/N)} \Delta N &= N \int_0^1 e^{-i\omega\tau_\gamma(n)} \mathrm{d}n \\ &= 2\pi N \int_{-\infty}^{\infty} \frac{\mathrm{d}t}{2\pi} \gamma(t) e^{-i\omega t} \\ &= 2\pi N \tilde{\gamma}(\omega). \end{aligned} \tag{3.50}$$

3.6 Finite element analysis (FEA)

For sufficiently simple and analytical source terms, such as a point particle charge and current density (see Sec. 3.4), one may find analytical solutions to the Maxwell equations. They are more extensively discussed in Chapters 4 and 6. For the work from Chapter 5, where the charge and current density is obtained from MC simulations (discretized data), a numerical solution of the Maxwell equations is necessary. Numerous computational approaches exist, which strongly depend on the application [181, 182]. For instance, the *finite-difference time-domain* (FDTD) method is commonly used for time-dependent cases, while the *method of moments* (MOM) is more relevant for frequency domain problems. For the work from Chapter 5, the *finite element method* or *finite element analysis* (FEA) has been chosen. For the sake of completeness, one could alternatively use integral methods [183], based on Jefimenko's equations [184]. For reasons that follow from the results of the following chapter, it is sufficient to consider a magnetostatic formulation. Only the magnetic field has been estimated in Chapter 5 and will be the focus of the following. Generally, there is a large body of literature for FEA. Especially for electromagnetics, Jin's book [185] provides an excellent and exhaustive overview. Alternatives are [186–188]. The following is partially based on theses references.

3.6.1 Formulation

The basic idea of FEA can be summarized as follows. In the potential form, where the electric and magnetic fields are represented through the scalar and vector potentials (see

Eqs. (3.9) and (3.10)), one may reformulate the Maxwell equations as a Lagrangian density. Minimizing the corresponding action solves the original differential equation according to the calculus of variations. This approach is known as *Ritz method*. An alternative is to consider weighted residuals, called *Galerkin's method*. In the following, two simplifying assumptions are made. The convolutional relationship between the displacement and electric field from Eq. (3.2) reduces in the static case, i.e. $\mathbf{E}(\mathbf{r}, t) = \mathbf{E}(\mathbf{r})$, to a simple and time-independent relation: $\mathbf{D} = \varepsilon_0 \varepsilon_s \mathbf{E}$. Recall that the static permittivity ε_s is embedded in the model from Eq. (3.21) or $\varepsilon_s = \varepsilon_\infty + \sum_j \Delta\varepsilon_j$, when represented through the Cole-Cole equation (see Eq. (3.23)), where $\omega \to 0$. For simplicity, it is abbreviated with $\varepsilon = \varepsilon_0 \varepsilon_s$. Secondly, a homogeneous target is assumed, i.e. $\varepsilon(\mathbf{r}) = \varepsilon$. While the inclusion of inhomogeneities is comparatively simple in a numerical approach, as opposed to an analytical approach (see Chapter 6), the comparability between the results obtained in Chapters 4 and 5 shall be maintained. The impact of boundaries is then further discussed in Chapter 6. Together with Eqs. (3.9) and (3.10), Ampère's circuital law becomes [153]

$$\left(-\nabla^2 + \frac{1}{c^2} \frac{\partial^2}{\partial t^2} \right) \mathbf{A} + \nabla \left(\nabla \cdot \mathbf{A} + \frac{1}{c^2} \frac{\partial \varphi}{\partial t} \right) = \mu \mathbf{J}_\mathrm{f}, \tag{3.51}$$

where $\mu\varepsilon \equiv 1/c^2$. In its current form, the vector and scalar potentials are coupled with a second equation that follows from Gauß' law, while one only needs to solve for $\mathbf{A}$ to estimate the magnetic field (see Eq. (3.10)). As mentioned above, a magnetostatic case is considered, so that $\partial \mathbf{A}/\partial t \overset{!}{=} \mathbf{0}$. It is usually paired with the electrostatic assumption, i.e. $\partial \varphi/\partial t \overset{!}{=} 0$ so that together with Eq. (A.69), Eq. (3.51) simplifies to what is known as the curl-curl equation [153, 189–191]:

$$\nabla \times \left(\frac{1}{\mu} \nabla \times \mathbf{A} \right) = \mathbf{J}_\mathrm{f}. \tag{3.52}$$

The result above is somewhat more general, i.e. it also applies to $\mu = \mu(\mathbf{r})$. With Eq. (3.52) being independent of the scalar potential, one could proceed with the approach outlined above, i.e. determining the associated Lagrangian density ($\mathcal{L}[\mathbf{A}] = (\nabla \times \mathbf{A})^2/(2\mu) - \mathbf{J}_\mathrm{f} \cdot \mathbf{A}$ [192]) and minimizing its action. However, Eq. (3.52) has a major limitation, which renders it ineligible for the present application. Since the divergence of a curl vanishes by definition, Eq. (3.52) implies that the current density has to be solenoidal, i.e. divergence-free: $\nabla \cdot \mathbf{J}_\mathrm{f} \overset{!}{=} 0$. This follows directly by taking the divergence of Eq. (3.52). Yet, the magnetic field of a stopping proton pencil beam is of interest, where the current density is decidedly non-solenoidal, especially at the range. The main issue is the electrostatic assumption. Consider the charges[2] that are primarily deposited at the range. They give rise to a changing electric field, which contributes to the magnetic field, according to Eq. (3.1d). If the beam current is constant then so is the rate of change of the electric field. Accordingly, a non-electrostatic scenario can give rise to a magnetostatic field. In other words, to maintain the magnetostatic assumption, which is to be expected from a constant current density ($\partial_t \mathbf{J}_\mathrm{f} = \mathbf{0}$), one needs to lift the electrostatic assumption: $\nabla \cdot \mathbf{J}_\mathrm{f} \neq 0 \Rightarrow \partial \varphi/\partial t \neq 0$. Reintroducing the scalar potential term in Eq. (3.52) leads to $\nabla \times (\nabla \times \mathbf{A}) = \mu \mathbf{J}_\mathrm{f} + 1/c^2 \nabla(\partial_t \varphi)$ so that the term on the RHS is not an independent source term anymore. The contribution from the scalar potential needs to be estimated separately, which has been done in an earlier work [193]. Firstly, realize that the electric field can be described by a gradient field

[2] Note that due to the conductivity of the target, they do not accumulate at the range. This will be further discussed in Chapter 5.

under the magnetostatic assumption: $\mathbf{E} = -\nabla\varphi$ (see Eq. (3.9) or Eq. (3.1c), whereby its curl vanishes). The Poisson equation follows directly from Eq. (3.1a):

$$\nabla^2\varphi = -\rho_\mathrm{f}/\varepsilon. \tag{3.53}$$

By differentiating it with respect to time and exchanging the derivatives, one obtains the Poisson equation for the derivative of the scalar potential: $\nabla^2(\partial_t\varphi) = -(\partial_t\rho_\mathrm{f})/\varepsilon$. The derivative of the charge density (source term) does not need to be estimated from the simulation but rather follows directly from the continuity equation Eq. (3.7): $\partial_t\rho_\mathrm{f} = -(\nabla\cdot\mathbf{J}_\mathrm{f})$. The constant current ($\partial_t\mathbf{J}_\mathrm{f} = \mathbf{0}$) implies that the source term $\partial_t\rho_\mathrm{f}$ is time independent, i.e. constant. Simultaneously it is non-zero, so that ρ_f can only change linearly. The Poisson equation can also be solved through the FEA so that one eventually obtains $\partial_t\varphi$. By taking the gradient, the second source term ($1/c^2\nabla(\partial_t\varphi)$) can be estimated and the curl-curl equation can be solved. $\mathbf{J}_\mathrm{f}$ serves as the input for both equations (Poisson and curl-curl), i.e. they are mutually dependent, so it stands to reason that $\mathbf{A}$ can be solved directly.

In Eq. (A.69), a gauge has yet not been chosen, while the sought simplification can be achieved by doing so. Through the Lorenz gauge (see Eq. (3.13), which translates to $\nabla\cdot\mathbf{A} + \varepsilon\mu\,\partial\varphi/\partial t = 0$ in the time domain), Eq. (3.51) simplifies to the vector Poisson equation

$$-\nabla^2\mathbf{A} = \mu\mathbf{J}_\mathrm{f}, \tag{3.54}$$

with the vector Laplacian on the LHS. It may not be immediately evident, but as opposed to Eq. (3.52), Eq. (3.54) does allow for non-solenoidal current densities and actually implies the continuity equation. Just as for Eq. (3.52), the divergence of Eq. (3.54) is taken, leading to $-\nabla\cdot(\nabla^2\mathbf{A}) = \mu\nabla\cdot\mathbf{J}_\mathrm{f}$. One may rewrite the LHS by the time derivative of the Poisson equation from Eq. (3.53), which has been considered before, together with the Lorenz gauge, $\partial_t\varphi$ can be replaced by the divergence of the vector potential so that the Poisson equation reads $\nabla^2(c^2\nabla\cdot\mathbf{A}) = (\partial_t\rho_\mathrm{f})/\varepsilon$. Through Eq. (A.70) and $\mu\varepsilon = 1/c^2$, the latter changes to $\nabla\cdot(\nabla^2\mathbf{A}) = \mu\,\partial_t\rho_\mathrm{f}$. Combined with the divergence of Eq. (3.54), the sought continuity equation emerges.

Interestingly enough, one may obtain Eq. (3.54) from Eq. (3.52) via Eq. (A.69) and the Coulomb gauge ($\nabla\cdot\mathbf{A} = 0$) [153, 173, 194]. The fact that the $\partial\varphi/\partial t$-term is included in this case is through this derivation not evident and actually contrary to the assumption. Recall that Eq. (3.52) followed from the electro- and magnetostatic assumptions.

Calculating the magnetic field based on Eq. (3.54) instead of Eq. (3.52) is occasionally discouraged [192], since gauge fixing is first of all not necessary to obtain a unique result of the magnetic field [185]. Secondly, imposing the Coulomb gauge can lead to numerical inaccuracies for cases with discontinuous and strongly varying permeability [195] and lastly, it is preferred when investigating non-linear **B**-**H**-relationships [194]. However, these issues do not arise in the present scenario, so Eq. (3.54) is selected due to the non-solenoidal current density.

3.6.2 Lagrangian and action of Eq. (3.54) with cylindrical symmetry

The simulated current density from Chapter 5 has a cylindrical symmetry, which shall be exploited in the following. The primary goal is to reduce the three-dimensional domain to two dimensions. Axial symmetries have long been considered in FEA [183, 188, 196–201], focusing primarily on a circular current along the azimuthal axis, i.e. $\mathbf{J}_\mathrm{f} = J_\phi\hat{\mathbf{e}}_\phi$. In the present case, however, the pencil beam current is predominantly longitudinal and somewhat radial due to scattering ($\mathbf{J}_\mathrm{f} = J_\rho\hat{\mathbf{e}}_\rho + J_z\hat{\mathbf{e}}_z$). Based on this, a few simplifications

regarding the associated vector potential are first considered. As will be further discussed in Chapters 4 and 6, Eq. (3.54) can be solved by means of Green's function, so that the vector potential can be represented as in Eq. (4.36):

$$\mathbf{A}(\mathbf{r}) = \frac{\mu}{4\pi} \int_{\mathbb{R}^3} \mathbf{J}_\mathrm{f}(\mathbf{r}') G(\mathbf{r}, \mathbf{r}') \mathrm{d}^3\mathbf{r}'. \tag{3.55}$$

The latter splits into its vector components so that also $\mathbf{A} = A_\rho \hat{\mathbf{e}}_\rho + A_z \hat{\mathbf{e}}_z$, i.e. $A_\phi = 0$. From the azimuthal component of Eq. (3.54) (see Eq. (A.77)), it then follows that $\partial A_\rho / \partial \phi = 0$. In addition, a ϕ-independent current cannot give rise to a ϕ-dependent magnetic field. Yet, according to Eq. (3.10), one may have $A_z \to A_z + \phi$, whereby $\mathbf{B}$ would still be ϕ-independent. Nonetheless, the rotational symmetry ($A_z(\phi) \overset{!}{=} A_z(\phi + 2\pi)$) excludes a linear ϕ-term, yielding $\partial A_z / \partial \phi = 0$. In summary, Eq. (3.54) reduces to

$$\frac{1}{\rho} \frac{\partial}{\partial \rho} \left(\rho \frac{\partial A_\rho}{\partial \rho} \right) + \frac{\partial^2 A_\rho}{\partial z^2} - \frac{A_\rho}{\rho^2} = -\mu J_\rho, \tag{3.56}$$

$$\frac{1}{\rho} \frac{\partial}{\partial \rho} \left(\rho \frac{\partial A_z}{\partial \rho} \right) + \frac{\partial^2 A_z}{\partial z^2} = -\mu J_z. \tag{3.57}$$

As outlined above, the associated Lagrangian is required. Generally, in an n-dimensional system ($\mathbf{r} = (x_1, \ldots, x_n)^\mathrm{T}$) with m unknown functions ($\mathbf{f} = (f_1, \ldots, f_m)^\mathrm{T}$), the minimization of Eq. (3.58) solves Eq. (3.59), according to the Euler-Lagrange equations:

$$\mathcal{I}[\mathbf{f}] = \int_\Omega \mathcal{L}(\mathbf{r}, \mathbf{f}, f_{1,1}, \ldots, f_{m,n}) \mathrm{d}^n\mathbf{r}, \tag{3.58}$$

$$\frac{\partial \mathcal{L}}{\partial f_i} - \sum_{j=1}^{n} \frac{\partial}{\partial x_j} \left(\frac{\partial \mathcal{L}}{\partial f_{i,j}} \right) = 0, \tag{3.59}$$

where $f_{i,j} \equiv \partial f_i / \partial x_j$ denotes the set of partial derivatives, which are also the entries of the Jacobian matrix. In the present case, $n = m = 3$ and $\mathbf{f} = \mathbf{A}$. The Lagrangian of Eq. (3.54) in cartesian coordinates can be found in the literature [195, 202][3]:

$$\mathcal{L}[\mathbf{A}] = \frac{1}{2\mu} (\nabla A_x \cdot \nabla A_x + \nabla A_y \cdot \nabla A_y + \nabla A_z \cdot \nabla A_z) - \mathbf{J} \cdot \mathbf{A} = \frac{1}{2\mu} \sum_{i,j} \left(\frac{\partial A_i}{\partial x_j} \right)^2 - \mathbf{J} \cdot \mathbf{A}. \tag{3.60}$$

Through the second representation of Eq. (3.60) one can easily confirm that $\partial \mathcal{L} / \partial (\partial_j A_i) = (\partial_j A_i) / \mu$ and subsequently verify that Eq. (3.59) leads back to Eq. (3.54). The transformation of Eqs. (3.58) and (3.60) to cylindrical coordinates is straightforward, but tedious. See Appendix A.13 for details. With the symmetry-related simplifications from above, Eq. (A.65) and the Lagrangian of Eqs. (3.56) and (3.57) becomes

$$\mathcal{I}\big[A_\rho, A_z\big] = \int_0^\infty \mathrm{d}\rho \int_{-\infty}^\infty \mathrm{d}z \, \mathcal{L}\big[A_\rho, A_z\big], \tag{3.61}$$

$$\mathcal{L}\big[A_\rho, A_z\big] = \frac{\rho}{2\mu} \left[\left(\frac{\partial A_\rho}{\partial \rho} \right)^2 + \left(\frac{A_\rho}{\rho} \right)^2 + \left(\frac{\partial A_\rho}{\partial z} \right)^2 + \left(\frac{\partial A_z}{\partial \rho} \right)^2 + \left(\frac{\partial A_z}{\partial z} \right)^2 \right] - \rho \big(J_\rho A_\rho + J_z A_z \big).$$

The sought reduction to two dimensions, i.e. the ρ-z-plane, has thereby been achieved. The factor of 2π from the ϕ-integral of Eq. (A.65) has no impact and has been dropped for this reason. Note that the ϕ-related geometrical ρ-weight has been collected within the Lagrangian. Through Eq. (3.59) one may recover Eqs. (3.56) and (3.57).

[3] Some sources [192, 203] give an incorrect Lagrangian of the form $\mathcal{L}[\mathbf{A}] \neq (\nabla \cdot \mathbf{A})^2 / (2\mu) - \mathbf{J} \cdot \mathbf{A}$, which does not correspond to Eq. (3.54).

3.6.3 Elemental matrices

The next step is to minimize Eq. (3.61). For this purpose, one discretizes the domain by expanding the vector potential components as

$$A_\kappa(\rho,z) \approx \sum_i \mathcal{A}_\kappa^i N_i(\rho,z), \qquad \kappa = \{\rho,z\}, \tag{3.62}$$

where $N_i(\rho,z)$ are the two-dimensional basis functions surrounding the nodal elements $\mathcal{A}_\kappa^i$, which are arranged on a two-dimensional grid covering the ρ-z-plane. When A_κ of Eq. (3.61) are represented through Eq. (3.62), the action shall be denoted as $\widetilde{\mathcal{I}}\left[\mathcal{A}_\rho^i, \mathcal{A}_z^i\right]$. The minimization is carried out by setting $\partial\widetilde{\mathcal{I}}/\partial\mathcal{A}_\kappa^j = 0$, which can be represented as the following set of systems of linear equations ($\partial/\partial a_j \left(\sum_i a_i b_i\right)^2 = 2b_j \sum_i a_i b_i$ is useful for the differentiation):

$$\underline{\mathrm{N}}_\kappa \boldsymbol{\mathcal{A}}_\kappa = \boldsymbol{\mathcal{J}}_\kappa, \qquad \kappa = \{\rho,z\}. \tag{3.63}$$

The vector $\boldsymbol{\mathcal{A}}_\kappa$ collects the nodal elements (i.e. $(\boldsymbol{\mathcal{A}}_\kappa)_i = \mathcal{A}_\kappa^i$) and the entries of the symmetric matrices $\underline{\mathrm{N}}_\kappa$ describe the overlap between the basis functions. $\boldsymbol{\mathcal{J}}_\kappa$ contains the integrated current densities, weighted with the basis functions. They are given by

$$(\underline{\mathrm{N}}_\rho)_{i,j} = \int_0^\infty \rho \mathrm{d}\rho \int_{-\infty}^\infty \mathrm{d}z \left(\frac{\partial N_i}{\partial\rho}\frac{\partial N_j}{\partial\rho} + \frac{N_i}{\rho}\frac{N_j}{\rho} + \frac{\partial N_i}{\partial z}\frac{\partial N_j}{\partial z} \right), \tag{3.64}$$

$$(\underline{\mathrm{N}}_z)_{i,j} = \int_0^\infty \rho \mathrm{d}\rho \int_{-\infty}^\infty \mathrm{d}z \left(\frac{\partial N_i}{\partial\rho}\frac{\partial N_j}{\partial\rho} + \frac{\partial N_i}{\partial z}\frac{\partial N_j}{\partial z} \right), \tag{3.65}$$

$$(\boldsymbol{\mathcal{J}}_\kappa)_i = \int_0^\infty \rho \mathrm{d}\rho \int_{-\infty}^\infty \mathrm{d}z \mu J_\kappa N_i. \tag{3.66}$$

Note that the matrix equations for $\boldsymbol{\mathcal{A}}_\kappa$ are disjoint, i.e. the vector field components can be solved separately. This is because Eq. (3.61) does not contain any mix terms between A_ρ and A_z, which is not the case for any Lagrangian. For instance, for the Lagrangian of Eq. (3.52), $\boldsymbol{\mathcal{A}}_\rho$ and $\boldsymbol{\mathcal{A}}_z$ have to be solved simultaneously.

3.6.4 Interpolation kernels / Basis functions

The accuracy of the FEA strongly depends on the discretization and the basis functions, which were defined in Eq. (3.62). For vector-valued problems, one distinguishes between node and edge elements. A comparison and their advantages/disadvantages are discussed elsewhere [204]. While a solution of the *vector* potential is desired, it has been separated into *scalar* its components in Eq. (3.63) so that only nodal elements come into question. Furthermore, a rectangular grid is considered for the present work. Triangular elements (or in three dimensions, tetrahedral) are more advantageous for curved geometries[4] Consequently, the two-dimensional elements can be constructed multiplicatively from one-dimensional kernels: $N(\rho,z) = N(\rho)N(z)$.

$N(\circ)$ can be chosen from a large variety of interpolation kernels. Generally, the order determines the size and thus the mutual overlap between the kernels. Also, the higher the order, the more accurately one may represent the sought solution. For instance, the linear (first order) interpolation kernel, shaped like a triangular function, is a common choice. It overlaps only with its nearest neighbors. In the FEA literature, higher order elements are usually constructed through the Lagrange polynomials. In the context of

[4] A more detailed description of the geometry is given in Appendix B.1.

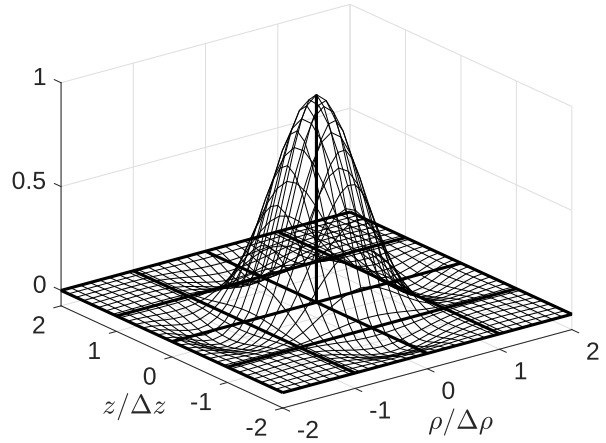

Figure 3.6: Two-dimensional cubic interpolation kernel on a rectangular grid, constructed via $N(\rho,z) = N(\rho)N(z)$, where $N(\kappa)$ is defined in Eq. (3.67). Note that it is not strictly positive.

medical imaging, an extensive survey of interpolation kernels is provided by Lehmann et al. [205] (see also [206,207]). Therein, the cubic kernel of Keys [208] is also discussed, which has been chosen for the present work:

$$N(\kappa) = \frac{1}{2}\begin{cases} 3\,|\bar{\kappa}|^3 - 5\,|\bar{\kappa}|^2 + 2 & 0 < |\bar{\kappa}| < 1 \\ -\,|\bar{\kappa}|^3 + 5\,|\bar{\kappa}|^2 - 8\,|\bar{\kappa}| + 4 & 1 < |\bar{\kappa}| < 2\,, \\ 0 & 2 < |\bar{\kappa}| \end{cases} \tag{3.67}$$

where $\bar{\kappa} = \kappa/\Delta\kappa$ is the coordinate κ normalized by its spacing $\Delta\kappa$, which is not necessarily uniform. To satisfy the defining criterion of an *interpolation kernel* it is unity at the center and vanishes at the surrounding nodes[5]. Being third order, it reaches to its four nearest neighbors. The two-dimensional kernel is shown in Fig. 3.6. It has been chosen, since it smoothly interpolates the first derivative. Recall that it is necessary to differentiate the estimated vector potential to obtain the magnetic field (see Eq. (3.10) or Eq. (A.75)).

Finally, in order to obtain the magnetic field from the vector potential, one needs to apply Eq. (3.10), i.e. Eq. (A.75):

$$\begin{aligned} B_\phi(\rho_i^B, z_j^B) &= \sum_k \mathcal{A}_\rho^k \frac{\partial N_k(\rho_i^B, z_j^B)}{\partial z} - \sum_k \mathcal{A}_z^k \frac{\partial N_k(\rho_i^B, z_j^B)}{\partial \rho} \\ &\equiv B_{\phi,\rho} \qquad\qquad + B_{\phi,z}, \end{aligned} \tag{3.68}$$

where ρ_i^B and z_j^B is the set of coordinates, where the magnetic field is evaluated. Since A_ρ originates solely from the radial current and the same goes for A_z (see Eq. (3.63)), the magnetic field that originates from the radial ($B_{\phi,\rho} = \partial A_\rho/\partial z$) and longitudinal ($B_{\phi,z} = -\,\partial A_z/\partial\rho$) current can also be separated, as has been done in Eq. (3.68).

3.6.5 Boundaries

Eqs. (3.56) and (3.57) are (static) boundary value problems, which require boundary conditions for a unique solution. Since it can be reasonably assumed that there are no discontinuities of the permeability (see Eq. (3.3) and text thereafter), a homogeneous and unbound

[5]For instance, B-splines do not satisfy this criterion and are thus *approximation kernels*.

domain is under consideration. Consequently, the boundary conditions are such that the field has to vanish at infinity. In three dimensions, this holds for both the magnetic field and the vector potential, which follows from the solution of Eq. (3.15) in the static case ($\omega = 0$) by means of Green's function [179]:

$$\mathbf{A}(\mathbf{r}) = \frac{\mu}{4\pi} \int_{\mathbb{R}^3} \mathrm{d}^3\mathbf{r}' \frac{\mathbf{J}_\mathrm{f}(\mathbf{r}')}{|\mathbf{r} - \mathbf{r}'|}, \tag{3.69}$$

$$\frac{1}{|\mathbf{r} - \mathbf{r}'|} \approx \frac{1}{|\mathbf{r}|} + \frac{\mathbf{r} \cdot \mathbf{r}'}{|\mathbf{r}|^3} + \dots . \tag{3.70}$$

Eq. (3.70) is the Taylor expansion (generally: $f(\mathbf{r} - \mathbf{r}') \approx f(\mathbf{r}) - \mathbf{r}' \cdot \nabla f(\mathbf{r}) + \dots$) or also known as the *multipole expansion* in this context, which is valid for $|\mathbf{r}| \gg |\mathbf{r}'|$. The first term of Eq. (3.70) dominates for large $|\mathbf{r}|$, so that Eq. (3.69) simplifies to an integral over the current density at large distances from the source, which decreases as $1/|\mathbf{r}|$. Consequently, the vector potential vanishes at infinity. For curvilinear coordinates, such as cylindrical and spherical coordinates, one may need to add that the result remains finite everywhere.

Since the solution of the magnetic field shall be obtained eventually, by initially solving for the vector potential, it might not be necessary to impose those boundary conditions. Some ambiguity does not impact the result due to Eq. (3.10). For instance, a constant modification of the type $A_z \to A_z + c$ still satisfies Eq. (3.57), but leaves $B_{\phi,z} = -\partial A_z/\partial\rho$ unchanged. On the other hand, given a linearly changing radial current[6] of the form $J_\rho(\rho, z) = J_\rho(\rho)\, z$, one can show that the $B_{\phi,\rho}$, originating from the associated A_ρ, is impacted by the boundary conditions. With the ansatz $A_\rho(\rho, z) = A_\rho(\rho)\, z$, Eq. (3.56) reduces to one dimension: $1/\rho\, \partial_\rho[\rho \partial_\rho A_\rho(\rho)] - A_\rho(\rho)/\rho^2 = -\mu J_\rho(\rho)$. The homogeneous solution takes the form $c_-/\rho + c_+\rho$. Together with the inhomogeneous solution, one can satisfy the boundary condition at infinity, while requiring a finite solution $\forall\rho$ leads to $A_\rho(\rho = 0) = 0$. (Also, a nonzero radial field at $\rho = 0$ is not sensible, since one cannot assign a unique direction pointing away from the origin.) Altogether, the solution is given by

$$A_\rho(\rho) = \frac{\mu}{2}\left[\rho \int_\rho^\infty J_\rho(\rho')\mathrm{d}\rho' + \frac{1}{\rho}\int_0^\rho \rho'^2 J_\rho(\rho')\mathrm{d}\rho'\right]. \tag{3.71}$$

Note that when $J_\rho(\rho) \propto \rho^n$, one needs at least $n > -2$, otherwise the current has an unphysical infinite weight around the origin. Recall the basis of FEA. To determine the solution, one minimizes the action (Eq. (3.58)), which along ρ only reduces to $\mathcal{I}[A_\rho] = \int_0^\infty \mathrm{d}\rho \mathcal{L}[A_\rho]$, where $\mathcal{L}[A_\rho] = \rho\left[(\partial A_\rho/\partial\rho)^2 + (A_\rho/\rho)^2\right]/(2\mu) - \rho J_\rho A_\rho$. Finally, how $B_{\phi,\rho}$ is impacted by the boundaries can be discussed for the present one-dimensional case. Adding the homogeneous solution to Eq. (3.71) remains valid: $A_\rho(\rho) \to A_\rho(\rho) + c_-/\rho + c_+\rho$, yet for $\rho \in [0, \infty)$, both homogeneous terms have an infinite contribution to the action. Accordingly, they will not appear in the solution as expected and A_ρ vanishes towards infinity ($c_+ = 0$) and remains finite $\forall\rho$ ($c_- = 0$). However, for a finite upper limit $\rho \in [0, \rho^A_\mathrm{max}]$, the action can be further minimized through the linear term $c_+\rho$. It is demonstrated in Fig. 3.7 for the case $J_\rho(\rho) = 6I[\theta(\rho) - \theta(\rho - \rho_0)]/\rho_0^3$. The normalization of J_ρ is chosen such that

$$A_\rho(\rho) = \frac{\mu I}{\rho}\begin{cases} (\rho/\rho_0)^2(3 - 2\,\rho/\rho_0) & \text{for } \rho \le \rho_0 \\ 1 & \text{for } \rho > \rho_0 \end{cases}, \tag{3.72}$$

is independent of the radius ρ_0 for $\rho > \rho_0$. It has been calculated from Eq. (3.71).

In Fig. 3.7, it is shown that $c_+ \neq 0$ minimizes the action and that the additional term distorts the results away from the expected A_ρ from Eq. (3.72). Note that this will

[6] Along the beam line and within the target, this assumption is indeed realistic, as can be seen in Fig. 5.18.

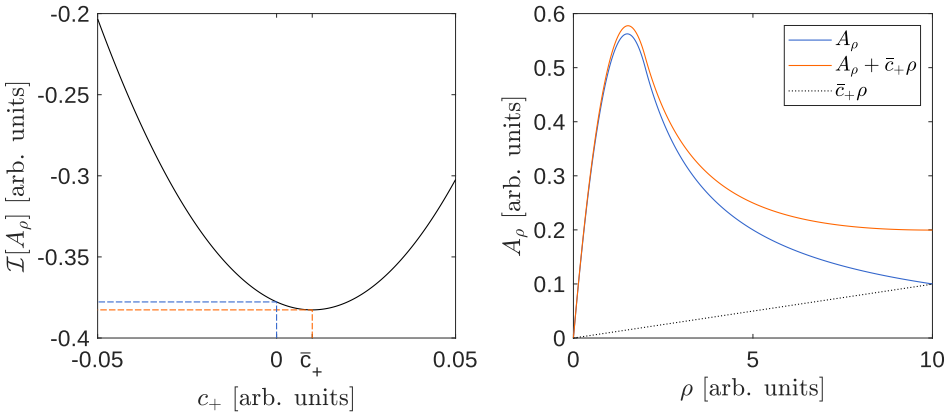

Figure 3.7: Qualitative minimization of the action $\mathcal{I}[A_\rho + c_+\rho]$ for different values of c_+ (left) in the case $\rho \in [0, 10]$. By minimizing the action within the finite domain, one obtains the slope $\bar{c}_+ \neq 0$, which differs from the expected A_ρ given in Eq. (3.72). The two solutions are shown on the right together with their difference $\bar{c}_+\rho$. The action of $A_\rho + \bar{c}_+\rho$ is lower, since it flattens out towards larger ρ, so that the term $\rho(\partial A_\rho/\partial\rho)^2/(2\mu)$ from $\mathcal{I}$ contributes less. $\rho_0 = 2$ and $I = \mu = 1$ has been set, hence the arbitrary units.

also not vanish upon differentiation to obtain the magnetic field: $B_{\phi,\rho} = \partial A_\rho(\rho, z)/\partial z = \partial(A_\rho(\rho)\, z)/\partial z = A_\rho(\rho)$.

Several techniques on how to handle infinite domains have been developed (see Zienkiewicz [209] and references therein), such as infinite elements [210–212]. Yet, in Fig. 3.7 one may also see that the inaccuracies related to c_+ would decrease if the upper limit $\rho^A_{\max}$ would be increased. Hence, for the present work, the probably simplest method is chosen, i.e. enlarging the domain such that the outer edges can approximately be considered infinite. At those boundaries, the field is then set to zero. In order to maintain moderate computational costs, the spacing is increased at larger distances, which is possible, since the field flattens for large ρ (see Fig. 3.7), allowing a wider spacing. Details are described in Appendix B.1. Recall that also $A_\rho(\rho = 0)$ has to be set, since also $\underline{\mathrm{N}}_\rho$ (see Eq. (3.64)) diverges at $\rho = 0$. In the literature, setting a specific value is known as Dirichlet boundary condition, while specifying a derivative at the boundary is named after Neumann [181,186]. To incorporate them, the symmetric modification of the linear system from Eq. (3.63) has been used, as described in [213]. Consider the general system $\underline{\mathrm{A}}\mathbf{x} = \mathbf{b}$, where $x_k = c_k$ is known. The necessary steps are:

1. $b_i \to b_i - \underline{\mathrm{A}}_{i,k} c_k$, $\forall i$
2. $\underline{\mathrm{A}}_{i,k} = \underline{\mathrm{A}}_{k,i} = 0$, $\forall i$
3. $\underline{\mathrm{A}}_{k,k} = 1$
4. $b_k = c_k$

3.6.6 Numerical solution

Finally, to obtain the nodal elements $\boldsymbol{\mathcal{A}}_\kappa$, expanding the vector potential A_κ (see Eq. (3.62)), from which the magnetic field is estimated by differentiation, one needs to solve the linear system given in Eq. (3.63). Its size and thus its complexity depends on the number of elements necessary to approximate the domain. In particular, the number of rows (and

columns - square matrix) can reach from ten thousands to millions. For this reason Eq. (3.63) is usually solved numerically. Numerous methods exist [214, 215], where the sparsity and symmetry of $\underline{\mathrm{N}}_\kappa$ can also be exploited. For instance, the *conjugate gradient method* is a well-known example. Yet, having reduced the problem to two dimensions, decreases the size of Eq. (3.63) to only a few ten thousand rows, which can be solved by inversion through the LU decomposition. In addition, the discretized current density elements, which are obtained from MC simulations, simplify the integral of Eq. (3.66) to a weighted sum[7]. In turn, this may be represented by a matrix multiplication: $\boldsymbol{\mathcal{J}}_\kappa = \underline{\mathrm{K}}_J \mathbf{J}_\kappa$, where the vector $\mathbf{J}_\kappa$ collects the discretized current density elements. Also, by representing the interpolation of Eq. (3.68) through another two matrices ($\mathbf{B}_{\phi,\kappa} = \underline{\mathrm{K}}_\kappa \boldsymbol{\mathcal{A}}_\kappa$) one may establish a direct connection between the current density elements and the magnetic field:

$$\mathbf{B}_{\phi,\kappa} = \underbrace{\underline{\mathrm{K}}_\kappa \underline{\mathrm{N}}_\kappa^{-1} \underline{\mathrm{K}}_J}_{\underline{\mathrm{M}}_\kappa} \mathbf{J}_\kappa, \tag{3.73}$$

where the vector $\mathbf{B}_{\phi,\kappa}$ contains the magnetic field at the set of coordinates (ρ_i^B, z_j^B). The magnetic field is thereby a weighted sum of the current density elements, with the weights collected in $\underline{\mathrm{M}}_\kappa$. Estimating the uncertainty of the magnetic field that originates from the fluctuations of the current density is particularly simple through this representation. The variance of a weighted sum of random variables[8] is given by $\mathrm{Var}[\sum_i a_i X_i] = \sum_i a_i^2 \mathrm{Var}[X_i] + \sum_{i \neq j} a_i a_j \mathrm{Cov}[X_i, X_j]$ [216], which further simplifies by neglecting the covariance[9]. By returning to the matrix notation, where the uncertainty of $\mathbf{J}_\kappa$ is denoted as $\boldsymbol{\sigma}_{J_\kappa}$, one eventually gets:

$$\boldsymbol{\sigma}_{B_{\phi,\kappa}} = \left(\underline{\mathrm{M}}_\kappa^{\circ 2} \boldsymbol{\sigma}_{J_\kappa}^{\circ 2} \right)^{\circ 1/2}, \tag{3.74}$$

where $\boldsymbol{\sigma}_{B_{\phi,\kappa}}$ is a vector of the magnetic field uncertainty at the (ρ_i^B, z_j^B). $\mathbf{v}^{\circ p}$ is the element-wise power as in $(\mathbf{v}^{\circ p})_i = v_i^p$. Without Eq. (3.73), i.e. if the direct inversion is not possible, one could also estimate $\boldsymbol{\sigma}_{B_{\phi,\kappa}}$ by repeatedly calculating $\mathbf{B}_{\phi,\kappa}$ from the different $\mathbf{J}_\kappa$ that were used to estimate $\boldsymbol{\sigma}_{J_\kappa}$, followed by analyzing the $\mathbf{B}_{\phi,\kappa}$ distributions. In fact, Eq. (3.74) has been verified by doing so.

[7] Assuming a constant value for each pixel without further interpolation.

[8] $\mathbf{J}_\kappa$ is treated as random variable.

[9] That the covariance can be neglected is not straightforward. For more details, see Sec. 5.1.4.

4 ELECTROMAGNETIC FIELD OF PRIMARY PROTONS

IN HOMOGENEOUS BIOLOGICAL TISSUES

Having laid out the physical basics in the previous two chapters, a proper quantification and analysis of the electromagnetic field that originates from the primary protons ensues. A first investigation has been carried out by Albert et al. [85], so a brief recap of their work follows. They proposed the detection of the electric field emerging from the primary protons as an alternative range verification method. Their calculations are based on an analytical solution of the Maxwell equations to numerically compute the electric field of a pulsed beam, following a simplified straight line in various biological tissues. The primary proton path was determined by the interaction with the target, which is described by the Bethe-Bloch formula (see Eq. (2.1) and Sec. 2.1.5). The biological tissues were characterized by their RSP, as defined in Eq. (2.3), and the permittivity was modeled with the Cole-Cole equation from Eq. (3.23). The point particle solutions were superimposed with a special case of what is described in Sec. 3.5. They used the electromagnetic interface conditions (Sec. 3.3) to obtain the field outside of a cylindrical volume. Finally, they consider rectangular beam pulses with a duration of 10 and 100 ns, which is 10^2-10^3 times shorter than what is possible with clinical accelerators (see Sec. 2.3). They concluded that the radial component of the electric field (perpendicular to the beam axis) peaks at the range and is with a magnitude of about 150 mV/cm in a detectable range by means of Mach-Zehnder sensors. They can detect fields as low as 10 mV/cm, according to their literature review [217,218]. In addition, they showed that their findings also hold under more realistic assumptions, such as energy and range straggling and a non-zero lateral beam spot size. In their discussion they argue that the field will remain detectable for a couple of seconds, only weakened by diffusion processes.

The contributions described in this chapter build upon the work of Albert et al. and carries it forward in numerous ways. The mathematical framework of Albert et al. is largely adapted and complemented by the estimation of the magnetic field. As opposed to the electric field, the magnetic field depends considerably on the properties of the current density as well as the pulse shape. For that matter and to enhance the interpretation/discussion of the results, their properties are analyzed separately. A generalization from rectangular to arbitrarily shaped pulses has been developed for this work and was already presented in the previous chapter. With respect to the electric field, the impact of the target's conductivity on the charges in the same cylindrical geometry as in Albert et al is investigated. While in their work the conductivity has been taken into account by including it within the permittivity model (see Eq. (3.32)), it has been found that this cannot be combined with the interface conditions. Instead, a simplified solution of the continuity equation, with boundaries included via a discontinuous conductivity, leads to considerably different results for the electric field. Within the homogeneous target, no simplifying assumptions for the Maxwell equations have been made. This means that the solutions entail electro-

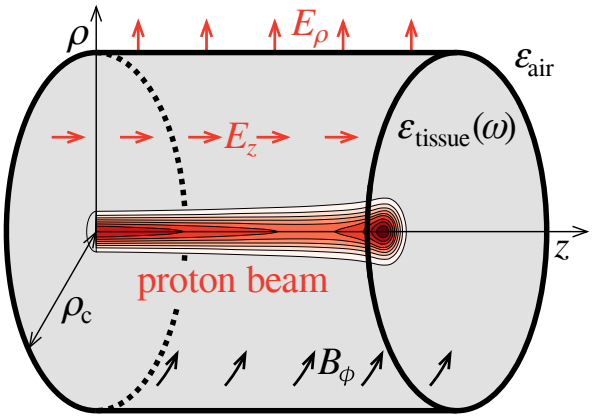

Figure 4.1: Geometrical setup with a radius of $\rho_c = 10$ cm, where only E_ρ, E_z and B_ϕ (indicated by arrows) are non-zero. The shaded gray volume has a frequency dependent permittivity (modeled through the Cole-Cole equation) and is surrounded by air, where $\varepsilon_{\text{air}} \approx \varepsilon_0$.

magnetic waves that originate from the primary protons. A comprehensive analysis is presented, including a separation into its well-known constituents. For this purpose, an alternative derivation of the electromagnetic field through the Liénard-Wiechert potentials is discussed. The flow of energy through the Poynting theorem is also shown. This work has been published in [177] and presented in [219].

4.1 Methods

The methods beyond the basics presented in the previous chapters will be shown in this section. A few simplifying assumptions have been made, which shall be mentioned briefly. With the chosen framework, nuclear reactions, which affect approximately 10% of the primaries [116] cannot be modeled. As mentioned above, the basic idea is to solve for the electromagnetic field of a point particle (described below), which will then be superimposed according to the beam structure (see Sec. 3.5). This path must be representative for all particles, which is not possible with particles that are impacted by nuclear reactions. They can occur all along the track, so that no single representative path exists. Lateral scattering is neglected for the same reason. Instead, the CSDA-based proton path has been used, which is predominantly decelerated by interactions with the electrons of the target. Effects that lead to a broadening of the Bragg peak, such as the statistical nature of the energy loss, variations of the ionization potential or even changing charge states of the primaries at the range were collectively estimated by Albert et al. by studying the influence of lateral and range straggling. They concluded that these effects do not impair the correlation of the field profile with the range and alter the magnitude in the order of 1%. Accordingly, it remains valid to study mono-energetic beams, where $Q = 150$ MeV has also been selected.

Regarding the geometry, the same cylindrical coordinate system as Albert et al. is considered, where the symmetry axis (z-axis) is aligned with the beam axis. A schematic drawing is shown in Fig. 4.1. The particles are launched at the origin and decelerate along the positive z-axis. The implications of creating charges at $(\mathbf{r}, t) = (\mathbf{0}, 0)$ are discussed in Sec. 4.1.6.

4.1.1 General solution of the homogeneous Maxwell equations

In the four-dimensional Fourier domain with respect to space and time, as defined in Eqs. (A.1a) and (A.1b), the Maxwell equations for a homogeneous medium ($\mu(\mathbf{r}) = \mu$, $\varepsilon(\mathbf{r}) = \varepsilon$) have a closed form solution. The expression for the electric field is already stated in Albert et al. [85], which follows directly from Eqs. (3.5a) to (3.5d). After a few algebraic manipulations (explicitly given in Eq. (A.9)), one obtains

$$\tilde{\tilde{\tilde{\mathbf{E}}}}(\mathbf{k},\omega) = -\frac{1}{\tilde{\varepsilon}_\mathrm{c}(\omega)} \frac{i\omega\tilde{\tilde{\tilde{\mathbf{J}}}}_\mathrm{f}(\mathbf{k},\omega)/\tilde{c}^2(\omega) - i\mathbf{k}\tilde{\tilde{\rho}}_\mathrm{f}(\mathbf{k},\omega)}{k^2 - \omega^2/\tilde{c}^2(\omega)}, \tag{4.1}$$

where $k^2 \equiv \mathbf{k}\cdot\mathbf{k} = k_x^2 + k_y^2 + k_z^2$ and the (complex) speed of light in the medium has been introduced:

$$1/\tilde{c}^2(\omega) = \mu\tilde{\varepsilon}_\mathrm{c}(\omega). \tag{4.2}$$

The solution for the magnetic field is obtained analogously (see Eq. (A.10)) and generally has a similar form:

$$\tilde{\tilde{\tilde{\mathbf{B}}}}(\mathbf{k},\omega) = \mu\frac{-i\mathbf{k}\times\tilde{\tilde{\tilde{\mathbf{J}}}}_\mathrm{f}(\mathbf{k},\omega)}{k^2 - \omega^2/\tilde{c}^2(\omega)}. \tag{4.3}$$

Both Eqs. (4.1) and (4.3) are closely related to and follow more evidently from the *inhomogeneous wave equations* [153]

$$-\nabla^2\mathbf{E} + \frac{1}{c^2}\frac{\partial^2}{\partial t^2}\mathbf{E} = -\mu_0\frac{\partial}{\partial t}\mathbf{J}_\mathrm{f} - \frac{1}{\varepsilon_0}\nabla\rho_\mathrm{f}, \tag{4.4}$$

$$-\nabla^2\mathbf{B} + \frac{1}{c^2}\frac{\partial^2}{\partial t^2}\mathbf{B} = \mu_0\nabla\times\mathbf{J}_\mathrm{f}, \tag{4.5}$$

which, for simplicity, have been stated as the microscopic form, i.e. in vacuum. In the following, the source terms, that are the charge and current density, will be stated and analyzed.

4.1.2 Analytical analysis of the point particle charge and current density

The lateral scattering into the x-y-plane has been neglected in this (and the sixth) chapter so that the point particle path follows a straight line along the z-axis. Accordingly, the position and velocity vectors for Eqs. (3.38) and (3.39) are $\mathbf{r}_\mathrm{p}(t) = (0,0,f_z(t))^\mathrm{T}$ and $\mathbf{v}_\mathrm{p}(t) = (0,0,\dot{f}_z(t))^\mathrm{T}$, so that

$$\rho_\mathrm{f}(\mathbf{r},t) = q_\mathrm{e}\,\delta(x)\delta(y)\delta(z - f_z(t))\theta(t), \tag{4.6}$$

$$\mathbf{J}_\mathrm{f}(\mathbf{r},t) = q_\mathrm{e}\dot{f}_z(t)\,\delta(x)\delta(y)\delta(z - f_z(t))\theta(t)\hat{\mathbf{e}}_z, \tag{4.7}$$

where the approach from Albert et al. has been adapted, which includes the step function $\theta(t)$. The charge is thereby created at the origin, which introduces a discontinuity of the charge and current density so that Eqs. (4.6) and (4.7) do not satisfy the continuity equation (Eq. (3.7)). This scenario has already been discussed in Sec. 3.4, while the implications will be analyzed in Sec. 4.1.6. The point particle path $f_z(t)$ is used with its velocity $\dot{f}_z(t)$ and acceleration $\ddot{f}_z(t)$, which is derived from the CSDA (see Sec. 2.1.5 for details) and are shown in Fig. 2.10.

A brief analysis of Eqs. (4.6) and (4.7) follows, which shall help to facilitate the interpretation of the results. In addition to the electric field, which is primarily discussed by Albert et al., also results of the magnetic field will be shown. While the influence of the pulse shape for the former is secondary, since it only dictates how the signal accumulates, it is all the more relevant for the latter, since it determines its signal strength.

It may initially seem counter-intuitive and it is not obvious that the charge density from Eq. (4.6) increases downstream, whereas the current density from Eq. (4.7) remains constant. In fact, based on Eq. (4.7), one may expect the opposite, since the current density scales with the decreasing velocity $\dot{f}_z(t)$. It may also seem mathematically unreasonable to consider a delta peak that increases its density. These issues may be resolved by taking into account how the delta function behaves when it is composed with another function $f(t)$: $\delta(f(t)) = \delta(t - t_0)/\left|\partial f(t)/\partial t \,\big|_{t_0}\right|$, where t_0 is the only root of the inner function, i.e. $f(t_0) = 0$ [220]. Accordingly, the delta functions of Eqs. (4.6) and (4.7) can be rewritten as

$$\delta\big(z - f_z(t)\big) = \delta\big(t - f_z^{-1}(z)\big)\,/\,\dot{f}_z(t), \tag{4.8}$$

where $\dot{f}_z(t) > 0$ has been assumed. When Eq. (4.8) is combined with Eqs. (4.6) and (4.7), then the velocity cancels for the current density and the charge density is inverse proportional to it. Eventually, this leads to the unexpected statement from above, i.e. the charge density increases, while the current density remains constant. While it may be rather abstract for a point particle, the same is more intuitive for a collection of particles in a beam. Barring the range and energy straggling, whose impact will be analyzed in the following chapter, and assuming a CSDA idealized path, it follows that the deceleration changes continuously in the target as a function of the depth. Particles further downstream undergo a stronger deceleration and move slower than particles further upstream so that they can "catch up". Consequently, the distance between consecutive particles decreases, which effectively increases the charge density. Finally, it is nonetheless interesting that a property, that is more sensible in the context of a beam, is also captured by a point particle representation of the charge and current density.

The increasing charge density can be visualized by studying the evolution of a pulse as it decelerates within the target. For this purpose, one maps the initial temporal pulse distribution $\gamma(t')$, like the one introduced in Sec. 3.5, to a spatial distribution $\zeta(z,t)$ along the z-axis after the time t passed. In general, given the distribution of the random variable X, denoted as $f_X(x)$, the distribution of the random variable $Y = g(X)$ can be expressed as [221]

$$\begin{aligned} f_Y(y) &= f_X\big(g^{-1}(y)\big)\left|\partial g^{-1}(y)/\partial y\right| \\ &= f_X\big(g^{-1}(y)\big)/\left|g'\big(g^{-1}(y)\big)\right|, \end{aligned} \tag{4.9}$$

where $g'(x) = \partial_x g(x)$ and the differentiation rule for inverse functions has been used: $\partial g^{-1}(y)/\partial y = 1/\partial_x g(x)|_{x=g^{-1}(y)}$. For simplicity, the time, when the first particle enters the decelerating medium at $z = 0$ is set to $t = 0$. With this reference point, the initial (pristine) distribution $\gamma(t')$, prior to the deceleration, vanishes for $t' > 0$. Certainly, this can always be achieved for any distribution by an appropriate shift. Accordingly, particles at $-t_0' < 0$ will take t_0' to enter the medium, while $\gamma(t')\mathrm{d}t'$ determines the number of particles entering. The distribution is then shifted to the desired time t ($\gamma(t') \to \gamma(t' - t)$), where each t' is mapped to $z = f_z(t')$:

$$\zeta(z,t) = \gamma\big(f_z^{-1}(z) - t\big)\,/\,\dot{f}_z\big(f_z^{-1}(z)\big)\,, \tag{4.10}$$

where once again $\dot{f}_z(t) \geq 0$ is assumed $\forall t$. Fig. 4.2 shows an example based on the beta distribution ($t \in [0,1]$)

$$\gamma(t) = \frac{t^{\alpha-1}(1-t)^{\beta-1}}{\Gamma(\alpha)\Gamma(\beta)/\Gamma(\alpha+\beta)}, \tag{4.11}$$

which has been chosen, since the parameter choice of $\alpha = \beta = 6$ bears a strong resemblance to a normal distribution, while it has a finite support, unlike a normal distribution. The

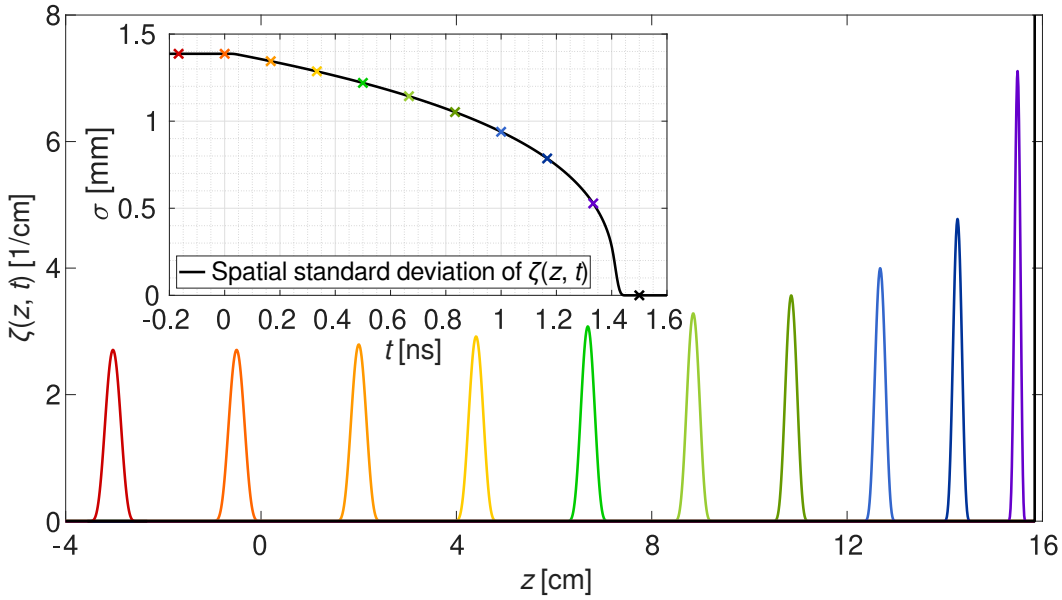

Figure 4.2: Shape evolution of an initially beta distributed pulse. For a few selected times t, marked as colored crosses in the insert, the color-coordinated $\zeta(z,t)$ are shown. The second (orange) pulse from the left is calculated from the pristine pulse $\gamma(t')$ prior to entering the decelerating medium (water). The original beta distribution, as stated in Eq. (4.11), has been shifted and rescaled so that the initial domain of $t' \in [0,1]$ changes to $t' \in [-\Delta t', 0]$. As described in the text, $\Delta t'$ is chosen so that the spatial extent of the pulse is $\Delta z = 10$ mm. The remaining pulses are shifted as $\gamma(t'-t)$ and transformed as in Eq. (4.10). With an initial energy of $Q_{\text{in}} = 150$ MeV, one can see how the pulse traverses along the z-axis and eventually culminates at the range of approximately 15.8 cm as a delta pulse. Scattering and energy straggling has been neglected. The insert shows the standard deviation of $\zeta(z,t)$ with respect to z. In particular, one first calculates the mean by definition as $\mu_\zeta(t) = \int_{\mathbb{R}} z\,\zeta(z,t)\mathrm{d}z$, followed by the spatial standard deviation: $\sigma_\zeta(t) = \int_{\mathbb{R}} (z-\mu_\zeta(t))^2\,\zeta(z,t)\mathrm{d}z$. The latter has been done with denser sampling, resulting in the black graph in the insert. It follows an almost identical shape as the velocity in Fig. 2.10, which confirms that the density increases proportional to the inverse velocity.

initial energy for Fig. 4.2 is $Q_{\text{in}} = 150$ MeV so that its initial velocity is $\beta_{\text{in}} = v_{\text{in}}/c_0 \approx 0.5066$ (see Eq. (2.18)). Due to the high velocity, a pulse with a finite width, which shall be smaller than the range, has an extremely short duration. In particular, a rectangular pulse with $\Delta z = 10$ mm has a temporal span of $\Delta t' = \Delta z / v_{\text{in}} \approx 65.84$ ps. Such parameters are clinically unreasonable, unless laser accelerated protons are taken into consideration [222]. Only for visualization purposes and to demonstrate a fundamental property (increasing charge density), a pulse duration of such a magnitude has been used. The same principle holds true for more realistic and longer pulses, where the charge density is locally increased. This will explicitly be shown in the following chapter, based on Monte Carlo data, where energy straggling is also taken into account.

Finally, for Eqs. (4.1) and (4.3), the four-dimensional Fourier transform of the charge and current density from Eqs. (4.6) and (4.7) is needed, which is defined in Eqs. (A.1a) and (A.1b):

$$\tilde{\tilde{\rho}}_{\text{f}}(\mathbf{k},\omega) = \frac{q_{\text{e}}}{(2\pi)^3} \int_0^\infty \frac{\mathrm{d}t}{2\pi} \exp[ik_z f_z(t) - i\omega t], \tag{4.12}$$

$$\tilde{\tilde{\mathbf{J}}}_{\text{f}}(\mathbf{k},\omega) = \frac{q_{\text{e}}}{(2\pi)^3} \int_0^\infty \frac{\mathrm{d}t}{2\pi} \dot{f}_z(t) \exp[ik_z f_z(t) - i\omega t] \hat{\mathbf{e}}_z. \tag{4.13}$$

With Eq. (4.8), a seemingly different result is obtained, which, however, is equal to Eqs. (4.12) and (4.13). Their equivalent follows from a dedicated integral transform. Equipped with the source terms, they can now be combined with Eqs. (4.1) and (4.3).

4.1.3 Direct solution of Eqs. (4.1) and (4.3) by inverse Fourier transform

The point particle solutions of both the electric and magnetic field are sought, which can now be stated through the results from Secs. 4.1.1 and 4.1.2. One can exploit the fact that Eqs. (4.1) and (4.3) as well as Eqs. (4.12) and (4.13) are sufficiently similar, so that the first steps can be generalized by introducing a placeholder $\tilde{\tilde{\mathbf{F}}} = \{\tilde{\tilde{\mathbf{E}}}, \tilde{\tilde{\mathbf{B}}}\}$ for both the electric and magnetic field. Combining the aforementioned equations, one can state

$$\tilde{\tilde{\mathbf{F}}}(\mathbf{k},\omega) = \frac{q_\mathrm{e}}{(2\pi)^3}\int_0^\infty \frac{\mathrm{d}t'}{2\pi}\tilde{\tilde{\mathbf{f}}}_F(\mathbf{k},\omega,t')\frac{\exp\left[ik_z f_z(t') - i\omega t'\right]}{k^2-\omega^2/\tilde{c}^2(\omega)}, \tag{4.14}$$

where $\tilde{\tilde{\mathbf{f}}}_F(\mathbf{k},\omega,t')$ are field specific. It will be shown below, that their dependency on $\mathbf{k}$ can be eliminated through differential operations. This is particularly helpful for the inverse Fourier transform, constituting the following step. It will allow a partial analytical evaluation. With the inverse Fourier transform defined in Eq. (A.1b), the general field variable from Eq. (4.14), back in temporal and spatial domain, becomes

$$\mathbf{F}(\mathbf{r},t) = \frac{q_\mathrm{e}}{(2\pi)^3}\int_{-\infty}^\infty \mathrm{d}\omega \int_0^\infty \frac{\mathrm{d}t'}{2\pi}\,\tilde{\mathbf{f}}_F(\omega,t')\,\mathrm{I}[\omega/\tilde{c}(\omega),\mathbf{r}-\mathbf{r}_\mathrm{p}(t')]\exp\left[i\omega(t-t')\right], \tag{4.15}$$

where the $\mathbf{k}$-space integral is summarized and already evaluated in the identity from Eq. (A.11). The $\mathbf{k}$-independent equivalent of $\tilde{\tilde{\mathbf{f}}}_F(\mathbf{k},\omega,t')$, denoted as $\tilde{\mathbf{f}}_F(\omega,t')$, has been used in Eq. (4.15). They will be derived in the following. Note that in Eq. (4.15), $\tilde{\mathbf{f}}_F(\omega,t')$ had deliberately been placed to the left of $\mathrm{I}[\ldots]\exp[\ldots]$, since its differential operators act on the expressions on its right. With Eq. (A.11),

$$\mathrm{I}[\omega/\tilde{c}(\omega),\mathbf{r}-\mathbf{r}_\mathrm{p}(t')] = 2\pi^2\exp\left[-i\omega d(\mathbf{r},t')/\tilde{c}(\omega)\right]/d(\mathbf{r},t')\,, \tag{4.16}$$

where the sign in the exponent is negative, since $\omega/\tilde{c}(\omega)$ has a negative imaginary part, which follows from Eq. (4.2) and Eq. (3.28). In Eq. (4.16), the absolute distance to the particle has been used

$$d(\mathbf{r},t') \equiv |\mathbf{r}-\mathbf{r}_\mathrm{p}(t')| = \sqrt{\rho^2+\Delta z^2(t')}, \qquad \Delta z(t') = z - f_z(t'). \tag{4.17}$$

As defined in Eq. (4.14), the $\tilde{\tilde{\mathbf{f}}}_F(\mathbf{k},\omega,t')$, with the help of Eqs. (4.1) and (4.3) as well as Eqs. (4.12) and (4.13) can now be identified as

$$\tilde{\tilde{\mathbf{f}}}_E(\mathbf{k},\omega,t') = -1/\tilde{\varepsilon}_\mathrm{c}(\omega)\left[i\omega\dot{f}_z(t')/\tilde{c}^2(\omega)\,\hat{\mathbf{e}}_z - i\mathbf{k}\right], \tag{4.18}$$

$$\tilde{\tilde{\mathbf{f}}}_B(\mathbf{k},\omega,t') = -i\mu\dot{f}_z(t')\mathbf{k}\times\hat{\mathbf{e}}_z. \tag{4.19}$$

As mentioned earlier, their dependency on $\mathbf{k}$ can be eliminated through differential operations. In particular, the factors to the right of $\tilde{\mathbf{f}}_F(\omega,t')$ in Eq. (4.15) are proportional to $\exp(-i\mathbf{k}\cdot\mathbf{r}+i\omega t)$. Accordingly, one can make use of the following identities

$$i\omega\exp(i\omega t) = \partial_t\exp(i\omega t), \tag{4.20}$$

$$-i\mathbf{k}\exp(-i\mathbf{k}\cdot\mathbf{r}) = \nabla\exp(-i\mathbf{k}\cdot\mathbf{r}), \tag{4.21}$$

$$-i\mathbf{k}\times\mathbf{u}\exp(-i\mathbf{k}\cdot\mathbf{r}) = \nabla\times\mathbf{u}\exp(-i\mathbf{k}\cdot\mathbf{r}), \tag{4.22}$$

where the vector $\mathbf{u}$ has been assumed to be independent of $\mathbf{r}$ (i.e. $\mathbf{u}(\mathbf{r}) = \mathbf{u}$). Accordingly, Eqs. (4.18) and (4.19) simplify to

$$\tilde{\mathbf{f}}_E(\omega, t') = -1/\tilde{\varepsilon}_\mathrm{c}(\omega)\big[i\omega \dot{f}_z(t')/\tilde{c}^2(\omega)\ \hat{\mathbf{e}}_z + \nabla\big], \tag{4.23}$$

$$\tilde{\mathbf{f}}_B(\omega, t') = \mu \dot{f}_z(t') \nabla \times \hat{\mathbf{e}}_z, \tag{4.24}$$

where $\mathbf{u} = \hat{\mathbf{e}}_z$ for Eq. (4.22). The $i\omega$ in the square brackets of Eq. (4.23) could have been transformed to ∂_t through Eq. (4.22). Yet, since the inverse Fourier transform with respect to time (i.e. the ω-integral of Eq. (4.15)) cannot be evaluated analytically, due to the complex permittivity models given in Eq. (3.23), there is no advantage in doing so. Interestingly enough, the simplifications in Eqs. (4.23) and (4.24) already foreshadow the alternative approach based on the scalar and vector potential, which is discussed in Sec. 4.1.5. In particular, the time derivative and gradient from Eq. (4.23) are also in Eq. (3.9), while the curl from Eq. (4.24) is connected to the definition of the vector potential in Eq. (3.10).

4.1.4 Frequency spectra of the vector field components

The point particle solution of the fields in the space and time domain are stated through Eqs. (4.15), (4.23) and (4.24). Within this section, the differential operation in Eqs. (4.23) and (4.24) will be carried out, and the different vector components will be separated. With the unidirectional current along z, it is advantageous to use a cylindrical coordinate system (Fig. 4.1), where vectorial quantities are expanded as in Eq. (A.71). As suggested in the title of this section, the inverse Fourier transform with respect to time is put on hold, so that in Eq. (4.15) the ω-integral and the factor $\exp(i\omega t)$ vanish.

4.1.4.1 Electric field

The azimuthal component of the electric field vanishes, since Eq. (4.16) is independent of ϕ and the ϕ-component of the gradient in cylindrical coordinates is proportional to ∂_ϕ. The radial and longitudinal components will be denoted as $\widetilde{E}_\rho^{①+}$ and $\widetilde{E}_z^{①+}$, where the superscript① shall separate the expressions given in this section from the alternative approach in Sec. 4.1.5, which yields the same results. The plus in the superscript indicates that the t'-integral in Eq. (4.15) only includes the positive domain. Recall that this originated from including $\theta(t)$ in Eqs. (4.6) and (4.7), which leads to the issues discussed in Sec. 3.4. With $\circ^{\pm}$, the negative half will also be included. Further details are provided below (see Sec. 4.1.6). By separating the original Fourier forward transform of Eqs. (4.12) and (4.13), the electric field components ($\kappa = \{\rho, z\}$), following from Eqs. (4.15), (4.16) and (4.23), can be written as

$$\widetilde{E}_\kappa^{①+}(\mathbf{r}, \omega) = \int_0^\infty \frac{\mathrm{d}t'}{2\pi} f_\kappa^{①}(\mathbf{r}, \omega, t') \exp\big(-i\omega t'\big), \tag{4.25}$$

where, by the use of the gradient in cylindrical coordinates (Eq. (A.73)) and

$$\frac{\partial}{\partial \rho} d(\mathbf{r}, t') = \frac{\rho}{d(\mathbf{r}, t')}, \tag{4.26}$$

$$\frac{\partial}{\partial z} d(\mathbf{r}, t') = \frac{\Delta z(t')}{d(\mathbf{r}, t')}, \tag{4.27}$$

one obtains

$$f_\rho^{①}(\mathbf{r}, \omega, t') = \frac{q_\mathrm{e}}{\tilde{\varepsilon}_\mathrm{c}(\omega)} \left[\frac{\rho}{d^2(\mathbf{r}, t')} + \frac{i\omega}{\tilde{c}(\omega)} \frac{\rho}{d(\mathbf{r}, t')} \right] \frac{\exp[-i\omega d(\mathbf{r}, t')/\tilde{c}(\omega)]}{4\pi\, d(\mathbf{r}, t')}, \tag{4.28}$$

$$f_z^{①}(\mathbf{r}, \omega, t') = \frac{q_\mathrm{e}}{\tilde{\varepsilon}_\mathrm{c}(\omega)} \left[\frac{\Delta z(t')}{d^2(\mathbf{r}, t')} + \frac{i\omega}{\tilde{c}(\omega)} \frac{\Delta z(t')}{d(\mathbf{r}, t')} - \frac{i\omega \dot{f}_z(t')}{\tilde{c}^2(\omega)} \right] \frac{\exp[-i\omega d(\mathbf{r}, t')/\tilde{c}(\omega)]}{4\pi\, d(\mathbf{r}, t')}. \tag{4.29}$$

The last terms outside of the square brackets of Eqs. (4.28) and (4.29) have deliberately been arranged as such, and are the (negative) Green's functions of the Helmholtz operator. Once again, this is related to the alternative approach shown in Sec. 4.1.5.

The particle's position $f_z(t')$ and velocity $\dot{f}_z(t')$ are independent of t' for $t' > t_\mathrm{r}$, where t_r is the stopping time, i.e. the average time it takes for a single proton to arrive at the range. For clinical energies, t_r lies in the nanosecond range, where a 150 MeV proton takes about 1.4 ns (Fig. 2.10), while a 100 MeV proton takes about 0.8 ns (Fig. 2.11) to reach the range z_r in water. In particular, $f_z(t' > t_\mathrm{r}) = z_\mathrm{r}$ and $\dot{f}_z(t' > t_\mathrm{r}) = 0$. Note that this does not imply that the charge proton remains stationary at the range. $f_z(t')$ merely describes the externally applied *free* charge and current density, while the total charge in the medium includes the *bound* charge, which can cancel the free charge so that conduction phenomena are effectively included. More details are provided in Secs. 4.1.8 and 4.1.9.

Under these assumptions Eq. (4.25) can partially be evaluated analytically. It can be separated into two domains

$$\widetilde{E}^{①+}_\kappa(\mathbf{r},\omega) = \int_0^{t_\mathrm{r}} \frac{\mathrm{d}t'}{2\pi} f^{①}_\kappa(\mathbf{r},\omega,t') \exp\bigl(-i\omega t'\bigr) + f^{①}_\kappa(\mathbf{r},\omega,t_\mathrm{r}) \int_{t_\mathrm{r}}^{\infty} \frac{\mathrm{d}t'}{2\pi} \exp\bigl(-i\omega t'\bigr), \tag{4.30}$$

where the first one has to be evaluated numerically, while the second one can be evaluated analytically. Upon inspection, the latter does not converge, so in order to assign a value to it, the following representation is helpful:

$$\int_{t_\mathrm{r}}^{\infty} \frac{\mathrm{d}t'}{2\pi} \exp\bigl(-i\omega t'\bigr) = \int_0^{\infty} \frac{\mathrm{d}t'}{2\pi} \exp\bigl(-i\omega t'\bigr) - \int_0^{t_\mathrm{r}} \frac{\mathrm{d}t'}{2\pi} \exp\bigl(-i\omega t'\bigr). \tag{4.31}$$

The second on the RHS can be evaluated elementarily, while an exponential relaxation is introduced to evaluate the former ($\epsilon > 0$):

$$\lim_{\epsilon\to 0^+} \int_0^{\infty} \frac{\mathrm{d}t'}{2\pi} \exp\bigl(-i\omega t' - \epsilon t'\bigr) = \lim_{\epsilon\to 0^+} \frac{1}{2\pi} \frac{-i}{\omega - i\epsilon} \overset{\text{Eq. (A.16)}}{=} \frac{\delta(\omega)}{2} + \mathcal{P}\frac{1}{2\pi i\omega}, \tag{4.32}$$

where the Sokhotski-Plemelj formula has been used. Altogether, Eq. (4.25) becomes

$$\widetilde{E}^{①+}_\kappa(\mathbf{r},\omega) = \int_0^{t_\mathrm{r}} \frac{\mathrm{d}t'}{2\pi} f^{①}_\kappa(\mathbf{r},\omega,t') \exp\bigl(-i\omega t'\bigr) + f^{①}_\kappa(\mathbf{r},\omega,t_\mathrm{r}) \left[\frac{\delta(\omega)}{2} + \mathcal{P}\frac{\exp(-i\omega t_\mathrm{r})}{2\pi i\omega}\right]. \tag{4.33}$$

4.1.4.2 Magnetic field

Using Eq. (A.73), Eq. (4.24) simplifies in cylindrical coordinates to $\tilde{\mathbf{f}}_B(\omega,t') = \mu\dot{f}_z(t')$ $(1/\rho\,\partial_\phi\hat{\mathbf{e}}_\rho - \partial_\rho\hat{\mathbf{e}}_z)$. As argued previously, $\mathrm{I}[\ldots]\exp[\ldots]$ in Eq. (4.15) is ϕ-independent so that the magnetic field only consists of an azimuthal component. Just like Eq. (4.25), its frequency spectrum can also be represented as

$$\widetilde{B}^{+}_\phi(\mathbf{r},\omega) = \int_0^{t_\mathrm{r}} \frac{\mathrm{d}t'}{2\pi} f_\phi(\mathbf{r},\omega,t') \exp\bigl(-i\omega t'\bigr), \tag{4.34}$$

where, by differentiating Eq. (4.16), one obtains

$$f_\phi(\mathbf{r},\omega,t') = \mu q_\mathrm{e}\dot{f}_z(t') \left[\frac{\rho}{d^2(\mathbf{r},t')} + \frac{i\omega}{\tilde{c}(\omega)}\frac{\rho}{d(\mathbf{r},t')}\right] \frac{\exp[-i\omega d(\mathbf{r},t')/\tilde{c}(\omega)]}{4\pi\, d(\mathbf{r},t')}. \tag{4.35}$$

Since Eq. (4.35) scales with the velocity and $\dot{f}_z(t' > t_\mathrm{r}) = 0$, Eq. (4.34) only needs to be integrated up to t_r. Additional terms, as in Eq. (4.33), vanish for the magnetic field. Note

that Eqs. (4.28) and (4.35) differ only by a factor, i.e. $f_\phi(\mathbf{r},\omega,t') = \mu\tilde{\varepsilon}_\mathrm{c}(\omega)\dot{f}_z(t')f_\rho^{①}(\mathbf{r},\omega,t') = \dot{f}_z(t')/\tilde{c}^2(\omega)f_\rho^{①}(\mathbf{r},\omega,t')$, since they were derived by carrying out the same differentiation with respect to ρ. With the alternative approach from the following section this connection will become more apparent.

4.1.5 Liénard-Wiechert potentials

Thus far, direct solutions of the Maxwell equations for the electric and magnetic field (Eqs. (4.1) and (4.3)) have been used as a basis to derive the results presented in Sec. 4.1.4. Yet, a more straightforward approach to obtain the same results makes use of the scalar and vector potentials, as defined in Eqs. (3.11) and (3.12). The simplicity of this alternative derivation may be expected from the associated equations for the scalar and vector potentials, given in Eqs. (3.14) and (3.15). Solving them for a point particle results in the so-called Liénard-Wiechert potentials. It generalizes the results from Sec. 4.1.4 regarding the particle path (lifting the assumption of a uni-directional path along z) without having to solve complicated integrals that originate from inverting the $\mathbf{k}$-space integral (Eq. (4.16)). Instead, a Fourier transform with respect to the spatial coordinates is not necessary, since Eqs. (3.14) and (3.15) decouple already in the spatial domain, unlike the electric and magnetic field in Eqs. (3.4a) to (3.4d). In fact, Eqs. (3.14) and (3.15) are sufficiently simple to be solved by means of *Green's function*.

In the literature, the Liénard-Wiechert potentials are usually discussed in the time domain, so in this section the slight modifications necessary to be applicable in the frequency domain will be shown. In particular, the *retarded time* does not have such a straightforward interpretation. Also, they are usually used to derive various properties of bremsstrahlung, since they can be transformed to reveal the electromagnetic field's dependency on the acceleration $\ddot{f}_z(t)$. For the result below, the separation of acceleration-related contributions will also be shown and help to analyze the frequency spectra.

Eqs. (3.14) and (3.15) are both manifestations of an *inhomogeneous Helmholtz equation*, which are of the form $(\nabla^2 + k^2)\psi(\mathbf{r}) = S(\mathbf{r})$, where $k^2 = \omega^2\mu\tilde{\varepsilon}_\mathrm{c}(\omega)$, ψ is either the scalar or vector potential and S are the source terms, i.e. charge or current density. As mentioned above, it can be solved through Green's function [223]:

$$\psi(\mathbf{r}) = \int_{\mathbb{R}^3} \mathrm{d}^3\mathbf{r}' G(\mathbf{r},\mathbf{r}')S(\mathbf{r}'), \qquad (4.36) \qquad G(\mathbf{r},\mathbf{r}') = -\frac{\exp(\pm ik|\mathbf{r}-\mathbf{r}'|)}{4\pi|\mathbf{r}-\mathbf{r}'|}, \qquad (4.37)$$

where Eq. (4.37) is the Green's function of the Helmholtz equation. The latter forms the basis for the work in Chapter 6, where more details regarding Green's function and specifically the derivation of Eq. (4.37) is given (see Sec. 6.1.4). Both signs in the exponent of Eq. (4.37) are valid solutions of the Helmholtz equation, yet, if $k \in \mathbb{C}$, then one of them diverges for large distances from the source $|\mathbf{r}-\mathbf{r}'|$, which is unphysical. The negative sign is necessary for Eq. (3.28) so that Eq. (4.37) *decreases* exponentially. The latter is also known as the *Sommerfeld radiation condition* [224]. Using the general point particle charge and current density from Eqs. (3.38) and (3.39), which only need to be formally Fourier transformed according to Eq. (A.3a), the solutions of Eqs. (3.14) and (3.15) are

$$\widetilde{\varphi}(\mathbf{r},\omega) = \frac{q_\mathrm{e}}{\tilde{\varepsilon}_\mathrm{c}(\omega)} \int_{-\infty}^{\infty} \frac{\mathrm{d}t'}{2\pi} \frac{\exp\left[-i\omega|\mathbf{r}-\mathbf{r}_\mathrm{p}(t')|/\tilde{c}(\omega) - i\omega t'\right]}{4\pi|\mathbf{r}-\mathbf{r}_\mathrm{p}(t')|}, \qquad (4.38)$$

$$\widetilde{\mathbf{A}}(\mathbf{r},\omega) = q_\mathrm{e}\mu \int_{-\infty}^{\infty} \frac{\mathrm{d}t'}{2\pi} \mathbf{v}_\mathrm{p}(t') \frac{\exp\left[-i\omega|\mathbf{r}-\mathbf{r}_\mathrm{p}(t')|/\tilde{c}(\omega) - i\omega t'\right]}{4\pi|\mathbf{r}-\mathbf{r}_\mathrm{p}(t')|}, \qquad (4.39)$$

where the δ^3-functions from Eqs. (3.38) and (3.39) collapsed the $\mathbb{R}^3$-integral from Eq. (4.36), which effectively replaces $\mathbf{r}'$ by $\mathbf{r}_\mathrm{p}(t')$. The remaining t'-integral is related to the Fourier transform of the charge and current density. It cannot be further evaluated without an explicit path $\mathbf{r}_\mathrm{p}(t')$ and velocity $\mathbf{v}_\mathrm{p}(t') = \mathrm{d}\mathbf{r}_\mathrm{p}(t')/\mathrm{d}t'$.

By straightforward differentiation, according to Eqs. (3.11) and (3.12), one obtains the electric and magnetic field from the scalar and vector potential, as given in Eqs. (4.38) and (4.39). When represented as in Eq. (4.25) or Eq. (4.34), the fields are calculated through

$$\widetilde{\mathbf{F}}^{①\pm}(\mathbf{r},\omega) = \int_{-\infty}^{\infty} \frac{\mathrm{d}t'}{2\pi} \mathbf{f}_F^{①}(\mathbf{r},\omega,t') \exp\big(-i\omega t'\big), \tag{4.40}$$

where the subscript $F = \{E, B\}$ and

$$\begin{aligned}&\mathbf{f}_E^{①}(\mathbf{r},\omega,t') \\ &\quad= \frac{q_\mathrm{e}}{\tilde{\varepsilon}_\mathrm{c}(\omega)} \left[\frac{\mathbf{r}-\mathbf{r}_\mathrm{p}(t')}{|\mathbf{r}-\mathbf{r}_\mathrm{p}(t')|^2} + \frac{i\omega}{\tilde{c}(\omega)} \frac{\mathbf{r}-\mathbf{r}_\mathrm{p}(t')}{|\mathbf{r}-\mathbf{r}_\mathrm{p}(t')|} - \frac{i\omega}{\tilde{c}^2(\omega)} \mathbf{v}_\mathrm{p}(t') \right] \frac{\exp\big[-i\omega|\mathbf{r}-\mathbf{r}_\mathrm{p}(t')|/\tilde{c}(\omega)\big]}{4\pi|\mathbf{r}-\mathbf{r}_\mathrm{p}(t')|},\end{aligned} \tag{4.41}$$

$$\mathbf{f}_B^{①}(\mathbf{r},\omega,t') = \mu\tilde{\varepsilon}_\mathrm{c}(\omega)\mathbf{v}_\mathrm{p}(t') \times \mathbf{f}_E^{①}(\mathbf{r},\omega,t'). \tag{4.42}$$

With Eq. (4.17) and $\mathbf{r}_\mathrm{p}(t')$ & $\mathbf{v}_\mathrm{p}(t')$ defined above Eqs. (4.6) and (4.7), on may confirm that Eq. (4.41) (split into $\hat{\mathbf{e}}_\rho$ and $\hat{\mathbf{e}}_z$) is equal to Eqs. (4.28) and (4.29). The same goes for the $\hat{\mathbf{e}}_\phi$ component of Eq. (4.42) and Eq. (4.35).

As stated above, Eq. (4.40) describes not quite the Liénard-Wiechert potentials, as they can be found in the literature [153]. They are usually stated in the time domain, make use of what is known as *retarded time* and the associated electric and magnetic fields depend on the point particles acceleration, unlike Eqs. (4.41) and (4.42). While the final result will still be given in the Fourier domain, the dependency on $\ddot{f}_z(t')$ is obtained by the introduction of the retarded time and an associated transformation. In particular, the retarded time t' is defined as

$$t = t' + |\mathbf{r}-\mathbf{r}_\mathrm{p}(t')|/\tilde{c}(\omega), \tag{4.43}$$

$$\mathrm{d}t'/\mathrm{d}t = 1/(1-\mathbf{n}_\mathrm{p}\cdot\tilde{\boldsymbol{\beta}}_\mathrm{p})\big|_{t'(\mathbf{r},t)}, \tag{4.44}$$

where $\mathbf{n}_\mathrm{p}(t') = (\mathbf{r}-\mathbf{r}_\mathrm{p}(t'))/|\mathbf{r}-\mathbf{r}_\mathrm{p}(t')|$ and $\tilde{\boldsymbol{\beta}}_\mathrm{p}(t') = \mathbf{v}_\mathrm{p}(t')/\tilde{c}(\omega)$. Eq. (4.44) follows from $(\mathrm{d}t/\mathrm{d}t')^{-1}$ in combination with Eq. (4.43). With the dispersion and therefore the complex-valued $\tilde{c}(\omega)$ it is not as straightforward to interpret Eq. (4.43) so that for simplicity $\tilde{\varepsilon}_\mathrm{c}(\omega) \to \varepsilon_0$ and therefore $\tilde{c}(\omega) \to c_0$ is assumed temporarily. An observer at $(\mathbf{r}, t)$ may detect the field that originated from a point particle at $t' < t$, since the associated electromagnetic wave moves at most with the speed of light c_0. By transforming the t'-integrals of Eqs. (4.38) and (4.39) to t via Eqs. (4.43) and (4.44) and inverting the remaining Fourier transform, one obtains the textbook Liénard-Wiechert potentials in vacuum [153]. In other words, Eqs. (4.38) and (4.39) are the Fourier transformed equivalents of the Liénard-Wiechert potentials that also allow for dispersion. This definition of the retarded time has implicitly been used in Eq. (4.40) so that upon transforming it with Eqs. (4.43) and (4.44), the exponential also simplifies significantly. The following results are only stated for the electric field, since only its spectrum will be analyzed in detail. The results for the magnetic field are analogous. The transformation yields

$$\begin{aligned}\widetilde{\mathbf{E}}^{\pm}(\mathbf{r},\omega) = \frac{q_\mathrm{e}}{4\pi\tilde{\varepsilon}_\mathrm{c}(\omega)} \int_{-\infty}^{\infty} \frac{\mathrm{d}t}{2\pi} \exp(-i\omega t) \\ \left[\left(\frac{\mathbf{r}-\mathbf{r}_\mathrm{p}}{|\mathbf{r}-\mathbf{r}_\mathrm{p}|^3} + \frac{i\omega}{\tilde{c}(\omega)} \frac{\mathbf{r}-\mathbf{r}_\mathrm{p}}{|\mathbf{r}-\mathbf{r}_\mathrm{p}|^2} - \frac{i\omega}{\tilde{c}^2(\omega)} \frac{\mathbf{v}_\mathrm{p}}{|\mathbf{r}-\mathbf{r}_\mathrm{p}|} \right) \frac{1}{1-\mathbf{n}_\mathrm{p}\cdot\tilde{\boldsymbol{\beta}}_\mathrm{p}} \right]_{t'(\mathbf{r},t)},\end{aligned} \tag{4.45}$$

where all time dependent quantities within the square brackets are to be evaluated at the retarded time t'. Eq. (4.45) turns out to be a Fourier transform (compare Eq. (A.3a)). Accordingly the factors of $i\omega$ in Eq. (4.45) may be transformed to time derivatives $\partial/\partial t$ (see Eq. (A.2a)). They then act on the t' dependent $\mathbf{r}_\mathrm{p}$ and $\mathbf{v}_\mathrm{p}$, whose derivative with respect to t is simplified through Eq. (4.44). The necessary algebraic manipulations are straightforward but rather tedious. More details are shown in Appendix A.5. Eventually, the transform from Eqs. (4.43) and (4.44) is inverted so that the second approach can also be written as

$$\widetilde{\mathbf{E}}^{②\pm}(\mathbf{r},\omega) = \int_{-\infty}^{\infty} \frac{\mathrm{d}t'}{2\pi} \mathbf{f}_E^{②}(\mathbf{r},\omega,t') \exp\bigl(-i\omega t'\bigr), \tag{4.46}$$

where

$$\mathbf{f}_E^{②}(\mathbf{r},\omega,t') = \frac{q_\mathrm{e}}{\tilde{\varepsilon}_\mathrm{c}(\omega)} \left\{ \left[\underbrace{\frac{(\mathbf{n}_\mathrm{p}-\tilde{\boldsymbol{\beta}}_\mathrm{p})(1-\tilde{\beta}_\mathrm{p}^2)}{(1-\mathbf{n}_\mathrm{p}\cdot\tilde{\boldsymbol{\beta}}_\mathrm{p})^2|\mathbf{r}-\mathbf{r}_\mathrm{p}|}}_{\mathbf{h}_v^{②}(\mathbf{r},\omega,t')} + \underbrace{\frac{\mathbf{n}_\mathrm{p}\times(\mathbf{n}_\mathrm{p}-\tilde{\boldsymbol{\beta}}_\mathrm{p})\times\dot{\tilde{\boldsymbol{\beta}}}_\mathrm{p}}{\tilde{c}(\omega)(1-\mathbf{n}_\mathrm{p}\cdot\tilde{\boldsymbol{\beta}}_\mathrm{p})^2}}_{\mathbf{h}_a^{②}(\mathbf{r},\omega,t')} \right] \frac{\exp\bigl[-i\omega|\mathbf{r}-\mathbf{r}_\mathrm{p}|/\tilde{c}(\omega)\bigr]}{4\pi|\mathbf{r}-\mathbf{r}_\mathrm{p}|} \right\}_{t'}. \tag{4.47}$$

Having eliminated $i\omega$ from Eq. (4.45), one sees that the electric field's dependency on the acceleration $\dot{\tilde{\boldsymbol{\beta}}}_\mathrm{p}(t') = \mathbf{a}_\mathrm{p}(t')/\tilde{c}(\omega)$ emerges, where $\mathbf{a}_\mathrm{p}(t') = \dot{\mathbf{v}}_\mathrm{p}(t') = \partial\mathbf{v}(t')/\partial t'$ denotes the particles acceleration. This finally establishes the connection between approach ①, as originally derived by Albert et al., and the classical Liénard-Wiechert potentials, here denoted as ②. The result stated in Eqs. (4.46) and (4.47) is practically identical to the results that can be found in the literature [179]. In particular, when Eqs. (4.43) and (4.44) are once again applied, the Fourier transform from Eq. (4.46) can be undone, since the exponent, including the part in Eq. (4.47), simplifies to the base function of the Fourier transform. Note that this is only possible for a non-dispersive medium, i.e. $\tilde{\varepsilon}_\mathrm{c}(\omega) \to \varepsilon_0$ and $\tilde{c}(\omega) \to c_0$. Regardless, the inclusion of a dispersive medium is remarkably simple, when starting from the electric and magnetic fields $\mathbf{F}(\mathbf{r},t)$ that originate from the Liénard-Wiechert potentials in vacuum. A set of canonical rules to transition from one to the other goes as follows: (a) Fourier transform $\mathbf{F}(\mathbf{r},t) \to \widetilde{\mathbf{F}}(\mathbf{r},\omega)$, (b) change the t-integral of the Fourier transform to the retarded time t' via Eqs. (4.43) and (4.44) and (c) replace $\varepsilon_0 \to \tilde{\varepsilon}_\mathrm{c}(\omega)$ and $c_0 \to \tilde{c}(\omega)$. This works for both the Liénard-Wiechert potentials and their associated electric and magnetic fields.

A separation between the velocity term $\mathbf{h}_v^{②}(\mathbf{r},\omega,t')$ and the acceleration term $\mathbf{h}_a^{②}(\mathbf{r},\omega,t')$, as referred to by Jackson [153], has been introduced in Eq. (4.47). The former describes the Coulomb field and the Cherenkov radiation, which is merely a superposition of Coulomb field wave fronts, while the latter, due to its dependency on the acceleration, gives rise to bremsstrahlung. A separation of the two will be presented in the results. To separate Eqs. (4.46) and (4.47) into radial and longitudinal components, like Eqs. (4.25), (4.28) and (4.29), a transformation to cylindrical coordinates is performed and the path defined above Eqs. (4.6) and (4.7) is used. In addition to Eq. (4.17), one can identify $\mathbf{r}-\mathbf{r}_\mathrm{p}(t') = \rho\hat{\mathbf{e}}_\rho + \Delta z(t')\hat{\mathbf{e}}_z$, $\mathbf{n}_\mathrm{p}(t')\cdot\tilde{\boldsymbol{\beta}}_\mathrm{p}(t') = \Delta z(t')\dot{f}_z(t')/(d(\mathbf{r},t')\tilde{c}(\omega))$ and $\mathbf{n}_\mathrm{p}(t')\cdot\dot{\tilde{\boldsymbol{\beta}}}_\mathrm{p}(t') = \Delta z(t')\ddot{f}_z(t')/(d(\mathbf{r},t')\tilde{c}(\omega))$. The explicit expression for the electric field

along z reads as follows (the ρ-component will not be discussed further):

$$h^{②}_{v,z}(\mathbf{r},\omega,t') = \frac{[\Delta z(t') - d(\mathbf{r},t')\dot{f}_z(t')/\tilde{c}(\omega)][\tilde{c}^2(\omega) - \dot{f}_z^2(t')]}{[d(\mathbf{r},t')\tilde{c}(\omega) - \Delta z(t')\dot{f}_z(t')]^2}, \tag{4.48}$$

$$h^{②}_{a,z}(\mathbf{r},\omega,t') = -\frac{\rho^2 \ddot{f}_z(t)}{[d(\mathbf{r},t')\tilde{c}(\omega) - \Delta z(t')\dot{f}_z(t')]^2}. \tag{4.49}$$

4.1.6 Violation of the continuity equation

In Sec. 3.4 it has already been discussed that the charge and current density given in Eqs. (4.6) and (4.7) violate the continuity equation (Eq. (3.7)). While it is computationally favorable to exclude the contributions from $t' < 0$, an identification of the unphysical contributions related to the discontinuity is necessary and the focus of the present section.

4.1.6.1 Complete path

One may gauge the impact of the discontinuity by comparing it to the field generated by a particle following a continuous and *complete path*. The simplest, albeit unphysical, approach is to assume that the particle drifted with the initial velocity v_0 through the same medium before starting to decelerate at $(\mathbf{r},t) = (\mathbf{0},0)$. The path for negative times is then described by $f_z(t' < 0) = v_0 t'$. Under this assumption, one does not need to take a boundary and its complex interactions into account. In particular, this will be subject to the work of Chapter 6. A comparison to such a path is nonetheless reasonable, since firstly, its constant velocity does not give rise to bremsstrahlung. Secondly, the Cherenkov wavefront, which is created since the particle moves faster than the speed of light in the medium, only has a small forward motion so that it does not interfere with the volume of interest ($\rho \sim \rho_\mathrm{c}$, $z \sim z_\mathrm{r}$). Instead, it drifts away at a reasonably shallow angle. More details are discussed in the results. While it was possible to evaluate Eq. (4.25) for $t' > t_\mathrm{r}$ analytically (see Eq. (4.33) and above), the same is not possible with the particle moving at a constant velocity for $t' < 0$. An approximation can be evaluated, which is given in Appendix A.6.

4.1.6.2 Appearance radiation

An alternative to removing the discontinuity is to modify the Maxwell equations so that they allow for a discontinuous charge and current density. The general idea has already been outlined in Sec. 3.4, where the current density is linearly modified as in Eq. (3.40). The additional current $\mathbf{\Sigma}_\mathrm{s}$ needs to satisfy Eq. (3.41), which is similar to Eq. (3.1a). Accordingly, the solution may be represented by a gradient field $\mathbf{\Sigma}_\mathrm{s} = -\nabla\varphi_\mathrm{s}$, while any rotational contribution cannot be determined by Eq. (3.41). The solution of $\nabla^2\varphi_\mathrm{s} = -\sigma_\mathrm{s}$ (recall that $\sigma_\mathrm{s} = q_\mathrm{e}\delta(\mathbf{r})\delta(t)$) is given by $\varphi_\mathrm{s} = q_\mathrm{e}\delta(t)/(4\pi r)$ so that $\mathbf{\Sigma}_\mathrm{s} = -q_\mathrm{e}\delta(t)\mathbf{r}/(4\pi r^3)$. In the four-dimensional Fourier domain, this translates to $\tilde{\tilde{\mathbf{\Sigma}}}_\mathrm{s} = -q_\mathrm{e} i\mathbf{k}/[(2\pi)^4 k^2]$. The linear modification of the source term $\tilde{\tilde{\mathbf{J}}}_\mathrm{f}$ gives rise to an additional electric field according to Eq. (4.1): $\tilde{\tilde{\mathbf{E}}}_\mathrm{s} = i\mu\omega\tilde{\tilde{\mathbf{\Sigma}}}_\mathrm{s}/[k^2 - \omega^2/\tilde{c}^2]$. Since $\tilde{\tilde{\mathbf{\Sigma}}}_\mathrm{s} \propto \mathbf{k}$ and $\tilde{\tilde{\mathbf{B}}} \propto \mathbf{k} \times \tilde{\tilde{\mathbf{\Sigma}}}_\mathrm{s}$ (Eq. (4.3)), there is no additional magnetic field. It is possible to invert the spatial Fourier transform of the additional electric field analytically:

$$\widetilde{\mathbf{E}}_\mathrm{s}(\mathbf{r},\omega) = \frac{q_\mathrm{e}}{2\pi\, i\omega\tilde{\varepsilon}_\mathrm{c}(\omega)} \frac{\hat{\mathbf{e}}_r}{4\pi r^2} \big\{\exp[-i\omega/\tilde{c}(\omega)\, r][1 + i\omega/\tilde{c}(\omega)\, r] - 1\big\}. \tag{4.50}$$

The details are provided in Appendix A.7. The result is a radial symmetric field around the origin, just like the "source current" $\mathbf{\Sigma}_\mathrm{s}$[1]. For the projection on the cylindrical components, $\hat{\mathbf{e}}_r \cdot \hat{\mathbf{e}}_\rho = \rho/r$ and $\hat{\mathbf{e}}_r \cdot \hat{\mathbf{e}}_z = z/r$ is used. Keep in mind that with Eq. (4.50), merely a "mathematical artifact"is being analyzed, since the discontinuity has been imposed for computational reasons. Interestingly enough though, there exists a physical interpretation for such an additional field. In the literature [225], the latter is known as *appearance radiation* and occurs during pair production.

4.1.6.3 Impact on approach ②

An issue that is related to the discontinuous charge and current density, is that the equivalence between factors of $i\omega$ and the time derivative ($i\omega \leftrightarrow \partial/\partial t$) requires adjustments. In particular, if the lower integral limit of Eq. (4.40) is set to zero, then the lower limit of Eq. (4.45) changes to Eq. (4.43) evaluated at $t' = 0$. It shall be abbreviated by $\ell = |\mathbf{r} - \mathbf{r}_\mathrm{p}(t' = 0)|/\tilde{c}(\omega) = r/\tilde{c}(\omega)$, where it has been assumed that $\mathbf{r}_\mathrm{p}(t' = 0) = \mathbf{0}$ and the absolute value of $\mathbf{r}$ is abbreviated as $|\mathbf{r}| \equiv r$. How a finite lower limit impacts Eq. (A.2a) is known from the Laplace transform [226]: $\int_\ell^\infty \mathrm{d}t/(2\pi)\, i\omega \exp(-i\omega t) f(t) = \exp(-i\omega\ell)/(2\pi)\, f(\ell) + \int_\ell^\infty \mathrm{d}t/(2\pi) \exp(-i\omega t) f'(t)$. In fact, this just follows from integration by parts. The additional term $\exp(-i\omega\ell)/(2\pi) f(\ell)$ requires $f(\ell)$, which is in turn to be evaluated at the retarded time (Eq. (4.45)), simplifying to $t'(\mathbf{r}, t = \ell) = 0$. Along z, it turns out to be

$$\varkappa_z(\mathbf{r}, \omega) = \frac{q_\mathrm{e}}{\tilde{\varepsilon}_\mathrm{c}(\omega)} \frac{\tilde{c}(\omega) z - v_0 r}{2\pi \tilde{c}(\omega)[\tilde{c}(\omega) r - v_0 z]} \frac{\exp[-i\omega r/\tilde{c}(\omega)]}{4\pi r}, \tag{4.51}$$

where $\dot{f}_z(t' = 0) = v_0$ is the initial velocity. In summary, when setting the lower limit of Eq. (4.46) to zero, one collects an additional term:

$$\widetilde{E}_z^{②+}(\mathbf{r}, \omega) = \varkappa_z(\mathbf{r}, \omega) + \int_0^\infty \frac{\mathrm{d}t'}{2\pi} f_z^{②}(\mathbf{r}, \omega, t') \exp\big(-i\omega t'\big). \tag{4.52}$$

4.1.7 Static field approximations

Equipped with the point particle solutions, compactly given in Eqs. (4.40) to (4.42) or Eqs. (4.46) and (4.47), the superposition described in Sec. 3.5 can be applied. In particular, the convolution with the normalized density function $\gamma(t)$, which describes the pulse shape, transforms the point particle solution to the field of a beam (Eq. (3.46)). In the Fourier domain, the latter translates to the product given in Eq. (3.47).

Constant beam For a constant beam with a hypothetical infinite duration, it is expected that the beam is surrounded by a static magnetic field, as opposed to the electric field. For a non-conductive medium, the electric field strength would accumulate indefinitely, while a conductive medium reaches an equilibrium between deposited and conducted charges, which strongly depends on the environment. Consequently, only the magnetic field will be analyzed regarding a constant beam. According to Eq. (3.46), the appropriate beam shape function needs to be determined. For this purpose, first a finite, symmetric and rectangular pulse $\Pi(t, T) = 1/T[\theta(t + T/2) - \theta(t - T/2)]$ is considered and then both the particle number and the duration are taken to infinity, while keeping the rate constant:

$$N\gamma_\infty(t) = \lim_{\substack{N,T\to\infty \\ N/T=\text{const.}}} N\,\Pi(t, T) = \Phi, \tag{4.53}$$

[1] As a side note, the Fourier forward transform of $\mathbf{\Sigma}_\mathrm{s}$ can be calculated with the same trick as shown in Appendix A.7.

where the rate of particles $\Phi = N/T$ has been introduced. Note that in this particular case, it is important to consider the product between the particle number and the beam shape function, since, isolated from one another, they cannot be normalized. In the Fourier domain, Eq. (4.53) becomes $N\tilde{\gamma}_\infty(\omega) = \Phi\delta(\omega)$, so when applied as in Eq. (3.47) in combination with Eqs. (4.34) and (4.35), one obtains for the beam (b)

$$\begin{aligned} B_\phi^{b+}(\mathbf{r}) &= \frac{\mu I}{4\pi}\int_{t_0}^{t_\mathrm{r}} \frac{\rho \dot{f}_z(t')}{\sqrt{\rho^2 + [z - f_z(t')]^2}^3}\mathrm{d}t' \\ &= \frac{\mu I}{4\pi\rho}\left(\frac{z - z_0}{\sqrt{\rho^2 + (z-z_0)^2}} - \frac{z - z_\mathrm{r}}{\sqrt{\rho^2 + (z-z_\mathrm{r})^2}}\right) \\ &\overset{z_0\to-\infty}{=} \frac{\mu I}{4\pi\rho}\left(1 - \frac{z - z_\mathrm{r}}{\sqrt{\rho^2 + (z-z_\mathrm{r})^2}}\right), \end{aligned} \tag{4.54}$$

where the current is defined as the elementary charge multiplied with the particle rate: $I = q_\mathrm{e}\Phi$. The integral with respect to t' has been evaluated through the change of variables $z' = f_z(t')$, $\mathrm{d}z'/\mathrm{d}t' = \dot{f}_z(t')$ and $f_z(t_0) = z_0$, $f_z(t_\mathrm{r}) = z_\mathrm{r}$. Also, by taking the lower limit $z_0 \to -\infty$ (i.e. $t_0 \to -\infty$), which was originally zero in Eq. (4.34), to negative infinity, one essentially assumes that the beam source is sufficiently far away from the range z_r. By taking $z_\mathrm{r} \to +\infty$, so that the particles do not stop at the range but continue moving towards infinity, then Eq. (4.54) would reduce to the well-known magnetic field of a straight wire $B_\phi = \mu I/(2\pi\rho)$. It is noteworthy that Eq. (4.54) does not depend on the specific single proton path anymore, except for the range. This result, albeit surprising, is supported by the constant current density, as analyzed in Sec. 4.1.2.

Approximation for the electric field Motivated by the apparent simplicity of the results from Albert et al. (Fig. (5) therein), approximate formulas for both the electric and magnetic field are sought. Generally, this is possible since a more realistic beam duration of ~ 10 µs is significantly longer than the delays related to the propagation of the field and the dominant relaxation times of the polarization, which are in the nanosecond range ($\tau_1 = 1/\omega_1$ with ω_1 listed in Table 3.1). Radiative contributions, such as bremsstrahlung and Cherenkov radiation, can be neglegted as analyzed through the alternative approach (Sec. 4.1.5). In particular, the terms proportional to $i\omega$ in Eq. (4.41) are associated to them and are therefore disregarded. On longer time-scales, they are considerably weaker than the static fields, due to their fleeting nature. From the Liénard-Wiechert potentials it follows that the exponent of Eqs. (4.40) and (4.41) is related to the retarded time (as defined in Eq. (4.43)). It leads to the aforementioned time delay (or retardation) in the nanosecond range and can thus be neglected. By neglecting radiative effects, one effectively sets $\omega = 0$, so that the permittivity will also be approximated by its DC value: $\tilde{\varepsilon}(\omega) = \tilde{\varepsilon}(0)$. In summary Eq. (4.41) becomes $\mathbf{f}_E^{①}(\mathbf{r},\omega,t') \approx q_\mathrm{e}/(4\pi\tilde{\varepsilon}(0))[\mathbf{r} - \mathbf{r}_\mathrm{p}(t')]/|\mathbf{r} - \mathbf{r}_\mathrm{p}(t')|^3$. The contribution from the interval $[0, t_\mathrm{r}]$ in Eq. (4.33) is negligible on longer time-scales so that only the second term will be further analyzed. Together with the superposition from Eq. (3.47), one eventually obtains $\mathbf{E}^{①+}(\mathbf{r},\omega) = \mathbf{f}_E^{①}(\mathbf{r},\omega,t_\mathrm{r})\big[\delta(\omega)/2 - \mathcal{P}\exp(-i\omega t_\mathrm{r})/(2\pi i\omega)\big]2\pi N\tilde{\gamma}(\omega)$. With $\mathbf{f}_E^{①}(\mathbf{r},\omega,t_\mathrm{r})$ being approximately independent of ω, one can re-interpret the remaining product as a convolution in the time domain. It can be shown that the term in the square brackets translates to a shifted step function $\theta(t - t_\mathrm{r})$. For the same reasons stated above, the t_r-shift is neglected. The result in the time domain is then proportional to the convolution between $\theta(t)$ and $\gamma(t)$. A convolution with a step function is equal to the integral of the other function, which for

$\gamma(t)$ has been defined as $\Gamma(t)$ (below Eq. (3.43) and Eq. (3.45)). Finally,

$$\mathbf{E}^{①b+}(\mathbf{r},t) \approx \frac{Nq_\mathrm{e}}{4\pi\tilde{\varepsilon}(0)} \frac{\mathbf{r}-\mathbf{r}_\mathrm{r}}{|\mathbf{r}-\mathbf{r}_\mathrm{r}|^3}\Gamma(t), \tag{4.55}$$

which is merely a Coulomb field that accumulates at the range $\mathbf{r}_\mathrm{r} = \mathbf{r}_\mathrm{p}(t_\mathrm{r}) = (0,0,z_\mathrm{r})^T$ according to the pulse shape. It is crucial to remind that Eq. (4.55) only holds for non-conductive targets, since otherwise the conduction diminishes the field. Details follow in Sec. 4.1.9.

Approximation for the magnetic field For the magnetic field, a similar line of reasoning leads to $f_\phi(\mathbf{r},\omega,t') \approx \mu q_\mathrm{e}/(4\pi)\dot{f}_z(t')\rho/d^3(\mathbf{r},t')$ for Eq. (4.35) so that in combination with Eqs. (3.47) and (4.34) one obtains

$$\begin{aligned}
B_\phi^{b+}(\mathbf{r},t) &\approx 2\pi N \int_{-\infty}^{\infty} \mathrm{d}\omega \int_{t_0}^{t_\mathrm{r}} \frac{\mathrm{d}t'}{2\pi} \frac{\mu q_\mathrm{e}}{4\pi} \frac{\rho \dot{f}_z(t')}{\sqrt{\rho^2+[z-f_z(t')]^2}^3} \tilde{\gamma}(\omega) \exp\left[i\omega(t-t')\right] \\
&= \frac{\mu N q_\mathrm{e}}{4\pi} \int_{t_0}^{t_\mathrm{r}} \frac{\rho \dot{f}_z(t')}{\sqrt{\rho^2+[z-f_z(t')]^2}^3} \gamma(t-t')\mathrm{d}t' \\
&\approx \frac{\mu N q_\mathrm{e}}{4\pi} \gamma(t) \int_{t_0}^{t_\mathrm{r}} \frac{\rho \dot{f}_z(t')}{\sqrt{\rho^2+[z-f_z(t')]^2}^3} \mathrm{d}t' \\
&\overset{t_0\to-\infty}{=} \frac{\mu N q_\mathrm{e}}{4\pi\rho} \gamma(t) \left(1 - \frac{z-z_\mathrm{r}}{\sqrt{\rho^2+(z-z_\mathrm{r})^2}}\right),
\end{aligned} \tag{4.56}$$

where the last step is almost identical to Eq. (4.54). Also, in the third step it has been assumed that the relatively small shift $t' \in [0, t_\mathrm{r}]$ is negligible compared to the scale of $\gamma(t)$, where it also can be assumed to be approximately constant. The result is effectively the static beam field from Eq. (4.54), which also follows the beam shape $\gamma(t)$. As expected, the magnetic field lasts only as long as the beam is active.

4.1.8 Inconsistencies regarding the interface condition

Albert et al. apply the classical interface conditions, which were discussed in Sec. 3.3. Yet, as already stated, they are derived under strongly simplifying assumptions, which limits their applicability to static fields and closed systems, such as e.g. one-dimensional capacitors [173]. They are not appropriate for a dynamic scenario with an open-ended geometry, as the one considered in this work. "Dynamic" refers here to the charge transport, caused by the conductivity. Together with the electric field, the associated conductivity current density points outwards (Eq. (3.31)), which effectively transports the charges away. Microscopically, this is rather to be understood as an exchange of electrons. With the relation between free and bound charge from Sec. 3.2.1, the charge relaxation can already be expected from first principles. In order to study the behavior of the charges for $t \to \infty$, one should consider the limit $\omega \to 0$ in the Fourier domain. Using Eqs. (3.19), (3.20) and (3.32),

$$\begin{aligned}
\lim_{\omega\to0} \tilde{\rho}_\mathrm{b}(\mathbf{r},\omega) &= \lim_{\omega\to0} -\frac{\tilde{\varepsilon}_\mathrm{c}(\omega)-\varepsilon_0}{\tilde{\varepsilon}_\mathrm{c}(\omega)} \tilde{\rho}_\mathrm{f}(\mathbf{r},\omega) \\
&= \lim_{\omega\to0} -\frac{\tilde{\varepsilon}(\omega)-i\sigma_\mathrm{DC}/\omega-\varepsilon_0}{\tilde{\varepsilon}(\omega)-i\sigma_\mathrm{DC}/\omega} \tilde{\rho}_\mathrm{f}(\mathbf{r},\omega) \\
&= -\tilde{\rho}_\mathrm{f}(\mathbf{r},0).
\end{aligned} \tag{4.57}$$

Since the total charge is $\tilde{\rho}_{\mathrm{tot}} = \tilde{\rho}_{\mathrm{f}} + \tilde{\rho}_{\mathrm{b}}$, it follows from Eq. (4.57) that the bound charge completely cancels the free charge so that the net charge vanishes. This does not mean that the charges disappear, but rather that the charges spread over an eventually infinite volume, whereby the charge density decreases to zero. With Eq. (4.40) derived for an homogeneous target, the charges would still cross the boundary (for non-zero σ_{DC}), despite an artificially introduced interface based on Eq. (3.36), which leads to inconsistencies. To summarize, the interface conditions cannot be applied for the present work due to the conductivity relaxation and thereby vanishing electric field. A more appropriate analysis is presented in the following section.

4.1.9 Conductivity relaxation

In the previous section it has been argued that the conductivity inhibits the application of the classical interface conditions. Also, the methods presented so far in this chapter *only* apply to homogeneous targets (as has been stated several times) and it is not possible to introduce a boundary through the interface conditions. Regardless, the impact that the conductivity and its associated charge relaxation have on the electric field and in particular on the results presented by Albert et al. can be assessed. A discontinuous and thus spatially dependent permittivity and conductivity ($\varepsilon_{\mathrm{c}}(t) \rightarrow \varepsilon_{\mathrm{c}}(\mathbf{r}, t)$) needs to be taken into account already at the constitutive relations (Eq. (3.2)). Precisely this is the starting point of Chapter 6 in Eq. (6.1a). Accordingly, the equations for both the electric and magnetic field complicate significantly. The four-dimensional Fourier transform, which enabled the closed form solutions of the electric and magnetic field (Eqs. (4.1) and (4.3)), does not exist in the discontinuous case, since the product between spatially dependent permittivity and the electric field turns into a **k**-space convolution: $\varepsilon(\mathbf{r}, t) *_t \mathbf{E}(\mathbf{r}, t) \leftrightarrow \tilde{\tilde{\varepsilon}}(\mathbf{k}, \omega) *_{\mathbf{k}} \tilde{\tilde{\mathbf{E}}}(\mathbf{k}, \omega)$. Besides, inverting the **k**-space with a **k**-dependent permittivity cannot be expected to have an analytical result when compared to the homogeneous case, which was already complicated (see Appendix A.3). In summary, the analytical and numerical complications would increase significantly. The approach from Chapter 6 could be applied to overcome those issues, yet, by considering the charge relaxation isolated from the initial charge deposition, a simpler analysis is possible. The cylindrical geometry remains under consideration, together with the assumption that the cylinder is sufficiently long when compared to the radius ρ_{c} so that end caps can be neglected. Thereby, the problem can be reduced to a two-dimensional problem in time and along the cylinder axis.

In particular, the spatio-temporal behavior of the charge density and its electric field under the influence and in the presence of a discontinuous conductivity is considered. The evolution of the charge density is governed by the continuity equation [173]. As described in Sec. 3.2.3, when separating the free current density $\mathbf{J}_{\mathrm{f}}$ from the conductivity current density $\mathbf{J}_{\mathrm{c}}$ so that the total current density is $\mathbf{J}_{\mathrm{t}} = \mathbf{J}_{\mathrm{f}} + \mathbf{J}_{\mathrm{c}}$, then also the charge density is separated as $\rho_{\mathrm{t}} = \rho_{\mathrm{f}} + \rho_{\mathrm{c}}$. As described above, the initial drift towards the range is neglected so that the free charges are placed at the range according to the beam shape: $\rho_{\mathrm{f}}(\mathbf{r}, t) = N q_{\mathrm{e}} \Gamma(t) \delta^3(\mathbf{r})$, where $\Gamma(t)$ is the cumulative beam shape defined in Eq. (3.45). Technically, the range is located at $\mathbf{r}_{\mathrm{r}} = (0, 0, z_{\mathrm{r}})^{\mathrm{T}}$ so that the argument of the delta-function should be replaced by $\mathbf{r} - \mathbf{r}_{\mathrm{r}}$, but for simplicity it has been shifted to zero, which is possible since the discontinuities along z were neglected. In the current scenario the charges "appear" at the range so that the free current density remains static: $\mathbf{J}_{\mathrm{f}} = \mathbf{0}$. To avoid the violation of the continuity equation, a source term of the form $\varsigma(\mathbf{r}, t) = N q_{\mathrm{e}} \delta^3(\mathbf{r}) \gamma(t)$ is necessary (see Secs. 3.4 and 4.1.6.2 for more details). With the DC approximation of Ohm's law (Eq. (3.31)) and the discontinuous conductivity, the conductivity current density is $\mathbf{J}_{\mathrm{c}}(\mathbf{r}, t) = \sigma_{\mathrm{DC}}(\mathbf{r}) \mathbf{E}(\mathbf{r}, t)$ [227].

Taking the target's convolutional permittivity model into account (Eq. (3.2)) makes the following steps easier in the Fourier domain with respect to time (Eq. (3.6)). In summary, the continuity equation for the total charge and current density (including source term) reads:

$$\begin{aligned}\tilde{\varsigma}(\mathbf{r},\omega) &= i\omega\tilde{\rho}_\mathrm{t}(\mathbf{r},\omega) + \nabla\cdot\big[\overbrace{\sigma_\mathrm{DC}(\mathbf{r})\widetilde{\mathbf{E}}(\mathbf{r},\omega)}^{\tilde{\mathbf{J}}_\mathrm{t}(\mathbf{r},\omega)}\big] \\ &= i\omega\tilde{\rho}_\mathrm{t}(\mathbf{r},\omega) + \sigma_\mathrm{DC}(\mathbf{r})\nabla\cdot\widetilde{\mathbf{E}}(\mathbf{r},\omega) + \widetilde{\mathbf{E}}(\mathbf{r},\omega)\cdot\nabla\sigma_\mathrm{DC}(\mathbf{r}) \\ &= i\omega\tilde{\rho}_\mathrm{t}(\mathbf{r},\omega) + \sigma_\mathrm{DC}(\mathbf{r})\tilde{\rho}_\mathrm{t}(\mathbf{r},\omega)/\tilde{\varepsilon}(\omega) + \widetilde{\mathbf{E}}(\mathbf{r},\omega)\cdot\nabla\sigma_\mathrm{DC}(\mathbf{r}),\end{aligned} \tag{4.58}$$

where Gauß' law (Eq. (3.4a)) has been used in the last step. Recall that the conductivity charge density remaines separate, i.e. it is not included as in Eq. (3.32). On the other hand, the polarization and bound charge are modeled with the frequency dependent permittivity. By using Eq. (3.4a), it has also been assumed that the latter is not discontinuous, as opposed to the conductivity. This simplifies the calculation of the electric field, whose more realistic counterpart with a discontinuous permittivity is not expected to drastically change the results. Eq. (4.58) simplifies considerably within $C = \{\mathbf{r}\in\mathbb{R}^3|[\nabla\sigma_\mathrm{DC}(\mathbf{r}) = 0]\cap[\sigma_\mathrm{DC}(\mathbf{r})\neq 0]\}$, i.e. the homogeneous and conductive domain. The total charge density inside C is denoted as $\tilde{\rho}_g(\mathbf{r},\omega)$, for which a multiplicative ansatz is used: $\tilde{\rho}_g(\mathbf{r},\omega) = Nq_\mathrm{e}\delta^3(\mathbf{r})\tilde{g}(\omega) \equiv \rho_g(\mathbf{r})\tilde{g}(\omega)$. Accordingly $\tilde{\varsigma}(\mathbf{r},\omega) = \rho_g(\mathbf{r})\tilde{\gamma}(\omega)$. For $\mathbf{r}\in C$, $\rho_g(\mathbf{r})$ factors out and Eq. (4.58) simplifies to

$$\tilde{\gamma}(\omega) = i\omega\tilde{g}(\omega) + \sigma_\mathrm{DC}\tilde{g}(\omega)/\tilde{\varepsilon}(\omega), \tag{4.59}$$

$$g(t) = \mathcal{F}_1^{-1}\left\{\frac{\tilde{\gamma}(\omega)}{i\omega + \sigma_\mathrm{DC}/\tilde{\varepsilon}(\omega)}\right\}, \tag{4.60}$$

where $\sigma_\mathrm{DC}(\mathbf{r}\in C) = \sigma_\mathrm{DC}$. The time domain solution of Eq. (4.59) is obtained by means of inverse Fourier transform and has been given in Eq. (4.60). Consider an instantaneously placed charge distribution $\rho_g(\mathbf{r})$, where $\gamma(t) = \delta(t)$. With $\rho_g(\mathbf{r},t) = \rho_g(\mathbf{r})g(t)$, the initial charge distribution in the homogeneous and conducting area will decay according to $g(t)$. That $g(t)$ describes a decay is not straightforward. Under the assumption that the permittivity is constant ($\tilde{\varepsilon}(\omega)\to\varepsilon$), Eq. (4.60) yields a simple exponential decay for the instantaneous excitation: $g(t) = \exp(-t/\tau)\theta(t)$, where $\tau = \varepsilon/\sigma_\mathrm{DC}$ is the relaxation time [228]. Except for the artificial origin of charges, it follows that charges can only accumulate and increase at the gradient $G = \{\mathbf{r}\in\mathbb{R}^3|\nabla\sigma_\mathrm{DC}\neq 0\}$. With respect to the geometry of Fig. 4.1 under consideration, charges are expected to accumulate on the cylinder surface. By taking advantage of the cylindrical symmetry, Eq. (4.58) can be reduced to a two-dimensional differential equation, one in space along the cylinder surface and one in time. Consequently, the ansatz for the total charge density is

$$\tilde{\rho}_\mathrm{t}(\mathbf{r},\omega) = \underbrace{Nq_\mathrm{e}\frac{\delta^+(\rho)\delta(z)}{2\pi\rho}\tilde{g}(\omega)}_{\text{ⓐ}} + \underbrace{Nq_\mathrm{e}\frac{\delta^+(\rho_\mathrm{c}-\rho)}{2\pi\rho}\tilde{f}(z,\omega)}_{\text{ⓑ}}, \tag{4.61}$$

where ρ_c is the cylinder radius and δ^+ is a positive sided delta function. The latter is described in Appendix A.8 together with its step function θ^+. The cylindrical discontinuity takes a very simple form in cylindrical coordinates:

$$\sigma_\mathrm{DC}(\mathbf{r}) = \sigma_\mathrm{DC}\theta^+(\rho_\mathrm{c}-\rho), \tag{4.62}$$

$$\nabla\sigma_\mathrm{DC}(\mathbf{r}) = -\sigma_\mathrm{DC}\delta^+(\rho_\mathrm{c}-\rho)\hat{\mathbf{e}}_\rho, \tag{4.63}$$

where the gradient has been estimated via Eq. (A.73), which only points along the radial direction. For the work in Chapter 6, similar assumptions regarding a discontinuous permittivity will be made. The solution of Eq. (4.58) for the total charge density with the ansatz from Eq. (4.61) is sought. For this purpose, the estimation of the electric field at the gradient and in particular its $\hat{\mathbf{e}}_\rho$-component due to the dot product with Eq. (4.63) is necessary. To a low-order approximation, one may neglect propagation and radiation-related effects and approximate the electric field by its static solution, i.e. the solution of Gauss' law from Eq. (3.4a), which is given by [153]:

$$\widetilde{\mathbf{E}}(\mathbf{r},\omega) = \frac{1}{4\pi\tilde{\varepsilon}(\omega)} \int_{\mathbb{R}^3} \frac{\tilde{\rho}_\mathrm{t}(\mathbf{r}',\omega)(\mathbf{r}-\mathbf{r}')}{|\mathbf{r}-\mathbf{r}'|^3} \mathrm{d}^3\mathbf{r}'. \tag{4.64}$$

To specify what is meant by a "low-order" approximation, consider Eqs. (4.36) and (4.37). For low frequencies ω, one can expand Eq. (4.37) for low values of $k \propto \omega$: $G(\mathbf{r},\mathbf{r}') = -1/(4\pi|\mathbf{r}-\mathbf{r}'|) + \mathcal{O}(k)$. In combination with the source term $S = -\tilde{\rho}/\tilde{\varepsilon}$, the scalar field can be represented with Eq. (4.36). The electric field in Eq. (4.64) follows then from Eq. (3.11), where $\omega \approx 0$ is assumed, and the identity $-\nabla(1/|\mathbf{r}-\mathbf{r}'|) = (\mathbf{r}-\mathbf{r}')/|\mathbf{r}-\mathbf{r}'|^3$. With the gradient of the conductivity being solely oriented along $\hat{\mathbf{e}}_\rho$ (Eq. (4.63)), one only needs the ρ-component for Eq. (4.58): $\widetilde{E}_\rho(\mathbf{r},\omega) = \widetilde{\mathbf{E}}(\mathbf{r},\omega)\cdot\hat{\mathbf{e}}_\rho$. The source term in Eq. (4.61) has been subdivided into two domains. ⓐ are the deposited charges in the center, which give rise to a classical Coulomb field around the origin. A straightforward evaluation of Eq. (4.64) leads to

$$\widetilde{E}_\rho^{\textcircled{a}}(\mathbf{r},\omega) = \frac{Nq_\mathrm{e}}{4\pi\tilde{\varepsilon}(\omega)} \frac{\rho}{\sqrt{\rho^2+z^2}^3} \tilde{g}(\omega). \tag{4.65}$$

The evaluation of Eq. (4.64) for the field associated with ⓑ is somewhat more involved and hence more explicitly shown in Appendix A.9. While the delta terms in ⓐ completely collapsed the integrals of Eq. (4.64), the z' integral remains for ⓑ. Since $a = a(z-z')$ in Eqs. (A.45) and (A.46), it can be written as a (spatial) convolution with respect to z:

$$\widetilde{E}_\rho^{\textcircled{b}}(\mathbf{r},\omega) = \frac{Nq_\mathrm{e}}{4\pi\tilde{\varepsilon}(\omega)} \frac{1}{\rho} \mathcal{Z}(\rho,z) * \tilde{f}(z,\omega). \tag{4.66}$$

The convolution kernel on the cylinder surface is given by

$$\mathcal{Z}(\rho_\mathrm{c},z) \equiv \mathcal{Z}(z) = \frac{1}{\pi|z|}\left[\mathcal{K}\big(-4\rho_\mathrm{c}^2/z^2\big) - \frac{1}{1+4\rho_\mathrm{c}^2/z^2}\mathcal{E}\big(-4\rho_\mathrm{c}^2/z^2\big)\right]. \tag{4.67}$$

Its normalization can easily be shown, since it has a closed form integral:

$$\int \mathcal{Z}(z)\mathrm{d}z = \frac{1}{\pi}\mathcal{K}(-4\rho_\mathrm{c}^2/z^2)\,\mathrm{sgn}(z), \tag{4.68}$$

$$\int_{-\infty}^{\infty} \mathcal{Z}(z)\mathrm{d}z = 1. \tag{4.69}$$

At this stage, one can assemble the previous results to obtain a differential equation for the unknown surface charge density $\tilde{f}(z,\omega)$. Eq. (4.61) can be applied in Eq. (4.58) and $\widetilde{\mathbf{E}}(\mathbf{r},\omega)\cdot\nabla\sigma_\mathrm{DC}(\mathbf{r}) = -\widetilde{E}_\rho(\mathbf{r},\omega)\sigma_\mathrm{DC}\delta^+(\rho_\mathrm{c}-\rho)$ is used, where $\widetilde{E}_\rho(\mathbf{r},\omega) = \widetilde{E}_\rho^{\textcircled{a}}(\mathbf{r},\omega) + \widetilde{E}_\rho^{\textcircled{b}}(\mathbf{r},\omega)$ from Eqs. (4.65) and (4.66). An important simplification comes from Eqs. (A.36) and (A.39). The source term on the LHS of Eq. (4.58) in cylindrical coordinates is $\tilde{\varsigma}(\mathbf{r},\omega) = Nq_\mathrm{e}\delta^+(\rho)\,\delta(z)/(2\pi\rho)\tilde{\gamma}(\omega)$, similar to ⓐ of Eq. (4.61). Eventually, one can factorize $Nq_\mathrm{e}\delta^+(\rho_\mathrm{c}-\rho)/(2\pi\rho)$ and integrate over ρ to obtain:

$$i\omega\tilde{f}(z,\omega) + \frac{\sigma_\mathrm{DC}}{2\tilde{\varepsilon}(\omega)}\left[\tilde{f}(z,\omega) - \rho_\mathrm{c}^2/\sqrt{\rho_\mathrm{c}^2+z^2}^3\,\tilde{g}(\omega) - \tilde{f}(z,\omega) * \mathcal{Z}(z)\right] = 0. \tag{4.70}$$

To separate the spatial from the temporal behavior, integration Eq. (4.70) over z is performed. For this purpose, the longitudinally integrated surface charge density is defined as $\tilde{f}(\omega) = \int_{-\infty}^{\infty} \tilde{f}(z,\omega)\mathrm{d}z$. Through a straightforward integral transform, it can be shown that the integral of a convolution is equal to the product of the individually integrated functions. With Eq. (4.69) the first and last term in the square brackets of Eq. (4.70) cancel. Eventually:

$$i\omega\tilde{f}(\omega) - \sigma_{\mathrm{DC}}/\tilde{\varepsilon}(\omega)\,\tilde{g}(\omega) = 0, \qquad (4.71) \qquad\qquad \tilde{f}(\omega) = \widetilde{\Gamma}(\omega) - \tilde{g}(\omega). \qquad (4.72)$$

Eq. (4.72) is the solution of Eq. (4.71). It can be confirmed with Eq. (4.60) and $i\omega\widetilde{\Gamma}(\omega) = \tilde{\gamma}(\omega)$, which follows directly from Eq. (3.45) and Eq. (A.2a). Recall that $g(t)$ quantifies the charge at the center and can be interpreted as a percentage of the total charge. Considering the case of a non-conductive medium ($\sigma_{\mathrm{DC}} = 0$), Eq. (4.60) simplifies to $g(t) = \mathcal{F}_1^{-1}\{\tilde{\gamma}(\omega)/(i\omega)\} = \Gamma(t)$, which follows from the inverse of Eq. (A.2a). Since $\Gamma(t) \in [0,1]$ is the normalized CDF, then also $g(t) \in [0,1]$. In the case of a conductive medium, $g(t)$ does not rise to 100%. Instead, the charge on the cylinder surface rises at exactly the same rate as it decreases at the center. In particular Eq. (4.72) is the difference between the available charge $\Gamma(t)$ and the charge at the center $g(t)$. The total charge $f(t) + g(t) = \Gamma(t)$ never exceeds the number of deposited charges at any given time and remains constant towards $t \to \infty$ (charge conservation).

With a convolutional law in the spatial domain in Eq. (4.70), it may be favorable to solve it also in the Fourier domain. The initial condition can be fixed through the source term and knowing that $f(z,t)$ vanishes at infinity. Thereby a Fourier approach is sufficient as opposed to the more general Laplace transform [226]. So in addition to the time-wise Fourier transform, Eq. (4.70) is also transformed with respect to z with the same convention as in Eq. (A.1a). Rearranging the result to the desired surface charge density yields

$$\tilde{\tilde{f}}(k_z,\omega) = \frac{1}{2\pi}\frac{\rho_{\mathrm{c}}|k_z|K_1(\rho_{\mathrm{c}}|k_z|)\tilde{\gamma}(\omega)/[i\omega\tilde{\varepsilon}(\omega)/\sigma_{\mathrm{DC}}+1]}{i\omega + [\sigma_{\mathrm{DC}}/2\tilde{\varepsilon}(\omega)][1-2\pi\widetilde{\mathcal{Z}}(k_z)]}, \qquad (4.73)$$

where $\mathcal{F}_z\left\{\rho_{\mathrm{c}}^2/\sqrt{\rho_{\mathrm{c}}^2+z^2}^3\right\} = \rho_{\mathrm{c}}|k_z|K_1(\rho_{\mathrm{c}}|k_z|)/\pi$ has been used and $K_1(\circ)$ is the modified Bessel function of the second kind. A few properties of the Bessel functions are summarized in Appendix A.17. For a numerical inversion of Eq. (4.73), first Eq. (4.67) needs to be forward Fourier transformed according to Appendix A.10. Through its low order approximation[2]

$$1 - 2\pi\widetilde{\mathcal{Z}}(k_z) = -\left[\gamma + \log(\rho_{\mathrm{c}}|k_z|/2)\right]\rho_{\mathrm{c}}^2k_z^2 + \mathcal{O}(k_z^4), \qquad (4.74)$$

where γ is the Euler–Mascheroni constant, it follows that Eq. (4.73) is singular around the origin ($k_z = 0, \omega = 0$). Note that the numerator remains finite, since $\lim_{k_z\to 0} \rho_{\mathrm{c}}|k_z|K_1(\rho_{\mathrm{c}}|k_z|) = 1$, $\tilde{\gamma}(\omega = 0) = 1/2\pi$ and $\tilde{\varepsilon}(\omega = 0)$ is finite as the conductivity term is not included. The singularity is not surprising, since $\int_{-\infty}^{\infty} f(z, t \to \infty)\mathrm{d}z$ is constant so that together with the integral across time, the DC component diverges. In fact, analyzing the behavior at the origin reveals a strong resemblance to the one-dimensional heat equation with a point source at the origin: $\partial_t u(z,t) - \alpha\partial_z^2 u(z,t) = \delta(z)\delta(t)$. In the Fourier domain, its solution reads $\tilde{\tilde{u}}(k_z,\omega) = 1/(2\pi)^2/(i\omega + \alpha k_z^2)$. Therefore one can expect similar dynamics (i.e. equilibrium seeking behavior) for the charge relaxation on the cylinder.

From the solution of $f(z,t)$ upon inversion of Eq. (4.73), one can estimate the associated electric field with Eq. (4.66). Recall that Eq. (4.67) has been calculated for the "radial center" of the surface charge density. Right above and beneath the surface, the electric

[2]The factor of 2π preceding it is related to Eq. (A.5).

field kernel behaves as $\lim_{\rho\to\rho_c^\pm} \mathcal{Z}(\rho,z) = \mathcal{Z}(z) \pm \delta(z)$, which can be shown with Eq. (A.47) from Appendix A.9. With the conductivity charges "under control", the issues described in Sec. 4.1.8 are resolved so that the interface conditions can be used. If the additional delta term is taken into account, one can apply Eq. (3.33) with $\rho_s = 0$. Without it, half the surface charge density lies between an external observer outside, so that $\rho_s = Nq_e f(z,t)/(4\pi\rho)$ is used (see Eq. (4.61)). Both approaches lead to the same result for the electric field outside the cylinder:

$$\begin{aligned}\widetilde{E}_\rho(\rho_c^+,z,\omega) &= \tilde{\varepsilon}(\omega)/\varepsilon_0\Big\{\widetilde{E}_\rho^{@}(\rho_c,z,\omega) + \frac{Nq_e}{4\pi\tilde{\varepsilon}(\omega)}\frac{1}{\rho}\big[\mathcal{Z}(z)+\delta(z)\big] * \tilde{f}(z,\omega)\Big\} \\ &\equiv \widetilde{E}_\rho^{@}(\rho_c^+,z,\omega) + \widetilde{E}_\rho^{(b)}(\rho_c^+,z,\omega),\end{aligned} \tag{4.75}$$

where the superscript ρ_c^+ shall underline that Eq. (4.75) represents the field outside.

4.1.10 Radiation yield

Having analyzed the constituents that make up the complete electromagnetic signal generated by the primary protons with an emphasis on a separation of radiative contributions in Sec. 4.1.5, the radiation yield and its absorption within the target shall be quantified. In electromagnetic theory the flow of energy is described by the Poynting vector $\mathbf{S} = \mathbf{E}\times\mathbf{H}$ in combination with the Poynting theorem given in Eq. (3.16). The total flow of energy through a given surface $\partial\Omega$ is given by

$$E^{\mathrm{rad}} = \oiint_{\partial\Omega}\left[\int_{-\infty}^{\infty}\mathbf{S}(\mathbf{r},t)\mathrm{d}t\right]\cdot\mathrm{d}\mathbf{A} = \oiint_{\partial\Omega}\left[2\pi\int_{-\infty}^{\infty}\widetilde{\mathbf{E}}(\mathbf{r},\omega)\times\widetilde{\mathbf{H}}^{\dagger}(\mathbf{r},\omega)\mathrm{d}\omega\right]\cdot\mathrm{d}\mathbf{A}, \tag{4.76}$$

where Eq. (A.7) has been used. The electric and magnetic fields are calculated with Eqs. (4.33) and (4.34), where the first terms in the square brackets of Eqs. (4.28), (4.29) and (4.35) are neglected as being related to the static fields, in order to focus on the radiative contributions. The flow of energy through a surface that encloses the beam, consisting of a cylinder up to the range z_r, which is capped off with a hemisphere is calculated as follows:

$$A_{\square} = \Big\{\mathbf{r}\in\mathbb{R}^3 | \rho = R, 0\le\varphi\le 2\pi, -\infty\le z\le z_r\Big\}, \tag{4.77}$$

$$A_{\mathbb{D}} = \Big\{\mathbf{r}\in\mathbb{R}^3 | r = R, 0\le\theta\le\pi/2, 0\le\varphi\le 2\pi\Big\}. \tag{4.78}$$

The cylinder has a radius of R and extends to negative infinity so that the contribution from the hypothetical cap at $z=-\infty$ can be neglected. This is possible, since only the path for $z>0$ is considered and one can rely on the absorption (see Fig. 3.2), which diminishes the signal for large z. Details regarding the evaluation of Eq. (4.76) are given in Appendix A.11.

The difference between E^{rad} at different radii R_1 and R_2 is the dielectric loss related to the absorption. This is confirmed by evaluating the volume integral on the RHS of Eq. (3.16) between the two surfaces associated with R_1 and R_2. Through the Lorentz force density $\mathbf{f} = \rho_f\mathbf{E} + \mathbf{J}_f\times\mathbf{B}$ one can relate the last term of Eq. (3.16) to the power transmitted to external charges [169, 229]. In the present scenario, this describes the mutual interaction between the primaries that leads primarily to conduction and partially to what is described in [230]. This term can be neglected as it is not associated with an electromagnetic radiation. Like Eq. (4.76), the total energy loss integrated over time can be estimated using [231]

$$u(\mathbf{r}) = -\int_{-\infty}^{\infty}\mathbf{E}(\mathbf{r},t)\cdot\frac{\partial}{\partial t}\mathbf{D}(\mathbf{r},t)\mathrm{d}t = 4\pi\int_0^{\infty}\omega\tilde{\varepsilon}''(\omega)|\widetilde{\mathbf{E}}(\mathbf{r},\omega)|^2\mathrm{d}\omega, \tag{4.79}$$

Table 4.1: Relative stopping power (RSP) of the same targets as in Fig. 3.1. The initial energies Q_{in} for the targets have been adjusted, in order to maintain the range of 150 MeV proton in water, which is $z_{\text{r}} = 15.84$ cm. The RSP values were adapted from Albert et al. [85], who took them from [232,233].

	Water	Muscle (Parallel)	Gray matter	Liver	Lung (Inflated)	Fat
RSP	1	1.032	1.032	1.032	0.273	0.984
Q_{in} [MeV]	150	152.73	152.73	152.73	72.12	148.62

where $\tilde{\varepsilon}''(\omega)$ is the imaginary part of the permittivity. Eq. (4.79) underlines what has been argued in Sec. 3.2.2, i.e. that the imaginary part of the permittivity leads to absorption. The second term on the RHS of Eq. (3.16) does not contribute, since the magnetic permeability and its comparatively weak imaginary part (see Eq. (3.3) and text thereafter) can be neglected. The explicit volume integral is given in Appendix A.11.

4.1.11 Numerical remarks

To obtain the results below, the expressions from above need to be evaluated numerically due to the non-analytical proton path shown in Fig. 2.10 and the permittivity model from Eq. (3.23), which has multiple resonances and non-integer exponents.

Parameters The parameter choice has been similar to the one of Albert et al. [85], i.e. $N = 10^8$ particles and a rectangular beam pulse of $T = 10$ ns. The corresponding beam shape function is $\gamma(t) = [\theta(t) - \theta(t-T)]/T$ with $\tilde{\gamma}(\omega) = (1 - e^{-i\omega T})/(2\pi i\omega T)$. While such short pulse durations are unreasonable from a technical point of view[3], they are necessary to show the polarization effects occurring in the nanosecond scale. While the electric field just accumulates faster, the magnetic field scales with the particle rate, i.e. beam current. The pulse duration is kept but the number of particles is scaled down to $N = 10^5$, which corresponds to a peak beam current of 1.6 µA. When effects in the nanosecond scale are less relevant, in this work a rather more realistic pulse duration of 10 µs is considered, which is the same three orders of magnitude longer as N is lowered for the magnetic field.

Permittivity The permittivity model given in Eq. (3.23) with the parameters from Table 3.1 is used. The values of water reduce to the Debye model. For simplicity water is assumed to be non-conductive, since Ref. [159] gives a very low conductivity of $\sigma_{\text{DC}} > 0.0001$. While water technically is conductive, its conductivity could be further reduced by distillation, whereby this assumption would be somewhat more realistic.

Energy scaling The different targets considered in this work have different RSP. For comparability purposes, the initial energy has been adjusted, so that the range within different targets is equal to the range of protons with $Q_{\text{in}} = 150$ MeV in water. With the RSP values from Table 4.1, the stopping power of the target is estimated with Eq. (2.3) and then the range is calculated via Eq. (2.17), which depends on Q_{in}. The modified Q_{in} are also in Table 4.1.

[3] Recall, the parameters are generally guided by Sec. 2.3.

Numerical integration The t'-integral of Eqs. (4.33), (4.34) and (4.46) has been integrated with the trapezoidal rule over 10^4 linearly spaced samples within $[0, t_\mathrm{r}]$. The latter is calculated for $\omega \in [-60, 60]$ GHz, which is also sampled 10^4 times. Frequencies beyond 60 GHz are absorbed exponentially and thus negligible (see Fig. 3.2). The result is then inverted as in Eq. (3.47), including the beam shape function.

Behavior around the origin With the singularity at the origin in combination with the Cauchy principal value in Eq. (4.33), one needs to analyze the behavior towards $\omega \to 0$. It strongly depends on the inclusion of conductivity and interface conditions. As argued in Sec. 4.1.8, the latter will not be applied. Instead, both cases with and without conductivity will be considered. In either case $\lim_{\omega\to 0} \omega/\tilde{c}(\omega) = 0$. For a conductive medium

$$\lim_{\omega\to 0} 1/\tilde{\varepsilon}_\mathrm{c}(\omega) = 0, \tag{4.80}$$

$$\lim_{\omega\to 0} f_\kappa^{①}(\mathbf{r}, \omega, t') = 0, \tag{4.81}$$

where the latter follows from the former. Accordingly, the delta-term in Eq. (4.33) vanishes, while the second analytical term remains finite:

$$\lim_{\omega\to 0} f_\rho^{①}(\mathbf{r}, \omega, t_\mathrm{r}) \frac{e^{-i\omega t_\mathrm{r}}}{2\pi i\omega} = \frac{q_\mathrm{e}\rho/\sigma_\mathrm{DC}}{8\pi^2 d^3(\mathbf{r}, t_\mathrm{r})}, \qquad \lim_{\omega\to 0} f_z^{①}(\mathbf{r}, \omega, t_\mathrm{r}) \frac{e^{-i\omega t_\mathrm{r}}}{2\pi i\omega} = \frac{q_\mathrm{e}\Delta z(t_\mathrm{r})/\sigma_\mathrm{DC}}{8\pi^2 d^3(\mathbf{r}, t_\mathrm{r})}.$$

For a non-conductive medium, the delta-term contributes, but the second analytical term leads to a singularity around $\omega = 0$. Its contribution remains finite and mostly cancels through its odd symmetry and the application of the principal value. How exactly it behaves depends on the permittivity and the pulse shape (from Eq. (3.47)). In particular, one can approximate both of them around $\omega = 0$ with a constant real part and a linearly changing imaginary part: $\tilde{\varepsilon}(\omega) \approx \tilde{\varepsilon}(0)(1 - i\omega/\omega_\varepsilon)$ and $2\tilde{\gamma}(\omega) \approx 1 - i\omega/\omega_\gamma$. Consequently, the low-order approximation around $\omega = 0$ becomes

$$\lim_{\omega\to 0} 2\pi\tilde{\gamma}(\omega) f_\kappa^{①}(\mathbf{r}, \omega, t_\mathrm{r}) e^{-i\omega t_\mathrm{r}}/(2\pi i\omega) = f_\kappa^{①}(\mathbf{r}, 0, t_\mathrm{r}) \left[1/i\omega - (t_\mathrm{r} + 1/\omega_\gamma - 1/\omega_\epsilon)\right]/(2\pi).$$

To allow a numerical integration across $\omega = 0$, one has to subtract the singularity $\widetilde{\mathcal{S}}_\kappa(\omega) = f_\kappa^{①}(\mathbf{r}, 0, t_\mathrm{r})/(2\pi i\omega)[\theta(\omega + \omega_\mathrm{c}) - \theta(\omega - \omega_\mathrm{c})]$ with a cut-off frequency of $\omega_\mathrm{c} = 30$ GHz in a symmetric window around zero and evaluate its Fourier transform analytically: $\mathcal{S}_\kappa(t) = f_\kappa^{①}(\mathbf{r}, 0, t_\mathrm{r}) \operatorname{Si}(\omega_\mathrm{c} t)/\pi$, where $\operatorname{Si}(t) = \int_0^t \sin(t')/t' \mathrm{d}t'$ is known as the sine integral [220].

Evaluation of Eq. (4.60) For low (i.e. early) values of time $t \sim$ fs, one needs to integrate over a wide frequency range up to PHz, which were sampled logarithmically with $\sim 10^7$ samples, starting from 0.1 Hz. The sampling around $\omega = 0$ is thereby sufficiently dense. A maximum frequency spacing of $\Delta\omega_\mathrm{max} \sim 10^5$ Hz has also been set. When the logarithmic sampling exceeds it, it is replaced by linear samples spaced by $\Delta\omega_\mathrm{max}$. To further increase the numerical precision, Simpson's rule for the numerical integration has been applied.

Inversion of Eq. (4.73) *and evaluation of Eq.* (4.75) For the numerical inversion of the two-dimensional Fourier transform, it is advantageous to begin with the temporal dimension, since the result is well behaved along k_z, i.e. has no singularities. For instance, this is also the case with the aforementioned analogy to the heat equation: $\tilde{u}(k_z, t) = \exp(-\alpha t k_z^2)\theta(t)/(2\pi)$. The integration across the singularity leads to a finite result. The angular frequency ω has been sampled 10^5 times up to 100 THz, while for k_z 10^4 linear samples up to 500 1/m are sufficient.

Table 4.2: Relaxation-related half-life in various biological tissues. These values are the intersections of the dotted lines in Fig. 4.6 with the horizontal axis. Recall that water has been assumed to be non-conductive, so its $t_{1/2}$ is technically infinite.

	Water	Muscle (Parallel)	Gray matter	Liver	Lung (Inflated)	Fat
$t_{1/2}$ [ns]	-	0.74	2.1	13	20	37

Frequency integral of Eqs. (4.76) *and* (4.79) When the pulse shape is taken into account (see Eq. (3.47)), then the ω-integral is weighted with $4\pi^2\tilde{\gamma}(\omega)\tilde{\gamma}^\dagger(\omega)$. This leads to strongly oscillating integrals for a rectangular pulse with a realistic duration of $T \sim 10$ µs, where $4\pi^2\tilde{\gamma}(\omega)\tilde{\gamma}^\dagger(\omega) = 2(1-\cos\omega T)/(\omega^2T^2)$ oscillates much faster than the point particle solution. To moderate the computational cost, it is replaced with a non-oscillating approximation with the same weight and asymptotic behavior: $4\pi^2\tilde{\gamma}(\omega)\tilde{\gamma}^\dagger(\omega) \approx 2/(1+\omega^2T^2)$, which tolerates a less dense sampling.

4.2 Results

Recall that all the methods presented above have an azimuthal symmetry. Accordingly, the results below lie in the ρ-z-plane and/or their time dependency is shown.

4.2.1 Magnetic field

The generated magnetic field in various tissues, as calculated from Eqs. (3.47) and (4.34), is shown in Fig. 4.3. The permeability gradients in biological tissues (including the surrounding air) are low, as already argued in the text below Eq. (3.3). Magnetic field discontinuities are therefore not expected, i.e. the magnetic interface conditions do not ned to be applied. In addition, magnetic field profiles of Fig. 4.3 along the vertical (time) axis are compared in Fig. 4.4.

Lastly, the complete spatial profile of the magnetic field for a constant beam, including the ρ-dependency, is shown in Fig. 4.5. It is calculated from Eq. (4.54), which is tissue independent.

4.2.2 Relaxation and its impact on the electric field

First, the time-scales of the relaxation are estimated by numerically evaluating the inverse Fourier transform of Eq. (4.60). In particular, the response of a delta-like excitation: $\gamma(t) = \delta(t)$ and $\tilde{\gamma}(\omega) = 1/2\pi$ is studied. The result is shown in Fig. 4.6 and indicates how fast charges within the conducting medium decay. In order to further quantify the results from Fig. 4.6, the time $t_{1/2}$ in which a delta-charge distribution decreases to half of its initial value (also referred to as half-life) due to the conductivity relaxation is calculated. Formally, it is defined as $g(t_{1/2}) = 1/2$. The results are listed in Table 4.2.

Not only do the results from Fig. 4.6 quantify the time-scale of the relaxation, $g(t)$ is the relative amount of charge remaining in the center, being part of the ansatz from Eq. (4.61) (part ⓐ). Through Eq. (4.65), it is also associated with the field from the center[4]. In the following, the focus is more on the cylindrical geometry (i.e. discontinuity) with its associated surface charge density (part ⓑ from Eq. (4.61)) and field (see Eq. (4.66)). Fig. 4.7

[4]Keep in mind that Fig. 4.6 only holds for $\gamma(t) = \delta(t)$.

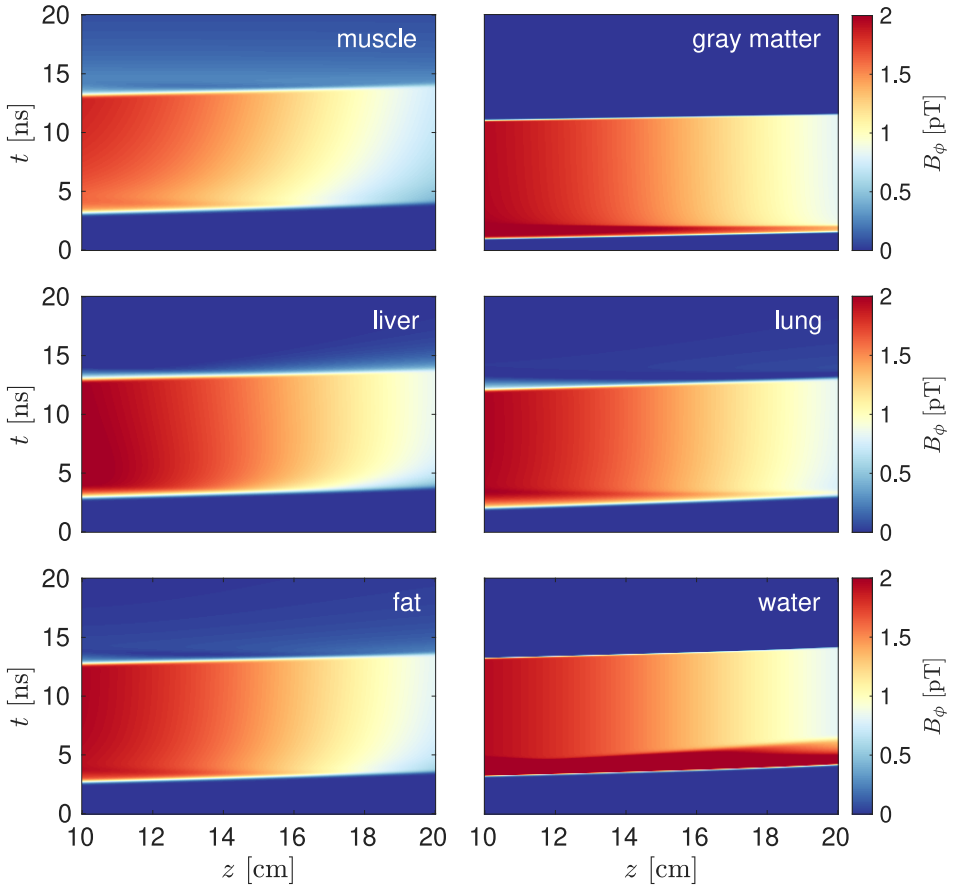

Figure 4.3: Magnetic field of a rectangular pulse with a duration of 10 ns and a peak beam current of 1.6 µA. The result is shown along the cylinder axis at $\rho = 10$ cm in various biological tissues. The field extends smoothly beyond the range at $z_\mathrm{r} \approx 15.84$ cm.

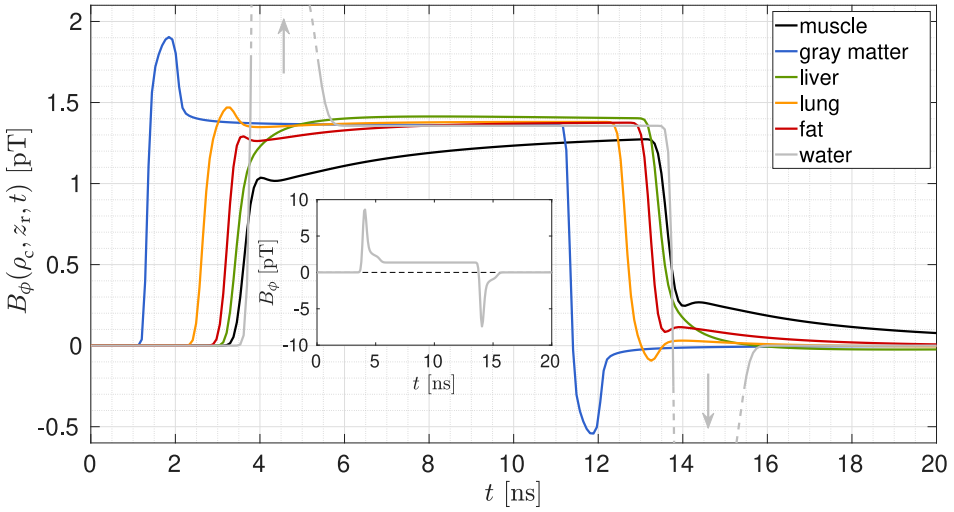

Figure 4.4: Vertical magnetic field profiles of Fig. 4.3 across time at $z_\mathrm{r} = 15.84$ cm. The profile of water is beyond the range of the main window, which can already be seen in Fig. 4.3, where the color-mapping is partially saturated for water. Accordingly, it has once again been plotted in the insert.

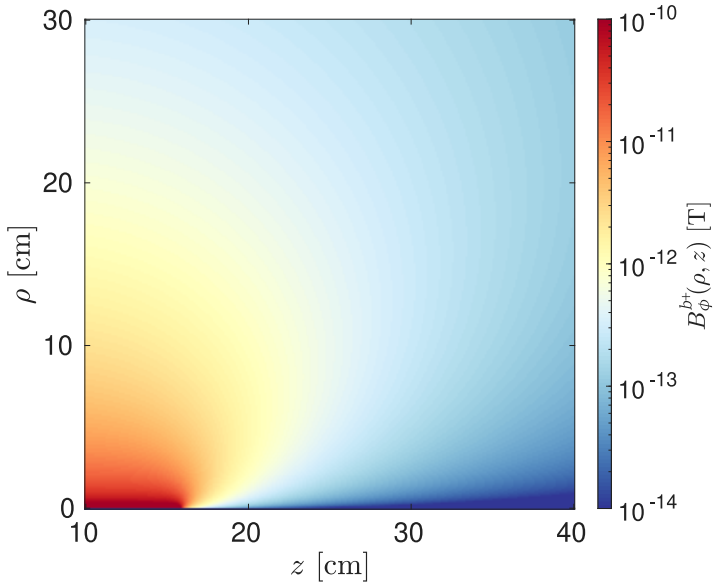

Figure 4.5: Spatial profile of the magnetic field for beam with a constant current of 2 µA. Note that the color-scaling is logarithmic.

shows $f(z,t)$, which is defined in Eq. (4.61) and estimated via Eq. (4.73). Being proportional to the surface charge density, it shows how the charges initially accumulate on the cylinder surface and subsequently spread out due to the charge relaxation. When (horizontally) integrated over z, the total amount of surface charge is limited by the remaining charge in the center (see Fig. 4.6) and the amount of charge administered: $f(t) = \Gamma(t) - g(t)$. The charge accumulation is dictated by the pulse shape $\gamma(t)$, where a delta and rectangular pulse have been chosen. For the latter, a more realistic pulse duration of 10 µs is used, which is significantly longer than the relaxation time-scales (see Table 4.2). Recall that the range has for simplicity been shifted to zero ($\hat{z}_\mathrm{r} = 0$), which also applies to the subsequent results presented in the current sect

With Eq. (4.75), which relies on the results from Figs. 4.6 and 4.7, the ρ-component of the electric field outside but just above the cylinder: $E_\rho(\rho_\mathrm{c}^+, z, t)$ (see Fig. 4.8) has been computed. A further separation into the field that originates from the center $E_\rho^{ⓐ}(\rho_\mathrm{c}^+, z, t)$ and the surface $E_\rho^{ⓑ}(\rho_\mathrm{c}^+, z, t)$ is shown in the profile plot from Fig. 4.9.

Finally, the relaxation was demonstrated by re-evaluating the results of Albert et al. (in particular their Fig. 3) *without* the boundary conditions. Several parameters have been adapted. The result is shown in Fig. 4.10. Since the parallel component of the electric field is continuous across a boundary (see Eq. (3.34)), E_z agrees with the results from Albert et al., except for fat. The profiles of E_ρ, equivalent to Fig. 4.4 showing the profiles of Fig. 4.3, are given in Fig. 4.11.

4.2.3 Radiative part

In order to fully comprehend the electromagnetic signal, the radiative part will be studied in this section. In particular, the focus is on the radiation that originates from the primary protons in (non-conductive) water. The analysis simplifies significantly when considering a point particle only, which will be the case for the following three figures. Also, only the electric field will be shown. The point-partilce's Coulomb field as well as its electromag-

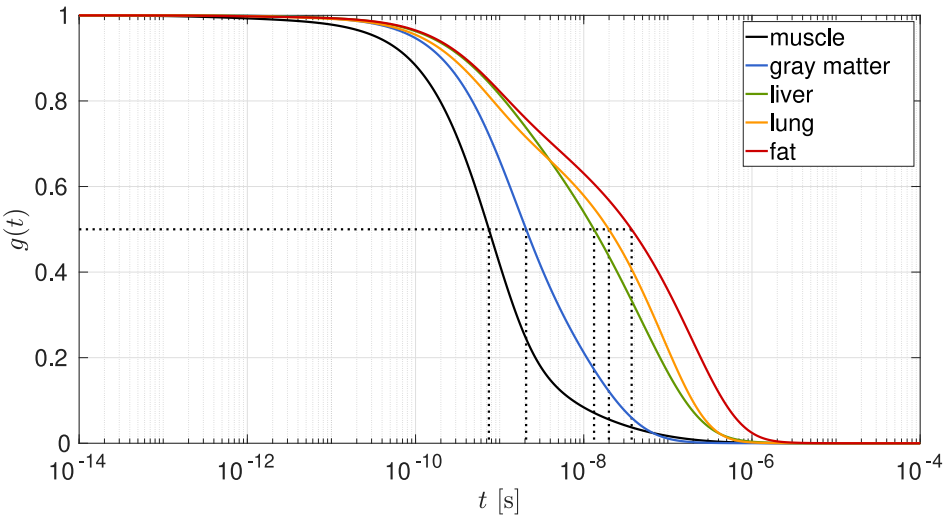

Figure 4.6: Charge relaxation in biological tissues, after an external charge imbalance is "placed" in a conducting and homogeneous volume at $t = 0$. $g(t)$ may be interpreted as the percentage of charge remaining in the center, when compared to its initial value. The times $t_{1/2}$, when $g(t_{1/2}) = 1/2$ have been indicated by dotted lines.

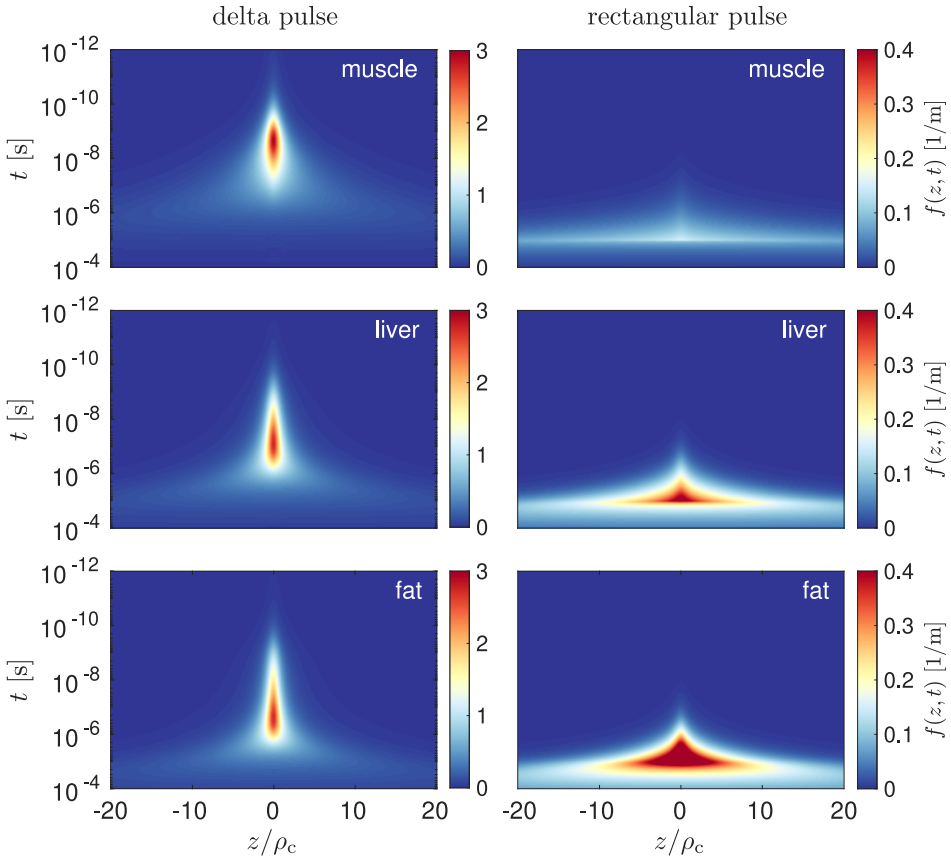

Figure 4.7: Semi-logarithmic plot of the surface charge density on the cylinder with a radius of $\rho_c = 10$ cm for a few select targets across the relaxation time spectrum (see Table 4.2). Note that the color scale for the delta pulse (left) differs from the color scale of the rectangular pulse (right).

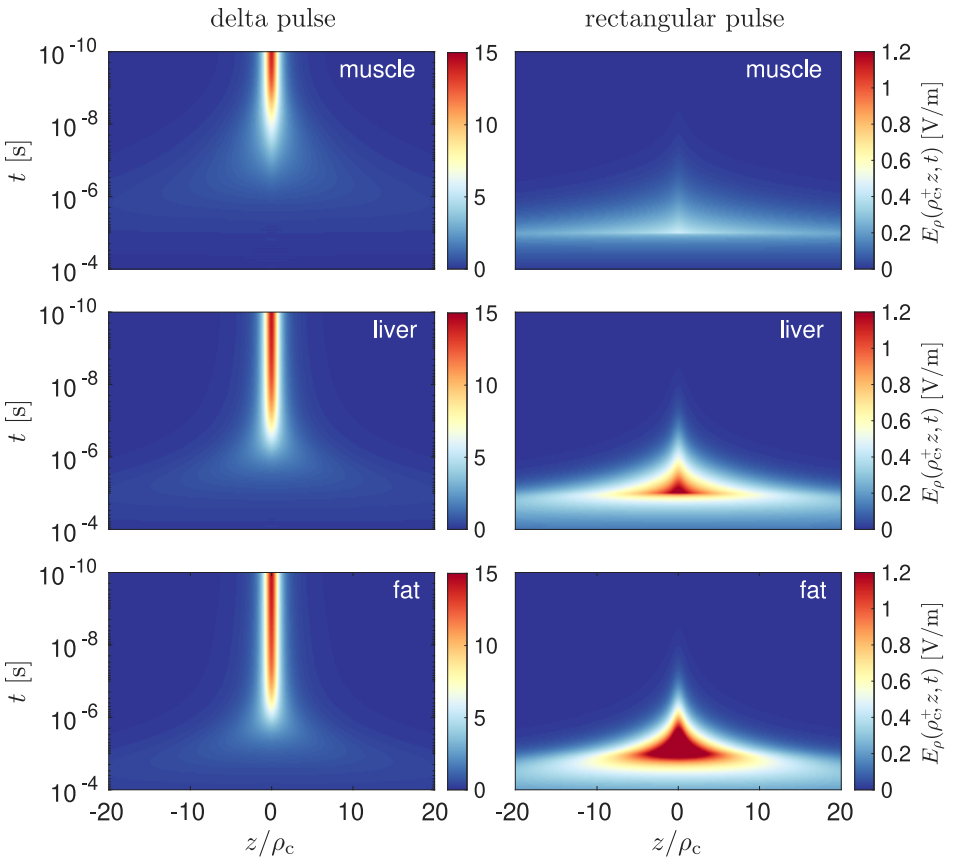

Figure 4.8: Semi-logarithmic plot showing the ρ-component of the electric field outside of the cylinder with a radius of $\rho_\mathbf{c} = 10$ cm. Note that the color scale for the delta pulse (left) differs from the color scale of the rectangular pulse (right).

netic wave front can be seen in Fig. 4.12. Both the radial and longitudinal components are shown at a fixed time $t = 2.5$ ns in the vicinity of the range. They were calculated from Eq. (4.33). Closely related to Fig. 4.12, the temporal profile of E_ρ and E_z at the range and 5 cm away from the central beam axis is shown in Fig. 4.13. The impact of the charge discontinuity through the inclusion of the path for $t < 0$ (see Appendix A.6) or the appearance radiation field (see Appendix A.7) are also investigated therein. The chosen position $\mathbf{r}_0 = (\rho_0, z_\mathrm{r}) = (5\ \mathrm{cm}, 15.84\ \mathrm{cm})$ is marked in Fig. 4.12. Also at $\mathbf{r}_0$, in Fig. 4.14 the frequency spectrum of the longitudinal electric field component is shown, which is affected by the charge discontinuity and appearance radiation. The separation into velocity and acceleration dependent parts via Eqs. (4.46) and (4.47) is shown, where Eqs. (4.51) and (4.52) need to be taken into account. For comparison, the frequency spectra of the Cherenkov radiation were added (see Eq. (A.63)), which are used for the derivation of the Frank-Tamm formula. The different (gray) profiles belong to different velocities $\beta = v/c_0 = \{0.12, 0.14, \ldots, 0.22\}$, which primarily contribute at the range.

The results are wrapped up with an estimation of the radiation yield in water from a rectangular beam with a duration of 10 µs and 10^8 particles. Due to the rotational symmetry with respect to the azimuthal angle, the surface and volume integrals, as described in Sec. 4.1.10 and Appendix A.11, reduce numerically to line and surface integrals, respectively. For the surface integral of the Poynting vector, the distribution of the Poynting vector along z projected onto the surface is denoted as $p_\mathbf{s}(\mathbf{r})$, which only needs to be integrated

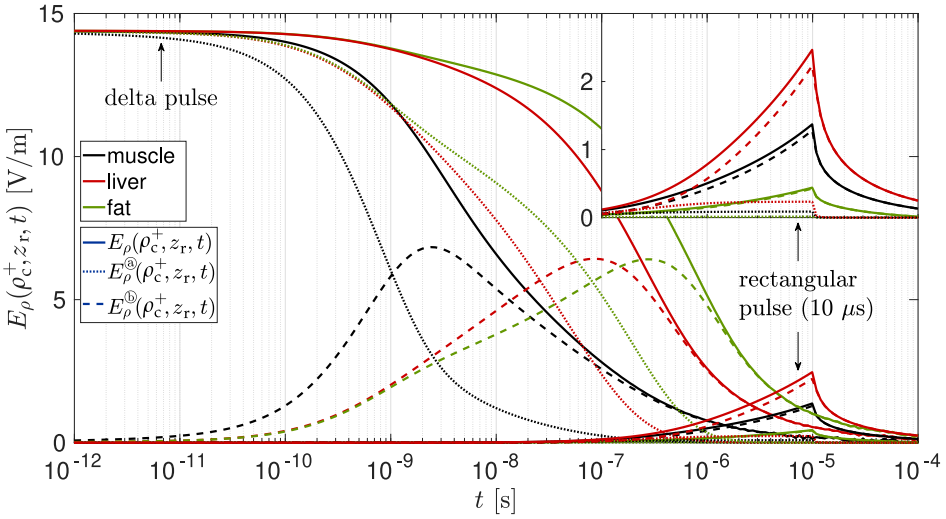

Figure 4.9: Vertical profiles of Fig. 4.8 at the range ($\hat{z}_r = 0$) across the same logarithmic time scale. Both the delta and rectangular pulses are shown. The color-coding was adapted from Fig. 4.6 to distinguish between the different tissues, while the different line styles correspond to the different field contributions. In particular, the dotted lines correspond to the field that originates from the center (ⓐ), while the dashed lines are the surface contributions (ⓑ). The solid lines lines show the total field, i.e. exactly what is shown in Fig. 4.8. The insert has the same units as the main plot.

along the surface $\partial\Omega_z$ in the z-direction to obtain the yield: $E^{\text{rad}} = \int_{\partial\Omega_z} p_{\mathbf{s}}(\mathbf{r})\mathrm{d}z$. (The θ-integral of $E^{\text{rad}}_{\text{ⓓ}}$, given in Eq. (A.56), has formally been parametrized through z.) It is shown in Fig. 4.15 for both contributions from the cylindrical and semi-spherical surfaces. One obtains $E^{\text{rad}} = 1.167$ eV at $R_1 = 10$ cm and $E^{\text{rad}} = 1.011$ eV at $R_2 = 20$ cm. The difference is explained by the electromagnetic absorption, which was confirmed by evaluating the volume integral of the energy density between R_1 and R_2 separately, where $\Delta E^{\text{rad}} = 0.151$ eV. The remaining inaccuracies are due to the fact that it was integrated only up to $z = -20$ cm instead of $-\infty$. This means that within a 10 cm propagation in water approximately 12.9 % of the energy is absorbed. With the peak frequency of about 9 GHz (see Fig. 4.14), a single rectangular pulse gives rise to approximately 2×10^5 photons.

4.3 Discussion

Prior to entering a detailed discussion of the results presented above, one aspect of the methods shall be highlighted. While the approach from Sec. 4.1.4 is mostly identical to the work from Albert et al., except for the delta-term from Eq. (4.32) and the estimation of the magnetic field, a major simplification has been achieved by realizing the connection to the Liénard-Wiechert potentials. To obtain the same result as in Eq. (4.15), given in Eqs. (4.40) to (4.42), it was not necessary to solve complicated integrals (see Appendix A.3). In addition, Eqs. (4.40) to (4.42) apply to arbitrary proton paths so that e.g. scattering can be modeled in future work.

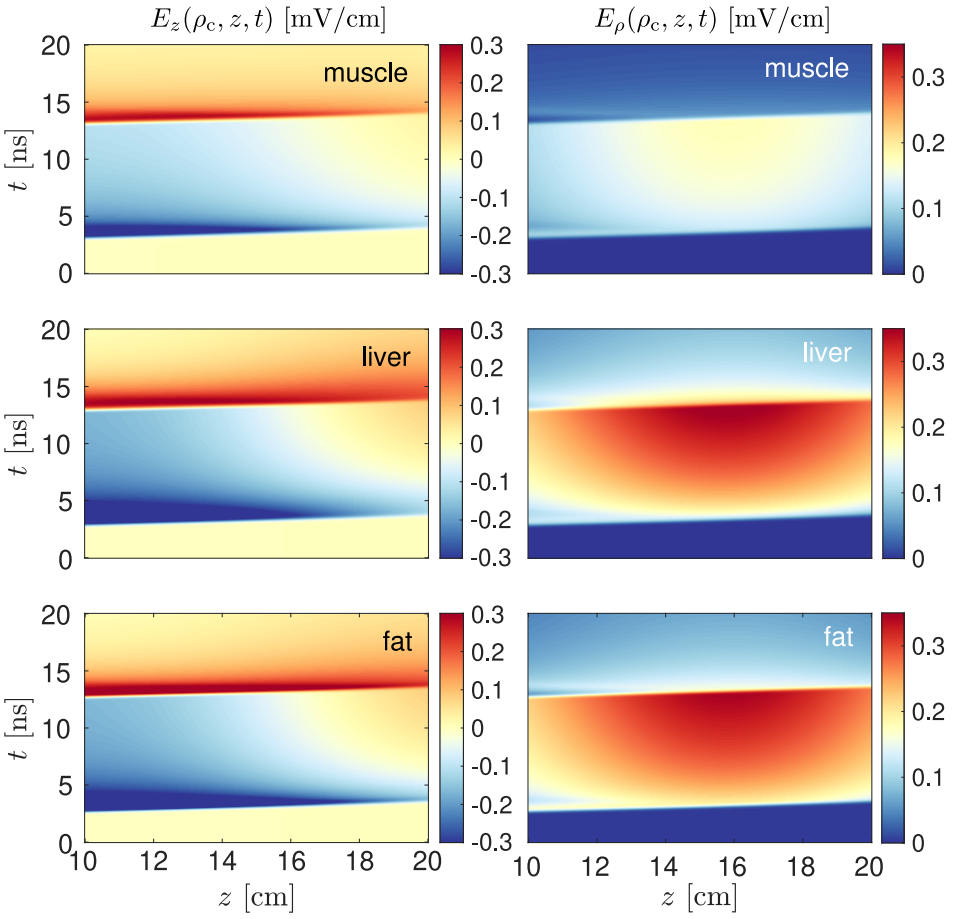

Figure 4.10: Longitudinal (left) and radial (right) component of the electric field at $\rho_c = 10$ cm along z and t without interface conditions. A rectangular pulse with a duration of 10 ns is considered.

4.3.1 Magnetic field

The first and probably most important observation is that when comparing different targets, the magnetic field (on the cylinder surface i.e. at a distance of 10 cm) is very similar and has little variability (see Figs. 4.3 and 4.4). This applies to both the behavior across time and the profile along z. Already after about 6 ns, the field strength has settled to an almost identical value in most tissues. Taking the static field limit as a reference (see Eq. (4.54)), the plateau value of Fig. 4.4 is expected to be $\mu I/(4\pi\rho)\, z_r/\sqrt{\rho^2 + z_r^2} \approx 1.377$ pT, which agrees well with the results. Also note that the profiles in Fig. 4.4 closely follow the rectangular beam pulse shape, as have been approximated and predicted in Eq. (4.56). The down-scaled pulse duration (nanoseconds vs. microseconds) has been chosen, as deviations from this approximation are only visible on such short timescales. First notice the slight variations regarding the horizontal offset of the rectangular profile, e.g. gray matter rises and drops first, while muscle last. This is related to the different propagation velocities of the electromagnetic waves inside the tissues, which are in turn determined by the refractive index. It has been plotted in Fig. 3.2 and results in the small time delay. Secondly, the preceding and trailing peaks and troughs can primarily be attributed to the electromagnetic radiation, which constructively interfere at the sharp pulse gradients. In terms of magnitude, their amplitudes are comparable to the DC field, as can be seen in Fig. 4.12. The radiative part

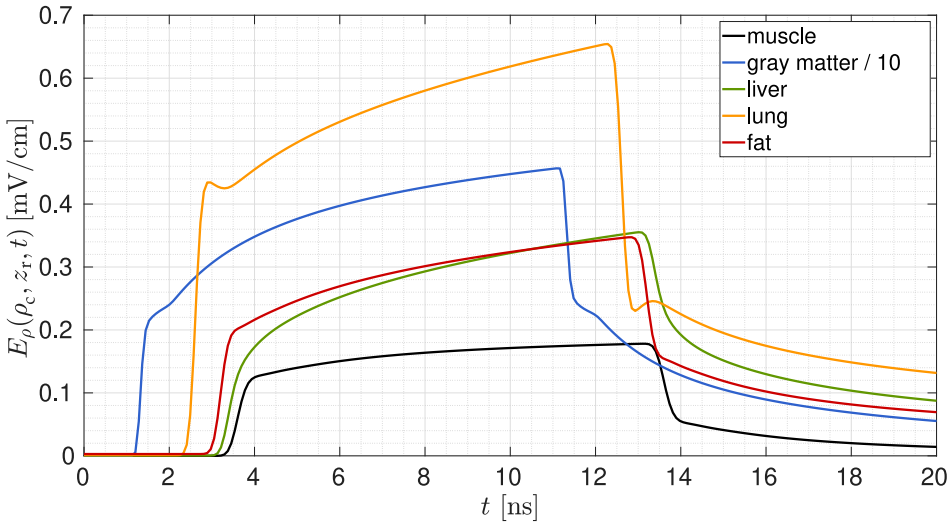

Figure 4.11: Radial component of the electric field, 10 cm above the range z_r. This corresponds to vertical profiles along the three panels on the right side of Fig. 4.10. Two additional tissues, i.e. gray matter and lung, have been added, completing the set from Fig. 4.6. Gray matter has been scaled down by a factor of 10 to fit into the vertical range.

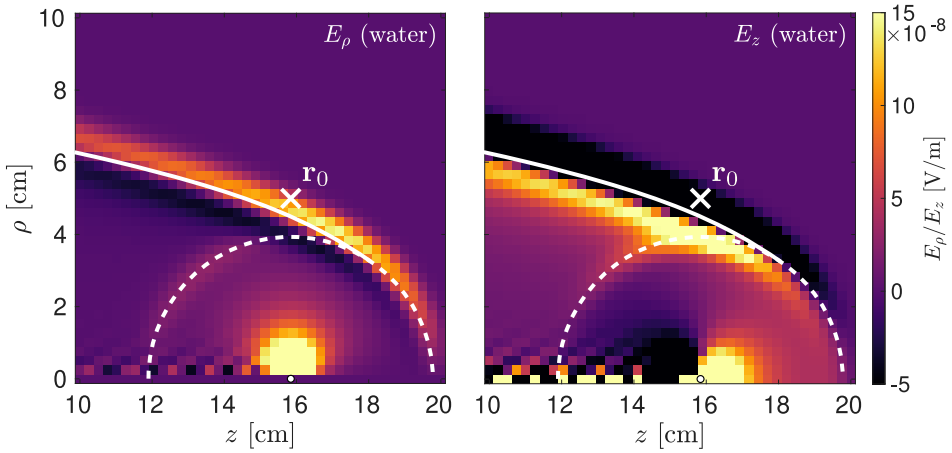

Figure 4.12: Radial and longitudinal component of the electric field in water (without conductivity and boundaries) at $t = 2.5$ ns. The black and white dot on the central axis ($\rho = 0$) indicates the range $z_r \approx 15.84$ cm. The solid line follows the Cherenkov radiation wave front, while the dashed line outlines the weaker radial pulse of bremsstrahlung. The origin of which is primarily at the range, where the deceleration is the largest (see Fig. 2.10). The fluctuations along the path of the proton (close to $\rho = 0$ and $10 < z < 15$ cm) are numerical noise.

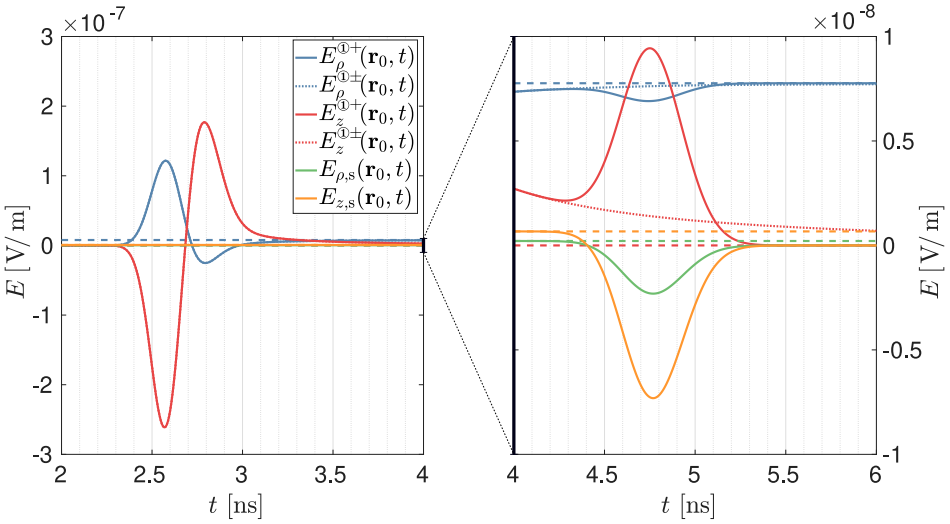

Figure 4.13: E_ρ and E_z across time at $\mathbf{r}_0 = (\rho_0, z_\mathrm{r}) = (5\ \mathrm{cm}, 15.84\ \mathrm{cm})$ in water (without conductivity and boundaries). Both field components $E_\kappa^{①+}(\mathbf{r}_0,t)$ are each compared to $E_\kappa^{①\pm}(\mathbf{r}_0,t)$, where the contribution from $t<0$ is included. The appearance radiation field $E_{\kappa,\mathrm{s}}$ is also shown, but only visible in the closeup on the right. The dashed lines of the same colors correspond to the respective asymptotes.

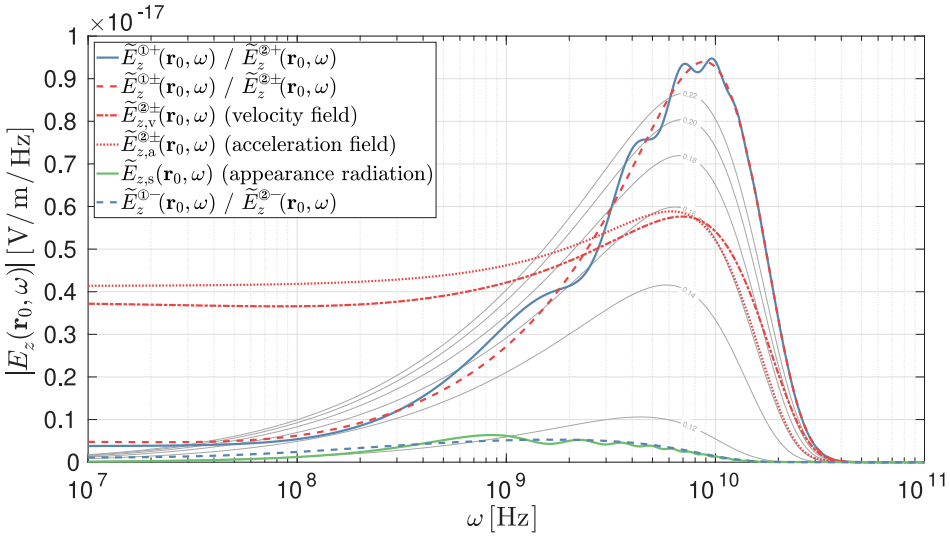

Figure 4.14: Frequency spectrum of E_z at $\mathbf{r}_0$, as shown in Fig. 4.13. The color-coding has been adapted. The data is further complemented by the separation into the velocity and acceleration field as well as the isolated contribution from $t<0$. The gray lines in the background are the frequency spectra of the Cherenkov radiation from particles with different velocities.

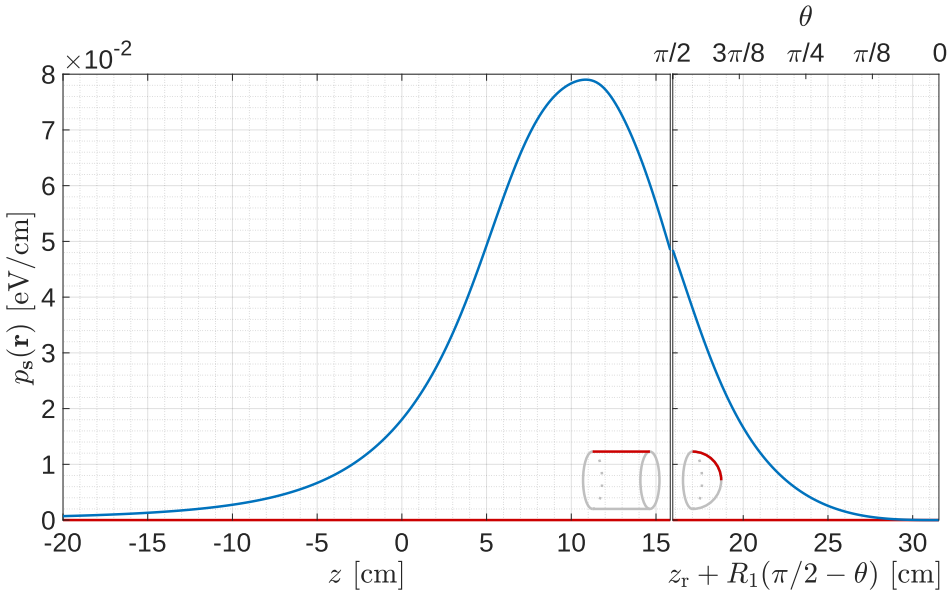

Figure 4.15: Radiation energy distribution $p_s(\mathbf{r})$, split into the flow through the cylinder (left) and the hemisphere (right) at $R_1 = 10$ cm. When integrated, it yields the emitted energy. The surfaces are explicitly defined in Eqs. (4.77) and (4.78). Note that the line associated with the hemisphere curves down, as indicated by the sketch.

is further discussed below. The small deviations in the plateau region, where the waves destructively interfere, are likely polarization effects. The overarching conclusion is the approximate independence of the tissue parameters. This is to be expected, since differences in the magnetic field are associated with differences in permeability, which are negligible (see Eq. (3.3) and text below). Recall that with Eq. (3.23), permittivity and conductivity differences are modeled. Yet in particular the conductivity, which is set to zero for water, appears to have little impact when compared to the remaining tissues.

In the spatial profile of Fig. 4.5, it is shown that the magnetic field close to the central beam axis (and for $z < z_r$) behaves like the magnetic field of a simple straight wire, which has been argued in Sec. 4.1.7. However, the magnetic field away from the central beam axis and beyond the range, as it is shown in Figs. 4.3 and 4.4, does not demonstrate an indicative peak or clear step along the z-axis. It decreases rather smoothly along the beam line. More specifically, the field drops from $\mu I/(2\pi\rho)$ downstream to half that value at the range. How fast this happens depends on the distance to the central beam axis. The derivative of Eq. (4.54) with respect to z is a bell-shaped curve (not Gaussian), whose FWHM can be used to quantify width. It is given by $2\sqrt{2^{3/2}-1}\,\rho$, i.e. the longitudinal profile smooths out linearly with the distance. As has been argued in Sec. 4.1.2 by means of an analytical and numerical analysis, this drop is not related to the decreasing velocity of the primary proton. For instance, a beam of protons traveling with a constant velocity until they are abruptly stopped at the range would have the same DC field. While the longitudinal profile does not have a distinctive feature, it is nonetheless characteristic and shifts together with the range. This correlation could form the basis of a range verification approach or beam diagnostics, similar to the detection of collimated prompt gammas along the beam axis [69]. One could deduce the range through a comparison of the measured profile with the theoretical model, where the Bragg-peak position is known. Under idealized assumptions, this is investigated in Sec. 5.3.7. The magnetic field strength lies in the order of picotesla and

is thereby detectable by means of sensitive magnetometry such as optical magnetometry [234] or SQUIDs [235]. Yet it remains low when compared to external magnetic fields, such as earth's magnetic field, which is on average about 45 µT [236]. Shielding will certainly be necessary. In addition, noise that originates from the patients's biomagnetism needs to be dealt with. Since it lies in a low frequency range (up to 100 Hz [237]), it might be separated from the magnetic field that originates from the beam in the frequency domain. A more detailed analysis regarding the frequency profile of a modulated beam is provided in Chapter 6.

4.3.2 Relaxation and electric field

As shown in Fig. 4.6, the relaxation times strongly depend on the tissue due to the different permittivity and conductivity parameters (see Table 3.1). The associated relaxation half-life (see Table 4.2) covers a relatively wide range, differing by about two orders of magnitude and are therefore 10^2-10^4 times shorter than a 10 µs pulse. Keep in mind that the conductivity has been approximated by its DC value. In reality, it rises towards higher frequencies [163] so that the results from Table 4.2 constitute a lower bound, i.e. the relaxation is likely somewhat faster. Keeping the focus on the behavior of the charges, the cylindrical geometry has been taken into account in Fig. 4.7. It is shown how the charges accumulate on the cylindrical boundary and simultaneously drift apart. The time-scales of the charge accumulation are identical to the relaxation in the center (Fig. 4.6), only inverted. In other words, $t_{1/2}$ also applies to the laterally integrated $f(t)$. The lateral spread is similarly fast so that the peak charge density drops by 50% within comparable time scales. As mentioned above, the pulse duration is orders of magnitude longer than the relaxation time so that the charges on the surface are already drifting apart while the beam is still on and delivering new charges. So when comparing the delta with the rectangular pulse (left vs. right column of Fig. 4.7), the same amount of charges is distributed significantly wider for the rectangular pulse.

The electric field, that on the one hand originates from the charges and on the other hand drives the charge relaxation and thereby changes the charge distribution (its own source), is shown in Figs. 4.8 and 4.9. Through the approach presented in Sec. 4.1.9, it was possible to solve this complex interplay by a simple Fourier inversion of Eq. (4.73). In particular, an iterative solution would have been significantly more complex due to the convolutional permittivity model. That the electric field peaks at approximately 144 mV/cm ($\sim$ 15 V/m), as has been calculated by Albert et al., can only be confirmed with the delta pulse. In the case of the rectangular 10 µs pulse, the observable field outside of the cylinder is approximately one order of magnitude weaker. In both cases, the field strength is not upheld, but vanishes in timescales that are somewhat longer than the relaxation times. In particular, the field is then dominated by the surface contributions (as shown in the insert of Fig. 4.9). A smaller fraction contributes from the center, which reaches an equilibrium. In other words, at this point the rate of deposited charges equals the rate of charges removed by the conduction current. The then constant amount of charges in the center can be estimated via Eq. (4.61), where the charge density in the center is given by $\tilde{\rho}_\mathrm{t}^{@}(\mathbf{r},t) = Nq_\mathrm{e}\delta^3(\mathbf{r})g(t)$. Mathematically, the equilibrium only settles for a beam with infinite duration, where the beam shape function is given by $N\tilde{\gamma}_\infty(\omega) = \Phi\delta(\omega)$ (see Eq. (4.53)). The inverse Fourier transform of Eq. (4.60) simplifies through the delta term so that eventually $\tilde{\rho}_\mathrm{t}^{@}(\mathbf{r},t) = I\tilde{\varepsilon}(0)/\sigma_\mathrm{DC}\delta^3(\mathbf{r})$, where $I = q_\mathrm{e}\Phi$. Relative to the total amount of charge that would lead to the peak value of 144 mV/cm at a distance of 10 cm ($Nq_\mathrm{e}\delta^3(\mathbf{r})$), one obtains the ratio $\tilde{\varepsilon}(0)/(\sigma_\mathrm{DC}T)$. The beam duration T has been extracted from the fluence $\Phi = N/T$. With the linear relationship

between the field and the charge density (see Eq. (4.64)), the ratio between 144 mV/cm and the plateau value should be identical. The DC permittivity (see Eq. (3.23)) is given by $\tilde{\varepsilon}(0) = \varepsilon_0(\varepsilon_\infty + \Delta\varepsilon_1 + \Delta\varepsilon_2)$ so that with the parameters from Table 3.1, the ratio for e.g. liver becomes $\tilde{\varepsilon}(0)/\sigma_{\mathrm{DC}}/T \approx 0.0164$. The expected equilibrium value is then 0.236 V/m, which agrees with what is shown in Fig. 4.9. It is yet almost another order of magnitude weaker than the originally expected peak value. Recall that the low-frequency resonances have been neglected in Table 3.1 so that the center contributions are likely larger. Nonetheless, with the field dominated by surface contributions, the peak at the range, as it is still present on the RHS of Fig. 4.8, cannot be expected with a patient's geometry. Also note that the field strength drops abruptly once the beam is turned of (after 10 µs). In summary, it was found that the field vanishes, even in the presence of cylindrical boundaries. This result disagrees with the finding of Albert et al., which predicted a sustained field strength following the initial build up. In addition, they argue that the field vanishes only through the diffusion of the charges, which is in the order of seconds or minutes. The discrepancy is caused by the issue with the interface conditions, as already discussed in Sec. 4.1.8. An accurate mapping of permittivity, conductivity and boundaries would be necessary to predict the field, which further complicates the situation. Detectability and sensitivity with respect to range shifts require a further analysis. A more promising approach is to collect the conducted charges through externally applied electrodes, as has been investigated by Cirrone et al. [238]. For this purpose, the patient needs to be electrically isolated. It has originally been suggested as a dose monitoring approach, but might also be used for range verification through multiple electrodes and triangulation. A broader discussion will be held in the conclusion (see Chapter 7).

A similarly rapid fall-off of the electric field is also shown in Figs. 4.10 and 4.11, where the field initially rises to a peak around the range. The differences in magnitude are attributed to the tissue's permittivity and conductivity. Also the short pulse duration of 10 ns impacts the strength. Notice that the electric field emerges in the same order as in Fig. 4.4, i.e. the field propagation velocity is (as expected) identical for electric and magnetic field. On that matter, a propagation-related delay of the electric field does not occur in Figs. 4.8 and 4.9, since the static approximation has been applied, which is solely based on Gauß' law: Eq. (4.64). However, since these delays are merely a couple of nanoseconds, a significant impact on the results cannot be expected. The linear rise of the electric field, as predicted by Eq. (4.55) is strongly damped and flattened due to the conductivity relaxation. The behavior $E_\rho \propto \Gamma(t)$ can be seen in the work of Albert et al. (in their Fig. 5), especially for $T = 100$ ns. However, such a result would only be observable for a non-conductive tissue.

A further elaboration on the analysis of Albert et al. ensues, where they considered the behavior of $\mathbf{E}(\mathbf{r}, t)$ ad $t \to \infty$. In this limit, the free charge density is described by the point charge located at the range: $\rho_{\mathrm{f}}(\mathbf{r}, t \to \infty) = q_{\mathrm{e}}\delta(x)\delta(y)\delta(z - z_{\mathrm{r}})$ or in Fourier domain $\tilde{\tilde{\rho}}_{\mathrm{f}}(\mathbf{k}, \omega) = q_{\mathrm{e}}/(2\pi)^3\delta(\omega)\exp(ik_z z_{\mathrm{r}})$. Therefore, in order to gauge the behavior as $t \to \infty$, one needs to consider $\tilde{\tilde{\mathbf{E}}}(\mathbf{k}, \omega \to 0)$. Firstly, $\tilde{\tilde{\mathbf{J}}}_{\mathrm{f}}(\mathbf{k}, \omega) = \mathbf{0}$, due to the static charge density. In combination with Eq. (3.47), Eq. (4.1) becomes $\tilde{\tilde{\mathbf{E}}}(\mathbf{k}, \omega) = 2\pi N\tilde{\gamma}(\omega)/\tilde{\varepsilon}_{\mathrm{c}}(\omega)\, i\mathbf{k}\tilde{\tilde{\rho}}_{\mathrm{f}}(\mathbf{k}, \omega)/[k^2 - \omega^2/\tilde{c}^2(\omega)]$. $1/\tilde{\varepsilon}_{\mathrm{c}}(\omega \to 0)$ vanishes so that the field inside the target vanishes completely. For the field outside and along $\hat{\mathbf{e}}_\rho$, the interface condition is (erronoeusly) applied so that the limit $\omega \to 0$ is well defined and the electric field becomes $\widetilde{\mathbf{E}}(\mathbf{k}, t) = Nq_{\mathrm{e}}/[(2\pi)^3\varepsilon_0]i\mathbf{k}/k^2$ $\exp(ik_z z_{\mathrm{r}})$, which is the spatial Fourier transform of a Coulomb field shifted to the range $\mathbf{r}_{\mathrm{r}} = (0, 0, z_{\mathrm{r}})^T$. Projected onto $\hat{\mathbf{e}}_\rho$ that is $E_\rho(\mathbf{r}, t) = Nq_{\mathrm{e}}/(4\pi\varepsilon_0)\,\rho/\sqrt{\rho^2 + (z - z_{\mathrm{r}})^2}^3$, while the longitudinal field $E_z(\mathbf{r}, t)$ vanishes. Eq. (3.33) would then imply a static surface charge

density of the form $\rho_s(\mathbf{r},t) = Nq_e/(4\pi)\,\rho_c/\sqrt{\rho_c^2+(z-z_r)^2}^3$, situated on the cylinder surface. With Eq. (4.64), an equivalent convolutional law as in Eq. (4.66), connects the surface charge density with the longitudinal field: $E_z(\mathbf{r},t) = 1/(4\pi\varepsilon_0)\rho_s(\rho_c,z) * \mathcal{R}(\rho_c,z)$, where $\mathcal{R}(\rho_c,z) = 4\rho_c\mathcal{E}(-4\rho_c^2/z^2)/(4\rho_c^2+z^2)\,\mathrm{sgn}(z)$ is the kernel for the field on the cylinder surface and non-zero. This contradicts with the conclusions from above, i.e. that the longitudinal field vanishes. In addition, a static surface charge density is equally unreasonable and contradicts with the results presented in Fig. 4.7. Finally, the conductivity-related charge relaxation already followed from first principles with the analysis of the bound charge, which was presented in Eq. (4.57).

4.3.3 Radiation

The basis of the present work (Eqs. (4.1) and (4.3)) is a general solution of the Maxwell equations in a homogeneous domain, as explicitly derived in Eqs. (A.9) and (A.10). Accordingly, the inherent wave-based nature of the Maxwell equations, as prominently apparent through the wave equations of Eqs. (4.4) and (4.5), comes into play. Beginning with the static frame of the electric field in Fig. 4.12, where the electromagnetic wave that originates from a primary proton is shown. Recall that water has been chosen as the target, where the conductivity was assumed to be negligible, i.e. set it to zero. Consequently, after the proton deceleration (taking on average about 1.39 ns, as shown in Fig. 2.10), the proton remains static at the range. It is then surrounded by its Coulomb field, which is gradually spreading. At the depicted 2.5 ns, the field has a radius of about 5 cm. It is accompanied by a spherical wave centered at the range (indicated by the dashed line in Fig. 4.12), which can be attributed to bremsstrahlung. The magnitude of bremsstrahlung scales with the deceleration (see Eq. (4.49)), so while the primary proton constantly decelerates, the major contribution is at the range, where the deceleration strongly peaks (Fig. 2.10). The amplitude of the wave decreases towards the central beam axis, which is a well-known characteristic of bremsstrahlung. Outside of the highly-relativistic regime, it radiates mostly perpendicularly to the primary proton's path [153]. A tilted wavefront propagates further out (delineated by a solid line), which can be attributed to Cherenkov radiation. Note that the wavefront is curved, due to the changing velocity of the primary proton. If it would move with a constant velocity, a straight wavefront would emerge.

The time profile in Fig. 4.13 shows the single cycle pulse for both E_ρ and E_z and further investigates the impact of the discontinuous charge and current density/appearance radiation, as discussed in Sec. 4.1.6. It emerges at the origin, i.e. $(\mathbf{r},t) = (\mathbf{0},0)$, and thus takes longer to reach $\mathbf{r}_0$ ($\sim$ 4.5 ns). It is comparatively weak, being further away and attenuated along the way, so that it is only visible in the closeup on the RHS. The appearance radiation (Eq. (4.50)) is almost identical to the wave that is created when only $t < 0$ is neglected. A proper inclusion of the path for $t < 0$ leads to a smoother and more reasonable profile. Regardless, the magnitude of this (physically unreasonable) deviation is very low. It is much rather acknowledged as a mathematical artifact, which can be neglected. For the numerical evaluation, it is less computationally expensive to neglect the path for $t < 0$. Primarily, it is an explanation for the unexpected delayed wave. The contribution from the appearance radiation has also been separated in the corresponding frequency spectrum shown in Fig. 4.14. Compared to the main signal, it may be neglected but leads to a slightly oscillating frequency profile. However, the main focus is the separation into the velocity and acceleration fields. At $\mathbf{r}_0$, they split into approximately equal parts, which agrees with what is shown in Fig. 4.12 regarding the separation of Cherenkov wavefront and the spherical bremsstrahlung wave. While the analytical expression of Eq. (4.33) is remarkably simple,

it comprises (rather abstractly) multiple phenomena. In terms of frequency, the spectrum reaches up to $\omega \sim 30$ GHz ($f \sim 5$ GHz), which corresponds to a wavelength of a couple of centimeters. Visually, this can be confirmed with Fig. 4.12. Generally, gigahertz frequencies are expected from the nanosecond primary proton dynamics.

Having partially attributed the electromagnetic wave of a primary proton with an initial energy of $Q = 150$ MeV to Cherenkov radiation, it raises the question how this can be reconciled with the well-known fact that the lower kinetic energy threshold for protons in water to emit Cherenkov radiation is approximately $Q = 485$ MeV [239,240]. Actually, Cherenkov radiation is more relevant in photon therapy [241], where one can use it to perform *optical dosimetry*. In this case, secondary electrons give rise to the Cherenkov radiation, where the energy threshold is significantly lower (0.264 MeV) due to their lower mass. Regardless, for protons, the key is to distinguish the frequency spectra. While the former typically peaks in the UV spectrum, the latter belongs to radio waves. The occurrence of Cherenkov radiation is tied to the particle's velocity β and the refractive index of the target n: $\beta > 1/n$. A proton with a kinetic energy of $Q = 150$ MeV moves initially with approximately half the speed of light (Eq. (2.18): $\beta \approx 0.507$), while the lowest relative permittivity in water at the highest included frequency (60 GHz) is approximately $\varepsilon_\mathrm{r} \approx 65.5$. For the initial velocity, $n > 2$ is necessary, while water has $n > 8$ ($n = \sqrt{\varepsilon_\mathrm{r}\mu_\mathrm{r}}$) in the radio frequency regime. Therefore the proton moves indeed faster than the speed of light in the medium. Even more so, $\beta \gtrsim 1/8$ is given for the majority of the path (see Fig. 2.10), so that the Cherenkov radiation is created almost all along the track. In summary, the high permittivity allows Cherenkov radiation at lower energies. To create the classical UV Cherenkov radiation, where $n \approx 1.33$, the aforementioned 485 MeV are necessary. Yet, not only $\beta > 1/n$ must be satisfied, also the absorption must be low. Water is sufficiently transparent for radio frequencies and in the visible spectrum, leading to the two regimes outlined in Fig. 4.16.

Lastly, the analysis of the energy yield shall be discussed. The peak in Fig. 4.15 is at the depth at which the circular Cherenkov waves, initially starting at the origin $(\mathbf{r}, t) = (\mathbf{0}, 0)$, collectively form the forward tilted wave front. In this case, including the path for $t < 0$ would be unreasonable, since the preceding drift through air does not create Cherenkov radiation. Generally, a superimposed pulse can give rise to this radiation, since the point particle fields have a non-zero average (see Fig. 4.13) so that subsequent particles cannot cancel their fields entirely. Regardless, the total amount of energy is extremely low, especially when compared to the initial energy of the primaries. An external detection is likely very challenging and/or completely masked by the natural background. In addition, the protons originating from the primary protons are probably significantly outnumbered by the emission from the secondary electron bremsstrahlung [242], which is also under investigation by Yamaguchi et al. for range verification. When compared to protons, electrons lose a significantly larger amount of energy to bremsstrahlung, due to their lower mass.

As a final remark, the analytical approach, which formed the basis of the work discussed in this chapter and which has been investigated and applied throughout, is limited in certain aspects. In particular, the following has been neglected: nuclear reactions and their fragments, changing charge states of the primaries at the range, range and energy straggling, lateral scattering as well as the impact of the secondary electrons. A MC-based approach can readily simulate these processes, and will be the focus of the following chapter.

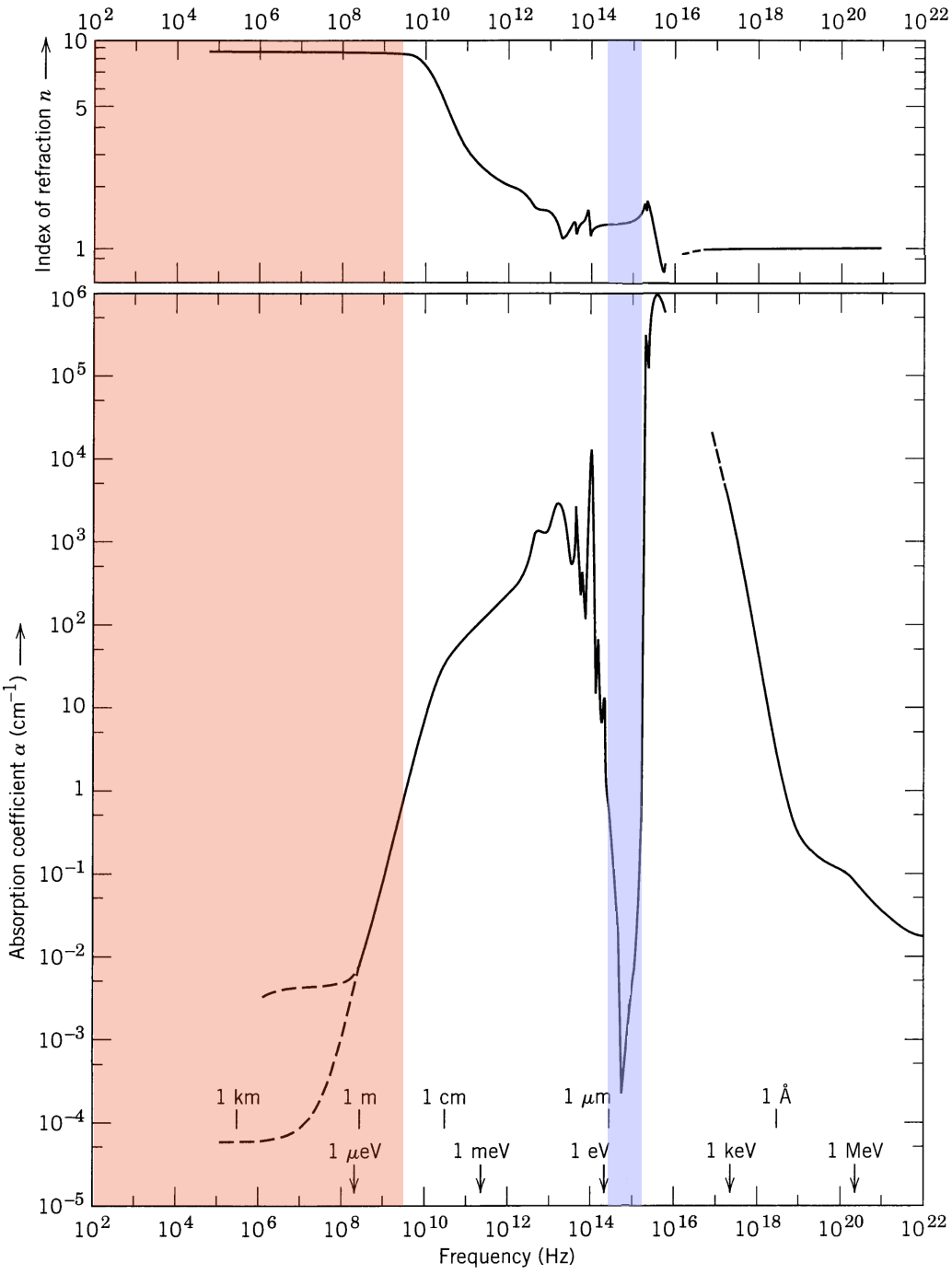

Figure 4.16: Index of refraction n and absorption coefficient α of water over a wide frequency range. A similar plot has also been shown in Fig. 3.2. The two frequency regimes where Cherenkov radiation can occur are indicated. They are in the radio (red) and visible/UV (blue) ranges. Adapted from Jackson [153] and modified.

5 IMPACT OF SECONDARY PARTICLES

WITH AN EMPHASIS ON SECONDARY ELECTRONS

One may summarize the results from the previous chapter as follows. The strong influence of the conductivity diminishes the electric field strength rapidly and causes a "washout" effect in a nanosecond time scale. The magnetic field, on the other hand, is not affected by the latter and remains constant during the beam pulse. Furthermore, the B-field is approximately independent of the environment (permittivity, conductivity) under the assumptions of Chapter 4 (homogeneous targets) and its longitudinal profile correlates with the range. Altogether, this renders the magnetic field as a favorable basis of a range verification approach. Whether this conclusion remains valid under more realistic assumptions shall be further investigated with the present chapter. The shortcomings and simplifications of the analytical work have already been highlighted in the discussion of Chapter 4. In particular, nuclear reactions, secondary protons and electrons, energy and range straggling and lateral scattering have been neglected. These effects will be taken into account by means of Monte Carlo (MC) simulations. Some simplifying assumptions remain, which will be discussed below.

The analytical solution of the Maxwell equations will be replaced by the numerical finite element analysis (FEA), which has already been described in Sec. 3.6. In fact, what has been shown is already a simplification of a closely related previous work that has been presented in [193, 243]. An extensive analysis of the MC-generated phase spaces and the associated charge and current densities is conducted. The magnetic field has been estimated from the latter and the impact of the hitherto neglected processes has been analyzed. With the error propagation described in Sec. 3.6.6, the magnitude of the magnetic field uncertainties that originate from the natural current density fluctuations, will be estimated. Finally, a few aspects towards an experimental detection will be discussed. A manuscript with the results from this chapter has been accepted for publication in *Medical Physics*. It has also been presented [244] separately.

Before presenting the specific methods of the present chapter, some underlying assumptions should be addressed. Firstly, a *magnetostatic* formalism has been used for the estimation of the magnetic field. This is based on the rapid response times (sub-nanoseconds) relative to the pulse duration (microseconds). See for this purpose Fig. 4.4. The magnetic field quickly reaches a static value, only briefly deviated by an initial peak. One can also observe that polarization-related relaxation effects vanish in the nanosecond scale. As has already been analyzed with Eq. (4.56) and stated in the discussion of Chapter 4, the temporal profile closely follows the beam pulse shape. Such a beam pulse shape (rectangular) is also extracted from the ion source of the S2C2 [245], a synchrocyclotron accelerator whose technical parameters have been used to guide the MC setting (see Secs. 2.3 and 5.1.4). By applying the magnetostatic formalism, one focuses on the constant plateau with respect to time and thus calculates the spatial profile (as in Fig. 4.5) through the FEA. This also means

that the general RF structure is neglected, i.e. the focus is on the DC part.

Already in Sec. 3.6.1, it has been discussed that the discontinuous current density of a stopping proton pencil beam ($\nabla \cdot \mathbf{J}_\mathrm{f} \neq 0$) is associated with a (constantly) changing charge density or charge deposition. These charges do not accumulate indefinitely. Quite the opposite, the charge relaxation, caused by the tissue's conductivity, diminishes the charges on timescales between a tenth and tens of nanoseconds (see Fig. 4.6), prohibiting charge accumulation[1]. Yet, the associated conductivity current density (see Eq. (3.31)) does not give rise to an additional magnetic field under the assumptions at hand. Firstly, the driving electric field that causes the conduction current is primarily a radial Coulomb field situated at the range (see Eq. (4.55)). The spatial distribution of this vector field translates through Eq. (3.31) to $\mathbf{J}_\mathrm{c}$, so that it is also a radial vector field. By virtue of symmetry, a radial current density cannot give rise to a magnetic field. This follows directly from Maxwell's equations. In addition, water, which has been modeled without conductivity in Fig. 4.4, behaves almost identically to the tissues, where the conductivity term is included. Nonetheless, this remains a simplifying assumption and will be further discussed in Chapter 7. It shall also be noted that external charges that may originate from the primary proton's drift through the preceding air or the patient's skin can be ruled out by the measurements of Cirrone et al. [238]. The amount of collected charges has been fully attributed to the beam current[2].

5.1 Methods

5.1.1 Geometry

The geometry under consideration is the same as in the previous chapter (see Fig. 5.1). Through MC simulations, multiple phase spaces of a single proton pencil beam in homogeneous water are obtained. As permittivity gradients between the surrounding air and biological tissues are negligible (see Eq. (3.3) and text below), an effectively homogeneous domain is under consideration. By taking advantage of its axial symmetry, it allowed a reduction of the vector potential, the magnetic field as well as the current density to the two-dimensional ρ-z-plane. In particular, the latter is collected azimuthally through square toroid-shaped voxels (red volume in Fig. 5.1). The magnetic field is numerically estimated from the simulated current density through the finite element analysis (FEA). As shown in Fig. 5.1, the corresponding mesh consists of rectangular elements, which are linearly spaced in the *area of interest* (AOI)[3]. In particular $\rho \in [0, 10]$ cm has $\Delta\rho = 1$ mm and $z \in [0, 15]$ cm has $\Delta z = 1$ mm. The beam begins to decelerate at $z = 0$, while is has been assumed that it drifts through air/vacuum for $z < 0$. With the chosen initial energy of 100 MeV, it has a range of approximately 75 mm in water, which is considered the midpoint of the entire domain. For reasons that are described in Sec. 3.6.5, the domain is enlarged beyond the AOI to a total of one meter from the midpoint along the axes: $0\ \text{mm} \leq \rho \leq 1000\ \text{mm}$ and $-925\ \text{mm} \leq z \leq 1075\ \text{mm}$. To maintain reasonably sized elemental matrices (defined in Eqs. (3.64) and (3.65)), the spacing increases exponentially beyond the AOI. In Fig. 5.1, the grid intersections are the nodes of the vector potential, while the pixels discretize the current density on the ρ-z-plane. They are associated with the aforementioned square toroidal volumes. The pixel centers are denoted as ρ_i^J and z_j^J. A more detailed description, including a drawing (to scale), is given in Appendix B.1. Finally, the magnetic field is evaluated at

[1] Note that the associated charge transport does not correspond to an actual displacement of the deposited protons, but rather to an exchange of electrons.

[2] Their work will be further discussed in the conclusion.

[3] The results below will be solely from the densely sampled AOI.

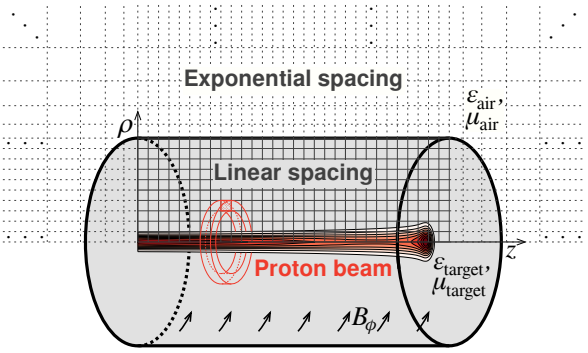

Figure 5.1: Schematic sketch of the geometrical setup, current density scoring and mesh for the FEA. A more accurate drawing to scale regarding the mesh is shown in Fig. B.1.

$\rho_i^B = (0.25 + i \times 0.5)$ mm for $i \in \{0..199\}$ and $z_j^B = (0.25 + j \times 0.5)$ mm for $j \in \{0..299\}$, i.e. between the nodes.

5.1.2 Magnetic field estimation

As mentioned above, the magnetic field is estimated through the FEA. Some basics and the specifics regarding the cylindrical symmetry and boundaries were already discussed in Sec. 3.6. Eventually, both the magnetic field and its uncertainty is estimated through the matrix multiplications from Eqs. (3.73) and (3.74). With the mesh described above, the elemental matrices $\underline{\mathrm{N}}_\kappa$ (Eqs. (3.64) and (3.65)) have 29850×29850 entries so that determining their inverse is computationally feasible. Limitations are mostly given by the necessary memory. While the $\underline{\mathrm{N}}_\kappa$ occupy only about 60 MB due to their sparsity, the $\underline{\mathrm{M}}_\kappa$ defined in Eq. (3.73) take approximately 13 GB each. The sparsity is lost through the inversion [186]. Denser sampling or a larger domain would be even more memory consuming. Regarding the mesh, note that the kernels from Eq. (3.67) need to be modified along the central beam axis, otherwise they would reach into $\rho < 0$. The details are described in Appendix B.2. Finally, in Sec. 3.6.5, it has been argued that the domain has to be "sufficiently large" to avoid the issue shown in Fig. 3.7. Unlike J_z, which is mostly a line source, J_ρ is only non-zero within the AOI, so it rather behaves like a point source whose field drops approximately quadratically. With the mesh (see Fig. B.1) ten times larger than the AOI, the boundary-related errors should be below 1%.

5.1.3 Current density accumulation

While the magnetic field profile down to the central beam axis ($\rho = 0$) will be shown in the results below, the primary interest is the behavior at the far field, a couple of centimeters away from the source. For this purpose, consider the integral representation of Ampère's circuital law[4]:

$$\oint_{\partial\Omega} \mathbf{H} \cdot \mathrm{d}\boldsymbol{\ell} = \iint_{\Omega} \mathbf{J}_\mathrm{f} \cdot \mathrm{d}\mathbf{S} + \frac{\mathrm{d}}{\mathrm{d}t} \iint_{\Omega} \mathbf{D} \cdot \mathrm{d}\mathbf{S}. \tag{5.1}$$

It directly shows the proportionality between the magnetic field and the surface integral over the current density. When the surface is chosen perpendicularly to the beam axis,

[4] Eq. (5.1) is obtained through a surface integral of Eq. (3.1d) over the area Ω. Through Stokes' theorem [246], the LHS reduces to a line integral along the boundary of the same area ($\partial\Omega$).

then there exists a radial outer edge $\rho_{\max}$ such that $\mathbf{J}_\mathrm{f}(\rho > \rho_{\max}) = \mathbf{0}$. If the area increases beyond $\rho_{\max}$, $\iint_\Omega \mathbf{J}_\mathrm{f} \cdot \mathrm{d}\mathbf{S}$ remains constant so that the magnetic field does not depend on the lateral profile of the current density in the far field[5]. Accordingly, one may accumulate the two-dimensional current density distributions in the ρ-z-plane to one-dimensional profiles along z, while maintaining the same far-field behavior. This enables a simple analysis of the impact of scattering and the beam spot size (as shown in Fig. 5.18). The contribution from $\partial_t \mathbf{D}$ complicates the simple proportionality to the current density surface integral. Yet through the vector potential and the arguments from Sec. 3.6.1, primarily that $\partial_t \mathbf{D} =$ const., one may obtain the sought proportionality. In the following, it is shown how the "accumulation rules" emerge under certain approximations. Keep in mind that they are only valid in the far field.

Accumulation of J_z

Assuming $\partial^2 A_z/\partial z^2 \approx 0$ in Eq. (3.57) allows an analytical solution of $B_{\phi,z} = -\partial A_z/\partial\rho$. With the aforementioned boundary condition $B_{\phi,z}(\rho \to \{0,\infty\}) = 0$, one obtains the result by straightforward integration:

$$B_{\phi,z}(\rho,z) = \frac{\mu}{\rho} \underbrace{\int_0^\rho \rho' J_z(\rho',z)\mathrm{d}\rho'}_{\mathfrak{J}_z(\rho,z)}. \tag{5.2}$$

The ρ'-weight has a purely geometrical interpretation, originating from the surface element of cylindrical coordinates. For $\rho > \rho_{\max}$, the quantity $\mathfrak{J}_z(\rho > \rho_{\max}, z) = \mathfrak{J}_z(z)$ is independent of ρ so that $B_{\phi,z}$ further decreases as $1/\rho$. As long as it equates to the same value, one can accumulate it to the aforementioned one-dimensional profile. In particular, the integral is approximated as

$$\mathfrak{J}_z(z_j^J) \approx \sum_i \bar{\rho}_i^J J_z(\rho_i^J, z_j^J), \qquad \bar{\rho}_i^J = \int_{\rho_i^J-\Delta\rho/2}^{\rho_i^J+\Delta\rho/2} \rho' \mathrm{d}\rho' = \rho_i^J \Delta\rho. \tag{5.3}$$

Finally, the accumulated current is then $J_z^{\mathrm{acc}}(\rho_0^J, z_j^J) = \mathfrak{J}_z(z_j^J)/\bar{\rho}_0^J$.

Accumulation of J_ρ

Likewise, Eq. (3.56) can be simplified through $\partial^2 A_\rho/\partial z^2 \approx 0$. Effectively, this leads to the same equation as discussed in Sec. 3.6.5, whose solution is given in Eq. (3.71). Solving for $B_{\phi,\rho} = \partial A_\rho/\partial z$ results in

$$B_{\phi,\rho} = \frac{\mu}{2\rho}\frac{\partial}{\partial z}\Bigg[\underbrace{\int_0^\rho \rho'^2 J_\rho(\rho',z)\mathrm{d}\rho'}_{\mathfrak{J}_\rho(\rho,z)} + \rho^2 \int_\rho^\infty J_\rho(\rho',z)\mathrm{d}\rho'\Bigg]. \tag{5.4}$$

The second term in the square brackets vanishes for $\rho > \rho_{\max}$, while $\mathfrak{J}_\rho(\rho,z)$ remains constant, just like $\mathfrak{J}_z(\rho,z)$. The interpretation of the quadratic weight is somewhat more intricate. Firstly, radial current further away from the central beam axis contributes more, i.e. beyond the geometrical linear weighting factor. It originates from the fact that the

[5] As discussed in numerous elementary textbooks on electromagnetic theory, one needs to choose Ω as discs perpendicular to the beam current density so that $\partial\Omega$ are rings surrounding the source.

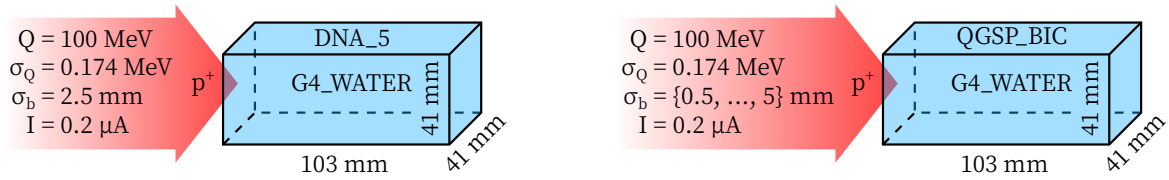

Figure 5.2: Overview of the MC simulation parameters. (a) uses the *Geant4-DNA option 5* (DNA_5), whereas (b) is based on a Geant4 standard physics list (QGSP_BIC) and tests a set of beam cross sections σ_b.

radial current flows outwards into larger volumes. Only a divergence-free (solenoidal) and therefore source-free radial current $J_\rho \propto 1/\rho$ (Eq. (A.74)) contributes equally like J_z, barring the surface element. $J_\rho \not\propto 1/\rho$ implies current sources along ρ giving rise to stronger magnetic fields. For the currently investigated scenario, Coulomb scattering (see Sec. 2.1.3) away or towards the central beam axis constitute such sources. In summary, the radial accumulation differs and has been implemented as follows

$$\mathfrak{J}_\rho(z_j^J) \approx \sum_i \bar{\rho}_i^J J_\rho(\rho_i^J, z_j^J), \qquad \bar{\rho}_i^J = \int_{\rho_i^J-\Delta\rho/2}^{\rho_i^J+\Delta\rho/2} \rho'^2 \mathrm{d}\rho' = \left(\rho_i^{J2} + \Delta\rho^2/12\right)\Delta\rho. \tag{5.5}$$

Similarly, $J_\rho^{\mathrm{acc}}(\rho_0^J, z_j^J) = \mathfrak{J}_\rho(z_j^J)/\bar{\rho}_0^J$.

5.1.4 Monte Carlo simulation

A volume of $41 \times 41 \times 103$ mm^3 has been set up in Geant4 (Version 10.05.p01) [247–249] to simulate a proton pencil beam in water (G4_WATER). With respect to the physical interactions, two different packages have been used: a standard physics list (QGSP_BIC), which is commonly used in medical physics applications for fast simulations, and the physics processes that are available through the Geant4-DNA extension [250–253]. The latter is further subdivided into different "options", three of which are recommended. They primarily differ in the interactions of the secondary electrons. The default is "option 2" being the first implementation of electron transport in Geant4. An improvement regarding the set of ionization and excitation cross sections [254] is available since 2016, referred to as "option 4". "option 6" is almost identical to "option 4" with respect to the types of interactions that are simulated (ionization, excitation, scattering), yet based on an alternative theoretical description. See [253] and references therein for an analysis of the differences between the options and details regarding the underlying models. To limit computational cost, an accelerated version of "option 4", called "option 5", has been chosen for the present work. Henceforth "Geant4-DNA option 5" is abbreviated as DNA_5. It shall be noted that Geant4-DNA places strong limitations on the target, since only water can be simulated.

As stated in Sec. 2.3, a pulsed beam from a synchrocyclotron with pulse durations in the microsecond scale are considered. While the average current remains relatively low, the temporarily stronger currents create temporarily stronger fields. Recall that the maximum peak beam current of the S2C2 is 18 µA. For the present work, a more moderate value of 0.2 µA has bee chosen. With respect to the launch time, it is assumed to be uniformly distributed, thereby neglecting the RF structure, as previously stated. The beam current determines the average time delay between two consecutive protons:

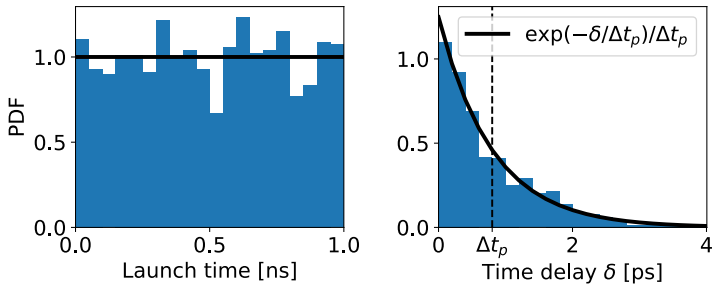

Figure 5.3: Distribution of both the launch time and the delay between two consecutive protons. The latter can be approximated by an exponential distribution.

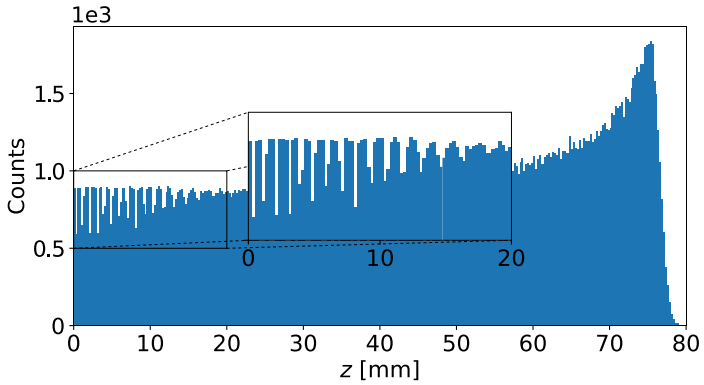

Figure 5.4: Initial fluctuations of the charge density, if the launch time is not randomized. An equivalent plot with the launch time randomized, is shown inFig. 5.8.

$\Delta t_p = q_e / I \approx 0.8$ ps. It is approximately exponentially distributed, so that it has been sampled from $f_{\Delta t_p}(\delta > 0) = \exp(-\delta/\Delta t_p)/\Delta t_p$, leading to random and on average uniform current. The exponential approximation is not straightforward and rather an empirical observation (see Fig. 5.3). Also, sampling δ on-the-fly from a static distribution is generally only possible for uniform distributions. Non-uniform beam distributions would require a variable Δt_p. If instead one would launch the protons with a constant Δt_p, then one can observe that protons tend to occupy some z_j^J bins more frequently than others, regardless of changing the random seeds, as is shown in Fig. 5.4. It occurs mostly at the entrance region and gradually averages out due to the longitudinal "shuffling" that originates from range straggling. More quantitatively, the penetration depth straggling increases within the first 20 mm by about 0.37 mm (see Fig. 2.3), which sufficiently exceeds the longitudinal spacing $\Delta z = 0.25$ mm of Fig. 5.4. In summary, a constant Δt_p is not appropriate.

The lateral distribution of the particles was sampled from a normal distribution, such as the one given in Eq. (2.21). A spot size of $\sigma_b = 2.5$ mm has been used for DNA_5, whereas multiple spot sizes $\sigma_b = \{0.5, 1.0, \ldots, 5.0\}$ were tested with QGSP_BIC. The chosen values were guided by [255]. To put this into perspective, with their arrangement of quadrupole lenses following the S2C2 accelerator, Henrotin et al. [149] achieve spot sizes as low as 1 mm. In addition, they or Van de Walle et al. [148] also quantified the uncertainty of the initial energy for the S2C2 from a 230 MeV beam to be as low as 0.4 MeV. In relative terms, this equates to only $\sigma_Q = 0.174\%$. For the chosen initial energy of $Q_{\text{in}} = 100$ MeV, this means that the initial energy is sampled from a normal distribution with a mean of

100 MeV and a standard deviation of $\sigma_Q = 0.174$ MeV.

With the beam launched at $t = 0$, the time up to $t = 0.9$ ns is independently (i.e. with different random seeds) and repeatedly simulated. Subsequently, the phase spaces (PSs) at a time within the interval $t_{\mathrm{PS}} \in [0.85, 0.9]$ ns were exported, ensuring to obtain a complete picture of an active beam. Recall that the average stopping time of 100 MeV protons is approximately $t_g \approx 0.81$ ns (see Fig. 2.11), which follows from the CSDA. The t_{PS} randomization has been introduced for the same purpose as the Δt_p variability. Only a single PS is extracted from each simulation, since they would otherwise be strongly correlated due to the predominantly straight proton paths and short electron scattering paths. The PS-based scoring of the MC results is necessary, since the primary interest is the current density, which is, unlike dose for instance, not an accumulated quantity. The specifics regarding the launch time had to be discussed for the same reason. It is noteworthy that the timing usually plays a minor role in typical MC simulations for medical physics applications, such as the MC-generated dose profile from Fig. 2.12. DNA_5 physics is computationally expensive. Note that the present application is not necessarily the intended use of DNA_5. A classical MC simulation on the scale of the target is performed, i.e. the proton pencil beam (recall the volume stated above). However, DNA_5 has rather been developed for detailed simulations on the micro and nanoscale [256]. While the simulations for each PS can be performed in parallel, computation times average about 37-40 hours on a single CPU. Taking this into account, $N_{\mathrm{PS}} = 300$ PSs is deemed as sufficient statistics, revealing the weak and strongly fluctuating radial current (see Fig. 5.15).

5.1.5 Extension of the proton data

The primary protons in the MC simulations are directly launched into the target (water) so that only $z > 0$ is simulated (with respect to the geometry shown in Fig. B.1). A discontinuous current density would imply an unphysical current source at the origin ($z = 0$), which strongly impacts the magnetic field, so the following describes how the current density is extended in the negative direction. To save further computational cost and memory, the drift has not been included in the MC simulations, but one can instead infer the charge and current density from first principles, under the assumption that the interaction with air is negligible (zero energy loss and scattering). Simultaneously, the random nature of the PS shall be maintained, which is why the current of the preceding drift is sampled from the appropriate distribution described in the following.

Current density As mentioned above, the initial current density is given by Eq. (2.21), or more formally $\mathbf{J}_{\mathrm{in}} = J_{\mathrm{in}}\hat{\mathbf{e}}_z$. For the following, recall the cylindrical voxels, indicated in Fig. 5.1. The portion of the total beam current impinging on a cylindrical current element Ω_{c} within the radii $\rho_0 \leq \rho \leq \rho_1$ and the angular element $\phi_0 \leq \phi \leq \phi_0 + \Delta\phi$ is then given by

$$I' = \iint_{\Omega} \mathbf{J}_{\mathrm{in}} \cdot \mathrm{d}\mathbf{A} = I\left[\exp\left(-\frac{\rho_0^2}{2\sigma_b^2}\right) - \exp\left(-\frac{\rho_1^2}{2\sigma_b^2}\right)\right]\frac{\Delta\phi}{2\pi}. \tag{5.6}$$

The average time delay between two adjacent protons within Ω_{c} follows then from the partial current I': $\Delta t'_p = q_{\mathrm{e}}/I'$ so that the average longitudinal distance is $\Delta z'_p = v_{\mathrm{in}}\Delta t'_p$. Given the longitudinal grid spacing Δz, which is only constant with the AOI and changes exponentially otherwise, one can determine the average number of primary protons within each Ω_{c}:

$$\overline{N}_p = \Delta z/\Delta z'_p = I'\Delta z/(q_{\mathrm{e}}v_{\mathrm{in}}). \tag{5.7}$$

The actual proton count is subject to random fluctuations, which are well described by a Poisson distribution. This has been demonstrated in Fig. 5.5. To finally estimate the initial current density, Eq. (3.37) is used. The charge density is then just N_p sampled from $p_{N_p} = \overline{N}_p^{N_p} \exp(-\overline{N}_p)/N_p!$, divided by the volume of the toroid-shaped voxels: $V_i^{\text{voxel}} = 2\pi\rho_i^J \Delta\rho\Delta z$, $(0 \leq i \leq 99)$. Subsequently, N_p random samples are drawn from the initial energy distribution. Their velocities are calculated through Eq. (2.18) and averaged, yielding $\overline{v}$ in order to finally obtain

$$J_z^{\text{in}} = q_e N_p / V_i^{\text{voxel}} \, \overline{v}. \tag{5.8}$$

Although this result might suggest otherwise, J_z^{in} does not depend on the voxelization, since $\overline{N}_p$ also scales with the voxel size. Yet, the same does not hold for the uncertainty of J_z^{in}. The impact of the voxelization and how it has been chosen is further examined in Appendix B.3.

Uncertainty of the current density Recall that the magnitude of the magnetic field fluctuations shall also be estimated from the current density fluctuations. For this reason, the sample standard deviation s_{J_z}, calculated from MC, is also extended via the (population) standard deviation. In particular, Eq. (5.8) is the product of the two random variables N_p and $\overline{v}$. Generally, error propagation of the product of two random variables $Z = XY$ yields $\sigma_Z^2 = \sigma_X^2 Y^2 + \sigma_Y^2 X^2$ [216]. Applied to Eq. (5.8):

$$\sigma_{J_z}^{\text{in}} = q_e / V_i^{\text{voxel}} \sqrt{\sigma_{N_p}^2 v_{\text{in}}^2 + \sigma_{\overline{v}}^2 N_p^2} = q_e N_p^{1/2} / V_i^{\text{voxel}} \sqrt{v_{\text{in}}^2 + \sigma_{v_{\text{in}}}^2}, \tag{5.9}$$

where the variance of the Poisson distribution is $\sigma_{N_p}^2 = N_p$ and the uncertainty of the mean velocity is given by *standard deviation of the mean*: $\sigma_{\overline{v}}^2 = \sigma_{v_{\text{in}}}^2 / N_p$. The first term under the square root of Eq. (5.9) dominates ($v_{\text{in}} \gg \sigma_{v_{\text{in}}}$), so that the relative current density uncertainty scales with the number of particles $\sigma_{J_z}^{\text{in}} / J_z^{\text{in}} \approx N_p^{-1/2}$. In Fig. B.3, Eq. (5.9) has been compared to the standard deviation of the DNA_5 data at the entrance region ($z = 0$). It confirms (i) the validity of Eq. (5.9) and (ii) that s_{J_z} can be estimated with the simple standard deviation formula, as opposed to requiring a more robust (Gaussian) fit. It has been argued above that N_p / V_i^{voxel} is effectively V_i^{voxel}-independent, so with Eq. (5.9) and $\sigma_{J_z}^{\text{in}} \propto N_p^{1/2} / V_i^{\text{voxel}}$ it is clear that $\sigma_{J_z}^{\text{in}}$ depends on the voxel volume. Once again, this is analyzed in Appendix B.3. Finally, J_ρ does not need to be extended, since an initially divergence-free beam is assumed. Same goes for the electron current, which is only generated in the dense target and negligible outside (in air).

5.1.6 Expected longitudinal beam profiles

Proton beam distributions from the DNA_5 data that are related to the current density will be compared to the theoretical expectations. They will be derived in the following, neglecting both lateral scattering and nuclear reactions.

Number density distribution Initially, range straggling is also neglected. The superposition law from Eq. (3.46) can also be applied to the point particle number density[6]: $f_n^{\text{pp}}(\mathbf{r}, t) = \delta(x)\delta(y)\delta(z - f_z(t))$, considering that a beam is just a superposition of point particles. Together with the beam shape function of a constant beam (see Eq. (4.53)), one obtains the

[6] Basically Eq. (3.38) divided by the elementary charge.

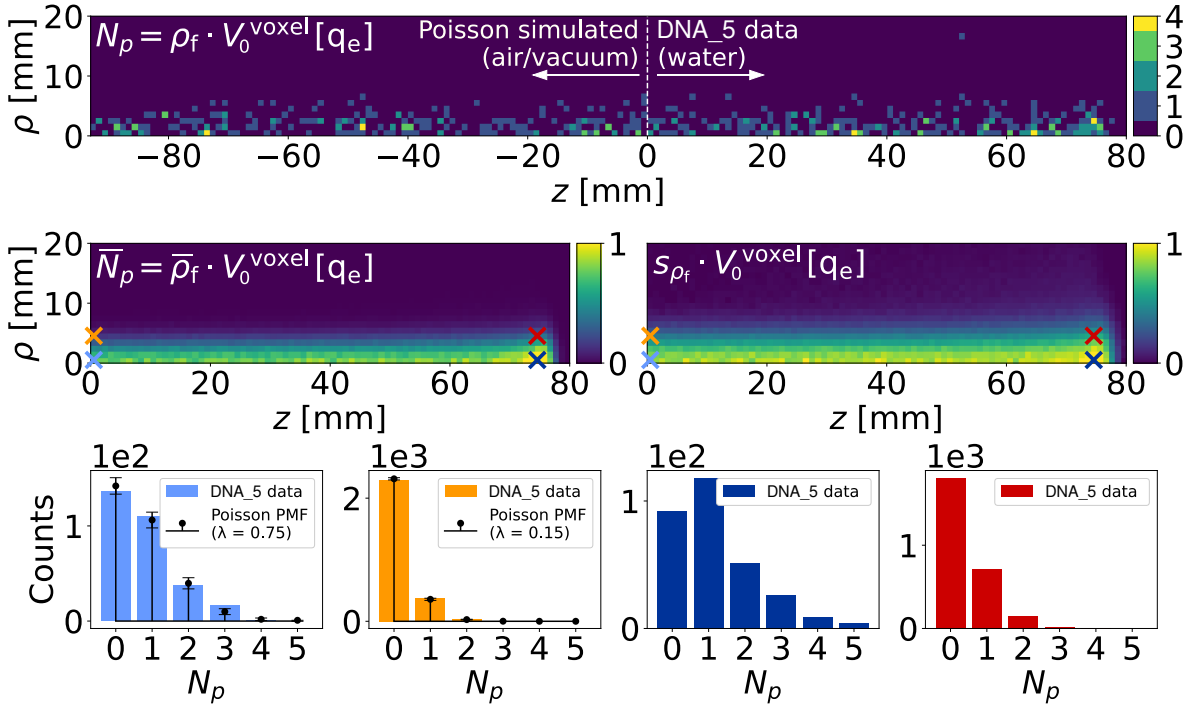

Figure 5.5: Number of protons per voxel $V_0^{\text{voxel}} = \pi$ mm^3 and their description through the Poisson distribution. The upper panel shows an exemplary proton count distribution for $z > 0$, which has been extracted from the MC phase spaces. The data for $z < 0$ has been sampled from the associated Poisson distribution with the mean calculated from Eq. (5.7). For this demonstration, the longitudinal spacing has been kept constant ($\Delta z = 1$ mm). For the actual geometry (see Fig. B.1) it increases exponentially for $z < 0$. The corresponding mean and standard deviation of the complete DNA_5 data set are shown in the two panels below. The underlying histograms at a few selected points (marked with an $\times$ and color-coded) are shown in the bottom row. The two histograms at the entrance region (light blue and orange) are further compared to the Poisson PMF (probability mass function), since they are most similar to the free-space drift that is described by the Poisson distribution and the mean from Eq. (5.7). The errorbars on the PMFs are the expected statistical deviations when considering only a finite sample. For M samples, the uncertainty is described by the standard deviation of the binomial distribution: $\sqrt{M p_{N_p}(1 - p_{N_p})}$. The equal volume subdivision has been used, which is further described in Appendix B.3. In this case M changes with the radius, so that the blue histograms add up to N_{PS}, whereas the red/orange histograms at $\rho_4^J = 4.5$ mm have a total of $9 \times N_{\text{PS}}$. As a final remark, technically the amount of charge ρ_f in units of the elementary charge is shown, which is equivalent to the number of protons.

proton number density distribution

$$f_n^{\mathrm{b}}(\mathbf{r}) = \Phi\delta(x)\delta(y)\int_{-\infty}^{t_\mathrm{r}} \delta(z - f_z(t'))\mathrm{d}t' \tag{5.10}$$

$$= \Phi\delta(x)\delta(y)\theta(z_\mathrm{r} - z)/|\dot{f}_z(f_z^{-1}(z))|, \tag{5.11}$$

where $f_z(t_\mathrm{r}) = z_\mathrm{r}$ is the proton range. The upper integral limit is set such that only moving protons are considered. Integrating Eq. (5.11) spatially gives the average number of protons that are moving within the target: $\overline{n} = \Phi(t_\mathrm{r} - t_0)$, which is merely the particle rate Φ multiplied with the average deceleration time $t_\mathrm{r} - t_0$, where t_0 is the entrance time. For $I = 0.2$ µA, $\overline{n} \approx 995$, whereas the DNA_5 data has an average of $\overline{n} \approx 962$ protons per PS. The difference is explained by the nuclear reactions. With the *equal volume* voxelization (see Appendix B.3), this means that there is less than one proton per voxel, which shall provide motivation for the analysis of the fluctuations. Eq. (5.11) is inverse proportional to the depth-dependent velocity, which is in line with the analysis from Sec. 4.1.2. Yet, it predicts an unphysical infinite charge density at z_r when the velocity drops to zero. In reality, it is spread out due to range straggling, which is readily included in Eq. (5.10) by replacing the sharp delta-distribution with a broader normal distribution. Its standard deviation is dictated by the penetration depth straggling theory that has been described in Sec. 2.1.2 and shown in Fig. 2.3. The z-dependence can be mapped to a time-dependence through the CSDA so that eventually

$$\hat{f}_n^{\mathrm{b}}(\mathbf{r}) = \Phi\delta(x)\delta(y)\int_{-\infty}^{t_\mathrm{r}} \frac{1}{\sqrt{2\pi\sigma_z^2(t')}}\exp\left[-\frac{(z - f_z(t'))^2}{2\sigma_z^2(t')}\right]\mathrm{d}t'. \tag{5.12}$$

Calculating both $f_z(t)$ and $\sigma_z(t)$ is based on the stopping power. It has been found that the NIST stopping power (see Fig. 2.2) does not accurately describe the DNA_5 data, but also that it can easily be modified to do so. The details are described in Appendix B.4.

Beam current profile Scaling the proton number density by the elementary charge results in the charge density: $q_\mathrm{e}\hat{f}_n^{\mathrm{b}}(\mathbf{r})$. Further multiplied by the average longitudinal velocity $\overline{v}_z(z)$[7] leads to the current density (see Eq. (3.39)). When laterally integrated, one gets the expected current $\hat{I} = q_\mathrm{e}\hat{f}_n^{\mathrm{b}}(z)\overline{v}_z(z)$. $f_n^{\mathrm{b}}(z)$ denotes the laterally integrated $f_n^{\mathrm{b}}(\mathbf{r})$ from Eq. (5.12).

Energy distribution The kinetic energy distribution of the moving protons in the target follows from a change of variables [221] of the number density distribution. In particular, depth and energy are related to one another by the CSDA (see Eq. (2.17)):

$$f_Q^{\mathrm{b}}(Q) = f_n^{\mathrm{b}}(z(Q))|\underbrace{\partial z(Q)/\partial Q}_{1/S(Q)}|. \tag{5.13}$$

5.1.7 Range estimation from the MC phase spaces

The range definition from Paganetti [13] is applied, which equates it to the peak of the diffluence[8]. More specifically, beam current instead of fluence (they are proportional and therefore equivalent) is used, where the former is calculated by laterally integrating the longitudinal current density J_z. A smooth function is fitted to the MC-generated profile

[7] $\overline{v}_z(z)$ differs from $\dot{f}_z(f_z^{-1}(z))$ at the range, where $\overline{v}_z(z)$ has been extrapolated beyond (see Fig. B.4).

[8] The diffluence is the derivative of the fluence along the beam line (z-axis).

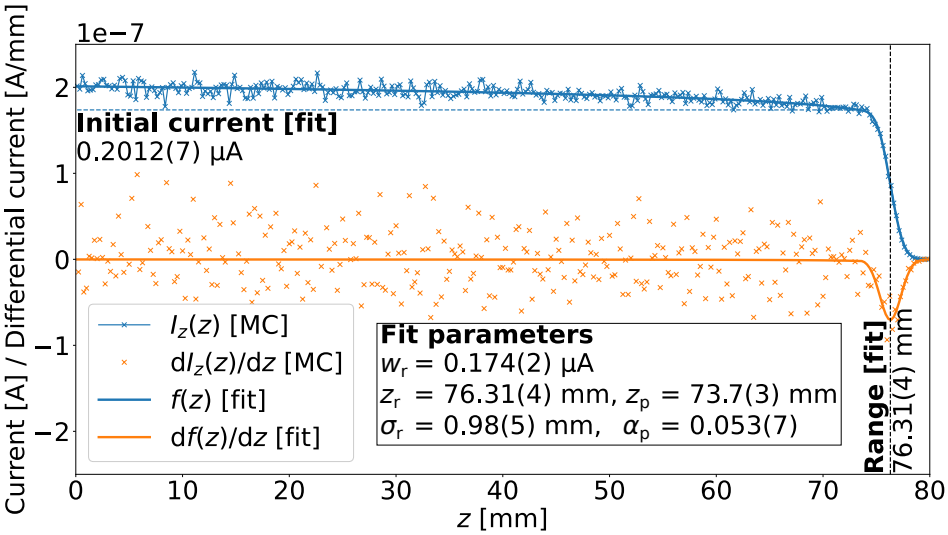

Figure 5.6: Longitudinal beam current profile of the DNA_5 data (all 300 PSs) fitted to Eq. (5.14) in order to determine the range z_r. The longitudinal spacing (0.25 mm) is smaller than the usual $\Delta z = 1$ mm. The values given in parenthesis are the 1σ-uncertainties of the fit parameters, applying each to the last digits. The horizontal dashed line (blue) is the error function $g(z)$ (see the text above Eq. (5.14)), which is technically only valid for $z > z_p$. It provides an estimate for the nuclear reaction-related losses.

Table 5.1: Proton range for different Geant4 physics packages and the CSDA, based on the NIST stopping power [90]. For clarity, "w/o e^-" abbreviates "without electrons".

Method	DNA_5 (fitted)	NIST (CSDA)	DNA_5 w/o e^- (fitted)	QGSP_BIC (fitted)
Range [mm]	76.31(4)	77.32	77.33(4)	77.72(4)

to compensate for noise, which is further enlarged by the necessary differentiation. From the Gaussian energy and range straggling theory presented in Sec. 2.1.2, it follows that the distal fall-off can be modeled by an error-function. In particular, the derivative of the current profile with respect to z is related to the charge deposition (see Eq. (3.7)), which is expected to be Gaussian, as is the derivative of the error function. Explicitly $g(z|w_r, z_r, \sigma_r) \equiv g(z) = w_r/2\{1 + \mathrm{erf}[-(z - z_r)/(2\sqrt{2}\sigma_r)]\}$, where the fit parameters w_r, z_r and σ_r quantify the current strength prior to the drop, the range and range straggling, respectively. It has been found that the preceding plateau and loss through nuclear interactions can be described by a simple power law of the form $(az + b)^\alpha$, which is smoothly and continuously attached to the error function (at $z_p < z_r$):

$$f(z) = \begin{cases} g(z_p)\left[1 + \dfrac{g'(z_p)}{\alpha_p g(z_p)}(z - z_p)\right]^{\alpha_p} & z \le z_p \\ g(z) & z > z_p \end{cases}. \tag{5.14}$$

The fit with Eq. (5.14) is shown in Fig. 5.6. It has been found that the MC physics packages have a non-negligible impact on the range, differing by up to 1.4 mm. The explicit values have been summarized in Table 5.1. Consequently, data from different physics packages will not be compared.

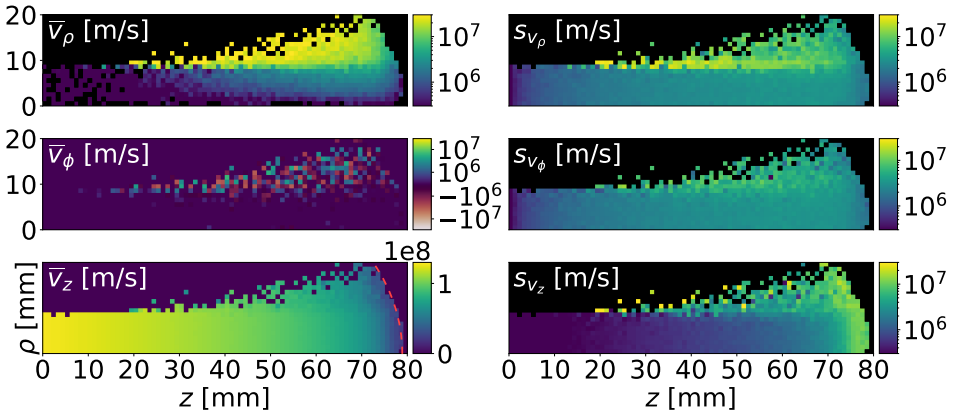

Figure 5.7: Average $\overline{v}_\kappa$ and standard deviation s_{v_κ} of the proton velocity along the components of a cylindrical coordinate system. The complete DNA_5 data set (300 PS) has been used, where pixels with less than 10 protons were excluded. Except for $\overline{v}_z$, all results are logarithmically scaled.

5.2 Results

The results below are primarily based on the DNA_5 data (Fig. 5.2 (a)), except for the analysis regarding the impact of the beam spot size (Fig. 5.2 (b)).

5.2.1 Phase space analysis

The current density as the source of the magnetic field is a statistical quantity, which can be represented as the product of the charge density and the average velocity within each volume element (see Eq. (3.37)). Consequently an analysis of PSs with an emphasis on the charge and velocity distributions of the dominant charged particles (protons and electrons) ensues to better comprehend their contribution to the total current density. $\kappa = \{\rho, \phi, z\}$ serves in the following as a placeholder for components of a cylindrical coordinate system. Due to their large absolute values, velocities are oftentimes represented in units of $\beta_\kappa = v_\kappa / c_0 \in [-1, 1]$, which is sometimes given as a percentage.

5.2.1.1 Protons

Spatial velocity distribution The spatial distribution of the average proton velocities $\overline{v}_\kappa$ and their standard deviations s_{v_κ} are shown in Fig. 5.7. Their distributions within each voxel are well approximated by normal distributions, so that $\overline{v}_\kappa$ and s_{v_κ} were determined through Gaussian fits. v_κ varies significantly in terms of counts, magnitude and uncertainty therefore the binning has been adjusted dynamically for each voxel. To ensure a balanced count per bin, mean and standard deviation have initially been approximated through the associated Gaussian percentiles. In particular, the 50^{th} percentile is the mean and the 84^{th} (approximately) is the mean plus standard deviation. Subsequently, the velocity binning has bee set to the mean plus/minus five standard deviations, which helps to compensate for outliers.

Longitudinal beam profiles Some accumulated longitudinal beam profiles are collectively shown in Fig. 5.8. The theoretical expectations have been derived in Sec. 5.1.6. As in Fig. 5.7, the complete DNA_5 data set has been used, yet the histograms have been normalized to a single phase space. For instance, a beam with a current of 0.2 µA has a density of 10

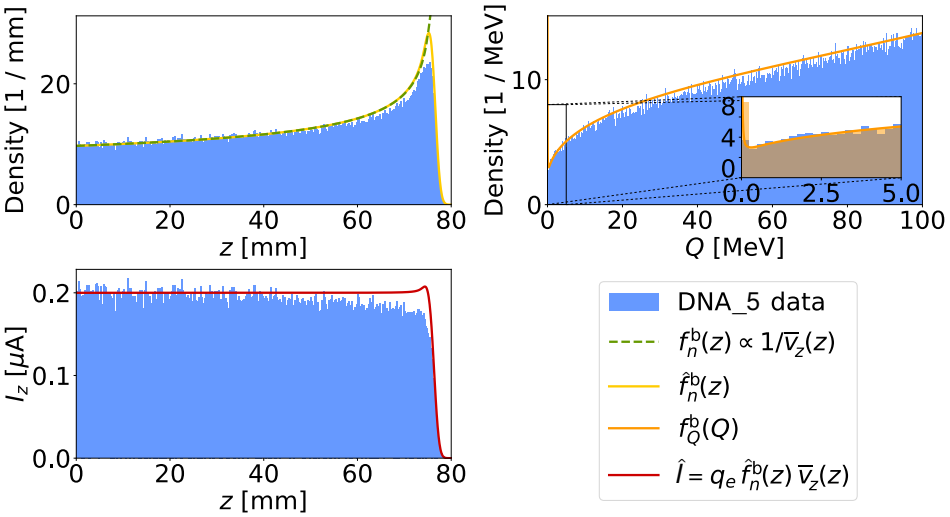

Figure 5.8: Accumulated proton beam distributions in the target and during irradiation, considering only protons in motion. $f_Q^b(Q)$ has been discretized (bin-wise integrated) in the insert of the upper right panel due to the sharp increase towards $Q = 0$. It remains finite nonetheless. The current profile in the lower left panel is essentially the same as Fig. 5.6. The longitudinal binning is 0.25 mm, whereas $\Delta Q = 0.25$ MeV.

protons per mm that increases to above 20 at the range, as is shown in the upper left panel of Fig. 5.8.

5.2.1.2 Electrons

The Geant4-DNA extension has primarily been chosen for its higher accuracy regarding electron production and transport, especially for low energies [251, 252]. To put it into perspective, secondary, tertiary, etc. electrons comprise about 92.3% of the DNA_5 data, whereas in QGSP_BIC they amount to only 0.02% so that protons are the vast majority. However, with 92.3% there are on average only 12 times more electrons than protons, while one might expect a factor between 10^5 and 10^6 (see Sec. 2.1.4). This expectation remains valid considering that DNA_5 tracks electrons down to 10 eV and does not use any production cuts for the DNA processes.

The apparent lack of electrons can be explained by their short lifetimes (sub-picoseconds) compared to the deceleration times of the primary protons (on average 0.81 ns for a 100 MeV beam, as shown in Fig. 2.11). More specifically, the average lifetime of the secondary electrons is just 7.5 fs (see Fig. 5.9), so when integrated over the deceleration time of a proton, there are approximately 0.81 ns/7.5 fs $\approx 1.1 \times 10^5$ electrons per primary proton. Considering that despite the short lifetimes, there are still 12 times more electrons than protons and that energies below 10 eV are not even included (there is a non-negligible amount of electrons below 10 eV, as shown in Fig. 2.9), there seem to be too many after all. However, the estimate from Sec. 2.1.4 considers only secondary electrons, while DNA_5 also simulates further daughter particles. In summary, the factor 12 refers to the *instantaneous* ratio between electrons and protons, not the integrated one.

With respect to the longitudinal velocity distribution, it has been found that the secondary electrons can empirically be separated into two classes via the kinetic energy threshold $Q_{\text{thr}} = 1$ keV (see Fig. 5.10), i.e. the threshold velocity $\beta_{\text{thr}} \approx 6.247 \times 10^{-2}$ (see Fig. 5.11). Electrons with energies below the threshold follow a narrow and isotropic distribution.

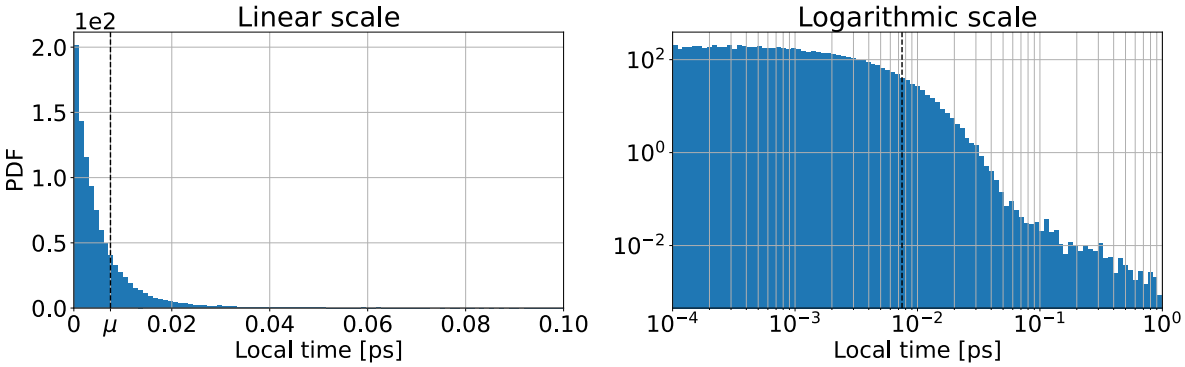

Figure 5.9: Lifetime distribution of secondary electrons. The *local time* is in Geant4 the time since creation. Its distribution for all electrons of the complete DNA_5 data set are shown in linear (left) and logarithmic (right) scale. The average of 7.5 fs is indicated with a dashed line.

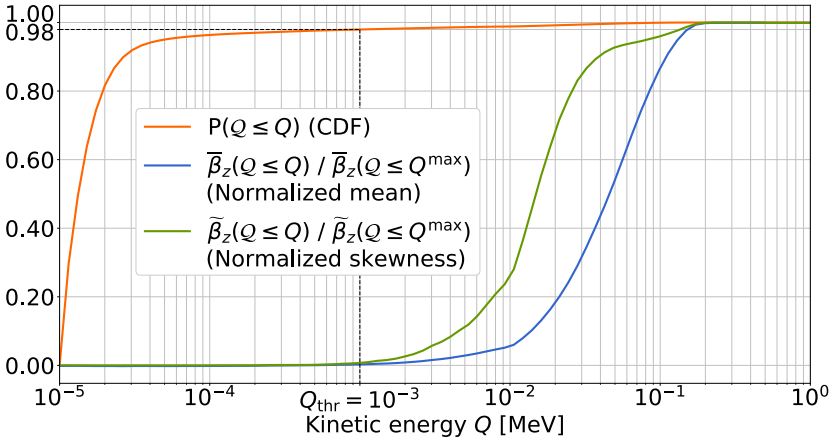

Figure 5.10: Normalized mean ($\bar{\beta}_z$) and skewness ($\tilde{\beta}_z$) of the secondary electron longitudinal velocity as a function of increasing energies included, starting from $Q_{\text{cut}} = 10$ eV. Both mean and skewness (serving as measures of symmetry) begin to deviate from a symmetric zero-mean distribution once energies above $Q_{\text{thr}} = 1$ keV are included. The proportion of electrons above (2%) and below (98%) Q_{thr} are shown with the CDF (cumulative distribution function): $\mathrm{P}(\mathcal{Q} \leq Q)$.

Their absolute velocity, relative to the speed of light, is denoted as $\mathcal{B}$ and the individual components as $\mathcal{B}_\kappa$. Almost all electrons ($\sim$ 98%) belong to this class. Conversely, the remaining ones above Q_{thr} have a broad distribution, which is anisotropic along z (see Fig. 5.11). They are represented by $\mathfrak{B}$ and $\mathfrak{B}_\kappa$.

Low energy electron velocity distribution The $\mathcal{B}$-distribution has in addition to the upper threshold β_{thr} a lower cut at $\beta_{\text{cut}} \approx 6.256 \times 10^{-3}$ related to MC energy cuts ($Q_{\text{cut}} = 10$ eV). This has a strong impact on the $\mathcal{B}_\kappa$-distributions for which a description to quantify the width of the distributions is sought. It follows from the upper left panel of Fig. 5.12 that $\mathcal{B}_\kappa / \mathcal{B} \sim \mathcal{U}_{[-1,1]}$. The present symmetry around zero confirms the aforementioned isotropic flow without a net drift across all $\mathcal{B}_\kappa$-components. The inverse of this observation states that one obtains $\mathcal{B}_\kappa$ by multiplying $\mathcal{B}$ with samples from a uniform distribution. $\mathcal{B}_\kappa$ is thereby

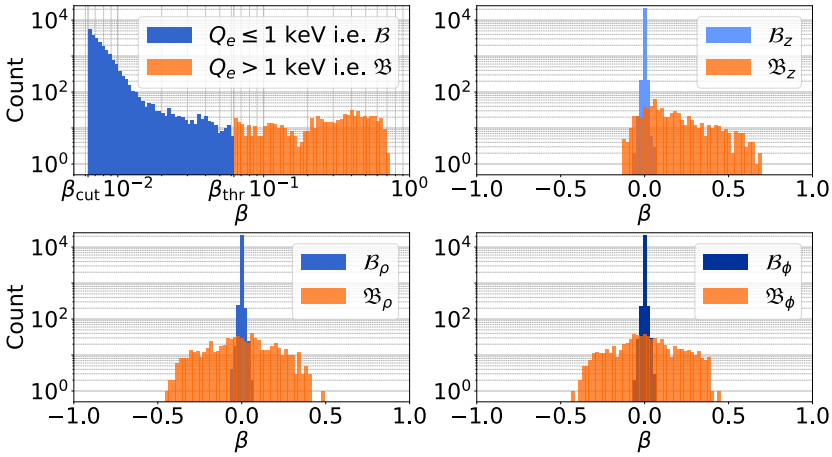

Figure 5.11: Electron velocity distribution in the entrance region ($z_0 = 0.5$ mm and $\Delta z = 1$ mm). They are separated into low energies $\mathcal{B}$ (blue) and high energies $\mathfrak{B}$ (orange). The upper left panel shows the absolute value, while the remaining ones are the components of cylindrical coordinates. Note the logarithmic axes.

the product of two random variables, which is then distributed as [216]

$$\begin{aligned} f_{\mathcal{B}_\kappa}(\beta) &= \int_{-\infty}^{\infty} f_{\mathcal{B}}(\beta') f_{\mathcal{U}}(\beta/\beta')/|\beta'| \mathrm{d}\beta' \\ &= \frac{1}{2}\int_{|\beta|}^{\infty} f_{\mathcal{B}}(\beta')/\beta' \mathrm{d}\beta', \end{aligned} \tag{5.15}$$

where $f_{\mathcal{B}}(\beta < 0) = 0$ (i.e. the absolute value is always positive) has been used. To model $\mathcal{B}$, a simple power law is chosen, that takes β_{cut} into account[9]: $f_{\mathcal{B}}(\beta) \approx \alpha \beta_{cut}^{\alpha}/\beta^{\alpha+1}\theta(\beta - \beta_{cut})$. It is based on the approximate linear drop in the double logarithmic histogram of Fig. 5.11 (upper right panel). Together with Eq. (5.15)

$$f_{\mathcal{B}_\kappa}(\beta) \approx \frac{\alpha}{2(\alpha+1)\beta_{cut}} \begin{cases} 1 & |\beta| \leq \beta_{cut} \\ (\beta_{cut}/|\beta|)^{\alpha+1} & |\beta| > \beta_{cut} \end{cases}. \tag{5.16}$$

The result is flat below β_{cut} and falls off symmetrically beyond β_{cut} with the same power law as $f_{\mathcal{B}}(\beta)$ (see Fig. 5.12). The full width at half maximum (FWHM) of the $\mathcal{B}_\kappa$ distribution is chosen as the desired measure for the width (see Fig. 5.12):

$$\mathrm{FWHM}_{\mathcal{B}_\kappa} = 2^{(\alpha+2)/(\alpha+1)}\beta_{cut}. \tag{5.17}$$

The standard deviation does not appear suitable due to its truncated shape.

High energy electron velocity distribution Among the broader $\mathfrak{B}_\kappa$-distributions, only $\mathfrak{B}_z$ shows a drift in the forward direction (Fig. 5.11), i.e. the high energy electrons tend to move along with the primary protons. This directionality can be attributed to single head-on proton collisions (see Eq. (2.16)), known as hard collisions [87]. The maximum energy

[9] For simplicity, the unphysical non-zero probability beyond one ($v > c_0$) is tolerated, which is nonetheless practically zero for the present parameter range (on average about 1.67×10^{-9}%).

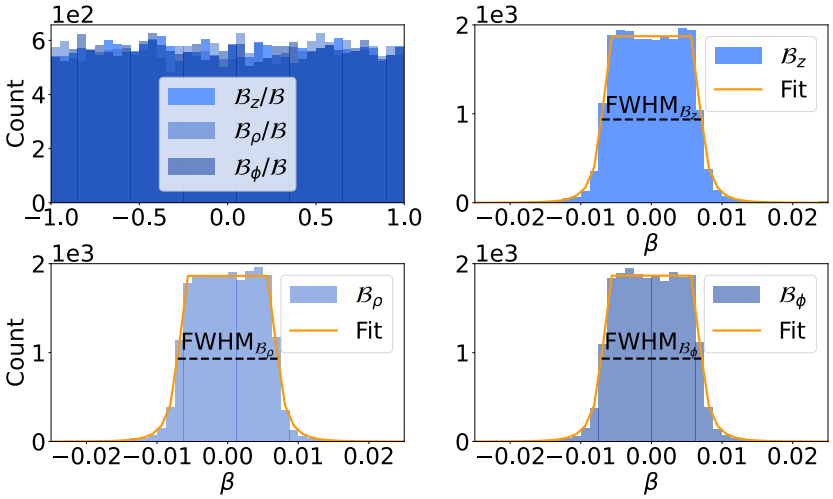

Figure 5.12: Low energy electron velocity distribution in the entrance region ($z_0 = 0.5$ mm and $\Delta z = 1$ mm). The upper left panel shows $\mathcal{B}_\kappa/\mathcal{B} \in [-1, 1]$, while the remaining ones are close-ups of $\mathcal{B}_\kappa$ also shown in Fig. 5.11 (now linear scale). The fit function for all $\mathcal{B}_\kappa$ is given in Eq. (5.15).

transfer W_m has already been stated in Eq. (2.2), from which one can calculate the maximum secondary electron velocity

$$\beta_e^{\max} \approx 2\beta_p\gamma_p^2/(1+2\beta_p^2\gamma_p^2), \tag{5.18}$$

where $\beta_p = v_p/c_0$ is the depth-dependent proton velocity and $\gamma_p^2 = 1/(1-\beta_p^2)$.

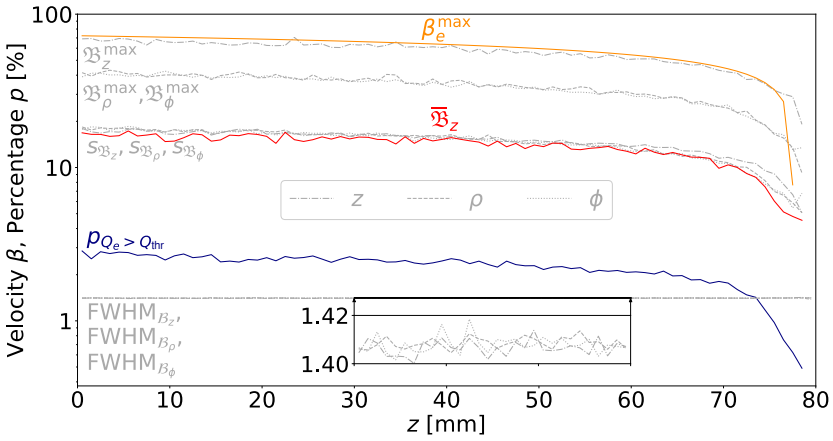

Figure 5.13: Statistical parameters from the laterally integrated electron velocity distributions as a function of the depth. FWHM$_{\mathfrak{B}_\kappa}$ is defined in Eq. (5.17), $p_{Q_e > Q_\mathrm{thr}}$ is the percentage of electrons with energies above Q_thr, $\overline{\mathfrak{B}}_\kappa$, $s_{\mathfrak{B}_\kappa}$ and $\mathfrak{B}_\kappa^{\max}$ are the mean, sample standard deviation and maximum values of the $\mathfrak{B}_\kappa$-distributions (shown in Fig. 5.11) and $\beta_e^{\max}$ is given in Eq. (5.18).

Longitudinal profiles Several statistical parameters were extracted from the depth dependent electron distributions (such as the one shown in Figs. 5.11 and 5.12 from the entrance region) and collected in Fig. 5.13. The data has been integrated laterally since the electron

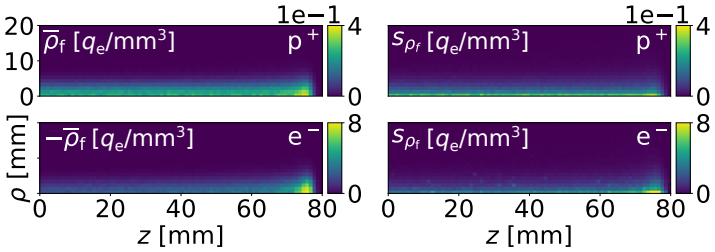

Figure 5.14: Charge density of protons (p^+) and electrons (e^-). The mean (left) and sample standard deviation (right) of the complete DNA_5 data set, voxelized with *increasing volumes* (see Appendix B.3), is shown. The opposite sign of e^- has been compensated.

behavior does not change significantly with the distance from the central beam axis. After all, the primary protons give rise to the secondary electrons, whereas the former do not differ significantly laterally either in terms of energy and direction. In other words, the mostly isotropic electron cloud surrounding the primary protons does not depend on the lateral position. The quantities shown in Fig. 5.13 are described from bottom to top in the following.

$\text{FWHM}_{\mathcal{B}_\kappa} \approx 1.41\%$ (defined in Eq. (5.17)) is almost perfectly constant across z. The percentage of high energy electrons $p_{Q_e > Q_{\text{thr}}}$, starting from almost 3%, decreases along z to about 0.8% at the range in accordance with the decreasing primary proton velocity, that gives rise to less energetic electrons. The 2% estimate from Fig. 5.10 is the average.

The sample standard deviation $s_{\mathfrak{B}_\kappa}$ and the mean longitudinal velocity $\overline{\mathfrak{B}}_z$ follow an almost identical behavior, gradually decreasing from about 17% to 7% at the range. The maximum absolute values of $\mathfrak{B}_\rho$ and $\mathfrak{B}_\phi$ (denoted as $\mathfrak{B}_\rho^{\max}$ and $\mathfrak{B}_\phi^{\max}$) were estimated from the 99.5$^{\text{th}}$ percentile, whereas $\mathfrak{B}_z^{\max}$ is the 99.9$^{\text{th}}$ percentile. These percentiles have been chosen over the overall maximum (100$^{\text{th}}$ percentile), since they follow the same trend and are not interrupted by some individual peaks that are likely related to electrons created in nuclear reactions. Primarily, the percentile of $\mathfrak{B}_z^{\max}$ is used to enhance the comparability to $\beta_e^{\max}$ from Eq. (5.18), which is shown as a function of the depth-dependent average primary proton velocity β_p.

5.2.2 Charge and current density

5.2.2.1 DNA_5 data

Charge and current density of a proton beam ($I = 0.2$ µA) and its secondary electrons are shown in Figs. 5.14 and 5.15. The maximum proton density of approximately 0.37 q_e/mm^3 is shown in the upper left panel of Fig. 5.14. As has been discussed in Sec. 5.2.1.2, there are on average about twelve times more electrons than protons. This ratio varies spatially, increasing to approximately 20 at the range, while it is about 10 in the preceding plateau (comparing $\overline{\rho}_f$ of protons and electrons in Fig. 5.14). Fig. 5.15 shows only the current density components with a non-zero average, from which the magnetic field has been estimated below. Note that J_z and s_{J_z} are longitudinally extended as described in Sec. 5.1.5.

The lateral scattering shortens the projected range, which is indicated by the red dashed line in the lower left panel of Fig. 5.7. Whether this has an impact on the overall range has been investigated with Fig. 5.16.

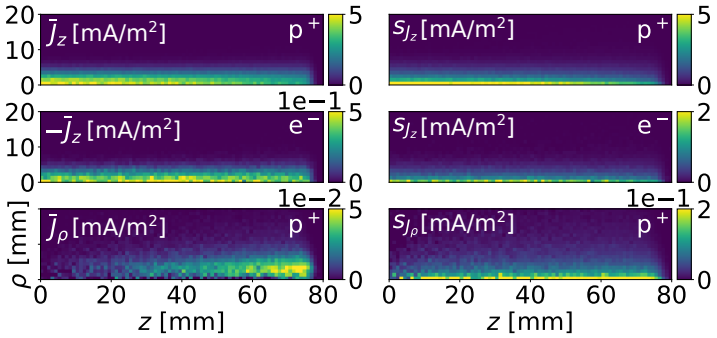

Figure 5.15: Current density of protons and electrons, sorted by magnitude from strongest to weakest. See the caption of Fig. 5.14 for details.

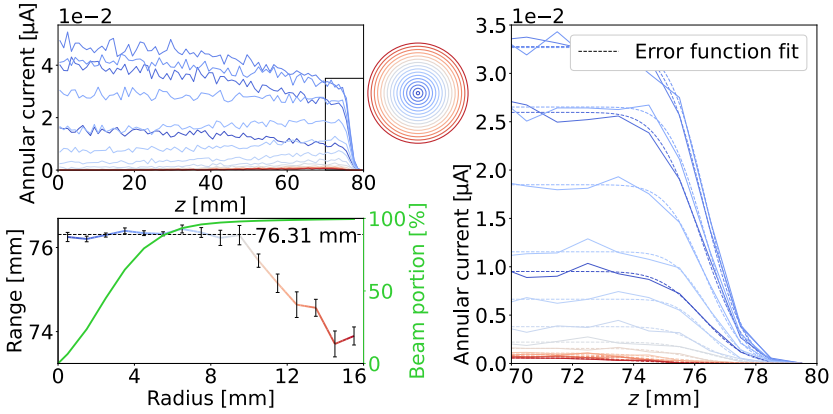

Figure 5.16: Radially separated range estimation. The DNA_5 data has been subdivided into annular rings (color-coded from small (blue) to large (red) radii) and the range from the distal fall-off has been determined with an error-function fit. The complete profiles are shown in the upper left panel, which add up to the 0.2 µA current profile of Fig. 5.6. The lower left panel collects the radius-dependent range values, which are compared to the overall range of 76.31 mm from Fig. 5.6. The radially accumulated beam profile is shown on its right vertical axis, associating the beam portion with the range.

5.2.2.2 QGSP_BIC data

A subset of the average longitudinal and lateral current densities from the QGSP_BIC simulations with different spot sizes is shown in Fig. 5.17. Applying the accumulation laws from Eqs. (5.3) and (5.5) to the data from Fig. 5.17 leads to the results shown in Fig. 5.18. The result is more reasonably presented when transformed to a current. For the accumulated current along z, the current through perpendicular circular disks with an area that corresponds to the innermost cylindrical pixel ($I_z = J_z^{\mathrm{acc}} \pi \Delta\rho^2$) is plotted. The radial current passes through the lateral area of the cylinder that changes from zero to $2\pi\Delta\rho\Delta z$. The average has been chosen, as depicted in Fig. 5.18: $I_\rho = J_\rho^{\mathrm{acc}} \pi \Delta\rho \Delta z$.

5.2.3 Magnetic field

Following the exhaustive analysis of the PSs and current density, the results continue with the estimation of the associated magnetic field. The spatial profile of the total magnetic field B_ϕ is further split into the proton current contributions from the radial ($B_{\phi,\rho}$) and

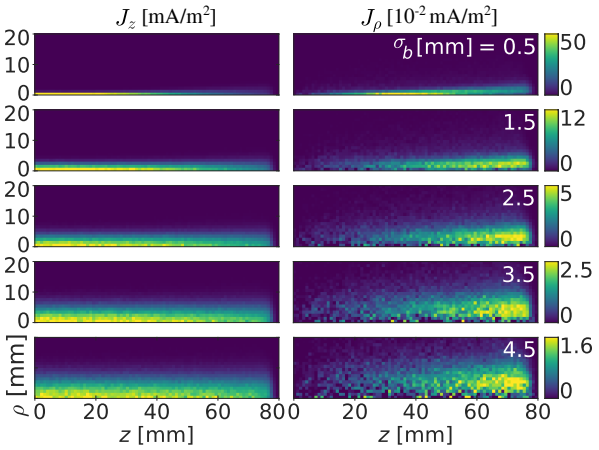

Figure 5.17: Longitudinal and lateral current densities of different spot sizes σ_b. The beam current is 0.2 µA in all cases.

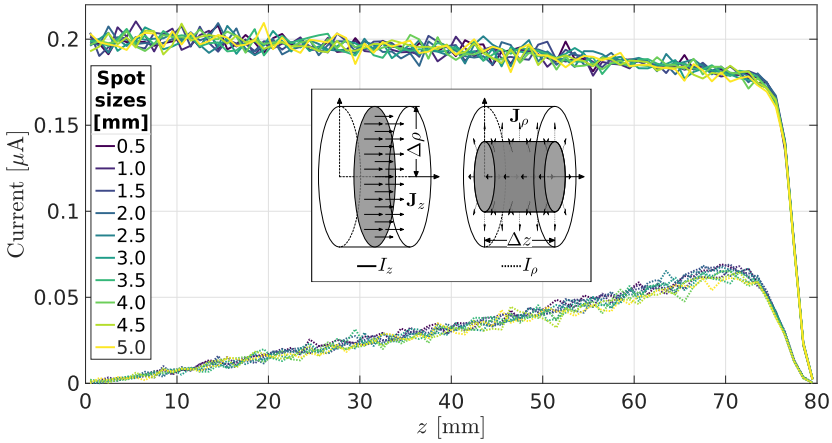

Figure 5.18: Accumulated longitudinal and radial current densities represented as currents through the gray shaded areas. All simulated σ_b are included, as opposed to the subset that is shown in Fig. 5.17.

longitudinal current ($B_{\phi,z}$) through Eq. (3.68) as well as the longitudinal electron current ($\underline{B}_{\phi,z}$). The result is shown in Fig. 5.19. Using Eq. (3.74), the magnetic field uncertainties, that originate from the current density fluctuations, were also estimated. They are represented as absolute *relative standard deviation* RSD $= \sigma/|\mu|$. The total uncertainty follows from the standard error propagation for additive quantities: $\sigma^2_{B_\phi} = \sigma^2_{B_{\phi,z}} + \underline{\sigma}^2_{B_{\phi,z}} + \sigma^2_{B_{\phi,\rho}}$.

The results from Fig. 5.19 are further analyzed in Fig. 5.20 along longitudinal profiles, 5 cm away from the central beam axis. Therein, they are compared to the magnetic field strength $B^{\text{acc}}_{\phi,z}$ and $B^{\text{acc}}_{\phi,\rho}$ from the accumulated proton currents J^{acc}_z and J^{acc}_ρ, which were described in Sec. 5.1.3. All the magnetic fields were calculated from the average of the 300 PSs of the DNA_5 data, which means that there is an uncertainty in the numerical calculation. This is not to be confused with the fluctuation-related RSD estimation. While the latter originates from the natural randomness of the beam current, the former is a computational inaccuracy. Regardless, it is almost identically quantified through Eq. (3.74), where the uncertainty of the average current density follows from the *standard deviation of the mean*: $\sigma_{J_\kappa} \to \sigma_{J_\kappa}/\sqrt{N_{\text{PS}}}$. In an effort to analyze the impact of the nuclear reaction related intensity loss (see Fig. 2.7), the magnetic field $B^{\text{fit}}_{\phi,z}$ from the longitudinal current profile of

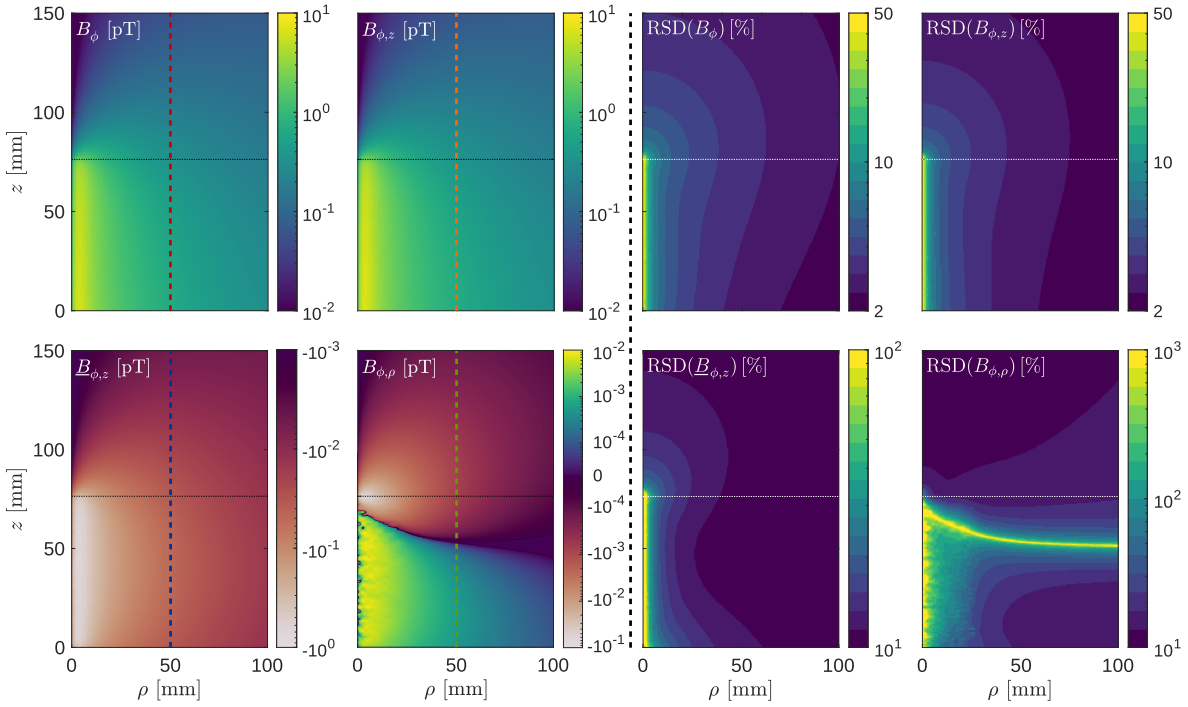

Figure 5.19: Magnetic field strength (left four panels) and its uncertainty represented as RSD (right four panels) of a 0.2 µA beam, calculated from the average current densities (300 PSs). The horizontal dotted lines (black/white) indicate the range at 76.31 mm, as estimated via Fig. 5.6. The vertical dashed lines correspond to the profile plots from Fig. 5.20. Note that $\underline{B}_{\phi,z}$ is flipped due to the electron's opposite charge.

Fig. 5.6, with the corresponding current density J_z^{fit}, is calculated. Barring small differences related to noise, J_z^{fit} is practically identical to J_z^{acc}, hence the agreement between $B_{\phi,z}^{\text{fit}}$ and $B_{\phi,z}^{\text{acc}}$. The fit current can now be further separated into the current that is described by the error function $J_z^{\text{erf}}(\rho_0^J, z_j^J) = g(z_j^J)/(\pi\Delta\rho^2)$ and the remaining current, which is affected by the attenuation: $J_z^{\text{att}}(\rho_0^J, z_j^J) = [f(z_j^J) - g(z_j^J)]/(\pi\Delta\rho^2)$. Consequently, $B_{\phi,z}^{\text{fit}} = B_{\phi,z}^{\text{erf}} + B_{\phi,z}^{\text{att}}$. Finally, the analytical reference from Eq. (4.54) is here denoted as $B_{\phi,z}^{\text{ref}}$, where $z_{\text{r}} = 76.31$ mm has been used. The magnetic field profiles of Fig. 5.20, which carry the information about the range, show an apparent longitudinal shift. An estimate of how much nuclear reactions, scattering and the electron current distort the profile with respect to $B_{\phi,z}^{\text{ref}}$ is sought. For this purpose, one can make use of the fact that the second derivative of $B_{\phi,z}^{\text{ref}}$ with respect to z has a root at the range

$$\frac{\partial^2 B_{\phi,z}^{\text{ref}}}{\partial z^2} = \frac{3\mu I \rho}{4\pi} \frac{z - z_{\text{r}}}{\sqrt{\rho^2 + (z - z_{\text{r}})^2}^5}. \tag{5.19}$$

Consequently, the second derivative of the profiles shown in Fig. 5.20 has been calculated[10] and presented Fig. 5.21 to analyze their zero crossings in the discussion.

[10] Numerically, the second order central difference has been used.

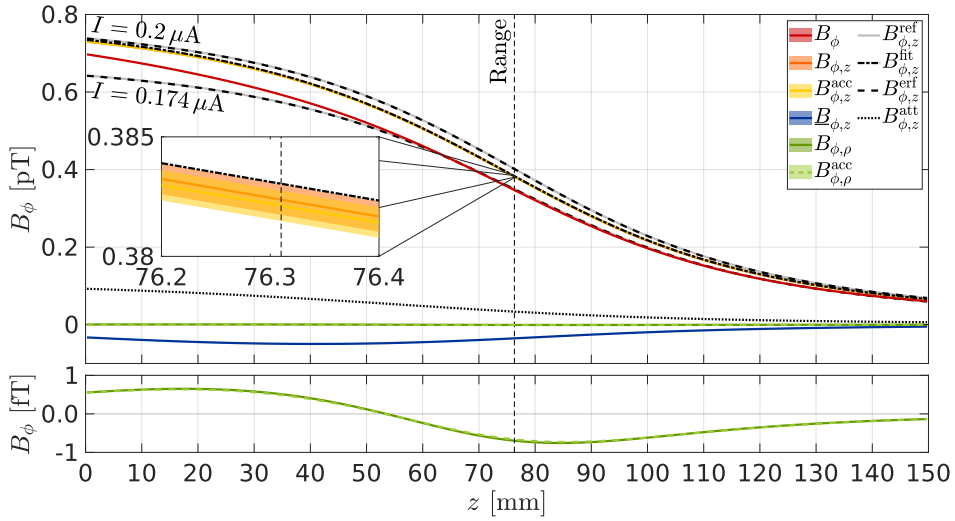

Figure 5.20: Magnetic field profiles along the vertical lines of Fig. 5.19. $B^{\mathrm{acc}}_{\phi,z}$ and $B^{\mathrm{acc}}_{\phi,\rho}$ from the accumulated currents described in Sec. 5.1.3 have been added. The analytical reference $B^{\mathrm{ref}}_{\phi,z}$ from Eq. (4.54) is shown for the initial current of $I = 0.2$ µA and the current $w_{\mathrm{r}} = 0.174$ µA, prior to the range drop (see Fig. 5.6). The separation of the profile from Fig. 5.6 ($B^{\mathrm{fit}}_{\phi,z} = B^{\mathrm{erf}}_{\phi,z} + B^{\mathrm{att}}_{\phi,z}$) has also been added. The colored lines are surrounded by an error estimate, which is small and therefore only visible in the insert. A closeup of $B_{\phi,\rho}$ and $B^{\mathrm{acc}}_{\phi,\rho}$ is shown at the bottom.

5.3 Discussion

5.3.1 Computational approach

Before entering the discussion on the results, presented in the previous section, a few comments regarding the chosen computational approach, as described in Secs. 3.6 and 5.1.2, shall be made. Recall that the FEA has been chosen to estimate the magnetic field, where it has been ensured that the underlying equation allows for non-solenoidal currents (see Sec. 3.6.1). The most prominent alternative might have been an estimation through integral equations, such as the well-known Biot–Savart law. Two points, one of which turned out to be inaccurate, initially discouraged a utilization of this alternative. Firstly, the singular weight in the integral[11] is not easily handled with discretized data. Secondly, derivations of the Biot-Savart law in well established literature [169] assume $\nabla \cdot \mathbf{J}_{\mathrm{f}} = 0$, contrary to the present requirements. As hinted, this assumption is *not* necessary [153], i.e. $\partial \mathbf{J}_{\mathrm{f}} / \partial t = \mathbf{0}$ is sufficient. Regardless, it is easy to take advantage of the cylindrical symmetry in FEA and separate the magnetic field from longitudinal and radial currents. Also, the matrix formulation given in Eq. (3.73) is handy, allowing a straightforward estimation of the uncertainties (Eq. (3.74)). By adjusting $\underline{\mathrm{K}}_\kappa$, a direct estimation of the second derivative, as required in Fig. 5.21, is possible. For future work, it also allows an easier inclusion of inhomogeneities.

5.3.2 Phase space analysis

5.3.2.1 Protons

The spatial proton velocity distributions from Fig. 5.7 compare the magnitude of the averages to their uncertainties, from which one can form expectations regarding the current

[11] Like in Eq. (3.69). Actually, taking the curl of Eq. (3.69) leads to the Biot-Savart law.

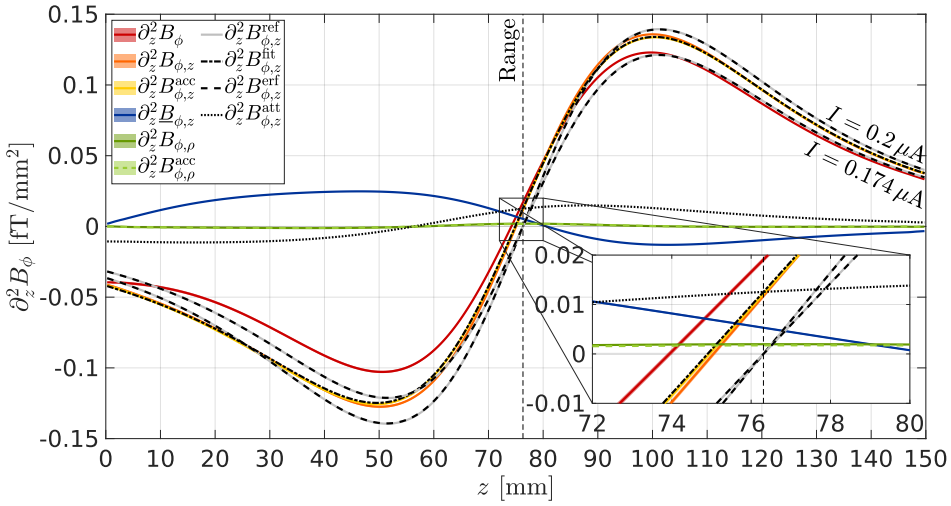

Figure 5.21: Second derivative of the profiles from Fig. 5.20 with respect to z. See its caption for details.

density fluctuations and offer some explanations. The average radial proton velocity $\overline{v}_\rho$ increases downstream, as one expects from lateral scattering accumulating (see Fig. 2.4). Its variability s_{v_ρ}, which is for the most part larger than $\overline{v}_\rho$, remains approximately constant so that v_ρ is generally highly fluctuating. As a consequence of cylindrical symmetry, $\overline{v}_\phi = 0$[12] and $s_{v_\phi} \approx s_{v_\rho}$, since both originate from the same process, i.e. multiple Coulomb scattering. $\overline{v}_z$ obviously dominates and is not exceeded by its uncertainty s_{v_z}, which nonetheless increases towards the range due to the increasing energy straggling (see Fig. 2.3). Generally, one can expect the magnetic field from the radial current to be subject to larger fluctuations than the field that originates from the longitudinal current.

The theoretically expected constancy of the beam current (see Sec. 4.1.2) depends on the charge density increasing at the same rate as the velocity decreases (see Eq. (3.37)). However, the penetration depth straggling (see Fig. 2.3) spreads the proton distribution longitudinally and has therefore the potential to reduce the charge density. Note that the density reduction due to lateral scattering, as for instance visible in Figs. 2.13 and 5.17, does not contribute, since the laterally integrated profiles are considered. Also, the portion that "vanishes" into the radial flow lies in the order of 1% (see Fig. 5.7). So the question is, whether the decreasing current shown in Fig. 5.6 can be partially attributed to energy straggling. In fact, this question motivated the work that led to Fig. 5.8. Keep in mind though, that the leading cause of fluence reduction are nonetheless the nuclear reactions, as shown in Fig. 2.7. Comparing the more accurate $\hat{f}_n^{\mathrm{b}}(z)$, which includes the energy straggling, with the ideal $f_n^{\mathrm{b}}(z) \propto 1/\dot{f}_z(f_z^{-1}(z))$, one can conclude that energy straggling has negligible impact on the fluence prior to the range. Its only impact is the smooth drop at the range, as opposed to an idealized sharp edge. Consequently, the gradually decreasing current (difference between the DNA_5 data and $\hat{I}$ in the lower left panel of Fig. 5.8) can be fully attributed to nuclear reactions, since only the latter has been neglected for $\hat{I}$. Regardless, the nuclear interactions do not eradicate the increasing proton charge density, which more than doubles towards the range. The latter is a crucial characteristic, which ensures an approximately constant current density. More quantitatively, the charge density decreases by about 15% with respect to $\hat{f}_n^{\mathrm{b}}(z)$, which also follows from the ratio between

[12] Deviations are related to low statistics.

the initial current $I = 0.2$ µA and $w_r \approx 0.174$ µA (see Fig. 5.6). Comparable magnitudes of nuclear reaction-related losses can also be found in the literature [257]. In summary, the theoretical expectations from Sec. 4.1.2 have been confirmed on a MC simulation basis. Note how $\hat{f}_n^b(z)$ close to the range briefly exceeds $f_n^b(z)$[13], which is explained by the fact that the longitudinal spread occurs in both directions. This means that the distribution of the idealized sharp peak of $f_n^b(z)$ also contributes prior to the range.

Finally, the energy distribution of the DNA_5 data is well described through the idealized $f_Q^b(Q)$ from Eq. (5.13), which means that the symmetric shuffling (caused by energy straggling) has little impact. Moreover, the energy distribution is insofar interesting, since its overall shape may be initially unexpected. In particular, the increasing charge density together with the decreasing energy downstream suggests that there should be more particles with lower energies. Yet, both the DNA_5 histogram as well as the theoretical description increase towards higher energies. The explanation of this (counter-intuitive) result lies in the concave shape of $Q(z)$. A comparatively low energy loss ΔQ is initially associated with a wide longitudinal interval Δz, which decreases downstream. This means that the majority of the beam line (within the target) is occupied with high energies, leading to the observed distribution. The naive expectation from above (based on the charge density distribution) is nonetheless not incorrect, but overshadowed by the $Q(z)$-effect. The fact that the stopping power flattens and decreases towards very low energies (see Fig. 2.2) together with the rising charge density leads to a reversal of the trend in $f_Q^b(Q)$, i.e. to a minimum close to zero (see the insert of Fig. 5.8).

5.3.2.2 Electrons

The empirical sub-division of the electrons at the threshold energy $Q_{thr} = 1$ keV is well justified through Fig. 5.10. It separates the data into few high-energy electrons with longitudinal drift (relevant) and a myriad of low-energy electrons with isotropic flow (negligible). A separation based on the built-in simulation settings would suggest a Q_{thr} of 100 eV (Eq. (2.16)). However, starting from 100 eV, only a very small forward-scattering trend is observable. Scattering directions at such low energies are almost perpendicular with respect to the primary proton (as mentioned in Sec. 2.1.4), so that very little forward momentum is generated. For future simulations, one could raise the tracking cut energy Q_{cut} to the threshold energy $Q_{thr} = 1$ keV, which accelerates the simulations significantly and lowers the necessary memory. Thereby one could obtain the same results (in terms of current density) by simulating only 2% of the DNA_5 data.

In the introductory statement of the present chapter, it has been argued that the symmetric conductivity current cannot give rise to an additional magnetic field. However, whether the numerous secondary electrons locally increase the conductivity along the beam line and thereby cause an asymmetric charge relaxation current, has not been discussed yet. For the following two reasons, one can argue that the latter is not the case. Firstly, while there are 10^5-10^6 secondary electrons per primary proton (see Sec. 2.1.4 for details), their density, shown in Fig. 5.14, remains low relative to the ionic charge carriers of the target or biological tissues in general, which is in the order of Avogadro's number. The fact that there are only 10^3 moving protons at any given time[14] (see Sec. 5.1.6) does not raise the electron numbers to a relevant level. The second reason are the immensely short lifetimes of the secondary electrons. These are mostly sub-picoseconds (as shown in Fig. 5.9) for electrons

[13] Visible in the upper left panel of Fig. 5.8 upon close inspection or more pronounced for $\hat{I}$, where it should be noted that its velocity $\overline{v}_z(z)$ is based on the DNA_5 data (see Fig. B.4) and not idealized.

[14] For a 100 MeV beam with a beam current of 0.2 µA.

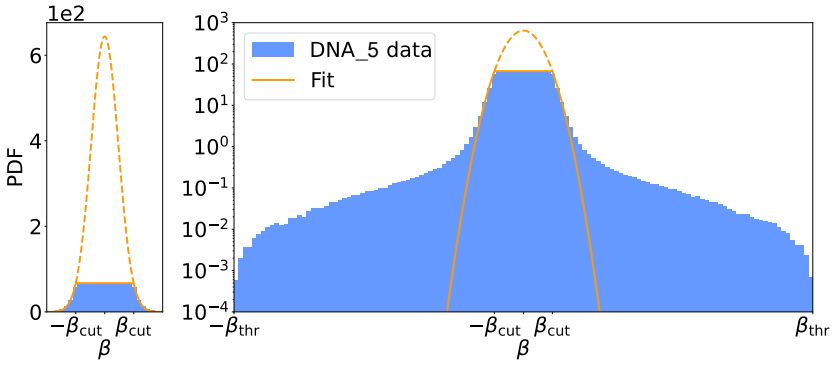

Figure 5.22: Truncated Gaussian fit on the low energy electron velocity distribution. All electrons below $Q_{\text{thr}} = 1$ keV of the complete DNA_5 data set were collected, including all three components. The solid line is Eq. (5.20), whereas the dashed line is continuing the Gaussian part, originally only valid for $|\beta| > \beta_{\text{cut}}$, to the entire domain.

above 10 eV and are captured quickly thereafter. Alternatively, they occupy a *solvated* state within the same timescales, that lies below the conduction band [258]. Compared to the primaries' declaration times (see Fig. 2.11), this means that the protons do not leave behind a trail of electrons, but are rather surrounded by a small electron cloud, that "moves" with them. In other words, the majority of secondary electrons is already absorbed, while the primary proton is still underway. Simultaneously, the charge relaxation times are above the nanosecond scale (see Table 4.2) so that the cohort of primary protons downstream cannot exert a drift on the short-lived electrons.

For the empirical description of the symmetric low-energy electron velocity distributions, it follows straight from Eq. (5.15) that any $\mathcal{B}$-distribution with a lower energy cut will display a plateau within $|\beta| \leq \beta_{\text{cut}}$ for its $\mathcal{B}_\kappa$-distributions, provided $\mathcal{B}_\kappa/\mathcal{B} \sim \mathcal{U}_{[-1,1]}$. This explains their perhaps unexpected shape as a mere consequence of the MC cuts. Based on the observational power law, Eq. (5.16) provides an apt description for the majority of the $\mathcal{B}_\kappa$-distributions, yet fails to capture the tails. It succeeds nonetheless in its primary purpose, a quantification of the width via FWHM. With the sharp drop of the power law (on average $\alpha_\kappa \approx 4.89(2)$), $f_{\mathcal{B}_\kappa(\beta)}$ is hardly broader than the cut velocity, such that $\text{FWHM}_{\mathcal{B}_\kappa} \approx 2\beta_{\text{cut}}$. Consequently, a somewhat higher Q_{cut} would have eradicated the vast majority of electrons. The latter also follows from the CDF shown in Fig. 5.10.

The small shift of the $\mathfrak{B}_z$-distribution in Fig. 5.11 towards positive velocities gives rise to the entire electron current. Note that despite the fact that the primaries exhibit a radial drift (see Fig. 5.7), it does not appear to be transmitted to the secondary electrons, whose $\mathfrak{B}_\rho$-distribution is symmetric. The low magnitude paired with strong variability of the proton's radial velocity suppresses a similar trend among the electrons.

A first conclusion of Fig. 5.13 is that the homogeneous electron cloud remains constant in terms of velocity distribution along the entire beam line (specifically the $\text{FWHM}_{\mathcal{B}_\kappa}$ are constant). This allows for an alternative analysis regarding the low-energy electron velocity distribution, collecting the complete electron data set across all z. Instead of the power-law, it is perhaps more natural to approximate $\mathcal{B}_\kappa$ with a normal distribution: $\mathcal{B}_\kappa \sim \mathcal{N}(\mu = 0, \sigma = \sigma_{\mathcal{B}})$. With $\mathcal{B} = \sqrt{\mathcal{B}_\rho^2 + \mathcal{B}_\phi^2 + \mathcal{B}_z^2}$, one may show through dedicated variable transforms (general law given in Eq. (4.9)) that the absolute value $\mathcal{B}$ follows a Maxwell-Boltzmann distribution[15]: $f_{\mathcal{B}}(\beta) = 2\beta^2/\left(\sqrt{2\pi}\sigma_{\mathcal{B}}^3\right) \exp\left[-\beta^2/(2\sigma_{\mathcal{B}}^2)\right]\theta(\beta)$.

[15]For consistency, one may recover the normal $\mathcal{B}_\kappa$ distributions through Eq. (5.15)

Upon application of the cut velocity, one obtains $\tilde{f}_{\mathcal{B}}(\beta) = f_{\mathcal{B}}(\beta)\theta(\beta - \beta_{\text{cut}})/N_{\text{cut}}$, where $N_{\text{cut}} = 1 - \{\text{erf}[\beta_{\text{cut}}/(\sqrt{2}\sigma_{\mathcal{B}})] - 2\beta_{\text{cut}}/(\sqrt{2\pi}\sigma_{\mathcal{B}})\exp\left[-\beta_{\text{cut}}^2/(2\sigma_{\mathcal{B}}^2)\right]\}$ readjusts the normalization. Combining $\tilde{f}_{\mathcal{B}}(\beta)$ with Eq. (5.15) yields the truncated Gaussian for $\mathcal{B}_\kappa$:

$$f_{\mathcal{B}_\kappa}(\beta) = \frac{1}{N_{\text{cut}}} \begin{cases} \dfrac{1}{\sqrt{2\pi}\sigma_{\mathcal{B}}} \exp\left(-\dfrac{\beta_{\text{cut}}^2}{2\sigma_{\mathcal{B}}^2}\right) & |\beta| \leq \beta_{\text{cut}} \\ \dfrac{1}{\sqrt{2\pi}\sigma_{\mathcal{B}}} \exp\left(-\dfrac{\beta^2}{2\sigma_{\mathcal{B}}^2}\right) & |\beta| > \beta_{\text{cut}} \end{cases} . \tag{5.20}$$

The fit with Eq. (5.20) is shown in Fig. 5.22. While Eq. (5.20) provides a good description in the linear scale, it fails to describe the tails shown in the logarithmic scale. Regardless, the Gaussian model is worthwhile since it enables an extrapolation of the contributions below $Q_{\text{cut}} = 10$ eV. In particular, it predicts $1/N_{\text{cut}} \approx 4.7(2)$ times more electrons[16]. Consequently, the fraction of high energy electrons would shrink from 2% (see Fig. 5.10) to below 0.5%. However, the latter is only briefly discussed here, being a somewhat crude extrapolation. What is safe to say, is that the 2% estimate is too large, or only valid when mentioning the 10 eV cut.

The magnitude of the longitudinal electron drift $\overline{\mathfrak{B}}_z$ (red line of Fig. 5.13) is almost identical to its uncertainty $s_{\mathfrak{B}_z}$ or for that matter identical to the uncertainties of all components $s_{\mathfrak{B}_\kappa}$. This has already been observed in Fig. 5.11. Consequently, one can expect large current density and magnetic field fluctuations from the electrons. Wrapping up the PS analysis, the upper threshold of the $\mathfrak{B}_z$-distributions $\mathfrak{B}_z^{\max}$ is well described by Eq. (5.18) (orange line of Fig. 5.13). It supports the previous statement, i.e. that the relevant current is caused by hard or head-on proton-electron collisions.

5.3.3 Charge and current density

That the proton charge density increases downstream (as expected from Fig. 5.8) is also present in Fig. 5.14. While the *increasing volume* voxelization (see Appendix B.3) somewhat distorts the density profile[17], the uncertainty s_{ρ_f} behaves approximately alike. This indicates, that the Poisson distribution, which made a valid description in the entrance region (see Sec. 5.1.5 and Fig. B.3), also applies further downstream, increasing with the square root of the proton counts. s_{ρ_f} is in terms of magnitude comparable to its mean $\overline{\rho}_f$, which is caused by the low proton counts (at most 0.37 protons per mm^3). The relatively large count of secondary electrons (recall the factor of twelve with respect to the protons, as discussed in Sec. 5.2.1.2) is of course visible in the charge density. However, the electrons undergo uncertainties of comparable size, from which one can follow that the Poisson statistics does not apply to them. The explanation is related to their microscopic behavior, i.e. that they do not scatter far away from the primary protons. If a proton occupies a voxel, then so do many electrons. Likewise, the absence of protons leads to an absence of electrons, or more compactly: *all-or-nothing*. The close correlation lets the electrons fluctuate like the protons, just in larger quantities. The instantaneous electrons density remains comparatively low, when compared to the target electrons, so that together with their short lifetimes (see Fig. 5.9), high velocities (10 eV still corresponds to 0.6% of c_0) and their random trajectories, one can neglect the mutual interactions. In hindsight, this justifies the use of MC for the present work and generally for low-scale track structure codes such as Geant4-DNA.

[16] Uncertainty estimate: $\sigma_{1/N_{\text{cut}}} \approx |\,\partial(1/N_{\text{cut}})/\partial\sigma_{\mathcal{B}}\,|_{\sigma_{\sigma_{\mathcal{B}}}}$, where $\sigma_{\sigma_{\mathcal{B}}}$ is the error estimate of the fit.

[17] Practically the same image of $\overline{\rho}_f$ and s_{ρ_f} with *equal volume* voxelization is given in the second row of Fig. 5.5.

The slightly decreasing longitudinal proton current strength $\bar{J}_z$ in Fig. 5.15 is related to lateral scattering and nuclear reaction losses. The impact of the increasing s_{ρ_f} on its uncertainty is suppressed, however, due to the decreasing velocity (see Eq. (3.37)). Also, the rising v_z-fluctuations (see Fig. 5.7), which are related to the increasing energy straggling, have negligible influence on s_{J_z} (for the same reason as in Eq. (5.9)). An observation, for which the PS analysis has been conducted to provide an explanation, is that there are on average about 12 times more electrons than protons[18], yet the electron current is in terms of strength one order of magnitude weaker than the proton current. One may imagine two extreme cases: either the spatial distribution of the electron velocity is like the protons' (pointing primarily in the forward direction, as shown in Fig. 5.7), just two orders of magnitude slower, or they scatter randomly so that their velocity cancels on average. The reality is somewhere in between, but leans more heavily towards the latter. With most of them flowing isotropically (see Fig. 5.12), the fact that only about 2% of electrons contribute[19] explains the majority of the two orders of magnitude difference. In addition, they ($\overline{\mathfrak{B}}_z$ from Fig. 5.13) are on average somewhat slower than the protons. The velocity of the latter has not been added to Fig. 5.13, but is comparable to $\mathfrak{B}_\rho^{\max}$ or $\mathfrak{B}_\phi^{\max}$. In summary, few swift electrons comprise the majority of the electron current, as opposed to many slow ones. Yet another order of magnitude weaker is the radial proton current (see Fig. 5.15), having a relative uncertainty below one, as expected from Fig. 5.7. Its contribution to the magnetic field will be negligible.

5.3.4 Spot size impact

For small beam spot sizes (0.5-2.5 mm), an apparent drop in the longitudinal current density J_z is visible in Fig. 5.17. The latter is caused by lateral scattering, which only affects the field close to the central beam axis. Further out, when J_z can be replaced by the accumulated J_z^{acc} (see Fig. 5.18), the current densities (or I_z for that matter) from different spot sizes are equal, implying no differences in terms of magnetic field (as can be expected from Eq. (5.2)). Scattering does not cause a significant flow outwards, but primarily "parallelizes" the beam current away from a more condensed flow[20]. This effect is less pronounced for larger beam spot sizes, due to an approximate equilibrium between scattering towards and away from the central beam axis.

Still considering Fig. 5.17, the radial current J_ρ increases downstream, except for the smallest beam spot size ($\sigma_b = 0.5$ mm), which is dominated by the aforementioned spreading (current running in parallel). In terms of strength J_z and J_ρ differ by two orders of magnitude, yet, when radially accumulated, the associated I_z and I_ρ in Fig. 5.18 appear quite comparable. To make reason of this, recall that $B_{\phi,z} \propto J_z$ (see Eq. (5.2)), but also $B_{\phi,\rho} \propto \partial J_\rho / \partial z$ (see Eq. (5.4)), i.e. it depends on how much J_ρ changes longitudinally. Consequently, it is not sensible to compare I_z and I_ρ with respect to their field strengths. Furthermore, it is not necessarily expected that also the radial current, when accumulated with a quadratic weight as in Eq. (5.5), is independent of the beam spot size. Nonetheless, one can explain this result on the basis of the Fermi-Eyges scattering theory, described in Sec. 2.1.3. In particular, through Bayes' theorem, one gets the ρ-dependent radial scattering angle distribution from Eq. (2.13): $P(z, \theta_\rho|\rho) = P(z, \rho, \theta_\rho)/P(z, \rho)$, where $P(z, \rho) = \int P(z, \rho, \theta_\rho) \mathrm{d}\theta_\rho$. It follows a normal distribution with the average angle linearly increasing with ρ: $\langle \theta_\rho(z) \rangle = A_1(z)/A_2(z)\rho$. The average radial velocity scales with the av-

[18] Probably even more, considering Fig. 5.22.

[19] Thereby, the charge density is effectively lower.

[20] Especially visible for $\sigma_b = 0.5$ mm and $z > 40$ mm.

erage scattering angle and $P(z,\rho)$ is proportional to the charge density so that according to Eq. (3.37), $J_\rho \propto P(z,\rho)\left\langle\theta_\rho(z)\right\rangle$. Consequently, the accumulated current, defined in Eq. (5.5), is

$$\mathfrak{J}_\rho \propto \int_0^\infty \rho^2 P(z,\rho)\left\langle\theta_\rho(z)\right\rangle \mathrm{d}\rho = 2A_1. \tag{5.21}$$

The result is independent of A_2, being the only parameter that depends on the beam spot size. The quadratic accumulation of the radial current is thereby spot size independent, just as the accumulation of the longitudinal current. In summary, both J_z and J_ρ are independent of the spot size in the far field. With the theoretical explanation in mind, one can state that this holds also for larger spot sizes, beyond the 5 mm simulated.

5.3.5 Two-dimensional magnetic field profiles

The individual currents that together give rise to the total azimuthal magnetic field B_ϕ are the longitudinal proton current (dominant), longitudinal electron current (small impact) and the radial proton current (negligible). The latter has its strongest contribution at the range (since $B_{\phi,\rho} \propto \partial J_\rho/\partial z$), where the current drops to zero and also changes its sign, since the slope of the current does as well. As it was neither necessary to longitudinally extend the radial proton current nor the longitudinal electron current (see Sec. 5.1.5), both $B_{\phi,\rho}$ and $\underline{B}_{\phi,z}$ approach zero towards $z = 0$, as opposed to $B_{\phi,z}$.

To clarify the interpretation of the RSD, it quantifies the variability among different *static* PSs. The dynamic nature is not taken into consideration, in particular the tissue dependent field propagation, which was investigated in the previous chapter. Nonetheless, the RSD shown in Fig. 5.19 confirms the general expectation, i.e. that the large current density fluctuations, that were shown in Fig. 5.15, lead to high RSD. When moving further away from the central beam axis, more current density elements contribute, which averages out their fluctuations. The peak of $\mathrm{RSD}(B_{\phi,\rho})$ is related to the zero crossing of $B_{\phi,\rho}$ around $z = 50$ mm. $\mathrm{RSD}(B_\phi)$ is dominated by s_{J_z}, just as B_ϕ is dominated by J_z. Fig. 5.19 only shows the azimuthal component of the magnetic field, whereas the v_ϕ-fluctuations shown in Fig. 5.7 will also lead to random radial and longitudinal magnetic fields. They likely have a comparable magnitude as $\mathrm{RSD}(B_{\phi,\rho})$, but cannot be estimated under the symmetry assumptions made in Sec. 3.6.2.

The fluctuations are expected to be in the nanosecond time scale (i.e. GHz frequencies), due to the rapid proton velocities (see Fig. 5.7). How they would affect a measurement over the duration τ by means of optical magnetometry (OM) shall be analyzed in the following. For this purpose, the basic principle of OM will be summarized briefly. An external magnetic field B (to be measured) rotates the spin of a perpendicularly polarized ensemble of alkali electrons by the angle $\phi_B = \gamma_\mathrm{e} B\tau$, where $\gamma_\mathrm{e} \approx -1.76 \times 10^{11}$ rad/T^{-1}s^{-1} is the gyromagnetic ratio of electrons. The precession creates a spin polarization $P \propto \phi_B$ along the third axis, which in turn rotates the polarization plane of a linearly polarized probe beam moving along this axis by the angle $\phi_P \propto P$ (Farady effect) [259]. The measured magnetic field B_m then scales with the measured polarization angle ϕ_P so that their relative uncertainties behave as $\sigma_{B,m}/B_m = \sigma_{\phi,P}/\phi_P = \sigma_{\phi,B}/\phi_B$, based on the error propagation between linear relationships. How the field fluctuations affect the ϕ_B can be estimated through the more general relationship between ϕ_B and B_m:

$$\phi_B = \gamma_\mathrm{e}\int_0^\tau B(t)\mathrm{d}t \approx \gamma_\mathrm{e}\sum_{i=0}^{\tau/\Delta t} B(i\Delta t)\Delta t. \tag{5.22}$$

The approximation of the integral by the sum is only valid, if Δt is sufficiently small to capture the B fluctuations, i.e. below the nanosecond scale. The uncertainty of the sum over the random $B(i\Delta t)$ is analogous to the *standard deviation of the mean* so that $\sigma_{\phi,B} = \gamma_e\sqrt{\tau/\Delta t}\sigma_B\Delta t$. Relative to ϕ_B one obtains

$$\frac{\sigma_{\phi,B}}{\phi_B} = \sqrt{\frac{\Delta t}{\tau}}\frac{\sigma_B}{B} = \sqrt{\frac{\Delta t}{\tau}}\mathrm{RSD}(B). \tag{5.23}$$

Eventually, $\mathrm{RSD}(B_m) = \sqrt{\Delta t/\tau}\,\mathrm{RSD}(B)$ so if the measurement time is comparable to the time scale of the fluctuations, then the RSD of B_m is equal to the RSD of B. While this is intuitively sensible, Eq. (5.23) is only an additional uncertainty. The study of noise in optical magnetometry is significantly more complex [260]. Especially measurement times in the order of Δt are unreasonable and rather a quantitative analysis. As expected though, the fluctuations average out for longer measurement times, which is expressed by the factor $\sqrt{\Delta t/\tau} \ll 1$ and thereby do not disturb a measurement.

5.3.6 One-dimensional magnetic field profiles

First and foremost, Fig. 5.20 confirms the accumulation rules derived in Sec. 5.1.3, judged by the excellent agreement between $B_{\phi,\kappa}$ and $B^{\mathrm{acc}}_{\phi,\kappa}$. Same goes for the analytical reference $B^{\mathrm{ref}}_{\phi,z}$ with the initial and final beam current of 0.2 and 0.174 µA, being almost indistinguishable from $B^{\mathrm{erf}}_{\phi,z}$. The latter are calculated from smoother profiles, where range straggling is taken into account, as opposed to $B^{\mathrm{ref}}_{\phi,z}$, based on an idealized sharp step. Consequently, range straggling does not affect the profile. With the two references belonging to the initial and final current, $B^{\mathrm{ref}}_{\phi,z}$ provide an envelope for the more accurate $B_{\phi,z}$, which includes nuclear reaction losses and thus transitions continuously from 0.2 to 0.174 µA (see Fig. 5.6). However, $B_{\phi,z}$ appears shifted with respect to the ideal 0.2 µA profile. A natural explanation might be that the projected range from the scattered and thus curved proton paths are shorter. This phenomenon has been indicated by the red dashed line in Fig. 5.7. This hypothesis has been inspected with Fig. 5.16. While the current profile is indeed shifted towards larger radii, 97.6% of the pencil beam has a range close to the average of 76.31 mm (within the margin of error). The scattering does not provide an explanation for the shift. The portion of the current that is associated with the attenuation has been separated for this reason, so that its magnetic field $B^{\mathrm{att}}_{\phi,z}$ can be further analyzed in Fig. 5.21.

The root of the second derivative of the magnetic field profiles has been introduced as an assessment tool to determine longitudinal shifts, since it is less susceptible to differences in magnitude. For instance in Fig. 5.20, $B^{\mathrm{ref}}_{\phi,z}(I = 0.174\ \mu\mathrm{A})$ appears horizontally shifted back with respect to $B^{\mathrm{ref}}_{\phi,z}(I = 0.2\ \mu\mathrm{A})$, yet in Fig. 5.21, both $\partial_z^2 B^{\mathrm{ref}}_{\phi,z}$ pass through zero precisely at $z_\mathrm{r} = 76.31$ mm. And indeed, with $\partial_z^2 B^{\mathrm{att}}_{\phi,z} > 0$ at the range z_r, $\partial_z^2 B_{\phi,z}$, $\partial_z^2 B^{\mathrm{acc}}_{\phi,z}$ and $\partial_z^2 B^{\mathrm{fit}}_{\phi,z}$ are all equally shifted back by about 1.3 mm. Electron current together with the radial current further enlarge the distance of the root to z_r for $B_{\phi,z}$ to roughly 2.4 mm. After analyzing the profile beyond the $\rho = 50$ mm, shown in Figs. 5.20 and 5.21, it has been found that this shift changes approximately linearly with the radius. The linear regression, including parameters, is shown in Fig. 5.23. In summary, the shift originates from the attenuation of the nuclear reactions, the electron current and the radial proton current, ordered from most to least contributing.

A more empirical observation is that the electron field $\underline{B}_{\phi,z}$ approximately cancels the attenuation-related field $B^{\mathrm{att}}_{\phi,z}$ so that the total B_ϕ is well approximated by the analytical reference with the lower current $B^{\mathrm{ref}}_{\phi,z}(I = 0.174\ \mu\mathrm{A})$. A final comment, also regarding the

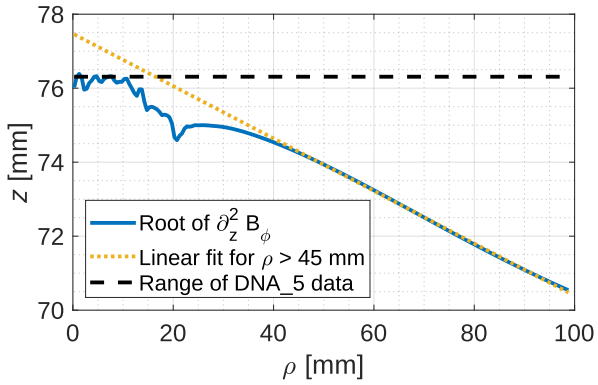

Figure 5.23: Linear regression for the quantification of the longitudinal profiles shift with respect to the range. The fit is described by z [mm] $= p_0 + p_1\rho$ [mm], where $p_0 = 77.47(1)$ mm and $p_1 = -0.0709(1)$.

magnitude, is that both $\underline{B}_{\phi,z}$ and $B_{\phi,\rho}$ vanish towards $z = 0$ and beyond, since their current only exists in the target.

5.3.7 Considerations towards an experimental detection

Having presented an exhaustive analysis of the magnetic field that originates from a proton pencil beam in water, one can now roughly evaluate its potential clinical applicability for range verification purposes. The physical principle for such an approach is that the longitudinal profile of the magnetic field carries information about the range, which may be inferred through an external measurement. For instance, one could deduce the range by optimizing the agreement between the measured and expected profile.

This may be feasible in terms of magnitude. In particular, assuming a sensitivity of 3.6 fT/$\sqrt{\text{Hz}}$ [261] and a pulse duration of 10 µs, one may detect field strengths of 1 pT. It follows from Eq. (2.22) that the dose of a single pulse with 37 mGy is comparatively low taking the beam parameters of the DNA_5 data (see Sec. 5.1.4). In particular, a relatively small beam spot size (2.5 mm) has been considered, whereas 7.5 mm would be more clinically relevant. Since larger spot sizes lower the dose ($\dot{D} \propto \sigma_b^{-2}$ from Eq. (2.22)), one may use a 20 times larger beam current[21], when allowing for a dose of 0.1 Gy. Accordingly, the field strength rises from 0.5 pT to 10 pT, i.e. one order of magnitude above the sensitivity limits. Longer beam pulses or averaging over multiple ones [80] would further enhance the detectability. In fact, with such beam currents, one enters the FLASH dose regime (see Sec. 2.2), where a magnetic field-based range verification may become interesting, as the field strength scales with the beam current.

As the signal strength decreases with the distance from the source (see Fig. 5.19), it is necessary to place detectors as close as possible to the proton beam. Furthermore, the longitudinal beam profile flattens with increasing ρ (see Eq. (4.54)) and thus diminishes its sensitivity with respect to the range, which provides further motivation to minimize the distance. How close sensitive magnetometry devices can be placed to the human body is also of interest in magnetoencephalography (MEG) [237], where one measures magnetic fields from brain currents. SQUID detectors are as close as 2 cm away from the scalp [262], whereas optical magnetometry devices allow a separation of only 5 mm [263, 264]. For a measurement of the beam profile, such as the one shown in Fig. 5.20, one would require an

[21] This is within the capabilities of S2C2, as discussed in Sec. 2.3.

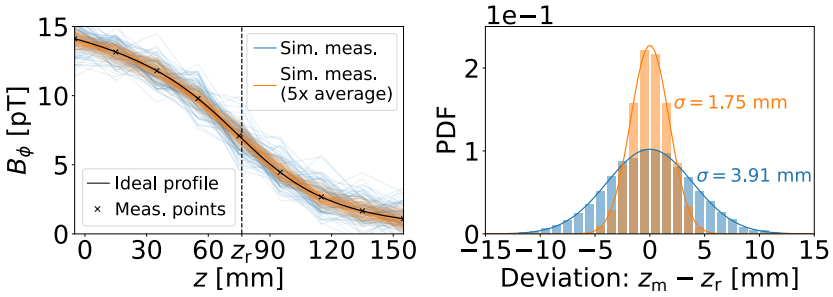

Figure 5.24: Theoretical accuracy of a range measurement. The simulated measurements are on the left, whereas the difference between measured (z_m) and actual range (z_r) is on the right. The latter is fitted with a normal distribution.

array of detectors. A spacing of about 20-30 mm is used in MEG [237], which is probably also sufficient for the present application, considering the rather smooth B-field profile. Having reduced the dimensionality to two and eventually one dimension, one may overlook the fact that multiple detectors could be placed for a single depth by arranging them on arcs. The field strengths are nonetheless low, so that shielding is necessary (common practice in MEG). The fringe fields in the treatment room are below mT, where the closest quadrupole magnet is 2.99 m away from the isocenter [265], which should be even lower with the setup of Paul et al. [266] and a separation of 6 m. Finally, the accuracy of a range estimation has been assessed by simulating measurements with the parameters discussed in this and the previous paragraph (see Fig. 5.24). The range accuracy is 1.75 mm with an average of 5 measurements.

What is of interest in MEG, is noise for the application under consideration. In fact, bioelectric fields have the potential to completely mask the sought field. This could be overcome by realizing that the electromagnetic fields from the human body are generally low frequency, specifically up to 100 Hz [237]. One may separate the signal of the proton beam by oscillating the beam current above the biological threshold or by directly exploiting the RF structure from the accelerators (see Sec. 2.3). As magnetometry can be tailored towards oscillating fields [267], one may detect the beam in the presence of noise by searching for the known reference frequency. Oscillating fields behave decidedly different in the presence of boundaries, which is further investigated in the following chapter.

6 IMPACT OF TISSUE BOUNDARIES

FOR OSCILLATING OR MODULATED BEAMS

Motivated by the discussion of the previous chapter, a beam whose intensity is periodically modulated shall be analyzed. The field that originates from such a source oscillates as well, so that the interaction with the boundary complicates significantly. In particular, one needs to take the reflection and transmission at the boundary into account, which depends on the angle of incidence. Also, the absorption within the target and evanescent waves contribute. For simplicity, the simple geometry from Fig. 4.1 is kept, which allows a sensible interpretation and analysis based only on the Fourier spectrum of the field. By analyzing modulated fields, the RF structure of the accelerators (Fig. 2.15) is taken more seriously and it will be able to gauge its impact.

Having stressed the importance of properly including the interfaces, recall that the interface conditions from Sec. 3.3 are not applicable, as has been discussed in Sec. 4.1.8. In Sec. 4.1.5, it has been shown that the presented derivation and solution can also be reinterpreted as a Green's function approach (see Eqs. (4.36) and (4.37)). This insight is taken as a basis to develop a Green's function that solves the Helmholtz equation in a cylindrical coordinate system with a radial discontinuity. By this approach, one operates in the familiar theory that has been established in Chapter 4, which enables comparisons and consistency checks. As will be presented in Sec. 6.1.17, the amplitude of the oscillating field is directly proportional to the absolute value of the Fourier transformed point-particle field. Thereby, estimating the point-particle field in the frequency domain suffices, which additionally spares the inverse Fourier transform. Conversely, the dedicated Green's functions cannot be represented in a closed form. An integration/summation cannot be solved analytically and needs to be evaluated numerically. In general, the presented analytical approach is limited to the simple cylindrical tissue boundaries. Caps at the ends of the cylinder, for instance, cannot be included already. With this approach, a fundamental analysis shall be presented in order to understand the processes involved. Not only the magnetic but the complete electromagnetic field will be presented, for which one needs to consider the associated scalar and vector potential equations, as presented in the following section. Finally, since an inhomogeneous target is considered, where the intermediate results are occasionally verified by taking the homogeneous limit, it needs to be clarified that (in)homogeneous is reserved to describe the geometry. The same phrase also carries a meaning in the study of differential equations, indicating whether a source term is included. In that case, "source-free" will be used.

With the present chapter, the main body of this thesis is concluded with *preliminary* work, which means that the following is primarily a presentation of the methods that were developed. Nonetheless, a few results have been generated, which were accepted for the IEEE NSS MIC RTSD 2022 conference [268].

6.1 Methods

6.1.1 Electromagnetic potential wave equations

In the following, the calculations are carried out in the Fourier time domain (see Eqs. (A.3a) and (A.3b)), while the spatial coordinates are *not* transformed to **k**-domain. A spatially dependent permittivity $\tilde{\varepsilon}(\omega) \rightarrow \tilde{\varepsilon}(\mathbf{r},\omega)$ is considered, whereas the permeability remains approximately constant and independent of the frequency: $\mu(\mathbf{r},\omega) = \mu$. Therefore, the constitutive relations read

$$\widetilde{\mathbf{D}}(\mathbf{r},\omega) = \tilde{\varepsilon}(\mathbf{r},\omega)\widetilde{\mathbf{E}}(\mathbf{r},\omega), \tag{6.1a}$$

$$\widetilde{\mathbf{H}}(\mathbf{r},\omega) = 1/\mu\widetilde{\mathbf{B}}(\mathbf{r},\omega). \tag{6.1b}$$

In analogy to the homogeneous approach, a solution for the scalar potential φ and vector potential $\mathbf{A}$ is sought. In the Fourier domain, they are defined through Eqs. (3.11) and (3.12). The gauge freedom is fixed to simplify the calculations. In the homogeneous case, the Lorenz gauge (Eq. (3.13)) decouples the scalar and vector equations (Eqs. (3.14) and (3.15)). The same gauge is used for the present problem, which now includes the spatially dependent permittivity. Under Eqs. (3.11), (3.12), (6.1a) and (6.1b), Ampère's circuital law (Eq. (3.4d)) becomes

$$\nabla^2\widetilde{\mathbf{A}} - (\nabla\tilde{\varepsilon})/\tilde{\varepsilon}(\nabla\cdot\widetilde{\mathbf{A}}) + \omega^2\mu\tilde{\varepsilon}\widetilde{\mathbf{A}} = -\mu\tilde{\mathbf{J}}_\mathrm{f}. \tag{6.2}$$

The explicit algebraic manipulations necessary to obtain Eq. (6.2) are given in the appendix in Eq. (A.78). Notably and favorably, the equation for the vector potential $\widetilde{\mathbf{A}}$ decouples from the scalar potential $\widetilde{\varphi}$ under the Lorenz gauge from Eq. (3.13), even in the presence of tissue inhomogeneities ($\nabla\tilde{\varepsilon}$). Yet the equations for the individual field components of $\widetilde{\mathbf{A}}$ are now linked through the scalar term $\nabla\cdot\widetilde{\mathbf{A}}$. The scalar potential, on the other hand, cannot be separated from the vector potential

$$\nabla^2\widetilde{\varphi} + (\nabla\tilde{\varepsilon})/\tilde{\varepsilon}\cdot(\nabla\widetilde{\varphi} + i\omega\widetilde{\mathbf{A}}) + \omega^2\mu\tilde{\varepsilon}\widetilde{\varphi} = -\tilde{\rho}_\mathrm{f}/\tilde{\varepsilon}. \tag{6.3}$$

With the gauge chosen in Eq. (3.13), $\widetilde{\mathbf{A}}$ and $\widetilde{\varphi}$ do not decouple. Yet, for inhomogeneous permittivities and permeabilities, one can also apply a *generalized Lorenz gauge* that separates $\widetilde{\mathbf{A}}$ and $\widetilde{\varphi}$ [269,270]. Regardless, the associated equations complicate significantly and couple the longitudinal and radial vector potential components (see Appendix A.16). They cannot be solved sequentially, as outlined in the following.

Without the tissue boundaries ($\nabla\tilde{\varepsilon} = 0$), Eqs. (6.2) and (6.3) have previously been solved by means of Green's function (see Eqs. (4.36) and (4.37)). Here, the same approach shall be used, where the dedicated Green's function, capable of coping with the tissue inhomogeneity, needs to be determiend. To simplify the problem at hand, the involved symmetries shall first be considered.

6.1.2 Cylindrical geometry and symmetries

From the analysis of MC simulated phase spaces, it has been concluded that the radial proton current J_ρ (caused by multiple Coulomb scattering) is approximately two orders of magnitude weaker than the longitudinal current (Fig. 5.15) and therefore negligible. Hence, in the following it will be dropped entirely and only a longitudinal source term of the form $\mathbf{J}_\mathrm{f} = J_z\hat{\mathbf{e}}_z$ will be taken into account. It has also been found that the beam spot size has no impact on the far field (see Fig. 5.18), so that one can go back to the infinitesimally narrow

line current from Chapter 4. A solely radial discontinuity of the permittivity, i.e. tissue boundary, is considered. Thereby, the target constitutes a long tube with a given radius ρ_c:

$$\tilde{\varepsilon}(\mathbf{r},\omega) = \varepsilon_0 + \underbrace{(\tilde{\varepsilon}(\omega) - \varepsilon_0)}_{\varepsilon_0\widetilde{\chi}_e(\omega)}\theta^+(\rho_c - \rho), \quad (6.4) \qquad \nabla\tilde{\varepsilon}(\mathbf{r},\omega) = -\varepsilon_0\widetilde{\chi}_e(\omega)\delta^+(\rho_c - \rho)\hat{\mathbf{e}}_\rho. \quad (6.5)$$

Having chosen a simple permittivity of the form given in Eq. (6.4) leads to a very simple gradient, consisting only of a radial component situated at the boundary (Eq. (6.5)), where the gradient transformed to cylindrical coordinates, given in Eq. (A.73), has been applied. Note that the positive-sided step and delta-functions θ^+ and δ^+ have been used as opposed to the regular symmetric ones. They are properly defined in Appendix A.8 and have been introduced due to the conductivity. From Sec. 4.1.9, it followed that the conducted charge can only collect at the gradient. From a physical point of view, one would expect the charges to remain within the confines of the target. Yet, using the θ- and δ-function, would imply a non-zero charge density for $\rho > \rho_c$. By definition, this is not the case for $\theta^+(\rho_c - \rho)$ and $\delta^+(\rho_c - \rho)$. Generally, this is rather a formality. The discontinuity remains in both cases infinitely sharp and this does not impact the base functions below.

With both boundary and source term being ϕ-independent and thus ϕ-symmetric, the resultant electromagnetic fields are expected to be equally symmetric. This, however, does not translate directly to ϕ-symmetric scalar and vector potentials due to the differential relationship between the two (see Eqs. (3.11) and (3.12)). In particular, a linearly ϕ-dependent scalar or vector potential turns constant and thus ϕ-independent under differentiation. Yet the periodicity, in particular $\widetilde{A}_\kappa(\rho,\phi,z) \overset{!}{=} \widetilde{A}_\kappa(\rho,\phi+2\pi,z)$ and $\widetilde{\varphi}(\rho,\phi,z) \overset{!}{=} \widetilde{\varphi}(\rho,\phi+2\pi,z)$, excludes this exception leading to

$$\frac{\partial\widetilde{A}_\kappa}{\partial\phi} = 0, \quad (6.6) \qquad \frac{\partial\widetilde{\varphi}}{\partial\phi} = 0. \quad (6.7)$$

With the symmetry and boundary simplifications at hand, one can move onto the equations for the scalar (Eq. (6.3)) and vector potential (Eq. (6.2)), starting with $\widetilde{A}_\phi$. By using Eq. (6.5) and expanding the azimuthal component of Eq. (6.2) with the identity from Eq. (A.77), one obtains $\nabla^2\widetilde{A}_\phi - \widetilde{A}_\phi/\rho^2 + \omega^2\mu\tilde{\varepsilon}\widetilde{A}_\phi = 0$, where Eq. (6.6) has been used. The latter is trivially solved with $\widetilde{A}_\phi = 0$ and thus vanishes altogether. The component along the beam axis, Eq. (6.2) reduces to

$$\nabla^2\widetilde{A}_z + \omega^2\mu\tilde{\varepsilon}\widetilde{A}_z = -\mu\tilde{J}_z, \quad (6.8)$$

once again under the simplified boundary from Eq. (6.5). Most importantly, the equation for $\widetilde{A}_z$ decouples entirely from the remaining vector potential components $\widetilde{A}_\rho$, $\widetilde{A}_z$ and the scalar potential $\widetilde{\varphi}$. It can thus be solved independently. Along the radial vector component from Eq. (6.2), one gets

$$\nabla^2\widetilde{A}_\rho - \frac{\widetilde{A}_\rho}{\rho^2} - \left[\frac{\nabla\tilde{\varepsilon}}{\tilde{\varepsilon}}\right]_\rho\frac{1}{\rho}\frac{\partial(\rho\widetilde{A}_\rho)}{\partial\rho} + \omega^2\mu\tilde{\varepsilon}\widetilde{A}_\rho = \left[\frac{\nabla\tilde{\varepsilon}}{\tilde{\varepsilon}}\right]_\rho\frac{\partial\widetilde{A}_z}{\partial z}, \quad (6.9)$$

where the notation $[\circ]_\kappa$ shall indicate that only the κ-component of the vectorial quantity $\circ$ is taken. First and foremost, the differential equation for $\widetilde{A}_\rho$ depends on $\widetilde{A}_z$. Hence, one either solves the coupled system of differential equations of $\widetilde{A}_\rho$ and $\widetilde{A}_z$ simultaneously, or, what is possible in this particular case, one solves for $\widetilde{A}_z$ a priori and reinterprets its contribution in Eq. (6.9) as a source term. The $\widetilde{A}_z$-term has deliberately been placed on the RHS of Eq. (6.9), in analogy to Eq. (6.8), where $-\mu\tilde{J}_z$ constitutes the regular source term, since the second approach, i.e. the source-term interpretation, has been chosen. Note that

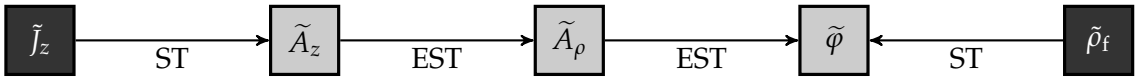

Figure 6.1: [Effective] source terms ([E]ST) for the vector potential components and the scalar potential. The two outer panels (point-particle charge and current density) are the independent and external source terms, while $\widetilde{A}_z$ and $\widetilde{A}_\rho$ are effective source terms in a more mathematical sense. Practically, one needs to solve $\widetilde{A}_z$ before $\widetilde{A}_\rho$, which needs to be solved before $\widetilde{\varphi}$.

it is multiplied with the gradient of the permittivity, therefore one only needs to calculate $\partial_z \widetilde{A}_z$ at the boundary in order to calculate $\widetilde{A}_\rho$.

Finally, the scalar potential from Eq. (6.3) simplifies to

$$\nabla^2 \widetilde{\varphi} + \left[\frac{\nabla \tilde{\varepsilon}}{\tilde{\varepsilon}}\right]_\rho \frac{\partial \widetilde{\varphi}}{\partial \rho} + \omega^2 \mu \tilde{\varepsilon} \widetilde{\varphi} = -\tilde{\rho}_\mathrm{f}/\tilde{\varepsilon} - \left[\frac{\nabla \tilde{\varepsilon}}{\tilde{\varepsilon}}\right]_\rho i\omega \widetilde{A}_\rho. \tag{6.10}$$

In turn, it depends on $\widetilde{A}_\rho$, which is in this case interpreted as a source term. The mutual dependencies of the vector potential components and the scalar potential are shown in Fig. 6.1. Eqs. (6.8) to (6.10) shall be solved by means of Green's function. For this purpose, the basics of Green's functions and how they can be derived are reviewed.

6.1.3 Green's function and its eigenfunction expansion

The $\tilde{\varepsilon}$-discontinuity of the present geometry needs to be incorporated in the Green's function. This specific application, however, cannot be found in the standard literature [271,272], encompassing a wide range of solutions. They rather emphasize the analysis of limited domains with specific boundary conditions, while an infinite domain is considered here. The Schrödinger equation bears a strong similarity to Eq. (6.9), when the permittivity is replaced with some potential V, for which asymptotic or approximate solutions have been devised, such as the WKB method [273] or the Born approximation [274]. Yet, the solution rather close to the source or scattering boundary will be calculated so that such approximations need to be justified thoroughly or do not even apply. Instead, the *exact* Green's function for the present discontinuous geometry shall be derived.

The basics of Green's functions will be briefly recapitulated. A given differential operator $\mathcal{L} - \lambda$, where λ is a scalar, acts on the sought solution $|\psi\rangle$ and yields a source term $|S\rangle$ [275]:

$$(\mathcal{L} - \lambda)\,|\psi\rangle = |S\rangle\,. \tag{6.11}$$

The corresponding set of eigenvectors $|n\rangle$ of $\mathcal{L}$ (i.e. basis functions in the continuous case) with their associated eigenvalues λ_n is defined by the eigenvalue equation

$$\mathcal{L}\,|n\rangle = \lambda_n\,|n\rangle\,, \tag{6.12}$$

$$\sum_n |n\rangle\langle n| = I, \tag{6.13}$$

where I is the unity operator. If one can find a complete and orthonormal set of eigenvectors and eigenvalues such that the completeness relation from Eq. (6.13) is fulfilled, then it is possible to construct a Green's function G so that the solution of Eq. (6.11) can be represented as [276]

$$|\psi\rangle = G\,|S\rangle\,, \tag{6.14}$$

$$G = \sum_n |n\rangle\langle n|/(\lambda_n - \lambda)\,. \tag{6.15}$$

It follows directly from Eq. (6.15) that G is also the solution of $(\mathcal{L} - \lambda)G = I$, which is usually regarded as the defining property of the Green's function. More important for the

present application in a three-dimensional space of continuous functions is the following definition of the Green's function [246]:

$$(\mathcal{L} - \lambda)G(\mathbf{r}, \mathbf{r}') = \delta(\mathbf{r} - \mathbf{r}'). \tag{6.16}$$

When defined through Eq. (6.16), one sees that the Green's function is the solution of Eq. (6.11) for a delta source term and thus characterizes the response of $\mathcal{L} - \lambda$ for a delta-excitation at a given $\mathbf{r}'$. The solution for a more complex source-term S is then their linear superposition, expressed as

$$\psi(\mathbf{r}) = \int_{\mathbb{R}^3} \mathrm{d}^3\mathbf{r}' G(\mathbf{r}, \mathbf{r}') S(\mathbf{r}'). \tag{6.17}$$

Simultaneously, Eq. (6.17) is also the continuous equivalent of Eq. (6.14). As it is defined, the Green's functions is not unique, unless boundary conditions are imposed. In an open-ended domain, as it is in the present case, the boundary conditions require the solution to vanish at negative and positive infinity. These introductory and defining concepts have been kept deliberately very general, in particular an inner product has not been chosen yet, since it varies in what follows below.

There are multiple methods to derive Green's functions and accordingly a large body of literature in addition to the ones already mentioned. In the one-dimensional case, the Green's function can be derived by dividing the domain into two regions and solving the source-free equation separately, under the two boundary conditions [220, 273, 274]. Subsequently, they are combined using the Wronskian and Abel's identity. This is usually discussed in the framework of Sturm–Liouville theory, which will be introduced below[1]. In three dimensions, this method cannot be applied. Instead, the approach from Eq. (6.15) is used [153, 277]. Especially for the Helmholtz equation, which originally motivated the development of Green's function, there is exhaustive material available [271, 278].

6.1.4 Green's function for the Helmholtz equation

Since Eqs. (6.2) and (6.3) reduce to the Helmholtz equation for a homogeneous tissue, i.e. $\nabla\tilde{\varepsilon} = 0$, it is instructive to recapitulate the derivation of its Green's function. Subsequently, it will be modified to account for an inhomogeneous target. The following steps can be found in the literature mentioned above. In order to apply Eq. (6.15), first one needs to choose an inner product. The Hilbert space is equipped with

$$\langle \psi_\alpha | \psi_\beta \rangle = \int_{\mathbb{R}^3} \mathrm{d}^3\mathbf{r}\, \psi_\alpha^\dagger(\mathbf{r}) \psi_\beta(\mathbf{r}), \tag{6.18}$$

where $\circ^\dagger$ indicates the complex conjugation. In $\mathbb{R}^3$, the discrete base vectors of Eq. (6.15) are replaced with continuous functions: $|n\rangle \to \psi(\mathbf{r})$. By introducing $k^2 = \omega^2\mu\tilde{\varepsilon}$, Eqs. (6.2) and (6.3) simplify in the homogeneous case to the aforementioned Helmholtz equation: $(\mathcal{L} + k^2)\widetilde{\mathbf{A}} = -\mu\tilde{\mathbf{J}}_\mathrm{f}$, $(\mathcal{L} + k^2)\widetilde{\varphi} = -\tilde{\rho}_\mathrm{f}/\tilde{\varepsilon}$, where $\mathcal{L} = \nabla^2$ is the Laplacian and $\nabla^2 + k^2$ the Helmholtz operator. Upon comparison with Eq. (6.11) one can already identify $\lambda = -k^2$. Following the strategy outlined in the previous section, a set of eigenvectors and eigenvalues is sought, that satisfy Eq. (6.12). For the given operator $\mathcal{L}$, one can easily verify

$$\mathcal{L}\psi_{\mathbf{k}'} = \nabla^2\psi_{\mathbf{k}'} = -k'^2\psi_{\mathbf{k}'}, \tag{6.19}$$

$$\psi_{\mathbf{k}'} = \frac{1}{(2\pi)^{3/2}} \exp\left(i\mathbf{k}' \cdot \mathbf{r}\right), \tag{6.20}$$

[1] Sturm–Liouville theory will only be used for the derivation of the basis function.

where the factor $1/(2\pi)^{3/2}$ has been chosen such that $\psi_{\mathbf{k}'}$ is orthonormal under the norm given in Eq. (6.18): $\langle\psi_{\mathbf{k}'}|\psi_{\mathbf{k}''}\rangle = \delta(\mathbf{k}' - \mathbf{k}'')$. Comparing Eq. (6.19) with Eq. (6.12), one gets $\lambda_n = -k'^2$. Note that one needs to carefully distinguish between the constant parameter k and the *continuous* variables in the vector $\mathbf{k}' = (k'_x, k'_y, k'_z)^{\mathrm{T}}$ or $k'^2 = k'^2_x + k'^2_y + k'^2_z$. Since no further restrictions (i.e. boundary conditions) that could discretize the $\mathbf{k}'$-values were set, one needs to turn the discrete sums of Eqs. (6.13) and (6.15) over the eigenvalues into continuous integrals:

$$\int_{\mathbb{R}^3} \mathrm{d}^3\mathbf{k}' \psi^\dagger_{\mathbf{k}'}(\mathbf{r}')\psi_{\mathbf{k}'}(\mathbf{r}) = \delta(\mathbf{r} - \mathbf{r}'), \qquad (6.21) \qquad G(\mathbf{r}, \mathbf{r}') = \int_{\mathbb{R}^3} \mathrm{d}^3\mathbf{k}' \frac{\psi^\dagger_{\mathbf{k}'}(\mathbf{r}')\psi_{\mathbf{k}'}(\mathbf{r})}{k^2 - k'^2}. \qquad (6.22)$$

On a side-note, when Eq. (6.11) is defined without "$-\lambda$" such that $\mathcal{L}' = \nabla^2 + k^2$, then one can easily modify Eq. (6.19) by adding $k^2\psi_{\mathbf{k}'}$ on both sides, yielding the necessary eigenvalue equation: $(\nabla^2 + k^2)\psi_{\mathbf{k}'} = (k^2 - k'^2)\psi_{\mathbf{k}'}$, where now $\lambda' = k^2 - k'^2$. To verify Eq. (6.21), one needs to apply the integral representation of the Dirac-delta function for each k_κ [220]:

$$\delta(t - t') = \frac{1}{2\pi}\int_{-\infty}^{\infty} \mathrm{d}\omega \exp\big[i\omega(t - t')\big]. \qquad (6.23)$$

Furthermore, Eq. (6.22) is evaluated with the identity from Eq. (A.11):

$$\begin{aligned} G(\mathbf{r}, \mathbf{r}') &= \int_{\mathbb{R}^3} \mathrm{d}^3\mathbf{k}' \frac{1}{(2\pi)^3} \frac{\exp(-i\mathbf{k}'\mathbf{r}')\exp(i\mathbf{k}'\mathbf{r})}{k^2 - k'^2} = -\frac{1}{(2\pi)^3}\,\mathrm{I}(k, \mathbf{r} - \mathbf{r}') \\ &\overset{\Im(k)<0}{=} -\frac{1}{4\pi}\frac{\exp(-ik|\mathbf{r} - \mathbf{r}'|)}{|\mathbf{r} - \mathbf{r}'|}. \end{aligned} \qquad (6.24)$$

The sign of the imaginary part of k, which has been assumed to be negative due to Eq. (3.28), determines the sign in the exponent. Eventually, the well-known Green's function for the Helmholtz equation in Eq. (6.24) has been derived. In order to modify this "blueprint" derivation of the Green's function to incorporate an inhomogeneous target, one needs to determine the base function equivalent of Eq. (6.20) for the new geometry. To facilitate the derivation of the adapted base functions, one can (a) move to a cylindrical coordinate system, where the discontinuity simplifies and (b) use the *separation of variables*.

6.1.5 Separation of variables

In the previous section, it has been shown how Green's function can be derived from the source-free equation $(\nabla^2 + k'^2)\psi_{\mathbf{k}'} = 0$ (Eq. (6.19)). For this reason, one considers only the source-free parts of Eqs. (6.8) to (6.10) and observe that, excluding the boundary, they can all be written as

$$\frac{1}{\rho}\frac{\partial}{\partial\rho}\left(\rho\frac{\partial F}{\partial\rho}\right) - \alpha^2\frac{F}{\rho^2} + \frac{1}{\rho^2}\frac{\partial^2 F}{\partial\phi^2} + \frac{\partial^2 F}{\partial z^2} + k'^2 F = 0, \qquad (6.25)$$

where $\alpha = 1$ for Eq. (6.9) and otherwise $\alpha = 0$. The theory regarding the separability of solutions to the Helmholtz equation above is tied to the *Stäckel determinant* [279–281], which is used to determine under which conditions a separation is possible, depending on the choice of coordinate system. A more detailed analysis goes back to Morse and Feshbach [278] or Spencer and Moon [282–285]. More recent work, providing a concise presentation of the mathematical derivation, is given by Tilburg [286]. Most importantly one can confirm that the Helmholtz equation is separable in cylindrical coordinates, even if the wavenumber k' takes the more general form [287]

$$k'^2(\rho, \phi, z) = k_0'^2 + g_\rho(\rho) + g_\phi(\phi)/\rho^2 + g_z(z), \qquad (6.26)$$

where g_ρ, g_ϕ and g_z are some univariate functions. While $g_\phi = g_z = 0$, g_ρ has a step-like shape, related to the permittivity $\tilde{\varepsilon}$. Further details are given below. The multiplicative separation of variables of the solution of Eq. (6.25) is defined as

$$F(\rho, \phi, z) = R(\rho)\Phi(\phi)Z(z). \tag{6.27}$$

The following steps are detailed in numerous textbooks [153, 285]. Aside, Weisstein [287] provides a concise and easily accessible overview. Combining Eq. (6.25) with Eq. (6.27) yields an additive term of $1/\Phi\, \partial^2\Phi/\partial\phi^2 = -m^2$, which depends exclusively on ϕ and therefore is set to a negative constant for periodicity purposes. The general solution of the emerging differential equation is $\Phi(\phi) = c_m \cos(m\phi) + s_m \sin(m\phi)$. To preserve the aforementioned continuity, m has to be an integer. At this stage, one can invoke the cylindrical symmetry and conclude that the only ϕ-symmetric solution is given for $m = 0$, therefore $\Phi(\phi) = c_0$. Subsequently, one arrives analogously at $1/Z\, \partial^2 Z/\partial z^2 = -k_z'^2$, with the general solution $Z(z) = c_+ \exp(ik_z' z) + c_- \exp(-ik_z' z)$. A negative separation constant $-k_z'^2$ has deliberately been chosen, seeking the equivalence with respect to Eq. (6.20). For the same reason, $c_- = 0$. The infinitely oscillating behavior of $Z(z)$ is in a physical scenario unreasonable, but tolerable when seeking an eigenfunction. Finally, the equation for the radial function becomes

$$\frac{\partial^2 R}{\partial \rho^2} + \frac{1}{\rho}\frac{\partial R}{\partial \rho} + \left(k'^2 - k_z'^2 - \frac{\alpha^2}{\rho^2}\right) R = 0, \tag{6.28}$$

which is known as *Bessel's differential equation* [220]. With $k'^2 = k_x'^2 + k_y'^2 + k_z'^2$ one can define k_ρ': $k'^2 - k_z'^2 = k_x'^2 + k_y'^2 \equiv k_\rho'^2$. Being a second order linear differential equation, there are two linearly independent solutions

$$R(\rho) = c_J J_\alpha(k_\rho'\rho) + c_Y Y_\alpha(k_\rho'\rho), \tag{6.29}$$

where $J_\alpha(\circ)$ and $Y_\alpha(\circ)$ are the *Bessel functions of the first and second kind* [220]. In Eq. (6.25), α is squared to eventually specify the order of the Bessel function (subscript). Since $\alpha = \{0, 1\}$, Eq. (6.25) is unaffected. The case $\alpha = 1$ only appears in the vector Laplacian of the radial component. This particular result is also tabulated in Spencer [282].

6.1.6 Homogeneous case in cylindrical geometry

With the separation of variables, one can construct a solution of Eq. (6.25) and thus determine the ϕ-symmetric equivalent of Eq. (6.20). To verify the consistency and applicability, the Green's function of the Helmholtz equation with Eq. (6.15) will also be derived, just as in Sec. 6.1.3. The cylindrical scalar Laplacian operator is obtained for $\alpha = 0$. For simplicity[2], the Bessel function of the second kind is excluded due to its singular behavior towards the origin by setting $c_Y = 0$. With Eq. (6.27), one eventually obtains

$$\overline{\psi}_{\mathbf{k}'}(\mathbf{r}) = \frac{1}{(2\pi)^{3/2}} J_0(k_\rho'\rho) \exp\left(ik_z' z\right) \tag{6.30}$$

where the product of the remaining constants $c_0 c_+ c_J = 1/(2\pi)^{3/2}$ is set to satisfy the normalization. As constructed, Eq. (6.30) solves Eq. (6.25) and is thus the sought equivalent of Eq. (6.20). Yet, there is a more direct connection between the two. The expression of Eq. (6.20) describes a planar wave oriented towards $\mathbf{k}'$ and thus possesses no cylindrical symmetry. It can be enforced however, by averaging over the azimuth. For this

[2] It would also be possible to construct a base function with Y_0, yet it is not orthogonal to itself, but the *Struve function*, which somewhat complicates matters.

purpose, the argument of Eq. (6.20) is represented in terms of cylindrical coordinates: $\mathbf{k}' \cdot \mathbf{r} = k'_\rho \rho \cos(\phi - \phi'_k) + k'_z z$, where $k'_x = k'_\rho \cos\phi'_k$, $k'_y = k'_\rho \sin\phi'_k$, $k'_z = k'_z$ and analogously for the spatial coordinates. Thereby, the equivalence between Eq. (6.20) and Eq. (6.30) is established:

$$\overline{\psi}_{\mathbf{k}'}(\mathbf{r}) = \frac{1}{2\pi} \int_0^{2\pi} \psi_{\mathbf{k}'}(\mathbf{r}) \mathrm{d}\phi, \tag{6.31}$$

where one needs Eq. (A.96). The orthogonality of Eq. (6.30) is verified with the inner product from Eq. (6.18) and the cylindrical volume element

$$\begin{aligned} \langle \overline{\psi}_{\mathbf{k}'} | \overline{\psi}_{\mathbf{k}''} \rangle &= \frac{1}{(2\pi)^3} \int_0^\infty \rho \mathrm{d}\rho \int_0^{2\pi} \mathrm{d}\phi \int_{-\infty}^\infty \mathrm{d}z J_0(k'_\rho \rho) J_0(k''_\rho \rho) \exp\left[i(k'_z - k''_z)z\right] \\ &= \frac{\delta^+(k'_\rho - k''_\rho)}{2\pi k'_\rho} \delta(k'_z - k''_z), \end{aligned} \tag{6.32}$$

where Eq. (6.23) has been used together with the orthogonality of the Hankel transform [220]:

$$\delta^+(k_\rho - k'_\rho)/k_\rho = \int_0^\infty J_\nu(k_\rho \rho) J_\nu(k'_\rho \rho) \rho \mathrm{d}\rho. \tag{6.33}$$

The continuous completeness relation from Eq. (6.21) can be verified analogously. The ρ-weight in Eq. (6.32) has been motivated geometrically and similarly one can argue with the transform defined above Eq. (6.31). Also, the result of Eq. (6.32) is a three-dimensional Dirac-delta function expressed in cylindrical coordinates:

$$\begin{aligned} \int_{\mathbb{R}^3} \mathrm{d}^3\mathbf{k}' \psi^\dagger_{\mathbf{k}'}(\mathbf{r}') \psi_{\mathbf{k}'}(\mathbf{r}) &= \frac{1}{(2\pi)^3} \int_0^\infty k'_\rho \mathrm{d}k'_\rho \int_0^{2\pi} \mathrm{d}\phi'_k \int_{-\infty}^\infty \mathrm{d}k'_z J_0(k'_\rho \rho) J_0(k'_\rho \rho') \exp\left[ik'_z(z - z')\right] \\ &= \frac{\delta^+(\rho - \rho')}{2\pi\rho} \delta(z - z') \end{aligned} \tag{6.34}$$

Both Eq. (6.23) and Eq. (6.33) have been applied, since ω and t as well as ρ and k are interchangeable. The integral weight k'_ρ is of special importance and cannot always be deduced geometrically. More details are presented in the framework of Sturm–Liouville theory (see Secs. 6.1.7 and 6.1.10). Proceeding with Green's function[3]:

$$\begin{aligned} G(\mathbf{r}, \mathbf{r}') &= \frac{1}{(2\pi)^3} \int_0^\infty k'_\rho \mathrm{d}k'_\rho \int_0^{2\pi} \mathrm{d}\phi'_k \int_{-\infty}^\infty \mathrm{d}k'_z J_0(k'_\rho \rho) J_0(k'_\rho \rho') \frac{\exp[ik'_z(z - z')]}{k^2 - (k'^2_\rho + k'^2_z)} \\ &\overset{\Im(k)<0}{=} \frac{1}{4\pi} \int_0^\infty k'_\rho \mathrm{d}k'_\rho J_0(k'_\rho \rho) J_0(k'_\rho \rho') \frac{\exp\left(-i\tilde{k}'_z |z - z'|\right)}{-i\tilde{k}'_z}, \end{aligned} \tag{6.35}$$

where Eq. (A.113) has been used and introduced $\tilde{k}'^2_z = k^2 - k'^2_\rho$. The equivalence between Eq. (6.24) and Eq. (6.35) is not straightforward. Beginning with a simplified assumption, i.e. that the source term is situated at the origin with $\rho' = 0$. In this case, since $J_0(x \to 0) = 1$, Eq. (6.35) reduces to the *Sommerfeld identity*, which is discussed in Appendix A.18 and given in Eq. (A.112). Thereby, Eq. (6.35) is consistent with Eq. (6.24). Yet, this cannot be applied for $\rho' \neq 0$. For this purpose, one can consider the cylindrical expansion of Eq. (6.24) [271]

$$-\frac{\exp(-ik|\mathbf{r} - \mathbf{r}'|)}{|\mathbf{r} - \mathbf{r}'|} = \sum_{n=-\infty}^\infty \cos[n(\phi - \phi')] \int_0^\infty k'_\rho \mathrm{d}k'_\rho J_n(k'_\rho \rho) J_n(k'_\rho \rho') \frac{\exp\left(-i\tilde{k}'_z |z - z'|\right)}{-i\tilde{k}'_z}, \tag{6.36}$$

[3] Eq. (3.28) is again assumed.

where $|\mathbf{r}-\mathbf{r}'|^2 = \rho^2+\rho'^2-2\rho\rho'\cos(\phi-\phi')+(z-z')^2$. Note that Eq. (6.35) is restricted to ϕ-symmetric and thereby ϕ-independent source terms $S(\mathbf{r}')$ when applied in Eq. (6.17). Similarly, when Eq. (6.24) is applied to a ϕ-independent source term, then the ϕ-integral from the cylindrical volume element of Eq. (6.15) only applies to Eq. (6.24). It can be evaluated with the representation from Eq. (6.36). The symmetry of $\cos[n(\phi-\phi')]$ in the interval $[0,2\pi]$ eliminates almost all terms of the sum over n on the RHS of Eq. (6.36), except for $n=0$, leading to

$$-\int_0^{2\pi}\frac{\exp(-ik|\mathbf{r}-\mathbf{r}'|)}{|\mathbf{r}-\mathbf{r}'|}\mathrm{d}\phi = 2\pi\int_0^\infty k'_\rho \mathrm{d}k'_\rho J_0(k'_\rho\rho)J_0(k'_\rho\rho')\frac{\exp\left(-i\tilde{k}'_z|z-z'|\right)}{-i\tilde{k}'_z}. \tag{6.37}$$

This identity can be considered as a generalized Sommerfeld identity since it includes the latter as $\rho'\to 0$. Comparing the RHS of both Eq. (6.37) and Eq. (6.35) finally completes the consistency of Eq. (6.24) and Eq. (6.35). Just as the eigenfunctions were cylindrically averaged in Eq. (6.31) to construct Eq. (6.30), so is the result in Eq. (6.35) also a cylindrically averaged Eq. (6.24), as can be concluded from Eq. (6.37).

Radial component

With the *scalar* base function given in Eq. (6.30), it was possible to confirm consistency, i.e. derive the Green's function of the Helmholtz equation in cylindrical coordinates by reducing it to an integral representation (Eq. (6.35)). Yet, for a *vectorial* unknown $|\psi\rangle$ and source term $|S\rangle$ in Eq. (6.11), one may need to take an extra step. For convenience, the previous result from Eqs. (4.36) and (4.37) is replicated. It states that Eq. (6.17) also applies to vectorial source terms

$$\widetilde{\mathbf{A}}(\mathbf{r}) = \int_{\mathbb{R}^3}\widetilde{\mathbf{S}}(\mathbf{r}')G(\mathbf{r},\mathbf{r}')\mathrm{d}\mathbf{r}', \tag{6.38}$$

$$G(\mathbf{r},\mathbf{r}') = -\frac{1}{4\pi}\frac{\exp(-ik|\mathbf{r}-\mathbf{r}'|)}{|\mathbf{r}-\mathbf{r}'|}, \tag{6.39}$$

where, upon comparison with Eq. (3.15), one can identify $\widetilde{\mathbf{S}} = -\mu\tilde{\mathbf{J}}_\mathrm{f}$ and $k^2=\omega^2\mu\tilde{\varepsilon}$. Eq. (6.38) splits into its vector components, which, for a Cartesian coordinate system, yields three independent equations. With a cylindrical coordinate system, however, some base vectors of the expansion ($\hat{\mathbf{e}}_\rho$, $\hat{\mathbf{e}}_\phi$) depend on the coordinates, which needs to be taken into account for the evaluation of Eq. (6.38). With the symmetries discussed around Eq. (6.6), it is still assumed that $\widetilde{A}_\phi = 0$, while $\widetilde{A}_\rho$ as well as its source term $\tilde{J}_\rho$ are assumed to be ϕ-independent. For the derivation of the eigenfunctions for $\widetilde{A}_\rho$ below (Sec. 6.1.8.2), an equivalent integral representation for the Green's function as in Eq. (6.35) is sought to establish a reference and enable a comparison for consistency checks.

Eq. (6.38) is split into its non-vanishing vector components: $\widetilde{\mathbf{A}} = \widetilde{A}_\rho\hat{\mathbf{e}}_\rho + \widetilde{A}_z\hat{\mathbf{e}}_z$ and $\widetilde{\mathbf{S}} = \widetilde{S}_\rho\hat{\mathbf{e}}_\rho + \widetilde{S}_z\hat{\mathbf{e}}_z$. With the cylindrical expansion of Eq. (6.39) in Eq. (6.36), the definition of $\hat{\mathbf{e}}_\rho$ (Eq. (A.72)) and the ϕ-independence of $\widetilde{S}_\rho$, one can evaluate the ϕ'-integral of Eq. (6.38):

$$\begin{aligned}\widetilde{A}_\rho(\mathbf{r})\hat{\mathbf{e}}_\rho &= \int_0^\infty\rho'\mathrm{d}\rho'\int_0^{2\pi}\mathrm{d}\phi'\int_{-\infty}^\infty\mathrm{d}z'\left[\widetilde{S}_\rho(\rho',z')\hat{\mathbf{e}}'_\rho\right]G(\mathbf{r},\mathbf{r}')\\ &= \int_0^\infty\rho'\mathrm{d}\rho'\int_{-\infty}^\infty\mathrm{d}z'\widetilde{S}_\rho(\mathbf{r}')2\pi\,\hat{\mathbf{e}}_\rho\frac{1}{4\pi}\int_0^\infty k'_\rho\mathrm{d}k'_\rho J_1(k'_\rho\rho)J_1(k'_\rho\rho')\frac{\exp\left(-i\tilde{k}'_z|z-z'|\right)}{-i\tilde{k}'_z}.\end{aligned} \tag{6.40}$$

For the evaluation of the ϕ'-integral, the following identity has been used:

$$\int_0^{2\pi} \cos\left[n(\phi-\phi')\right] \mathrm{trig}(\phi')\mathrm{d}\phi' = \begin{cases} \pi\,\mathrm{trig}(\phi) & \text{for } n=\{-1,+1\} \\ 0 & \text{for } n\in\mathbb{Z}\setminus\{-1,+1\} \end{cases}, \tag{6.41}$$

where $\mathrm{trig} = \{\cos,\sin\}$ is a placeholder for the trigonometric functions that correspond to the first and second component of $\hat{\mathbf{e}}'_\rho$. Eq. (6.41) collapses the sum of Eq. (6.36) to two equally contributing terms $\{-1,+1\}$, since the two negative signs cancel while mapping $J_{-1} \to -J_1$ (Eq. (A.88)). Since the result of Eq. (6.41) is proportional to $\mathrm{trig}(\phi)$, one can also identify $\hat{\mathbf{e}}_\rho$ on the RHS so that by evaluating the ϕ'-integral, effectively $\hat{\mathbf{e}}'_\rho \to \hat{\mathbf{e}}_\rho$ has been mapped. The two contributions also produce a factor of 2π, which can be collected into the volume element $\mathrm{d}\mathbf{r}'$ via $2\pi = \int_0^{2\pi}\mathrm{d}\phi'$ so that the ρ-component of Eq. (6.40) (its only component) can be written as

$$\widetilde{A}_\rho(\mathbf{r}) = \int_{\mathbb{R}^3} \widetilde{S}_\rho(\mathbf{r}')G_\rho(\mathbf{r},\mathbf{r}')\mathrm{d}\mathbf{r}', \tag{6.42}$$

where

$$G_\rho(\mathbf{r},\mathbf{r}') \equiv \frac{1}{4\pi}\int_0^\infty k'_\rho \mathrm{d}k'_\rho J_1(k'_\rho\rho)J_1(k'_\rho\rho')\frac{\exp\left(-i\tilde{k}'_z|z-z'|\right)}{-i\tilde{k}'_z} \tag{6.43}$$

has been introduced. The upper equation is the sought integral representation of Green's function for the radial component.

6.1.7 Brief review of Sturm–Liouville theory

Sturm–Liouville theory considers a class of second-order ordinary differential equations of the type [220]

$$\mathcal{L}u = p_0(x)\frac{\partial^2}{\partial x^2}u(x) + p_1(x)\frac{\partial}{\partial x}u(x) + p_2(x)u(x), \tag{6.44}$$

where $x\in[a,b]$. If $p'_0(x) = p_1(x)$, then $\mathcal{L}$ is self-adjoint. For differential operators, where the latter is not satisfied as in Eq. (6.28), one can achieve self-adjointness [223] by multiplying Eq. (6.44) with

$$w(x) = \frac{1}{p_0(x)}\exp\left(\int^x \frac{p_1(x)}{p_0(x)}\mathrm{d}x\right). \tag{6.45}$$

Thereby, the operator of Eq. (6.44) takes the so-called *first canonical form* [275]:

$$\mathcal{L} = \frac{1}{w(x)}\frac{\partial}{\partial x}\left[p(x)\frac{\partial}{\partial x}\right] + \frac{q(x)}{w(x)}, \tag{6.46}$$

where $p(x) = p_0(x)$ and $q(x) = p_2(x)$ has been re-labeled. The distinct eigenfunctions ψ_α and ψ_β of $\mathcal{L}$ with their associated eigenvalues λ_α and λ_β are then orthogonal under the scalar product

$$\langle\psi_\alpha|\psi_\beta\rangle = \int_a^b w(x)\psi^\dagger_\alpha(x)\psi_\beta(x)\mathrm{d}x. \tag{6.47}$$

Sturm–Liouville theory also provides an explicit expression to evaluate Eq. (6.47), which can be used to determine the eigenvalues under which orthogonality is guaranteed [288]

$$(\lambda_\alpha-\lambda_\beta)\int_a^b w(x)\psi^\dagger_\alpha(x)\psi_\beta(x)\mathrm{d}x = w(x)p_0(x)\left[\psi^\dagger_\alpha(x)\psi'_\beta(x) - \psi^{\dagger\prime}_\alpha(x)\psi_\beta(x)\right]\Big|_a^b. \tag{6.48}$$

Within the finite interval $[a, b]$, Eq. (6.48) allows the construction of a series expansion through a discrete but infinite set of eigenfunctions ψ_α. If $\lambda_\alpha \neq \lambda_\beta$ are chosen such that either ψ or ψ' vanishes at the boundaries [275], then one can construct an orthogonal system. When appropriately normalized, then this set of eigenfunctions obeys [223]

$$\int_a^b w(x)\psi_\alpha^\dagger(x)\psi_\beta(x)\mathrm{d}x = \delta_{\alpha\beta}, \tag{6.49}$$

where $\delta_{\alpha\beta}$ is the *Kronecker delta*, which equates to unity only for $\alpha = \beta$ and vanishes otherwise. With Eq. (6.49) it is straightforward to construct a series expansion for $f(x)$, provided that ψ_n are *complete* within $[a, b]$:

$$f(x) = \sum_n c_n\psi_n(x), \tag{6.50}$$

$$c_n = \int_a^b w(x)\psi_n^\dagger(x)f(x)\mathrm{d}x. \tag{6.51}$$

The latter is referred to as the *generalized Fourier series* with the *generalized Fourier coefficients* c_n [220], since by choosing $\psi_n \propto e^{inx}$ one recovers the standard Fourier series. The notion of completeness is formally stated as the vanishing mean square error between the original functions and its expansion [220]:

$$\lim_{N\to\infty}\int_a^b w(x)\left[f(x) - \sum_{n=0}^{N} c_n\psi_n(x)\right]^2\mathrm{d}x = 0. \tag{6.52}$$

Bayin [223] describes the proof of completeness as "rather technical" and refers to Courant and Hilbert [289] for details. He also provides another formal expression for completeness:

$$\sum_n \psi_n^\dagger(x')\psi_n(x) = \delta(x - x')/w(x'), \tag{6.53}$$

which is in fact the continuous equivalent of Eq. (6.13) in the framework of Sturm–Liouville theory. Verifying Eq. (6.53) shall suffice to confirm the completeness for the present application.

6.1.8 Eigenfunctions

With the separation of variables from Sec. 6.1.5 and the basics of Sturm–Liouville theory from the previous section, the eigenfunctions of the source-free Eqs. (6.8) to (6.10) are desired, which are then used to derive the Green's function, analogous to the steps presented in Sec. 6.1.6. The estimation of the eigenfunctions proceeds in the standardized fashion. Solutions of the operators of Eqs. (6.8) to (6.10) will first be determined in the homogeneous domains with their respective outer boundary conditions satisfied. Towards the origin, this translates to an exclusion of solutions with singular behavior. By requiring C^1 continuity at the transition, one can set the open constants. This approach is commonly used, seeking solutions to Schrödinger [290] or Klein-Gordon equation [291] in the presence of a discontinuous potential. With the separation of variables (Sec. 6.1.5), the following general ansatz will be used for all cases

$$\psi_{\mathbf{k}'}^{(n)} = \frac{1}{(2\pi)^{3/2}}R^{(n)}(k'_\rho, \rho)\exp\left(ik'_z z\right), \tag{6.54}$$

where the index $n = \{1, 2, 3\}$ corresponds to the eigenfunctions of $\{\widetilde{A}_z, \widetilde{A}_\rho, \tilde{\varphi}\}$ from Eqs. (6.8) to (6.10). They were ordered according to their mutual dependencies from Fig. 6.1, i.e. they

also need to be solved in this order. With the step-like permittivity $\tilde{\varepsilon}$ defined in Eq. (6.4), one can also define the complex-valued wavenumber

$$\tilde{k}^2 \equiv \omega^2\mu\tilde{\varepsilon} = k_0^2 + \tilde{k}_\chi^2\theta^+(\rho_c - \rho) = \begin{cases} k_0^2 + \tilde{k}_\chi^2 & \text{for } \rho \le \rho_c \\ k_0^2 & \text{for } \rho > \rho_c \end{cases}, \tag{6.55}$$

which has been split into the vacuum wavenumber $k_0^2 \equiv \omega^2\mu\varepsilon_0$ and the tissue wave number $\tilde{k}_\chi^2 \equiv \omega^2\mu\varepsilon_0\widetilde{\chi}_e = k_0^2\widetilde{\chi}_e$. This separation simplifies consistency checks below, since one returns to homogeneous case by taking $\tilde{k}_\chi \to 0$. Both Eqs. (6.9) and (6.10) contain the expression $[\nabla\tilde{\varepsilon}/\tilde{\varepsilon}]_\rho$, which shall be simplified with Eqs. (6.4) and (6.5):

$$\left[\frac{\nabla\tilde{\varepsilon}}{\tilde{\varepsilon}}\right]_\rho = \frac{-\widetilde{\chi}_e\delta^+(\rho_c - \rho)}{1 + \widetilde{\chi}_e\theta^+(\rho_c - \rho)} = -\underbrace{\log(1+\widetilde{\chi}_e)}_{\equiv\eta}\,\delta^+(\rho_c - \rho), \tag{6.56}$$

where Eq. (A.37) has been used.

6.1.8.1 Eigenfunctions for the longitudinal vector potential

The equation for the longitudinal vector potential, given in Eq. (6.8), shall be considered first. Just as in Eqs. (6.19) and (6.20) and since k_0 is already included as λ in Eq. (6.15), it is re-labeled as the eigenvalue ($k_0 \to k'$). With Eq. (6.54), the source-free variation of Eq. (6.8) reduces to

$$\frac{\partial^2 R^{(1)}}{\partial\rho^2} + \frac{1}{\rho}\frac{\partial R^{(1)}}{\partial\rho} - k_z'^2 R^{(1)} + \left[k'^2 + \tilde{k}_\chi^2\theta^+(\rho_c - \rho)\right]R^{(1)} = 0. \tag{6.57}$$

Just as for Eq. (6.28), $k_\rho'^2 = k'^2 - k_z'^2$ has been introduced. The $\tilde{k}_\chi$-term now divides Eq. (6.57) into two regions with ρ above and below ρ_c. With Eq. (6.29), where $\alpha = 0$, one can state the general solution of Eq. (6.57) in the inner region

$$R_{\text{in}}^{(1)}(k_\rho', \rho < \rho_c) = \mathfrak{c}_J^{(1)} J_0\left(\sqrt{k_\rho'^2 + \tilde{k}_\chi^2}\rho\right) + \mathfrak{c}_Y^{(1)} Y_0\left(\sqrt{k_\rho'^2 + \tilde{k}_\chi^2}\rho\right). \tag{6.58}$$

Since Y_0 has a singular behavior towards $\rho = 0$ and $0 \le \rho \le \rho_c$, its contribution is excluded by setting $\mathfrak{c}_Y^{(1)} = 0$ on a physical basis, requiring a finite solution $\forall\rho \ge 0$. This sort of reasoning can also be found in the literature [290, 292]. The remaining constant $\mathfrak{c}_J^{(1)}$ can be chosen to satisfy the normalization, which is already included in Eq. (6.54), so $\mathfrak{c}_J^{(1)} = 1$. For $\rho \ge \rho_c$, the general solution of Eq. (6.57) is given by

$$R_{\text{out}}^{(1)}(k_\rho', \rho > \rho_c) = c_J^{(1)} J_0(k_\rho'\rho) + c_Y^{(1)} Y_0(k_\rho'\rho). \tag{6.59}$$

To finally obtain a solution of Eq. (6.57), C^1-continuity at ρ_c is required:

$$R_{\text{in}}^{(1)}(k_\rho', \rho) = R_{\text{out}}^{(1)}(k_\rho', \rho)\Big|_{\rho=\rho_c}, \tag{6.60}$$

$$\partial_\rho\, R_{\text{in}}^{(1)}(k_\rho', \rho) = \partial_\rho R_{\text{out}}^{(1)}(k_\rho', \rho)\Big|_{\rho=\rho_c}. \tag{6.61}$$

As opposed to the previous cases, the Bessel function of the second kind is not discarded in the outer region. In fact, it provides a second parameter that is necessary to satisfy both Eqs. (6.60) and (6.61):

$$c_J^{(1)} = \frac{\pi}{2}\left[yJ_1(y)Y_0(x) - xJ_0(y)Y_1(x)\right], \tag{6.62}$$

$$c_Y^{(1)} = \frac{\pi}{2}\left[xJ_0(y)J_1(x) - yJ_0(x)J_1(y)\right], \tag{6.63}$$

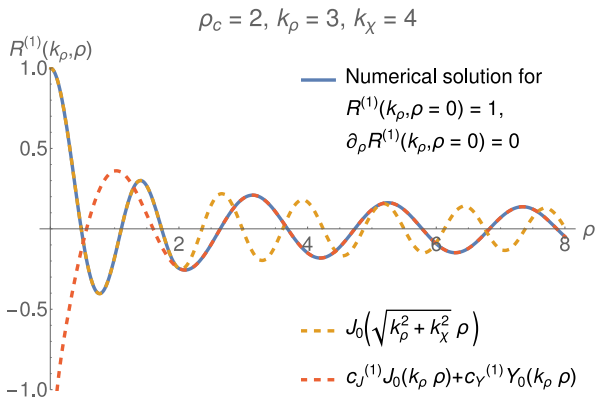

Figure 6.2: Numerical solution of Eq. (6.57) via `NDSolve` from Mathematica [293] with the initial conditions at $\rho = 0$ chosen so that $R^{(1)}(k_\rho, \rho)$ matches the initial value of J_0. Since the second term of Eq. (6.57) is proportional to $1/\rho$, the initial point of the numerical solution has been set to $\rho = 10^{-3}$ instead of $\rho = 0$ with a maximum step size of `MaxStepSize`$\rightarrow 10^{-4}$. The step function θ^+ has been smoothly approximated via the expression in Eq. (A.30) with $\epsilon = 4 \times 10^{-3}$. The result has been compared to the analytical solution from Eq. (6.66) within the respective domains. The chosen exemplary parameters are given above.

where the following dimensionless quantities were introduced

$$x \equiv k'_\rho \rho_\mathrm{c}, \tag{6.64}$$

$$y \equiv \sqrt{k'^2_\rho + \tilde{k}^2_\chi}\rho_\mathrm{c}. \tag{6.65}$$

The factor π appears in Eqs. (6.62) and (6.63), since the results can be simplified with the identity from Eq. (A.91), which is based on the so-called *Wronskian* that relates solutions of Eq. (6.28). In summary

$$R^{(1)}(k'_\rho, \rho) = \begin{cases} J_0\left(\sqrt{k'^2_\rho + \tilde{k}^2_\chi}\rho\right) & \text{for } \rho \leq \rho_\mathrm{c} \\ c_J^{(1)} J_0(k'_\rho \rho) + c_Y^{(1)} Y_0(k'_\rho \rho) & \text{for } \rho > \rho_\mathrm{c} \end{cases}. \tag{6.66}$$

In Fig. 6.2, this result has been compared to a numerical solution with exemplary parameters.

6.1.8.2 Eigenfunctions for the radial vector potential

Applying Eq. (6.54) to Eq. (6.9), and simplifying the gradient term with Eq. (6.56) leads to the following equation for the radial function

$$\frac{\partial^2 R^{(2)}}{\partial \rho^2} + \frac{1}{\rho}\frac{\partial R^{(2)}}{\partial \rho} - \frac{R^{(2)}}{\rho^2} + \eta \delta^+(\rho_\mathrm{c} - \rho)\frac{1}{\rho}\frac{\partial(\rho R^{(2)})}{\partial \rho} + \left[k'^2_\rho + \tilde{k}^2_\chi \theta^+(\rho_\mathrm{c} - \rho)\right] R^{(2)} = 0, \tag{6.67}$$

where $\eta = \log(1 + \widetilde{\chi}_\mathrm{e})$ has been abbreviated and $k'^2_\rho = k'^2 - k'^2_z$ already summarized. ρ_c also subdivides $R^{(2)}$ into two homogeneous regions. The inner domain is analogous to Eq. (6.58) and thus solved with Eq. (6.29), where in this case $\alpha = 1$:

$$R^{(2)}_\mathrm{in}(k'_\rho, \rho < \rho_\mathrm{c}) = \mathfrak{c}_J^{(2)} J_1\left(\sqrt{k'^2_\rho + \tilde{k}^2_\chi}\rho\right) + \mathfrak{c}_Y^{(2)} Y_1\left(\sqrt{k'^2_\rho + \tilde{k}^2_\chi}\rho\right). \tag{6.68}$$

Similarly, the singularity with $\mathfrak{c}_Y^{(2)} = 0$ is excluded, while $\mathfrak{c}_J^{(2)} = 1$ for normalization purposes. For the outer domain, one also takes the superposition from Eq. (6.29)

$$R^{(2)}_\mathrm{out}(k'_\rho, \rho > \rho_\mathrm{c}) = c_J^{(2)} J_1(k'_\rho \rho) + c_Y^{(2)} Y_1(k'_\rho \rho). \tag{6.69}$$

For $\widetilde{A}_z$, the constants were determined by requiring C^1 continuity for Eq. (6.69) with Eq. (6.68) at $\rho = \rho_c$. Yet the δ^+-term in Eq. (6.67) complicates the estimation of $c_J^{(2)}$ and $c_Y^{(2)}$. In fact, by requiring C^1 continuity in this case, one would ignore the δ^+-term, i.e. if $\eta = 0$, only then one could determine the constants through the C^1-continuity. To estimate the impact of the δ^+-term, Eq. (6.67) is integrated within a small domain around ρ_c:

$$\int_{\rho_c-\epsilon}^{\rho_c+\epsilon} \left\{ \frac{\partial^2 R^{(2)}}{\partial\rho^2} + \frac{1}{\rho}\frac{\partial R^{(2)}}{\partial\rho} - \frac{R^{(2)}}{\rho^2} + \eta\delta^+(\rho_c-\rho)\frac{1}{\rho}\frac{\partial(\rho R^{(2)})}{\partial\rho} + \left[k_\rho'^2 + \tilde{k}_\chi^2\theta^+(\rho_c-\rho)\right]R^{(2)} \right\} \mathrm{d}\rho$$
$$\approx \frac{\partial R^{(2)}}{\partial\rho} + \frac{R^{(2)}}{\rho}\bigg|_{\rho_c-\epsilon}^{\rho_c+\epsilon} + \eta\frac{1}{\rho}\frac{\partial(\rho R^{(2)})}{\partial\rho}\bigg|_{\rho_c} + 2\epsilon\left[k_\rho'^2 + \tilde{k}_\chi^2\theta^+(\rho_c-\rho)\right]R^{(2)}\bigg|_{\rho_c} = 0. \tag{6.70}$$

The approximation sign only applies to the last term, where $\int_a^b f(x)\mathrm{d}x \approx (b-a)f((a+b)/2)$ has been used, which holds if $b-a$ is sufficiently small, i.e. if $f(x)$ changes negligibly within $[a,b]$. One can choose ϵ arbitrarily small due to the infinitely compact nature of δ^+, justifying the approximation. For the same reason one can argue that the last term can be neglected altogether, due to its proportionality to ϵ. In summary, in the neighborhood around ρ_c, Eq. (6.67) can be approximated by

$$\frac{\partial^2\hat{R}^{(2)}}{\partial\rho^2} + \frac{1}{\rho}\frac{\partial\hat{R}^{(2)}}{\partial\rho} - \frac{\hat{R}^{(2)}}{\rho^2} + \eta\delta^+(\rho_c-\rho)\frac{1}{\rho}\frac{\partial(\rho\hat{R}^{(2)})}{\partial\rho} = 0, \tag{6.71}$$

where effectively only the last term with respect to Eq. (6.67) has been dropped. The solution of this somewhat simpler equation is studied in order to gauge the impact of the δ^+-term. In the homogeneous regions, i.e. $\rho \neq \rho_c$, it is easy to verify that Eq. (6.71) is generally solved by $c^-/\rho + c^+\rho$, where c^- and c^+ are constants that can be adjusted to satisfy some initial conditions. This is equivalent to the two linearly independent solutions (see Eqs. (6.68) and (6.69)) from the original differential equation Eq. (6.67). For the inner domain below ρ_c, the constants c_{in}^- and c_{in}^+ are used, being determined by the initial conditions at ρ_0, which has also been assumed to lie within the inner region ($\rho_0 < \rho_c$). For completeness they are explicitly given by $c_{\mathrm{in}}^- = \rho_0[\hat{R}^{(2)}(\rho_0) - \hat{R}'^{(2)}(\rho_0)\rho_0]/2$ and $c_{\mathrm{in}}^+ = [\hat{R}^{(2)}(\rho_0) + \hat{R}'^{(2)}(\rho_0)\rho_0]/(2\rho_0)$. Taking the δ^+-term into account, one arrives at

$$\hat{R}^{(2)}(\rho) = \begin{cases} c_{\mathrm{in}}^-/\rho + c_{\mathrm{in}}^+\rho & \text{for } \rho \leq \rho_c \\ c_{\mathrm{out}}^-/\rho + c_{\mathrm{out}}^+\rho & \text{for } \rho > \rho_c \end{cases}, \tag{6.72}$$

for the general solution of Eq. (6.71). Naturally, the solution in the outer domain is also just a superposition of the same type as for $\rho < \rho_c$. Yet, they cannot be chosen freely, but are related to the inner constants and the η-parameter from Eq. (6.71):

$$c_{\mathrm{out}}^- = c_{\mathrm{in}}^- + (1-e^{-\eta})c_{\mathrm{in}}^+\rho_c^2, \tag{6.73}$$
$$c_{\mathrm{out}}^+ = e^{-\eta}c_{\mathrm{in}}^+. \tag{6.74}$$

Certainly, one can alternatively first determine c_{out}^- and c_{out}^+ through the initial conditions and find equivalent relations for c_{in}^- and c_{in}^+. Yet, since the initial conditions in the inner domain were chosen (see Eq. (6.68) and the text below), the former approach has been selected. To confirm that Eq. (6.72) indeed solves Eq. (6.71), a non-piecewise representation of Eq. (6.72) is favorable:

$$\hat{R}^{(2)} = \left\{c_{\mathrm{in}}^- + \left[1-e^{-\eta\theta^+(\rho-\rho_c)}\right]c_{\mathrm{in}}^+\rho_c^2\right\}\Big/\rho + c_{\mathrm{in}}^+e^{-\eta\theta^+(\rho-\rho_c)}\rho, \tag{6.75}$$

which can be applied in Eq. (6.71). With the solution at hand, one can now seek appropriate boundary conditions that can also be used to solve for the constants in Eq. (6.69). One can easily verify that Eq. (6.72) is continuous at $\rho = \rho_c$ with the constants from Eqs. (6.73) and (6.74), which is why one can already state

$$\hat{R}^{(2)}_{\text{in}}(\rho) = \hat{R}^{(2)}_{\text{out}}(\rho)\Big|_{\rho=\rho_c}. \tag{6.76}$$

Yet, the first derivative is decidedly not continuous and changes proportionally to the value of $\hat{R}^{(2)}$ and its derivative (referring to the factors preceding the δ^+-term of Eq. (6.71)). Hence the discontinuity of the boundary condition regarding the derivative cannot be additive. Concurrently, the derivative of Eq. (6.72) at $\rho = \rho_c$ does not differ by a multiplicative factor either. By changing the derivative, inspired by the appearance of $\partial_\rho(\rho f(\rho))$-like derivatives and the power law structure of Eq. (6.72), one can achieve the desired result. In particular

$$\partial_\rho\Big[\rho\hat{R}^{(2)}_{\text{in}}(\rho)\Big] = \partial_\rho\Big[\rho\hat{R}^{(2)}_{\text{out}}(\rho)\Big]e^{\eta}\Big|_{\rho=\rho_c} \tag{6.77}$$

differs only by the multiplicative factor e^{η}. To determine $c^{(2)}_J$ and $c^{(2)}_Y$ from Eq. (6.69), the same boundary conditions, i.e. Eq. (6.77) with $\hat{R} \to R$ can be applied. This is valid, since they only specify the behavior at $\rho = \rho_c$, where the original differential equation (Eq. (6.67)) and its approximation (Eq. (6.71)), which has been used to derive the boundary conditions, agree. Eventually, one obtains

$$c^{(2)}_J = \pi/2\big[xJ_1(y)Y_0(x) - yJ_0(y)Y_1(x)e^{-\eta}\big], \tag{6.78}$$

$$c^{(2)}_Y = \pi/2\big[yJ_0(y)J_1(x)e^{-\eta} - xJ_0(x)J_1(y)\big]. \tag{6.79}$$

Interestingly enough and somewhat unexpectedly, η appears in the exponent, while it has been defined logarithmically (see Eq. (6.67) and below). In summary, the solution of Eq. (6.67) is

$$R^{(2)}(k'_\rho, \rho) = \begin{cases} J_1\Big(\sqrt{k'^2_\rho + \tilde{k}^2_\chi}\rho\Big) & \text{for } \rho \leq \rho_c \\ c^{(2)}_J J_1(k'_\rho\rho) + c^{(2)}_Y Y_1(k'_\rho\rho) & \text{for } \rho > \rho_c \end{cases}. \tag{6.80}$$

Just as in Fig. 6.2, a numerical confirmation of Eq. (6.80) is shown in Fig. 6.3.

6.1.8.3 Eigenfunctions for the scalar potential

Finally, for the scalar potential the solution of

$$\frac{\partial^2 R^{(3)}}{\partial\rho^2} + \frac{1}{\rho}\frac{\partial R^{(3)}}{\partial\rho} - \eta\delta^+(\rho_c - \rho)\frac{\partial R^{(3)}}{\partial\rho} + \big[k'^2_\rho + \tilde{k}^2_\chi\theta^+(\rho_c - \rho)\big]R^{(3)} = 0 \tag{6.81}$$

is sought, which is obtained by applying the general ansatz from Eq. (6.54) to Eq. (6.10) together with Eqs. (6.55) and (6.56). Eq. (6.81) can similarly be reduced to an approximate form around $\rho = \rho_c$, just as in Eqs. (6.70) and (6.71). For this purpose, Eq. (6.81) is multiplied by ρ, since the first two terms can be summarized as $1/\rho\partial_\rho(\rho\partial_\rho R^{(3)})$, which can then be integrated. As shown in Sec. 6.1.8.2, only the last term of Eq. (6.81) is proportional to ϵ and is thereby negligible. The simplified equation is then

$$\frac{\partial^2\hat{R}^{(3)}}{\partial\rho^2} + \frac{1}{\rho}\frac{\partial\hat{R}^{(3)}}{\partial\rho} - \eta\delta^+(\rho_c - \rho)\frac{\partial\hat{R}^{(3)}}{\partial\rho} = 0. \tag{6.82}$$

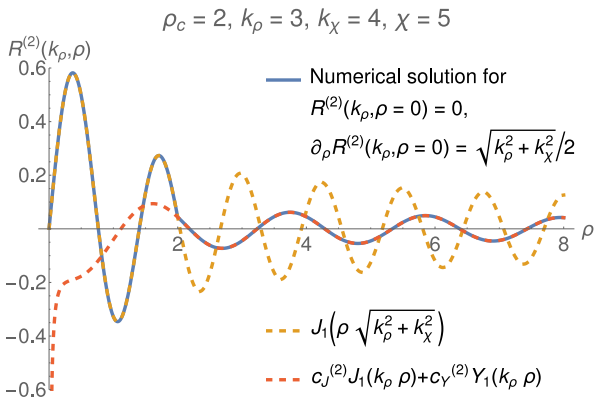

Figure 6.3: Numerical solution of Eq. (6.67) with the initial conditions at $\rho = 10^{-3}$ chosen so that $R^{(2)}(k_\rho, \rho)$ matches the initial value of J_1. The numerical solution is somewhat sensitive to the initial conditions, which is why it was necessary to use $R^{(2)}(k_\rho, \rho = 10^{-3}) = \sqrt{k_\rho^2 + k_\chi^2}/2 \times 10^{-3}$, based on $J_1(\alpha\rho) \approx \alpha\rho/2$. The result has been compared to the analytical solution from Eq. (6.80) within the respective domains. Further details are provided in the caption of Fig. 6.2.

For $\rho \neq \rho_c$, the general solution of Eq. (6.82) is $c^0 + c^\ell \log(\rho)$. Inside the cylinder, some initial conditions at $\rho_0 < \rho_c$ specify the constants: $c^0_{\text{in}} = \hat{R}^{(3)}(\rho_0) - \hat{R}'^{(3)}(\rho_0)\rho_0 \log(\rho_0)$ and $c^\ell_{\text{in}} = \hat{R}'^{(3)}(\rho_0)\rho_0$. Since for $\rho > \rho_c$, Eq. (6.82) is also homogeneous, the outer solution takes the same form

$$\hat{R}^{(3)}(\rho) = \begin{cases} c^0_{\text{in}} + c^\ell_{\text{in}} \log(\rho) & \text{for } \rho \leq \rho_c \\ c^0_{\text{out}} + c^\ell_{\text{out}} \log(\rho) & \text{for } \rho > \rho_c \end{cases}, \tag{6.83}$$

where the constants for the outer domain are similarly related to the constants in the inner domain as in Eqs. (6.73) and (6.74):

$$c^0_{\text{out}} = c^0_{\text{in}} + (1 - e^\eta) c^\ell_{\text{in}} \log(\rho_c), \tag{6.84}$$

$$c^\ell_{\text{out}} = c^\ell_{\text{in}} e^\eta. \tag{6.85}$$

The validity of Eq. (6.83) can be confirmed again by a non-piecewise representation, as in Eq. (6.75). By definition, Eq. (6.83) is C^0-continuous, while its derivative merely differs by a multiplicative factor so that the necessary boundary conditions at $\rho = \rho_c$ for Eq. (6.82) are

$$\hat{R}^{(3)}_{\text{in}}(\rho) = \hat{R}^{(3)}_{\text{out}}(\rho)\Big|_{\rho=\rho_c}, \tag{6.86}$$

$$\partial_\rho \hat{R}^{(3)}_{\text{in}}(\rho) = \partial_\rho \hat{R}^{(3)}_{\text{out}}(\rho) e^{-\eta}\Big|_{\rho=\rho_c}. \tag{6.87}$$

To eventually solve Eq. (6.81), Eqs. (6.86) and (6.87) is applied to the ansatz already given in Eqs. (6.58) and (6.59), which only need to be relabeled: $(1) \to (3)$, so that

$$R^{(3)}(k'_\rho, \rho) = \begin{cases} J_0\left(\sqrt{k'^2_\rho + \tilde{k}^2_\chi}\rho\right) & \text{for } \rho \leq \rho_c \\ c^{(3)}_J J_0(k'_\rho \rho) + c^{(3)}_Y Y_0(k'_\rho \rho) & \text{for } \rho > \rho_c \end{cases}, \tag{6.88}$$

with the constants given as

$$c^{(3)}_J = \pi/2\left[y J_1(y) Y_0(x) e^\eta - x J_0(y) Y_1(x)\right], \tag{6.89}$$

$$c^{(3)}_Y = \pi/2\left[x J_0(y) J_1(x) - y J_0(x) J_1(y) e^\eta\right]. \tag{6.90}$$

An exemplary plot of Eq. (6.88) is shown in Fig. 6.4. Note that since Eq. (6.57) is equal to Eq. (6.81) when $\eta = 0$, so are Eqs. (6.62) and (6.63) equal to Eqs. (6.89) and (6.90) when η vanishes. Recall that to obtain Eq. (6.82), Eq. (6.81) has been multiplied by ρ, so that the first

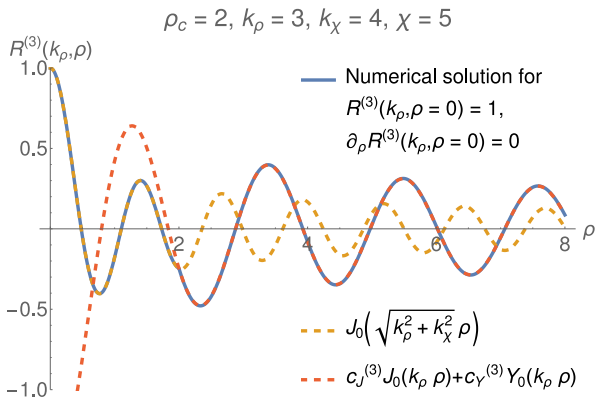

Figure 6.4: Numerical solution of Eq. (6.81) with the initial conditions at $\rho = 0$ chosen so that $R^{(3)}(k_\rho, \rho)$ matches the initial value of J_0. The result has been compared to the analytical solution from Eq. (6.88) within the respective domains. Further details are provided in the caption of Fig. 6.2.

two terms can be integrated elementary. Yet, this step is not strictly necessary, which shall be discussed briefly. When Eq. (6.81) is integrated as in Eq. (6.70), then $1/\rho\partial_\rho \hat{R}^{(3)}$ collects the 2ϵ factor, as it cannot be evaluated elementary. Its contribution thereby vanishes in the $\epsilon \to 0$ limit so that Eq. (6.81) simplifies to $\partial_\rho^2 \hat{R}^{(3)} - \eta\delta^+(\rho_c - \rho)\partial_\rho \hat{R}^{(3)} = 0$. The general solution in this case is particularly simple: $\hat{R}^{(3)}_{\text{in}} = c^0_{\text{in}} + c^+_{\text{in}}\rho$ with $c^0_{\text{in}} = \hat{R}^{(3)}(\rho_0) - \hat{R}'^{(3)}(\rho_0)\rho_0$, $c^+_{\text{in}} = \hat{R}'^{(3)}(\rho_0)$ and the usual assumption that $\rho_0 < \rho_c$. For the outer domain, one then gets $\hat{R}^{(3)}_{\text{out}}(\rho) = c^0_{\text{out}} + c^+_{\text{out}}\rho$, where $c^0_{\text{out}} = c^0_{\text{in}} + (1 - e^\eta)c^+_{\text{in}}\rho_c$ and $c^+_{\text{out}} = c^+_{\text{in}}e^\eta$. This result can be used to deduce the same boundary conditions as given in Eqs. (6.86) and (6.87), so in summary the multiplication with ρ is not strictly necessary. What matters is that the terms that do not vanish under differentiation agree regarding the discontinuity, which is in both cases the e^η-factor (see e.g. Eq. (6.85)).

6.1.9 Orthogonality of $\psi^{(n)}$

The scheme outlined in Secs. 6.1.4 and 6.1.6 for the homogeneous case will be followed. In particular, the focus lies on the orthogonality (below Eq. (6.20) and Eq. (6.32)), where one needs to choose an inner product as in Eq. (6.18). With the general ansatz from Eq. (6.54), the inner product from Eq. (6.18) for z and k_z will be examined. Notably, the complex conjugation is necessary so that the identity from Eq. (6.23) can be invoked to establish both orthogonality and completeness. Along the radial coordinate, however, it has been found that $R^{(n)}$ are *not* orthogonal for a complex-valued $\tilde{k}_\chi$ under the inner product given in Eq. (6.47). Instead, orthogonality can numerically (and analytically; see below) be confirmed if the complex conjugation in Eq. (6.47) is dropped so that the inner product takes the general form

$$\langle R^{(n)}(k'_\rho)|R^{(n)}(k_\rho)\rangle_p = \int_0^\infty R^{(n)}(k'_\rho,\rho)R^{(n)}(k_\rho,\rho)w^{(n)}(\rho)\mathrm{d}\rho. \tag{6.91}$$

In the literature, such an inner product *without* complex conjugation is referred to as a *pseudo inner product* or *symmetric product* [294]. It lacks the usual requirement that $\langle\circ|\circ\rangle > 0$ such that even $\langle\circ|\circ\rangle_p \in \mathbb{C}$. Yet, "it generates enough mathematical structure to be useful in electromagnetic applications" [294]. Note that the $R^{(n)}$ as they are defined in Eqs. (6.66), (6.80) and (6.88) are not complex-valued per se. Imaginary parts are introduced by the parameters $\tilde{k}_\chi$ and $\widetilde{\chi}_e$. If those were real-valued, then $R^{(n)}$ would be real-valued as well

so that a complex conjugation would have no effect. So one could argue that it would be nonsensical to introduce a complex conjugation, where the necessity depends on the parameter choice. Furthermore, since these calculations are carried out in the time frequency Fourier domain, one should not be restricted to real-valued eigenvalues. In addition, the transform of Eq. (6.45) and its inner product (Eq. (6.47)) are introduced to convert Eq. (6.44) to a self-adjoint operator, which is by definition *not* given, since Eqs. (6.57), (6.67) and (6.81) contain complex numbers. A more formal reasoning for the application of the pseudo inner product is however beyond this work.

The weight function $w^{(n)}(\rho)$ depends on the differential equation and can be derived with Eq. (6.45). Upon comparison of Eqs. (6.57), (6.67) and (6.81) with Eq. (6.44), one can identify that in all cases $p_0^{(n)}(\rho) = 1$. Instead, $p_1^{(n)}(\rho)$ differs and is listed below together with the corresponding weight functions for the $R^{(n)}$ that follow from Eq. (6.45):

$$\begin{aligned} w^{(1)}(\rho) &= \exp\big(\textstyle\int^{\rho} 1/\rho' \mathrm{d}\rho'\big) && p_1^{(1)}(\rho) = 1/\rho, \\ &= \exp\big(\log\rho\big) \\ &= \rho, \end{aligned} \tag{6.92}$$

$$\begin{aligned} w^{(2)}(\rho) &= \exp\left\{\int^{\rho}\left[\frac{1}{\rho'} - \frac{-\widetilde{\chi}_\mathrm{e}\delta^+(\rho_\mathrm{c}-\rho')}{1+\widetilde{\chi}_\mathrm{e}\theta^+(\rho_\mathrm{c}-\rho')}\right]\mathrm{d}\rho'\right\} && p_1^{(2)}(\rho) = 1/\rho - [\nabla\tilde{\varepsilon}/\tilde{\varepsilon}]_\rho, \\ &= \exp\big\{\log\rho - \log\big[1+\widetilde{\chi}_\mathrm{e}\theta^+(\rho_\mathrm{c}-\rho)\big]\big\} \\ &= \rho/\big[1+\widetilde{\chi}_\mathrm{e}\theta^+(\rho_\mathrm{c}-\rho)\big], \end{aligned} \tag{6.93}$$

$$\begin{aligned} w^{(3)}(\rho) &= \exp\left\{\int^{\rho}\left[\frac{1}{\rho'} + \frac{-\widetilde{\chi}_\mathrm{e}\delta^+(\rho_\mathrm{c}-\rho')}{1+\widetilde{\chi}_\mathrm{e}\theta^+(\rho_\mathrm{c}-\rho')}\right]\mathrm{d}\rho'\right\} && p_1^{(3)}(\rho) = 1/\rho + [\nabla\tilde{\varepsilon}/\tilde{\varepsilon}]_\rho, \\ &= \exp\big\{\log\rho + \log\big[1+\widetilde{\chi}_\mathrm{e}\theta^+(\rho_\mathrm{c}-\rho)\big]\big\} \\ &= \rho\big[1+\widetilde{\chi}_\mathrm{e}\theta^+(\rho_\mathrm{c}-\rho)\big]. \end{aligned} \tag{6.94}$$

For $\widetilde{A}_z$, the weight $w^{(1)}$ in the radial direction does not differ from the weight function in the homogeneous case (see Eq. (6.32)), while $w^{(2)}$ and $w^{(3)}$ are scaled with $1/(1+\widetilde{\chi}_\mathrm{e})$ and $1+\widetilde{\chi}_\mathrm{e}$, respectively for $\rho \leq \rho_\mathrm{c}$.

An evaluation of the finite inner product (integrating in Eq. (6.91) only up to ρ_max instead of infinity) and a comparison with and without complex conjugation is shown in Fig. 6.5. The expected result is a delta function situated at k'_ρ. Consequently, an integral along k_ρ, which is shown in the inserts of Fig. 6.5, should be a step function that changes its value at k'_ρ. The latter can only be observed for the inner product *without* the complex conjugation. Most importantly, both real and imaginary part follow the step-like behavior. They should not be considered as separate delta peaks for real and imaginary part, but rather a single delta peak multiplied with a complex number, which is allowed by the pseudo inner product from Eq. (6.91). Also note that the complex conjugation causes the imaginary part of Fig. 6.5 (a) to pass through zero at k'_ρ as the result is at this point by definition real-valued due to the real-valued weight function $w^{(1)}$ from Eq. (6.92). Besides, orthogonality of $R^{(2)}$ and $R^{(3)}$ can only be observed if the piecewise and complex-valued weight functions from Eqs. (6.93) and (6.94) are used. The equivalent of Eq. (6.48) with the re-defined inner product from Eq. (6.91) so that the complex conjugation on the RHS is analogously dropped also holds:

$$\begin{aligned} &(k_\rho^2 - k_\rho'^2)\int_a^b w^{(n)}(\rho)R^{(n)}(k_\rho,\rho)R^{(n)}(k'_\rho,\rho)\mathrm{d}\rho \\ &\qquad = w^{(n)}(\rho)\Big\{R^{(n)}(k_\rho,\rho)\big[\partial_\rho R^{(n)}(k'_\rho,\rho)\big] - \big[\partial_\rho R^{(n)}(k_\rho,\rho)\big]R^{(n)}(k'_\rho,\rho)\Big\}\Big|_a^b. \end{aligned} \tag{6.95}$$

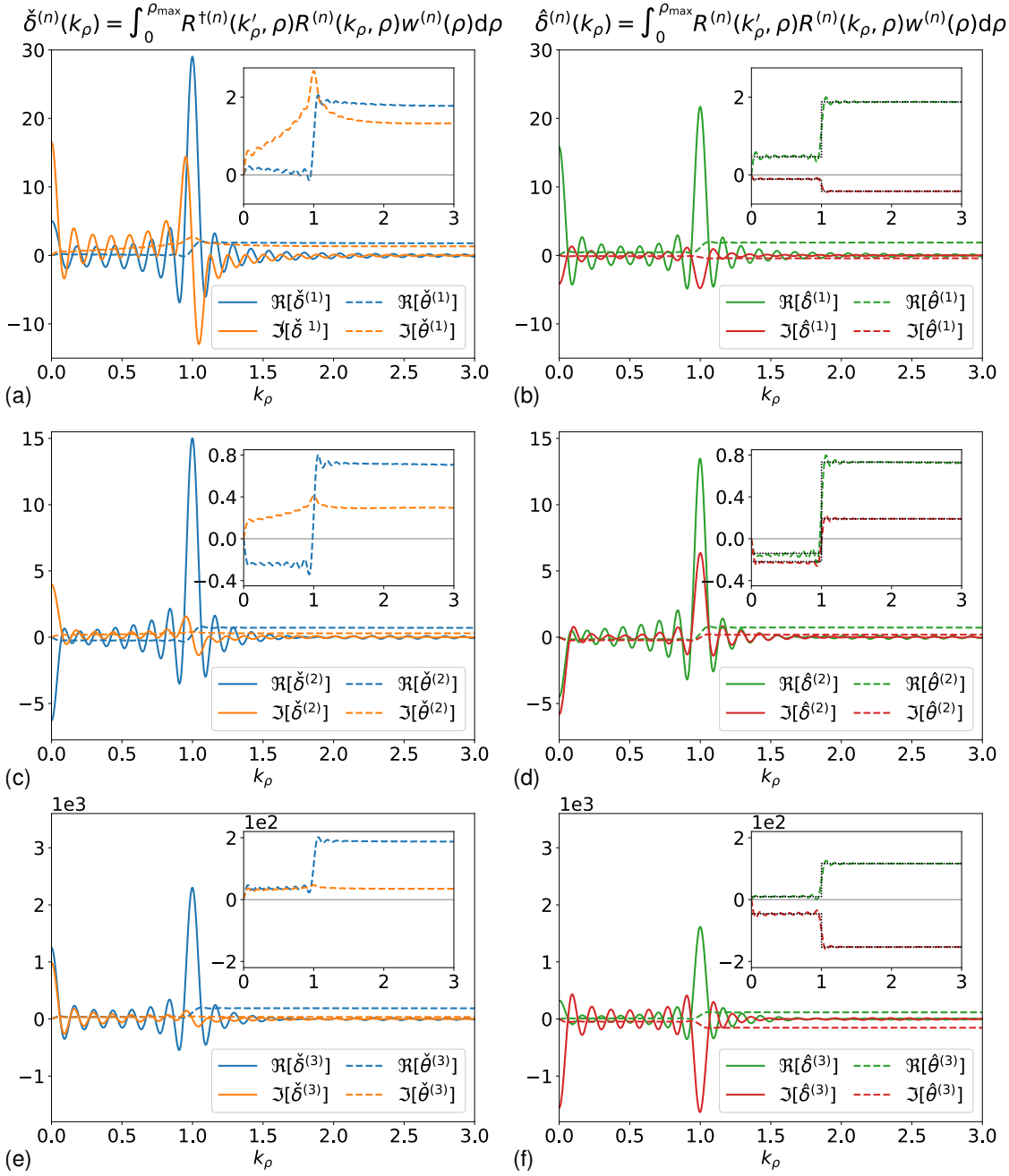

Figure 6.5: Evaluation of Eq. (6.91) with (left) and without (right) complex conjugation with a finite upper limit $\rho_{\max}$ for $R^{(n)}$ from Eq. (6.66): (a) & (b), Eq. (6.80): (c) & (d) and Eq. (6.88): (e) & (f). The exemplary parameters are: $\rho_{\max} = 50$, $\rho_c = 2$, $k'_\rho = 1$, $\tilde{k}_\chi = 0.8 - 0.4i$ and $\widetilde{\chi}_e = 8 - 4i$. The integrals of the expressions on the top are also shown and defined as $\check{\theta}^{(n)}(k_\rho) = \int_0^{k_\rho} \check{\delta}^{(n)}(k''_\rho) \mathrm{d}k''_\rho$ and $\hat{\theta}^{(n)}(k_\rho) = \int_0^{k_\rho} \hat{\delta}^{(n)}(k''_\rho) \mathrm{d}k''_\rho$.

It can actually be confirmed by a repeated application of an integral identity of Bessel functions (*Lommel's integrals*) that follows from Eq. (6.48) when studying the homogeneous Bessel differential equation:

$$\int W_\nu(k_\rho\rho)Z_\nu(k'_\rho\rho)\rho\mathrm{d}\rho = \rho\frac{k'_\rho W_\nu(k_\rho\rho)Z_{\nu-1}(k'_\rho\rho) - k_\rho W_{\nu-1}(k_\rho\rho)Z_\nu(k'_\rho\rho)}{k_\rho^2 - k_\rho'^2}. \tag{6.96}$$

Most importantly though, the orthogonality of $R^{(n)}$ follows directly from Eq. (6.95), since $R^{(n)}$ or $\partial_\rho R^{(n)}$ vanish at the limits zero and infinity. Yet, the graphs in the inserts of Fig. 6.5 (b), (d) and (f) all show a non-negligible initial offset at $k_\rho = 0$. Such offsets can already be observed with Eq. (6.33) when it is similarly evaluated up to a finite limit ρ_max:

$$\int_0^{\rho_\mathrm{max}} J_0(k_\rho\rho)J_0(k'_\rho\rho)\rho\mathrm{d}\rho = \rho_\mathrm{max}\frac{k_\rho J_0(k'_\rho\rho_\mathrm{max})J_1(k_\rho\rho_\mathrm{max}) - k'_\rho J_0(k_\rho\rho_\mathrm{max})J_1(k'_\rho\rho_\mathrm{max})}{k_\rho^2 - k_\rho'^2}. \tag{6.97}$$

Eq. (6.97) follows from Eq. (6.96) by leveraging the symmetry property from Eq. (A.88). For a given $k'_\rho > 0$, the value of Eq. (6.97) at $k_\rho = 0$ behaves as $-\left[2\rho_\mathrm{max}/(\pi k_\rho'^3)\right]^{1/2}\cos\left(k'_\rho\rho_\mathrm{max} + \pi/4\right) \propto \sqrt{\rho_\mathrm{max}}$ and hence rises to infinity as $\rho_\mathrm{max} \to \infty$. At the same time, the width of the initial peak is well approximated by $j_{0,1}/\rho_\mathrm{max} \propto 1/\rho_\mathrm{max}$, where $j_{0,1} \approx 2.40$ is the first root of J_0. It follows that the weight of the initial peak behaves as $1/\sqrt{\rho_\mathrm{max}}$ and thereby vanishes in the limit. An analogous bound for the offset shown in Fig. 6.5 (b), (d) and (f) shall be established. Eq. (6.95) is used, where one can first note that the contribution from the lower limit $a = 0$ vanishes. For $b = \rho_\mathrm{max}$, one first needs to know how Eqs. (6.66), (6.80) and (6.88) behave as $R^{(n)}(k_\rho \to 0, \rho > \rho_\mathrm{c})$. A careful evaluation of the limits yields

$$\lim_{k_\rho\to 0} R^{(1)}(k_\rho, \rho > \rho_\mathrm{c}) = J_0(\tilde{k}_\chi\rho_\mathrm{c}) + \tilde{k}_\chi\rho_\mathrm{c}\, J_1(\tilde{k}_\chi\rho_\mathrm{c})\log(\rho_\mathrm{c}/\rho), \tag{6.98}$$

$$\lim_{k_\rho\to 0} R^{(2)}(k_\rho, \rho > \rho_\mathrm{c}) = \left[\tilde{k}_\chi(\rho^2/2 - \rho_\mathrm{c}^2/2)/(1+\widetilde{\chi}_\mathrm{e})J_0(\tilde{k}_\chi\rho_\mathrm{c}) + \rho_\mathrm{c}J_1(\tilde{k}_\chi\rho_\mathrm{c})\right]/\rho, \tag{6.99}$$

$$\lim_{k_\rho\to 0} R^{(3)}(k_\rho, \rho > \rho_\mathrm{c}) = J_0(\tilde{k}_\chi\rho_\mathrm{c}) + \tilde{k}_\chi\rho_\mathrm{c}(1+\widetilde{\chi}_\mathrm{e})J_1(\tilde{k}_\chi\rho_\mathrm{c})\log(\rho_\mathrm{c}/\rho), \tag{6.100}$$

where they have been simplified with $\sqrt{\tilde{k}_\chi^2} = \tilde{k}_\chi$, which holds true for $\Re[\tilde{k}_\chi] > 0$. The appearance of the logarithms are related to the series expansion of the Bessel function of the second kind around $x = 0$: $Y_0(x) = 2[\log(x/2) + \gamma]/\pi + \mathcal{O}(x^2)$, where γ is the *Euler–Mascheroni constant*. The terms of Eq. (6.95) with the constant parameter $k'_\rho > 0$ behave for large ρ_max as

$$R^{(n)}(k'_\rho, \rho)\Big|_{\rho=\rho_\mathrm{max}} \propto 1/\sqrt{\rho_\mathrm{max}}, \tag{6.101}$$

$$\partial_\rho R^{(n)}(k'_\rho, \rho)\Big|_{\rho=\rho_\mathrm{max}} \propto 1/\sqrt{\rho_\mathrm{max}}. \tag{6.102}$$

By combining the results from Eqs. (6.98) to (6.100), Eqs. (6.92) to (6.94) and Eqs. (6.101) and (6.102), one can find that the highest order terms regarding ρ_max for the value of Eq. (6.95) at $k_\rho = 0$ (height of the initial peak) behave as $\sqrt{\rho_\mathrm{max}}\log(\rho_\mathrm{max})$ for $R^{(1)}$ and $R^{(3)}$ and $\sqrt{\rho_\mathrm{max}^3}$ for $R^{(2)}$. Note that $\partial_\rho R^{(n)}(k_\rho, \rho)$ in Eq. (6.95) produces a k_ρ-factor such that the second term is not relevant for for $k_\rho \to 0$. Notably, their initial peak rises faster than in Eq. (6.97), which is why it is so prominently featured in Fig. 6.5. To characterize the width, note that $c_J^{(1)} \approx J_0(\tilde{k}_\chi\rho_\mathrm{c}) + \tilde{k}_\chi\rho_\mathrm{c}J_1(\tilde{k}_\chi\rho_\mathrm{c})\left[\log\left(k_\rho\rho_\mathrm{c}/2\right) + \gamma\right]$ diverges for small k_ρ, while $c_Y^{(1)} \approx -\pi\tilde{k}_\chi\rho_\mathrm{c}J_1(\tilde{k}_\chi\rho_\mathrm{c})/2$ remains constant so that in order to suppress the $c_J^{(1)}J_0(k_\rho\rho_\mathrm{max})$, one needs to choose $k_\rho \approx j_{0,1}/\rho_\mathrm{max}$, which shall approximate the width of the initial peak. An almost identical result follows for the width of the initial peak of

Eq. (6.95) for $n = 3$, only that $c_J^{(3)}$ and $c_Y^{(3)}$ carry factors of $1 + \widetilde{\chi}_\mathrm{e}$. For $n = 2$, only $c_J^{(2)} J_1(k_\rho \rho_\mathrm{max}) \approx \tilde{k}_\chi J_0(\tilde{k}_\chi \rho_\mathrm{c})/(1 + \widetilde{\chi}_\mathrm{e}) J_1(k_\rho \rho_\mathrm{max})/k_\rho$ dominates. It enables the same conclusion as for all initial peaks, i.e. that the width behaves as $1/\rho_\mathrm{max}$.

In the limit $\rho_\mathrm{max} \to 0$, the weight of the initial peak for $n = \{1, 3\}$ is proportional to $\log(\rho_\mathrm{max})/\sqrt{\rho_\mathrm{max}}$ and thus vanishes, just as for Eq. (6.97). On the contrary, the contribution of the initial peak for $n = 2$ increases as $\sqrt{\rho_\mathrm{max}}$. This leads to the conclusion that for $n = 2$, $k_\rho = 0$ needs to be strictly excluded. In general, the offsets caused by the initial peaks in (a) & (b) and (e) & (f) of Fig. 6.5 are somewhat larger than in Eq. (6.97), since they rise somewhat faster (by $\log \rho_\mathrm{max}$) and are scaled with factors containing $J_\nu(\tilde{k}_\chi \rho_\mathrm{c})$ and $Y_\nu(\tilde{k}_\chi \rho_\mathrm{c})$, which increase exponentially for complex-valued inputs. Finally, in the same inserts, the graphs of $\hat{\theta}^{(n)}$ have been complemented with idealized steps (black dotted lines). The height of those, both real and imaginary part, provides the normalization for the completeness relation, which will be discussed in the following section.

6.1.10 Completeness relation for $\psi^{(n)}$

The last remaining step, prior to the expansion of Green's function, is to verify the completeness relation (see Eqs. (6.13) and (6.53)). Eventually, only a slight modification of the completeness relation, i.e. division by the eigenvalues, leads to Green's function. Yet, for Eq. (6.54) it is not as straightforward as for Eq. (6.20) with Eq. (6.21) or Eq. (6.30) with Eq. (6.34). Especially in the latter case, the orthogonality of the Hankel transform from Eq. (6.33), used to verify the orthogonality of Eq. (6.30), is also used to confirm the completeness relation. This was possible since ρ and k_ρ in Eq. (6.33) are symmetric and thereby interchangeable. It also provided the k'_ρ-integral weight without the necessity of a geometrical interpretation. Yet, this convenient symmetry does not hold for $R^{(n)}$ so that Eq. (6.95) cannot be used to confirm their completeness relation.

In the following, two separate approaches to derive the *continuous* spectrum for $R^{(1)}$ will be considered. The first one is based on the generalized Fourier series and somewhat more rigorous. From there it follows that one also needs to include a *discrete* spectrum. The second one relies on an evaluation of Eq. (6.95). The continuous spectrum for $R^{(2)}$ and $R^{(3)}$ is then presented more compactly via the second approach. Details on the discrete spectrum are presented thereafter, followed by the combined completeness relation. The results are confirmed numerically, but no proof of completeness is given. In particular, the introduction of the discrete, in addition to the continuous spectrum, deserves more attention in a different context[4].

Note that Eq. (6.54) did not alter the z-dependent part compared to Eq. (6.30) so that the corresponding completeness with respect to z, based on Eq. (6.23), still holds and does not require a separate analysis.

6.1.10.1 Continuous spectrum for $R^{(1)}$: Series approach

The first observation is that the k'_ρ-weight in Eq. (6.34) is not straightforward. In fact, the weight function as well as set of eigenvalues are the unknowns that need to be adjusted to obtain the completeness relation for $R^{(n)}$. Therefore, an approach to derive the integral weight in the k_ρ-domain (and confirm Eq. (6.33)) is sought, that can also be applied to $R^{(1)}$. The present approach is inspired by the *Fourier series* and in particular how its continuous equivalent, the *Fourier transform*, emerges in the limit of an infinite domain [246].

[4] In the framework of this thesis, the mathematical rigor that perhaps would do it justice cannot be provided, however.

With the generalized Fourier series (see Eq. (6.50)) applied to Bessel's differential equation (Eq. (6.28)), one can construct the so-called *Fourier-Bessel series* [220,223,275] in the domain $[0,\rho_{\max}]$:

$$f(\rho)=\sum_{n=1}^{\infty}c_{\nu,n}J_{\nu}\left(j_{\nu,n}\frac{\rho}{\rho_{\max}}\right), \tag{6.103}$$

$$c_{\nu,n}=\frac{2}{\rho_{\max}^2 J_{\nu+1}^2(j_{\nu,n})}\int_0^{\rho_{\max}}f(\rho)J_{\nu}\left(j_{\nu,n}\frac{\rho}{\rho_{\max}}\right)\rho\mathrm{d}\rho, \tag{6.104}$$

where $j_{\nu,n}>0$ is the n^{th} zero of J_{ν}. The set of discrete eigenfunctions is obtained with Eq. (6.48), where one can ensure the orthogonality regarding the inner product of Eq. (6.47) by requiring that either ψ or ψ' vanishes at the boundaries. With the weight function $w^{(1)}(\rho)=\rho$, the contribution from the lower bound $a=0$ vanishes, regardless of having chosen the Bessel function of the first kind. The term from the upper bound $b=\rho_{\max}$ vanishes if either $J_{\nu}(\rho)$ or $\partial_{\rho}J_{\nu}(\rho)$ at $\rho=\rho_{\max}$ is zero. In Eqs. (6.103) and (6.104), the former has been chosen, since the argument $j_{\nu,n}\rho/\rho_{\max}$ reduces at $\rho=\rho_{\max}$ to the *defined* zeros of the Bessel function. In Eq. (6.103), one effectively squeezes J_{ν} with rising n into $[0,\rho_{\max}]$ so that more and more oscillations of J_{ν} are contained. Note that Eq. (6.103) is a family of series expansions (different for each order ν), whereas the focus is now on the special case $\nu=0$. The goal is to obtain the Hankel transform [220]

$$f(\rho)=\int_0^{\infty}F(k_{\rho})J_0(k_{\rho}\rho)k_{\rho}\mathrm{d}k_{\rho}, \tag{6.105}$$

$$F(k_{\rho})=\int_0^{\infty}f(\rho)J_0(k_{\rho}\rho)\rho\mathrm{d}\rho, \tag{6.106}$$

from the Fourier-Bessel series of Eqs. (6.103) and (6.104) in the limit $\rho_{\max}\to\infty$. In particular Eq. (6.105) contains the sought integral weight k_{ρ}. As a first step, the normalization constant $2/[\rho_{\max}^2 J_1^2(j_{0,n})]$ of Eq. (6.104), which has been introduced to satisfy Eq. (6.49), is moved to the sum of Eq. (6.103). The discrete frequencies $k_{\rho,n}=j_{0,n}/\rho_{\max}$ are then identified. Pushing $\rho_{\max}$ to infinity, $c_{0,n}$, without the normalization constant, turns directly into the forward Hankel transform of Eq. (6.106) with the argument $k_{\rho,n}$. For sufficiently large n, the zeros of the Bessel function can be expanded as $j_{0,n}=(n-1/4)\pi+\mathcal{O}(1/n)$ so that the difference between two adjacent frequencies is approximately given by $\Delta k_{\rho,n}\approx\pi/\rho_{\max}$. It vanishes for large $\rho_{\max}$, so that $k_{\rho}=\lim_{\rho_{\max}\to\infty}k_{\rho,n}$ is continuous. To simplify $J_1^2(j_{0,n})$ from the normalization, its asymptotic form is used: $J_1^2(x)\approx 2/(\pi x)\sin^2(x-\pi/4)$, evaluated at $j_{0,n}$: $J_1^2(j_{0,n})\approx 2/(\pi j_{0,n})$. Finally, the sum of Eq. (6.103) transforms to the desired result, while it collects the sought weight function k_{ρ} in the limit $\rho_{\max}\to\infty$:

$$\lim_{\rho_{\max}\to\infty}\sum_{n=1}^{\infty}F(k_{\rho,n})J_0\big(k_{\rho,n}\rho\big)\underbrace{j_{0,n}/\rho_{\max}}_{k_{\rho,n}}\underbrace{\pi/\rho_{\max}}_{\Delta k_{\rho,n}}=\int_0^{\infty}F(k_{\rho})J_0(k_{\rho}\rho)k_{\rho}\mathrm{d}k_{\rho}. \tag{6.107}$$

The same approach shall be applied to $R^{(1)}$ to determine its weight function. Thus, first an equivalent series expansion, based upon $R^{(1)}$, needs to be constructed.

Eq. (6.66) has a minimum length scale imposed by the discontinuity, so that $\rho_{\max}>\rho_{\mathrm{c}}$. In Eqs. (6.103) and (6.104), the discrete spatial frequencies $k_{\rho,n}=j_{0,n}/\rho_{\max}$ were expressible in terms of the tabulated zeros of the Bessel function of the first kind and the size of the domain. With the superposition in Eq. (6.66) for $\rho>\rho_{\max}$, one instead needs to define the set of $j_{(1),n}$ as

$$R^{(1)}\big(j_{(1),n}/\rho_{\max},\rho\big)\Big|_{\rho=\rho_{\max}}=0. \tag{6.108}$$

Note that $c_J^{(1)}$ and $c_Y^{(1)}$ also depend on the discrete set of frequencies $k_{\rho,n}^{(1)} = j_{(1),n}/\rho_{\max}$. First, a special case is considered, i.e. a real-valued $\tilde{k}_\chi > 0$. Eq. (6.108) is thereby a linear superposition of oscillating functions with an approximate phase shift of $\pi/2$, which provides an infinite set of solutions, just as $j_{0,n}$ did. The associated series expansion is then

$$f(\rho) = \sum_{n=1}^{\infty} c_{(1),n}\, R^{(1)}(j_{(1),n}/\rho_{\max}, \rho) \tag{6.109}$$

$$c_{(1),n} = \frac{1}{N} \int_0^{\rho_{\max}} f(\rho) R^{(1)}(j_{(1),n}/\rho_{\max}, \rho) \rho \mathrm{d}\rho \tag{6.110}$$

where the normalization is given by

$$\begin{aligned} N &= \int_0^{\rho_{\max}} \left[R^{(1)}(j_{(1),n}/\rho_{\max}, \rho)\right]^2 \rho \mathrm{d}\rho \\ &= \frac{\rho_c^2}{2} \left\{ J_1^2\left(\sqrt{j_{(1),n}^2/\rho_{\max}^2 + \tilde{k}_\chi^2}\, \rho_c\right) - \left[c_J^{(1)} J_1\left(j_{(1),n}\, \rho_c/\rho_{\max}\right) + c_Y^{(1)} Y_1\left(j_{(1),n}\, \rho_c/\rho_{\max}\right)\right]^2 \right\} \\ &\quad + \frac{\rho_{\max}^2}{2} \left[c_J^{(1)} J_1\left(j_{(1),n}\right) + c_Y^{(1)} Y_1\left(j_{(1),n}\right)\right]^2. \end{aligned} \tag{6.111}$$

In order to simplify Eq. (6.111) and eventually transform Eq. (6.109) to an integral containing the sought weight function, realize that the first term of Eq. (6.111), proportional to ρ_c^2, vanishes in the limit $\rho_{\max} \to \infty$ in comparison to the second term. The definition of $j_{(1),n}$ (Eq. (6.108)) explicitly reads

$$0 = c_J^{(1)} J_0\left(j_{(1),n}\right) + c_Y^{(1)} Y_0\left(j_{(1),n}\right) \approx \sqrt{\frac{2}{\pi j_{(1),n}}} \left[c_J^{(1)} \cos\left(j_{(1),n} - \frac{\pi}{4}\right) + c_Y^{(1)} \sin\left(j_{(1),n} - \frac{\pi}{4}\right)\right], \tag{6.112}$$

which has been approximated with Eqs. (A.103) and (A.105). The result is a linear superposition of cosine and sine, which can be represented as a single scaled and phase-shifted cosine [295, 296]: $a\cos x + b \sin x = \mathrm{sgn}(a)\sqrt{a^2+b^2}\cos(x-\alpha)$, where $\tan\alpha = b/a$. Thereby, the definition of $j_{(1),n}$ (Eq. (6.108)) can approximately be rephrased as $j_{(1),n} - \pi/4 - \arctan c_{(1)} = (n+1/2)\pi$, where $c_{(1)} = c_Y^{(1)}/c_J^{(1)}$ and $n \in \mathbb{N}$. Simultaneously, the dominating term of Eq. (6.111) has a similar form and one can proceed analogously

$$c_J^{(1)} J_1\left(j_{(1),n}\right) + c_Y^{(1)} Y_1\left(j_{(1),n}\right) \approx \sqrt{\frac{2}{\pi j_{(1),n}}} \left[c_J^{(1)} \sin\left(j_{(1),n} - \frac{\pi}{4}\right) - c_Y^{(1)} \cos\left(j_{(1),n} - \frac{\pi}{4}\right)\right], \tag{6.113}$$

where Eqs. (A.104) and (A.106) have been used. This superposition can also be summarized, where the cosine term is as follows: $\cos\left(j_{(1),n} - \pi/4 + \arctan 1/c_{(1)}\right)$. With the simplified definition of $j_{(1),n}$ (Eq. (6.112) and below), one gets $\cos\left[(n+1/2)\pi + \arctan c_{(1)} + \arctan 1/c_{(1)}\right] = \cos\left[(n+1/2)\pi \pm \pi/2\right] = \pm 1$. The sign depends on n and the sign of $c_{(1)}$, which cancels due to the square in Eq. (6.111). Same goes for $\mathrm{sgn}(a)$. Eventually, only the $\sqrt{a^2+b^2}$ remains. More intuitively, Eq. (6.113) is proportional to the derivative of Eq. (6.112), which defines the zeros. So Eq. (6.112) is effectively evaluated in Eq. (6.113) at the extrema between the roots. Finally, the limit can be taken just as in Eq. (6.107):

$$\lim_{\rho_{\max}\to\infty} \frac{1}{N} = \lim_{\rho_{\max}\to\infty} \frac{\overbrace{j_{(1),n}/\rho_{\max}}^{k_{\rho,n}^{(1)}}}{\left(c_J^{(1)}\right)^2 + \left(c_Y^{(1)}\right)^2} \overbrace{\pi/\rho_{\max}}^{\Delta k_{\rho,n}^{(1)}} = \frac{k_\rho}{\left(c_J^{(1)}\right)^2 + \left(c_Y^{(1)}\right)^2} \mathrm{d}k_\rho \equiv \frac{\mathrm{d}k_\rho}{N^{(1)}}, \tag{6.114}$$

where the integral norm has been defined

$$\boxed{\frac{1}{N^{(1)}(k_\rho)} \equiv \frac{k_\rho}{\left(c_J^{(1)}\right)^2 + \left(c_Y^{(1)}\right)^2}.} \tag{6.115}$$

This result is consistent with the Hankel transform from Eqs. (6.105) and (6.106), since $R^{(1)}(k_\rho, \rho)$ reduces to the base function of the Hankel transform (i.e. $J_0(k_\rho \rho)$) if $\tilde{k}_\chi$ vanishes, where $c_J^{(1)} = 1$ and $c_Y^{(1)} = 0$. Accordingly, Eq. (6.115) also reduces to the expected integral weight: $1/N^{(1)}(k_\rho) = k_\rho$.

Recall that in Eqs. (6.103) and (6.104) a fixed lower limit of $\rho_{\min} = 0$ has been chosen. In order to allow for an expansion across an arbitrary interval $\rho_{\min} \leq \rho \leq \rho_{\max}$, one requires a linear superposition of the Bessel functions of the first and second kind [275]. This is conceptually very similar to the superposition in Eq. (6.66) and indeed if one constructs the corresponding continuous transform (with the so-called *cylinder functions*), then the necessary integral weight in the k_ρ-domain is the sum of the squared coefficients as in Eq. (6.115) [297, 298].

In the derivation of Eq. (6.115), one obtains a continuous spectrum of $k_\rho \geq 0$. Yet, considering only the discrete $j_{(1),n}/\rho_{\max} > 0$ back in the Fourier-Bessel series of Eq. (6.109) creates an *incomplete* expansion (orange line of Fig. 6.6 vs. the expected gray line). Consequently, further solutions of Eq. (6.108) are sought. Along the purely imaginary k_ρ-axis at $\rho_{\max} > \rho_c$, Eq. (6.66) is real-valued for $|ik_\rho| < \tilde{k}_\chi$:

$$R^{(1)}(ik_\rho, \rho_{\max}) = c_I^{(1)} I_0(k_\rho \rho_{\max}) + c_K^{(1)} K_0(k_\rho \rho_{\max}), \tag{6.116}$$

where

$$c_I^{(1)} = -zJ_1(z)K_0(x) + xJ_0(z)K_1(x), \tag{6.117}$$

$$c_K^{(1)} = zJ_1(z)I_0(x) + xJ_0(z)I_1(x), \tag{6.118}$$

and

$$z \equiv \sqrt{\tilde{k}_\chi^2 - k_\rho^2}\rho_c. \tag{6.119}$$

Eqs. (A.92) and (A.93) have been used, which involve the *modified Bessel functions of the first and second kind*: $I_\nu(z)$ and $K_\nu(z)$ [5]. $I_\nu(z)$ possesses an exponential rise (Eq. (A.107)) as opposed to the exponentially decreasing behavior of $K_\nu(z)$ (Eq. (A.108)), so that Eq. (6.116) is dominated by the first term and changes across several orders of magnitude. In order to normalize Eq. (6.116), it is scaled with $e^{-k_\rho(\rho_{\max}-\rho_c)}$ to suppress the exponential rise, which does not change the roots of Eq. (6.116).

The roots of Eq. (6.116) for $k_\rho \in [0, i\tilde{k}_\chi]$ (keeping in mind that $\tilde{k}_\chi > 0$ has been assumed) are of interest, since they provide further solutions of Eq. (6.108) and need to be included to satisfy the completeness. These specific complex-valued solutions lie in the closed interval $[0, i\tilde{k}_\chi]$, since the oscillating behavior of $J_0(z)$ and $J_1(z)$ changes the sign and thereby leads to zero crossings. For $|ik_\rho| > \tilde{k}_\chi$, these oscillations are also replaced with the exponential rise (Eq. (A.92)), since z (Eq. (6.119)) is then also complex-valued. This leads to the conclusion that there exists only a finite set of complex-valued $j^\star_{(1),n}$ that solve Eq. (6.108), while the real-valued $j_{(1),n}$ lie in an open interval $[0, \infty)$ and provide an infinite set of solutions.

[5] The factor of $\pi/2$, originally present in Eqs. (6.62) and (6.63), does not appear in Eqs. (6.117) and (6.118), since $K_\nu(z)$ is scaled with $2/\pi$ in Eq. (A.93).

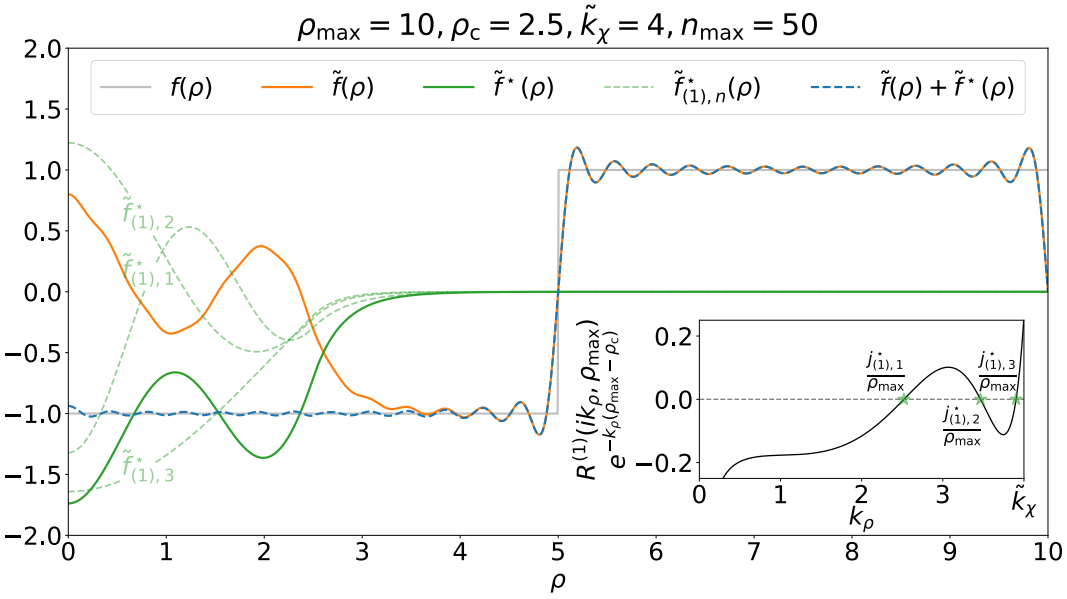

Figure 6.6: Finite Fourier-Bessel series expansion of an exemplary step function of the following type: $f(\rho) = 2\theta(\rho - \rho_{max}/2) - 1$ (gray line). The remaining expressions of the legend are defined in Eqs. (6.120) and (6.121), while the (arbitrarily) chosen parameters are given above. The insert shows Eq. (6.116) with its exponential normalization. The highlighted zero crossings (green stars) define the set of $j^\star_{(1),n}$. Only when both real ($j_{(1),n}/\rho_{max}$) and imaginary ($j^\star_{(1),n}/\rho_{max}$) spatial frequencies are taken into account, then one obtains an accurate approximation of $f(\rho)$ (blue dashed line).

For a numerical example, the finite series expansion is considered:

$$\tilde{f}(\rho) = \sum_{n=1}^{n_{max}} c_{(1),n} R^{(1)}(j_{(1),n}/\rho_{max}, \rho), \tag{6.120}$$

$$\tilde{f}^\star(\rho) = \sum_{n=1}^{n^\star} c^\star_{(1),n} R^{(1)}(j^\star_{(1),n}/\rho_{max}, \rho) \equiv \sum_{n=1}^{n^\star} \tilde{f}^\star_{(1),n}(\rho), \tag{6.121}$$

where the contributions from the real- and complex-valued spatial frequencies were separated, so that $f(\rho) \approx \tilde{f}(\rho) + \tilde{f}^\star(\rho)$ is an approximation of a given $f(\rho)$. For the plot in Fig. 6.6, some $n_{max} = 50$ needs to be chosen, while $n^\star$ is finite and depends on the choice of $\tilde{k}_\chi$, ρ_c and ρ_{max}. For the chosen parameters, there are three terms for the sum in Eq. (6.121) with the individual constituents ($\tilde{f}^\star_{(1),n}(\rho)$), shown as green transparent dashed lines. They add up to $\tilde{f}^\star(\rho)$ but also allow for a more intuitive interpretation regarding the finite set of complex-valued spatial frequencies. Note that for $\rho \leq \rho_c$ and the aforementioned requirement that $|ik_\rho| < \tilde{k}_\chi$, $R^{(1)}(ik_\rho, \rho) = J_0\left(\sqrt{\tilde{k}_\chi^2 - k_\rho^2}\rho\right)$ is just a Bessel function, which shows the fastest oscillations for $ik_\rho = 0$. For $\rho > \rho_c$, it changes into the modified Bessel functions (see Eq. (6.116)). Especially with the dominating and exponentially rising $I_0(k_\rho \rho_{max})$, one can only satisfy the requirement of Eq. (6.108), when $c_K^{(1)}$ practically vanishes [6]. This occurs when the slope of $R^{(1)}(ik_\rho, \rho)$ matches the slope of $c_K^{(1)} K_0(k_\rho \rho)$ at $\rho = \rho_c$. In the example of Fig. 6.6, this is for the first time satisfied for $j^\star_{(1),1}/\rho_{max} \approx 2.52i$ (see insert), where the corresponding $\tilde{f}^\star_{(1),1}$ has two maxima for $\rho > 0$ (as a criterion of how many oscillations there are). The larger the $j^\star_{(1),n}/\rho_{max}$, the fewer oscillations are present in $\tilde{f}^\star_{(1),n}$ until $\tilde{f}^\star_{(1),n^\star}$ approaches the zero-line directly. Fewer oscillations would be nonsensical and the fastest

[6] For $\rho_{max} \to \infty$ it has to vanish entirely.

oscillations are thresholded by $\tilde{k}_\chi$. In summary, the latter provides an intuitive picture for the finite complex spatial frequencies.

On a side-note, since the $j_{(1),n}$ were defined through Eq. (6.108), all contributing terms in the expansion of Eqs. (6.120) and (6.121) vanish at $\rho = \rho_{\max}$ so that the approximation of $f(\rho)$ is forced to vanish there as well. This would not be the case, if one alternatively defines the $j_{(1),n}$ by setting the derivative at $\rho = \rho_{\max}$ to zero. Secondly, Eq. (6.116) rises beyond 10^{12} (for the chosen parameters) towards $k_\rho \to i\tilde{k}_\chi$, which justifies the introduction of the exponential normalization. Lastly, since $\tilde{f}^\star_{(1),n}$ decrease exponentially beyond ρ_c, the contributions from Eq. (6.121) are primarily necessary within the cylinder for $\rho < \rho_{\max}$.

Under the assumption of a real-valued $\tilde{k}_\chi > 0$, it was comparatively easy to determine both the real and complex-valued spatial frequencies. Especially, since Eq. (6.66) is real-valued along the imaginary k_ρ-axis, one only needs to determine the roots along this axis to obtain the $j^\star_{(1),n}$ (insert of Fig. 6.6). If, however, $\tilde{k}_\chi$ is complex-valued, then the $j_{(1),n}$ do not lie on the real axis (but rather close to it) and $j^\star_{(1),n}$ are also not purely complex anymore. On the other hand, the imaginary part of $j_{(1),n}$ has to vanish in the limit $\rho_{\max} \to \infty$, since otherwise Eq. (6.66) would not be normalizable. $j^\star_{(1),n}$ remain complex-valued in the limit of an infinite domain. Methods to determine the set of the complex-valued spatial frequencies (Sec. 6.1.12) will be discussed below.

Altogether, one can derive the sought integral normalization (Eq. (6.115)) by first constructing the associated Fourier-Bessel series and secondly increasing the domain to infinity. Through the exemplary expansion presented in Fig. 6.6, one could infer that Eq. (6.109) is incomplete when limited to $j_{(1),n} > 0$. Yet, the condition to derive the positive ones (see Eq. (6.108)) could also be used to determine the missing (complex-valued) contributions. An equivalent condition in the continuous case will be sought. While the Fourier-Bessel series is strictly a discrete sum, it foreshadows that in the $\rho_{\max} \to \infty$ limit the complete expansion consists of a continuous and discrete spectrum. The latter is due to the finite nature of the $j^\star_{(1),n}$.

In the following, a more straightforward derivation of Eq. (6.115) is considered. The drawback is that the introduction of the discrete (and complex-valued) frequencies to achieve the completeness is somewhat arbitrary.

6.1.10.2 Continuous spectrum for $R^{(n)}$: Direct evaluation of Eq. (6.91)

With the orthogonality of $R^{(n)}$ established in Sec. 6.1.9 via a numerical demonstration (see Fig. 6.5) and an analytical argument using Eq. (6.95), a formal statement of orthogonality reads

$$\int_0^\infty R^{(n)}(k'_\rho, \rho) R^{(n)}(k_\rho, \rho) w^{(n)}(\rho) \mathrm{d}\rho = N^{(n)}(k'_\rho) \delta(k_\rho - k'_\rho). \tag{6.122}$$

The sought normalization factor $N^{(n)}(k'_\rho)$ has been identified as the weight of the delta function. This originates from the completeness statement of Sturm-Liouville theory in Eq. (6.53), where the sum over the eigenfunctions equates to a delta function in the ρ-domain. The weight function $w(x)$ appears in the denominator so that the RHS is indeed a delta function with respect to the inner product from Eq. (6.47). Transforming Eq. (6.53) to a continuous spectrum requires the introduction of the normalization factor defined in Eq. (6.122):

$$\int \frac{\mathrm{d}k_\rho}{N^{(n)}(k_\rho)} R^{(n)}(k_\rho, \rho') R^{(n)}(k_\rho, \rho) = \frac{\delta(\rho - \rho')}{w^{(n)}(\rho)}. \tag{6.123}$$

The integral limits in this equivalent "inner product" in the k_ρ-domain were not specified, as it shall indicate that the aforementioned discrete k_ρ-values off the real number line also

need to be included. Both Eqs. (6.122) and (6.123) form a symmetric pair and so the weight functions $w^{(n)}$ and the normalization factors $N^{(n)}(k_\rho)$ fulfill the same role.

In the following, Eq. (6.122) is used to solve for $N^{(n)}$. Just as in the previous section, the principle method is demonstrated with an analogy to the Hankel transform, focusing on $n = 1$. If the discontinuity is removed ($\tilde{k}_\chi \to 0$), then Eq. (6.122) reduces to

$$\int_0^\infty J_0(k'_\rho\rho)J_0(k_\rho\rho)\rho \mathrm{d}\rho = N(k'_\rho)\delta(k_\rho - k'_\rho). \tag{6.124}$$

Integrating both sides of Eq. (6.124) with respect to $\int_0^\infty \mathrm{d}k_\rho$ leaves $N(k'_\rho)$ on the RHS, while the LHS yields a factor of $1/\rho$ through the identity of Eq. (A.90), when the $\mathrm{d}k_\rho$-integral is evaluated first. On the LHS one can apply the same identity once again for the $\mathrm{d}\rho$-integral, which generates a factor of $1/k'_\rho$. Eventually, Eq. (6.124) reads: $1/k'_\rho = N(k'_\rho)$, which is the desired result and consistent with Eq. (6.33) or Eq. (6.105). Yet, to arrive at this result, it was necessary to evaluate the $\mathrm{d}k_\rho$-integral, which is not possible for $R^{(n)}(k_\rho, \rho)$ due to its complicated and nested dependency on k_ρ (see Eqs. (6.66), (6.80) and (6.88)). Instead, an alternative approach is sought, that avoids the evaluation of the k_ρ-integral. For this purpose, Eq. (6.124) with a finite upper limit is considered

$$\check{\delta}(k_\rho, k'_\rho, \rho_{\max}) = \int_0^{\rho_{\max}} J_0(k'_\rho\rho)J_0(k_\rho\rho)\rho \mathrm{d}\rho, \tag{6.125}$$

which can be evaluated explicitly, as given in Eq. (6.97). In this form, it can be analyzed as a function and does not exhibit the marginal properties of the Dirac delta distribution, that is only rigorously defined inside an integral. In particular, the value at the peak $k_\rho = k'_\rho$ is studied:

$$\lim_{k_\rho \to k'_\rho} \check{\delta}(k_\rho, k'_\rho, \rho_{\max}) = \rho_{\max}^2/2\Big[J_0^2(k'_\rho\rho_{\max}) + J_1^2(k'_\rho\rho_{\max})\Big] \approx \frac{\rho_{\max}}{\pi}\frac{1}{k'_\rho}, \tag{6.126}$$

where Eq. (6.97) has been used and subsequently approximated for large $\rho_{\max}$ via Eqs. (A.103) and (A.104) and $\cos^2 + \sin^2 = 1$. Furthermore, the explicit result of Eq. (6.125) from Eq. (6.97) is approximated through Eqs. (A.103) and (A.104) for large $\rho_{\max}$:

$$\check{\delta}(k_\rho, k'_\rho, \rho_{\max}) \approx \frac{1}{\sqrt{k_\rho k'_\rho}}\frac{\sin\left[(k_\rho - k'_\rho)\rho_{\max}\right]}{\pi(k_\rho - k'_\rho)} - \frac{1}{\sqrt{k_\rho k'_\rho}}\frac{\cos\left[(k_\rho + k'_\rho)\rho_{\max}\right]}{\pi(k_\rho + k'_\rho)}. \tag{6.127}$$

Only the first term of Eq. (6.127) dominates, particularly around $k_\rho = k'_\rho$. It is proportional to an oscillating representation of the delta function through the sinc-function [246]:

$$\hat{\delta}(k_\rho, k'_\rho, \rho_{\max}) = \frac{\sin\left[(k_\rho - k'_\rho)\rho_{\max}\right]}{\pi(k_\rho - k'_\rho)}, \tag{6.128}$$

which is appropriately normalized, i.e. $\int \hat{\delta}(k_\rho, k'_\rho, \rho_{\max})\mathrm{d}k_\rho = 1$. Consequently, the first term on the RHS of Eq. (6.127) already displays the desired product of the normalization factor $N(k'_\rho)$ and the delta function as defined in Eq. (6.124) so that one can directly read off the normalization factor via $N(k'_\rho) = \lim_{k_\rho \to k'_\rho} 1/\sqrt{k_\rho k'_\rho} = 1/k'_\rho$. Alternatively, one can compare the peak values and thus isolate the contribution from the delta function via Eq. (6.128):

$$\lim_{k_\rho \to k'_\rho} \hat{\delta}(k_\rho, k'_\rho, \rho_{\max}) = \frac{\rho_{\max}}{\pi}. \tag{6.129}$$

Upon comparison of Eqs. (6.126) and (6.129), one can also identify $N(k'_\rho) = 1/k'_\rho$, since the peak value also scales with the normalization factor. Alternatively, factoring $\rho_{\max}/\pi$ from Eq. (6.126) or evaluating the limit

$$N(k'_\rho) = \lim_{\rho_{\max}\to\infty}\left[\frac{\pi}{\rho_{\max}}\lim_{k_\rho\to k'_\rho}\check{\delta}(k_\rho, k'_\rho, \rho_{\max})\right] \tag{6.130}$$

separates the desired normalization factor. Finally, this approach is also applicable to $R^{(n)}$. With Eq. (6.95), one can evaluate the equivalent of Eq. (6.125):

$$\begin{aligned}\check{\delta}^{(n)}(k_\rho, k'_\rho, \rho_{\max}) &= \int_0^{\rho_{\max}} w^{(n)}(\rho) R^{(n)}(k_\rho,\rho) R^{(n)}(k'_\rho,\rho)\mathrm{d}\rho \\ &= \frac{w^{(n)}(\rho)}{k_\rho^2 - k_\rho'^2}\Big\{R^{(n)}(k_\rho,\rho)\left[\partial_\rho R^{(n)}(k'_\rho,\rho)\right] - \left[\partial_\rho R^{(n)}(k_\rho,\rho)\right] R^{(n)}(k'_\rho,\rho)\Big\}\Big|_{\rho=\rho_{\max}} .\end{aligned} \tag{6.131}$$

For both $n = \{1,3\}$, Eq. (6.131) cannot be further simplified, since $\partial_\rho W_0(k_\rho\rho) = -k_\rho W_1(k_\rho\rho)$, where $W_\nu = \{J_\nu, Y_\nu\}$. The case $n = 2$ does allow a further simplification via $\partial_\rho W_1(k_\rho\rho) = k_\rho W_0(k_\rho\rho) - W_1(k_\rho\rho)/\rho$, which follows from the recurrence relations of the Bessel functions [220]. In particular the second term cancels as it is not proportional to the constant k_ρ. The quality of the $\hat{\delta}$-approximation on $\check{\delta}^{(1)}$ is demonstrated in Fig. 6.7. To derive the normalization, first the limits for the peak values are considered:

$$\lim_{k_\rho\to k'_\rho}\check{\delta}^{(1)} = \frac{\rho_{\max}^2}{2}\left\{\left[c_J^{(1)}J_0(\tilde{x}) + c_Y^{(1)}Y_0(\tilde{x})\right]^2 + \left[c_J^{(1)}J_1(\tilde{x}) + c_Y^{(1)}Y_1(\tilde{x})\right]^2\right\} + \widetilde{N}^{(1)} \tag{6.132}$$

$$\begin{aligned}&= \frac{\rho_{\max}^2}{2}\Big\{\left(c_J^{(1)}\right)^2\left[J_0^2(\tilde{x}) + J_1^2(\tilde{x})\right] + \left(c_Y^{(1)}\right)^2\left[Y_0^2(\tilde{x}) + Y_1^2(\tilde{x})\right] \\ &\qquad + 2c_J^{(1)}c_Y^{(1)}\left[J_0(\tilde{x})Y_0(\tilde{x}) + J_1(\tilde{x})Y_1(\tilde{x})\right]\Big\} + \widetilde{N}^{(1)},\end{aligned} \tag{6.133}$$

$$\begin{aligned}\lim_{k_\rho\to k'_\rho}\check{\delta}^{(2)} &= \frac{\rho_{\max}^2}{2}\Big\{\left[c_J^{(2)}J_1(\tilde{x}) + c_Y^{(2)}Y_1(\tilde{x})\right]^2 \\ &\qquad - \left[c_J^{(2)}J_0(\tilde{x}) + c_Y^{(2)}Y_0(\tilde{x})\right]\left[c_J^{(2)}J_2(\tilde{x}) + c_Y^{(2)}Y_2(\tilde{x})\right]\Big\} + \widetilde{N}^{(2)}\end{aligned} \tag{6.134}$$

$$\begin{aligned}&= \frac{\rho_{\max}^2}{2}\Big\{\left(c_J^{(2)}\right)^2\left[J_1^2(\tilde{x}) - J_0(\tilde{x})J_2(\tilde{x})\right] + \left(c_Y^{(2)}\right)^2\left[Y_1^2(\tilde{x}) - Y_0(\tilde{x})Y_2(\tilde{x})\right] \\ &\qquad - c_J^{(2)}c_Y^{(2)}\left[J_0(\tilde{x})Y_2(\tilde{x}) - 2J_1(\tilde{x})Y_1(\tilde{x}) + J_2(\tilde{x})Y_0(\tilde{x})\right]\Big\} + \widetilde{N}^{(2)},\end{aligned} \tag{6.135}$$

$$\lim_{k_\rho\to k'_\rho}\check{\delta}^{(3)} = \frac{\rho_{\max}^2}{2}\left\{\left[c_J^{(3)}J_0(\tilde{x}) + c_Y^{(3)}Y_0(\tilde{x})\right]^2 + \left[c_J^{(3)}J_1(\tilde{x}) + c_Y^{(3)}Y_1(\tilde{x})\right]^2\right\} + \widetilde{N}^{(3)} \tag{6.136}$$

$$\begin{aligned}&= \frac{\rho_{\max}^2}{2}\Big\{\left(c_J^{(3)}\right)^2\left[J_0^2(\tilde{x}) + J_1^2(\tilde{x})\right] + \left(c_Y^{(3)}\right)^2\left[Y_0^2(\tilde{x}) + Y_1^2(\tilde{x})\right] \\ &\qquad + 2c_J^{(3)}c_Y^{(3)}\left[J_0(\tilde{x})Y_0(\tilde{x}) + J_1(\tilde{x})Y_1(\tilde{x})\right]\Big\} + \widetilde{N}^{(3)},\end{aligned} \tag{6.137}$$

where $\tilde{x} \equiv k'_\rho\rho_{\max}$ and the $c_J^{(n)}$, $c_Y^{(n)}$ are to be evaluated at k'_ρ. The $\widetilde{N}^{(n)}$ do not scale with $\rho_{\max}$ and vanish in the limit $\rho_{\max} \to \infty$. They are relevant for the normalization of the

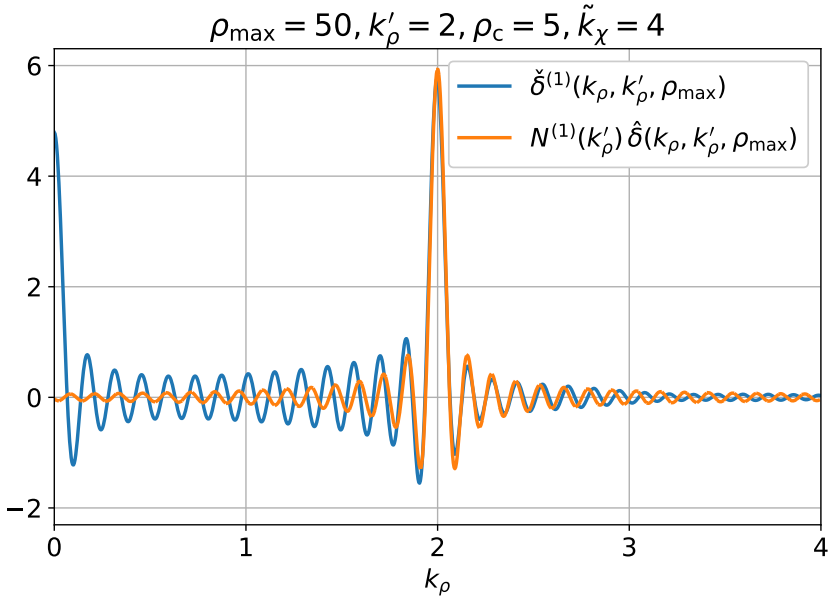

Figure 6.7: Approximation of Eq. (6.131) through the RHS of Eq. (6.122) for $n = 1$. The delta-function representation from Eq. (6.128) has been used, while normalization factor is taken from Eq. (6.138). Already at $\rho_{\max} = 50$, the approximation follows $\check{\delta}^{(1)}$ very closely around $k'_\rho = 2$ and is eventually identical in the limit $\rho_{\max} \to \infty$.

discrete spectrum and will be discussed in Sec. 6.1.13, but are dropped for now. With the leading terms of Eqs. (A.98) and (A.99), one can easily verify that all terms in the square brackets of Eqs. (6.133), (6.135) and (6.137) that are multiplied with the square of $c_J^{(n)}$ or $c_Y^{(n)}$ can for large $\rho_{\max}$ be approximated via $2/(\pi\tilde{x})$. The remaining terms, proportional to $c_J^{(n)} c_Y^{(n)}$, vanish in the same limit. Finally, Eq. (6.130) is evaluated:

$$N^{(1)}(k'_\rho) = \lim_{\rho_{\max}\to\infty} \frac{\pi}{\rho_{\max}} \left\{ \frac{\rho_{\max}^2}{2} \left[\left(c_J^{(1)}\right)^2 \frac{2}{\pi\tilde{x}} + \left(c_Y^{(1)}\right)^2 \frac{2}{\pi\tilde{x}} \right] \right\} = \frac{1}{k'_\rho} \left[\left(c_J^{(1)}\right)^2 + \left(c_Y^{(1)}\right)^2 \right], \tag{6.138}$$

which is consistent with Eq. (6.115). Similar results are obtained for the remaining two normalization factors so that generally

$$N^{(n)}(k'_\rho) = \frac{1}{k'_\rho} \left[\left(c_J^{(n)}\right)^2 + \left(c_Y^{(n)}\right)^2 \right], \tag{6.139}$$

These results have already been used in Fig. 6.5 for the dotted black lines in the inserts that show the step size as calculated with Eq. (6.139). As previously mentioned, this second approach, based on Eq. (6.130), offers a more direct method, while the introduction of the discrete spectrum is not as apparent.

6.1.11 Discrete spectrum

As discussed in Sec. 6.1.10.1 and demonstrated in Fig. 6.6, one needs to introduce a finite set of complex-valued frequencies, hereafter referred to as $k^\star_\rho$, to enable a complete expansion. It has been shown how the continuous spectrum emerges from the $j_{(1),n}$ in the limit $\rho_{\max} \to \infty$. Yet, the behavior of the $j^\star_{(1),n}$ in the same limit requires separate attention. The *complete* set of frequencies in the Fourier-Bessel series (both real and complex-valued) was defined

by Eq. (6.108). The equivalent requirement for an infinite domain reads

$$\lim_{\rho\to\infty} R^{(n)}\big(k_\rho,\rho\big) = 0. \tag{6.140}$$

As has been mentioned towards the end of Sec. 6.1.10.1, the continuous spectrum $k'_\rho \in (0,\infty)$ is strictly on the real axis, which follows from Eq. (6.140). In particular Eqs. (6.66), (6.80) and (6.88) are superpositions of $J_\nu(k'_\rho\rho)$ and $Y_\nu(k'_\rho\rho)$, which both vanish for positive and real valued k'_ρ, if $\rho\to\infty$. Still, complex-valued $k^\star_\rho$ can also satisfy Eq. (6.140). For $\tilde{k}_\chi > 0$, these were solely on the imaginary axis, where $k^\star_\rho$ is adjusted so that $c_I^{(n)}$, and thus the exponentially increasing part, vanishes. Here, the more general $\tilde{k}_\chi \in \mathbb{C}$ is considered together with the assumption that $\Im(\tilde{k}_\chi) < 0$. The principle is that $J_\nu(k^\star_\rho\rho)$ and $Y_\nu(k^\star_\rho\rho)$, which are individually dominated by an exponential increase, can be superimposed so that only the exponentially decreasing part remains. For this purpose, the asymptotic expansions of the Bessel functions (see Eqs. (A.98) and (A.99)) are considered, which are valid for large complex-valued arguments $z = k^\star_\rho\rho = x + iy$. In this representation, one can split the sine and cosine terms of Eqs. (A.98) and (A.99) into an exponentially increasing part $\acute{e}_\nu(z)$ and an exponentially decreasing part $\grave{e}_\nu(z)$:

$$\begin{aligned}\cos\Big(z-\frac{\pi}{4}-\nu\frac{\pi}{2}\Big) &= \underbrace{\exp\Big[i\Big(x-\frac{\pi}{4}-\nu\frac{\pi}{2}\Big)\Big]\frac{\exp(-y)}{2}}_{\grave{e}_\nu(z)} + \underbrace{\exp\Big[-i\Big(x-\frac{\pi}{4}-\nu\frac{\pi}{2}\Big)\Big]\frac{\exp(y)}{2}}_{\acute{e}_\nu(z)}\\ &= \grave{e}_\nu(z) + \acute{e}_\nu(z),\end{aligned} \tag{6.141}$$

$$\sin\Big(z-\frac{\pi}{4}-\nu\frac{\pi}{2}\Big) = -i\grave{e}_\nu(z) + i\acute{e}_\nu(z), \tag{6.142}$$

which are also scaled with a complex oscillating term, depending on x. In anticipation of the results and consistency with Sec. 6.1.10.1, it has been assumed that the imaginary part of $\Im(k^\star_\rho\rho) = y > 0$, which is tied to the previous assumption, i.e. $\Im(\tilde{k}_\chi) < 0$. Otherwise, $\acute{e}_\nu(z)$ and $\grave{e}_\nu(z)$ would be inverted. At this stage, one can give the asymptotic approximation for the superposition of the Bessel functions in Eqs. (6.66), (6.80) and (6.88) using Eqs. (A.98) and (A.99) in combination with Eqs. (6.141) and (6.142):

$$\begin{aligned}c_J^{(n)}J_\nu(z) + c_Y^{(n)}Y_\nu(z) &\sim c_J^{(n)}\sqrt{\frac{2}{\pi z}}\Big\{\big[\grave{e}_\nu(z)+\acute{e}_\nu(z)\big]\overline{p}_\nu(z) - \big[-i\grave{e}_\nu(z)+i\acute{e}_\nu(z)\big]\widetilde{p}_\nu(z)\Big\}\\ &\quad + c_Y^{(n)}\sqrt{\frac{2}{\pi z}}\Big\{\big[-i\grave{e}_\nu(z)+i\acute{e}_\nu(z)\big]\overline{p}_\nu(z) + \big[\grave{e}_\nu(z)+\acute{e}_\nu(z)\big]\widetilde{p}_\nu(z)\Big\}\\ &= \sqrt{\frac{2}{\pi z}}\Big\{\overline{p}_\nu(z)\Big[\Big(c_J^{(n)}-ic_Y^{(n)}\Big)\grave{e}_\nu(z) + \Big(c_J^{(n)}+ic_Y^{(n)}\Big)\acute{e}_\nu(z)\Big]\\ &\quad + i\widetilde{p}_\nu(z)\Big[\Big(c_J^{(n)}-ic_Y^{(n)}\Big)\grave{e}_\nu(z) - \Big(c_J^{(n)}+ic_Y^{(n)}\Big)\acute{e}_\nu(z)\Big]\Big\}\end{aligned} \tag{6.143}$$

The re-bracketing in the second step reveals that the exponentially increasing contributions from $\acute{e}_\nu(z)$ vanish under the following condition:

$$\boxed{c_J^{(n)} + ic_Y^{(n)} = 0} \tag{6.144}$$

Thereby, the eigenfunctions are dominated by an exponential decrease so that Eq. (6.140) is satisfied and thus also normalizable. In order to solve Eq. (6.144), one needs to adjust k_ρ. The details are presented in the following section.

6.1.12 Calculation of the discrete spectrum

It is not trivial to determine the sets of $k_\rho^\star$, that are defined as the solutions of Eq. (6.144). Numerical methods and approximations are necessary, which will be motivated in the following for the case $n = 1$. The analytical expressions for all $n = \{1, 2, 3\}$ are summarized in Table A.1.

For simplicity, $\tilde{k}_\chi > 0$ is considered initially. From Sec. 6.1.10.1 and Fig. 6.6, it is known that the $k_\rho^\star$ are in this case purely imaginary, hence $k_\rho \to ik_\rho''$ is considered. Also, by splitting Eq. (6.144) into its real and imaginary part, one needs to solve

$$\Re\Big[c_J^{(1)}\Big] = \Im\Big[c_Y^{(1)}\Big], \qquad (6.145) \qquad\qquad \Im\Big[c_J^{(1)}\Big] = -\Re\Big[c_Y^{(1)}\Big]. \qquad (6.146)$$

Using Eqs. (A.92) and (A.93), it follows that Eq. (6.146) is satisfied by definition. Since the RHS of Eq. (6.145) vanishes, it reduces to

$$\Re\Big[c_J^{(1)}\Big] = -z''J_1(z'')K_0(x'') + x''J_0(z'')K_1(x'') = 0 \qquad (6.147)$$

$$\approx \frac{\exp(-x'')}{\sqrt{x''z''}}\left[x''\cos\Big(z'' - \frac{\pi}{4}\Big) - z''\sin\Big(z'' - \frac{\pi}{4}\Big)\right], \qquad (6.148)$$

where $x'' = k_\rho''\rho_\mathrm{c}$ as in Eq. (6.64) and $z'' = \sqrt{\tilde{k}_\chi^2 - k_\rho''^2}\rho_\mathrm{c}$ as in Eq. (6.119). For the approximation in the second step, Eqs. (A.103), (A.104) and (A.108) have been used. All quantities involved in Eq. (6.147), except for $J_0(z'')$ and $J_1(z'')$, are larger than zero for $k_\rho'' < \tilde{k}_\chi$ so that Eq. (6.147) can only vanish if $J_0(z'')$ and $J_1(z'')$ have the same sign, which is true if z'' is larger than a root of J_1 but smaller than the subsequent root of J_0. New solutions are created around $k_\rho'' = 0$ as $\tilde{k}_\chi$ rises. They can be approximated by calculating the root of the low-order approximation of Eq. (6.144) around the origin (see the third and fourth row of Table A.1):

$$c_J^{(1)} + ic_Y^{(1)} \approx J_0(\tilde{x}) + \tilde{x}J_1(\tilde{x})\left[\log\Big(-i\frac{x}{2}\Big) + \gamma\right] \quad \Leftrightarrow \quad k_\rho^\star \approx \frac{2i}{\rho_\mathrm{c}}\exp\left[-\frac{J_0(\tilde{x})}{\tilde{x}J_1(\tilde{x})} - \gamma\right], \quad (6.149)$$

where $\tilde{x} = \tilde{k}_\chi\rho_\mathrm{c}$ and γ is the Euler–Mascheroni constant. It follows that $k_\rho^\star$ can get exponentially close to zero if $J_1(\tilde{x})$ is sufficiently small. It also applies to the more general case $\tilde{k}_\chi \in \mathbb{C}$, which will be addressed in the following. There, Eq. (6.148) is *not* satisfied by definition, so that one needs to revert to the definition from Eq. (6.144). Also, Eqs. (A.92) and (A.93) are not helpful, since the solutions $k_\rho^\star$ are not purely imaginary anymore. Yet, a computational issue arises for large $\tilde{k}_\chi$. Since both constants are proportional to the Bessel functions ($c_J^{(1)}, c_Y^{(1)} \propto J_\alpha, Y_\alpha$), their magnitude scales with both $e^{\pm ik_\rho\rho_\mathrm{c}}$ and thus increases exponentially along the imaginary axis. However, their superposition, i.e. Eq. (6.144), decreases exponentially, as already apparent in Eq. (6.148). For k_ρ with large imaginary parts, the difference between the addends and the result can exceed 15 orders of magnitude and thus the float precision. One can overcome this issue by re-bracketing Eq. (6.144) with the definition from Eqs. (6.62) and (6.63) so that the exponential rise in the complex plane cancels:

$$\begin{aligned} c_J^{(1)} + ic_Y^{(1)} =& \frac{\pi}{2}\Big[yJ_1(y)Y_0(x) - xJ_0(y)Y_1(x)\Big] + i\frac{\pi}{2}\Big[xJ_0(y)J_1(x) - yJ_0(x)J_1(y)\Big] \\ =& \frac{i\pi}{2}\Big\{xJ_0(y)\underbrace{\big[J_1(x) + iY_1(x)\big]}_{H_1^{(1)}(x)} - yJ_1(y)\underbrace{\big[J_0(x) + iY_0(x)\big]}_{H_0^{(1)}(x)}\Big\}, \end{aligned} \qquad (6.150)$$

where the so-called *Hankel function* (see Eq. (A.94)) has been introduced. From its asymptotic behavior (Eq. (A.109)) follows the aforementioned exponential decrease, which now also applies to both addends. Note that Eq. (6.150) is also the equivalent of Eq. (6.147). Likewise, an equivalent of Eq. (6.148), that is valid for complex-valued $k_\rho^\star$, is sought. Using Eqs. (A.103), (A.104) and (A.109) in combination with Eq. (6.150) one obtains

$$c_J^{(1)} + ic_Y^{(1)} \sim \frac{e^{i(x-\pi/4)}}{\sqrt{xy}} \left[x\cos\left(y - \frac{\pi}{4}\right) - iy\sin\left(y - \frac{\pi}{4}\right) \right] \equiv \tilde{c}_J^{(1)} + i\tilde{c}_Y^{(1)}. \tag{6.151}$$

The validity of Eq. (6.151) is demonstrated in Fig. 6.8 (a)-(d). Analogous re-bracketing and approximations as in Eqs. (6.150) and (6.151) are possible for all n and are given in the first two rows of Table A.1. By evaluating Eq. (6.151) along the imaginary axis, so that $x \to ix''$ and $y \to z''$, one recovers Eq. (6.148). (The complex unit vanishes via $e^{-i\pi/4} i^{-1/2} i = 1$). Yet, Eq. (6.151) is now also valid along arbitrary complex-valued k_ρ-paths and allows a computationally efficient approximation. It is used to generate a set of initial guesses that are further improved via a dedicated root-finding algorithm, e.g. the Newton–Raphson method [299].

Just like Eq. (6.116), Eq. (6.150) decreases exponentially along the imaginary axis. It cannot necessarily be seen in Fig. 6.8 though, with its relatively low exemplary parameters. Recall that Eq. (6.116) required an exponential scaling of the type $e^{-k_\rho(\rho_{\max}-\rho_c)}$, as shown in the insert of Fig. 6.6. It is computationally advantageous to rescale Eq. (6.150) and its approximation from Eq. (6.151) with e^{-ix} so that their magnitude remains approximately constant in the vicinity of $k_\rho^\star$. For Eq. (6.151) one only needs to remove the e^{ix} factor, while one can use the exponentially scaled Hankel functions for Eq. (6.150) [300]. Certainly, this has no impact on the roots $k_\rho^\star$.

In Sec. 6.1.10.1, where $\tilde{k}_\chi > 0$ has been considered, it has been argued that the $k_\rho^\star$ are on the imaginary axis within the interval $0 \leq k_\rho^\star \leq i\tilde{k}_\chi$. To see how the $k_\rho^\star$ change for $\tilde{k}_\chi \in \mathbb{C}$, consider adding a small and negative imaginary part to the initially real-valued $\tilde{k}_\chi$ or correspondingly $\tilde{x}$ as $\tilde{x} \to \tilde{x} - i\tilde{\epsilon}$. Recall that the imaginary part is negative ($\tilde{\epsilon} > 0$) since $\tilde{k}_\chi \propto \tilde{\varepsilon}$, which has a negative imaginary part for positive frequencies ω. Assuming $x^\star = k_\rho^\star \rho_c$ solves Eq. (6.144) with the initially real-valued $\tilde{x}$, it is estimated how much $x^\star$ needs to change so that Eq. (6.144) is still satisfied: $x^\star \to x^\star + \epsilon^\star$. For this purpose, Eq. (6.151) is expanded with respect to $\tilde{\epsilon}$ and $\epsilon^\star$ around zero and solved for $\epsilon^\star$. With $x^\star$ being a root, it is sufficient to focus on the expression in the square brackets of Eq. (6.151):

$$\epsilon^\star = \frac{\tilde{\epsilon}}{\tilde{x}} \frac{\tilde{x}^2 - ix^\star}{1 - ix^\star}.$$

Since $x^\star$ was (initially) purely imaginary and $\tilde{x} > 0$, the infinitesimal change of $x^\star$ is positive and real $\epsilon^\star > 0$. In other words, the $k_\rho^\star$ move into the upper right quadrant of the complex plane. Together with the aforementioned requirement from Sec. 6.1.10.1 (that now applies to the imaginary part of $k_\rho^\star$ only) the following domain for the $k_\rho^\star$ is obtained:

$$\Re[k_\rho^\star] \geq 0, \tag{6.152}$$

$$0 \leq \Im[k_\rho^\star] \leq \Re[\tilde{k}_\chi]. \tag{6.153}$$

Though it has been attempted to motivate Eqs. (6.152) and (6.153), they remain somewhat empirical. A more rigorous analysis lies beyond the scope of this work. Nonetheless, they have been used to narrow the search domain of the $k_\rho^\star$ for all n. With the numerical examples regarding the completeness below, a $k_\rho^\star$ outside of Eqs. (6.152) and (6.153) has not been identified.

The representation in Fig. 6.8 (a)-(d) and specifically the contour lines at zero reveal that the real and imaginary part of Eq. (6.150) are individually solved along continuous

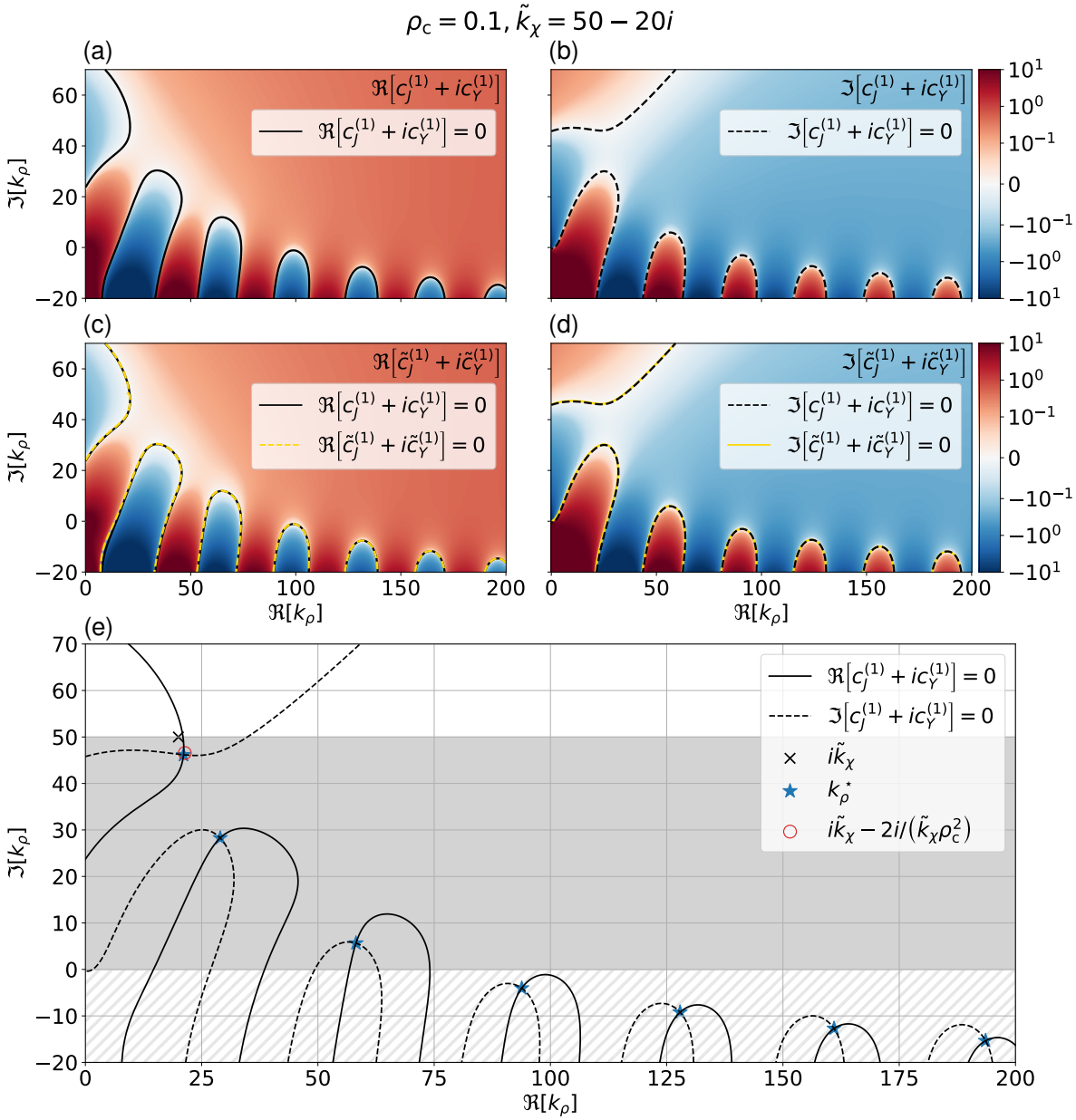

Figure 6.8: The upper panels (a)-(d) show a comparison between Eq. (6.150) and its asymptotic approximation from Eq. (6.151). They have been evaluated in the complex k_ρ-plane and split into real part (left) and imaginary part (right) and are represented in a symmetric logarithmic scale. The (arbitrarily) chosen parameters are given above. Contour lines have been added and are compared in the lower two panels. Only slight deviations of the contours on the edges of the depicted domain are visible, which confirms the validity of Eq. (6.151). Panel (e) superimposes the contour lines from (a) & (b), where the intersections (blue stars) are the solutions of Eq. (6.144).

lines. Yet, to satisfy Eq. (6.144), both need to vanish so that the intersections of the contour lines constitute the sought $k_\rho^\star$. Accordingly, the contour lines of Fig. 6.8 (a)-(b) have been superimposed in Fig. 6.8 (e) with their intersections highlighted. Also, Eqs. (6.152) and (6.153) are indicated with a gray box. On a side-note, even though it may appear in Fig. 6.8 (e) that there are no $k_\rho^\star$ to the left of $i\tilde{k}_\chi$, one can find counterexamples for lower $\tilde{k}_\chi$-values. $\Im[k_\rho^\star] > 0$ from Eq. (6.153) has been introduced due to the assumption that followed Eqs. (6.141) and (6.142). It is not a criterion that follows from Eq. (6.144), as there exist solutions with a negative imaginary part (see Fig. 6.8 (e)). These solutions are special in the sense that they increase, instead of decrease, purely exponentially. Consequently, they cannot be normalized and are not of interest in this context.

With $i\tilde{k}_\chi$ lying on the upper edge of the domain specified in Eqs. (6.152) and (6.153) and that y vanishes for $k_\rho = i\tilde{k}_\chi$, a low-order approximation and its approximate $k_\rho^\star$ is relatively simple:

$$c_j^{(1)} + ic_Y^{(1)} \approx -\tilde{x}/2\big(ix\tilde{x} + \tilde{x}^2 - 2\big)K_1(\tilde{x}) \quad \Leftrightarrow \quad k_\rho^\star \approx i\tilde{k}_\chi - 2i/\big(\tilde{k}_\chi \rho_\mathrm{c}^2\big). \tag{6.154}$$

The equivalents for the remaining n are given in the last two columns of Table A.1. The latter is an estimate for the solution with the largest imaginary part. From $i\tilde{k}_\chi$ one subtracts $2i/(\tilde{k}_\chi\rho_\mathrm{c}^2)$ so that it provides some justification that the $k_\rho^\star$ are below the horizontal $\Im[i\tilde{k}_\chi]$-line. It is also shown in Fig. 6.8 (e). The approximation can only be accurate, if $k_\rho^\star$ is sufficiently close to $i\tilde{k}_\chi$, which is given if $|\tilde{k}_\chi\rho_\mathrm{c}| \gg 1$. It also follows that the first $k_\rho^\star$ moves closer to $i\tilde{k}_\chi$ as $\tilde{k}_\chi$ rises with the frequency. This needs to be taken into account regarding the sampling rate, while evaluating Eq. (6.151), when a set of initial guesses is sought. Also, the spacing between the $k_\rho^\star$ impacts the sampling. For large k_ρ, the arguments of cos and sin in Eq. (6.151) are approximately $y \sim x$. It follows that the $k_\rho^\star$ are approximately vertically spaced by π/ρ_c. This estimate improves as $k_\rho^\star$ increases, as apparent in Fig. 6.8 (e).

For the case $n = 2$, the low-order approximation around $k_\rho = i\tilde{k}_\chi$ (like Eq. (6.154)) reveals the trivial solution $k_\rho^\star = i\tilde{k}_\chi$. It is discarded since its base function vanishes everywhere. Also, the approximation around $k_\rho = 0$ is too complicated and does not offer a simple estimate of $k_\rho^\star$. For $n = \{2,3\}$, the equivalent of Fig. 6.8 (e) is shown in Fig. 6.9. Upon comparison, there are considerably more solutions, despite otherwise equal parameters. Accordingly, the range on the real axis is twice as large. This can be explained by the fact that Eqs. (6.80) and (6.88) (see Figs. 6.3 and 6.4) are not continuous at ρ_c anymore, unlike Eq. (6.66) (see Fig. 6.2). The discontinuity can "kick" $R^{(2,3)}$ into an exponentially decreasing solution, even if the derivative of the inner part is initially too steep.

6.1.13 Normalization for the discrete spectrum

The contributions from the discrete spectrum also need to be normalized with respect to the inner product from Eq. (6.91). It was generally evaluated Eq. (6.131) and specifically given in Eqs. (6.132), (6.134) and (6.136). It has been found that the normalization rises to infinity at $k_\rho = k_\rho'$, which is only mathematically rigorous with a continuous spectrum and a delta-like behavior. For the discrete contributions, this is not the case anymore, i.e. the normalization is finite. To see this, recall that the $k_\rho^\star$ are defined such that the superposition of Bessel functions of $R^{(n)}$ for large radii vanishes exponentially fast (see Eq. (6.143)). The square of the same superposition and its derivative (without the k_ρ'-factor) is present in Eqs. (6.132) and (6.136) so that the $\rho_\mathrm{max}^2/2$-terms vanish as the quadratic rise is suppressed. For Eq. (6.134), the first term is again the squared superposition for the $n = 2$-case, but the second term is not a straightforward derivative. In order to argue, that its $\rho_\mathrm{max}^2/2$-term also vanishes for the discrete frequencies, the following identities are

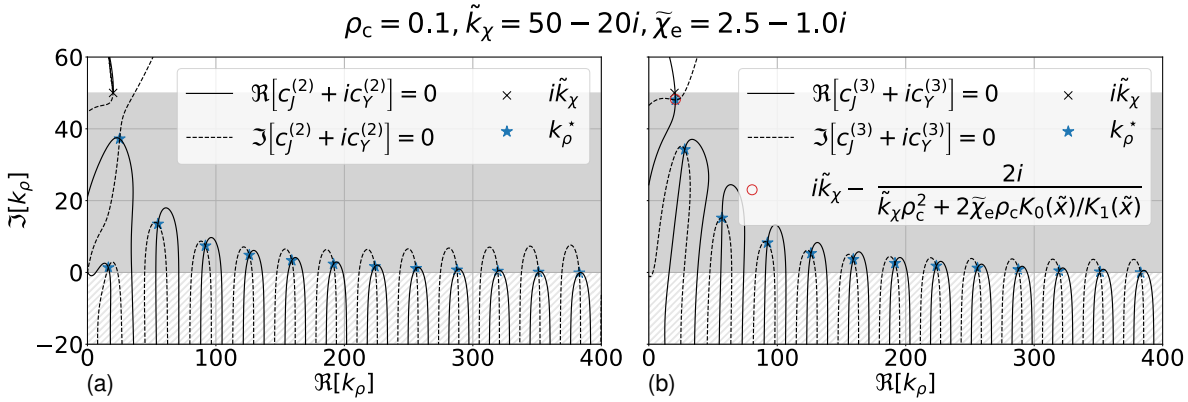

Figure 6.9: Solutions of Eq. (6.144) for (a) $n = 2$ and (b) $n = 3$. When both the real part (solid lines) and the imaginary part (dashed lines) vanish, Eq. (6.144) is satisfied (blue stars). The rightmost solution is the first one with a negative imaginary part and thus lies in the excluded zone. The approximate $k_\rho^\star$ for $n = 3$ (red circle) is also given in Table A.1.

necessary: $\partial_\rho[\rho W_1(\rho)] = \rho W_0(\rho)$ and $\partial_\rho[1/\rho W_1(\rho)] = -1/\rho W_2(\rho)$. With this perspective, the second term in the curly brackets of Eq. (6.134) is proportional to the product of the "scaled" derived superpositions, i.e. multiplied with ρ and $1/\rho$. Thereby, the exponential fall-off also dominates and the $\rho_{\max}^2/2$-term vanishes. A more straightforward, but potentially misleading argument is that the continuous normalization factors (see Eq. (6.139)), which were all derived from the $\rho_{\max}^2/2$-terms of Eqs. (6.132), (6.134) and (6.136) are proportional to

$$\left(c_J^{(n)}\right)^2 + \left(c_Y^{(n)}\right)^2 = \left(c_J^{(n)} - ic_Y^{(n)}\right)\left(c_J^{(n)} + ic_Y^{(n)}\right). \tag{6.155}$$

The RHS contains the requirement from Eq. (6.144) and therefore $N^{(n)}$ vanish as well. Yet, the $N^{(n)}$ have been derived with the simplified asymptotic expansions from Eqs. (A.103) to (A.106) which are not valid for the complex-valued $k_\rho^\star$. However, a more detailed evaluation should validate this approach as well.

In both cases, the previously neglected $\widetilde{N}^{(n)}$ remain, which are now explicitly given and further simplified with Eqs. (6.62), (6.63), (6.78), (6.79), (6.89) and (6.90):

$$\begin{aligned}\widetilde{N}^{(1)} &= \frac{\rho_c^2}{2}\left\{J_0^2(y) + J_1^2(y) - \left[c_J^{(1)}J_0(x) + c_Y^{(1)}Y_0(x)\right]^2 - \left[c_J^{(1)}J_1(x) + c_Y^{(1)}Y_1(x)\right]^2\right\} \\ &= \frac{\rho_c^2}{2}\,\frac{x^2 - y^2}{x^2}\,J_1^2(y),\end{aligned} \tag{6.156}$$

$$\begin{aligned}\widetilde{N}^{(2)} &= \frac{\rho_c^2}{2}\Big\{e^{-\eta}\left[J_1^2(y) - J_0(y)J_2(y)\right] - \left[c_J^{(2)}J_1(x) + c_Y^{(2)}Y_1(x)\right]^2 \\ &\qquad + \left[c_J^{(2)}J_0(x) + c_Y^{(2)}Y_0(x)\right]\left[c_J^{(2)}J_2(x) + c_Y^{(2)}Y_2(x)\right]\Big\} \\ &= \frac{\rho_c^2}{2}\left\{e^{-\eta}\,\frac{x^2 - e^{-\eta}y^2}{x^2}\,J_0^2(y) + (e^{-\eta} - 1)\,J_1^2(y) - e^{-\eta}\,\frac{x^2 - y^2}{x^2}\left[J_0^2(y) + J_0(y)J_2(y)\right]\right\},\end{aligned} \tag{6.157}$$

$$\begin{aligned}\widetilde{N}^{(3)} &= \frac{\rho_c^2}{2}\left\{e^{\eta}\left[J_0^2(y)+J_1^2(y)\right]-\left[c_J^{(3)}J_0(x)+c_Y^{(3)}Y_0(x)\right]^2-\left[c_J^{(3)}J_1(x)+c_Y^{(3)}Y_1(x)\right]^2\right\}\\ &= \frac{\rho_c^2}{2}\left[e^{\eta}\frac{x^2-e^{\eta}y^2}{x^2}J_1^2(y)+\left(e^{\eta}-1\right)J_0^2(y)\right].\end{aligned} \tag{6.158}$$

These are the sought normalization factors for the discrete eigenfunctions

$$\widetilde{N}^{(n)}(k_\rho^\star)=\int_0^\infty\left[R^{(n)}(k_\rho^\star,\rho)\right]^2 w^{(n)}(\rho)\mathrm{d}\rho, \tag{6.159}$$

which are only finite (and complex-valued) if $k_\rho^\star$ indeed solve Eq. (6.144).

A computational issue occurs during the evaluation of $R^{(n)}(k_\rho^\star,\rho)$, which arises from the fact that the $k_\rho^\star$ can only be determined with a finite and at most float precision. Consequently, Eq. (6.144) cannot be solved perfectly so that

$$\left|c_J^{(n)}+ic_Y^{(n)}\right|\leq t, \tag{6.160}$$

where t is the chosen tolerance from the Newton-Raphson root finder and in the order of 10^{-12}. Simultaneously, the second terms in the square brackets of Eq. (6.143) do not vanish, so their influence is gauged by calculating the absolute ratio to the first term:

$$r=\left|\left(c_J^{(n)}+ic_Y^{(n)}\right)\acute{e}_\nu(k_\rho^\star\rho)\right|\Big/\left|\left(c_J^{(n)}-ic_Y^{(n)}\right)\grave{e}_\nu(k_\rho^\star\rho)\right| = t\Big/\left|c_J^{(n)}-ic_Y^{(n)}\right|e^{2\Im(k_\rho^\star)\rho}. \tag{6.161}$$

To ensure that the exponentially decreasing term dominates, $r=10^{-6}\ll 1$ has been chosen, which yields the threshold radius

$$\rho_{\mathrm{thr}}=\frac{1}{2\Im(k_\rho^\star)}\log\left[\left|c_J^{(n)}-ic_Y^{(n)}\right|r\Big/t\right], \tag{6.162}$$

up to which $R^{(n)}$ can be used. Beyond ρ_{thr}, Eq. (6.143) is used without the $\acute{e}_\nu$-term, where it has been assumed that Eq. (6.144) is perfectly solved. The polynomials $\overline{p}_\nu$ and $\widetilde{p}_\nu$ were expanded up to and including the third order. The necessity and the quality of the approximation is demonstrated in Fig. 6.10.

6.1.14 Combined completeness relation

The aim of this last subsection is to provide the combined completeness statement along with some numerical tests. As already formally stated in Eq. (6.123), the completeness relation is given by

$$\boxed{\frac{\delta(\rho-\rho')}{w^{(n)}(\rho')}=\underbrace{\int_0^\infty\frac{\mathrm{d}k_\rho}{N^{(n)}(k_\rho)}R^{(n)}(k_\rho,\rho')R^{(n)}(k_\rho,\rho)}_{\equiv\delta^{(n)}_{\mathrm{cont.}}(\rho,\rho')}+\underbrace{\sum_{k_\rho^\star}\frac{1}{\widetilde{N}^{(n)}(k_\rho^\star)}R^{(n)}(k_\rho^\star,\rho')R^{(n)}(k_\rho^\star,\rho)}_{\equiv\delta^{(n)}_{\mathrm{disc.}}(\rho,\rho')},} \tag{6.163}$$

which has been separated into the discrete and continuous spectrum. Generally, a mixed spectrum, with discrete and continuous contributions, cannot necessarily be found in the standard literature. It is briefly mentioned in Sec. 5.2.4 of [294] or discussed in mathematical

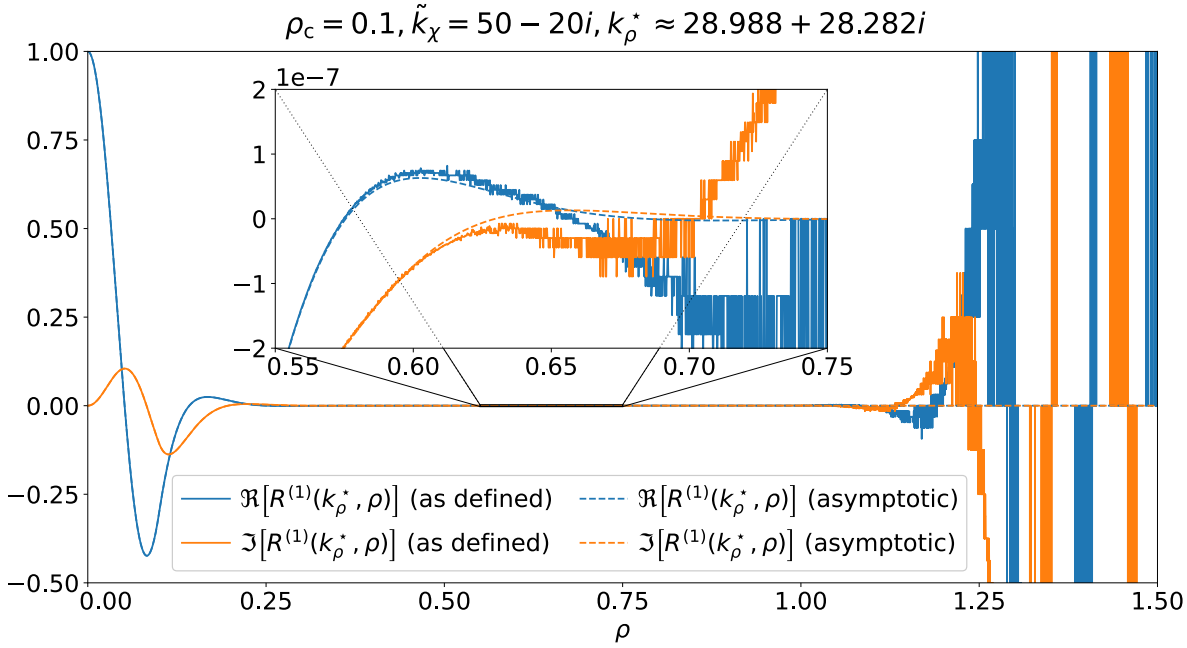

Figure 6.10: Computational issues regarding the evaluation of the discrete base function. $R^{(1)}$ as defined in Eq. (6.66) is compared to the computationally more stable approach, where $R^{(1)}$ is replaced with Eq. (6.143) for $\rho > \rho_{\text{thr}}$ from Eq. (6.162). In the present example, the $k_\rho^\star$-value (given above the plot and also shown in Fig. 6.8 (e) as the second solution from the left) has been calculated to high accuracy, i.e. $t \approx 4 \times 10^{-15}$ (see Eq. (6.160)), which is close to the limit of the float precision. Yet, the remaining deviation eventually leads to large inaccuracies for $\rho > 1$. One can also use Eq. (6.162) to determine the ρ-value, where Eq. (6.66) becomes too inaccurate. When $r = 1$ (from Eq. (6.161)), then the exponentially increasing and decreasing parts are equal in magnitude. With the present tolerance value, Eq. (6.162) states that for $\rho > 0.644$, Eq. (6.66) cannot be used anymore, which is approximately where Eq. (6.66) and Eq. (6.143) begin to deviate, as shown in the insert. With the more conservative tolerance value of $t = 10^{-12}$, and requiring a dominant exponential decrease ($r = 10^{-4}$), the threshold value of the present example is given by $\rho_{\text{thr}} \approx 0.385$, i.e. Eq. (6.143) has been used for $\rho > \rho_{\text{thr}}$ to plot the dashed graphs.

physics, when solving the Schrödinger equation [301]. For the numerical and visual confirmation, the incomplete contribution from the continuous spectrum with a finite upper integral limit shall be defined as:

$$\tilde{\delta}^{(n)}_{\text{cont.}}(\rho, \rho', k_\rho^{\max}) \equiv \int_0^{k_\rho^{\max}} \frac{\mathrm{d}k_\rho}{N^{(n)}(k_\rho)} R^{(n)}(k_\rho, \rho') R^{(n)}(k_\rho, \rho). \tag{6.164}$$

For the same purpose, its combination with the discrete spectrum and the integral with respect to ρ is introduced:

$$\tilde{\delta}^{(n)}_{\text{tot.}}(\rho, \rho', k_\rho^{\max}) \equiv \tilde{\delta}^{(n)}_{\text{cont.}}(\rho, \rho', k_\rho^{\max}) + \delta^{(n)}_{\text{disc.}}(\rho, \rho'), \tag{6.165}$$

$$\tilde{\theta}^{(n)}_{\text{tot.}}(\rho, \rho', k_\rho^{\max}) \equiv \int_0^{\rho} \tilde{\delta}^{(n)}_{\text{tot.}}(\rho'', \rho', k_\rho^{\max}) \mathrm{d}\rho''. \tag{6.166}$$

By definition, Eqs. (6.165) and (6.166) are consistent with Eq. (6.163) in the limit:

$$\lim_{k_\rho^{\max} \to \infty} \tilde{\delta}^{(n)}_{\text{tot.}}(\rho, \rho', k_\rho^{\max}) = \frac{\delta(\rho - \rho')}{w^{(n)}(\rho')}, \tag{6.167}$$

$$\lim_{k_\rho^{\max} \to \infty} \tilde{\theta}^{(n)}_{\text{tot.}}(\rho, \rho', k_\rho^{\max}) = \frac{\theta(\rho - \rho')}{w^{(n)}(\rho')}. \tag{6.168}$$

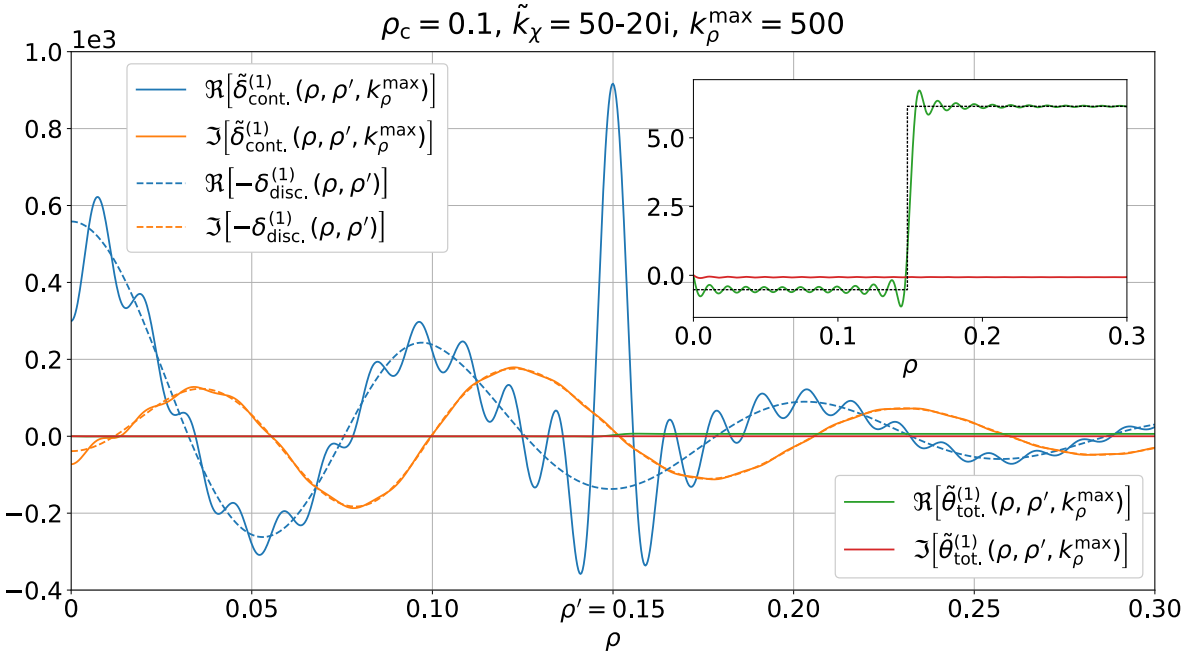

Figure 6.11: Completeness of $R^{(1)}$. The contributions from the incomplete continuous spectrum (Eq. (6.164)) and the discrete spectrum (defined in Eq. (6.163)) are shown separately. The negative of the latter has been shown so that one may observe how it flattens the real part of Eq. (6.164) and removes the imaginary part when properly added up as in Eq. (6.165). The result is the expected delta-function so that its integral (Eq. (6.166)) is a step function with a step size of $1/w^{(1)}(\rho') = 1/\rho' \approx 6.67$.

The completeness of $R^{(1)}$ is demonstrated in Fig. 6.11 with the same parameters as in Fig. 6.8 so that only three $k_\rho^\star$-values contribute to the sum of $\delta^{(1)}_{\text{disc.}}(\rho, \rho')$. The completeness of the remaining two cases, i.e. $n = \{2, 3\}$, is shown in Fig. 6.12.

6.1.15 Green's function

With the completeness relation in place, one can finally construct the sought Green's function according to Eq. (6.15). The previous sections were solely focused on the radial part $R^{(n)}$, yet at this stage the complete ansatz from Eq. (6.54) for the three-dimensional case is again considered. For $n = 1$, it fulfills $\left[\nabla^2 + \tilde{k}_\chi^2 \theta^+(\rho_c - \rho)\right] \psi^{(1)}_{\mathbf{k}} = -k^2 \psi^{(1)}_{\mathbf{k}}$, where the source-free Eq. (6.8) and Eq. (6.55) were combined. The defining equation of $R^{(1)}$ (see Eq. (6.57)) verifies the eigenvalue equation. Just as in Sec. 6.1.4, one can identify $\mathcal{L}^{(1)} = \nabla^2 + \tilde{k}_\chi^2 \theta^+(\rho_c - \rho)$ with the missing scalar $\lambda = -k_0^2$ and the eigenvalues $\lambda_n = -k^2 = -(k_\rho^2 + k_z^2)$. Analogous operators $\mathcal{L}^{(n)}$ can be identified for the remaining cases, yet the scalar as well as the eigenvalues remain the same. In analogy to Eq. (6.22), the Green's functions are constructed as follows

$$G^{(n)}(\mathbf{r}, \mathbf{r}') = \frac{1}{(2\pi)^3} \int_0^{2\pi} \mathrm{d}k_\phi \int_{-\infty}^{\infty} \mathrm{d}k_z \left[\int_0^{\infty} \frac{\mathrm{d}k_\rho}{N^{(n)}(k_\rho)} \frac{R^{(n)}(k_\rho, \rho') R^{(n)}(k_\rho, \rho)}{k_0^2 - (k_\rho^2 + k_z^2)} + \sum_{k_\rho^\star} \frac{1}{\widetilde{N}^{(n)}(k_\rho^\star)} \frac{R^{(n)}(k_\rho^\star, \rho') R^{(n)}(k_\rho^\star, \rho)}{k_0^2 - (k_\rho^{\star 2} + k_z^2)} \right] e^{ik_z(z - z')}. \quad (6.169)$$

For the correct application of Eq. (6.169), the defining property of the Green's function (Eq. (6.16)) is reconsidered. The more general equivalent is mentioned in the paragraph

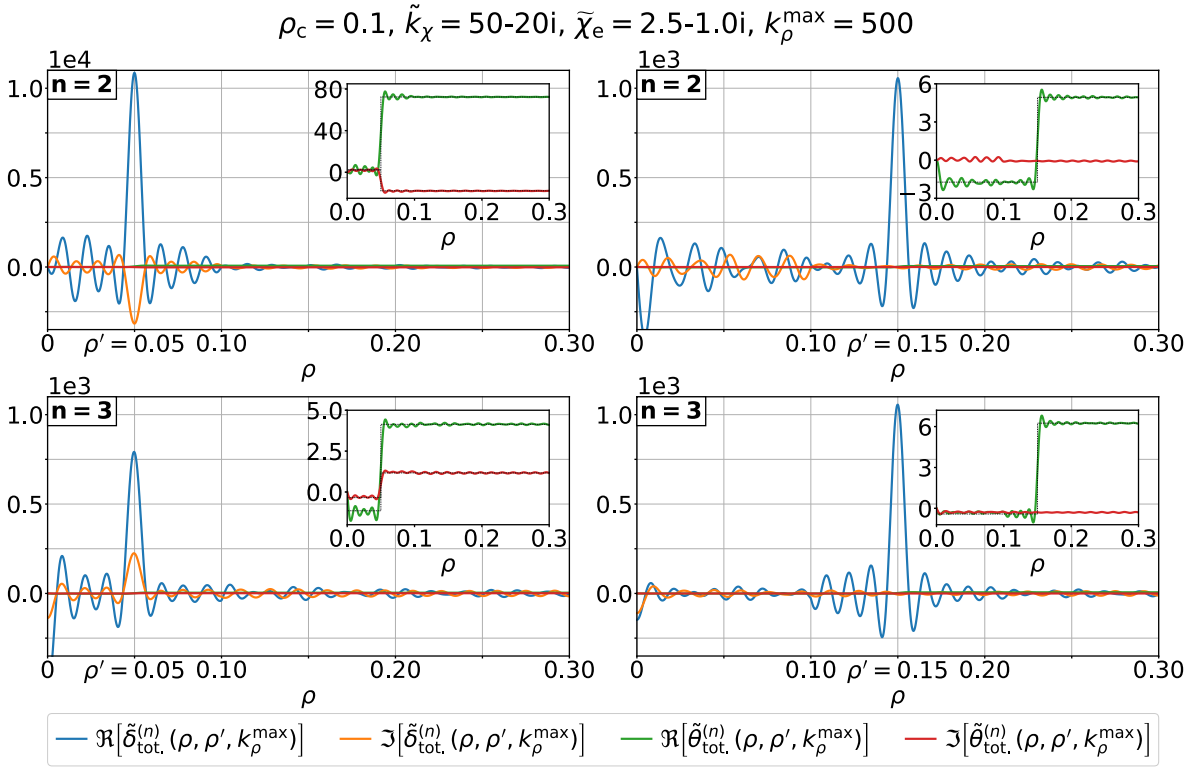

Figure 6.12: Completeness of $R^{(2)}$ and $R^{(3)}$. As opposed to Fig. 6.11, only Eqs. (6.165) and (6.166) without their separation into discrete and contributions are shown. For both $n = 2$ (upper two panels) and $n = 3$ (lower two panels) two ρ'-values are shown ($\rho' = 0.05$ (left) and $\rho' = 0.15$ (right)), since $w^{(n)}(\rho')$ is discontinuous at $\rho_c = 0.1$ for $n = \{2, 3\}$. In particular, the weights and therefore the step sizes in the inserts, change from $1/w^{(2)}(\rho' = 0.05) = (1 + \widetilde{\chi}_e)/\rho' = 70 - 20i$ and $1/w^{(3)}(\rho' = 0.05) = 1/[\rho'(1 + \widetilde{\chi}_e)] \approx 5.28 + 1.51i$ to $1/w^{(2,3)}(\rho' = 0.15) = 1/\rho' \approx 6.67$, which has been outlined by the dotted lines in the inserts.

above: $(\mathcal{L} - \lambda)G = I$, where I is the unity operator. Notably, it depends on the definition of the inner product, therefore one can calculate

$$\left(\mathcal{L}^{(n)} - \lambda\right) G^{(n)}(\mathbf{r}, \mathbf{r}') = \frac{1}{2\pi} \frac{\delta^+(\rho - \rho')}{w^{(n)}(\rho')} \delta(z - z'), \tag{6.170}$$

which follows from Eq. (6.163) and Eq. (6.23). By multiplying Eq. (6.170) with the source term $S(\mathbf{r}')$ and integrating it with respect to $\mathrm{d}^3\mathbf{r}'$, one can identify the solution of Eqs. (6.8) to (6.10)

$$f^{(n)}(\mathbf{r}) = \int_0^\infty w^{(n)}(\rho')\mathrm{d}\rho' \int_0^{2\pi} \mathrm{d}\phi' \int_{-\infty}^{\infty} \mathrm{d}z'\, G^{(n)}(\mathbf{r}, \mathbf{r}') S^{(n)}(\mathbf{r}'), \tag{6.171}$$

where $f^{(n)} = \{\widetilde{A}_z, \widetilde{A}_\rho, \widetilde{\varphi}\}$ and $S^{(n)}$ is a placeholder for the RHS of Eqs. (6.8) to (6.10). In summary, Eq. (6.169) needs to be applied with the weight function from the inner product in the spatial domain, as defined in Eq. (6.91). Yet, as it stands, Eq. (6.17) is not wrong. Only the volume element needs to be adjusted: $\mathrm{d}^3\mathbf{r}' = w^{(n)}(\rho')\mathrm{d}\rho'\mathrm{d}\phi'\mathrm{d}z'$.

The k_ϕ and k_z-integral in Eq. (6.169) can already be evaluated for an initial simplification:

$$G^{(n)}(\mathbf{r},\mathbf{r}') = \frac{1}{4\pi}\Bigg[\int_0^\infty \frac{\mathrm{d}k_\rho}{N^{(n)}(k_\rho)} R^{(n)}(k_\rho,\rho')R^{(n)}(k_\rho,\rho)\,\mathrm{E}(\hat{k}_z, z-z') + \sum_{k_\rho^\star} \frac{1}{\widetilde{N}^{(n)}(k_\rho^\star)} R^{(n)}(k_\rho^\star,\rho')R^{(n)}(k_\rho^\star,\rho)\,\mathrm{E}(\hat{k}_z^\star, z-z')\Bigg], \tag{6.172}$$

where Eq. (A.113) has been used for the evaluation of the k_z-integral and $\hat{k}_z^2 = k_0^2 - k_\rho^2$ and $\hat{k}_z^{\star 2} = k_0^2 - k_\rho^{\star 2}$. When one lets $\tilde{k}_\chi \to 0$ in Eq. (6.172), then it reduces to Eq. (6.35) for $n = \{1,3\}$ and to Eq. (6.43) for $n = 2$.

6.1.16 Formal solution and implementation of the potentials and fields

Finally, one can put together the solutions of the point particle fields. For convenience, the source terms from Eqs. (4.6) and (4.7) are reprinted, Fourier-time transformed via Eq. (A.3a) and represented in cylindrical coordinates:

$$\tilde{\rho}_\mathrm{f}(\mathbf{r},\omega) = q_\mathrm{e}\frac{\delta^+(\rho)}{2\pi\rho}\int_{-\infty}^\infty \frac{\mathrm{d}t'}{2\pi}\delta\big(z - f_z(t')\big)e^{-i\omega t'}, \tag{6.173}$$

$$\tilde{J}_z(\mathbf{r},\omega) = q_\mathrm{e}\frac{\delta^+(\rho)}{2\pi\rho}\int_{-\infty}^\infty \frac{\mathrm{d}t'}{2\pi}\dot{f}_z(t')\delta\big(z - f_z(t')\big)e^{-i\omega t'}. \tag{6.174}$$

The delta-functions in Eq. (6.173) and Eq. (6.174) collapse the volume integral of Eq. (6.171), as initially only a point-particle charge and current density is considered.

6.1.16.1 Longitudinal vector potential

From Eq. (6.8), one can identify the source term as $S^{(1)} = -\mu\tilde{J}_z$. It is situated at the origin ($\rho' = 0$), so when the $\mathrm{d}\rho'$-integral in Eq. (6.171) is evaluated, ρ' is set to zero in Eq. (6.172). In the present case ($n = 1$), the eigenfunctions are well-defined and non-zero at the origin: $R^{(1)}(k_\rho, \rho' \to 0) = 1$ and $R^{(1)}(k_\rho^\star, \rho' \to 0) = 1$. The evaluation of the $\mathrm{d}z'$-integral replaces z' by $f_z(t')$, which eventually leads to:

$$\widetilde{A}_z(\mathbf{r},\omega) = -\frac{\mu q_\mathrm{e}}{4\pi}\int_{-\infty}^\infty \frac{\mathrm{d}t'}{2\pi}\dot{f}_z(t')e^{-i\omega t'}\Bigg\{\int_0^\infty \frac{\mathrm{d}k_\rho}{N^{(1)}(k_\rho)} R^{(1)}(k_\rho,\rho)\,\mathrm{E}\Big[\hat{k}_z, z - f_z(t')\Big] + \sum_{k_\rho^\star}\frac{1}{\widetilde{N}^{(1)}(k_\rho^\star)} R^{(1)}(k_\rho^\star,\rho)\,\mathrm{E}\Big[\hat{k}_z^\star, z - f_z(t')\Big]\Bigg\}. \tag{6.175}$$

A consistency check is given in Appendix A.20.1. The upper result contributes to the electric field, as given in Eq. (3.11). For the magnetic field (see Eq. (3.12) and the ϕ-component of Eq. (A.75)), the derivative with respect to ρ is necessary, whereas the source term of Eq. (6.9) requires $\partial_z\widetilde{A}_z(\mathbf{r},\omega)$. For the former, the following replacement is necessary: $R^{(1)}(\dots) \to \partial_\rho R^{(1)}(\dots)$, while for the latter, one needs to change $\mathrm{E}[\dots] \to \partial_z\,\mathrm{E}[\dots]$ in Eq. (6.175).

6.1.16.2 Radial vector potential

The RHS of Eq. (6.9) in combination with Eq. (6.56) gives the following source term: $S^{(2)} = [\nabla\tilde{\varepsilon}/\tilde{\varepsilon}]_\rho\,\partial_z\widetilde{A}_z$. Since it does not have a point-particle character along z unlike Eqs. (6.173)

and (6.174), the z'-integral of Eq. (6.171) cannot be simplified immediately. For the integral with respect to ρ', one needs to revert to the weight from Eq. (6.93). It is discontinuous at ρ_c, where also the source term is located. Using Eq. (A.38), one can identify $[\nabla\tilde{\varepsilon}/\tilde{\varepsilon}]_\rho w^{(2)}(\rho') = -\rho'\widetilde{\chi}_\mathrm{e}/(1+\widetilde{\chi}_\mathrm{e})\delta^+(\rho_\mathrm{c}-\rho')$ and obtain via Eq. (6.171):

$$\begin{aligned}\widetilde{A}_\rho(\mathbf{r},\omega) = -\frac{\rho_\mathrm{c}}{2}\frac{\widetilde{\chi}_\mathrm{e}}{1+\widetilde{\chi}_\mathrm{e}}\int_{-\infty}^{\infty}\mathrm{d}z'\frac{\partial\widetilde{A}_z(\mathbf{r}'_\mathrm{c},\omega)}{\partial z'} \\ \left[\int_0^\infty \frac{\mathrm{d}k_\rho}{N^{(2)}(k_\rho)}R^{(2)}(k_\rho,\rho_\mathrm{c})R^{(2)}(k_\rho,\rho)\,\mathrm{E}(\hat{k}_z,z-z') \right. \\ \left. + \sum_{k_\rho^\star}\frac{1}{\widetilde{N}^{(2)}(k_\rho^\star)}R^{(2)}(k_\rho^\star,\rho_\mathrm{c})R^{(2)}(k_\rho^\star,\rho)\,\mathrm{E}(\hat{k}_z^\star,z-z')\right] \qquad (6.176)\end{aligned}$$

$$\begin{aligned}= \frac{\rho_\mathrm{c}}{2}\frac{\widetilde{\chi}_\mathrm{e}}{1+\widetilde{\chi}_\mathrm{e}}\int_{-\infty}^{\infty}\mathrm{d}z'\,\widetilde{A}_z(\mathbf{r}'_\mathrm{c},\omega) \\ \left[\int_0^\infty \frac{\mathrm{d}k_\rho}{N^{(2)}(k_\rho)}R^{(2)}(k_\rho,\rho_\mathrm{c})R^{(2)}(k_\rho,\rho)\partial_{z'}\,\mathrm{E}(\hat{k}_z,z-z') \right. \\ \left. + \sum_{k_\rho^\star}\frac{1}{\widetilde{N}^{(2)}(k_\rho^\star)}R^{(2)}(k_\rho^\star,\rho_\mathrm{c})R^{(2)}(k_\rho^\star,\rho)\partial_{z'}\,\mathrm{E}(\hat{k}_z^\star,z-z')\right], \qquad (6.177)\end{aligned}$$

where $\mathbf{r}'_\mathrm{c} = (\rho_\mathrm{c}, z')$ indicates that $\widetilde{A}_z$ is evaluated along the cylindrical boundary. This result has been verified in Appendix A.20.2. In the second step, the *integration by parts* has been invoked so that $\partial_z\widetilde{A}_z$ does not need to be evaluated. Also $\partial_{z'}\,\mathrm{E}(\hat{k}_z^\star, z-z')$ does not have a singularity at $k_\rho = k_0$, which simplifies the implementation. $\widetilde{A}_\rho$ itself is a source term in Eq. (6.10) and its time derivative contributes directly to the electric field (Eq. (3.12)).

6.1.16.3 Scalar potential

Finally, the source term of the scalar potential is $S^{(3)} = -\tilde{\rho}_\mathrm{f}/\tilde{\varepsilon} - [\nabla\tilde{\varepsilon}/\tilde{\varepsilon}]_\rho i\omega\widetilde{A}_\rho$, which follows from Eq. (6.10). Since the source term is linear in Eq. (6.171), it is separated into $S^{(3)} = S_\rho^{(3)} + S_A^{(3)}$, where $S_\rho^{(3)} = -\tilde{\rho}_\mathrm{f}/\tilde{\varepsilon}$ and $S_A^{(3)} = -[\nabla\widetilde{\varepsilon}/\tilde{\varepsilon}]_\rho i\omega\widetilde{A}_\rho$. Likewise, the scalar potential is separated into $\widetilde{\varphi} = \widetilde{\varphi}_\rho + \widetilde{\varphi}_A$. $\tilde{\rho}_\mathrm{f}$ is explicitly given in Eq. (6.173). For the integral with respect to ρ' of Eq. (6.171), $-[\nabla\tilde{\varepsilon}/\tilde{\varepsilon}]_\rho w^{(3)}(\rho') = \rho'\widetilde{\chi}_\mathrm{e}\delta^+(\rho_\mathrm{c}-\rho')$ is used:

$$\begin{aligned}\widetilde{\varphi}_\rho(\mathbf{r},\omega) = -(1+\widetilde{\chi}_\mathrm{e})\frac{q}{4\pi\tilde{\varepsilon}}\int_{-\infty}^{\infty}\frac{\mathrm{d}t'}{2\pi}e^{-i\omega t'}\left\{\int_0^\infty\frac{\mathrm{d}k_\rho}{N^{(3)}(k_\rho)}R^{(3)}(k_\rho,\rho)\,\mathrm{E}\left[\hat{k}_z,z-f_z(t')\right]\right. \\ \left. + \sum_{k_\rho^\star}\frac{1}{\widetilde{N}^{(3)}(k_\rho^\star)}R^{(3)}(k_\rho^\star,\rho)\,\mathrm{E}\left[\hat{k}_z^\star,z-f_z(t')\right]\right\}, \qquad (6.178)\end{aligned}$$

$$\begin{aligned}\widetilde{\varphi}_A(\mathbf{r},\omega) = i\omega\widetilde{\chi}_\mathrm{e}\frac{\rho_\mathrm{c}}{2}\int_{-\infty}^{\infty}\mathrm{d}z'\,\widetilde{A}_\rho(\mathbf{r}'_\mathrm{c},\omega)\left[\int_0^\infty\frac{\mathrm{d}k_\rho}{N^{(3)}(k_\rho)}R^{(3)}(k_\rho,\rho_\mathrm{c})R^{(3)}(k_\rho,\rho)\,\mathrm{E}\big(\hat{k}_z,z-z'\big)\right. \\ \left. + \sum_{k_\rho^\star}\frac{1}{\widetilde{N}^{(3)}(k_\rho^\star)}R^{(3)}(k_\rho^\star,\rho_\mathrm{c})R^{(3)}(k_\rho^\star,\rho)\,\mathrm{E}\big(\hat{k}_z^\star,z-z'\big)\right]. \qquad (6.179)\end{aligned}$$

Finally, for Eq. (3.11), the derivative with respect to ρ and z is required, which applies to $R^{(3)}(\dots)$ and $\mathrm{E}[\dots]$, respectively. Eqs. (6.178) and (6.179) are verified in Appendix A.20.3.

Due to their complicated dependency on k_ρ, the k_ρ-integrals of Eqs. (6.175), (6.176), (6.178) and (6.179) need to be evaluated numerically. A few complications arise, which will be addressed in the following.

6.1.16.4 Implementation

Sampling The k_ρ-integrands have an oscillating nature, as they are largely composed of Bessel functions. An estimate of the oscillation period is desired to sample the k_ρ-domain with a fixed number of samples per period. All k_ρ-integrands of Eqs. (6.175), (6.176), (6.178) and (6.179) are normalized with $N^{(n)}(k_\rho)$. They are well approximated via Eqs. (A.103) to (A.106) and are given in the last row of Table A.1. Their arguments y of the sine- and cosine-terms (barring the $\pi/4$ phase shift), are initially "decelerated" due to $\tilde{k}_\chi$. For $k_\rho \gg \tilde{k}_\chi$ they approach $y \sim x = k_\rho \rho_\mathrm{c}$, which oscillates slightly faster. In addition, sine and cosine raised to the n^{th} power can be represented as linear superpositions of sine and cosine, with the fastest oscillation having the argument $nk_\rho\rho_\mathrm{c}$. $n = 2$ in the present case so that the period is given by $T_N = 2\pi/(2\rho_\mathrm{c})$. When $\rho \leq \rho_\mathrm{c}$, then the $R^{(n)}(k_\rho, \rho)$ oscillate with the argument $k_\rho\rho$ and the period of $T_\rho = 2\pi/\rho$. (ρ_c is included, since the $R^{(n)}(k_\rho, \rho)$ are by definition continuous.) For $\rho > \rho_\mathrm{c}$, the $c_J^{(n)}$ and $c_Y^{(n)}$ contribute as well. Just as for $N^{(n)}(k_\rho)$, Eqs. (A.103) to (A.106) are used to approximate Eqs. (6.62), (6.63), (6.78), (6.79), (6.89) and (6.90). It follows that the sine- and cosine-terms also appear quadratically so that one needs to take $T_c = T_N = 2\pi/(2\rho_\mathrm{c})$ into account. These separate contributions are multiplied together so that when they are expanded as linear sine- and cosine-terms, the argument of the fastest oscillation is just the linear sum of the original arguments. Consequently, the periods add inversely. The total period T_tot for Eqs. (6.175), (6.176), (6.178) and (6.179) in- and outside of the target is summarized in Table 6.1.

Table 6.1: Approximate total inverse period $1/T_\mathrm{tot}$ of the k_ρ-integrand oscillations.

$1/T_\mathrm{tot}$	$\widetilde{A}_z$	$\widetilde{A}_\rho$	$\widetilde{\varphi}_\rho$	$\widetilde{\varphi}_A$
$\rho \leq \rho_\mathrm{c}$	$\frac{1}{T_N} + \frac{1}{T_\rho}$	$\frac{1}{T_N} + \frac{1}{T_{\rho_\mathrm{c}}} + \frac{1}{T_\rho}$	$\frac{1}{T_N} + \frac{1}{T_\rho}$	$\frac{1}{T_N} + \frac{1}{T_{\rho_\mathrm{c}}} + \frac{1}{T_\rho}$
$\rho > \rho_\mathrm{c}$	$\frac{1}{T_N} + \frac{1}{T_c} + \frac{1}{T_\rho}$	$\frac{1}{T_N} + \frac{1}{T_{\rho_\mathrm{c}}} + \frac{1}{T_c} + \frac{1}{T_\rho}$	$\frac{1}{T_N} + \frac{1}{T_c} + \frac{1}{T_\rho}$	$\frac{1}{T_N} + \frac{1}{T_{\rho_\mathrm{c}}} + \frac{1}{T_c} + \frac{1}{T_\rho}$

Singularity When Eqs. (6.175), (6.178) and (6.179) are evaluated without a derivative with respect to z, then the k_ρ-integrand passes through a singularity at $k_\rho = k_0$, since $\mathrm{E}[\dots] \propto 1/\hat{k}_z$ and $\hat{k}_z$ vanishes at k_0. The weight of the singularity is finite but the integrand is infinitely sharp at this point so that an integration with the trapezoidal rule in combination with a sample that lies too close to k_0 leads to a strong overestimation of the area. Consequently, the integrand will *not* be sampled around k_0, but instead integrated analytically. The following approximation is chosen:

$$g^{(n)}(k_\rho)\,\mathrm{E}\left[\hat{k}_z, z - f_z(t')\right] \overset{k_\rho \sim k_0}{\approx} g^{(n)}(k_0)\; i/\sqrt{k_0^2 - k_\rho^2}\,, \tag{6.180}$$

where $g^{(n)}(k_\rho)$ collects the remaining factors of the k_ρ-integrands, e.g. $g^{(1)}(k_\rho) = 1/N^{(1)}(k_\rho)$ $R^{(1)}(k_\rho, \rho)$. In addition, an estimate of the width of the singularity is required, i.e. in which domain the upper approximation is valid. It holds, if the exponent of Eq. (A.113),

i.e. $-i\hat{k}_z|\Delta z|$, where $\Delta z \equiv z - f_z(t')$, is sufficiently small. Around k_0 it is approximated by $-i[2k_0(k_0 - k_\rho)]^{1/2}|\Delta z|$. If one lets $k_\rho \in k_0 \pm \epsilon_s^2/(2k_0\Delta z^2)$, then the magnitude of the exponent is given by the dimensionless parameter ϵ_s, which can be chosen arbitrarily small. Yet, for small k_0 and/or Δz, the interval diverges so that $g^{(n)}(k_0)$ in Eq. (6.180) is not valid anymore. Therefore $k_\rho \in k_0 \pm \Delta k_\rho^{\mathrm{sgl}}$ is chosen, where

$$\Delta k_\rho^{\mathrm{sgl}} = \begin{cases} \epsilon_s^2 k_0/2 & \text{for } k_0|\Delta z| \leq 1 \\ \epsilon_s^2/(2k_0\Delta z^2) & \text{for } k_0|\Delta z| > 1 \end{cases}. \tag{6.181}$$

The latter also holds, if $f_z(t')$ is replaced by z', as is the case for Eq. (6.179). Finally, the integral is evaluated via

$$\int \mathrm{d}k_\rho/\sqrt{k_0^2 - k_\rho^2} = \arctan\Big(k_\rho/\sqrt{k_0^2 - k_\rho^2}\Big). \tag{6.182}$$

Exponential decrease For $k_\rho > k_0$, the E-function suppresses the integrand exponentially so that the upper integral limit (infinity) can be relaxed by a finite value. With $\Delta z \equiv |z - f_z(t')|$ and introducing the dimensionless tolerance value $\epsilon_e \sim 10^{-6}$, one only needs to integrate up to $k_\rho^{\max}$:

$$e^{-i\sqrt{k_0^2-k_\rho^2}\Delta z} \leq \epsilon_e, \qquad \Leftrightarrow \qquad k_\rho^{\max} = \sqrt{k_0^2\Delta z^2 + \log^2(\epsilon_e)}/\Delta z\,. \tag{6.183}$$

If z is below the range, then Δz vanishes for certain t'-values so that Eq. (6.183) diverges. This is expected, since also the exponent vanishes for $\Delta z = 0$. To avoid requiring large amounts of samples, these specific t'-values are excluded and interpolated based on the surrounding results. Afterwards, the t'-integral is carried out.

6.1.17 Superposition to a modulated beam

The results from Eqs. (6.175), (6.176), (6.178) and (6.179) are point-particle solutions. The superposition from Sec. 3.5 is applied in order to obtain the field that originates from an intensity modulated beam. Note that an intensity modulation of a single proton pencil beam at high frequencies is considered. It is not to be confused with the *intensity modulation in proton therapy* (IMPT) [302], which is optimized to cover more complex targets. Such a modulation could either be active, utilizing beam choppers [79, 151, 303, 304], or by exploiting the RF structure from the accelerators shown in Fig. 2.15.

In Sec. 3.5, the applicability of the convolutional superposition has been discussed, in particular the interplay between the distance from the source ρ and the beam current I (see Fig. 3.5). Here, one also has to take into account that the beam current is high enough so that it can be modulated under the quantization into elementary particles. In particular, when the beam is sinusoidally modulated with ω_{mod}, then the intensity drops within $T_{\mathrm{mod}}/2 = 1/(2f_{\mathrm{mod}})$. The charge drops then by $\Delta Q = IT_{\mathrm{mod}}/2$, given the beam current I. The change of charge is limited by the elementary charge: $\Delta Q = n_{\min}\, e^+$ so that the necessary current for a given modulation frequency is given by

$$I_{\min} = n_{\min}\, e^+ \omega_{\mathrm{mod}}/\pi. \tag{6.184}$$

The highest relevant modulation frequencies are of the order of 10 GHz (see Fig. 4.14), so when assuming $n_{\min} = 10$, one would need to deliver a beam current of at least 5 nA. This corresponds to a quite moderate dose rate (see Eq. (2.22)), so that a beam modulation would be possible from this point of view.

At this stage, one only needs to apply the superposition described in Sec. 3.5. The beam modulation will be described by an idealized sinusoidal curve, since it simplifies significantly given the Fourier domain point particle solutions. In order to determine the shape function necessary for Eq. (3.47) of a beam modulated at ω_{mod}, a modulated beam with finite duration is considered first

$$\hat{\gamma}_{\text{mod}}(t) = \frac{1}{\widehat{N}_{\text{mod}}}\big[1+\cos\left(\omega_{\text{mod}}t\right)\big]\Pi(t;T), \tag{6.185}$$

where $\Pi(t;T) = 1/T\big[\theta(t+T/2)-\theta(t-T/2)\big]$ is a normalized boxcar function, which limits the duration. N_{mod} ensures the normalization from Eq. (3.44) and is given by

$$\widehat{N}_{\text{mod}} = 1+\frac{\sin(\omega_{\text{mod}}T/2)}{\omega_{\text{mod}}T/2}. \tag{6.186}$$

For a beam with infinite duration, the limit $T\to\infty$ is taken, but one also needs to allow for an infinite number of particles ($N\to\infty$) so that the average fluence $\Phi = N/T$ remains constant:

$$N\gamma_{\text{mod}}(t) = \lim_{\substack{N,T\to\infty \\ N/T=\text{const.}}} N\hat{\gamma}_{\text{mod}}(t) = \Phi\big[1+\cos\left(\omega_{\text{mod}}t\right)\big]. \tag{6.187}$$

In particular $\widehat{N}_{\text{mod}}\to 1$, since the second term of Eq. (6.186) is a sinc-function that vanishes for large arguments. As mentioned above, Φ is the *average* fluence, whereas the actual profile fluctuates from zero to 2Φ. To apply Eq. (3.47), the Fourier transform of Eq. (6.187) is required: $N\tilde{\gamma}_{\text{mod}}(t) = \Phi\delta(\omega)+\Phi\delta(\omega-\omega_{\text{mod}})/2+\Phi\delta(\omega+\omega_{\text{mod}})/2$, which eventually leads to

$$\begin{aligned}\mathbf{F}_b(\mathbf{r},t) &= 2\pi\int_{-\infty}^{\infty} N\tilde{\gamma}_{\text{mod}}(\omega)\widetilde{\mathbf{F}}(\mathbf{r},\omega)e^{i\omega t}\mathrm{d}\omega \\ &= 2\pi\Phi\Big[\widetilde{\mathbf{F}}(\mathbf{r},0)+\widetilde{\mathbf{F}}(\mathbf{r},\omega_{\text{mod}})e^{i\omega_{\text{mod}}t}/2+\widetilde{\mathbf{F}}(\mathbf{r},-\omega_{\text{mod}})e^{-i\omega_{\text{mod}}t}/2\Big].\end{aligned} \tag{6.188}$$

Knowing that $\widetilde{\mathbf{F}}(\mathbf{r},\omega)$ is real-valued in the time domain, it follows that its real part is symmetric and its imaginary part is anti-symmetric with respect to $\omega = 0$ (see Eq. (A.6)) so that

$$\mathbf{F}_b(\mathbf{r},t) = 2\pi\Phi\Big\{\widetilde{\mathbf{F}}(\mathbf{r},0)+\Re\Big[\widetilde{\mathbf{F}}(\mathbf{r},\omega_{\text{mod}})\Big]\cos(\omega_{\text{mod}}t)-\Im\Big[\widetilde{\mathbf{F}}(\mathbf{r},\omega_{\text{mod}})\Big]\sin(\omega_{\text{mod}}t)\Big\}. \tag{6.189}$$

The first term is discarded, as the focus is on the oscillating contributions. The remaining linear superposition of sine and cosine can be combined to a single scaled and phase shifted cosine, as has been shown below Eq. (6.113). The amplitude is the square root of the sum of the squared coefficients, which are the real and imaginary parts of the point particle field at the modulation frequency. The latter is by definition its absolute value, so that the field modulates with the same frequency and has an amplitude of

$$A_{\text{mod}} = 2\pi\Phi\Big\|\widetilde{\mathbf{F}}(\mathbf{r},\omega_{\text{mod}})\Big\|. \tag{6.190}$$

6.2 Results & Discussion

The modulation frequency dependent amplitude of the magnetic field relative to the beam current I is shown in Fig. 6.13. One may easily factor out I from Eq. (6.190), since the

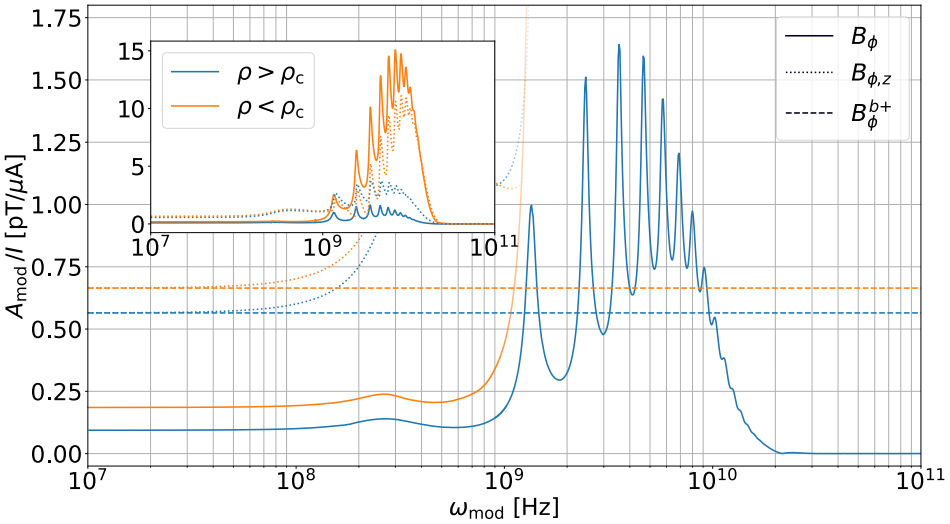

Figure 6.13: Amplitude of the oscillating magnetic field relative to the beam current as a function of the modulation frequency. Two frequency spectra, 5 mm above ($\rho > \rho_c$) and below ($\rho < \rho_c$) the cylindrical boundary at $\rho_c = 10$ cm are shown. With the field inside being less relevant for an external detection, it is shown only in the insert. Also, the low frequency behavior of $B_{\phi,z} = -\partial A_z/\partial\rho$ (dotted line) as well as the DC result from Eq. (4.54) (dashed line) are shown.

point particle vector and scalar potentials from Eqs. (6.175), (6.176), (6.178) and (6.179) and therefore also their fields (see Eqs. (3.11) and (3.12)) scale with the elementary charge. With current and particle fluence related as $I = q_e\Phi$, one obtains $A_{mod}/I = 2\pi\|\widetilde{\mathbf{F}}(\mathbf{r},\omega_{mod})\|$.

What is shown in Fig. 6.13 is then also a scaled version of the point particle frequency spectrum with boundaries taken into account. Hence, before discussing the amplitude, one may qualitatively compare Fig. 6.15 to Fig. 4.14. In particular, a comparison regarding the frequency spectra of the longitudinal electric and azimuthal magnetic field is reasonable, due to their close relationship, specified in Eq. (4.42). One should keep in mind, however, that Fig. 4.14 and Fig. 6.15 are calculated with different initial energies, i.e. 150 and 100 MeV, respectively so that the comparability has some limitations. Notwithstanding, they were both evaluated at the respective ranges, i.e. 15.84 cm and 7.73 cm. The overall shape is very similar, peaking at about 10 GHz. This applies in particular to the spectrum inside the target (i.e. $\rho < \rho_c$), as shown in the insert of Fig. 6.13. The primary difference between the two frequency spectra are the distinct peaks. In fact, with the boundary being the principle difference between the two calculations, one can attribute the peaks to the cylindrical boundary. From a physics point of view, the reflections at the boundaries lead to a repeated recurrence of the primary pulse. From a more mathematical point of view, the resulting field is thereby a time delayed superposition of itself. This kind of description formed the basis of the convolutional superposition described in Sec. 3.5. In particular, at the end of this section, it has also been discussed under which circumstances the continuum approximation does not apply. The result is still a convolutional law, yet the field is not convolved with the beam shape function, but the sum of complex exponential functions, as given in Eq. (3.49). The latter converges in an ideal case (reflecting infinitely many times) to a train of delta-pulses (Dirac comb). It remains a set of pulses in a more realistic scenario, including attenuation, dispersion, transmission and the longitudinal propagation. Yet, these pulses broaden somewhat, which leads to and explains the spiked profile in

Fig. 6.15. With the simple cylindrical geometry, one can further characterize the peaks in terms of their spacing in the frequency domain. Say the pulse repeatedly returns after $\Delta\tau$. Upon comparison with the Fourier series representation of a Dirac comb, one finds that the peaks in Eq. (3.49) have a frequency spacing of $\Delta\omega = 2\pi/\Delta\tau$. After reaching the boundary at $\rho_c = 10$ cm for the first time, the wave has to travel a distance of $2\rho_c$ to arrive at the opposite site. Recall that the result from Fig. 6.15 has been simulated with the parameters for water. Across the frequencies relevant for Fig. 6.15, water has an approximate refractive index of $n \approx 8.6$ (see Fig. 3.2). Consequently, one may represent the time delay as $\Delta\tau = 2\rho_c/(c_0/n)$ so that the frequency spacing becomes $\Delta\omega = \pi/\rho_c\, c_0/n \approx 1.1$ GHz. Compare this value to what is shown in Fig. 6.13. While the logarithmic scale might be deceiving, note how the first peak sits right in between 1 GHz and 2 GHz and that the few following ones are between the grid lines spaced by 1 GHz. They each move towards the higher grid line with the frequency spacing being somewhat larger than 1 GHz. The fact that the approximate $\Delta\omega$ offers such a good description tells us that dispersion has little impact, which makes sense considering that the refractive index begins to deviate from the aforementioned value only after about 100 GHz.

The behavior towards low frequencies has also been analyzed in Fig. 6.13. Considering only the contribution from the longitudinal vector potential ($B_{\phi,z} = -\partial A_z/\partial\rho$, as introduced in Eq. (3.68)), it has been found to agree with Eq. (4.54) (labeled as B_ϕ^{b+}) towards $\omega_{\mathrm{mod}} \to 0$ and thus it provides a reassuring consistency with the previous DC results. One may wonder, why the first term of Eq. (6.189) is not necessary to achieve the present agreement. Recall that a modulated beam current with an average fluence Φ has been chosen. When letting $\omega_{\mathrm{mod}} \to 0$ in Eq. (6.187), one gets a fluence of 2Φ, while the low frequency limit of the term in curly brackets from Eq. (6.189) is $2\widetilde{\mathbf{F}}(\mathbf{r}, 0)$. If a modulated beam current with a DC fluence of Φ instead of 2Φ would have been chosen, then one would require the first term of Eq. (6.189) to obtain the agreement. On the other hand, the low frequency behavior of B_ϕ deviates, which originates from the $B_{\phi,\rho} = \partial A_\rho/\partial z$-term. It impacts the DC value, which might not have been expected from first principles. Consider the $\omega \to 0$ limit back in Eq. (6.2). The last term on the LHS vanishes immediately and one may argue through the Lorenz gauge from Eq. (3.13) that $\nabla \cdot \widetilde{\mathbf{A}} = 0$, whereby the second term would vanish as well. Eventually Eq. (6.2) would reduce to Eq. (3.54), whose solution for a longitudinal beam current is not affected by the boundary and given by Eq. (4.54). Yet, $\nabla \cdot \widetilde{\mathbf{A}} = 0$ is a faulty assumption. As a reminder, the results presented in Chapters 4 and 5 are only valid in the homogeneous case. In Sec. 3.6.1, it has already been argued that both the electric field as well as the scalar potential change linearly. With $i\omega \leftrightarrow \partial_t$, it follows that $i\omega\mu\tilde{\varepsilon}\widetilde{\varphi} \neq 0$ in Eq. (3.13) so that the divergence of the vector potential does not vanish and neither does the second term of Eq. (6.2). The resulting boundary dependence that reaches down to the DC part, can be traced back to the charge deposition. If the beam current was hypothetically infinitely long, then its longitudinal vector potential would be constant along z. Given that $\widetilde{A}_\rho$ depends on $\partial_z \widetilde{A}_z$ (see Eq. (6.176)), $\widetilde{A}_\rho$ would vanish. $\widetilde{A}_\rho$ is therefore only non-zero if there are current sources and sinks. In summary, while the magnetic field does not interact with the permittivity gradient, the changing electric field at the range does, which translates to the magnetic field. The interface conditions for the magnetic field remain valid nonetheless. Note how the DC difference between $\rho < \rho_c$ and $\rho > \rho_c$ is equal for both B_ϕ and $B_{\phi,z}$, since there is not permeability gradient.

A further analysis similar to Fig. 4.13 has been presented in Fig. 6.14. Therein, the frequency spectrum from Fig. 6.13 has been transformed to the time domain via Eq. (A.3b). The expected pulsed structure emerges, caused by repeated reflections. One sees that the first pulse from Fig. 6.14 arrives somewhat later than the one shown in Fig. 4.13. This is due

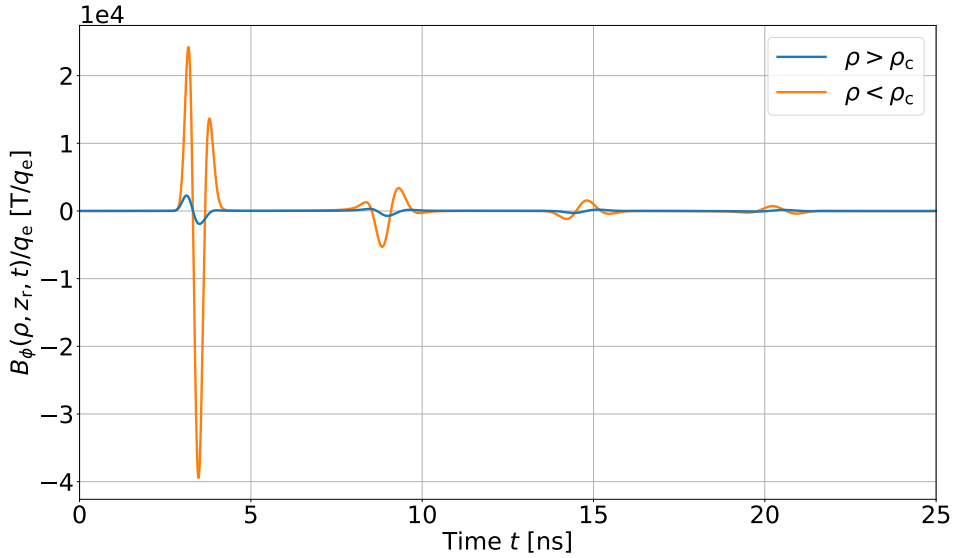

Figure 6.14: Magnetic field of a point particle in- and outside of a cylindrical target. The inverse Fourier transform of Fig. 6.13 is displayed here relative to the elementary charge.

to the fact that the latter is evaluated at a smaller radius of 5 cm, whereas the former is at 10 cm. The time delay is not twice as long though, since Fig. 4.13 has a longer deceleration time due to its higher energy (compare Figs. 2.10 and 2.11). With the field inside and outside shown, one can see the portion of the beam that is transmitted and also how much is reflected. In particular, the third peak of the first wave of Fig. 6.14 for $\rho < \rho_c$ can be attributed to the part that travels in the opposite direction, as it does not exist for the field outside. The wave packages reoccur after a constant time delay of about $\Delta\tau \approx 5.76$ ns, while they decrease in strength and broaden in time. The loss of field strength is explained by multiple processes: (a) the attenuation of 12.9% per 10 cm, as described in Sec. 4.2.3, (b) the amount of radiation that is transmitted and (c) the scattering of initially circular waves on the cylindrical boundaries, which broadens the wavefront.

Finally, the original purpose of Eq. (6.190) is considered, i.e. the analysis of the amplitude. A large decrease of intensity can be observed across the boundary, in particular comparing the B_ϕ-profiles of Fig. 6.13. This is related to the large permittivity gradient, which changes abruptly from $\varepsilon_r^{\text{target}} \sim 75$ to $\varepsilon_r^{\text{air}} \sim 1$ and leads to large reflection and low transmission coefficients. In particular, the critical angle with respect to the surface normal is only about 6.7° for the water-air boundary, so that transmission is only permitted for waves that travel approximately perpendicular to the surface. Similar effects occur also for the interaction between the RF signal and the human body in MRI [305]. With respect to the current strength, it follows from Fig. 6.13 that one would require current strengths in the µA range to generate signals that can be detected with sensitive instrumentation, such as SQUIDs [306], which allows a detection of GHz fields. The DC field is approximately six times weaker than what is shown in Fig. 5.20. Accordingly one would require higher currents than those being discussed for Fig. 5.24.

Finally, the longitudinal profile along the cylinder axis, as initially investigated in Chapter 5 is reconsidered, and a dependency on the frequency in Fig. 6.15 is investigated. For frequencies below say 100 MHz, the profile takes the same shape as the DC profile shown in Fig. 5.20, i.e. gradually decreasing along the z-axis. The profile associated with the frequency $\omega_{\text{mod}} \sim 3.6$ GHz at the highest peak of Fig. 6.13 shows no correlation with the range.

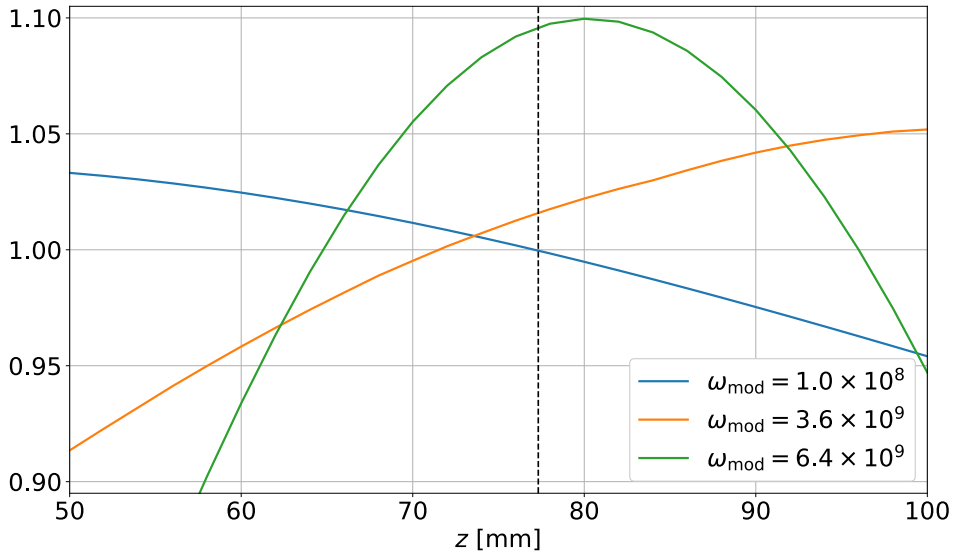

Figure 6.15: Normalized longitudinal amplitude profile of the magnetic field oscillating at different modulation frequencies ω_{mod}. In particular, the profiles are normalized to the average between $z = 50$ and 100 mm at $\rho = 105$ mm ($\rho > \rho_c$). The vertical dashed line indicates the proton range at 77.3 mm.

The latter is not surprising, knowing that these peaks are associated with the cylindrical geometry. More interestingly, the profile at a frequency between the frequency spectrum spikes (e.g. $\omega_{mod} \sim 6.4$ GHz) peaks close to the range, which is likely associated with the circular wave fronts shown in Fig. 4.12.

7 CONCLUSIONS AND PERSPECTIVES

Within Chapters 4 to 6, various aspects of the electric and magnetic field of a proton pencil beam have been analyzed through dedicated analytical and numerical methods. In the following, they shall be summarized together with the conclusions that can be drawn from them. The contributions from the present thesis were structured as follows. In Chapter 4, the electromagnetic field of a proton pencil beam has been evaluated through an analytical method, that has been derived from first principles. Following that, Monte Carlo simulations were leveraged to further investigate how the source (proton beam) and its magnetic field are affected by the secondaries. Finally, the preliminary work from Chapter 6 dealt with the impact of boundaries on a modulated or oscillating (RF-structure) beam.

In Chapter 4, the methods that were laid out by Albert et al. were further advanced and thoroughly analyzed regarding their applicability. Hence, before reviewing the associated results, some of the crucial developments shall be highlighted. Firstly, the superposition of point particle solutions has been generalized to arbitrary pulse shapes, which has also been exploited for the analysis reported in Chapter 6. Secondly, the analysis from Sec. 4.1.2 showed the favorable property that the current density remains constant along the entire beam axis (under ideal assumptions) and that this fact may also be represented by individual point particles. As opposed to Albert et al. both the electric and magnetic field were considered through a simplified and unified approach (see Eq. (6.171)), where some details were previously overlooked (see Secs. 4.1.4.1 and 4.1.6.2). Furthermore, the somewhat intransparent derivation of Albert et al. has been identified to be equivalent to a Green's function approach and in particular to the Liénard-Wiechert-potentials, which has formed the basis for the work of Chapter 6 and further enabled an analysis of the frequency spectrum. Yet, the limitations of this analytical approach were also pointed out. In particular, their erroneous application of the well-known interface conditions has led to inconsistent results. A dedicated effort (see Sec. 4.1.9) has been undertaken in order to present a more accurate result. Finally, the associated electromagnetic waves were further analyzed.

Based on the developed methods, it has been found that the magnetic field is approximately independent of the environment and follows a smooth profile along the beam line, which is correlated to the range. One may deduce the range through a measurement of the magnetic field by comparing it to the expected depth profile. Very sensitive instrumentation (optical magnetometry or SQUIDs) and shielding would be necessary, while noise, in particular from bioelectricity, needs to be accounted for. In part, the latter has sparked the investigations presented in Chapter 6. Certainly, a potential clinical application is far down the line. Efforts to detect and confirm the results of this work are nonetheless currently ongoing. With respect to the electric field, it has been found that the optimistic findings of Albert et al. cannot be confirmed. In particular, their argument that the field strength is only diminished through diffusion processes and is thereby sustained for a duration in the order of seconds does not hold up. In fact, the results from this work show that with the con-

ductivity of biological tissues, the field strength vanishes within nanoseconds through the conductivity-related charge relaxation. This statement remains valid, even with a boundary where the charges eventually collect. Nonetheless, the field does not vanish entirely. The contribution to the field that originates from the charges downstream, from which the range could be determined, reaches an equilibrium between deposited and conducted charges. Its magnitude depends on the beam current and the tissue's permittivity and conductivity. Yet, for the comparatively high beam current chosen, the field is already two orders of magnitude weaker than what has been predicted by Albert et al. Therefore, performing range verification based on an electric field measurement does not appear feasible, especially when considering the fast washout effects from the relaxation. While these findings might be initially discouraging, the fact that biological tissues are conductive opens up the possibility to collect the charges with surface electrodes. In fact, Cirrone et al. [238] have recently performed such experiments with very promising results. They investigated this approach for dose monitoring, where they were able to collect the entire charge imbalance (in the order of nanocoulomb) with a single electrode. For this purpose, electrical isolation of the target and eventually the patient is necessary. Finally, a comprehensive analysis of the proton point particle frequency spectrum has been carried out. The primary purpose has been to provide an explanation and interpretation of the obtained spectrum. Interestingly enough, both Bremsstrahlung and Cherenkov radiation contribute. Especially Cherenkov radiation is not expected at such low energies. However, with a peak frequency of 9 GHz, it is not associated with the "usual" Cherenkov radiation in the visible/UV spectrum. While this might be interesting from a purely academic point of view, the low amount of energy transmitted does not necessarily appear applicable to range verification, considering the large background from secondary electron bremsstrahlung, which has not been considered here. To put this into perspective, bremsstrahlung, which has also been shown to be part of the frequency spectrum, is usually the first process neglected when discussing the stopping of heavy particles [87].

With the work summarized thus far, only the primary protons were considered, so a further analysis of the secondary charged particles has been carried out in Chapter 5. The basic question has been, whether the current from the numerous secondary electrons overshadows the primary proton current. For this purpose, dedicated Monte Carlo simulations were conducted with a focus on the physics of the secondary electrons down to energies as low as 10 eV. It has been found that the electrons do have a non-negligible but small impact in the order of 10% compared to the proton current. Their primarily isotropic scattering at low energies together with their short lifetimes diminish the contribution from the electrons, despite the larger charge densities. The aforementioned 10% are the electrons that undergo head-on collisions with the primary protons, receiving a strong forward scattering. So barring these minor deviations, this validates the findings of Chapter 4. In addition, the magnetic field has been estimated numerically from the Monte Carlo simulated current densities through the finite element analysis. As described in Chapter 3, it has been crucial to make sure that the chosen formalism allows for non-solenoidal current densities. The radial beam current, which originates from multiple Coulomb scattering and has therefore been neglected in Chapter 4, has been confirmed to be an appropriate simplification, since it (and its associated magnetic field) is two orders of magnitude weaker than the longitudinal current. The magnetic field from both the longitudinal and lateral current is generally independent of the beam spot size, hence larger spot sizes can be chosen that distribute the dose over a wider area. Of course, this has limitations, since the target needs to be sufficiently homogeneous laterally. Random current density fluctuations and their impact on the magnetic field have been widely analyzed and also found to be negligible, averaging

out in the context of a measurement. Furthermore, the longitudinal magnetic field profile shifts slightly with respect to the result from Chapter 4 through the loss of intensity caused by nuclear reactions, the electron current and the radial current. The magnitude of the shift has been quantified and needs to be compensated for a measurement of the range. Up to minor deviations, the assumptions made in Chapter 4 have been found to be valid.

Knowing that the total current density is dominated by the protons, despite the electrons, some conclusions regarding (currently) investigated imaging techniques can now be drawn, starting with *current density imaging* (CDI). It is based on the principle that the field from the current to be determined affects the phase of the spins, which can be measured through dedicated sequences. This can be done with either conventional [307] or low-field MRI [308], reporting sensitivities in the order of 1 $\mu A/mm^2$ for pulses lasting $\sim$ 70 ms. However, the beam currents presented in Fig. 5.15 are significantly lower (5×10^{-3} $\mu A/mm^2$). A reduction of the beam cross section, which would raise the current density, has technical (focusing) and physical (scattering) limitations and increases the dose locally. With the necessary pulse durations being about four orders of magnitude longer, one quickly runs into dose constraints. Another approach has been motivated by the aim to detect brain currents through MRI. This led to several studies some twenty years ago [309–312], stating the ability to detect fields in the order of 100 pT lasting between tens and hundreds of milliseconds. While one might generate field strengths of comparable magnitude (with a current ten times larger than what has been considered for Fig. 5.19), a beam with the necessary duration would administer an excessive amount of dose. Considering low- or ultra-low-field MRI has not significantly enhanced the sensitivity [313–315]. The recent integration of an MR scanner with a proton beam line [316] has gained considerable interest, not least due to the on-line MR images of proton beams [317]. However, large necessary doses and a limitation to fluid targets, which has been explained by heat convection [318], likely narrow an application to quality assurance. Yet, the probably simplest approach appears feasible, i.e. the direct detection of the field. The principle is similar to MEG, yet without the *inverse problem*, since the source term is practically known, expect for the range. An applicability guided by parameters from MEG has been discussed in Chapter 5, where a range sensitivity in the order of millimeters has been concluded.

Finally, boundaries, the RF structure of the beam[1] and the possibility to modulate the beam have been considered in Chapter 6. Therein, the familiar formalism from Chapter 4 has been adjusted to include a radial discontinuity of the permittivity, thereby circumventing the necessity to use the interface conditions. The principle idea has been rather simple, i.e. construct the Green's function through the eigenvalue expansion. Yet, analytically and numerically it has been rather complex, requiring, for instance, both a continuous and discrete spectrum. Nonetheless, the preliminary results have highlighted some crucial aspects. In particular, that the magnetic field is not completely independent of the environment, since the contribution from the changing electric field at the range depends on the permittivity. This definitely needs to be taken into account, however, being a range-related effect, it might be advantageous for range verification purposes. A further analysis is certainly necessary and shall also include the electric field.

Throughout this work, simple geometries (cylinder) have been considered, which may be valid for a first evaluation as the present one, but should be extended to more realistic phantoms (beyond water) in future work. Also, the impact of conductivity requires a more thorough analysis. The symmetry arguments that have been used to simplify the work from Chapter 5 cannot hold up for an inhomogeneous target. An entirely different plat-

[1] To exploit the RF structure of the beam is currently also under investigation in ionoacoustics.

form that unlike MC simulates the interactions among particles is required. To allow for a simpler description, first experiments could be carried out with non-conductive targets such as PMMA. Regarding conductivity, the aforementioned dose monitoring investigated by Cirrone et al. also has the potential to be applied for range verification. By using multiple electrodes, one could compare the charge collected within each electrode and deduce the range by triangulation. How the charges eventually distribute also depends on the tissue's permittivity and conductivity, which would have to be determined beforehand. MRI offers methodologies to obtain permittivity and conductivity maps, the so-called *electrical property tomography* [319]. This can be subject to future investigations.

A APPENDIX ON ANALYTICAL METHODS

Details for the the work from Chapters 4 and 6, being primarily based on analytical methods, are collected below. For some explicit manipulations (e.g. Eqs. (A.9) and (A.10)), the equations that have been used for the expressions on the left are given in the square brackets on the right.

A.1 Fourier transform convention and some basic properties

Throughout this work, the following forward and inverse Fourier transform pair with respect to space $\mathbf{r}$ and time t, transforming to spatial frequency $\mathbf{k}$ and angular frequency ω, respectively, has been used:

$$\mathcal{F}_4\{\mathbf{f}(\mathbf{r},t)\} = \tilde{\tilde{\mathbf{f}}}(\mathbf{k},\omega) = \int_{-\infty}^{\infty} \frac{\mathrm{d}t}{2\pi} \int_{\mathbb{R}^3} \frac{\mathrm{d}^3\mathbf{r}}{(2\pi)^3} \exp(+i\mathbf{k}\cdot\mathbf{r} - i\omega t)\mathbf{f}(\mathbf{r},t), \tag{A.1a}$$

$$\mathcal{F}_4^{-1}\{\tilde{\tilde{\mathbf{f}}}(\mathbf{k},\omega)\} = \mathbf{f}(\mathbf{r},t) = \int_{-\infty}^{\infty} \mathrm{d}\omega \int_{\mathbb{R}^3} \mathrm{d}^3\mathbf{k} \exp(-i\mathbf{k}\cdot\mathbf{r} + i\omega t)\tilde{\tilde{\mathbf{f}}}(\mathbf{k},\omega), \tag{A.1b}$$

where $\mathbf{f}(\mathbf{r},t)$ is some general vector-valued function and $\tilde{\tilde{\mathbf{f}}}(\mathbf{k},\omega)$ its Fourier space counterpart. The sign and normalization convention of Eqs. (A.1a) and (A.1b) have been chosen in accordance with the work of Albert et al. [85]. An alternative definition is, for instance, given in [320]. Through *integration by parts*, one can show that differential operations turn multiplicative in the Fourier domain

$$\mathcal{F}_4\{\partial/\partial t\, \mathbf{f}(\mathbf{r},t)\} = i\omega\tilde{\tilde{\mathbf{f}}}(\mathbf{k},\omega), \tag{A.2a}$$

$$\mathcal{F}_4\{\nabla\cdot\mathbf{f}(\mathbf{r},t)\} = -i\mathbf{k}\cdot\tilde{\tilde{\mathbf{f}}}(\mathbf{k},\omega), \tag{A.2b}$$

$$\mathcal{F}_4\{\nabla\times\mathbf{f}(\mathbf{r},t)\} = -i\mathbf{k}\times\tilde{\tilde{\mathbf{f}}}(\mathbf{k},\omega). \tag{A.2c}$$

The Fourier transform with respect to time *only* uses the same conventions, but is for convenience stated explicitly

$$\mathcal{F}_1\{f(t)\} = \tilde{f}(\omega) = \int_{-\infty}^{\infty} \frac{\mathrm{d}t}{2\pi} \exp(-i\omega t) f(t), \tag{A.3a}$$

$$\mathcal{F}_1^{-1}\{\tilde{f}(\omega)\} = f(t) = \int_{-\infty}^{\infty} \mathrm{d}\omega \exp(i\omega t)\tilde{f}(\omega). \tag{A.3b}$$

Note that $\mathcal{F}_4$ is abbreviated with double tilde, while $\mathcal{F}_1$ is represented through a single tilde. Eq. (A.2a) also holds for Eqs. (A.3a) and (A.3b). The so-called "shift property" follows from a change of variables of the t-integral:

$$\mathcal{F}_1\{f(t-t_0)\} = e^{-i\omega t_0}\mathcal{F}_1\{f(t)\}. \tag{A.4}$$

A convolution in time domain corresponds to a product in the frequency domain

$$h(t) = f(t) * g(t) = \int_{-\infty}^{\infty} f(\tau) g(t-\tau) \mathrm{d}\tau \qquad \Leftrightarrow \qquad \tilde{h}(\omega) = 2\pi \tilde{f}(\omega)\tilde{g}(\omega). \tag{A.5}$$

Note the factor of 2π, which is related to the definition chosen in Eqs. (A.3a) and (A.3b). The latter can be shown by Fourier transforming the integral representation of $h(t)$ and changing the time-integral variable from the Fourier transform to $\tau' = t - \tau$ so that $\mathrm{d}t = \mathrm{d}\tau'$. The Fourier transform of a real-valued function $f(t)$ has a symmetric real part and an antisymmetric imaginary part with respect to the origin at $\omega = 0$, which can be summarized as

$$\tilde{f}(\omega) = \tilde{f}^{\dagger}(-\omega), \tag{A.6}$$

where $\circ^{\dagger}$ denotes the complex conjugation. It can be shown by requiring that the real-valued function is identical to its complex conjugate: $f^{\dagger}(t) \overset{!}{=} f(t)$ in combination with the representation of Eq. (A.3b). Finally, Parseval's theorem states that the integrated product of two square-integrable function has the same weight both in time and frequency domain:

$$\int_{-\infty}^{\infty} f(t) g^{\dagger}(t) \mathrm{d}t = 2\pi \int_{-\infty}^{\infty} \tilde{f}(\omega)\tilde{g}^{\dagger}(\omega) \mathrm{d}\omega. \tag{A.7}$$

A.2 Electric and magnetic field solutions for a homogeneous medium

The following manipulations only hold for a homogeneous medium, i.e. $\tilde{\varepsilon}(\mathbf{r}) = \tilde{\varepsilon}$ and $\mu(\mathbf{r}) = \mu$. The triple product identity will be useful:

$$\mathbf{A} \times (\mathbf{B} \times \mathbf{C}) = (\mathbf{A} \cdot \mathbf{C})\mathbf{B} - (\mathbf{A} \cdot \mathbf{B})\mathbf{C}. \tag{A.8}$$

Solving for the electric field, one gets

$$\begin{aligned}
\mathbf{k} \times (-i\mathbf{k} \times \tilde{\tilde{\mathbf{E}}}) &= \mathbf{k} \times (-i\omega \tilde{\tilde{\mathbf{B}}}), && \text{[Eq. (3.5c)]} \\
(-i\mathbf{k} \cdot \tilde{\tilde{\mathbf{E}}})\mathbf{k} + ik^2 \tilde{\tilde{\mathbf{E}}} &= \omega\mu \tilde{\tilde{\mathbf{J}}}_{\mathrm{f}} + i\omega^2 \mu \tilde{\tilde{\mathbf{D}}}, && \text{[Eqs. (3.5d) and (A.8)]} \\
i(k^2 - \omega^2 \mu\tilde{\varepsilon}) \tilde{\tilde{\mathbf{E}}} &= \omega\mu \tilde{\tilde{\mathbf{J}}}_{\mathrm{f}} - \tilde{\rho}_{\mathrm{f}}/\tilde{\varepsilon}\mathbf{k}, && \text{[Eqs. (3.5a) and (3.6)]} \\
\tilde{\tilde{\mathbf{E}}} &= (-i)\frac{1}{\tilde{\varepsilon}} \frac{\omega \tilde{\tilde{\mathbf{J}}}_{\mathrm{f}}/\tilde{c}^2 - \tilde{\rho}_{\mathrm{f}}\mathbf{k}}{k^2 - \omega^2/\tilde{c}^2}. && \text{[Eq. (4.2)]}
\end{aligned} \tag{A.9}$$

The manipulations for the magnetic field proceed analogously:

$$\begin{aligned}
\mathbf{k} \times (-i\mathbf{k} \times \tilde{\tilde{\mathbf{B}}}) &= \mathbf{k} \times (\mu \tilde{\tilde{\mathbf{J}}}_{\mathrm{f}} + i\omega\mu \tilde{\tilde{\mathbf{D}}}), && \text{[Eqs. (3.3) and (3.5d)]} \\
(-i\mathbf{k} \cdot \tilde{\tilde{\mathbf{B}}})\mathbf{k} + ik^2 \tilde{\tilde{\mathbf{B}}} &= \mu\mathbf{k} \times \tilde{\tilde{\mathbf{J}}}_{\mathrm{f}} + i\omega\mu\tilde{\varepsilon}\, \mathbf{k} \times \tilde{\tilde{\mathbf{E}}}, && \text{[Eqs. (3.2) and (A.8)]} \\
i(k^2 - \omega^2\mu\tilde{\varepsilon}) \tilde{\tilde{\mathbf{B}}} &= \mu\mathbf{k} \times \tilde{\tilde{\mathbf{J}}}_{\mathrm{f}}, && \text{[Eq. (3.5c)]} \\
\tilde{\tilde{\mathbf{B}}} &= (-i)\mu \frac{\mathbf{k} \times \tilde{\tilde{\mathbf{J}}}_{\mathrm{f}}}{k^2 - \omega^2/\tilde{c}^2}. && \text{[Eq. (4.2)]}
\end{aligned} \tag{A.10}$$

A.3 $\mathbf{k}$-space integral

The following identity shall be confirmed in the following:

$$\mathrm{I}(\tilde{k}, \mathbf{r}) \equiv \int_{\mathbb{R}^3} \mathrm{d}^3\mathbf{k} \frac{\exp(\pm i\mathbf{k} \cdot \mathbf{r})}{k^2 - \tilde{k}^2} = 2\pi^2 \frac{\exp\left[i\tilde{k}\,\mathrm{sgn}(\tilde{k}'')r\right]}{r}, \tag{A.11}$$

where $\mathbf{k} = (k_x, k_y, k_z)^{\mathrm{T}}$ and $\mathbf{r} = (x, y, z)^{\mathrm{T}} \in \mathbb{R}^3$ with their absolute values abbreviated as $|\mathbf{k}| \equiv k$ and $|\mathbf{r}| \equiv r$, and $\tilde{k} = \tilde{k}' + i\tilde{k}'' \in \mathbb{C}$. Eq. (A.11) is evaluated in spherical coordinates with the volume element $\mathrm{d}^3\mathbf{k} = k^2 \mathrm{d}k \mathrm{d}\phi_k \sin\theta_k \mathrm{d}\theta_k = k^2 \mathrm{d}k \mathrm{d}\phi_k \mathrm{d}\mu_k$ where $\mu_k = \cos\theta_k$:

$$\begin{aligned} \mathrm{I}(\tilde{k}, \mathbf{r}) &= \int_0^\infty k^2 \mathrm{d}k \int_0^{2\pi} \mathrm{d}\phi_k \int_{-1}^1 \mathrm{d}\mu_k \frac{\exp(\pm ikr\mu_k)}{k'^2 - \tilde{k}^2} \\ &= 2\pi \int_0^\infty k^2 \mathrm{d}k \frac{1}{k^2 - \tilde{k}^2} \frac{\exp(\pm ikr) - \exp(\mp ikr)}{\pm ikr} \\ &= 2\pi \int_{-\infty}^\infty \frac{k}{r} \frac{\sin(kr)}{k^2 - \tilde{k}^2} \mathrm{d}k, \end{aligned} \tag{A.12}$$

where the exponent $\mathbf{k} \cdot \mathbf{r}$ has been expressed as $kr\cos\theta_k = kr\mu_k$, since the k_z-axis is assumed to be aligned with $\mathbf{r}$. The remaining k-integral is evaluated with the residue theorem, similar to Eq. (A.113).

In [177], Eq. (A.11) has been evaluated in cylindrical coordinates, which will be shown for completeness. With $\mathbf{k} = (k_x = \rho_k \cos\phi_k, k_y = \rho_k \sin\phi_k, k_z)^{\mathrm{T}}$ and $\mathbf{r} = (x = \rho\cos\phi, y = \rho\sin\phi, z+)^{\mathrm{T}}$, $\mathbf{k} \cdot \mathbf{r} = \rho\rho_k \cos(\phi - \phi_k) + k_z z$ follows. One gets

$$\begin{aligned} \mathrm{I}(\tilde{k}, \mathbf{r}) &= \int_0^\infty \rho_k \mathrm{d}\rho_k \int_0^{2\pi} \mathrm{d}\phi_k \int_{-\infty}^\infty \mathrm{d}k_z \frac{\exp(\pm i\rho\rho_k \cos(\phi - \phi_k) \pm ik_z z)}{\rho_k^2 + k_z^2 - \tilde{k}^2} \\ &= 2\pi \int_0^\infty \rho_k \mathrm{d}\rho_k \int_{-\infty}^\infty \mathrm{d}k_z \frac{J_0(\rho\rho_k)}{\rho_k^2 + k_z^2 - \tilde{k}^2} \exp(\pm ik_z z), \end{aligned} \tag{A.13}$$

where Eq. (A.96) has been used. The k_z-integral can now be evaluated with Eq. (A.113) followed by using Eq. (A.112) for the ρ_k-integral. In [177], Eq. (A.97) has been used for the ρ_k-integral. For the k_z-integral, one can modify the Sommerfeld identity with $J_0(z) = [H_0^{(1)}(z) + H_0^{(2)}(z)]/2$, which follows by definition from Eqs. (A.94) and (A.95). Together with the reflection formula $H_0^{(1)}(-z) = H_0^{(2)}(z)$ and by extending the lower integral limit to negative infinity, one obtains an alternative version of the Sommerfeld identity [321]:

$$\begin{aligned} -\frac{\exp(ikr)}{r} &= \frac{1}{2} \int_{-\infty}^\infty k'_\rho \mathrm{d}k'_\rho H_0^{(1)}(k'_\rho \rho) \frac{\exp\left(i\tilde{k}'_z |z|\right)}{i\tilde{k}'_z} \\ &= \frac{1}{\pi} \int_{-\infty}^\infty \mathrm{d}\tilde{k}'_z K_0\left(\rho\sqrt{\tilde{k}_z'^2 - k^2}\right) \exp\left(i\tilde{k}'_z |z|\right), \end{aligned} \tag{A.14}$$

where $K_0(z) = i\pi/2 H_0^{(1)}(iz)$ has been applied. Just like Eq. (A.111), it also only holds for $\Im(k) > 0$. The equivalent of Eq. (A.112) is analogous.

A.4 Sokhotski-Plemelj formula

The Sokhotski-Plemelj formula considers the following limit [322]

$$\lim_{\epsilon \to 0^+} \int_a^b \frac{f(x)}{x - x_0 \pm i\epsilon} \mathrm{d}x = \mp i\pi f(x_0) + \mathcal{P} \int_a^b \frac{f(x)}{x - x_0} \mathrm{d}x, \tag{A.15}$$

where $f(x)$ is a generic uni-variate function, $\mathcal{P}$ is the Chauchy principal value and $a < x_0 < b$. Less formally, it can also be stated as

$$\lim_{\epsilon \to 0^+} \frac{1}{x - x_0 \pm i\epsilon} = \mp i\pi\delta(x - x_0) + \mathcal{P}\frac{1}{x - x_0}, \tag{A.16}$$

which is only sensible in combination with an integral across x_0.

A.5 Derivation of Eqs. (4.46) and (4.47)

The subject of this section is to present a more detailed derivation of Eqs. (4.46) and (4.47). The following steps are similar to what is shown in [169]. On a side note, it has explicitly been requested during the revision of [177]. When transforming $i\omega \to \partial/\partial t$ in Eq. (4.45), then the time derivative acts on quantities that are evaluated at the retarded time defined in Eq. (4.43). In particular, one needs to evaluate

$$\frac{\mathrm{d}}{\mathrm{d}t}\left[\frac{\mathbf{n}_\mathrm{p}}{|\mathbf{r}-\mathbf{r}_\mathrm{p}|}\frac{1}{1-\mathbf{n}_\mathrm{p}\cdot\tilde{\boldsymbol{\beta}}_\mathrm{p}}\right]_{t'(\mathbf{r},t)}, \tag{A.17}$$

$$\frac{\mathrm{d}}{\mathrm{d}t}\left[\frac{\mathbf{v}_\mathrm{p}}{|\mathbf{r}-\mathbf{r}_\mathrm{p}|}\frac{1}{1-\mathbf{n}_\mathrm{p}\cdot\tilde{\boldsymbol{\beta}}_\mathrm{p}}\right]_{t'(\mathbf{r},t)}, \tag{A.18}$$

which are the second and third terms in the round brackets of Eq. (4.45). Recall that $\mathbf{n}_\mathrm{p} = (\mathbf{r}-\mathbf{r}_\mathrm{p})/|\mathbf{r}-\mathbf{r}_\mathrm{p}|$, as defined below Eq. (4.43). Though Eq. (4.44), the differentiation with respect to t is simplified considerably by using Eq. (4.44):

$$\left[\frac{\mathrm{d}}{\mathrm{d}t'}\left(\frac{\mathbf{n}_\mathrm{p}}{|\mathbf{r}-\mathbf{r}_\mathrm{p}|}\frac{1}{1-\mathbf{n}_\mathrm{p}\cdot\tilde{\boldsymbol{\beta}}_\mathrm{p}}\right)\right]\frac{1}{1-\mathbf{n}_\mathrm{p}\cdot\tilde{\boldsymbol{\beta}}_\mathrm{p}}, \tag{A.19}$$

$$\left[\frac{\mathrm{d}}{\mathrm{d}t'}\left(\frac{\mathbf{v}_\mathrm{p}}{|\mathbf{r}-\mathbf{r}_\mathrm{p}|}\frac{1}{1-\mathbf{n}_\mathrm{p}\cdot\tilde{\boldsymbol{\beta}}_\mathrm{p}}\right)\right]\frac{1}{1-\mathbf{n}_\mathrm{p}\cdot\tilde{\boldsymbol{\beta}}_\mathrm{p}}. \tag{A.20}$$

Using

$$\frac{\mathrm{d}}{\mathrm{d}t'}|\mathbf{r}-\mathbf{r}_\mathrm{p}| = -\mathbf{n}_\mathrm{p}\cdot\tilde{\boldsymbol{\beta}}_\mathrm{p}\tilde{c}, \tag{A.21}$$

$$\frac{\mathrm{d}}{\mathrm{d}t'}\mathbf{n}_\mathrm{p} = \frac{\mathbf{n}_\mathrm{p}(\mathbf{n}_\mathrm{p}\cdot\tilde{\boldsymbol{\beta}}_\mathrm{p})-\tilde{\boldsymbol{\beta}}_\mathrm{p}}{|\mathbf{r}-\mathbf{r}_\mathrm{p}|}\tilde{c}, \tag{A.22}$$

one can easily show

$$\frac{\mathrm{d}}{\mathrm{d}t'}\frac{\mathbf{n}_\mathrm{p}}{|\mathbf{r}-\mathbf{r}_\mathrm{p}|} = \frac{2\mathbf{n}_\mathrm{p}(\mathbf{n}_\mathrm{p}\cdot\tilde{\boldsymbol{\beta}}_\mathrm{p})-\tilde{\boldsymbol{\beta}}_\mathrm{p}}{|\mathbf{r}-\mathbf{r}_\mathrm{p}|^2}\tilde{c}, \tag{A.23}$$

$$\frac{\mathrm{d}}{\mathrm{d}t'}\frac{\tilde{\boldsymbol{\beta}}_\mathrm{p}}{|\mathbf{r}-\mathbf{r}_\mathrm{p}|} = \frac{\tilde{\boldsymbol{\beta}}_\mathrm{p}(\mathbf{n}_\mathrm{p}\cdot\tilde{\boldsymbol{\beta}}_\mathrm{p})}{|\mathbf{r}-\mathbf{r}_\mathrm{p}|^2}\tilde{c}+\frac{\dot{\tilde{\boldsymbol{\beta}}}_\mathrm{p}}{|\mathbf{r}-\mathbf{r}_\mathrm{p}|}. \tag{A.24}$$

With Eqs. (A.21) to (A.24), Eqs. (A.19) and (A.20) can be evaluated and simplified. Replacing the result in Eq. (4.45) and transforming the t-integral back to the retarded time t' leads to Eq. (4.47).

A.6 Integral approximations for a complete path

The lower integral limits of Eqs. (4.25) and (4.52) are extended to negative infinity, when assuming a path for $t' < 0$. A linear path, which is described by $f_z(t'<0) = v_0 t'$, is considered. Consequently, $\dot{f}_z(t'<0) = v_0$ and $\ddot{f}_z(t'<0) = 0$. Despite its simplicity, the resulting integrand cannot be evaluated analytically. Instead, it is only possible for an approximation (provided in the following) which can then be subtracted from the complete integrand. The result is then integrated numerically with a finite lower limit. Finally, the analytically evaluated approximation is added on top. Most importantly, this requires an approximation that improves as t' goes to negative infinity. For such large negative values of t', $\Delta z(t') \gg \rho$ so that $d(\mathbf{r},t') \approx \Delta z(t')$. (For $z > 0$ and $t' < 0$, the absolute value can be dropped.) Together with the linear path described above, Eq. (4.29) is approximated by

$$f_z^{①}(\mathbf{r},\omega,t') \approx \frac{q_\mathrm{e}}{\tilde{\varepsilon}_\mathrm{c}(\omega)}\left[\frac{1}{\Delta z(t')}+\frac{i\omega}{\tilde{c}(\omega)}\frac{\tilde{c}(\omega)-v_0}{\tilde{c}(\omega)}\right]\frac{\exp[-i\omega\Delta z(t')/\tilde{c}(\omega)]}{4\pi\Delta z(t')}. \tag{A.25}$$

Likewise, Eqs. (4.47) and (4.49) simplify to

$$f_z^{②}(\mathbf{r},\omega,t') \approx \frac{q_\mathrm{e}}{\tilde{\varepsilon}_\mathrm{c}(\omega)}\left[\frac{1}{\Delta z(t')}\frac{\tilde{c}(\omega)+v_0}{\tilde{c}(\omega)}\right]\frac{\exp[-i\omega\Delta z(t')/\tilde{c}(\omega)]}{4\pi\Delta z(t')}, \tag{A.26}$$

where the acceleration term vanished entirely. With these approximations it is possible to express the associated integral in terms of the exponential integral $\mathrm{E}_1(z) = \int_1^\infty \exp(-zt)/t\,\mathrm{d}t$ [220]:

$$\int_{-\infty}^{0}\frac{\mathrm{d}t'}{2\pi}f_z^{①}(\mathbf{r},\omega,t')\exp\big(-i\omega t'\big) \approx \frac{1}{2\pi}\,\frac{q_\mathrm{e}}{\tilde{\varepsilon}_c(\omega)}\,\frac{\tilde{c}(\omega)+v_0}{\tilde{c}(\omega)v_0}\,\frac{\exp[-i\omega z/\tilde{c}(\omega)]}{4\pi z} \left[\frac{\tilde{c}(\omega)}{\tilde{c}(\omega)+v_0} - a\exp(a)\,\mathrm{E}_1(a)\right], \tag{A.27}$$

$$\int_{-\infty}^{0}\frac{\mathrm{d}t'}{2\pi}f_z^{②}(\mathbf{r},\omega,t')\exp\big(-i\omega t'\big) \approx \frac{1}{2\pi}\,\frac{q_\mathrm{e}}{\tilde{\varepsilon}_c(\omega)}\,\frac{\tilde{c}(\omega)+v_0}{\tilde{c}(\omega)v_0}\,\frac{\exp[-i\omega z/\tilde{c}(\omega)]}{4\pi z} \big[1 - a\exp(a)\,\mathrm{E}_1(a)\big], \tag{A.28}$$

where $a = -i\omega z[1/v_0 - 1/\tilde{c}(\omega)]$.

A.7 Electric field of the charge source term

The derivation of Eq. (4.50) is presented. The expression for $\tilde{\tilde{\mathbf{E}}}_\mathrm{s}(\mathbf{k},\omega)$ is given in Sec. 4.1.6.2. The following is just the inversion of the spatial Fourier transform:

$$\begin{aligned}
\widetilde{\mathbf{E}}_\mathrm{s}(\mathbf{r},\omega) &= \int_{\mathbb{R}^3}\mathrm{d}^3\mathbf{k}\exp(-i\mathbf{k}\cdot\mathbf{r})\tilde{\tilde{\mathbf{E}}}_\mathrm{s}(\mathbf{k},\omega)\\
&= \frac{q_\mathrm{e}\mu\omega}{(2\pi)^4}\int_{\mathbb{R}^3}\mathrm{d}^3\mathbf{k}\exp(-i\mathbf{k}\cdot\mathbf{r})\frac{\mathbf{k}}{k^2(k^2-\omega^2/\tilde{c}^2)}\\
&= \frac{q_\mathrm{e}\mu i\omega}{(2\pi)^4}\nabla\int_{\mathbb{R}^3}\mathrm{d}^3\mathbf{k}\frac{\exp(-i\mathbf{k}\cdot\mathbf{r})}{k^2(k^2-\omega^2/\tilde{c}^2)}\\
&= \frac{q_\mathrm{e}\mu i\omega}{(2\pi)^4}\nabla\int_0^\infty k^2\mathrm{d}k\int_0^{2\pi}\mathrm{d}\phi_k\int_{-1}^{1}\mathrm{d}\mu_k\frac{\exp(-ikr\mu_k)}{k^2(k^2-\omega^2/\tilde{c}^2)}\\
&= \frac{q_\mathrm{e}\mu i\omega}{(2\pi)^3}\nabla\int_0^\infty \mathrm{d}k\frac{2\sin(kr)}{kr(k^2-\omega^2/\tilde{c}^2)}\\
&= \frac{q_\mathrm{e}\mu i\omega}{(2\pi)^3}\nabla\left[\pi\frac{\exp(-i\omega/\tilde{c}\,r)-1}{\omega^2/\tilde{c}^2\,r}\right]\\
&= \frac{q_\mathrm{e}}{2\pi\,i\omega\tilde{\varepsilon}_\mathrm{c}}\frac{\hat{\mathbf{e}}_r}{4\pi r^2}\big[\exp(-i\omega/\tilde{c}\,r)(1+i\omega/\tilde{c}\,r)-1\big].
\end{aligned} \tag{A.29}$$

A.8 Boundary step

The discontinuity at the boundary is analytically modeled through infinitely sharp but finite step. For reasons detailed in the main text, an asymmetric representation, so that the step lies entirely in the positive half, is chosen:

$$\theta_\epsilon^+(x) = \begin{cases} 0 & \text{for } x \le 0\\ 6(x/\epsilon)^5 - 15(x/\epsilon)^4 + 10(x/\epsilon)^3 & \text{for } 0 < x < \epsilon\\ 1 & \text{for } x \ge \epsilon \end{cases}. \tag{A.30}$$

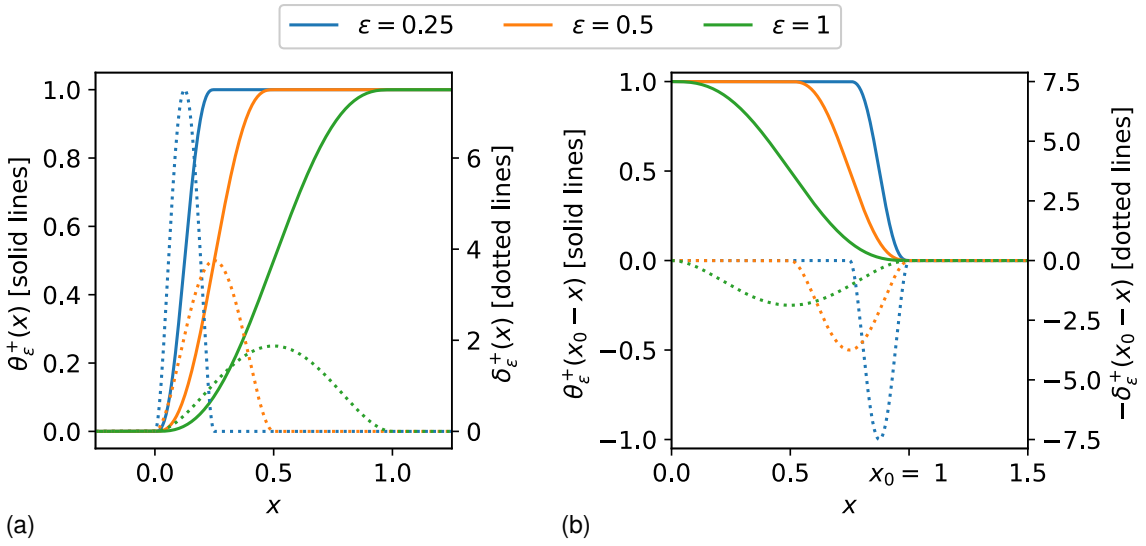

Figure A.1: Exemplary plots of Eq. (A.30) (left vertical axes) and Eq. (A.31) (right vertical axes) for different values of ϵ. (b) also shows Eq. (A.30) with an argument that causes a flip and shift. In both cases the right vertical axis shows the derivative of the function depicted with the left vertical axis, so that for (b) an additional minus appears.

With the differential relationship between the Heaviside step function and the Dirac-delta function ($\partial_x \theta^+(x) = \delta^+(x)$), one can also provide

$$\delta^+_\epsilon(x) = \frac{30}{\epsilon} \begin{cases} (x/\epsilon)^2 - 2(x/\epsilon)^3 + (x/\epsilon)^4 & \text{for } 0 < x < \epsilon \\ 0 & \text{else} \end{cases}. \tag{A.31}$$

Both Eqs. (A.30) and (A.31) are shown in Fig. A.1. The limit then defines the sharp step function:

$$\theta^+(x) = \lim_{\epsilon \to 0^+} \theta^+_\epsilon(x), \tag{A.32}$$

$$\delta^+(x) = \lim_{\epsilon \to 0^+} \delta^+_\epsilon(x). \tag{A.33}$$

The aforementioned asymmetry of Eq. (A.33) can formally be stated as

$$\int_{-\infty}^{0} \delta^+(x)\mathrm{d}x = 0, \tag{A.34}$$

$$\int_{0}^{\infty} \delta^+(x)\mathrm{d}x = 1. \tag{A.35}$$

Throughout this work, the argument of Eqs. (A.32) and (A.33) is oftentimes given by $x_0 - x$, where $x_0 > 0$ is some vertical shift. Thereby, $\theta^+(x_0 - x)$ and $\delta^+(x_0 - x)$ flip so that the entire weight is then contained in $x < x_0$ (see Fig. A.1 (b)).

Three specific combinations of the step- and delta-function are relevant in the main text. Since they all scale with the delta-function in the numerator, they can be represented as a single delta-function paired with an adjusted normalization:

$$-\delta^+(x_0 - x)\theta^+(x_0 - x) = N_1 \delta^+(x_0 - x), \tag{A.36}$$

$$\frac{-\chi\delta^+(x_0 - x)}{1 + \chi\theta^+(x_0 - x)} = N_2 \delta^+(x_0 - x), \tag{A.37}$$

$$\frac{-\chi\delta^+(x_0 - x)}{\left[1 + \chi\theta^+(x_0 - x)\right]^2} = N_3 \delta^+(x_0 - x), \tag{A.38}$$

where N_1, N_2 and N_3 are the normalization factors, which are determined in the following. Eqs. (A.36) to (A.38) all have elementary integrals, since they are combinations of a function

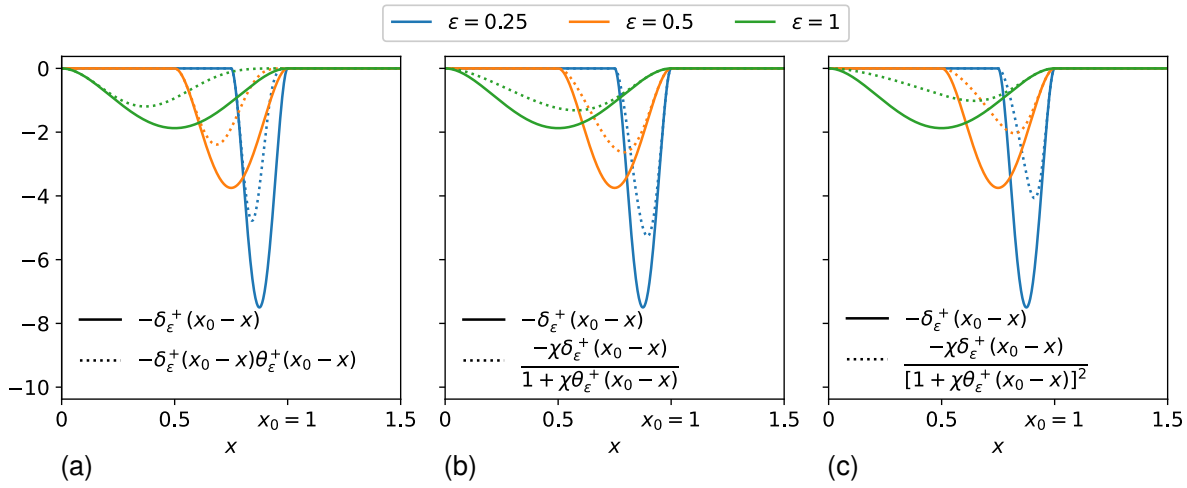

Figure A.2: Qualitative confirmation of Eqs. (A.36) to (A.38). In (a), the area under the dotted vs the solid line for a given ϵ is half as large, as stated in Eq. (A.39). For (b) and (c), $\chi = 1$ has been chosen so that the weight of the dotted line is $\log(2)$ and $1/2$, respectively, following from Eqs. (A.40) and (A.41).

(θ^+) and its derivative (δ^+):

$$N_1 = \int_{-\infty}^{\infty} [-\delta^+(x_0 - x)]\theta^+(x_0 - x)\mathrm{d}x = \frac{1}{2}\theta^{+2}(x_0 - x)\Big|_{-\infty}^{\infty} = -\frac{1}{2}, \tag{A.39}$$

$$N_2 = \int_{-\infty}^{\infty} \frac{-\chi\delta^+(x_0 - x)}{1 + \chi\theta^+(x_0 - x)}\mathrm{d}x = \log[1 + \chi\theta^+(x_0 - x)]\Big|_{-\infty}^{\infty} = -\log(1 + \chi), \tag{A.40}$$

$$N_3 = \int_{-\infty}^{\infty} \frac{-\chi\delta^+(x_0 - x)}{[1 + \chi\theta^+(x_0 - x)]^2}\mathrm{d}x = -\frac{1}{1 + \chi\theta^+(x_0 - x)}\Big|_{-\infty}^{\infty} = -\frac{\chi}{1 + \chi}. \tag{A.41}$$

With the expressions of Eqs. (A.30) and (A.31), one can visually confirm that Eqs. (A.36) to (A.38) are compacted in an arbitrarily narrow interval of $[x_0 - \epsilon, x_0]$, as shown in Fig. A.2. They also possess the same asymmetry as stated in Eqs. (A.34) and (A.35), so one can conclude that in the limit $\epsilon \to 0^+$, the LHSs of Eqs. (A.36) to (A.38) and $\delta^+(x_0 - x)$ differ only by the multiplicative factors given in Eqs. (A.39) to (A.41).

Finally, the importance of the asymmetry (Eqs. (A.34) and (A.35)), which is maintained under the identities of Eqs. (A.36) to (A.38), shall be underlined. In fact, a symmetric step and delta function pair turns asymmetric under e.g. Eq. (A.36). With the same approach as in Eq. (A.39), one can evaluate

$$\int_{-\infty}^{x} \delta(x')\theta(x')\mathrm{d}x' = \frac{1}{2}\theta^2(x), \tag{A.42}$$

from which follows

$$\int_{-\infty}^{0} \delta(x)\theta(x)\mathrm{d}x = \frac{1}{8}, \tag{A.43}$$

$$\int_{0}^{\infty} \delta(x)\theta(x)\mathrm{d}x = \frac{3}{8}, \tag{A.44}$$

where a symmetric step has been assumed: $\theta(0) = 1/2$. The resulting distribution of $\delta(x)\theta(x)$ has the same weight as in Eq. (A.36) $(1/8 + 3/8 = 1/2)$, but is now asymmetric as can be concluded in Eqs. (A.43) and (A.44). Hence, one cannot justifiably arrive at Eq. (A.36) when multiplying $\theta(x)$ and $\delta(x)$ so that $\delta(x)\theta(x) \neq \delta(x)/2$. Generally, asymmet-

ric representations of the delta function exist. The construction through the Airy function is one example.

A.9 Electric field of the surface charge density

The explicit evaluation of the ρ-component of Eq. (4.64) with the source term ⓑ given in Eq. (4.61) is presented in the following. With $\mathbf{r} = \rho\hat{\mathbf{e}}_\rho + z\hat{\mathbf{e}}_z$, the projection onto $\hat{\mathbf{e}}_\rho$ is straightforward ($\mathbf{r}\cdot\hat{\mathbf{e}}_\rho = \rho$), yet more complex for $\mathbf{r}' = \rho'\hat{\mathbf{e}}'_\rho + z'\hat{\mathbf{e}}'_z$: $\mathbf{r}'\cdot\hat{\mathbf{e}}_\rho = \rho'\cos(\phi-\phi')$ and $|\mathbf{r}-\mathbf{r}'|^3 = [\rho^2 - 2\rho\rho'\cos(\phi-\phi') + \rho'^2 + (z-z')^2]^{3/2}$. With a complete integral over the azimuth $\phi' \in [0, 2\pi]$, it follows that ϕ only offsets the interval of the periodic cosine function. With Eq. (4.61) being ϕ-independent, its electric field will also be ϕ-independent. The integral over the azimuth in Eq. (4.64) can be evaluated with the following identities

$$\int_0^{2\pi} \frac{\mathrm{d}\phi'}{(a - b\cos\phi')^{3/2}} = 4\frac{\mathcal{E}[-2b/(a-b)]}{\sqrt{a-b}(a+b)}, \tag{A.45}$$

$$\int_0^{2\pi} \frac{\cos\phi'\mathrm{d}\phi'}{(a - b\cos\phi')^{3/2}} = 4\frac{a\mathcal{E}[-2b/(a-b)] - (a+b)\mathcal{K}[-2b/(a-b)]}{\sqrt{a-b}(a+b)b}, \tag{A.46}$$

where $\mathcal{K}(\circ)$ and $\mathcal{E}(\circ)$ are the complete elliptic integrals of he first [323] and second [324] kind. In the present case the parameters are given by $a = \rho^2 + \rho'^2 + (z-z')^2$ and $b = 2\rho\rho'$. The integral with respect to ρ' is collapsed by the delta function, while the z'-integral can be represented as the convolution given in Eq. (4.66), where the convolution kernel is given by

$$\mathcal{Z}(\rho, z) = \frac{1}{\pi}\frac{1}{\sqrt{(\rho-\rho_\mathrm{c})^2+z^2}}\left\{\mathcal{K}\left[\frac{-4\rho\rho_\mathrm{c}}{(\rho-\rho_\mathrm{c})^2+z^2}\right] + \frac{\rho^2-\rho_\mathrm{c}^2-z^2}{(\rho+\rho_\mathrm{c})^2+z^2}\mathcal{E}\left[\frac{-4\rho\rho_\mathrm{c}}{(\rho-\rho_\mathrm{c})^2+z^2}\right]\right\}. \tag{A.47}$$

When evaluated on the cylinder surface ($\rho = \rho_\mathrm{c}$), one obtains Eq. (4.67).

A.10 Fourier transform of $\mathcal{Z}(z)$

The Fourier transform of Eq. (4.67) can be expressed through the Meijer-G function [325]:

$$\begin{aligned}\widetilde{\mathcal{Z}}(k_z) = \int_{-\infty}^{\infty}\frac{\mathrm{d}z}{2\pi}\mathcal{Z}(z)\exp(ik_z z) &= \frac{1}{4\pi^{3/2}}\left[\overbrace{\mathrm{G}^{2,1}_{1,3}\left(\begin{matrix}1/2\\0,0,0\end{matrix}\middle|\rho_\mathrm{c}^2k_z^2\right)}^{2\pi^{1/2}I_0(\rho_\mathrm{c}k_z)K_0(\rho_\mathrm{c}|k_z|)} - 2\,\mathrm{G}^{2,1}_{1,3}\left(\begin{matrix}-1/2\\0,0,0\end{matrix}\middle|\rho_\mathrm{c}^2k_z^2\right)\right] \\ &= \frac{1}{2\pi^{3/2}}\,\mathrm{G}^{2,1}_{1,3}\left(\begin{matrix}1/2\\0,1,0\end{matrix}\middle|\rho_\mathrm{c}^2k_z^2\right).\end{aligned} \tag{A.48}$$

A.11 Poynting theorem-related surface and volume integrals

Here, details for the evaluation of Eq. (4.76) and the volume integral over Eq. (4.79) are provided. Based on Eqs. (4.28), (4.29) and (4.35), one can write

$$\widetilde{\mathbf{E}}(\mathbf{r},\omega) = \widetilde{E}^+_\rho(\mathbf{r},\omega)\hat{\mathbf{e}}_\rho + \widetilde{E}^+_z(\mathbf{r},\omega)\hat{\mathbf{e}}_z, \tag{A.49}$$

$$\mathbf{H}(\mathbf{r},\omega) = \widetilde{B}^+_\phi(\mathbf{r},\omega)/\mu\hat{\mathbf{e}}_\phi. \tag{A.50}$$

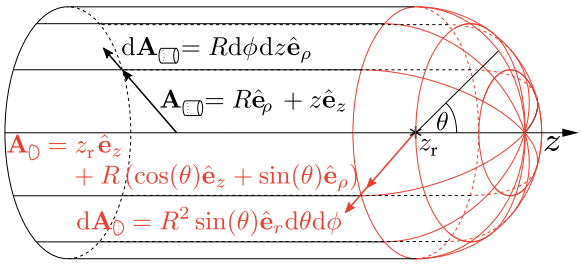

Figure A.3: The two surfaces, cylinder (black) and hemisphere (red), through which the energy flow is calculated.

The time-integrated (which is equal to frequency-integrated) Poynting vector is defined as

$$\bar{\mathbf{S}}(\mathbf{r}) \equiv 2\pi \int_{-\infty}^{\infty} \widetilde{\mathbf{E}}(\mathbf{r},\omega) \times \widetilde{\mathbf{H}}^{\dagger}(\mathbf{r},\omega)\mathrm{d}\omega = \bar{S}_\rho(\mathbf{r})\hat{\mathbf{e}}_\rho + \bar{S}_z(\mathbf{r})\hat{\mathbf{e}}_z \tag{A.51}$$

where its components are given by

$$\bar{S}_\rho(\mathbf{r}) = -2\pi \int_{-\infty}^{\infty} \widetilde{E}_z^{+}(\mathbf{r},\omega)\widetilde{B}_\phi^{+\dagger}(\mathbf{r},\omega)/\mu\mathrm{d}\omega, \tag{A.52}$$

$$\bar{S}_z(\mathbf{r}) = 2\pi \int_{-\infty}^{\infty} \widetilde{E}_\rho^{+}(\mathbf{r},\omega)\widetilde{B}_\phi^{+\dagger}(\mathbf{r},\omega)/\mu\mathrm{d}\omega. \tag{A.53}$$

The two surfaces defined in Eqs. (4.77) and (4.78) with their parametrizations, including surface elements, are shown in Fig. A.3. The surface integral of Eq. (4.76) is separated accordingly:

$$E^{\mathrm{rad}} = E^{\mathrm{rad}}_{\square} + E^{\mathrm{rad}}_{\bigcirc}, \tag{A.54}$$

$$E^{\mathrm{rad}}_{\square} = \int_0^{2\pi} R\mathrm{d}\phi \int_{-\infty}^{z_\mathrm{r}} \mathrm{d}z\bar{S}_\rho(\mathbf{A}_{\square}), \tag{A.55}$$

$$E^{\mathrm{rad}}_{\bigcirc} = \int_0^{\pi/2} R\mathrm{d}\theta \int_0^{2\pi} R\sin\theta\mathrm{d}\phi \left[\bar{S}_z(\mathbf{A}_{\bigcirc})\cos\theta + \bar{S}_\rho(\mathbf{A}_{\bigcirc})\sin\theta\right]. \tag{A.56}$$

The volume integral over Eq. (4.79) between two surfaces with radii R_1 and R_2 is

$$\begin{aligned}\Delta E^{\mathrm{rad}} &= \overbrace{\int_{\Delta\square} u(\mathbf{r})\mathrm{d}^3\mathbf{r}} + \overbrace{\int_{\Delta\bigcirc} u(\mathbf{r})\mathrm{d}^3\mathbf{r}} \\ &= \overbrace{\int_{R_1}^{R_2}\mathrm{d}\rho\int_0^{2\pi}\rho\mathrm{d}\phi\int_{-\infty}^{z_\mathrm{r}}\mathrm{d}z\,u(\mathbf{r})} + \overbrace{\int_{R_1}^{R_2}\mathrm{d}r\int_0^{\pi/2}r\mathrm{d}\theta\int_0^{2\pi}r\sin\theta\mathrm{d}\phi\,u(\mathbf{r})}.\end{aligned} \tag{A.57}$$

A.12 Cherenkov radiation

The textbook derivation of the Frank–Tamm formula, which describes the Cherenkov radiation, first estimates the associated electromagnetic fields. Their estimation is presented in the following, being mostly a translation to SI units from Jackson [153]. Starting from

Eq. (4.15):

$$\begin{aligned}
\widetilde{\mathbf{F}}(\mathbf{r},\omega) &= \frac{q_\mathrm{e}}{(2\pi)^3}\int_{\mathbb{R}^3}\mathrm{d}^3\mathbf{k}\int_{-\infty}^{\infty}\frac{\mathrm{d}t'}{2\pi}\,\tilde{\mathbf{f}}_F(\omega,t')\frac{\exp[-i\mathbf{k}\cdot\mathbf{r}+ik_z f_z(t')-i\omega t']}{k^2-\omega^2/\tilde{c}^2(\omega)}\\
&= \frac{q_\mathrm{e}}{(2\pi)^3}\int_0^\infty \rho_k\mathrm{d}\rho_k\int_0^{2\pi}\mathrm{d}\phi_k\int_{-\infty}^{\infty}\mathrm{d}k_z\int_{-\infty}^{\infty}\frac{\mathrm{d}t'}{2\pi}\tilde{\mathbf{f}}_F(\omega,t')\\
&\qquad\qquad \frac{\exp[-i\rho\rho_k\cos(\phi-\phi_k)-ik_z z+ik_z f_z(t')-i\omega t']}{\rho_k^2+k_z^2-\omega^2/\tilde{c}^2(\omega)}\\
&= \frac{q_\mathrm{e}}{(2\pi)^2}\int_0^\infty \rho_k\mathrm{d}\rho_k\int_{-\infty}^{\infty}\mathrm{d}k_z\int_{-\infty}^{\infty}\frac{\mathrm{d}t'}{2\pi}\tilde{\mathbf{f}}_F(\omega,t')J_0(\rho\rho_k)\frac{\exp[-ik_z z+ik_z f_z(t')-i\omega t']}{\rho_k^2+k_z^2-\omega^2/\tilde{c}^2(\omega)}\\
&= \frac{q_\mathrm{e}}{(2\pi)^2}\int_0^\infty \mu_k\mathrm{d}\mu_k\int_{-\infty}^{\infty}\mathrm{d}k_z\int_{-\infty}^{\infty}\frac{\mathrm{d}t'}{2\pi}\tilde{\mathbf{f}}_F(\omega,t')J_0(\mu_k)\frac{\exp[-ik_z z+ik_z f_z(t')-i\omega t']}{\mu_k^2+\rho^2[k_z^2-\omega^2/\tilde{c}^2(\omega)]}\\
&= \frac{q_\mathrm{e}}{(2\pi)^2}\int_{-\infty}^{\infty}\mathrm{d}k_z\int_{-\infty}^{\infty}\frac{\mathrm{d}t'}{2\pi}\tilde{\mathbf{f}}_F(\omega,t')K_0\Big(\rho\sqrt{k_z^2-\omega^2/\tilde{c}^2(\omega)}\Big)\\
&\qquad\qquad \exp\big[-ik_z z+ik_z f_z(t')-i\omega t'\big],
\end{aligned} \tag{A.58}$$

where both Eqs. (A.96) and (A.97) have been used. Following Appendix A.3 the next step would be to carry out the k_z-integral via Eq. (A.14) to obtain the Green's function of the Helmholtz equation. However, for a point particle moving with the constant velocity v along z, where $f_z(t') = vt'$ and $\dot{f}_z(t') = v$, one can evaluate the t'-integral first. This is possible since the $\tilde{\mathbf{f}}_F(\omega,t')$ become independent of t' for a linearly moving particle. Consequently, one can use (see Eq. (6.23))

$$\int_{-\infty}^{\infty}\frac{\mathrm{d}t'}{2\pi}\exp\big[i(k_z v-\omega)t'\big] = \delta(k_z v-\omega)\overset{v\gtrless 0}{=}\delta(k_z-\omega/v)/v, \tag{A.59}$$

where the scaling property of the delta function has been used in the last step. With Eq. (4.23) and Eq. (A.73), the radial electric field becomes

$$\begin{aligned}
\widetilde{E}_\rho(\mathbf{r},\omega) &= \frac{q_\mathrm{e}}{(2\pi)^2}\int_{-\infty}^{\infty}\mathrm{d}k_z\frac{(-\partial_\rho)}{\tilde{\varepsilon}_\mathrm{c}(\omega)}\delta(k_z-\omega/v)/v\,K_0\Big(\rho\sqrt{k_z^2-\omega^2/\tilde{c}^2(\omega)}\Big)\exp(-ik_z z)\\
&= \frac{q_\mathrm{e}}{(2\pi)^2\tilde{\varepsilon}_\mathrm{c}(\omega)v}(-\partial_\rho)K_0(\rho\lambda)\exp(-i\omega/v\,z)\\
&= \frac{q_\mathrm{e}\lambda}{(2\pi)^2\tilde{\varepsilon}_\mathrm{c}(\omega)v}K_1(\rho\lambda)\exp(-i\omega/v\,z),
\end{aligned} \tag{A.60}$$

where λ has been introduced and is defined by

$$\lambda^2 = \omega^2[1/v^2-1/\tilde{c}^2(\omega)]. \tag{A.61}$$

Since the azimuthal component of $\tilde{\mathbf{f}}_B(\omega,t')$ differs only multiplicatively from the radial component of $\tilde{\mathbf{f}}_E(\omega,t')$, one also gets

$$\widetilde{B}_\phi(\mathbf{r},\omega) = v/\tilde{c}^2(\omega)\widetilde{E}_\rho(\mathbf{r},\omega). \tag{A.62}$$

For the longitudinal component of the electric field, Eqs. (4.23) and (A.73) are also needed:

$$\begin{aligned}\widetilde{E}_z(\mathbf{r},\omega) &= \frac{q_\mathrm{e}}{(2\pi)^2}\int_{-\infty}^{\infty}\mathrm{d}k_z\Big[-\frac{i\omega v/\tilde{c}^2(\omega)+\partial_z}{\tilde{\varepsilon}_\mathrm{c}(\omega)}\Big]\delta(k_z-\omega/v)/v \\ &\qquad\qquad K_0\Big(\rho\sqrt{k_z^2-\omega^2/\tilde{c}^2(\omega)}\Big)\exp(-ik_z z) \\ &= \frac{q_\mathrm{e}}{(2\pi)^2\tilde{\varepsilon}_\mathrm{c}(\omega)}\big[-i\omega/\tilde{c}^2(\omega)-\partial_z/v\big]K_0(\rho\lambda)\exp(-i\omega/v\,z) \\ &= \frac{q_\mathrm{e}}{(2\pi)^2\tilde{\varepsilon}_\mathrm{c}(\omega)}\big[\underbrace{-i\omega/\tilde{c}^2(\omega)+i\omega/v^2}_{i\lambda^2/\omega}\big]K_0(\rho\lambda)\exp(-i\omega/v\,z) \\ &= \frac{iq_\mathrm{e}\lambda^2}{(2\pi)^2\tilde{\varepsilon}_\mathrm{c}(\omega)\omega}K_0(\rho\lambda)\exp(-i\omega/v\,z). \end{aligned} \tag{A.63}$$

In summary, the textbook results for the electromagnetic fields associated with the Cherenkov radiation have been derived from Eq. (4.15). Eqs. (A.60), (A.62) and (A.63) are slightly more general though, since they are valid also for $z \neq 0$. Unfortunately, this approach cannot be applied for the problem from Appendix A.6, since (see Eq. (4.32))

$$\int_{-\infty}^{0}\frac{\mathrm{d}t'}{2\pi}\exp\big[i(k_z v-\omega)t'\big] = \frac{1}{2}\delta(k_z v-\omega)+\mathcal{P}\frac{1}{2\pi i(k_z v-\omega)}, \tag{A.64}$$

where the second term cannot be evaluated analytically in Eq. (A.58).

A.13 Transformation of Eqs. (3.58) and (3.60)

With Eq. (A.71) and $\mathbf{A} = A_x\hat{\mathbf{e}}_x + A_y\hat{\mathbf{e}}_y + A_z\hat{\mathbf{e}}_z$, (A_x, A_y, A_z) are represented through (A_ρ, A_ϕ, A_z). Together with Eq. (A.73), one gets

$$\begin{aligned}\nabla A_x &= \Big(\frac{\partial A_\rho}{\partial\rho}\mathfrak{c}-\frac{\partial A_\phi}{\partial\rho}\mathfrak{s}\Big)\hat{\mathbf{e}}_\rho+\Big(\frac{\partial A_\rho}{\partial\phi}\frac{\mathfrak{c}}{\rho}-A_\rho\frac{\mathfrak{s}}{\rho}-\frac{\partial A_\phi}{\partial\phi}\frac{\mathfrak{s}}{\rho}-A_\phi\frac{\mathfrak{c}}{\rho}\Big)\hat{\mathbf{e}}_\phi+\Big(\frac{\partial A_\rho}{\partial z}\mathfrak{c}-\frac{\partial A_\phi}{\partial z}\mathfrak{s}\Big)\hat{\mathbf{e}}_z, \\ \nabla A_y &= \Big(\frac{\partial A_\rho}{\partial\rho}\mathfrak{s}+\frac{\partial A_\phi}{\partial\rho}\mathfrak{c}\Big)\hat{\mathbf{e}}_\rho+\Big(\frac{\partial A_\rho}{\partial\phi}\frac{\mathfrak{s}}{\rho}+A_\rho\frac{\mathfrak{c}}{\rho}+\frac{\partial A_\phi}{\partial\phi}\frac{\mathfrak{c}}{\rho}-A_\phi\frac{\mathfrak{s}}{\rho}\Big)\hat{\mathbf{e}}_\phi+\Big(\frac{\partial A_\rho}{\partial z}\mathfrak{s}+\frac{\partial A_\phi}{\partial z}\mathfrak{c}\Big)\hat{\mathbf{e}}_z, \\ \nabla A_z &= \frac{\partial A_z}{\partial\rho}\hat{\mathbf{e}}_\rho+\frac{\partial A_z}{\partial\phi}\frac{1}{\rho}\hat{\mathbf{e}}_\phi+\frac{\partial A_z}{\partial z}\hat{\mathbf{e}}_z,\end{aligned}$$

where $\mathfrak{c} = \cos\phi$ and $\mathfrak{s} = \sin\phi$. With the cylindrical volume element, Eq. (3.58) transforms and simplifies through a repeated application of $\cos^2\phi + \sin^2\phi = \mathfrak{c}^2 + \mathfrak{s}^2 = 1$ to:

$$\begin{aligned}\mathcal{I}[\mathbf{A}] = \int_0^\infty\mathrm{d}\rho\int_0^{2\pi}\rho\mathrm{d}\phi\int_{-\infty}^{\infty}\mathrm{d}z\Bigg\{ \\ \frac{1}{2\mu}\Bigg[\Big(\frac{\partial A_\rho}{\partial\rho}\Big)^2+\Big(\frac{\partial A_\phi}{\partial\rho}\Big)^2+\frac{1}{\rho^2}\Big(\frac{\partial A_\phi}{\partial\phi}+A_\rho\Big)^2+\frac{1}{\rho^2}\Big(\frac{\partial A_\rho}{\partial\phi}-A_\phi\Big)^2 \\ +\Big(\frac{\partial A_\rho}{\partial z}\Big)^2+\Big(\frac{\partial A_\phi}{\partial z}\Big)^2+\Big(\frac{\partial A_z}{\partial\rho}\Big)^2+\frac{1}{\rho^2}\Big(\frac{\partial A_z}{\partial\phi}\Big)^2+\Big(\frac{\partial A_z}{\partial z}\Big)^2\Bigg]-\mathbf{J}\cdot\mathbf{A}\Bigg\}.\end{aligned} \tag{A.65}$$

A.14 Vector calculus identities in cylindrical coordinates

The identities that have been summarized in this section can be found in numerous textbooks, such as [220, 246]. General vector calculus identities, independent of the choice of coordinate system, are:

$$\nabla(\psi\chi) = \chi\nabla\psi + \psi\nabla\chi, \tag{A.66}$$

$$\nabla\left(\frac{\psi}{\chi}\right) = \frac{\chi\nabla\psi - \psi\nabla\chi}{\chi^2} \tag{A.67}$$

$$\nabla\cdot(\psi\mathbf{A}) = (\nabla\psi)\cdot\mathbf{A} + \psi\nabla\cdot\mathbf{A}, \tag{A.68}$$

$$\nabla\times\nabla\times\mathbf{A} = \nabla(\nabla\cdot\mathbf{A}) - \nabla^2\mathbf{A}, \tag{A.69}$$

$$\nabla^2(\nabla\cdot\mathbf{A}) = \nabla\cdot(\nabla^2\mathbf{A}), \tag{A.70}$$

where ψ and χ are scalar functions and $\mathbf{A}$ is a vector. The latter can be expanded into the cylindrical components A_ρ, A_ϕ and A_z:

$$\mathbf{A} = A_\rho\hat{\mathbf{e}}_\rho + A_\phi\hat{\mathbf{e}}_\phi + A_z\hat{\mathbf{e}}_z, \tag{A.71}$$

where $\hat{\mathbf{e}}_\rho$, $\hat{\mathbf{e}}_\phi$ and $\hat{\mathbf{e}}_z$ are the unit vectors, defined through

$$\hat{\mathbf{e}}_\rho = \begin{pmatrix}\cos\phi\\ \sin\phi\\ 0\end{pmatrix}, \qquad \hat{\mathbf{e}}_\phi = \begin{pmatrix}-\sin\phi\\ \cos\phi\\ 0\end{pmatrix}, \qquad \hat{\mathbf{e}}_z = \begin{pmatrix}0\\ 0\\ 1\end{pmatrix}. \tag{A.72}$$

How the Nabla-operator acts on scalar or vectorial quantities depends on the coordinate system. For cylindrical coordinates, one obtains

$$\nabla\psi = \frac{\partial\psi}{\partial\rho}\hat{\mathbf{e}}_\rho + \frac{1}{\rho}\frac{\partial\psi}{\partial\phi}\hat{\mathbf{e}}_\phi + \frac{\partial\psi}{\partial z}\hat{\mathbf{e}}_z, \qquad \text{(Gradient)} \tag{A.73}$$

$$\nabla\cdot\mathbf{A} = \frac{1}{\rho}\frac{\partial(\rho A_\rho)}{\partial\rho} + \frac{1}{\rho}\frac{\partial A_\phi}{\partial\phi} + \frac{\partial A_z}{\partial z}, \qquad \text{(Divergence)} \tag{A.74}$$

$$\nabla\times\mathbf{A} = \left(\frac{1}{\rho}\frac{\partial A_z}{\partial\phi} - \frac{\partial A_\phi}{\partial z}\right)\hat{\mathbf{e}}_\rho + \left(\frac{\partial A_\rho}{\partial z} - \frac{\partial A_z}{\partial\rho}\right)\hat{\mathbf{e}}_\phi + \frac{1}{\rho}\left(\frac{\partial(\rho A_\phi)}{\partial\rho} - \frac{\partial A_\rho}{\partial\phi}\right)\hat{\mathbf{e}}_z, \qquad \text{(Curl)} \tag{A.75}$$

$$\nabla^2\psi = \frac{1}{\rho}\frac{\partial}{\partial\rho}\left(\rho\frac{\partial\psi}{\partial\rho}\right) + \frac{1}{\rho^2}\frac{\partial^2\psi}{\partial\phi^2} + \frac{\partial^2\psi}{\partial z^2}, \qquad \text{(Laplacian)} \tag{A.76}$$

$$\nabla^2\mathbf{A} = \left(\nabla^2 A_\rho - \frac{A_\rho}{\rho^2} - \frac{2}{\rho^2}\frac{\partial A_\phi}{\partial\phi}\right)\hat{\mathbf{e}}_\rho + \left(\nabla^2 A_\phi - \frac{A_\phi}{\rho^2} + \frac{2}{\rho^2}\frac{\partial A_\rho}{\partial\phi}\right)\hat{\mathbf{e}}_\phi + \nabla^2 A_z\hat{\mathbf{e}}_z. \qquad \text{(Vector laplacian)} \tag{A.77}$$

A.15 Scalar and vector potential equations for an inhom. permittivity

Here, the explicit derivations of Eqs. (6.2) and (6.3) are presented. The manipulations for the vector potential are

$$\begin{aligned}
\nabla \times \widetilde{\mathbf{H}} &= \tilde{\mathbf{J}} + i\omega\widetilde{\mathbf{D}}, && \text{[Eq. (3.4d)]}\\
\nabla \times (\widetilde{\mathbf{B}}/\mu) &= \tilde{\mathbf{J}} + i\omega(\tilde{\varepsilon}\widetilde{\mathbf{E}}), && \text{[Eqs. (6.1a) and (6.1b)]}\\
\nabla \times \nabla \times \widetilde{\mathbf{A}} &= \mu\tilde{\mathbf{J}} + i\omega\mu\tilde{\varepsilon}\big(-\nabla\widetilde{\varphi} - i\omega\widetilde{\mathbf{A}}\big), && \text{[Eqs. (3.11) and (3.12)]}\\
\nabla(\nabla\cdot\widetilde{\mathbf{A}}) - \nabla^2\widetilde{\mathbf{A}} &= \mu\tilde{\mathbf{J}} - i\omega\mu\tilde{\varepsilon}\nabla\widetilde{\varphi} + \omega^2\mu\tilde{\varepsilon}\widetilde{\mathbf{A}}, && \text{[Eq. (A.69)]}\\
\nabla(-i\omega\mu\tilde{\varepsilon}\widetilde{\varphi}) - \nabla^2\widetilde{\mathbf{A}} &= \mu\tilde{\mathbf{J}} - i\omega\mu\tilde{\varepsilon}\nabla\widetilde{\varphi} + \omega^2\mu\tilde{\varepsilon}\widetilde{\mathbf{A}}, && \text{[Eq. (3.13)]}\\
-i\omega\mu(\nabla\tilde{\varepsilon})\widetilde{\varphi} - \nabla^2\widetilde{\mathbf{A}} &= \mu\tilde{\mathbf{J}} + \omega^2\mu\tilde{\varepsilon}\widetilde{\mathbf{A}}, && \text{[Eq. (A.66)]}\\
\nabla^2\widetilde{\mathbf{A}} - (\nabla\tilde{\varepsilon})/\tilde{\varepsilon}(\nabla\cdot\widetilde{\mathbf{A}}) + \omega^2\mu\tilde{\varepsilon}\widetilde{\mathbf{A}} &= -\mu\tilde{\mathbf{J}}, && \text{[Eq. (3.13)]} \qquad \text{(A.78)}
\end{aligned}$$

whereas the scalar potential equation is obtained through

$$\begin{aligned}
\nabla\cdot\widetilde{\mathbf{D}} &= \tilde{\rho}_\mathrm{f}, && \text{[Eq. (3.4a)]}\\
\nabla\cdot(\tilde{\varepsilon}\widetilde{\mathbf{E}}) &= \tilde{\rho}_\mathrm{f}, && \text{[Eq. (6.1a)]}\\
\nabla\cdot[\tilde{\varepsilon}(-\nabla\widetilde{\varphi} - i\omega\widetilde{\mathbf{A}})] &= \tilde{\rho}_\mathrm{f}, && \text{[Eq. (3.11)]}\\
\nabla\tilde{\varepsilon}\cdot(-\nabla\widetilde{\varphi} - i\omega\widetilde{\mathbf{A}}) + \tilde{\varepsilon}(-\nabla^2\widetilde{\varphi} - i\omega\nabla\cdot\widetilde{\mathbf{A}}) &= \tilde{\rho}_\mathrm{f}, && \text{[Eq. (A.68)]}\\
\nabla\tilde{\varepsilon}\cdot(-\nabla\widetilde{\varphi} - i\omega\widetilde{\mathbf{A}}) + \tilde{\varepsilon}(-\nabla^2\widetilde{\varphi} - i\omega(-i\omega\mu\tilde{\varepsilon}\widetilde{\varphi})) &= \tilde{\rho}_\mathrm{f}, && \text{[Eq. (3.13)]}\\
\nabla^2\widetilde{\varphi} + (\nabla\tilde{\varepsilon})/\tilde{\varepsilon}\cdot(\nabla\widetilde{\varphi} + i\omega\widetilde{\mathbf{A}}) + \omega^2\mu\tilde{\varepsilon}\widetilde{\varphi} &= -\tilde{\rho}_\mathrm{f}/\tilde{\varepsilon}. && \text{(A.79)}
\end{aligned}$$

A.16 Alternative gauge

An alternative gauge to Eq. (3.13) is the generalized Lorenz gauge [270]:

$$\nabla\cdot(\tilde{\varepsilon}\widetilde{\mathbf{A}}) + i\omega\mu\tilde{\varepsilon}^2\widetilde{\varphi} = 0, \tag{A.80}$$

which separates the equations for the scalar and vector potential, like Eq. (3.13) does in the homogeneous case (Eqs. (3.14) and (3.15)):

$$1/\tilde{\varepsilon}\,\nabla\cdot(\tilde{\varepsilon}\nabla\widetilde{\varphi}) + \omega^2\mu\tilde{\varepsilon}\widetilde{\varphi} = -\tilde{\rho}_\mathrm{f}/\tilde{\varepsilon} \tag{A.81}$$

$$-\mu\nabla\times(\mu^{-1}\nabla\times\widetilde{\mathbf{A}}) + \omega^2\mu\tilde{\varepsilon}\widetilde{\mathbf{A}} + \mu\tilde{\varepsilon}\nabla[\mu^{-1}\tilde{\varepsilon}^{-2}\nabla\cdot(\tilde{\varepsilon}\widetilde{\mathbf{A}})] = -\mu\tilde{\mathbf{J}}_\mathrm{f} \tag{A.82}$$

Assuming a spatially dependent permittivity and a homogeneous permeability, i.e. $\tilde{\varepsilon} = \tilde{\varepsilon}(\mathbf{r})$ and $\mu(\mathbf{r}) = \mu$, the equation for the scalar potential is almost identical to Eq. (6.3), without the vector potential term:

$$\begin{aligned}
1/\tilde{\varepsilon}\,\nabla\cdot(\tilde{\varepsilon}\nabla\widetilde{\varphi}) + \omega^2\mu\tilde{\varepsilon}\widetilde{\varphi} &= -\tilde{\rho}_\mathrm{f}/\tilde{\varepsilon}\\
\nabla^2\widetilde{\varphi} + (\nabla\tilde{\varepsilon})/\tilde{\varepsilon}\cdot(\nabla\widetilde{\varphi}) + \omega^2\mu\tilde{\varepsilon}\widetilde{\varphi} &= -\tilde{\rho}_\mathrm{f}/\tilde{\varepsilon}. && \text{[Eq. (A.68)]} \qquad \text{(A.83)}
\end{aligned}$$

This could readily be solved with the methods from Sec. 6.1.8.3. The equation for the vector potential simplifies to

$$\begin{aligned}
-\mu\nabla\times(\mu^{-1}\nabla\times\widetilde{\mathbf{A}}) + \omega^2\mu\tilde{\varepsilon}\widetilde{\mathbf{A}} + \mu\tilde{\varepsilon}\nabla[\mu^{-1}\tilde{\varepsilon}^{-2}\nabla\cdot(\tilde{\varepsilon}\widetilde{\mathbf{A}})] &= -\mu\tilde{\mathbf{J}}_\mathrm{f}\\
-\nabla(\nabla\cdot\widetilde{\mathbf{A}}) + \nabla^2\widetilde{\mathbf{A}} + \omega^2\mu\tilde{\varepsilon}\widetilde{\mathbf{A}} + \underbrace{\tilde{\varepsilon}\nabla[\tilde{\varepsilon}^{-2}\nabla\cdot(\tilde{\varepsilon}\widetilde{\mathbf{A}})]}_{(*)} &= -\mu\tilde{\mathbf{J}}_\mathrm{f}. \qquad \text{[Eq. (A.69)]} \qquad \text{(A.84)}
\end{aligned}$$

The last term on the LHS further expands to

$$
\begin{aligned}
(*) &= \tilde{\varepsilon}\nabla\left[\frac{(\nabla\tilde{\varepsilon})\cdot\widetilde{\mathbf{A}}+\tilde{\varepsilon}(\nabla\cdot\widetilde{\mathbf{A}})}{\tilde{\varepsilon}^2}\right] && \text{[Eq. (A.68)]}\\
&= \tilde{\varepsilon}\frac{\tilde{\varepsilon}^2\nabla[(\nabla\tilde{\varepsilon})\cdot\widetilde{\mathbf{A}}+\tilde{\varepsilon}(\nabla\cdot\widetilde{\mathbf{A}})]-[(\nabla\tilde{\varepsilon})\cdot\widetilde{\mathbf{A}}+\tilde{\varepsilon}(\nabla\cdot\widetilde{\mathbf{A}})]\nabla\tilde{\varepsilon}^2}{\tilde{\varepsilon}^4} && \text{[Eq. (A.67)]}\\
&= \nabla[(\nabla\tilde{\varepsilon})\cdot\widetilde{\mathbf{A}}]/\tilde{\varepsilon}+(\nabla\tilde{\varepsilon})/\tilde{\varepsilon}\,(\nabla\cdot\widetilde{\mathbf{A}})+\nabla(\nabla\cdot\widetilde{\mathbf{A}})\\
&\qquad -2(\nabla\tilde{\varepsilon})/\tilde{\varepsilon}\,[(\nabla\tilde{\varepsilon})/\tilde{\varepsilon}\cdot\widetilde{\mathbf{A}}]-2(\nabla\tilde{\varepsilon})/\tilde{\varepsilon}\,(\nabla\cdot\widetilde{\mathbf{A}}) && \text{[Eq. (A.66)]}\\
&= \nabla[(\nabla\tilde{\varepsilon})\cdot\widetilde{\mathbf{A}}]/\tilde{\varepsilon}-(\nabla\tilde{\varepsilon})/\tilde{\varepsilon}\,(\nabla\cdot\widetilde{\mathbf{A}})+\nabla(\nabla\cdot\widetilde{\mathbf{A}})-2(\nabla\tilde{\varepsilon})/\tilde{\varepsilon}\,[(\nabla\tilde{\varepsilon})/\tilde{\varepsilon}\cdot\widetilde{\mathbf{A}}]. && \text{(A.85)}
\end{aligned}
$$

As in Eq. (6.5), one can further simplify under the assumption that the gradient of the permittivity only has a radial component:

$$(\nabla\tilde{\varepsilon})/\tilde{\varepsilon}=\tilde{\eta}\,\hat{\mathbf{e}}_\rho. \tag{A.86}$$

Accordingly Eq. (A.84) becomes

$$\nabla^2\widetilde{\mathbf{A}}+\omega^2\mu\tilde{\varepsilon}\widetilde{\mathbf{A}}+\nabla[\tilde{\eta}\tilde{\varepsilon}\widetilde{A}_\rho]/\tilde{\varepsilon}-\tilde{\eta}(\nabla\cdot\widetilde{\mathbf{A}})\hat{\mathbf{e}}_\rho-2\tilde{\eta}[\tilde{\eta}\widetilde{A}_\rho]\hat{\mathbf{e}}_\rho=-\mu\tilde{\mathbf{J}}_{\mathrm{f}}. \tag{A.87}$$

The third and forth term mix $\widetilde{A}_z$ and $\widetilde{A}_\rho$ so that they cannot be solved separately as outlined in Fig. 6.1.

A.17 Bessel function identities

A.17.1 General properties

The solutions of the Helmholtz equation in cylindrical coodinates are by definition the Bessel functions. Some of their basis properties will be summarized here. This list is limited to the identities that were used throughout this work. Further important and defining properties can be found in [220, 223], together with the ones listed below. For integer ν, the following symmetry holds:

$$J_{-\nu}(z)=(-1)^\nu J_\nu(z), \tag{A.88}$$

$$Y_{-\nu}(z)=(-1)^\nu Y_\nu(z), \tag{A.89}$$

where $J_\nu(z)$ and $Y_\nu(z)$ are the Bessel functions of the first and second kind, respectively. The former obeys the following normalization

$$\int_0^\infty J_\nu(az)\mathrm{d}z=\frac{1}{a}. \tag{A.90}$$

By definition J_ν and Y_ν are the two independent solutions of a second-order linear ordinary differential equation, i.e. Bessel's differential equation from Eq. (6.28). It follows from Abel's identity that their Wronskian has a simple form:

$$J_\nu(z)\frac{\partial Y_\nu(z)}{\partial z}-\frac{\partial J_\nu(z)}{\partial z}Y_\nu=\frac{2}{\pi z}. \tag{A.91}$$

Along the imaginary axis, they can be expressed through the modified Bessel functions of the first and second kind $I_\nu(z)$ and $K_\nu(z)$:

$$J_\nu(iz)=e^{i\nu\pi/2}I_\nu(z), \tag{A.92}$$

$$Y_\nu(iz)=e^{i(\nu+1)\pi/2}I_\nu(z)-2/\pi\, e^{-i\nu\pi/2}K_\nu(z). \tag{A.93}$$

In analogy to $e^{\pm i\phi} = \cos\phi \pm i\sin\phi$, one also defines the Hankel functions

$$H_\nu^{(1)}(z) = J_\nu(z) + iY_\nu(z), \quad (A.94) \qquad H_\nu^{(2)}(z) = J_\nu(z) - iY_\nu(z). \quad (A.95)$$

Two integral representations of the Bessel functions are relevant [220]:

$$J_0(z) = \frac{1}{2\pi}\int_0^{2\pi} \exp(\pm iz\cos\phi)\mathrm{d}\phi, \quad (A.96) \qquad K_0\big(\sqrt{z^2}\big) = \int_0^\infty \rho\mathrm{d}\rho \frac{J_0(\rho)}{\rho^2+z^2}. \quad (A.97)$$

A.17.2 Asymptotic expansions

Asymptotic expansions of the Bessel functions of the first and second kind are [297, 326]

$$J_\nu(z) \sim \sqrt{\frac{2}{\pi z}}\left[\cos\Big(z - \frac{\pi}{4} - \nu\frac{\pi}{2}\Big)\overline{p}_\nu(z) - \sin\Big(z - \frac{\pi}{4} - \nu\frac{\pi}{2}\Big)\widetilde{p}_\nu(z)\right], \quad (A.98)$$

$$Y_\nu(z) \sim \sqrt{\frac{2}{\pi z}}\left[\sin\Big(z - \frac{\pi}{4} - \nu\frac{\pi}{2}\Big)\overline{p}_\nu(z) + \cos\Big(z - \frac{\pi}{4} - \nu\frac{\pi}{2}\Big)\widetilde{p}_\nu(z)\right], \quad (A.99)$$

where the even and odd power series have been introduced

$$\overline{p}_\nu(z) = \sum_{m=0}^{\infty} \frac{(-1)^m(\nu, 2m)}{(2z)^{2m}} = 1 - \frac{(4\nu^2-1)(4\nu^2-9)}{128z^2} + \mathcal{O}(z^{-4}), \quad (A.100)$$

$$\widetilde{p}_\nu(z) = \sum_{m=0}^{\infty} \frac{(-1)^m(\nu, 2m+1)}{(2z)^{2m+1}} = \frac{4\nu^2-1}{8z} - \frac{(4\nu^2-1)(4\nu^2-9)(4\nu^2-25)}{3072z^3} + \mathcal{O}(z^{-5}), \quad (A.101)$$

with

$$(\nu, m) \equiv \frac{\Gamma(\nu+m+1/2)}{\Gamma(\nu-m+1/2)m!}, \quad (A.102)$$

where $\Gamma(\circ)$ is the gamma function, i.e. the continuous extension of the factorial. These formulas, are valid for large values of $|z|$, provided that $|\arg(z)| < \pi$, which just excludes the negative real axis. Some important low order approximations are:

$$J_0(z) \sim \sqrt{\frac{2}{\pi z}}\cos\Big(z - \frac{\pi}{4}\Big), \quad (A.103) \qquad Y_0(z) \sim \sqrt{\frac{2}{\pi z}}\sin\Big(z - \frac{\pi}{4}\Big), \quad (A.105)$$

$$J_1(z) \sim \sqrt{\frac{2}{\pi z}}\sin\Big(z - \frac{\pi}{4}\Big), \quad (A.104) \qquad Y_1(z) \sim -\sqrt{\frac{2}{\pi z}}\cos\Big(z - \frac{\pi}{4}\Big). \quad (A.106)$$

The modified Bessel functions are dominated by an exponential increase or decrease. Their low-order asymptotic forms do not depend on the order ν:

$$I_\nu(z) \sim \frac{1}{\sqrt{2\pi z}}\exp(z), \quad (A.107) \qquad K_\nu(z) \sim \sqrt{\frac{\pi}{2z}}\exp(-z). \quad (A.108)$$

With the aforementioned equivalence to Euler's formula, the asymptotic expansions of the Hankel functions are

$$H_\nu^{(1)} \sim \sqrt{\frac{2}{\pi z}}\exp\left[i\left(z - \frac{\pi}{4} - \nu\frac{\pi}{2}\right)\right], \quad (A.109)$$

$$H_\nu^{(2)} \sim \sqrt{\frac{2}{\pi z}}\exp\left[-i\left(z - \frac{\pi}{4} - \nu\frac{\pi}{2}\right)\right]. \quad (A.110)$$

A.18 Sommerfeld identity

The Sommerfeld identity plays a crucial role in the theory of electromagnetic waves. It states that a spherical wave can be expanded as a superposition of cylindrical waves along ρ multiplied with plane waves along z [327]. It is discussed in numerous text books [224, 328, 329]:

$$-\frac{\exp(ikr)}{r} = \int_0^\infty k'_\rho \mathrm{d}k'_\rho J_0(k'_\rho \rho) \frac{\exp\big(i\tilde{k}'_z|z|\big)}{i\tilde{k}'_z}, \tag{A.111}$$

where $r^2 = x^2 + y^2 + z^2$ and $\tilde{k}'^2_z = k^2 - k'^2_\rho$, which holds for $\Im(k) > 0$. The complex conjugate of Eq. (A.111) requires $\Im(k) < 0$. Both cases can be summarized as

$$-\frac{\exp[\pm i(k' \pm ik'')r]}{r} = \int_0^\infty k'_\rho \mathrm{d}k'_\rho J_0(k'_\rho \rho) \frac{\exp\big[\pm i\tilde{k}'_z|z|\big]}{\pm i\tilde{k}'_z}, \tag{A.112}$$

where k has been separated into its real and imaginary part: $k = k' \pm ik''$, so that $\Im(k) = \pm k''$ and $k'' > 0$. Also, $\tilde{k}'^2_z = (k' \pm ik'')^2 - k'^2_\rho$.

A.19 k_z-integral

The following integral identity is defined here as a separate function:

$$\mathrm{E}(k,z) \equiv \frac{1}{\pi}\int_{-\infty}^{\infty} \frac{\exp(ik_z z)}{k^2 - k_z^2}\mathrm{d}k_z = \begin{cases} \dfrac{\exp[ik\,\mathrm{sgn}(k'')|z|]}{ik\,\mathrm{sgn}(k'')} & k'' \neq 0 \\ \dfrac{\exp[ik|z|]}{ik} & k'' \to 0^+ \\ \dfrac{\exp[-ik|z|]}{-ik} & k'' \to 0^- \end{cases}, \tag{A.113}$$

where the complex-valued $k = k' + ik''$ is separated into its real part k' and imaginary part k''. A detailed derivation can be found in Bayin [223] in their *Example 18.5*.

A.20 Consistency checks for Eqs. (6.175), (6.176), (6.178) and (6.179)

In this section, the solutions of the scalar and vector potentials are directly verified by checking whether they solve the original differential equations. In all cases, the following identity is needed

$$\begin{aligned} \frac{\partial^2}{\partial z^2}\mathrm{E}(k,z) &= \frac{\partial^2}{\partial z^2}\left[\frac{\exp(\pm ik|z|)}{\pm ik}\right] \\ &= \frac{\partial}{\partial z}\big[\exp(\pm ik|z|)\,\mathrm{sgn}(z)\big] \\ &= \exp(\pm ik|z|)\big[\pm ik\,\mathrm{sgn}^2(z) + 2\delta(z)\big] \\ &= \mathrm{E}(k,z)\big[-k^2 \pm 2ik\delta(z)\big]. \end{aligned} \tag{A.114}$$

Under the assumption of a real-valued z, $\partial_z|z| = \mathrm{sgn}(z)$ and the following representation of the sign function: $\mathrm{sgn}(z) \equiv 2\theta(z) - 1$ has been used, so that $\partial_z\,\mathrm{sgn}(z) = 2\delta(z)$.

A.20.1 $\widetilde{A}_z$

The original differential equation from Eq. (6.8) in combination with Eq. (6.55) reads

$$\nabla^2 \widetilde{A}_z + \left[k_0^2 + \tilde{k}_\chi^2 \theta^+(\rho_\mathrm{c} - \rho)\right] \widetilde{A}_z = -\mu \tilde{J}_z, \tag{A.115}$$

where the Laplace operator in the cylindrical coordinate system is defined in Eq. (A.76). For the differentiation with respect to ρ, the following identities are necessary: $1/\rho\, \partial_\rho \left[\rho\, \partial_\rho Z_0(a\rho)\right] = -a^2 Z_0(a\rho)$, where $Z_0 = \{J_0, Y_0\}$. The Laplacian acting on Eq. (6.175), will be evaluated first, where $\widetilde{A}_z$ is factorized from the following expressions, since it is rather lengthy. Note that when the integral variables t' or k_ρ appear outside, they are meant to be included in the integrals from $\widetilde{A}_z$.

$$\begin{aligned}\nabla^2 \widetilde{A}_z &= \widetilde{A}_z \left[-k_\rho^2 - \tilde{k}_\chi^2 \theta^+(\rho_\mathrm{c} - \rho)\right] + \widetilde{A}_z \left[-\hat{k}_z^2 \pm 2i\hat{k}_z \delta(z - f_z(t'))\right] \\ &= -\widetilde{A}_z \left[k_0^2 + \tilde{k}_\chi^2 \theta^+(\rho_\mathrm{c} - \rho)\right] + \widetilde{A}_z \left[\pm 2i\hat{k}_z \delta(z - f_z(t'))\right],\end{aligned} \tag{A.116}$$

where $\hat{k}_z^2 = k_0^2 - k_\rho^2$ has been used. The first term cancels with the second term from the LHS of Eq. (A.115). With the δ-function, only the case $z - f_z(t') = 0$ contributes, which is also the argument from the E-function. By definition, $\pm i\hat{k}_z\, \mathrm{E}(\hat{k}_z, z \to 0) = 1$ (see Eq. (A.113)) so that the E-function drops. Finally the LHS of Eq. (A.115) reduces to

$$\begin{aligned}&-\frac{\mu q}{2\pi} \int_{-\infty}^{\infty} \frac{\mathrm{d}t'}{2\pi} \dot{f}_z(t') \delta(z - f_z(t')) e^{-i\omega t'} \underbrace{\left[\int_0^\infty \frac{\mathrm{d}k_\rho}{N^{(1)}(k_\rho)} R^{(1)}(k_\rho, \rho) + \sum_{k_\rho^\star} \frac{1}{\widetilde{N}^{(1)}(k_\rho^\star)} R^{(1)}(k_\rho^\star, \rho) \right]}_{\text{Eq. (6.163)}} \\ &= -\mu \underbrace{q \frac{\delta^+(\rho)}{2\pi\rho} \int_{-\infty}^{\infty} \frac{\mathrm{d}t'}{2\pi} \dot{f}_z(t') \delta(z - f_z(t')) e^{-i\omega t'}}_{\text{Eq. (6.174)}} \\ &= -\mu \tilde{J}_z,\end{aligned} \tag{A.117}$$

as desired from the RHS of Eq. (A.115).

A.20.2 $\widetilde{A}_\rho$

The original differential equation from Eq. (6.9) in combination with Eq. (6.55) reads

$$\nabla^2 \widetilde{A}_\rho - \frac{\widetilde{A}_\rho}{\rho^2} - \left[\frac{\nabla \tilde{\varepsilon}}{\tilde{\varepsilon}}\right]_\rho \frac{1}{\rho} \frac{\partial(\rho \widetilde{A}_\rho)}{\partial \rho} + \left[k_0^2 + \tilde{k}_\chi^2 \theta^+(\rho_\mathrm{c} - \rho)\right] \widetilde{A}_\rho = \left[\frac{\nabla \tilde{\varepsilon}}{\tilde{\varepsilon}}\right]_\rho \frac{\partial \widetilde{A}_z}{\partial z}. \tag{A.118}$$

The LHS of Eq. (A.118) simplifies significantly, since $\widetilde{A}_\rho \propto R^{(2)}$, which solves Eq. (6.67) by definition. Together with Eq. (A.114), only the following term remains: $\widetilde{A}_\rho \left[\pm 2i\hat{k}_z \delta(z - z')\right]$. Together with the $\pm i\hat{k}_z$-factor, the E-function is unity at $z = z'$ so that the LHS, after evaluation of the z'-integral, becomes

$$\begin{aligned}&-\rho_\mathrm{c} \frac{\widetilde{\chi}_\mathrm{e}}{1 + \widetilde{\chi}_\mathrm{e}} \frac{\partial \widetilde{A}_z(\mathbf{r}_\mathrm{c}, \omega)}{\partial z} \\ &\qquad \underbrace{\left[\int_0^\infty \frac{\mathrm{d}k_\rho}{N^{(2)}(k_\rho)} R^{(2)}(k_\rho, \rho_\mathrm{c}) R^{(2)}(k_\rho, \rho) + \sum_{k_\rho^\star} \frac{1}{\widetilde{N}^{(2)}(k_\rho^\star)} R^{(2)}(k_\rho^\star, \rho_\mathrm{c}) R^{(2)}(k_\rho^\star, \rho) \right]}_{\text{Eq. (6.163)}} \\ &-\rho_\mathrm{c} \frac{\widetilde{\chi}_\mathrm{e}}{1 + \widetilde{\chi}_\mathrm{e}} \frac{\partial \widetilde{A}_z(\mathbf{r}_\mathrm{c}, \omega)}{\partial z} \frac{\delta(\rho - \rho_\mathrm{c})}{w^{(2)}(\rho_\mathrm{c})}.\end{aligned} \tag{A.119}$$

Finally, both Eq. (A.119) and the RHS of Eq. (A.118) are integrated with the volume element of Eq. (6.171). While $w^{(2)}$ cancels on the LHS so that the integral with respect to ρ is trivial, Eq. (A.38) is used again on the RHS. Thereby, LHS and RHS are equal, as desired.

A.20.3 $\widetilde{\varphi}$

The original differential equation from Eq. (6.10) in combination with Eq. (6.55) reads

$$\nabla^2\widetilde{\varphi} + \left[\frac{\nabla\tilde{\varepsilon}}{\tilde{\varepsilon}}\right]_\rho \frac{\partial\widetilde{\varphi}}{\partial\rho} + \left[k_0^2 + \tilde{k}_\chi^2\theta^+(\rho_\mathrm{c}-\rho)\right]\widetilde{\varphi} = -\tilde{\rho}_\mathrm{f}/\tilde{\varepsilon} - \left[\frac{\nabla\tilde{\varepsilon}}{\tilde{\varepsilon}}\right]_\rho i\omega\widetilde{A}_\rho. \tag{A.120}$$

Similar to what is explicitly shown in Eq. (A.116) or argued in Appendix A.20.2, the remaining term on the LHS is $\widetilde{\varphi}_\rho[\pm 2i\hat{k}_z\delta(z-f_z(t'))] + \widetilde{\varphi}_A[\pm 2i\hat{k}_z\delta(z-z')]$. For the former, the LHS becomes

$$\begin{aligned}
&-(1+\widetilde{\chi}_\mathrm{e})\frac{q}{2\pi\tilde{\varepsilon}}\int_{-\infty}^{\infty}\frac{\mathrm{d}t'}{2\pi}\delta(z-f_z(t'))e^{-i\omega t'} \\
&\qquad\qquad \underbrace{\left[\int_0^\infty \frac{\mathrm{d}k_\rho}{N^{(3)}(k_\rho)}R^{(3)}(k_\rho,\rho) + \sum_{k_\rho^\star}\frac{1}{\widetilde{N}^{(3)}(k_\rho^\star)}R^{(3)}(k_\rho^\star,\rho)\right]}_{\text{Eq. (6.163)}} \\
&= -\frac{1}{\tilde{\varepsilon}}\underbrace{q\frac{\delta^+(\rho)}{2\pi\rho}\int_{-\infty}^{\infty}\frac{\mathrm{d}t'}{2\pi}\delta(z-f_z(t'))e^{-i\omega t'}}_{\text{Eq. (6.173)}} \\
&= -\tilde{\rho}_\mathrm{f}/\tilde{\varepsilon}.
\end{aligned} \tag{A.121}$$

The result is the sought source term of $\widetilde{\varphi}_\rho$. The E-function vanished through the same argument as given above Eq. (A.117), which is conceptually very similar. Finally, the $\widetilde{\varphi}_A$-term leads to

$$\begin{aligned}
&i\omega\widetilde{\chi}_\mathrm{e}\rho_\mathrm{c}\widetilde{A}_\rho\underbrace{\left[\int_0^\infty \frac{\mathrm{d}k_\rho}{N^{(3)}(k_\rho)}R^{(3)}(k_\rho,\rho_\mathrm{c})R^{(3)}(k_\rho,\rho) + \sum_{k_\rho^\star}\frac{1}{\widetilde{N}^{(3)}(k_\rho^\star)}R^{(3)}(k_\rho^\star,\rho_\mathrm{c})R^{(3)}(k_\rho^\star,\rho)\right]}_{\text{Eq. (6.163)}} \\
&= -\frac{-\widetilde{\chi}_\mathrm{e}\delta(\rho_\mathrm{c}-\rho)}{1+\widetilde{\chi}_\mathrm{e}\theta^+(\rho_\mathrm{c}-\rho)}i\omega\widetilde{A}_\rho,
\end{aligned} \tag{A.122}$$

which is equal to $S_A^{(3)}$.

Table A.1: Asymptotic and local approximations of Eq. (6.144) and its approximate solutions. x and y are defined in Eqs. (6.64) and (6.65). Also $z = y - \pi/4$ and $\tilde{x} = \tilde{k}_\chi \rho_\mathrm{c}$ has been used. γ is the Euler–Mascheroni constant. The last row lists the asymptotic approximations of Eq. (6.139).

n	1	2	3
$C^{(n)} \equiv c_J^{(n)} + i c_Y^{(n)}$	$i\frac{\pi}{2}\left[xJ_0(y)H_1^{(1)}(x) - yJ_1(y)H_0^{(1)}(x)\right]$	$i\frac{\pi}{2}\left[yJ_0(y)H_1^{(1)}(x)e^{-\eta} - xJ_1(y)H_0^{(1)}(x)\right]$	$i\frac{\pi}{2}\left[xJ_0(y)H_1^{(1)}(x) - yJ_1(y)H_0^{(1)}(x)e^{\eta}\right]$
$C^{(n)}$ (Asymp.)	$\frac{e^{i(x-\pi/4)}}{\sqrt{xy}}\left[x\cos(z) - iy\sin(z)\right]$	$\frac{e^{i(x-\pi/4)}}{\sqrt{xy}}\left[y\cos(z)e^{-\eta} - ix\sin(z)\right]$	$\frac{e^{i(x-\pi/4)}}{\sqrt{xy}}\left[x\cos(z) - iy\sin(z)e^{\eta}\right]$
$C^{(n)}$ (Appr. at 0)	$J_0(\tilde{x}) + \tilde{x}J_1(\tilde{x})\left[\log\left(-i\frac{x}{2}\right) + \gamma\right]$	$\tilde{x}J_0(\tilde{x})\frac{e^{-\eta}}{x}$	$J_0(\tilde{x}) + \tilde{x}J_1(\tilde{x})\left[\log\left(-i\frac{x}{2}\right) + \gamma\right]e^{\eta}$
$C^{(n)} = 0$ (Appr. at 0)	$\frac{2i}{\rho_\mathrm{c}}\exp\left[-\frac{J_0(\tilde{x})}{\tilde{x}J_1(\tilde{x})} - \gamma\right]$	N/A	$\frac{2i}{\rho_\mathrm{c}}\exp\left[-\frac{e^{-\eta}J_0(\tilde{x})}{\tilde{x}J_1(\tilde{x})} - \gamma\right]$
$C^{(n)}$ (Appr. at $i\tilde{k}_\chi$)	$-\tilde{x}\big(ix\tilde{x} + \tilde{x}^2 - 2\big)K_1(\tilde{x})/2$	$\sqrt{i\tilde{x}(i\tilde{x} - x)/2}\left[\tilde{x}K_0(\tilde{x}) + 2K_1(\tilde{x})e^{-\eta}\right]$	$-\tilde{x}\big(ix\tilde{x} + \tilde{x}^2 - 2\big)K_1(\tilde{x})/2 - \widetilde{\chi}_\mathrm{e}\tilde{x}\big(ix + \tilde{x}\big)K_0(\tilde{x})$
$C^{(n)} = 0$ (Appr. at $i\tilde{k}_\chi$)	$i\tilde{k}_\chi - \frac{2i}{\tilde{k}_\chi\rho_\mathrm{c}^2}$	$i\tilde{k}_\chi$	$i\tilde{k}_\chi - \frac{2i}{\tilde{k}_\chi\rho_\mathrm{c}^2 + 2\widetilde{\chi}_\mathrm{e}\rho_\mathrm{c}K_0(\tilde{x})/K_1(\tilde{x})}$
$N^{(n)}$ (Asymp.)	$\frac{1}{k_\rho}\left[\frac{x}{y}\cos^2(z) + \frac{y}{x}\sin^2(z)\right]$	$\frac{1}{k_\rho}\left[\frac{y}{x}\cos^2(z)e^{-2\eta} + \frac{x}{y}\sin^2(z)\right]$	$\frac{1}{k_\rho}\left[\frac{x}{y}\cos^2(z) + \frac{y}{x}\sin^2(z)e^{2\eta}\right]$

B APPENDIX ON NUMERICAL METHODS

B.1 Mesh for the finite element analysis

Here, explicit formulas describing the mesh that has been used for the FEA are described. Along the radial axis, the nodes of the vector potential are

$$\rho_i^A = \Delta\rho \begin{cases} i & 0 \le i \le N_\rho^{\text{lin}} \\ \widehat{\exp}_{b_\rho}(i, N_\rho^{\text{lin}} - 1) & N_\rho^{\text{lin}} < i \le N_\rho^{\text{lin}} + N_\rho^{\text{exp}} \end{cases}, \tag{B.1}$$

where $N_\rho^{\text{lin}} = 100$ and $N_\rho^{\text{exp}} = 49$ are the numbers of linearly (with $\Delta\rho = 1$ mm) and exponentially spaced samples, respectively. In Eq. (B.1), $\widehat{\exp}_b(i, i_0)$ has been introduced, which obeys $\widehat{\exp}_b(i_0, i_0) = i_0$ and $\widehat{\exp}_b(i_0 + 1, i_0) = i_0 + 1$, followed by a subsequent exponential rise. This guarantees a smooth continuation after the linear section. Explicitly, it is given by $\widehat{\exp}_b(i, i_0) = i_0 + (e^{b(i-i_0)} - 1)/(e^b - 1)$. Along ρ, the exponent $b_\rho \approx 0.0888$ has been adjusted such that $\rho_{\text{max}}^A = \widehat{\exp}_{b_\rho}(N_\rho^{\text{lin}} + N_\rho^{\text{exp}}, N_\rho^{\text{lin}} - 1) = 10^3\Delta\rho$. Similarly, for the z-axis, the following has been chosen

$$z_i^A = \Delta z \begin{cases} -\widehat{\exp}_{b_z}(-i, -1) & -N_z^{\text{exp}} \le i < 0 \\ i & 0 \le i \le N_z^{\text{lin}} \\ \widehat{\exp}_{b_z}(i, N_z^{\text{lin}} - 1) & N_z^{\text{lin}} < i \le N_z^{\text{lin}} + N_z^{\text{exp}} \end{cases}, \tag{B.2}$$

where $N_z^{\text{lin}} = 150$, $N_z^{\text{exp}} = 24$ and $\Delta z = 1$ mm. The approximate range of 75 mm has been chosen as the midpoint, such that $b_z \approx 0.2166$ has been adjusted to satisfy $z_{\text{min}}^A = \widehat{\exp}_{b_z}(-N_z^{\text{exp}}, -1) = (-10^3 + 75)\Delta z$ and $z_{\text{max}}^A = \widehat{\exp}_{b_z}(N_z^{\text{lin}} + N_z^{\text{exp}}, N_z^{\text{lin}} - 1) = (10^3 + 75)\Delta z$. The comprehensive drawing of Fig. B.1 (to scale) summarizes the chosen mesh. Therein, one can also see that the linearly sampled area of interest (100×150 mm^2 around z_{r}) occupies only 0.75% of the total area, yet it uses 51% of the nodes.

B.2 Modified interpolation kernels along the central beam axis

The interpolation kernels for the expansion of the vector components (see Eq. (3.62)) can be written as $N_{i,j}(\rho, z) = N_i(\rho)N_j(z)$[1]. Along $z \in \mathbb{R}$, Eq. (3.67) can be used throughout and in addition, they satisfy the property $\sum_{j\in\mathbb{Z}} N_j(z) = 1$ [187], where $N_j(z) = N(z - j\Delta z)$. The radial coordinate $\rho \ge 0$ is discontinuous, so in order to satisfy the equivalent $\sum_{i\ge 0} N_i(\rho) = \theta(\rho)$, where $N_{i>1}(\rho) = N(\rho - i\Delta\rho)$, the first two kernels are modified. The one at the origin

[1] The linear indexing ($N_i(\rho, z)$) has been changed to a two-dimensional indexing ($N_{i,j}(\rho, z)$).

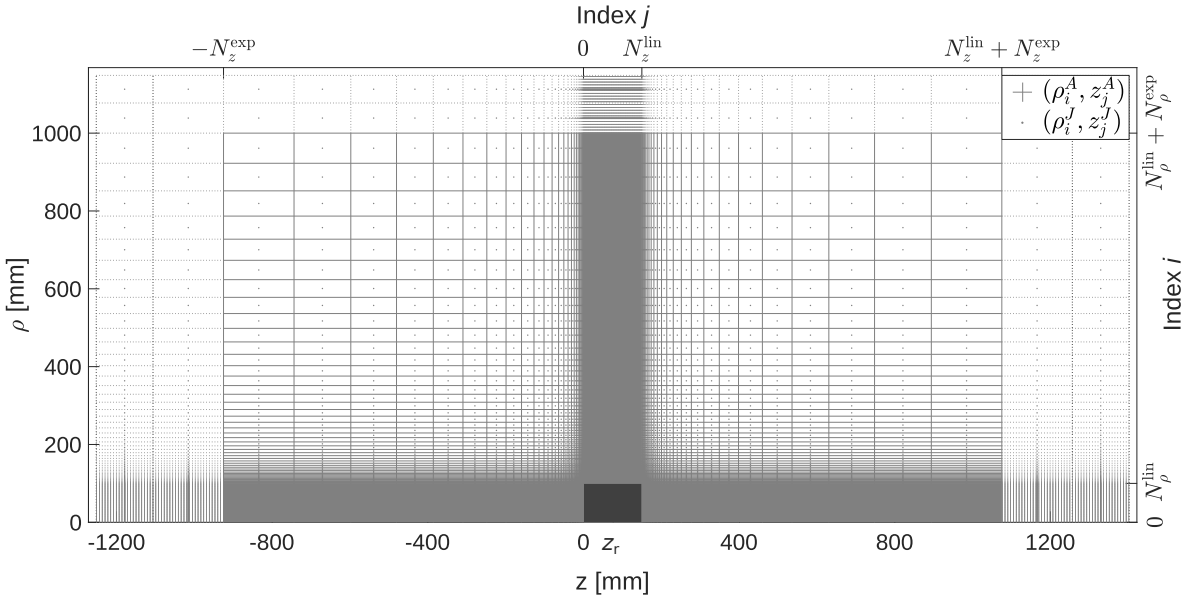

Figure B.1: Mesh for the FEA in the two-dimensional plane along ρ and z. The range $z_\mathrm{r} \approx 76.31\ \mathrm{mm} \approx 75\ \mathrm{mm}$ has been chosen as the center, from which the main grid of the vector potential nodes (ρ_i^A, z_j^A) reaches out one meter along the positive and negative z-axis ($z_{\min}^A = (-10^3 + 75)\Delta z$ and $z_{\max}^A = (10^3 + 75)\Delta z$) as well as one meter along ρ ($\rho_{\max}^A = 10^3 \Delta\rho$). They are the intersections between the solid lines. The surrounding dotted lines indicate the necessary margin, so that the 4×4-kernels (see Fig. 3.6) can maintain their size. Their dimensions were chosen by mirroring the last two nodes, which means that their spacing does not continue exponentially. The node indices ($N_\rho^{\lim} = 100$, $N_\rho^{\exp} = 49$, $N_z^{\lim} = 150$ and $N_z^{\exp} = 24$) are each indicated on the opposite sides of the axes. The area that is both linearly sampled along ρ and z ($\Delta\rho = \Delta z = 1$ mm) is the darker rectangle around z_r. The simulated current density as well as the calculated magnetic field shown in Fig. 5.19 are entirely contained within this are of interest ($100 \times 150\ \mathrm{mm}^2$). The midpoints (dots) are the pixel centers of the discretized current density.

is cut in half: $N_0(\rho) = N(\rho)\theta(\rho)$, while the following one is defined by ($\bar{\rho} = \rho/\Delta\rho$)

$$N_1(\rho) = \frac{1}{2} \begin{cases} -4\bar{\rho}^3 + 6\bar{\rho}^2 & 0 \le \bar{\rho} < 1 \\ 3\bar{\rho}^3 - 14\bar{\rho}^2 + 19\bar{\rho} - 6 & 1 \le \bar{\rho} < 2 \\ -\bar{\rho}^3 + 8\bar{\rho}^2 - 21\bar{\rho} + 18 & 2 \le \bar{\rho} < 3 \\ 0 & \text{else} \end{cases}. \tag{B.3}$$

Effectively, only the first interval ($0 \le \bar{\rho} < 1$) is modified, while the other two are as Eq. (3.67), shifted by $\Delta\rho$. The first few kernels along the radial coordinate are shown in Fig. B.2.

B.3 Volume subdivision

The toroidal voxel volumes V_i^{voxel} (exemplary drawing in Fig. 5.1) increase linearly with the distance from the central beam axis. To compensate, one may subdivide the square toroid volumes along the azimuth into separate arcs. In fact, with the spacing in the AOI, one may write: $V_i^{\mathrm{voxel}} = (2i+1)V_0^{\mathrm{voxel}}$, i.e. that the outer volumes are odd integer multiples of the innermost cylindrical volume. Thereby, one can tile the lateral plane with cylindrical voxels of equal size (without gaps), as drawn in Fig. B.3 (*equal volume*). When calculating

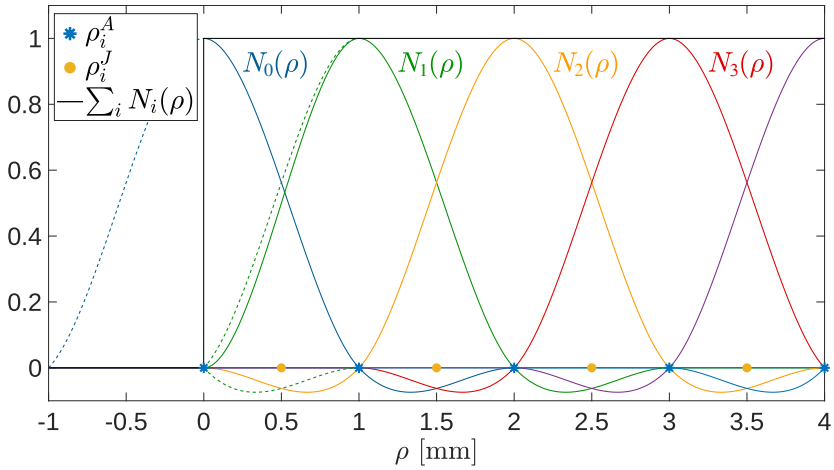

Figure B.2: Interpolation kernels along the radial direction close to $\rho = 0$. The first two kernels $N_0(\rho)$ and $N_1(\rho)$ have been modified, since $\rho \geq 0$ and to satisfy $\sum_i N_i(\rho) = \theta(\rho)$ (black line). $N_0(\rho)$ is cut in half, but otherwise as in Eq. (3.67). $N_1(\rho)$ is defined in Eq. (B.3). A comparison to Eq. (3.67) is indicated by the dashed line, while the difference is shown below. From $N_2(\rho)$ onwards, the kernels are given by Eq. (3.67), shifted to ρ_i^A.

the average current density $\bar{J}_\kappa$ from the MC PSs, there is no difference between an equal or an increasing volume subdivision[2]. However, this does not apply to standard deviation s_{J_z}, as demonstrated in Fig. B.3. The increasing proton count along ρ decreases the relative uncertainty for larger radii. Upon inspection, one may infer that the *equal volume* subdivision is more sensible as it shows an overall smoother uncertainty profile in the ρ-z-plane. Note in particular how sharply the uncertainty drops from ρ_0^J to ρ_1^J in the *increasing volume* case.

Regardless, any pixel away from the central beam axis represents a current ring. If the geometry had not been collapsed to the ρ-z-plane, then all the arc-shaped current elements would contribute to the sum from Eq. (3.74), including the ones from the opposite side of the measurement/detector location. The larger statistics would further lower the fluctuations, so that one can conclude that the *equal volume* subdivision underrepresents the number of protons involved in the aggregate current density and thereby overestimates the uncertainty. In summary, the *increasing volume* subdivision has been chosen for the estimation of $\boldsymbol{\sigma}_{J_\kappa}$.

B.4 Linear modification of the stopping power

$S^{\mathrm{NIST}}(Q)$ shall be denoted as the NIST [90] stopping power shown in Fig. 2.2. Through Eq. (2.17), one obtains $Q^{\mathrm{NIST}}(z)$, which is however not in agreement with $Q^{\mathrm{DNA\_5}}(z)$. To enable a seamless comparison between the DNA_5 data and the theoretical description, $S^{\mathrm{NIST}}(Q)$ is empirically modified through a linear shift: $\widetilde{S}^{\mathrm{NIST}}(Q) = S^{\mathrm{NIST}}(Q) + p_0 + p_1 Q$, where $p_0 = -0.998(6)$ MeV/cm and $p_1 = 0.0119(1)$ 1/cm. The corresponding $\widetilde{Q}^{\mathrm{NIST}}(z)$ offers a good description of $Q^{\mathrm{DNA\_5}}(z)$, which is demonstrated in Fig. B.4.

[2]When subdivided into equal volumes, note that the average/standard deviation is taken over more than N_{PS} samples for larger radii, in particular $(2i+1)N_{\mathrm{PS}}$.

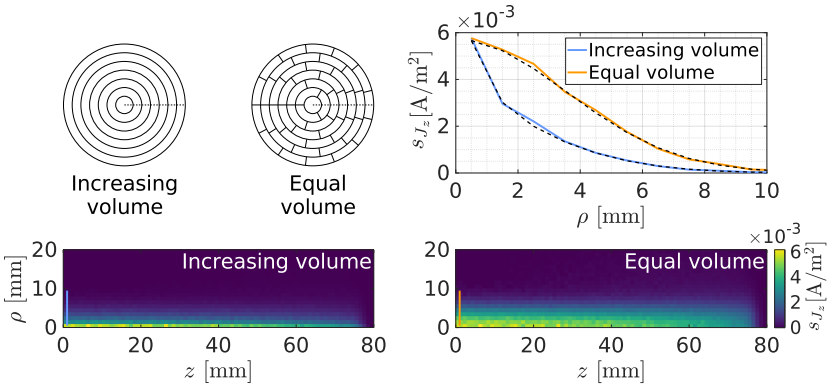

Figure B.3: Impact of the voxelization on the standard deviation of the proton current density along z. The dashed lines in the upper right panel have been calculated with Eq. (5.9).

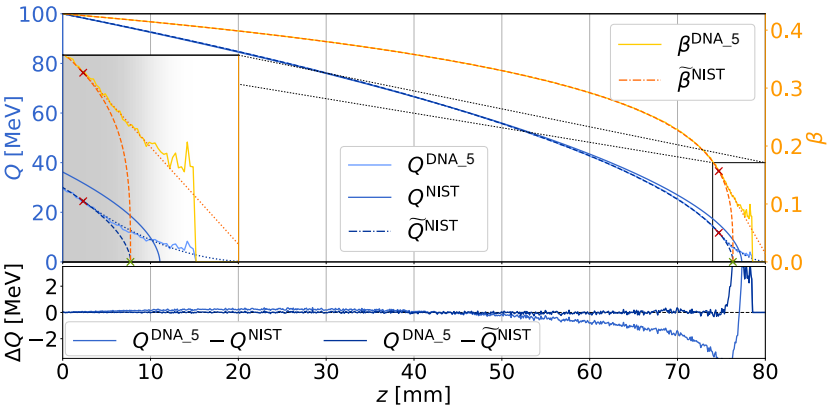

Figure B.4: Linear modification of the NIST stopping power $S^{\mathrm{NIST}} \rightarrow \widetilde{S}^{\mathrm{NIST}}$ to fit the DNA_5 data. Both Q^{NIST} and $\widetilde{Q}^{\mathrm{NIST}}$ are calculated from Eq. (2.17), whereas $Q^{\mathrm{DNA\_5}}$ and $\beta^{\mathrm{DNA\_5}}$ were determined via Gaussian fits. The $\widetilde{S}^{\mathrm{NIST}}$ ($\widetilde{Q}^{\mathrm{NIST}}$) decreases the differences between $Q^{\mathrm{DNA\_5}}$ and Q^{NIST} along the entire z-axis (see the lower panel). Also the intersection of $\widetilde{Q}^{\mathrm{NIST}}$ with $Q = 0$ (range) agrees well with $z_{\mathrm{r}} \approx 76.31$ mm from Fig. 5.6 (marked with a green $\times$ and better visible in the insert). The modified velocity $\tilde{\beta}^{\mathrm{DNA\_5}}$ (calculated via Eq. (2.18)) has been linearly extrapolated (dotted line) starting from the red $\times$ at 74.7 mm. The gray coloring in the insert indicates the reliability of the DNA_5 data changing left through right from high to low statistics. The extrapolation of $\widetilde{Q}^{\mathrm{NIST}}$ was then calculated from the inverse of Eq. (2.18).

C SCIENTIFIC CONTRIBUTIONS

Publications

- **M Rädler**, C Gianoli, P Palaniappan, K Parodi, and M Riboldi: "Electromagnetic Signal of a Proton Beam in Biological Tissues for a Potential Range-Verification Approach in Proton Therapy" *Physical Review Applied* 15, 024066 (2021)
- **M Rädler**, G Buizza, M Kawula, P Palaniappan, C Gianoli, G Baroni, C Paganelli, K Parodi and M Riboldi: "Impact of secondary particles on the magnetic field generated by a proton pencil beam: A finite element analysis based on Geant4-DNA simulations" *Accepted for publication in Medical Physics* (2022)

Conferences

- **M Rädler**, Martin, G Dedes, K Parodi, and M Riboldi: "Exploring a Novel Concept for Direct Proton Beam Measurement Via Its Magnetic Field: A Simulation Study" *AAPM 61st Annual Meeting & Exhibition 2019, San Antonio* WE-HI-SAN2-4 (Imaging for Particle Therapy)
- **M Rädler**, K Parodi, G Dedes and M Riboldi: "Proton beam detection via the generated magnetic field – A simulation study towards a novel measurement concept" *50. Jahrestagung Deutsche Gesellschaft für Medizinische Physik 2019* Session 17, V 77 (Adaptive und bildgeführte Strahlentherapie)
- **M Rädler**, C Gianoli, M Riboldi: "Characterization of the electromagnetic signal generated by a proton beam in biological tissues" *IEEE Nuclear Science Symposium, Medical Imaging Conference and Room Temperature Semiconductor Detector Conferences 2020* M-03-256
- **M Rädler**, G Buizza, P Palaniappan, C Gianoli, G Baroni, C Paganelli, K Parodi and M Riboldi: "Magnetic field of a proton pencil beam as range verification method: The impact of secondaries" *ESTRO Congress 2022, Copenhagen* PD-0899 (Implementation of new technology & techniques)
- **M Rädler**, L Schmidt, M Riboldi: "Magnetic field originating from a modulated proton beam as a range verification approach: Investigating boundary effects" *IEEE Nuclear Science Symposium, Medical Imaging Conference and Room Temperature Semiconductor Detector Conferences 2022* MIC-17-438

Contributions to publications

- J Dickmann, P Wesp, **M Rädler**, S Rit, M Pankuch, RP Johnson, V Bashkirov, RW Schulte, K Parodi, G Landry" "Prediction of image noise contributions in proton computed tomography and comparison to measurements" *Physics in Medicine & Biology* 64 145016 (2019)
- C Gianoli, M Göppel, S Meyer, P Palaniappan, **M Rädler**, F Kamp, C Belka, M Riboldi and K Parodi: "Patient-specific CT calibration based on ion radiography for different detector configurations in ^{1}H, ^{4}He and ^{12}C ion pencil beam scanning" *Physics in Medicine & Biology* 65, 245014 (2020)
- P Palaniappan, S Meyer, **Martin Rädler**, F Kamp, C Belka, M Riboldi, K Parodi and C Gianoli: "X-ray CT adaptation based on a 2D–3D deformable image registration framework using simulated in-room proton radiographies" *Physics in Medicine & Biology* 67, 045003 (2022)

Additional publications

- **M Rädler**, G Landry, S Rit, RW Schulte, K Parodi and G Dedes: "Two-dimensional noise reconstruction in proton computed tomography using distance-driven filtered back-projection of simulated projections" *Physics in Medicine & Biology* 63 215009 (2018)
- C Gianoli, CS Seller Oria, M Würl, **M Rädler**, S Meyer, T Ostermayr, J Schreiber and K Parodi: "Analytical Proof of Principle for a Novel Approach to Imaging with Polyenergetic Proton Beams" *IEEE Nuclear Science Symposium and Medical Imaging Conference Proceedings (2018)*

ACKNOWLEDGMENTS

The completion of this thesis has only been possible through the help of many people to whom I would like to express my gratitude. While such acknowledgments cannot do them justice, I will attempt to do my best in this opportunity.

First and foremost, I would like to acknowledge Prof. Dr. Marco Riboldi. Thank you Marco for accepting me as Your first PhD student upon Your arrival in Munich. I am grateful that I was given the time and opportunity to publish the work of my Master thesis during the first year. Regarding my project, Your supervision has guided me through an entirely novel subject, which is special and exciting in and of itself. I was given the freedom to learn and explore throughout, for which I am very grateful for. Your calm and positive attitude has helped me to overcome stressful times, especially during last-minute abstract submissions. Mille grazie! The connection to Marco in the first place, has been made possible through Dr. Chiara Gianoli. Thank you very much for that and all the scientific and personal advice and guidance you have given already since my time as a Master student. I also would like to thank our Chair and my former supervisor Prof. Dr. Katia Parodi, who despite her busy schedule, always finds the time to listen to my concerns. Thank you especially for establishing the contact to the Group of Pablo Cirrone. I highly valued the exchange with them and their interesting work.

An external collaboration with the group of Prof. Guido Baroni & Prof. Chiara Paganelli has enabled the work from Chapter 5. Especially I would like to acknowledge the dedicated work of Dr. Giulia Buizza, in particular during the revision, which required some after hours sessions. Experimental efforts were running in parallel with the present work, which were carried out by Maximilian Kähler, Benedikt Fischer and Lars-Tamino Breckenfelder for their Bachelor projects. Thank you all for your bringing this work closer to an experimental realization. Special thanks goes to Lukas Schmidt, who has joined me during my last year for his Bachelor thesis, which has led to the work from Chapter 6. I highly appreciated our discussions.

I am indebted to Dr. Prasannakumar Palaniappan as a collaborator, office mate and good friend. I have always enjoyed your excellent cooking and the tasty Indian sweets you brought back to Germany. Exercising with you was always enjoyable, be it bike tours, squash or badminton, even through I do not stand a change against you. Thank you also for enduring me during the writing phase. I know it has been tough. I am very glad to have shared the office with you!

I highly appreciate to have been so actively involved in teaching and tutoring, where I was allowed to satisfy my own curiosity in topics beyond this thesis. My thanks go especially to Marco, Chiara and George. On that regard, I would also like to acknowledge the former students from the tutorials, whose feedback has motivated me to further improve upon the material. In particular, Pratik and Elia were highly engaged and I am glad to know that they stayed in academia and embarked on their own PhD journeys.

I would like to thank my former supervisor Prof. Guillaume Landry and his group in Großhadern, who made the time during ESTRO 2022 all the more enjoyable. Guillaume, I hope we find more time to go hiking in the future!

I would like to acknowledge PD Dr. Walter Assmann, who drew our attention to the work of Albert et al., which has shaped a large part of this thesis and provided an ideal starting point. He also included me as a supervisor for the seminar *Einführung in Medizinische Physik*, from which I was able to recruit some students for the present project. I am also glad that Jona has carried on the seminar, building such an enjoyable atmosphere.

I would like to thank Prof. Dr. Joao Seco for practically instantly accepting to be the second reviewer of my thesis[1]. I would also like to thank Prof. Joachim Rädler, Prof. Hartmut Ruhl, Prof. Jörg Schreiber and Prof. Jochen Weller for accepting the invitation to my defense committee.

I am grateful to the Chair of Medical Physics for providing such a welcoming and scientifically stimulating atmosphere with many exciting seminars and nice social events, despite lockdown. Thank you to Jannis, Kathrin, Giulio, Bea, Tim, EG, Sonja, Pratik, Ze, Mune, Juliana, Lenny, Hans Peter, Julie, Andrea, Romy, Felix. Thanks to Prof. Peter Thirolf for making me feel less alone during long office hours. Franz, I have met you already during my Bachelor project and I am very glad you're still around. I am very much looking forward to the next fitness training and sauna.

Lastly, my deepest gratitude belongs to my family and closest friends for being there for me. Fabi, dieser einzige deutsche Satz gebührt dir. Bas, I am so grateful about all the positive influences you had on my life. I would like to thank my Parents Christine and Reinhard for their continued support and love throughout my studies as well as my sisters Alex, Katja and Moni. Special thanks goes to my mother, who has now read my third thesis from beginning to end, always protecting me from typos and errors that are easily missed. Finally, I am indebted to the Chair of Medical Physics in yet another way, having brought Maria and me together. Marysia, I cannot thank you enough for all the countless hours you spent with me discussing my work, bug-fixing, proofreading, listening to my (unreasonable) concerns and your seemingly endless patience. You have enriched my life in so many ways, wiesz przecież!

[1] E-mail sent: 10:30 a.m. - Confirmation received: 10:31 a.m. (same day)

LIST OF FIGURES

LIST OF TABLES

BIBLIOGRAPHY

[1] Oleg D Jefimenko. Presenting electromagnetic theory in accordance with the principle of causality. *European journal of physics*, 25(2):287, 2004.

[2] J Ferlay, M Ervik, F Lam, M Colombet, L Mery, M Piñeros, A Znaor, I Soerjomataram, and Bray F. Global cancer observatory: Cancer today. International Agency for Research on Cancer (`https://gco.iarc.fr/today`). Accessed: September 26th 2022.

[3] Robert A Weinberg. How cancer arises. *Scientific American*, 275(3):62–70, 1996.

[4] Josep M Borras, Yolande Lievens, Peter Dunscombe, Mary Coffey, Julian Malicki, Julieta Corral, Chiara Gasparotto, Noemie Defourny, Michael Barton, Rob Verhoeven, et al. The optimal utilization proportion of external beam radiotherapy in european countries: an estro-hero analysis. *Radiotherapy and Oncology*, 116(1):38–44, 2015.

[5] SØREN M Bentzen. Dose-response relationships in radiotherapy. *Basic clinical radiobiology*, 4, 2002.

[6] Timur Mitin and Anthony L Zietman. Promise and pitfalls of heavy-particle therapy. *Journal of Clinical Oncology*, 32(26):2855, 2014.

[7] Manuel Lederman. The early history of radiotherapy: 1895–1939. *International Journal of Radiation Oncology* Biology* Physics*, 7(5):639–648, 1981.

[8] Robert R Wilson et al. Radiological use of fast protons. *Radiology*, 47(5):487–491, 1946.

[9] Particle Therapy Co-Operative Group (PTCOG). Particle Therapy Centers. `https://www.ptcog.ch`, August 2022.

[10] Vivek Verma, Mark V Mishra, and Minesh P Mehta. A systematic review of the cost and cost-effectiveness studies of proton radiotherapy. *Cancer*, 122(10):1483–1501, 2016.

[11] Guillaume Landry and Chia-ho Hua. Current state and future applications of radiological image guidance for particle therapy. *Medical Physics*, 45(11):e1086–e1095, 2018.

[12] Thorsten M Buzug. Computed tomography. In *Springer handbook of medical technology*, pages 311–342. Springer, 2011.

[13] H. Paganetti. *Proton Therapy Physics*. Series in Medical Physics and Biomedical Engineering. CRC Press, 2016.

[14] Sophia C Kamran, Jay O Light, and Jason A Efstathiou. Proton versus photon-based radiation therapy for prostate cancer: emerging evidence and considerations in the era of value-based cancer care. *Prostate cancer and prostatic diseases*, 22(4):509–521, 2019.

[15] Steven H Lin, Brian P Hobbs, Vivek Verma, Rebecca S Tidwell, Grace L Smith, Xiudong Lei, Erin M Corsini, Isabel Mok, Xiong Wei, Luyang Yao, et al. Randomized phase iib trial of proton beam therapy versus intensity-modulated radiation therapy for locally advanced esophageal cancer. *Journal of Clinical Oncology*, 38(14):1569, 2020.

[16] Xin Wang, Nicolas L Palaskas, Syed Wamique Yusuf, Jun-ichi Abe, Juan Lopez-Mattei, Jose Banchs, Gregory W Gladish, Percy Lee, Zhongxing Liao, Anita Deswal, et al. Incidence and onset of severe cardiac events after radiotherapy for esophageal cancer. *Journal of Thoracic Oncology*, 15(10):1682–1690, 2020.

[17] Nina N Sanford, Jennifer Pursley, Bridget Noe, Beow Y Yeap, Lipika Goyal, Jeffrey W Clark, Jill N Allen, Lawrence S Blaszkowsky, David P Ryan, Cristina R Ferrone, et al. Protons versus photons for unresectable hepatocellular carcinoma: liver decompensation and overall survival. *International Journal of Radiation Oncology* Biology* Physics*, 105(1):64–72, 2019.

[18] Christopher Kurz. Deep learning applications in medical physics II. Lecture on "Digital Image Processing in Medical Physics" at LMU Munich, Summer 2020.

[19] Neil G Burnet, Simon J Thomas, Kate E Burton, and Sarah J Jefferies. Defining the tumour and target volumes for radiotherapy. *Cancer Imaging*, 4(2):153, 2004.

[20] Harald Paganetti, Chris Beltran, Stefan Both, Lei Dong, Jacob Flanz, Keith Furutani, Clemens Grassberger, David R Grosshans, Antje-Christin Knopf, Johannes A Langendijk, et al. Roadmap: proton therapy physics and biology. *Physics in Medicine & Biology*, 66(5):05RM01, 2021.

[21] Antje-Christin Knopf and Antony Lomax. In vivo proton range verification: a review. *Physics in Medicine & Biology*, 58(15):R131, 2013.

[22] Rudi Apolle, Steffen Appold, Henk P Bijl, Pierre Blanchard, Johan Bussink, Corinne Faivre-Finn, Jonathan Khalifa, Anne Laprie, Yolande Lievens, Indira Madani, et al. Inter-observer variability in target delineation increases during adaptive treatment of head-and-neck and lung cancer. *Acta Oncologica*, 58(10):1378–1385, 2019.

[23] Maria Kawula, Dinu Purice, Minglun Li, Gerome Vivar, Seyed-Ahmad Ahmadi, Katia Parodi, Claus Belka, Guillaume Landry, and Christopher Kurz. Dosimetric impact of deep learning-based ct auto-segmentation on radiation therapy treatment planning for prostate cancer. *Radiation Oncology*, 17(1):1–12, 2022.

[24] Nicole Grosse, Andrea O Fontana, Eugen B Hug, Antony Lomax, Adolf Coray, Marc Augsburger, Harald Paganetti, Alessandro A Sartori, and Martin Pruschy. Deficiency in homologous recombination renders mammalian cells more sensitive to proton versus photon irradiation. *International Journal of Radiation Oncology* Biology* Physics*, 88(1):175–181, 2014.

[25] Guillaume Landry, Reinoud Nijhuis, George Dedes, Josefine Handrack, Christian Thieke, Guillaume Janssens, Jonathan Orban de Xivry, Michael Reiner, Florian Kamp, Jan J Wilkens, et al. Investigating ct to cbct image registration for head and neck proton therapy as a tool for daily dose recalculation. *Medical physics*, 42(3):1354–1366, 2015.

[26] Lone Hoffmann, Markus Alber, Maria Fuglsang Jensen, Marianne Ingerslev Holt, and Ditte Sloth Møller. Adaptation is mandatory for intensity modulated proton therapy of advanced lung cancer to ensure target coverage. *Radiotherapy and Oncology*, 122(3):400–405, 2017.

[27] Barbara Schaffner and Eros Pedroni. The precision of proton range calculations in proton radiotherapy treatment planning: experimental verification of the relation between ct-hu and proton stopping power. *Physics in Medicine & Biology*, 43(6):1579, 1998.

[28] George Dedes, Jannis Dickmann, Katharina Niepel, Philipp Wesp, Robert P Johnson, Mark Pankuch, Vladimir Bashkirov, Simon Rit, Lennart Volz, Reinhard W Schulte, et al. Experimental comparison of proton ct and dual energy x-ray ct for relative stopping power estimation in proton therapy. *Physics in Medicine & Biology*, 64(16):165002, 2019.

[29] Jiasen Ma, Hok Seum Wan Chan Tseung, Michael G Herman, and Chris Beltran. A robust intensity modulated proton therapy optimizer based on monte carlo dose calculation. *Medical Physics*, 45(9):4045–4054, 2018.

[30] Fernando Hueso-González, Fine Fiedler, Christian Golnik, Thomas Kormoll, Guntram Pausch, Johannes Petzoldt, Katja E Römer, and Wolfgang Enghardt. Compton camera and prompt gamma ray timing: two methods for in vivo range assessment in proton therapy. *Frontiers in oncology*, 6:80, 2016.

[31] Harald Paganetti. Range uncertainties in proton therapy and the role of monte carlo simulations. *Physics in Medicine & Biology*, 57(11):R99, 2012.

[32] Nils Peters, Patrick Wohlfahrt, Christian Hofmann, Christian Möhler, Stefan Menkel, Maria Tschiche, Mechthild Krause, Esther GC Troost, Wolfgang Enghardt, and Christian Richter. Reduction of clinical safety margins in proton therapy enabled by the clinical implementation of dual-energy ct for direct stopping-power prediction. *Radiotherapy and Oncology*, 166:71–78, 2022.

[33] Jerimy C Polf and Katia Parodi. Imaging particle beams for cancer treatment. *Physics Today*, 68(10):28, 2015.

[34] Katia Parodi. Latest developments in in-vivo imaging for proton therapy. *The British journal of radiology*, 93(1107):20190787, 2020.

[35] Katia Parodi and Walter Assmann. Ionoacoustics: A new direct method for range verification. *Modern Physics Letters A*, 30(17):1540025, 2015.

[36] Uwe Schneider and Eros Pedroni. Proton radiography as a tool for quality control in proton therapy. *Medical physics*, 22(4):353–363, 1995.

[37] Yading Yuan, Ovidiu C Andronesi, Thomas R Bortfeld, Christian Richter, Russell Wolf, Alexander R Guimaraes, Theodore S Hong, and Joao Seco. Feasibility study of in vivo mri based dosimetric verification of proton end-of-range for liver cancer patients. *Radiotherapy and Oncology*, 106(3):378–382, 2013.

[38] P. G. Thirolf. On the role of nuclear fragmentation for the advancement of in-vivo medical imaging. In *Fourth International Conference on Nuclear Fragmentation*, October 2013.

[39] Xuping Zhu and Georges El Fakhri. Proton therapy verification with pet imaging. *Theranostics*, 3(10):731, 2013.

[40] Howard D Maccabee, Udipi Madhvanath, and Mudundi R Raju. Tissue activation studies with alpha-particle beams. *Physics in Medicine & Biology*, 14(2):213, 1969.

[41] J Pawelke, W Enghardt, Th Haberer, BG Hasch, R Hinz, M Kramer, E Lauckner, and M Sobiella. In-beam pet imaging for the control of heavy-ion tumour therapy. *IEEE Transactions on nuclear science*, 44(4):1492–1498, 1997.

[42] DW Litzenberg, DA Roberts, MY Lee, K Pham, AM Vander Molen, R Ronningen, and FD Becchetti. On-line monitoring of radiotherapy beams: Experimental results with proton beams. *Medical physics*, 26(6):992–1006, 1999.

[43] K Parodi, W Enghardt, and T Haberer. In-beam pet measurements of β+ radioactivity induced by proton beams. *Physics in Medicine & Biology*, 47(1):21, 2001.

[44] Wolfgang Enghardt, P Crespo, F Fiedler, R Hinz, K Parodi, J Pawelke, and Falk Poenisch. Charged hadron tumour therapy monitoring by means of pet. *Nuclear Instruments and Methods in Physics Research Section A: Accelerators, Spectrometers, Detectors and Associated Equipment*, 525(1-2):284–288, 2004.

[45] Yasushi Iseki, Hideyuki Mizuno, Yasuyuki Futami, Takehiro Tomitani, Tatsuaki Kanai, Mitsutaka Kanazawa, Atsushi Kitagawa, Takeshi Murakami, Teiji Nishio, Mitsuru Suda, et al. Positron camera for range verification of heavy-ion radiotherapy. *Nuclear Instruments and Methods in Physics Research Section A: Accelerators, Spectrometers, Detectors and Associated Equipment*, 515(3):840–849, 2003.

[46] Katia Parodi, Thomas Bortfeld, and Thomas Haberer. Comparison between in-beam and offline positron emission tomography imaging of proton and carbon ion therapeutic irradiation at synchrotron-and cyclotron-based facilities. *International Journal of Radiation Oncology* Biology* Physics*, 71(3):945–956, 2008.

[47] Hideaki Tashima, Taiga Yamaya, Eiji Yoshida, Shoko Kinouchi, Mitsuo Watanabe, and Eiichi Tanaka. A single-ring openpet enabling pet imaging during radiotherapy. *Physics in Medicine & Biology*, 57(14):4705, 2012.

[48] Teiji Nishio, Aya Miyatake, Takashi Ogino, Keiichi Nakagawa, Nagahiro Saijo, and Hiroyasu Esumi. The development and clinical use of a beam on-line pet system mounted on a rotating gantry port in proton therapy. *International Journal of Radiation Oncology* Biology* Physics*, 76(1):277–286, 2010.

[49] Yoshio Hishikawa, Kazufumi Kagawa, Masao Murakami, Hiroto Sakai, Takashi Akagi, and Mitsuyuki Abe. Usefulness of positron-emission tomographic images after proton therapy. *International Journal of Radiation Oncology* Biology* Physics*, 53(5):1388–1391, 2002.

[50] Katia Parodi, Harald Paganetti, Helen A Shih, Susan Michaud, Jay S Loeffler, Thomas F DeLaney, Norbert J Liebsch, John E Munzenrider, Alan J Fischman, Antje Knopf, et al. Patient study of in vivo verification of beam delivery and range, using positron emission tomography and computed tomography imaging after proton therapy. *International Journal of Radiation Oncology* Biology* Physics*, 68(3):920–934, 2007.

[51] Chul Hee Min, Xuping Zhu, Brian A Winey, Kira Grogg, Mauro Testa, Georges El Fakhri, Thomas R Bortfeld, Harald Paganetti, and Helen A Shih. Clinical application of in-room positron emission tomography for in vivo treatment monitoring in proton radiation therapy. *International Journal of Radiation Oncology* Biology* Physics*, 86(1):183–189, 2013.

[52] W Enghardt, K Parodi, P Crespo, F Fiedler, J Pawelke, and F Pönisch. Dose quantification from in-beam positron emission tomography. *Radiotherapy and Oncology*, 73:S96–S98, 2004.

[53] Sebastian P Nischwitz, Julia Bauer, Thomas Welzel, Harald Rief, Oliver Jäkel, Thomas Haberer, Kathrin Frey, Jürgen Debus, Katia Parodi, Stephanie E Combs, et al. Clinical implementation and range evaluation of in vivo pet dosimetry for particle irradiation in patients with primary glioma. *Radiotherapy and Oncology*, 115(2):179–185, 2015.

[54] Veronica Ferrero, Elisa Fiorina, Matteo Morrocchi, Francesco Pennazio, Guido Baroni, Giuseppe Battistoni, Nicola Belcari, Niccolo' Camarlinghi, Mario Ciocca, Alberto Del Guerra, et al. Online proton therapy monitoring: clinical test of a silicon-photodetector-based in-beam pet. *Scientific Reports*, 8(1):1–8, 2018.

[55] GW Bennett, JO Archambeau, BE Archambeau, JI Meltzer, and CL Wingate. Visualization and transport of positron emission from proton activation in vivo. *Science*, 200(4346):1151–1153, 1978.

[56] Paulo Crespo, Thomas Barthel, H Frais-Kolbl, Erich Griesmayer, Klaus Heidel, Katia Parodi, Jörg Pawelke, and Wolfgang Enghardt. Suppression of random coincidences during in-beam pet measurements at ion beam radiotherapy facilities. *IEEE transactions on nuclear science*, 52(4):980–987, 2005.

[57] Benzion Kozlovsky, Ronald J Murphy, and Reuven Ramaty. Nuclear deexcitation gamma-ray lines from accelerated particle interactions. *The Astrophysical Journal Supplement Series*, 141(2):523, 2002.

[58] Joost M Verburg, Helen A Shih, and Joao Seco. Simulation of prompt gamma-ray emission during proton radiotherapy. *Physics in Medicine & Biology*, 57(17):5459, 2012.

[59] M Moteabbed, S Espana, and H Paganetti. Monte carlo patient study on the comparison of prompt gamma and pet imaging for range verification in proton therapy. *Physics in Medicine & Biology*, 56(4):1063, 2011.

[60] Y Jongen and F Stichelbaut. Verification of the proton beam position in the patient by the prompt gamma rays emission. In *PTCOG Conf Rec*, page 16, 2003.

[61] Chul Hee Min, Han Rim Lee, Chan Hyeong Kim, and Se Byeong Lee. Development of array-type prompt gamma measurement system for in vivo range verification in proton therapy. *Medical physics*, 39(4):2100–2107, 2012.

[62] Julien Smeets, F Roellinghoff, D Prieels, F Stichelbaut, A Benilov, C Fiorini, Roberta Peloso, M Basilavecchia, Tommaso Frizzi, JC Dehaes, et al. Prompt gamma imaging with a slit camera for real-time range control in proton therapy. *Physics in Medicine & Biology*, 57(11):3371, 2012.

[63] S Aldawood, PG Thirolf, A Miani, M Böhmer, G Dedes, R Gernhäuser, C Lang, S Liprandi, L Maier, T Marinšek, et al. Development of a compton camera for prompt-gamma medical imaging. *Radiation Physics and Chemistry*, 140:190–197, 2017.

[64] E Draeger, D Mackin, S Peterson, H Chen, S Avery, S Beddar, and JC Polf. 3d prompt gamma imaging for proton beam range verification. *Physics in Medicine & Biology*, 63(3):035019, 2018.

[65] Joost M Verburg and Joao Seco. Proton range verification through prompt gamma-ray spectroscopy. *Physics in Medicine & Biology*, 59(23):7089, 2014.

[66] Christian Golnik, Fernando Hueso-González, Andreas Müller, Peter Dendooven, Wolfgang Enghardt, Fine Fiedler, Thomas Kormoll, Katja Roemer, Johannes Petzoldt, Andreas Wagner, et al. Range assessment in particle therapy based on prompt γ-ray timing measurements. *Physics in Medicine & Biology*, 59(18):5399, 2014.

[67] Theresa Werner, Jonathan Berthold, Fernando Hueso-González, Toni Koegler, Johannes Petzoldt, Katja Roemer, Christian Richter, Andreas Rinscheid, Arno Straessner, Wolfgang Enghardt, et al. Processing of prompt gamma-ray timing data for proton range measurements at a clinical beam delivery. *Physics in Medicine & Biology*, 64(10):105023, 2019.

[68] C Lang, Dietrich Habs, K Parodi, and PG Thirolf. Sub-millimeter nuclear medical imaging with high sensitivity in positron emission tomography using $\beta+$ γ coincidences. *Journal of Instrumentation*, 9(01):P01008, 2014.

[69] Fernando Hueso-González, Moritz Rabe, Thomas A Ruggieri, Thomas Bortfeld, and Joost M Verburg. A full-scale clinical prototype for proton range verification using prompt gamma-ray spectroscopy. *Physics in Medicine & Biology*, 63(18):185019, 2018.

[70] Yunhe Xie, El Hassane Bentefour, Guillaume Janssens, Julien Smeets, François Vander Stappen, Lucian Hotoiu, Lingshu Yin, Derek Dolney, Stephen Avery, Fionnbarr O'Grady, et al. Prompt gamma imaging for in vivo range verification of pencil beam scanning proton therapy. *International Journal of Radiation Oncology* Biology* Physics*, 99(1):210–218, 2017.

[71] J Krimmer, D Dauvergne, JM Létang, and É Testa. Prompt-gamma monitoring in hadrontherapy: A review. *Nuclear Instruments and Methods in Physics Research Section A: Accelerators, Spectrometers, Detectors and Associated Equipment*, 878:58–73, 2018.

[72] JunIchiro Tada, Yoshinori Hayakawa, Katsuhisa Hosono, and Tetsuo Inada. Time resolved properties of acoustic pulses generated in water and in soft tissue by pulsed proton beam irradiation—a possibility of doses distribution monitoring in proton radiation therapy. *Medical physics*, 18(6):1100–1104, 1991.

[73] Yoshinori Hayakawa, Junichiro Tada, Norio Arai, Katsuhisa Hosono, Masaru Sato, Toshio Wagai, Hiroshi Tsuji, and Hirohiko Tsujii. Acoustic pulse generated in a patient during treatment by pulsed proton radiation beam. *Radiation Oncology Investigations*, 3(1):42–45, 1995.

[74] VI Albul, VB Bychkov, SS Vasil'Ev, KE Gusev, VS Demidov, EV Demidova, NK Krasnov, AF Kurchanov, VE Luk'yashin, and A Yu Sokolov. Measuring the ultrasonic field generated in water upon the deceleration of a proton beam. *Instruments and Experimental Techniques*, 47(4):502–507, 2004.

[75] VI Albul, VB Bychkov, SS Vasil'ev, KE Gusev, VS Demidov, EV Demidova, NK Krasnov, AF Kurchanov, VE Luk'yashin, and A Yu Sokolov. Acoustic field generated by a beam of protons stopping in a water medium. *Acoustical Physics*, 51(1):33–37, 2005.

[76] Toshiyuki Terunuma, Takeji Sakae, Yoshinori Hayakawa, Akihiro Nohtomi, Yoshihisa Takada, Kiyoshi Yasuoka, and Akira Maruhashi. Waveform simulation based on 3d dose distribution for acoustic wave generated by proton beam irradiation. *Medical physics*, 34(9):3642–3648, 2007.

[77] W Assmann, S Kellnberger, S Reinhardt, S Lehrack, A Edlich, PG Thirolf, M Moser, G Dollinger, M Omar, V Ntziachristos, et al. Ionoacoustic characterization of the proton bragg peak with submillimeter accuracy. *Medical physics*, 42(2):567–574, 2015.

[78] Stephan Kellnberger, Walter Assmann, Sebastian Lehrack, Sabine Reinhardt, Peter Thirolf, Daniel Queirós, George Sergiadis, Günther Dollinger, Katia Parodi, and Vasilis Ntziachristos. Ionoacoustic tomography of the proton bragg peak in combination with ultrasound and optoacoustic imaging. *Scientific reports*, 6(1):1–7, 2016.

[79] SK Patch, M Kireeff Covo, A Jackson, YM Qadadha, KS Campbell, RA Albright, P Bloemhard, AP Donoghue, CR Siero, TL Gimpel, et al. Thermoacoustic range verification using a clinical ultrasound array provides perfectly co-registered overlay of the bragg peak onto an ultrasound image. *Physics in Medicine & Biology*, 61(15):5621, 2016.

[80] Sebastian Lehrack, Walter Assmann, Damien Bertrand, Sebastien Henrotin, Joel Herault, Vincent Heymans, Francois Vander Stappen, Peter G Thirolf, Marie Vidal, Jarno Van de Walle, et al. Submillimeter ionoacoustic range determination for protons in water at a clinical synchrocyclotron. *Physics in Medicine & Biology*, 62(17):L20, 2017.

[81] Kevin C Jones, Chandra M Seghal, and Stephen Avery. How proton pulse characteristics influence protoacoustic determination of proton-beam range: simulation studies. *Physics in Medicine & Biology*, 61(6):2213, 2016.

[82] Kevin C Jones, Wei Nie, James CH Chu, Julius V Turian, Alireza Kassaee, Chandra M Sehgal, and Stephen Avery. Acoustic-based proton range verification in heterogeneous tissue: simulation studies. *Physics in Medicine & Biology*, 63(2):025018, 2018.

[83] Julie Lascaud, Pratik Dash, Matthias Würl, Hans-Peter Wieser, Benjamin Wollant, Ronaldo Kalunga, Walter Assmann, Dirk-André Clevert, Alfredo Ferrari, Paola Sala, et al. Enhancement of the ionoacoustic effect through ultrasound and photoacoustic contrast agents. *Scientific reports*, 11(1):1–15, 2021.

[84] F. Caspers. Electromagnetic Signals and Sonic Methods for Dosimetry in Hadron Therapy. In *2nd Workshop on Hadron Beam Therapy of Cancer*, May 2011. `http://erice2011.na.infn.it/TalkContributions/Caspers.pdf`.

[85] Jaroslav Albert, Rudi Labarbe, and Edmond Sterpin. Electric field from a proton beam in biological tissues for proton radiotherapy. *Physical Review Applied*, 10(4):044054, 2018.

[86] Wayne D Newhauser and Rui Zhang. The physics of proton therapy. *Physics in Medicine & Biology*, 60(8):R155, 2015.

[87] Ervin B Podgoršak et al. *Radiation physics for medical physicists*, volume 1. Springer, 2006.

[88] U Fano. Penetration of protons, alpha particles, and mesons. *Ann. Rev. Nucl. Sci.*, 13, 1963.

[89] Hans Bethe. Zur Theorie des Durchgangs schneller Korpuskularstrahlen durch Materie. *Annalen der Physik*, 397(3):325–400, 1930.

[90] M.J. Berger, J.S. Coursey, M.A. Zucker, and J. Chang. ESTAR, PSTAR, and ASTAR: Computer Programs for Calculating Stopping-Power and Range Tables for Electrons, Protons, and Helium Ions. `http://physics.nist.gov/Star`, 2005. National Institute of Standards and Technology (NIST), Gaithersburg, MD. *Accessed April 9th 2019*.

[91] Geant4 extracted stopping power data. Courtesy of Georgios Dedes, 2016.

[92] H Bichsel. *Passage of Charged Particles through Matter, AIP Handbook 3rd Ed*. McGraw-Hill, New York, 1972.

[93] Hans Geissel and Christoph Scheidenberger. Slowing down of relativistic heavy ions and new applications. *Nuclear Instruments and Methods in Physics Research Section B: Beam Interactions with Materials and Atoms*, 136:114–124, 1998.

[94] International Commission on Radiation Units and Measurements. *Stopping powers and ranges for protons and alpha particles*. International Commission on Radiation Units and Measurements, 1993.

[95] Niels Bohr. Lx. on the decrease of velocity of swiftly moving electrified particles in passing through matter. *The London, Edinburgh, and Dublin Philosophical Magazine and Journal of Science*, 30(178):581–612, 1915.

[96] P. Sigmund. *Particle Penetration and Radiation Effects: General Aspects and Stopping of Swift Point Charges*. Springer Series in Solid-State Sciences. Springer Berlin Heidelberg, 2006.

[97] C Scheidenberger, H Geissel, HH Mikkelsen, F Nickel, S Czajkowski, H Folger, H Irnich, G Münzenberg, W Schwab, Th Stöhlker, et al. Energy-loss-straggling experiments with relativistic heavy ions in solids. *Physical review letters*, 77(19):3987, 1996.

[98] Keith R Symon. Fluctuations in energy lost by high energy charged particles in passing through matter. *Ph. D. Thesis*, 1948.

[99] C Tschalär. Straggling distributions of large energy losses. *Nuclear Instruments and Methods*, 61(2):141–156, 1968.

[100] MG Payne. Energy straggling of heavy charged particles in thick absorbers. *Physical Review*, 185(2):611, 1969.

[101] Martin Rädler. Noise Reconstruction in Proton Computed Tomography. Master thesis, Ludwig Maximilian University of Munich (LMU), November 2017.

[102] Gert Moliere. Theorie der streuung schneller geladener teilchen i. einzelstreuung am abgeschirmten coulomb-feld. *Zeitschrift für Naturforschung A*, 2(3):133–145, 1947.

[103] Gert Moliere. Theorie der streuung schneller geladener teilchen ii mehrfach-und vielfachstreuung. *Zeitschrift für Naturforschung A*, 3(2):78–97, 1948.

[104] Hans A Bethe. Moliere's theory of multiple scattering. *Physical review*, 89(6):1256, 1953.

[105] Bernard Gottschalk. Techniques of proton radiotherapy: transport theory. *arXiv preprint arXiv:1204.4470*, 2012.

[106] Anders Brahme. Multiple scattering of relativistic electrons in air. Technical report, Kungliga Tekniska Hoegskolan, 1971.

[107] B. Povh et al. *Teilchen und Kerne - Eine Einführung in die physikalischen Konzepte*. Springer Spektrum, 2014.

[108] Bernard Gottschalk. On the scattering power of radiotherapy protons. *Medical physics*, 37(1):352–367, 2010.

[109] H. Svensson, P. Almond, A. Brahme, A. Dutreix, and H. K. Leetz. Radiation Dosimetry: Electron Beams with Energies Between 1 and 50 MeV. *Journal of the International Commission on Radiation Units and Measurements*, 18(2), September 1984.

[110] Bruno Rossi and Kenneth Greisen. Cosmic-ray theory. *Reviews of Modern Physics*, 13(4):240, 1941.

[111] Leonard Eyges. Multiple scattering with energy loss. *Physical Review*, 74(10):1534, 1948.

[112] K Gunzert-Marx, H Iwase, D Schardt, and RS Simon. Secondary beam fragments produced by 200 mev u- 1 12c ions in water and their dose contributions in carbon ion radiotherapy. *New journal of physics*, 10(7):075003, 2008.

[113] Marco Durante and Harald Paganetti. Nuclear physics in particle therapy: a review. *Reports on Progress in Physics*, 79(9):096702, 2016.

[114] HL Bradt and B Peters. The heavy nuclei of the primary cosmic radiation. *Physical Review*, 77(1):54, 1950.

[115] Clemens Grassberger and Harald Paganetti. Elevated let components in clinical proton beams. *Physics in Medicine & Biology*, 56(20):6677, 2011.

[116] Harald Paganetti. Nuclear interactions in proton therapy: dose and relative biological effect distributions originating from primary and secondary particles. *Physics in Medicine & Biology*, 47(5):747, 2002.

[117] Peter Sigmund, Andreas Schinner, and Helmut Paul. Errata and addenda for icru report 73, stopping of ions heavier than helium. *J ICRU*, 5(1):1–10, 2009.

[118] Pablo de Vera, Isabel Abril, and Rafael Garcia-Molina. Energy spectra of protons and generated secondary electrons around the bragg peak in materials of interest in proton therapy. *Radiation research*, 190(3):282–297, 2018.

[119] Pablo de Vera, Eugene Surdutovich, Isabel Abril, Rafael Garcia-Molina, and Andrey V Solov'yov. Analytical model of ionization and energy deposition by proton beams in subcellular compartments. *The European Physical Journal D*, 68(4):1–8, 2014.

[120] Mohammad Reza Kia and Houshyar Noshad. Comparison of the secondary electrons produced by proton and electron beams in water. *Physics of Plasmas*, 23(5):053120, 2016.

[121] C Villagrasa, Z Francis, and S Incerti. Physical models implemented in the geant4-dna extension of the geant-4 toolkit for calculating initial radiation damage at the molecular level. *Radiation protection dosimetry*, 143(2-4):214–218, 2011.

[122] I Kyriakou, M Šefl, V Nourry, and S Incerti. The impact of new geant4-dna cross section models on electron track structure simulations in liquid water. *Journal of Applied Physics*, 119(19):194902, 2016.

[123] Millard E Rudd, Y-K Kim, Don H Madison, and Timothy J Gay. Electron production in proton collisions with atoms and molecules: energy distributions. *Reviews of modern physics*, 64(2):441, 1992.

[124] D Emfietzoglou, G Papamichael, Kostas Kostarelos, and M Moscovitch. A monte carlo track structure code for electrons (˜ 10 ev-10 kev) and protons (˜ 0.3-10 mev) in water: partitioning of energy and collision events. *Physics in Medicine & Biology*, 45(11):3171, 2000.

[125] Z Francis, S Incerti, R Capra, Barbara Mascialino, Gerard Montarou, V Stepan, and C Villagrasa. Molecular scale track structure simulations in liquid water using the geant4-dna monte-carlo processes. *Applied radiation and isotopes*, 69(1):220–226, 2011.

[126] Wolfgang Schlegel, Christian P Karger, and Oliver Jäkel. *Medizinische Physik: Grundlagen–Bildgebung–Therapie–Technik*. Springer-Verlag, 2018.

[127] Bernard Gottschalk. Radiotherapy proton interactions in matter. *arXiv preprint arXiv:1804.00022*, 2018.

[128] Harald Paganetti. Proton relative biological effectiveness–uncertainties and opportunities. *International journal of particle therapy*, 5(1):2–14, 2018.

[129] Giulia Giovannini, Till Böhlen, Gonzalo Cabal, Julia Bauer, Thomas Tessonnier, Kathrin Frey, Jürgen Debus, Andrea Mairani, and Katia Parodi. Variable rbe in proton therapy: comparison of different model predictions and their influence on clinical-like scenarios. *Radiation Oncology*, 11(1):1–16, 2016.

[130] Radhe Mohan and David Grosshans. Proton therapy–present and future. *Advanced drug delivery reviews*, 109:26–44, 2017.

[131] Hywel Owen, Ranald MacKay, Ken Peach, and Susan Smith. Hadron accelerators for radiotherapy. *Contemporary Physics*, 55(2):55–74, 2014.

[132] Vincent Favaudon, Laura Caplier, Virginie Monceau, Frédéric Pouzoulet, Mano Sayarath, Charles Fouillade, Marie-France Poupon, Isabel Brito, Philippe Hupé, Jean Bourhis, et al. Ultrahigh dose-rate flash irradiation increases the differential response between normal and tumor tissue in mice. *Science translational medicine*, 6(245):245ra93–245ra93, 2014.

[133] Pierre Montay-Gruel, Audrey Bouchet, Maud Jaccard, David Patin, Raphael Serduc, Warren Aim, Kristoffer Petersson, Benoit Petit, Claude Bailat, Jean Bourhis, et al.

X-rays can trigger the flash effect: Ultra-high dose-rate synchrotron light source prevents normal brain injury after whole brain irradiation in mice. *Radiotherapy and Oncology*, 129(3):582–588, 2018.

[134] Pierre Montay-Gruel, Munjal M Acharya, Kristoffer Petersson, Leila Alikhani, Chakradhar Yakkala, Barrett D Allen, Jonathan Ollivier, Benoit Petit, Patrik Gonçalves Jorge, Amber R Syage, et al. Long-term neurocognitive benefits of flash radiotherapy driven by reduced reactive oxygen species. *Proceedings of the National Academy of Sciences*, 116(22):10943–10951, 2019.

[135] Marie-Catherine Vozenin, Pauline De Fornel, Kristoffer Petersson, Vincent Favaudon, Maud Jaccard, Jean-François Germond, Benoit Petit, Marco Burki, Gisèle Ferrand, David Patin, et al. The advantage of flash radiotherapy confirmed in mini-pig and cat-cancer patientsthe advantage of flash radiotherapy. *Clinical Cancer Research*, 25(1):35–42, 2019.

[136] P Maxim, Paul Keall, and Jing Cai. Flash radiotherapy: Newsflash or flash in the pan? *Medical physics*, 2019.

[137] Joseph D Wilson, Ester M Hammond, Geoff S Higgins, and Kristoffer Petersson. Ultra-high dose rate (flash) radiotherapy: silver bullet or fool's gold? *Frontiers in oncology*, 9:1563, 2020.

[138] Jean Bourhis, Pierre Montay-Gruel, Patrik Gonçalves Jorge, Claude Bailat, Benoît Petit, Jonathan Ollivier, Wendy Jeanneret-Sozzi, Mahmut Ozsahin, François Bochud, Raphaël Moeckli, et al. Clinical translation of flash radiotherapy: Why and how? *Radiotherapy and Oncology*, 139:11–17, 2019.

[139] Konrad P Nesteruk and Serena Psoroulas. Flash irradiation with proton beams: beam characteristics and their implications for beam diagnostics. *Applied Sciences*, 11(5):2170, 2021.

[140] Jean Bourhis, Wendy Jeanneret Sozzi, Patrik Gonçalves Jorge, Olivier Gaide, Claude Bailat, Fréderic Duclos, David Patin, Mahmut Ozsahin, François Bochud, Jean-François Germond, et al. Treatment of a first patient with flash-radiotherapy. *Radiotherapy and oncology*, 139:18–22, 2019.

[141] Simon Jolly, Hywel Owen, Marco Schippers, and Carsten Welsch. Technical challenges for FLASH proton therapy. *Physica Medica*, 78:71–82, 2020.

[142] S. Humphries. *Principles of Charged Particle Acceleration*. Dover Publications, 2013.

[143] Kazuo Hiramoto, Masumi Umezawa, Kazuyoshi Saito, Satoshi Tootake, Hideaki Nishiuchi, Shigemistu Hara, Masanobu Tanaka, Koji Matsuda, Hiroaki Sakurabata, and Kunio Moriyama. The synchrotron and its related technology for ion beam therapy. *Nuclear Instruments and Methods in Physics Research Section B: Beam Interactions with Materials and Atoms*, 261(1-2):786–790, 2007.

[144] DL Friesel and TA Antaya. Medical cyclotrons. In *Reviews Of Accelerator Science And Technology: Volume 2: Medical Applications of Accelerators*, pages 133–156. World Scientific, 2009.

[145] V Smirnov and S Vorozhtsov. Modern compact accelerators of cyclotron type for medical applications. *Physics of Particles and Nuclei*, 47(5):863–883, 2016.

[146] E Pearson, W Kleeven, J Van de Walle, and S Zaremba. The New IBA Superconducting Synchrocyclotron (S2C2): From Modelling to Reality. In *Eleventh International Topical Meeting or Nuclear Applications of Accelerators*, August 2013.

[147] Mike Seidel. Cyclotrons. In *Introduction to Accelerator Physics*, September 2018.

[148] J van de Walle, M Abs, M Conjat, E Forton, S Henrotin, Y Jongen, W Kleeven, J Mandrillon, P Mandrillon, and P Verbruggen. The S2C2: From source to extraction. In *Proceedings of the 21st International Conference on Cyclotrons and their Applications*, pages 285–289, 2016.

[149] S Henrotin, M Abs, E Forton, Y Jongen, W J G M Kleeven, P Verbruggen, and J van de Walle. Commissioning and testing of the first IBA S2C2. In *Proceedings of the 21st International Conference on Cyclotrons and their Applications*, pages 178–180, 2016.

[150] Arash Darafsheh, Yao Hao, Townsend Zwart, Miles Wagner, Daniel Catanzano, Jeffrey F Williamson, Nels Knutson, Baozhou Sun, Sasa Mutic, and Tianyu Zhao. Feasibility of proton flash irradiation using a synchrocyclotron for preclinical studies. *Medical physics*, 47(9):4348–4355, 2020.

[151] Michele M Kim, Arash Darafsheh, Jan Schuemann, Ivana Dokic, Olle Lundh, Tianyu Zhao, José Ramos-Méndez, Lei Dong, and Kristoffer Petersson. Development of ultra-high dose rate (flash) particle therapy. *IEEE Transactions on Radiation and Plasma Medical Sciences*, 2021.

[152] Pengyu Wang, Jinxing Zheng, and Wuquan Zhang. Research on the design of scanning magnets for proton therapy nozzle. In *2018 IEEE International Conference on Applied Superconductivity and Electromagnetic Devices (ASEMD)*, pages 1–2. IEEE, 2018.

[153] John David Jackson. *Classical Electrodynamics*. Wiley, New York, NY, 3rd edition, 1999.

[154] Sophocles J Orfanidis. *Electromagnetic waves and antennas*. Rutgers University New Brunswick, NJ, 2002.

[155] John F Schenck. The role of magnetic susceptibility in magnetic resonance imaging: Mri magnetic compatibility of the first and second kinds. *Medical physics*, 23(6):815–850, 1996.

[156] Robert B Leighton and Matthew Sands. *The Feynman lectures on physics*. Addison-Wesley Boston, MA, USA, 1965.

[157] Robert G. Brown. Lecture: Classical Electrodynamics Part II. Lecture notes of Physics 318/319 at Duke University, 2007. `https://webhome.phy.duke.edu/~rgb/Class/phy319/phy319/phy319.html`.

[158] H. Fröhlich. *Theory of dielectrics: dielectric constant and dielectric loss*. Monographs on the physics and chemistry of materials. Clarendon Press, 1958.

[159] Sami Gabriel, RW Lau, and Camelia Gabriel. The dielectric properties of biological tissues: Iii. parametric models for the dielectric spectrum of tissues. *Physics in medicine & biology*, 41(11):2271, 1996.

[160] WJ Ellison. Permittivity of pure water, at standard atmospheric pressure, over the frequency range 0–25 thz and the temperature range 0–100 c. *Journal of physical and chemical reference data*, 36(1):1–18, 2007.

[161] Yu Feldman, Yu A Gusev, and MA Vasilyeva. Dielectric relaxation phenomena in complex systems. *Tutorial, Kazan Federal University, Institute of Physics*, 2012.

[162] Camelia Gabriel, Sami Gabriel, and YE Corthout. The dielectric properties of biological tissues: I. literature survey. *Physics in medicine & biology*, 41(11):2231, 1996.

[163] Sami Gabriel, RW Lau, and Camelia Gabriel. The dielectric properties of biological tissues: Ii. measurements in the frequency range 10 hz to 20 ghz. *Physics in medicine & biology*, 41(11):2251, 1996.

[164] Charles Polk and Elliot Postow. *Handbook of Biological Effects of Electromagnetic Fields, -2 Volume Set*. CRC press, 1995.

[165] Kensuke Sasaki, Kanako Wake, and Soichi Watanabe. Development of best fit cole-cole parameters for measurement data from biological tissues and organs between 1 mhz and 20 ghz. *Radio Science*, 49(7):459–472, 2014.

[166] Sverre Holm. Time domain characterization of the cole-cole dielectric model. *Journal of electrical bioimpedance*, 11(1):101–105, 2020.

[167] Roberto Garrappa, Francesco Mainardi, and Maione Guido. Models of dielectric relaxation based on completely monotone functions. *Fractional Calculus and Applied Analysis*, 19(5):1105–1160, 2016.

[168] Roberto Garrappa and Marina Popolizio. Computing the matrix mittag-leffler function with applications to fractional calculus. *Journal of Scientific Computing*, 77(1):129–153, 2018.

[169] D.J. Griffiths. *Introduction to Electrodynamics*. Pearson Education, 2014.

[170] Eugene Hecht. *Optics*. Pearson Education India, 2012.

[171] Jaakko Malmivuo, Robert Plonsey, et al. *Bioelectromagnetism: principles and applications of bioelectric and biomagnetic fields*. Oxford University Press, USA, 1995.

[172] Chris Bishop. The relationship between loss, conductivity, and dielectric constant. *Adv. Eng. Electromagn*, 2001.

[173] Hermann A Haus and James R Melcher. *Electromagnetic fields and energy*, volume 107. Prentice Hall Englewood Cliffs, NJ, 1989.

[174] Barry Marder. A method for incorporating gauss' law into electromagnetic pic codes. *Journal of Computational Physics*, 68(1):48–55, 1987.

[175] Andreas Dedner, Friedemann Kemm, Dietmar Kröner, C-D Munz, Thomas Schnitzer, and Matthias Wesenberg. Hyperbolic divergence cleaning for the mhd equations. *Journal of Computational Physics*, 175(2):645–673, 2002.

[176] Claus-Dieter Munz, Rudolf Schneider, Eric Sonnendrücker, and Ursula Voss. Maxwell's equations when the charge conservation is not satisfied. *Comptes Rendus de l'Académie des Sciences-Series I-Mathematics*, 328(5):431–436, 1999.

[177] Martin Rädler, Chiara Gianoli, Prasannakumar Palaniappan, Katia Parodi, and Marco Riboldi. Electromagnetic signal of a proton beam in biological tissues for a potential range-verification approach in proton therapy. *Physical Review Applied*, 15(2):024066, 2021.

[178] L. Devroye. *Non-Uniform Random Variate Generation*. Springer New York, 2013. **Chapter 2**.

[179] David Tong. Lectures on Electromagnetism. University of Cambridge, 2015. `https://www.damtp.cam.ac.uk/user/tong/em.html`.

[180] Miles N Wernick and John N Aarsvold. *Emission tomography: the fundamentals of PET and SPECT*. Elsevier, 2004.

[181] Jian-Ming Jin. *Theory and computation of electromagnetic fields*. John Wiley & Sons, 2011.

[182] Anders Bondeson, Thomas Rylander, and Pär Ingelström. *Computational electromagnetics*. Springer, 2012.

[183] Q. Wang. *Practical Design of Magnetostatic Structure Using Numerical Simulation*. Wiley, 2013.

[184] Oleg D Jefimenko. Solutions of maxwell's equations for electric and magnetic fields in arbitrary media. *American journal of physics*, 60(10):899–902, 1992.

[185] Jian-Ming Jin. *The finite element method in electromagnetics*. John Wiley & Sons, 2015.

[186] A.C. Polyfcarpou. *Introduction to the Finite Element Method in Electromagnetics*. Synthesis lectures on computational electromagnetics. Morgan & Claypool Publishers, 2006.

[187] G. Meunier. *The Finite Element Method for Electromagnetic Modeling*. ISTE. Wiley, 2010.

[188] J.R. Cardoso. *Electromagnetics through the Finite Element Method: A Simplified Approach Using Maxwell's Equations*. CRC Press, 2016.

[189] M. Plonus. *Applied Electromagnetics*. McGraw-Hill electrical engineering series. McGraw-Hill, 1978.

[190] Nabeel Demerdash, T Nehl, and F Fouad. Finite element formulation and analysis of three dimensional magnetic field problems. *IEEE Transactions on Magnetics*, 16(5):1092–1094, 1980.

[191] Oszkar Biro and Kurt Preis. On the use of the magnetic vector potential in the finite-element analysis of three-dimensional eddy currents. *IEEE Transactions on magnetics*, 25(4):3145–3159, 1989.

[192] Jaewook Lee. *Structural design optimization of electric motors to improve torque performance*. PhD thesis, University of Michigan, 2010.

[193] Martin Rädler, Georgios Dedes, Katia Parodi, and Marco Riboldi. Exploring a Novel Concept for Direct Proton Beam Measurement Via Its Magnetic Field: A Simulation Study. *AAPM 61st Annual Meeting & Exhibition, San Antonio*, WE-HI-SAN2-4 (Imaging for Particle Therapy), 2019.

[194] David Meeker. *Finite Element Method Magnetics: User's Manual*. FEMM, Waltham, United States, 2018.

[195] NA Demerdash and R Wang. Theoretical and numerical difficulties in 3-d vector potential methods in finite element magnetostatic computations. *IEEE Transactions on Magnetics*, 26(5):1656–1658, 1990.

[196] JBM Melissen and J Simkin. A new coordinate transform for the finite element solution of axisymmetric problems in magnetostatics. *IEEE Transactions on Magnetics*, 26(2):391–394, 1990.

[197] B Lencova and M Lenc. Linear finite element method in axisymmetric magnetostatic problems. *IEEE transactions on magnetics*, 28(2):1107–1110, 1992.

[198] Anjam Khursheed. *The finite element method in charged particle optics*. Springer Science & Business Media, 1999.

[199] João Pedro A Bastos and Nelson Sadowski. *Electromagnetic modeling by finite element methods*. CRC press, 2003.

[200] Dries Vanoost, Herbert De Gersem, Joan Peuteman, Georges Gielen, and Davy Pissoort. 2d magnetostatic finite element simulation for devices with a radial symmetry. *IEEE Trans. Magn.*, 2013.

[201] Rachid Touzani and Jacques Rappaz. *Mathematical Models for Eddy Currents and Magnetostatics: With Selected Applications*. Scientific Computation. Springer, 2014.

[202] MVK Chari, ZJ Csendes, P Silvester, A Konrad, and MA Palmo. Three-dimensional magnetostatic field analysis of electrical machinery by the finite-element method. *IEEE Transactions on Power Apparatus and Systems*, 8:4007–4019, 1981.

[203] Cazacu Dumitru. Numerical problems in 3D magnetostatic FEM analysis. *Advances in Automatic Control, Modeling & Simulation, Recent Advances in Electrical Engineering Series*, 13:385–390, 2013.

[204] Pavel Mintchev, Marin Dimitrov, and Stoimen Balinov. Comparative analysis of nodal and edge finite element method for numerical analysis of 3-d magnetostatic systems. *3. Japanese-Bulgarian-Macedonian Joint Seminar on Applied Electromagnetics*, 2002.

[205] Thomas Martin Lehmann, Claudia Gonner, and Klaus Spitzer. Survey: Interpolation methods in medical image processing. *IEEE transactions on medical imaging*, 18(11):1049–1075, 1999.

[206] Hsieh Hou and H Andrews. Cubic splines for image interpolation and digital filtering. *IEEE Transactions on acoustics, speech, and signal processing*, 26(6):508–517, 1978.

[207] Don P Mitchell and Arun N Netravali. Reconstruction filters in computer-graphics. *ACM Siggraph Computer Graphics*, 22(4):221–228, 1988.

[208] Robert Keys. Cubic convolution interpolation for digital image processing. *IEEE transactions on acoustics, speech, and signal processing*, 29(6):1153–1160, 1981.

[209] Olek C Zienkiewicz, Robert L Taylor, and Jian Z Zhu. *The finite element method: its basis and fundamentals*. Elsevier, 2005.

[210] Prabhat Kumar. Static infinite element formulation. *Journal of structural engineering*, 111(11):2355–2372, 1985.

[211] Prabhat Kumar. Finite element method computations in unbounded domains with nonzero but uniform far field decay. *Computers & Structures*, 75(5):457–462, 2000.

[212] Euclides Mesquita and Renato Pavanello. Numerical methods for the dynamics of unbounded domains. *Computational & applied Mathematics*, 24(1):1–26, 2005.

[213] Hans Petter Langtangen and Kent-Andre Mardal. *Introduction to numerical methods for variational problems*, volume 21. Springer Nature, 2019. *Sec. 5.2.4 Symmetric modification of the linear system*.

[214] Y. Saad. *Iterative Methods for Sparse Linear Systems: Second Edition*. Other Titles in Applied Mathematics. Society for Industrial and Applied Mathematics, 2003.

[215] D.M. Young and W. Rheinboldt. *Iterative Solution of Large Linear Systems*. Computer science and applied mathematics. Elsevier Science, 2014.

[216] V.K. Rohatgi, A.K.M.E. Saleh, and ProQuest (Firm). *An Introduction to Probability Theory and Mathematical Statistics*. Wiley Series In Probability And Statistics. John Wiley & Sons, Incorporated, 2015.

[217] H Bassen and G Smith. Electric field probes–a review. *IEEE Transactions on Antennas and propagation*, 31(5):710–718, 1983.

[218] VMN Passaro, F Dell'Olio, and F De Leonardis. Electromagnetic field photonic sensors. *Progress in quantum electronics*, 30(2-3):45–73, 2006.

[219] Martin Rädler, Chiara Gianoli, and Marco Riboldi. Characterization of the electromagnetic signal generated by a proton beam in biological tissues. *IEEE Nuclear Science Symposium, Medical Imaging Conference and Room Temperature Semiconductor Detector Conferences*, M-03-256, 2020.

[220] G.B. Arfken and H.J. Weber. *Mathematical Methods For Physicists International Student Edition*. Elsevier Science, 2005.

[221] Geoffrey Grimmett and Dominic Welsh. *Probability: an introduction*. Oxford University Press, 2014.

[222] Hiroyuki Daido, Mamiko Nishiuchi, and Alexander S Pirozhkov. Review of laser-driven ion sources and their applications. *Reports on progress in physics*, 75(5):056401, 2012.

[223] S.S. Bayin. *Mathematical Methods in Science and Engineering*. Wiley, 2018.

[224] Arnold Sommerfeld. *Partial differential equations in physics*. Academic press, 1949.

[225] David Blair Melrose and Ross C McPhedran. *Electromagnetic processes in dispersive media*. Cambridge University Press, 2005. **Section 20.7**.

[226] Hiroyuki Shima and Tsuneyoshi Nakayama. *Higher mathemfatics for physics and engineering*. Springer Science & Business Media, 2010. **Chapter 13**.

[227] A. Kovetz and S.P.A.A. Kovetz. *The Principles of Electromagnetic Theory*. Cambridge University Press, 1990.

[228] Albert E Seaver. An equation for charge decay valid in both conductors and insulators. *arXiv preprint arXiv:0801.4182*, 2008.

[229] Francesco Lacava and Lacava. *Classical electrodynamics*. Springer, 2016.

[230] QZ Lv, S Norris, Q Su, and R Grobe. Self-interactions as predicted by the dirac-maxwell equations. *Physical Review A*, 90(3):034101, 2014.

[231] Lev Davidovich Landau, JS Bell, MJ Kearsley, LP Pitaevskii, EM Lifshitz, and JB Sykes. *Electrodynamics of continuous media*, volume 8. elsevier, 2013.

[232] Hemalata Singh, SK Rathi, and AS Verma. Stopping powers of protons in biological human body substances. *Universal Journal of Medical Science*, 1(2):17–22, 2013.

[233] Gregory Michalak, Vicki Taasti, Bernhard Krauss, Amanda Deisher, Ahmed Halaweish, and Cynthia McCollough. A comparison of relative proton stopping power measurements across patient size using dual-and single-energy ct. *Acta Oncologica*, 56(11):1465–1471, 2017.

[234] Dmitry Budker and Michael Romalis. Optical magnetometry. *Nature physics*, 3(4):227–234, 2007.

[235] RL Fagaly. Superconducting quantum interference device instruments and applications. *Review of scientific instruments*, 77(10):101101, 2006.

[236] R. Lanza and A. Meloni. *The Earth's Magnetism: An Introduction for Geologists*. Springer Berlin Heidelberg, 2006.

[237] Matti Hämäläinen, Riitta Hari, Risto J Ilmoniemi, Jukka Knuutila, and Olli V Lounasmaa. Magnetoencephalography—theory, instrumentation, and applications to noninvasive studies of the working human brain. *Reviews of modern Physics*, 65(2):413, 1993.

[238] GA Pablo Cirrone, Nino Amato, Roberto Catalano, Alessandro Di Domenico, Giacomo Cuttone, Pietro Lojacono, Alfio Mazzaglia, Fabrizio Pace, Giuseppe Pittà, Luigi Raffaele, et al. On the possibility to use the charge imbalance in patients undergoing radiotherapy: a new online, in vivo, noninvasive dose monitoring system. *Applied Sciences*, 11(15):7005, 2021.

[239] Y Helo, A Kacperek, I Rosenberg, G Royle, and AP Gibson. The physics of cerenkov light production during proton therapy. *Physics in Medicine & Biology*, 59(23):7107, 2014.

[240] Adam K Glaser, Rongxiao Zhang, David J Gladstone, and Brian W Pogue. Optical dosimetry of radiotherapy beams using cherenkov radiation: the relationship between light emission and dose. *Physics in Medicine & Biology*, 59(14):3789, 2014.

[241] Johan Axelsson, Scott C Davis, David J Gladstone, and Brian W Pogue. Cerenkov emission induced by external beam radiation stimulates molecular fluorescence. *Medical physics*, 38(7):4127–4132, 2011.

[242] Mitsutaka Yamaguchi, Yuto Nagao, Koki Ando, Seiichi Yamamoto, Toshiyuki Toshito, Jun Kataoka, and Naoki Kawachi. Secondary-electron-bremsstrahlung imaging for proton therapy. *Nuclear Instruments and Methods in Physics Research Section A: Accelerators, Spectrometers, Detectors and Associated Equipment*, 833:199–207, 2016.

[243] Martin Rädler, Katia Parodi, Georgios Dedes, and Marco Riboldi. Proton beam detection via the generated magnetic field – A simulation study towards a novel measurement concept. *50. Jahrestagung Deutsche Gesellschaft für Medizinische Physik*, Session 17, V 77 (Adaptive und bildgeführte Strahlentherapie), 2019.

[244] Martin Rädler, Giulia Buizza, Prasannakumar Palaniappan, Chiara Gianoli, Guido Baroni, Chiara Paganelli, Katia Parodi, and Marco Riboldi. Magnetic field of a proton pencil beam as range verification method: The impact of secondaries. *ESTRO Congress, Copenhagen*, PD-0899 (Implementation of new technology & techniques), 2022.

[245] Wiel Kleeven. Accelerators for industrial and medical applications: The Superconducting Synchrocyclotron Project S2C2 (Part IV). In *European Scientific Institute (Archamps): Joint Universities Accelerator School (JUAS)*, March 2014.

[246] Alexander Altland and Jan von Delft. *Mathematics for physicists: introductory concepts and methods*. Cambridge University Press, 2019.

[247] S. Agostinelli et al. Geant4—a simulation toolkit. *Nuclear Instruments and Methods in Physics Research Section A: Accelerators, Spectrometers, Detectors and Associated Equipment*, 506(3):250–303, 2003.

[248] J. Allison et al. Geant4 developments and applications. *IEEE Transactions on Nuclear Science*, 53(1):270–278, 2006.

[249] J. Allison et al. Recent developments in geant4. *Nuclear Instruments and Methods in Physics Research Section A: Accelerators, Spectrometers, Detectors and Associated Equipment*, 835:186–225, 2016.

[250] S Incerti et al. The Geant4-DNA project. *Int. J. Model. Simulation, Sci. Comput.*, 1(02):157–178, jun 2010.

[251] S Incerti et al. Comparison of Geant4 very low energy cross section models with experimental data in water. *Med. Phys.*, 37(9):4692–4708, aug 2010.

[252] M.A. Bernal et al. Track structure modeling in liquid water: A review of the Geant4-DNA very low energy extension of the Geant4 Monte Carlo simulation toolkit. *Phys. Medica*, 31(8):861–874, December 2015.

[253] S. Incerti et al. Geant4-DNA example applications for track structure simulations in liquid water: A report from the Geant4-DNA Project. *Med. Phys.*, 45(8):e722–e739, August 2018.

[254] Sebastien Incerti, Ioanna Kyriakou, Marie-Claude Bordage, Susanna Guatelli, V Ivanchenko, and Dimitris Emfietzoglou. Track structure simulations of proximity functions in liquid water using the geant4-dna toolkit. *Journal of Applied Physics*, 125(10):104301, 2019.

[255] Maryam Moteabbed, Torunn I Yock, Nicolas Depauw, Thomas M Madden, Hanne M Kooy, and Harald Paganetti. Impact of spot size and beam-shaping devices on the treatment plan quality for pencil beam scanning proton therapy. *International Journal of Radiation Oncology* Biology* Physics*, 95(1):190–198, 2016.

[256] Sebastien Incerti, Michael Douglass, Scott Penfold, Susanna Guatelli, and Eva Bezak. Review of geant4-dna applications for micro and nanoscale simulations. *Physica Medica*, 32(10):1187–1200, 2016.

[257] Catherine Thérèse Quiñones. *Proton computed tomography*. PhD thesis, Université de Lyon, 2016.

[258] Michele Pizzochero, Francesco Ambrosio, and Alfredo Pasquarello. Picture of the wet electron: a localized transient state in liquid water. *Chemical science*, 10(31):7442–7448, 2019.

[259] D. Budker and D.F.J. Kimball. *Optical Magnetometry*. Optical Magnetometry. Cambridge University Press, 2013.

[260] M Auzinsh, Dmitry Budker, DF Kimball, SM Rochester, JE Stalnaker, AO Sushkov, and VV Yashchuk. Can a quantum nondemolition measurement improve the sensitivity of an atomic magnetometer? *Physical review letters*, 93(17):173002, 2004.

[261] D Drung, C Abmann, J Beyer, A Kirste, M Peters, F Ruede, and Th Schurig. Highly sensitive and easy-to-use squid sensors. *IEEE Transactions on Applied Superconductivity*, 17(2):699–704, 2007.

[262] Nicolas Coquelet, Xavier De Tiège, Florian Destoky, Liliia Roshchupkina, Mathieu Bourguignon, Serge Goldman, Philippe Peigneux, and Vincent Wens. Comparing meg and high-density eeg for intrinsic functional connectivity mapping. *NeuroImage*, 210:116556, 2020.

[263] Joonas Iivanainen, Matti Stenroos, and Lauri Parkkonen. Measuring meg closer to the brain: Performance of on-scalp sensor arrays. *NeuroImage*, 147:542–553, 2017.

[264] Ryan M Hill, Elena Boto, Molly Rea, Niall Holmes, James Leggett, Laurence A Coles, Manolis Papastavrou, Sarah K Everton, Benjamin AE Hunt, Dominic Sims, et al. Multi-channel whole-head opm-meg: Helmet design and a comparison with a conventional system. *NeuroImage*, 219:116995, 2020.

[265] Sebastian Gantz, Volker Hietschold, and Aswin Louis Hoffmann. Characterization of magnetic interference and image artefacts during simultaneous in-beam mr imaging and proton pencil beam scanning. *Physics in Medicine & Biology*, 65(21):215014, 2020.

[266] K. Paul et al. Towards MR-guided particle radiotherapy: Compatibility of an open MR scanner with an ion beamline. In *ESTRO*, May 2022.

[267] Igor M Savukov, SJ Seltzer, MV Romalis, and KL Sauer. Tunable atomic magnetometer for detection of radio-frequency magnetic fields. *Physical review letters*, 95(6):063004, 2005.

[268] Martin Rädler, Lukas Schmidt, and Marco Riboldi. Magnetic field originating from a modulated proton beam as a range verification approach: Investigating boundary effects. *IEEE Nuclear Science Symposium, Medical Imaging Conference and Room Temperature Semiconductor Detector Conferences*, MIC-17-438, 2022.

[269] A Nisbet. Electromagnetic potentials in a heterogeneous non-conducting medium. *Proceedings of the Royal Society of London. Series A. Mathematical and Physical Sciences*, 240(1222):375–381, 1957.

[270] Weng Cho Chew. Vector potential electromagnetics with generalized gauge for inhomogeneous media: Formulation. *Progress In Electromagnetics Research*, 149:69–84, 2014.

[271] D.G. Duffy. *Green's Functions with Applications*. Advances in Applied Mathematics. CRC Press, 2015.

[272] U.D. Jentschura. *Advanced Classical Electrodynamics: Green Functions, Regularizations, Multipole Decompositions*. World Scientific Publishing Company, 2017.

[273] C.M. Bender and S.A. Orszag. *Advanced Mathematical Methods for Scientists and Engineers*. Advanced Book Program - McGraw-Hill Book Company. McGraw-Hill, 1978.

[274] P.K. Kythe. *Green's Functions and Linear Differential Equations: Theory, Applications, and Computation*. Chapman & Hall/CRC Applied Mathematics & Nonlinear Science. CRC Press, 2011.

[275] L.M. Jones. *An Introduction to Mathematical Methods of Physics*. Benjamin/Cummings Publishing Company, 1979.

[276] Kim Milton. Lecture: Mathematical Methods of Physics. Lecture notes of Physics 5013 at the University of Oklahoma, Fall 2011. `https://www.nhn.ou.edu/~milton/p5013-11`.

[277] J. Mathews, R.L. Walker, and W.R. L. *Mathematical Methods of Physics*. Addison-Wesley world student series. W. A. Benjamin, 1970.

[278] P.M.C. Morse and H. Feshbach. *Methods of Theoretical Physics*. International series in pure and applied physics. McGraw-Hill, 1953.

[279] Paul G.S. Stäckel. *Integration of Hamiltonian-Jacobian differential equations by means of separation of variables*. Habilitation, Martin-Luther-University Halle-Wittenberg, 1891.

[280] Luther Pfahler Eisenhart. Separable systems of Stäckel. *Annals of Mathematics*, pages 284–305, 1934.

[281] Eric W. Weisstein. Stäckel Determinant. MathWorld–A Wolfram Web Resource: `https://mathworld.wolfram.com/StaeckelDeterminant.html`. Accessed: Febuary 3rd 2022.

[282] Domina Eberle Spencer. Separation of variables in electromagnetic theory. *Journal of Applied Physics*, 22(4):386–389, 1951.

[283] Parry Moon and Domina Eberle Spencer. Separability conditions for the laplace and helmholtz equations. *Journal of the Franklin Institute*, 253(6):585–600, 1952.

[284] Parry Moon and Domina Eberle Spencer. The meaning of the vector laplacian. *Journal of the Franklin Institute*, 256(6):551–558, 1953.

[285] P.H. Moon and D.E. Spencer. *Field Theory Handbook: Including Coordinate Systems, Differential Equations and Their Solutions*. Springer-Verlag, 1971.

[286] Gerrit van Tilburg. *Separability and Applications of the Helmholtz Equation*. Bachelor thesis, University of Groningen, 2018.

[287] Eric W. Weisstein. Helmholtz Differential Equation–Circular Cylindrical Coordinates. MathWorld–A Wolfram Web Resource: `https://mathworld.wolfram.com/HelmholtzDifferentialEquationCircularCylindricalCoordinates.html`. Accessed: Febuary 3rd 2022.

[288] Jim Lambers. Lecture: Differential Equations and Special Functions. Lecture notes of Mathematics 415/515 at the University of Southern Mississippi, Fall 2013. https://www.math.usm.edu/lambers/mat415/.

[289] Richard Courant and David Hilbert. *Methods of mathematical physics: partial differential equations*. John Wiley & Sons, 2008.

[290] G Gulyamov, AG Gulyamov, AB Davlatov, and Kh N Juraev. Energy levels in nanowires and nanorods with a finite potential well. *Advances in Condensed Matter Physics*, 2020, 2020.

[291] Ed Hungerford. Lecture: Introduction to Classical Electrodynamics. Lecture notes of Physics 4322 at the University of Huston, Spring 2018. http://nsmn1.uh.edu/hunger/class/fall_2011/lectures/lecture_7.pdf.

[292] X Leyronas and M Combescot. Quantum wells, wires and dots with finite barrier: Analytical expressions for the bound states. *Solid state communications*, 119(10-11):631–635, 2001.

[293] Wolfram Research, Inc. Mathematica, Version 12.1.1.0. Champaign, IL, 2020.

[294] George W Hanson and Alexander B Yakovlev. *Operator theory for electromagnetics: an introduction*. Springer Science & Business Media, 2013.

[295] T.M. Apostol. *Calculus: One-variable calculus, with an introduction to linear algebra*. Calculus. Wiley, 1967.

[296] Eric W. Weisstein. Harmonic Addition Theorem. MathWorld–A Wolfram Web Resource: https://mathworld.wolfram.com/HarmonicAdditionTheorem.html. Accessed: March 11th 2022.

[297] G.N. Watson. *A Treatise on the Theory of Bessel Functions*. Cambridge Mathematical Library. Cambridge University Press, 1995.

[298] A. Poularikas. *The Transforms and Applications Handbook*. Electrical Engineering Handbook. CRC-Press, 2000.

[299] Alfio Quarteroni, Riccardo Sacco, and Fausto Saleri. *Numerical mathematics*, volume 37. Springer Science & Business Media, 2010.

[300] The SciPy community. Exponentially scaled Hankel function of the first kind. https://docs.scipy.org/doc/scipy/reference/generated/scipy.special.hankel1e.html. Accessed: June 2nd 2022.

[301] Naomichi Hatano and Gonzalo Ordonez. Time-reversal symmetric resolution of unity without background integrals in open quantum systems. *Journal of Mathematical Physics*, 55(12):122106, 2014.

[302] AJ Lomax, T Boehringer, A Coray, E Egger, G Goitein, M Grossmann, P Juelke, S Lin, E Pedroni, B Rohrer, et al. Intensity modulated proton therapy: a clinical example. *Medical Physics*, 28(3):317–324, 2001.

[303] Shinian Fu and Takao Kato. Rf-chopper for the jhf proton linac. *Nuclear Instruments and Methods in Physics Research Section A: Accelerators, Spectrometers, Detectors and Associated Equipment*, 440(2):296–306, 2000.

[304] Friedhelm Caspers. Review of fast beam chopping. Technical report, CERN, 2004.

[305] Jinfeng Tian. Electromagnetic waves and fields in the human body in mri. *Theory and Applications of Heat Transfer in Humans*, 1:183–201, 2018.

[306] François Couëdo, Eliana Recoba Pawlowski, Julien Kermorvant, Juan Trastoy, Denis Crété, Yves Lemaître, Bruno Marcilhac, Christian Ulysse, Cheryl Feuillet-Palma, Nicolas Bergeal, et al. High-Tc superconducting detector for highly-sensitive microwave magnetometry. *Applied Physics Letters*, 114(19):192602, 2019.

[307] B MURAT EYÜPOĞLU, Ravinder Reddy, and John S Leigh. Imaging electrical current density using nuclear magnetic resonance. *Turkish Journal of Electrical Engineering and Computer Sciences*, 6(3):201–214, 1998.

[308] P Hömmen, J-H Storm, N Höfner, and R Körber. Demonstration of full tensor current density imaging using ultra-low field mri. *Magnetic resonance imaging*, 60:137–144, 2019.

[309] J Bodurka, A Jesmanowicz, JS Hyde, H Xu, L Estkowski, and SJ Li. Current-induced magnetic resonance phase imaging. *Journal of magnetic resonance (San Diego, Calif.: 1997)*, 137(1):265–271, 1999.

[310] Jerzy Bodurka and Peter A Bandettini. Toward direct mapping of neuronal activity: Mri detection of ultraweak, transient magnetic field changes. *Magnetic Resonance in Medicine: An Official Journal of the International Society for Magnetic Resonance in Medicine*, 47(6):1052–1058, 2002.

[311] Daniel Konn, Penny Gowland, and Richard Bowtell. Mri detection of weak magnetic fields due to an extended current dipole in a conducting sphere: a model for direct detection of neuronal currents in the brain. *Magnetic Resonance in Medicine: An Official Journal of the International Society for Magnetic Resonance in Medicine*, 50(1):40–49, 2003.

[312] PA Bandettini, N Petridou, and J Bodurka. Direct detection of neuronal activity with mri: fantasy, possibility, or reality? *Applied Magnetic Resonance*, 29(1):65–88, 2005.

[313] Antonino Mario Cassará, Bruno Maraviglia, Stefan Hartwig, Lutz Trahms, and Martin Burghoff. Neuronal current detection with low-field magnetic resonance: simulations and methods. *Magnetic resonance imaging*, 27(8):1131–1139, 2009.

[314] Martin Burghoff, Hans-Helge Albrecht, Stefan Hartwig, Ingo Hilschenz, Rainer Körber, Nora Höfner, Hans-Jürgen Scheer, Jens Voigt, Lutz Trahms, and Gabriel Curio. On the feasibility of neurocurrent imaging by low-field nuclear magnetic resonance. *Applied Physics Letters*, 96(23):233701, 2010.

[315] Rainer Körber, Jaakko O Nieminen, Nora Höfner, Vojko Jazbinšek, Hans-Jürgen Scheer, Kiwoong Kim, and Martin Burghoff. An advanced phantom study assessing the feasibility of neuronal current imaging by ultra-low-field nmr. *Journal of Magnetic Resonance*, 237:182–190, 2013.

[316] Sonja M Schellhammer, Aswin L Hoffmann, Sebastian Gantz, Julien Smeets, Erik Van Der Kraaij, Sébastien Quets, Stefan Pieck, Leonhard Karsch, and Jörg Pawelke. Integrating a low-field open mr scanner with a static proton research beam line: proof of concept. *Physics in Medicine & Biology*, 63(23):23LT01, 2018.

[317] Sonja Schellhammer. *Technical Feasibility of MR-Integrated Proton Therapy: Beam Deflection and Image Quality*. PhD thesis, Dissertation, Dresden, Technische Universität Dresden, 2019, 2019.

[318] S Schellhammer, S Gantz, L Karsch, Erik van der Kraaij, J Smeets, A Serra, J Pawelke, and A Hoffmann. On-line MRI-based proton beam range verification: First experimental proof-of-concept. *ESTRO Online Congress*, Award Lecture: Donal Hollywood Award, 2020.

[319] Xiaotong Zhang, Jiaen Liu, and Bin He. Magnetic-resonance-based electrical properties tomography: a review. *IEEE reviews in biomedical engineering*, 7:87–96, 2014.

[320] Chun Wa Wong. Maxwell equations and the redundant gauge degree of freedom. *European journal of physics*, 30(6):1401, 2009.

[321] W.C. Chew. Lecture: Electromagnetic Field Theory. Purdue University, Fall 2019. `https://engineering.purdue.edu/wcchew/ece604f19/Lecture%20Notes/Lect35.pdf`.

[322] P. Blanchard and E. Brüning. *Mathematical Methods in Physics: Distributions, Hilbert Space Operators, and Variational Methods*. Progress in Mathematical Physics. Birkhäuser, 2003. *Example 3.3.1 - 4*.

[323] Eric W. Weisstein. Complete Elliptic Integral of the First Kind, n.d. MathWorld–A Wolfram Web Resource.

[324] Eric W. Weisstein. Complete Elliptic Integral of the Second Kind, n.d. MathWorld–A Wolfram Web Resource.

[325] Izrail Solomonovich Gradshteyn and Iosif Moiseevich Ryzhik. *Table of integrals, series, and products*. Academic press, 2014.

[326] Diogo Oliveira e Silva and Christoph Thiele. Estimates for certain integrals of products of six bessel functions. *Revista Matemática Iberoamericana*, 33(4):1423–1462, 2017.

[327] W.C. Chew. *Waves and Fields in Inhomogeneous Media*. Electromagnetic waves. IEEE Press, 1995.

[328] J.A. Kong. *Electromagnetic Wave Theory*. A Wiley Interscience publication. Wiley, 1990.

[329] G. Tyras, H.G. Booker, and N. Declaris. *Radiation and Propagation of Electromagnetic Waves*. Elsevier Science, 2013.